

Special Issue Reprint

Mathematical Modelling and Numerical Analysis in Electrical Engineering, 2nd Edition

Edited by
Udochukwu B. Akuru, Ogbonnaya I. Okoro and Yacine Amara

mdpi.com/journal/mathematics

Mathematical Modelling and Numerical Analysis in Electrical Engineering, 2nd Edition

Mathematical Modelling and Numerical Analysis in Electrical Engineering, 2nd Edition

Guest Editors

Udochukwu B. Akuru

Ogbonnaya I. Okoro

Yacine Amara



Basel • Beijing • Wuhan • Barcelona • Belgrade • Novi Sad • Cluj • Manchester

Guest Editors

Udochukwu B. Akuru
Department of Electrical
Engineering
Tshwane University of
Technology
Pretoria
South Africa

Ogbonnaya I. Okoro
Department of Electrical and
Electronic Engineering
Michael Okpara University of
Agriculture
Umudike
Nigeria

Yacine Amara
GREAH
Université Le Havre
Normandie
Le Havre
France

Editorial Office

MDPI AG
Grosspeteranlage 5
4052 Basel, Switzerland

This is a reprint of the Special Issue, published open access by the journal *Mathematics* (ISSN 2227-7390), freely accessible at: https://www.mdpi.com/si/mathematics/Math_Model_Numer_Anal_Electr_Eng_2nd.

For citation purposes, cite each article independently as indicated on the article page online and as indicated below:

Lastname, A.A.; Lastname, B.B. Article Title. <i>Journal Name</i> Year , Volume Number, Page Range.
--

ISBN 978-3-7258-4683-2 (Hbk)

ISBN 978-3-7258-4684-9 (PDF)

<https://doi.org/10.3390/books978-3-7258-4684-9>

© 2025 by the authors. Articles in this book are Open Access and distributed under the Creative Commons Attribution (CC BY) license. The book as a whole is distributed by MDPI under the terms and conditions of the Creative Commons Attribution-NonCommercial-NoDerivs (CC BY-NC-ND) license (<https://creativecommons.org/licenses/by-nc-nd/4.0/>).

Contents

About the Editors	vii
-----------------------------	-----

Ermin Rahmanović and Martin Petrun

Analysis of Higher-Order Bézier Curves for Approximation of the Static Magnetic Properties of NO Electrical Steels

Reprinted from: *Mathematics* **2024**, 12, 445, <https://doi.org/10.3390/math12030445> 1

Mitja Garmut, Simon Steentjes and Martin Petrun

Optimization of an IPMSM for Constant-Angle Square-Wave Control of a BLDC Drive

Reprinted from: *Mathematics* **2024**, 12, 1418, <https://doi.org/10.3390/math12101418> 24

Carlos R. Baier, Pedro E. Melin, Miguel A. Torres, Roberto O. Ramirez, Carlos Muñoz and Agustín Quinteros

Developing and Evaluating the Operating Region of a Grid-Connected Current Source Inverter from Its Mathematical Model

Reprinted from: *Mathematics* **2024**, 12, 1775, <https://doi.org/10.3390/math12121775> 49

Robert Brezovnik and Jožef Ritonja

Derivation of Analytical Expressions for Fast Calculation of Resistance Spot Welding System Currents

Reprinted from: *Mathematics* **2024**, 12, 2454, <https://doi.org/10.3390/math12162454> 71

Manh-Dung Nguyen, Woo-Sung Jung, Duy-Tinh Hoang, Yong-Joo Kim, Kyung-Hun Shin and Jang-Young Choi

Fast Analysis and Optimization of a Magnetic Gear Based on Subdomain Modeling

Reprinted from: *Mathematics* **2024**, 12, 2922, <https://doi.org/10.3390/math12182922> 96

Manh-Dung Nguyen, Tae-Seong Kim, Kyung-Hun Shin, Gang-Hyeon Jang and Jang-Young Choi

Fast Prediction of Characteristics in Wound Rotor Synchronous Condenser Using Subdomain Modeling

Reprinted from: *Mathematics* **2024**, 12, 3526, <https://doi.org/10.3390/math12223526> 114

Anthony O. Onokwai, Udochukwu B. Akuru and Dawood A. Desai

Mathematical Modelling and Optimisation of Operating Parameters for Enhanced Energy Generation in Gas Turbine Power Plant with Intercooler

Reprinted from: *Mathematics* **2025**, 13, 174, <https://doi.org/10.3390/math13010174> 127

Duy-Tinh Hoang, Manh-Dung Nguyen, Yong-Joo Kim, Anh-Tuan Phung, Kyung-Hun Shin and Jang-Young Choi

Improved Design of an Eddy-Current Speed Sensor Based on Harmonic Modeling Technique

Reprinted from: *Mathematics* **2025**, 13, 844, <https://doi.org/10.3390/math13050844> 165

Duy-Tinh Hoang, Joon-Ku Lee, Kwang-Il Jeong, Kyung-Hun Shin and Jang-Young Choi

A Rotational Speed Sensor Based on Flux-Switching Principle

Reprinted from: *Mathematics* **2025**, 13, 1341, <https://doi.org/10.3390/math13081341> 183

Kyung-Soo Cha, Jae-Hyun Kim, Soo-Gyung Lee and Min-Ro Park

Design of a High-Efficiency External Rotor Interior Permanent Magnet Synchronous Motor Without Magnetic Leakage Flux Path

Reprinted from: *Mathematics* **2025**, 13, 1865, <https://doi.org/10.3390/math13111865> 203

About the Editors

Udochukwu B. Akuru

Udochukwu B. Akuru holds B.Eng. and M.Eng. degrees from the University of Nigeria, Nsukka (2008 and 2013), and a Ph.D. in Electrical Engineering from Stellenbosch University, South Africa (2017). He completed a Postdoctoral Fellowship at Stellenbosch University (2018–2019) and lectured at the University of Nigeria from 2011 to 2019. Currently, he is a Senior Lecturer in the Department of Electrical Engineering at the Tshwane University of Technology. His core research interests lie in the design and optimisation of electrical machines for renewable energy applications. Dr. Akuru has published extensively and reviews for numerous journals and conferences. He served as General Chair of SAUPEC 2025 and is a Registered Engineer with COREN, a Senior Member of both the IEEE and SAIEE, and a NRF South Africa C1-rated researcher. He has received several grants and awards, including the 2020 TWAS-DFG Fellowship and the UKRI Ayrton consortium grant on circular microgrids, where he leads CEPREC at TUT. He has collaborated with *Mathematica*, *GET/DAAD*, *UNIDO* and others, and serves as Track Chair at *IEEE ECCE*, Guest Editor for *MDPI Mathematics*, and Associate Editor for *IEEE Transactions on Industry Applications* and *IET Electric Power Applications*. He is currently Chairperson of *IEEE South Africa Section*.

Ogbonnaya I. Okoro

Ogbonnaya I. Okoro received his B.Eng. and M.Eng. degrees in Electrical Engineering from the University of Nigeria, Nsukka, in 1991 and 1997, respectively, and earned his Ph.D. in Electrical Machines from the University of Kassel, Germany, through the DAAD scholarship programme. He is a Professor of Electrical Power and Machines, a registered engineer with COREN, and a Senior Member of the IEEE. Prof. Okoro has held several academic leadership roles, including former Dean of the College of Engineering and Engineering Technology and former Head of the Department of Electrical/Electronic Engineering at Michael Okpara University of Agriculture, Umudike, Nigeria, where he currently serves as Dean of the Postgraduate School. His research interests include the dynamic simulation and control of induction machines, and the thermal and dynamic analysis of AC machines. He has published widely in reputable international journals and is the author of two engineering textbooks published by *JUTA*, South Africa: *Concise Higher Electrical Engineering* and *The Essential Matlab/Simulink for Engineers and Scientists*. He serves as a Guest Editor for the Special Issue on “Mathematical Modelling and Numerical Analysis in Electrical Engineering” by *MDPI Mathematics* journal and is also an Editorial Board Member of the *Nigerian Journal of Technology*.

Yacine Amara

Yacine Amara graduated as an Electrical Engineer from the École Nationale Polytechnique of Algiers (Algeria) in 1997. He began his doctoral studies in 1998 at the SATIE Laboratory, focusing on hybrid excited synchronous machines, and earned his Ph.D. in Applied Physics from Université de Paris-Sud in December 2001. Following a short-term lectureship at the same university, he undertook a postdoctoral position at SATIE on the Power Optimized Aircraft European Project. In 2003, he joined the Electrical Machines & Drives (EMD) group at the University of Sheffield (UK) as a research associate, working on the Free Piston Energy Converter Project. He later became a lecturer at Université de Technologie de Belfort-Montbéliard, conducting research at the L2ES laboratory. Since 2008, he has been with the Université du Havre, where he teaches electrical engineering and conducts research at the GREAH laboratory. He was promoted to Professor of Electrical Engineering

in September 2017. Prof. Amara's research focuses on the modelling, analysis and design of electrical machines and actuators, with significant contributions to the development and control of radial field hybrid excited synchronous machines. He has published extensively in these areas and is recognised for his work in advanced machine design.

Article

Analysis of Higher-Order Bézier Curves for Approximation of the Static Magnetic Properties of NO Electrical Steels

Ermin Rahmanović * and Martin Petrun

Institute of Electrical Power Engineering, UM FERI, Koroška cesta 46, 2000 Maribor, Slovenia;
martin.petrun@um.si

* Correspondence: ermin.rahmanovic@um.si

Abstract: Adequate mathematical description of magnetization curves is indispensable in engineering. The accuracy of the description has a significant impact on the design of electric machines and devices. The aim of this paper was to analyze the capability of Bézier curves systematically, to describe the nonlinear static magnetic properties of non-oriented electrical steels, and to compare this approach versus the established mathematical descriptions. First, analytic functions versus measurements were analyzed. The Bézier curves were then compared systematically with the most adequate analytic functions. Next, the most suitable orders of Bézier curves were determined for the approximation of nonlinear magnetic properties, where the influence of the range of the input measurement dataset on the approximation process was analyzed. Last, the extrapolation capabilities of the Bézier curves and analytic functions were evaluated. The general conclusion is that Bézier curves have adequate flexibility and significant potential for the approximation and extrapolation of nonlinear properties of non-oriented electrical steels.

Keywords: analytical modeling; anhysteretic curve; applied mathematics; Bézier curve; curve fitting; first magnetization curve; major loop; mathematical modeling; non-oriented electrical steel

MSC: 65D10

1. Introduction

The magnetic properties of soft magnetic materials are highly nonlinear and reflect intricate underlying phenomena in hysteresis behavior. In engineering applications, these properties are often described using basic magnetization curves, e.g., the anhysteretic curve, the first magnetization curve, the major loop, and the minor loops. For example, the major loop represents the input data of several well-known hysteresis models [1–3]. Examples of using the anhysteretic curve as input data are the widespread Jiles–Atherton hysteresis model and its variations [4,5] and various finite element simulation tools. Hysteresis models are used to describe nonlinear magnetization and power loss in iron cores, whereas the nonlinear behavior is indispensable in the design of electromagnetic machines and devices [6,7]. For these reasons, it is important to find adequate methods or analytic functions to describe such nonlinear curves with high accuracy and with low computational power.

Researchers have applied various approaches to model all the discussed magnetization curves. On the one hand, researchers try to establish adequate links between the physical parameters of materials and various mathematical descriptions, which would result in adequate physics-based material models [4]. This is a very complex task, and essential for understanding the intricate phenomena within soft magnetic materials, and, consequently, for their design and optimization processes. The complexity arises from the fact that hysteresis is a macroscopic property that emerges from the collective behavior of microscopic entities, and this behavior can be influenced by a multitude of factors [8]. On

the other hand, researchers also try to model nonlinear magnetization in a more practical way to predict the magnetization behavior, which is based on measured datasets. These models are phenomenological, i.e., they simply attempt to describe nonlinear relationships with the assumption that the modeled relationships extend past the measured values without a deep understanding of the underlying mechanisms [9–12]. These models are equally as important as the physical ones, and are essential in applied engineering, where the existing soft magnetic materials are applied in electromagnetic devices and machines. The most important requirements are accuracy and computational simplicity. A common and straightforward method is to use mathematical functions [2,10,13] or curves [14] that approximate the data obtained from measurements. This method has its difficulties, as it needs costly and specific instruments for measurement, and the data obtained may be limited in both amount (i.e., volume) and quality. To measure the magnetization curves, the measurement equipment can reach different levels of saturation, depending on its capability. The equipment also has different degrees of accuracy that affect the noise and errors in the obtained curves. The quality of the approximations depends on several factors: the size and noise level of the input dataset, the properties of the functions used, and the type of the fitting method. For example, an analysis based on the application of sigmoid functions is described in [15]. The authors investigated the relevant sigmoid functions and used them to construct the major hysteresis loop. Recently, the sigmoid functions from [15] were modified and fitted using different optimization algorithms to match measured data [10]. The modified analytic functions offered more degrees of freedom during the fitting process. In this paper, we examined different methods for estimating and extending the data obtained from measurements.

An approach used in many fields for the description of a wide range of different shapes and curves is (classical) Bézier curves. Bézier curves enable the construction of free-form curves and surfaces. The shape of a Bézier curve depends on the placement of the so-called control points. This feature makes them intuitive, easy to implement, and flexible. It is possible to construct very complex shapes only by placing control points in adequate positions. Bézier curves were first used for the shape optimization of automobile bodies [16]. Nowadays, these curves are used widely in computer graphics and animation. Examples of using them in computer graphics are font generation (Chinese [16] and Arabic [17]), image processing, and path design in various animations. However, they are not limited to the field of computer graphics. Due to their simplicity and continuous curvature, Bézier curves are being used in path planning for ground vehicles [18–20] and for unmanned aerial vehicles [21]. Their free-form ability made them popular in the field of shape design. An example of shape optimization with Bézier curves is the modeling of laminated plates of variable stiffness [22]. To expand their usability in shape optimization, Bézier curves are used to construct circular arcs in CAD applications (e.g., SolidWorks) [23] using mainly cubic Bézier curves [22]. The free-form ability to represent various shapes and geometries enhanced and is useful in the field of additive manufacturing, e.g., for the topology optimization of electrical machines [24,25]. Their ability to fit any dataset smoothly also makes them useful in the field of electrical engineering. The applications include the modeling of the flux linkage characteristics of a switched reluctance motor [26] and the modeling of PV module characteristics [27,28].

Classical Bézier curves are often used for simple smooth curve approximations. The number of control points defines the order of the corresponding Bézier curve. The order can be set to any arbitrary number for more flexibility, but it will increase the complexity due to an increasing number of control points [22]. Furthermore, Bézier curves constructed by a large number of control points are numerically unstable [19], and the calculation is slower since additional coordinates have to be calculated. For this reason, an alternative approach is to join low-order Bézier curves together in a smooth way to form a composite curve. This concept is called piecewise Bézier curves, and it builds a curve as a union of Bézier curves connected end to end [29]. Using this concept, even more complex shapes can be described by joining a larger number of lower orders of Bézier curves. A few rules

must be followed to obtain a smooth curve when joining Bézier curves, e.g., the so-called parametric continuity rules [22,30]. Bézier curves are also used for spline interpolations, especially in the known B-spline group. Any piecewise Bézier curves with arbitrary order can be converted into a B-spline, and any B-spline can be converted into one or more Bézier curves [29]. The B-spline curve has one main disadvantage compared with piecewise Bézier curves. The B-spline concept requires more computation, and the mathematics used to describe them are more complicated [29].

Based on the discussed flexibility that Bézier curves offer, especially the smooth fitting of datasets, we performed an analysis of the Bézier curve fitting process on various fundamental magnetization curves of non-oriented (NO) electrical steels (i.e., the anhysteretic curve, the major loop, and the first magnetization curve). This work is an extension of the preliminary study [31], and the aim was to investigate the approximation capabilities of classical Bézier curves systematically. We limited this study to classical Bézier curves because of their straightforward approximation of datasets without the need to implement additional rules, e.g., the continuity rules [22,30]. To demonstrate their ability to approximate magnetization curves, we identified established analytic functions [10,15] in parallel and performed a systematic comparison based on the deviation from the measured curves. We analyzed the deviation from the measured data in different regions of individual curves, e.g., the high-permeability region and the region of high saturation. This analysis resulted in the identification of the most suitable orders of classical Bézier curves and the most adequate analytic functions for different input datasets. The high-saturation region is, in most cases, very challenging to evaluate experimentally; therefore, we further analyzed the extrapolation capabilities of the identified Bézier curves and analytic functions. The main challenge during the curve-fitting process was to find the position of the control points, which determine the shape and curvature of the curve [18]. The main goal was to find a precise and elegant way to represent the observed data mathematically beyond the range of observation and to examine how the size of the input data sets affected the results.

The article is split into six sections. Section 2 presents the considered analytic functions, as well as the description of the theoretical background and properties of the Bézier curves. Two methods are presented for calculating the Bézier curves. The materials and the methodology used are presented in Section 3. Section 4 contains the obtained results. The influence of the order of Bézier curves on the approximation of the measured data is analyzed. Additionally, the extrapolation capabilities of Bézier curves of selected orders and analytic functions are analyzed. In Section 5, a discussion is provided. Finally, in Section 6, the concluding remarks are presented with a description of future work.

2. Mathematical Descriptions of Nonlinear Magnetic Properties

Mathematical functions, which are adequate for the description of the nonlinear curves in hysteresis, must have specific properties. They must be continuous, differentiable, single valued, and monotone; have odd symmetry; approach saturation polarization J_s , as magnetic field strength H tends toward negative or positive infinity (e.g., in ideal cases they have asymptotes); and must have a knee point where the second derivative reaches its minimal value [4].

Natural candidates that have those properties are the so-called sigmoid functions. The aim of this work is to introduce and analyze a novel concept for the approximation of nonlinear magnetic properties that is based on curves instead of functions, where classical Bézier curves of different orders are considered.

2.1. Analytic Functions

Analytic functions that describe a curve shaped in the form of the letter “S” are called sigmoid functions. Besides their shape, sigmoid functions have further important properties. Sigmoid functions are real valued, differentiable, and have a pair of horizontal asymptotes [15]. Due to their intrinsic properties, sigmoid functions are suitable candidates to describe nonlinear magnetic properties. The described favorable basic properties are

the reason for the frequent use of sigmoid functions in the description of the discussed magnetization curves [4]. The most adequate (and, for the discussed purpose, applied) sigmoid functions [10,15] are presented in Table 1 with Functions (1)–(5). In addition, many functions exist that have a similar shape to sigmoid functions but do not have all their properties, e.g., do not have horizontal asymptotes. Such functions are still applicable to the discussed problem and are widely used in applied engineering. During the preliminary analysis [31], we determined that the inverse hyperbolic sine function is promising, especially in the saturation region, because of its logarithmic character for higher input values. Therefore, the inverse hyperbolic sine of Function (6) was included in the presented analysis.

Table 1. Mathematical equations of selected analytic functions.

Analytic Function	Equation	
Logistic	$\frac{2a}{d+e^{-bx-c}} - a$	(1)
Hyperbolic tangent	$a \cdot \tanh(b \cdot (x + c))$	(2)
Elliot	$\frac{a \cdot (x+c)}{d+b \cdot x+c }$	(3)
Gompertz	$2a \cdot e^{-e^{-bx-c}} - a$	(4)
Langevin	$a \cdot \left(\coth\left(\frac{x+c}{b}\right) - \frac{b}{x+c} \right)$	(5)
Inverse hyperbolic sine	$a \cdot \operatorname{asinh}(b \cdot (x + c))$	(6)

Original analytic functions were modified with additional parameters to enable better agreement with the measured data during the approximation process. Functions (1)–(6) all have parameters:

- a —determines the value of the asymptote;
- b —controls the slope of the curve;
- c —enables the shifting of the function along the x -axis in an xy -coordinate system [15].

Functions (1) and (3) have a fourth parameter d , which also influences the slope [15].

Functions (1)–(4) are analytic functions without any physical background. In contrast to this, the Langevin function (Function (5)) has a physical origin. The Langevin function is a special case of the quantum mechanical Brillouin function when the function is limited to infinity [32]. The function was originally derived for paramagnets. Because of its physical foundation, it is used in many models to describe the magnetization curves, e.g., in the Jiles–Atherton hysteresis model [5]. Further, in applied engineering, the so-called Frölich–Kennelly approximation is often used for the description of nonlinear properties, especially for extrapolation purposes [6,33]. The Frölich–Kennelly equation has an equivalent mathematical description in the Elliot function (Function (3)). Therefore, all results obtained for the Elliot function also apply for the Frölich–Kennelly description.

In addition, we analyzed the inverse hyperbolic sine function (Function (6)). Generally, the inverse hyperbolic sine function has all the properties needed for adequate approximation of nonlinear magnetic properties. The difference compared with sigmoid functions (Functions (1)–(5)) is that the inverse hyperbolic sine function does not have asymptotes. However, the function value of the inverse hyperbolic sine function increases almost linearly (with a small slope), as the input x values increase at very high values. For that reason, parameter a has a scaling role for the inverse hyperbolic sine function.

Figure 1 presents a graphical comparison of the functions from Table 1. The parameters were set to $a = 1$, $b = 1$, $c = 0$, and $d = 1$ for the sigmoid functions. Such a choice ensured that Functions (1)–(5) approached horizontal asymptotes at -1 and 1 , as the x -value tended to negative and positive infinities, respectively. For the sake of graphic comparison, the parameters of the inverse hyperbolic sine function were set to $a = 1/\operatorname{asinh}(5)$, $b = 1$, and $c = 0$ to ensure that the first and last point of the function reached values of -1 and 1 in the presented interval $x \in [-5, 5]$ in Figure 1.

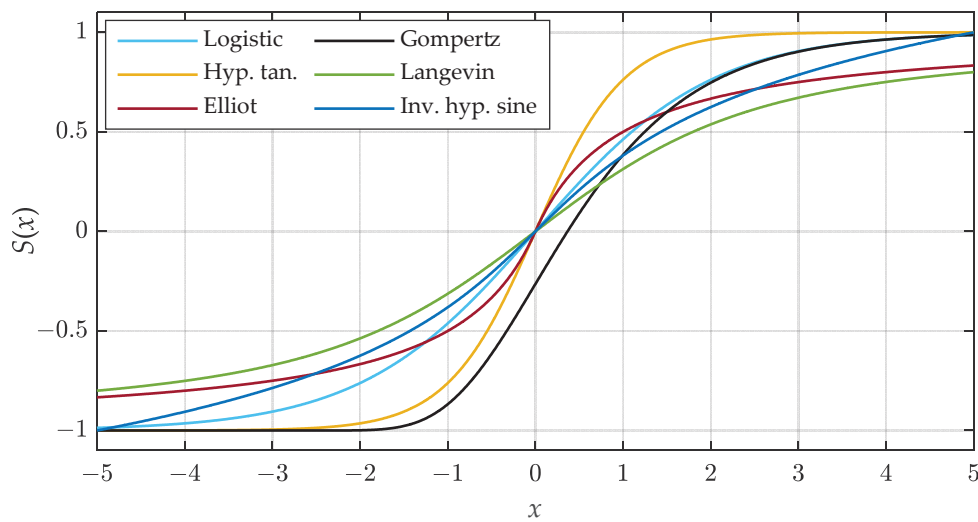


Figure 1. Graphical presentation and comparison of the analyzed mathematical functions.

2.2. Bézier Curves

Bézier curves are parametric curves with Bernstein polynomials as their basis functions. Paul de Casteljaou contributed significantly to their first development, but they are named after Pierre Bézier, who invented them in 1962 and made them widely popular for the shape design of automobile bodies while working for Renault [16,19]. Parametric curves are not defined as $y(x)$ dependencies, but they describe the shape of a curve based on a (local) input variable t that is defined along the curve. Variable t is 0 at the start of the curve and 1 at the end. For each value of t , two values are defined (i.e., $x(t)$ and $y(t)$), which, combined, define the coordinates $(x(t), y(t))$ of all the points on the curve. This means that the coordinates of a Bézier curve are obtained using two polynomials $x(t) = B_x(t)$ and $y(t) = B_y(t)$ [34]. Due to this property, parametric curves enable the description of highly complex curves. The free-form ability of Bézier curves, explained in Section 1, is demonstrated in Figure 2. It is possible to form a single-valued curve, as shown in Figure 2a; self-intersecting curves, as shown in Figure 2b,c; and complex shapes, as shown in Figure 2d.

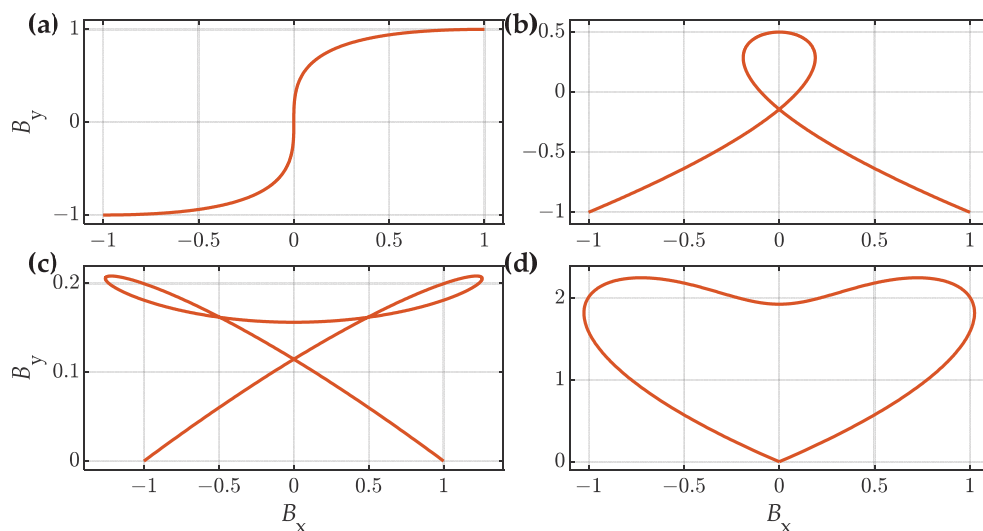


Figure 2. Various shapes formed with Bézier curves of different orders: (a) $n = 3$, (b) $n = 3$, (c) $n = 5$, and (d) $n = 10$.

Bézier curves are defined by their order n and a corresponding set of $(n + 1)$ control points $\mathbf{P} = (P_0, P_1, \dots, P_n)$. Each control point has its x and y coordinates $P_i(x_i, y_i)$ ($i = 0, 1, \dots, n$) in the 2D Cartesian coordinate system. Considering order n and corresponding vector of control points \mathbf{P} , the Bézier curve $B(t) = (B_x(t), B_y(t))$ can be expressed in polynomial form by Equations (7) and (8)

$$B_x(t) = x(t) = \sum_{i=0}^n b_{i,n}(t)x_i, \quad 0 \leq t \leq 1, \quad (7)$$

$$B_y(t) = y(t) = \sum_{i=0}^n b_{i,n}(t)y_i, \quad 0 \leq t \leq 1, \quad (8)$$

where $b_{i,n}(t)$ represents the Bernstein basis polynomials and (x_i, y_i) are the coordinates of control point P_i . The Bernstein basis polynomials of order n are defined by Equation (9) [18]:

$$b_{i,n}(t) = \binom{n}{i} t^i (1-t)^{n-i}, \quad i = 0, \dots, n \quad (9)$$

where $t \in [0, 1]$, in which 0 is the starting point of the curve and 1 is the end point of the curve [18], and $\binom{n}{i}$ is a binomial coefficient defined by Equation (10):

$$\binom{n}{i} = \frac{n!}{i!(n-i)!} \quad (10)$$

Besides Bézier curves, Bernstein polynomials are also known as basis functions for splines [35]. The basis functions of the Bézier curve can be enhanced to be able to reproduce various shapes, such as those presented in [30]. De Casteljau's recursive algorithm is used to evaluate Bézier curve polynomials because of its numerical stability [18].

Another feature of Bézier curves is their matrix representation, which allows for a straightforward calculation of the polynomial coefficients for functions $B_x(t)$ and $B_y(t)$. For a Bézier curve of order n , the matrix equation is defined by Equation (11) [36]:

$$B_x(t) = \begin{bmatrix} t^n & t^{n-1} & \dots & t & 1 \end{bmatrix} \mathbf{M}_{\text{Béz},n} \begin{bmatrix} x_0 \\ x_1 \\ \vdots \\ x_{n-1} \\ x_n \end{bmatrix} \quad (11)$$

The $B_x(t)$ polynomial of the Bézier curve is obtained with Equation (11). To obtain the $B_y(t)$ polynomial of the Bézier curve, the y coordinates of control points P_i must be considered in Equation (11). The matrix $\mathbf{M}_{\text{Béz},n}$ is an $(n + 1) \times (n + 1)$ -sized coupling matrix between the variable t and the control point's coordinates \mathbf{P} . By evaluating the matrix $\mathbf{M}_{\text{Béz},n}$ for Bézier curves of orders of up to 6 [36,37], the general form of matrix $\mathbf{M}_{\text{Béz},n}$ for curves of order n is determined by Equation (12) [38]:

$$\mathbf{M}_{\text{Béz},n} = \begin{bmatrix} \binom{n}{0} \binom{n}{n} & \binom{n}{1} \binom{n-1}{n-1} & \dots & \binom{n}{n-1} \binom{1}{1} & \binom{n}{n} \binom{0}{0} \\ \binom{n}{0} \binom{n}{n-1} & \binom{n}{1} \binom{n-1}{n-2} & \dots & \binom{n}{n-1} \binom{1}{0} & 0 \\ \binom{n}{0} \binom{n}{n-2} & \binom{n}{1} \binom{n-1}{n-3} & & 0 & 0 \\ \vdots & \vdots & & \vdots & \vdots \\ \binom{n}{0} \binom{n}{1} & \binom{n}{1} \binom{n-1}{0} & & 0 & 0 \\ \binom{n}{0} \binom{n}{0} & 0 & \dots & 0 & 0 \end{bmatrix} \quad (12)$$

Each non-zero element in $\mathbf{M}_{\text{Béz},n}$ is calculated as the product of two binomial coefficients by applying Equation (10). The elements within $\mathbf{M}_{\text{Béz},n}$ have a positive or negative sign depending on the matrix order. A general rule is that the main counter diagonal elements of matrix $\mathbf{M}_{\text{Béz},n}$ always have a positive sign, and then the sign alternates between negative and positive for all other diagonals above the main counter diagonal. The formation of matrix $\mathbf{M}_{\text{Béz},n}$ is presented in [36,37].

2.2.1. Properties of Bézier Curves

The basic properties of Bézier curves are:

- First, control point P_0 defines the beginning, and the last control point P_n defines the end of the curve.
- The tangent vector formed by the first two control points P_0 and P_1 ($\overline{P_0P_1}$) defines the initial direction, and the tangent vector formed by the last two points $\overline{P_{n-1}P_n}$ defines the ending direction of the curve.
- The Bézier curve lies within the area that is formed by the control points [18–20].

Furthermore, an important property of Bézier curves is the straightforward calculation of its derivative in terms of the variable t . If the Bézier curve for x coordinates is $x(t) = B_x(t)$ and for y coordinates is $y(t) = B_y(t)$, then the first derivative dy/dx is calculated by Equation (13):

$$\frac{dy}{dx} = \frac{dy/dt}{dx/dt} \quad (13)$$

and the second derivative d^2y/dx^2 by Equation (14):

$$\frac{d^2y}{dx^2} = \frac{\frac{d}{dt}(dy/dx)}{dx/dt} \quad (14)$$

The equations for the first and second derivatives allow for the calculation of the curvature of Bézier curves [18,19,39]. Bézier curves offer the possibility to form symmetric curves. Symmetric Bézier curves are generated by placing pairwise control points into symmetrical positions [40].

2.2.2. Impact of the Control Point's Placement on the Bézier Curve

In this subsection, we demonstrate the impact of the positioning of control points on the shape of a cubic (i.e., order of $n = 3$) Bézier curve. As presented in Figure 2, Bézier curves enable the formation of various shapes—continuous single-valued curves, as shown in Figure 2a; self-intersecting curves, as presented in Figure 2b,c; and closed shapes, as shown in Figure 2d. Figure 3 shows the various possibilities regarding the change in shape of a cubic Bézier curve from Figure 2a only by changing the position of the control points P_1 and P_2 (the first P_0 and last P_3 control points have fixed positions).

We chose to fix the first and last points for the presented comparison to show the variety of curves that start and end in the same points. As explained in Section 2.2.1, the starting and ending directions of the curve were defined by the tangents $\overline{P_0P_1}$ and $\overline{P_2P_3}$, respectively. The cases shown in Figure 3a,b are examples of changing the slope and curvature by moving the control points but preserving the property analogous to a single-valued function. In the case presented in Figure 3c, when the control point P_1 was below control point P_0 and P_2 was above P_3 , we obtained an overshoot over the normalized value of 1. That behavior is not adequate for the description of magnetization curves. Another nonphysical behavior was observed when the absolute values of the x coordinates of points P_1 and P_2 were higher than the x values of the last and first control points, respectively, as shown in Figure 3d. The obtained curve was not single valued in respect to x and thus not appropriate for the description of magnetization curves. Control points are decisive for the curvature and shape of the final curve [26].

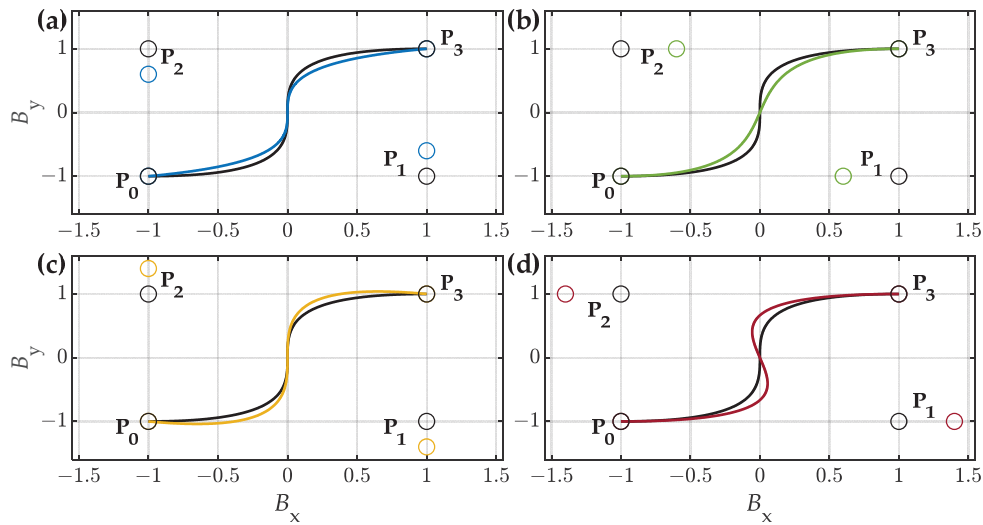


Figure 3. Impact of the placement of control points P_1 and P_2 on the shape of a 3rd-order Bézier curve: (a,b) changing the curvature and slope of a single valued curve, (c) overshoot over normalized value of 1 (d) non single valued curve.

3. Methodology

3.1. Assumptions and Limitations

The discussed analytical functions in Section 2.1 have limited ability to approximate various curves with high accuracy because they have only three or four adjustable parameters. In contrast to this, the Bézier curves can be based on many theoretically arbitrary control points; therefore, they offer higher flexibility for the approximation of measured data.

The focus of the presented analysis was on a systematic analysis of which functions and curves would result in the best fit based on different sets of measured data. Further, the extrapolation capabilities of the presented functions and curves were analyzed. During the analyses, we assumed that different sets of measured data for two NO steels were available. We limited the analyses to the application of the presented analytical functions and classical Bézier curves of different orders. One of the goals was to identify the most adequate orders for approximation of the discussed curves.

3.2. Measured Data

The analysis was performed systematically based on measured characteristic magnetization curves $J(H)$, where J is the magnetic polarization and H is the magnetic field strength. In the analysis, we considered three of the most basic curves that describe the nonlinear properties of soft magnetic materials:

- (1) First magnetization curves;
- (2) Anhysteretic curves;
- (3) Descending branches of the major loops.

We determined the discussed curves for two NO electrical steels with different thicknesses, i.e., 0.27 mm (NO27) and 0.35 mm (NO35), which are both commonly used in contemporary electrical machines. The measurement setup was based on a single sheet tester within a computer-aided measurement setup, in accordance with the International Standard IEC 60404-3. The measurements were performed at low excitation frequencies (i.e., under the so-called quasi-static conditions) up to $H = 50$ kA/m at 5000 J -equidistant measurement points. Based on the measured curves, it was assumed that $H = H_s = 50$ kA/m was the saturation point of both materials. Consequently, the available measured dataset was $\mathbf{H}_{\text{meas}} = [-H_s, H_s]$, where $[-H_s, H_s]$ denotes the interval of the discrete measured dataset, starting from $-H_s$ and ending with H_s .

The anhysteretic curve was calculated as the average value of polarization J between the ascending and descending branches of the major loop.

3.3. Definition of the Data Subsets and Evaluation (Sub)Regions

All the discussed functions and curves were evaluated systematically on different input subsets \mathbf{H}_{in} of the available measured data \mathbf{H}_{meas} (i.e., $\mathbf{H}_{meas} = [-H_s, H_s]$). The input subset \mathbf{H}_{in} was, in all cases, a subinterval of the measured data \mathbf{H}_{meas} , i.e., $\mathbf{H}_{in} \subseteq \mathbf{H}_{meas}$. The evaluation subregions \mathbf{H}_{eval} were defined within the discussed input subsets \mathbf{H}_{in} . Special attention was paid to evaluation of the following characteristic subregions:

- (1) The high-permeability (HP) subregion ($\mathbf{H}_{eval,2} = [-H_1, H_1]$);
- (2) The saturation (SAT) subregion ($\mathbf{H}_{eval,3} = [-H_{in,max}, -H_1] \cup [H_1, H_{in,max}]$);
- (3) The extrapolation (EXT) subregion ($\mathbf{H}_{eval,6} = [-H_s, -H_{in,max}] \cup [H_{in,max}, H_s]$).

The HP and SAT subregions were important for the first part of the analysis, i.e., evaluation of the approximation capabilities, whereas the EXT subregion was crucial for the analysis of the extrapolation capabilities. These subregions are very important in applied engineering and are presented schematically in Figure 4.

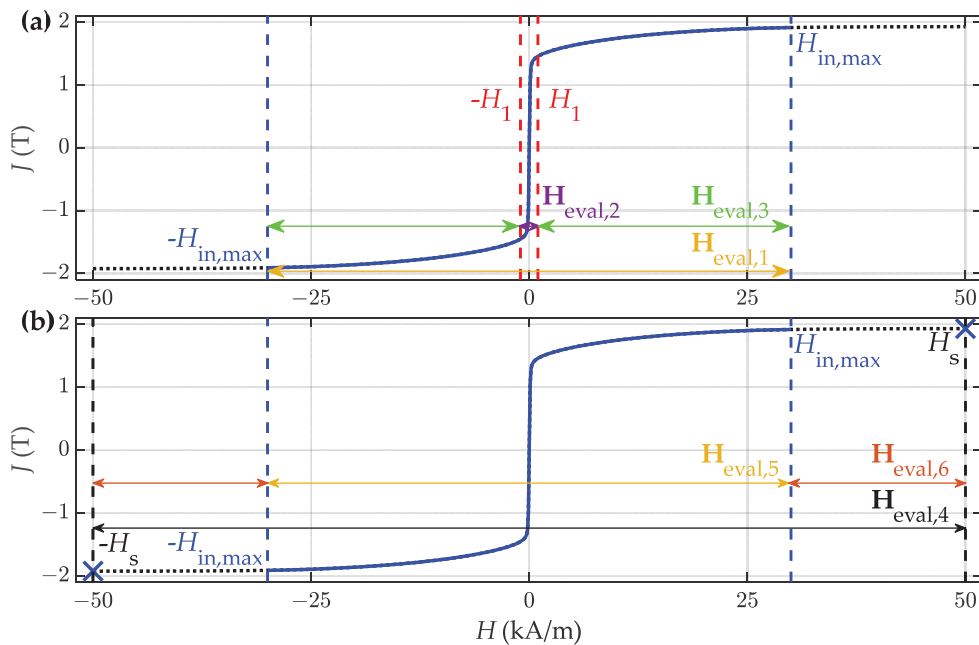


Figure 4. Graphic presentation of the input subsets of measured data \mathbf{H}_{in} and characteristic subregions for evaluation of the goodness of fit ($\mathbf{H}_{eval,1}$ to $\mathbf{H}_{eval,6}$) in the cases of (a) approximation and (b) extrapolation.

The input subset \mathbf{H}_{in} used in the process of fitting analytical functions and Bézier curves is plotted in blue in Figure 4. The measured data between $[-H_{in,max}, H_{in,max}]$ represented the input subset \mathbf{H}_{in} in individual cases for approximation, as presented in Figure 4a. It was slightly different for the case of extrapolation, where, additionally, the saturation points H_s were added to both sides of the input subset \mathbf{H}_{in} , highlighted with the blue cross in Figure 4b. The characteristic subregions of the magnetization curves were identified in both cases. Considering those subregions, the measured data were divided accordingly into evaluation subsets, denoted with $\mathbf{H}_{eval,1}$ to $\mathbf{H}_{eval,6}$ and presented in Figure 4a,b. This approach and division enabled us to perform a systematic analysis via local evaluation of the goodness of fit of the approximated curves in specific subregions individually as well as a global evaluation on the input subset \mathbf{H}_{in} .

It is important to note that H_s and H_1 were fixed at $H_s = 50$ kA/m and $H_1 = 1$ kA/m, respectively. In contrast to this, $H_{in,max}$ was varied (i.e., 1, 2, 5, 10, 15, 20, 30, 40, and

50 kA/m) and determined various input datasets for approximation and extrapolation of the discussed functions and curves.

3.4. Curve Fitting

The parameters (a , b , c , and d) of the analytic function from Table 1 were fitted to the input subsets \mathbf{H}_{in} of the measured magnetization curves using the Matlab function *fit* by applying the nonlinear least squares method.

For the process (i.e., the placement of control points) of fitting Bézier curves to the input subsets \mathbf{H}_{in} , we applied the differential evolution (DE) algorithm [10,41]. We set the value of the mutation factor to 0.5 and the crossover factor to 0.7 and used the DE algorithm for 15,000 iterations for each curve. In each iteration, the x and y coordinates of the control points were calculated to minimize the deviation of the calculated Bézier and measured magnetization curves. Within the process, the first and last control points (which were assumed to be equal to the first and last points, respectively, of the input subset \mathbf{H}_{in}) were fixed according to the adequate position of the measured curve. The goal was to determine the intermediate control points. To find the optimum values, we minimized the objective function F in Equation (15):

$$F = \sum_{i=1}^{N_{\max}} [J_{in,i}(H_{in,i}) - J_{calc,i}(H_{in,i})]^2, \quad (15)$$

where $J_{in,i}(H_{in,i})$ are the input measured values of the magnetic polarization at the corresponding magnetic field strengths $H_{in,i}$, $J_{calc,i}(H_{in,i})$ is the magnetic polarization approximated by a Bézier curve at $H_{in,i}$, and N_{\max} is the number of elements of the input subset \mathbf{H}_{in} .

In general, $2 \cdot (n - 1)$ parameters had to be determined for an arbitrary order n of a Bézier curve. Therefore, higher orders of Bézier curves naturally led to longer computational effort in the fitting procedure.

3.5. Evaluation of the Goodness of Fit

To evaluate the goodness of fit for the calculated curves, we applied the statistical measure normalized root mean square (NRMS) ε , defined by Equation (16) [7].

$$\varepsilon = \sqrt{\frac{1}{N_{\max}} \sum_{i=1}^{N_{\max}} \left(\frac{J_{in,i}(H_{eval,i}) - J_{calc,i}(H_{eval,i})}{\Delta J_{eval}} \right)^2} \quad (16)$$

In Equation (16), $J_{in,i}(H_{eval,i})$ are the measured values of magnetic polarization at corresponding magnetic field strengths $H_{eval,i}$ in the observed subregion for the evaluation of \mathbf{H}_{eval} . Furthermore, $J_{calc,i}(H_{eval,i})$ are the corresponding calculated values of magnetic polarization, and ΔJ_{eval} is the range of the evaluated subregion \mathbf{H}_{eval} . This range ΔJ_{eval} is defined as the difference between the maximum $J_{eval,max}$ and minimum $J_{eval,min}$ values of such a subregion, i.e., $\Delta J_{eval} = J_{eval,max} - J_{eval,min}$.

During the analysis, we evaluated both the approximation and the extrapolation capabilities of the presented functions and curves. Individual curves were evaluated by Equation (16) in different subregions individually (i.e., HP, SAT, and EXT regions) by selecting the adequate evaluation region \mathbf{H}_{eval} .

3.5.1. Approximation Capabilities

We analyzed the goodness of fit and evaluated the approximation capabilities of the analytic functions and Bézier curves of different orders in specific subregions within the input subset \mathbf{H}_{in} . The available measured data \mathbf{H}_{meas} were divided into nine input subsets \mathbf{H}_{in} between $[-H_{in,max}, H_{in,max}]$, where $H_{in,max}$ equaled 1, 2, 5, 10, 15, 20, 30, 40, and 50 kA/m, respectively. An exemplary case of an input subset \mathbf{H}_{in} , where $H_{in,max} = 30$ kA/m, is presented in Figure 4a with the blue curve. The first magnetization curves were fitted on the input subset $\mathbf{H}_{in} = [0, H_{in,max}]$, whereas all the other curves were fitted on a symmetric

subset $\mathbf{H}_{\text{in}} = [-H_{\text{in,max}}, H_{\text{in,max}}]$. In the first step, individual analytic functions were fitted, and Bézier curves of different orders were obtained for each individual input subset \mathbf{H}_{in} . The evaluation of the goodness of fit ε was carried out in three subregions of each subset, where the evaluation was performed in the following ranges \mathbf{H}_{eval} ($\mathbf{H}_{\text{eval}} \subseteq \mathbf{H}_{\text{in}}$):

- (a) The input subset $\mathbf{H}_{\text{eval},1} = \mathbf{H}_{\text{in}} = [-H_{\text{in,max}}, H_{\text{in,max}}]$;
- (b) The HP subregion (within the input subset), i.e., $\mathbf{H}_{\text{eval},2} = [-H_1, H_1]$;
- (c) The SAT region (within the input subset), i.e., $\mathbf{H}_{\text{eval},3} = [-H_{\text{in,max}}, -H_1] \cup [H_1, H_{\text{in,max}}]$.

The evaluation subregions $\mathbf{H}_{\text{eval},1}$ to $\mathbf{H}_{\text{eval},3}$ are depicted graphically in Figure 4a. It is important to note that $J_{\text{eval,max}}$ and $J_{\text{eval,min}}$ for case (c) were determined at $H_{\text{in,max}}$ and H_1 , respectively.

The result of this analysis was the identification of the most suitable analytic functions and the most adequate orders of Bézier curves for the approximation of nonlinear magnetic properties for different input data subsets. These were included in the next analysis, i.e., the analysis of the extrapolation capabilities.

3.5.2. Extrapolation Capabilities

In the analysis of the extrapolation capabilities, the fitting was carried out analogously with the previous analysis. The difference was that the positive and negative saturation points $J_s(H_s)$ were added to all symmetric input subsets between $[-H_{\text{in,max}}, H_{\text{in,max}}]$. Therefore, the input subset \mathbf{H}_{in} consisted of the negative saturation point $-H_s$, the measured data between $[-H_{\text{in,max}}, H_{\text{in,max}}]$, and the positive saturation point H_s , i.e., $\mathbf{H}_{\text{in}} = -H_s \cup [-H_{\text{in,max}}, H_{\text{in,max}}] \cup H_s$. This input subset for a specific case, where $H_{\text{in,max}} = 30 \text{ kA/m}$, is presented with the blue line and blue crosses in Figure 4b. The result of the fitting process was analytic functions and Bézier curves that ranged from $-H_s$ to H_s . They also enabled the analysis of the goodness of fit in the assumed EXT subregion. The evaluation of the goodness of fit ε was carried out again in three evaluation subregions \mathbf{H}_{eval} , where $\mathbf{H}_{\text{eval}} \subseteq \mathbf{H}_{\text{meas}}$:

- (d) The full measured dataset up to saturation $\mathbf{H}_{\text{eval},4} = \mathbf{H}_{\text{meas}}$;
- (e) The subregion which contained the measured data $\mathbf{H}_{\text{eval},5} = [-H_{\text{in,max}}, H_{\text{in,max}}]$;
- (f) The EXT subregion ($\mathbf{H}_{\text{eval},6} = [-H_s, -H_{\text{in,max}}] \cup [H_{\text{in,max}}, H_s]$).

Analogous to the previous subsection, $J_{\text{eval,max}}$ and $J_{\text{eval,min}}$ for case (f) were determined at H_s and $H_{\text{in,max}}$, respectively.

4. Results

The available range (defined by $H_{\text{in,max}}$) of the (measured) input data $\mathbf{H}_{\text{in}} = [-H_{\text{in,max}}, H_{\text{in,max}}]$ has, in general, a high impact on the goodness of fit of the approximated functions and curves. The impact of the range on the approximated curves using both analytic functions and Bézier curves is presented in Figure 5. The curves in Figure 5a,b were approximated on the input subset limited by $H_{\text{in,max}} = 0.5 \text{ kA/m}$ and in Figure 5c,d on the input subset limited by $H_{\text{in,max}} = 15 \text{ kA/m}$. The curves approximated on a bigger subset ($H_{\text{in,max}} = 15 \text{ kA/m}$) deviated more in the HP region in comparison to those approximated on the input subset \mathbf{H}_{in} , which coincided with the observed region ($H_{\text{in,max}} = 0.5 \text{ kA/m}$). The approximated curves in Figure 5 confirm that the size of the input subset \mathbf{H}_{in} (i.e., the range of measured input data defined by $H_{\text{in,max}}$) had a high impact on the approximation accuracy.

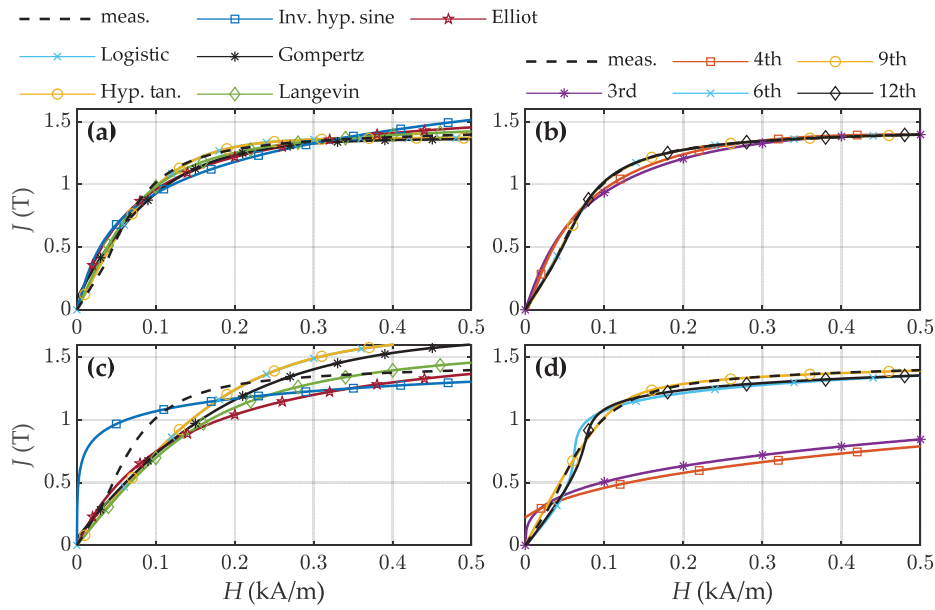


Figure 5. Impact of the range of measured data $H_{in,max}$ on the goodness of fit in the region $[0, 0.5]$ kA/m: (a) analytic functions, $H_{in,max} = 0.5$ kA/m; (b) Bézier curves of different orders, $H_{in,max} = 0.5$ kA/m; (c) analytic functions, $H_{in,max} = 15$ kA/m; and (d) Bézier curves of different orders, $H_{in,max} = 15$ kA/m.

4.1. Approximation with Analytic Functions

In general, all analytic functions produced the overall shape to describe the discussed nonlinear relationships, as demonstrated, e.g., in Figure 5a,c. For the sigmoid functions (Functions (1)–(5)) similar conclusions are presented in [10,15].

4.1.1. Anhysteretic Curves

To determine the most adequate analytic function for the approximation of the anhysteretic curve, we calculated the NRMS deviations ε on different regions within different input subsets \mathbf{H}_{in} for all the discussed functions, as described in Section 3.5.1. The obtained results are presented in Figure 6.

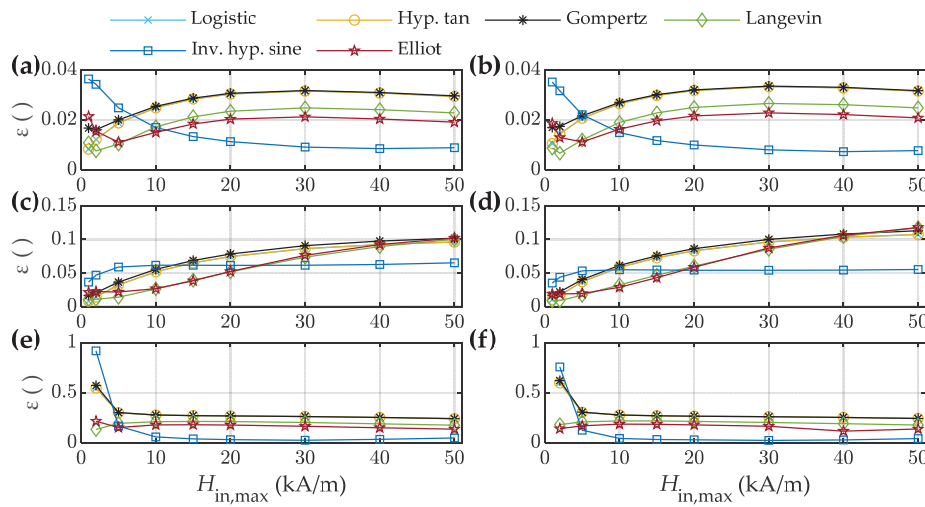


Figure 6. Calculated NRMS deviation ε within the individual input subsets $\mathbf{H}_{in} = [-H_{in,max}, H_{in,max}]$ for the anhysteretic curve of two materials NO35 (left column) and NO27 (right column) approximated with analytic functions (a,b) within the individual input subsets \mathbf{H}_{in} , (c,d) within the HP subregion of the individual subsets, and (e,f) within the SAT subregion of the individual subsets.

First, we evaluated the global goodness of fit (i.e., within different symmetric input subsets $\mathbf{H}_{\text{eval},1} = \mathbf{H}_{\text{in}}$ of the measured data) systematically, as described in case (a) of Section 3.5.1. Based on the presented results in Figure 6a,b, it was observed that the Langevin function had the best overall fit for the smaller input subsets up to $H_{\text{in,max}} = 5$ kA/m. Further, the Elliot function had the best goodness of fit for the measured anhysteretic curve of both materials when a symmetric input subset from $H_{\text{in,max}} = 5$ kA/m up to $H_{\text{in,max}} = 10$ kA/m was applied. These results agree with the findings in [10]. The goodness of fit with the Langevin function was slightly worse compared to the one evaluated with the Elliot function in the latter region. However, if the input subsets exceeded $H_{\text{in,max}} = 10$ kA/m, the global goodness of fit of the inverse hyperbolic sine function was the best.

To support the obtained results further, we analyzed the deviations in two specific subregions of the anhysteretic curve. The first local goodness of fit was defined between $\mathbf{H}_{\text{eval},2} = [-H_1, H_1]$, where $H_1 = 1$ kA/m (the so-called HP region), as explained in case (b) of Section 3.5.1. The local goodness of fit for the HP region is shown in Figure 6c,d. The obtained results supported the premise that, as the input subset \mathbf{H}_{in} increased into the saturation region, the deviations were more significant. This was expected due to the high nonlinearity of the input data, whereas individual subregions were not considered separately, and, consequently, could not be approximated with equal accuracy. In the HP region, the best results were again obtained using the Elliot and Langevin functions, whereas in the cases of larger input subsets above $H_{\text{in,max}} = 20$ kA/m, the inverse hyperbolic sine function again became the best option. If limited measured data not deep into saturation are available, the Elliot and Langevin functions are the best choice for approximation.

The second local subregion $\mathbf{H}_{\text{eval},3}$ (SAT region) was defined from 1 kA/m to the maximum value in the individual input subset $H_{\text{in,max}}$, i.e., when the materials were significantly saturated (i.e., case (c) in Section 3.5.1). The values of ε within this analysis are presented in Figure 6e,f. In this region the inverse hyperbolic sine function had superior results to other analytic functions, especially for input subsets that were measured deeper into saturation.

4.1.2. Major Loop Curves

Next, we analyzed the goodness of fit of the approximated analytic functions on the descending branch of the major loop. The calculated NRMS values ε are presented in Figure 7. The results obtained for the major loop are in line with those obtained for the anhysteretic curve. This could be attributed to the fact that the anhysteretic curve was calculated as the average value between both branches of the major loop, and, consequently, closely related to the major loop. It was concluded that the offset in H of the major loop curves did not introduce a significant change in the results.

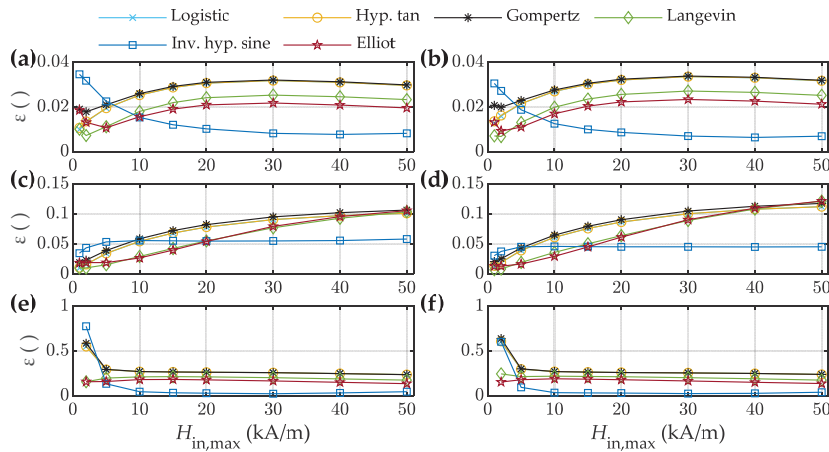


Figure 7. Calculated NRMS deviation ε within the individual input subsets $\mathbf{H}_{in} = [-H_{in,max}, H_{in,max}]$ for the descending branch of the major loop of two materials, NO35 (left column) and NO27 (right column), approximated with analytic functions (a,b) within the individual input subsets \mathbf{H}_{in} , (c,d) within the HP subregion of the individual subsets, and (e,f) within the SAT subregion of the individual subsets.

4.1.3. First Magnetization Curves

The results obtained were slightly different in the case of the first magnetization curves. The calculated NRMS errors ε for the case of the first magnetization curve are shown in Figure 8. In the input subset between 0 and $H_{in,max}$, i.e., $\mathbf{H}_{in} = [0, H_{in,max}]$, the Elliot and Langevin functions gave best results in the case of sheet NO35, as shown in Figure 8a. In the case of NO27, presented in Figure 8b, the Elliot and Langevin functions gave the best results up to $H_{in,max} = 30$ kA/m. Beyond this subregion, the inverse hyperbolic sine function became the most adequate analytic function. In the HP region, the Langevin function had the lowest deviation from the measured data in the case of NO35, as presented in Figure 8c. Figure 8d shows the results for NO27, where the Langevin function gave better results for the intermediate fields (up to $H_{in,max} = 20$ kA/m), and, after that region, the Langevin and Elliot functions had similar goodness of fit. In the case of the SAT region (i.e., from 1 kA/m to $H_{in,max}$), the results for both materials in Figure 8e,f were similar; overall, the inverse hyperbolic sine function yielded the best results. The Elliot and Langevin functions can be used for lower fields of up to $H_{in,max} = 10$ kA/m.

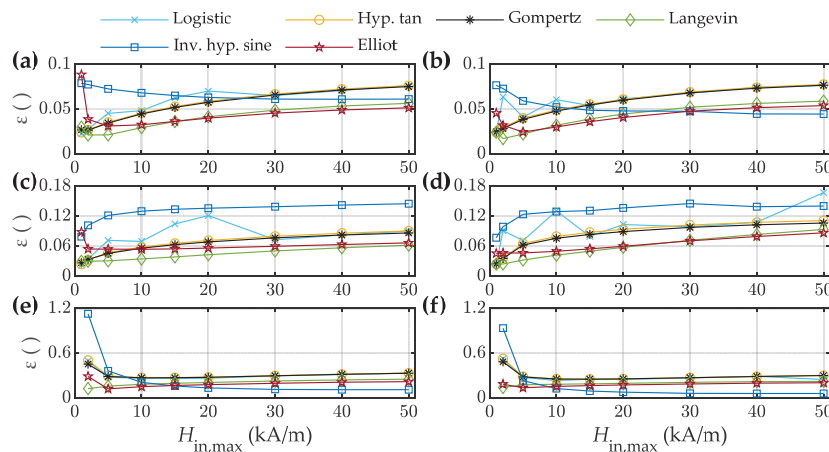


Figure 8. Calculated NRMS deviation ε within the individual input subsets $\mathbf{H}_{in} = [-H_{in,max}, H_{in,max}]$ for the first magnetization curve of two materials, NO35 (left column) and NO27 (right column), approximated with analytic functions (a,b) within the individual input subsets \mathbf{H}_{in} between 0 and $H_{in,max}$, (c,d) within the HP subregion between 0 and 1 kA/m of the individual subsets, and (e,f) within the SAT subregion between 1 kA/m and $H_{in,max}$ of the individual subsets.

4.2. Approximation with Higher-Order Bézier Curves

Next, we analyzed the ability of Bézier curves of different orders systematically to describe the measured magnetization curves. We performed the analysis starting with Bézier curves of the order $n = 3$ (order three is commonly used in many applications, e.g., in splines [42]) and increased the order up to $n = 12$.

Based on the results that are presented in Figure 5b,d we concluded that lower-order Bézier curves (e.g., the third and fourth orders) had limited ability to approximate magnetization curves adequately. Hence, we excluded these orders from further analysis. We applied the analysis presented in cases (a)–(c) in Section 3.5.1 to the approximation with Bézier curves.

4.2.1. Anhysteretic Curves

The obtained values of ε for the anhysteretic curves are presented in Figure 9. This part of the analysis was performed with Bézier curves from the 5th to 12th orders. For the sake of clarity, we did not plot ε for the Bézier curves of all the discussed orders but only representative ones. From the ε obtained for the individual symmetrical input subsets $\mathbf{H}_{\text{eval},1} = \mathbf{H}_{\text{in}}$ (as explained in Section 3.5.1 case (a)) in Figure 9a,b, we concluded that the most suitable were the eighth- and ninth-order Bézier curves. In general, it is reasonable to select a curve with the lowest number of control points. The obtained results showed that all Bézier curves starting from order six already had significantly improved goodness of fit compared to the analytic functions in all the analyzed scenarios.

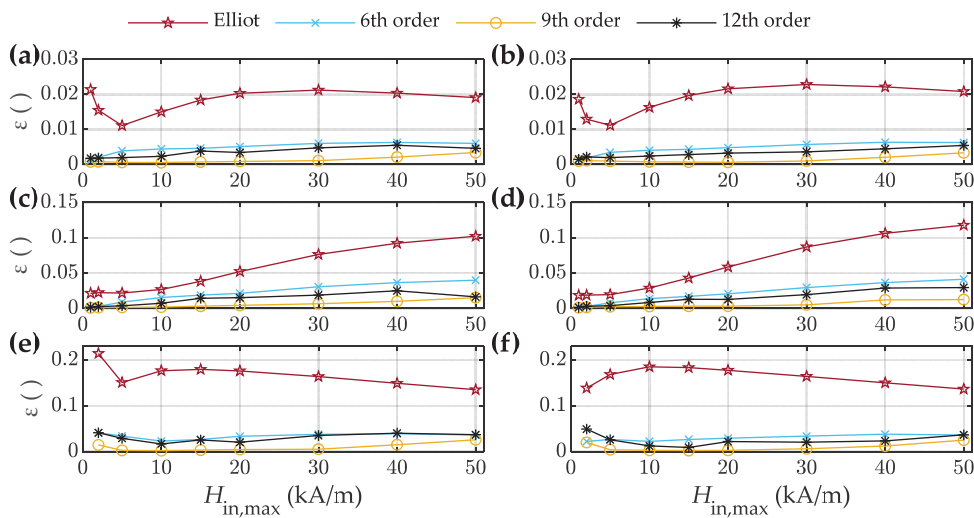


Figure 9. Calculated NRMS deviation ε within the individual input subsets $\mathbf{H}_{\text{in}} = [-H_{\text{in,max}}, H_{\text{in,max}}]$ for the anhysteretic curves of two materials, NO35 (left column) and NO27 (right column), approximated with Bézier curves (a,b) within the individual input subsets \mathbf{H}_{in} , (c,d) within the HP subregion of the individual subsets, and (e,f) within the SAT subregion of the individual subsets.

For the HP region (case (b) in Section 3.5.1) in Figure 9c,d, the ninth-order Bézier curve offered the best approximation, which is in line with the results in Figure 5b,d. Along with the 9th order, the 7th-, 8th-, and 10th-order Bézier curves yielded a very good approximation of this region. In this case, we observed that, as \mathbf{H}_{in} increased, the fit in the HP region became less accurate, which was analogous with the results for the analytic functions. The same orders of Bézier curves were estimated as the best for the remaining SAT region of the curve (case (c) in Section 3.5.1) presented in Figure 9e,f.

4.2.2. Major Loop Curves

The results for the descending branch of the major loop are similar to the results obtained for the anhysteretic curve. The results are presented in Figure 10. The ninth-order

Bézier curve had the lowest deviation from the measured major loop in all cases. The results obtained with the ninth-order curve were followed closely by the eighth-order Bézier curve.

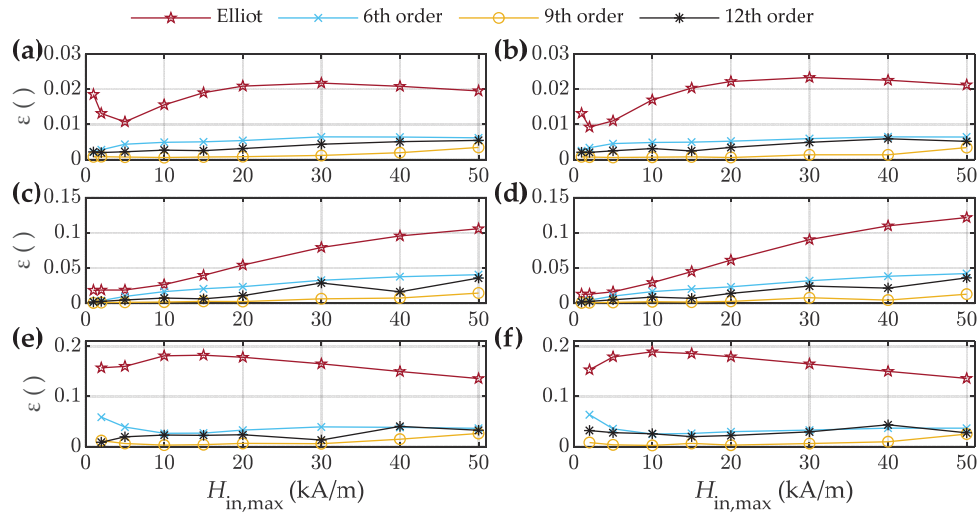


Figure 10. Calculated NRMS deviation ε within the individual input subsets $\mathbf{H}_{in} = [-H_{in,max}, H_{in,max}]$ for the descending branch of the major loop of two materials, NO35 (left column) and NO27 (right column), approximated with Bézier curves: (a,b) within the individual input subsets \mathbf{H}_{in} , (c,d) within the HP subregion of the individual subsets, and (e,f) within the SAT subregion of the individual subsets.

4.2.3. First Magnetization Curves

In the case of approximating the first magnetization curve, Bézier curves were superior to analytic functions, whereas the obtained NRMS values ε were significantly lower. The calculated NRMS deviation values ε for the Bézier curves are presented in Figure 11. For this specific curve, even the fourth-order Bézier curve demonstrated low deviation from the measured data. For input subsets up to $H_{in,max} = 30$ kA/m, shown in Figure 11a,b, the sixth- and seventh-order Bézier curves yielded the best goodness of fit, and, above 30 kA/m, the eighth- and ninth-order Bézier curves yielded the best results. In the HP region, presented in Figure 11c,d, the seventh-order Bézier curve had the best overall goodness of fit. Those results are followed closely by the results obtained with the eighth-order Bézier curve. In the SAT region, presented in Figure 11e,f, the seventh-order Bézier curve had the best goodness of fit. Additionally, in the region with magnetic field strength values of up to $H_{in,max} = 30$ kA/m, the sixth-order Bézier curves demonstrated low deviation from the measured data. In regions with high magnetic field strength values beyond 30 kA/m, the eighth- and ninth-order Bézier curves had the lowest NRMS deviation values ε .

Based on the results in this subsection, we concluded that suitable orders of Bézier curves for approximation of the discussed nonlinear magnetic properties were the sixth to ninth.

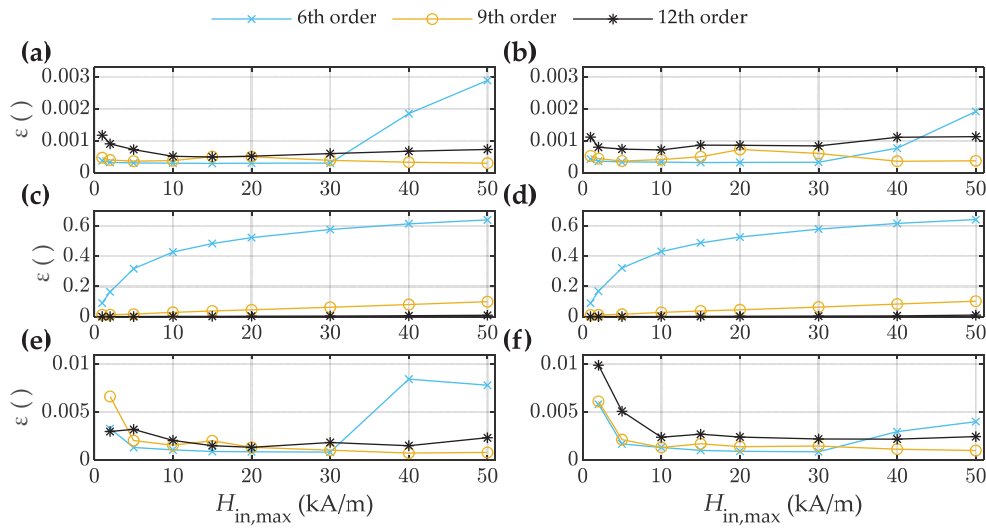


Figure 11. Calculated NRMS deviation ε within the individual input subsets $\mathbf{H}_{in} = [-H_{in,max}, H_{in,max}]$ for the first magnetization curve of two materials, NO35 (left column) and NO27 (right column), approximated with Bézier curves (a,b) within the individual input subsets \mathbf{H}_{in} between 0 and $H_{in,max}$, (c,d) within the HP subregion between 0 and 1 kA/m of the individual subsets, and (e,f) within the SAT subregion between 1 kA/m and $H_{in,max}$ of the individual subsets.

4.3. Analysis of Extrapolation Capabilities

It is often not feasible to measure the hysteresis properties deep into saturation. Therefore, only measured magnetization curves in limited regions are available, as presented schematically in Figure 12a. The reasons for this are the highly nonlinear properties and the corresponding complexity and challenges in the measurement procedures. The measurement accuracy is decreased significantly when measurements are performed at values of high magnetic field strength H . Because of that, it is important to have a reliable method to determine the magnetic curves up to high saturation values, even if measured data are not available for the whole magnetization curve. This can be performed by extrapolation, which is the technique used most often for this purpose in applied engineering. Two of the most used functions for this purpose are the Langevin and the Elliot functions (the latter is often referred to as the Frölich–Kennelly extrapolation).

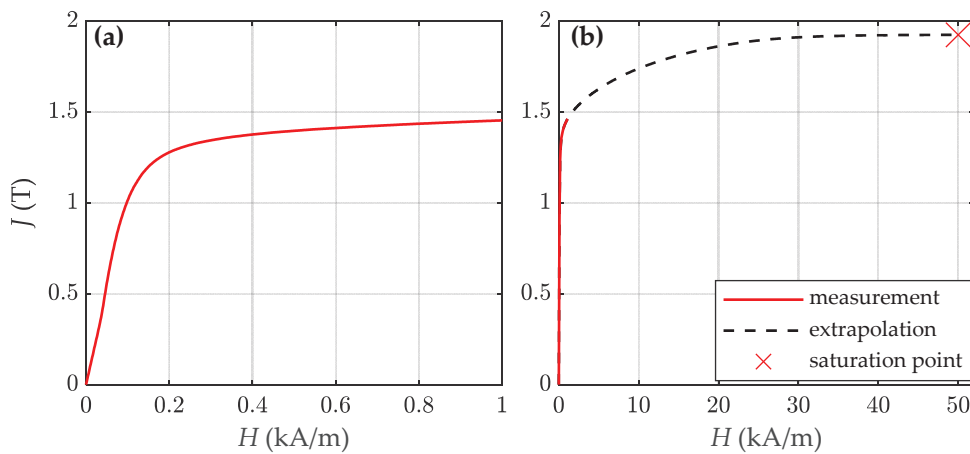


Figure 12. (a) Anhyseretic curve in the HP region and (b) anhyseretic curve measured up to saturation.

In Figure 12b, an example of limited available measured data is presented schematically. In such cases, a significant part of the magnetization curve is unknown and must be estimated with extrapolation. In the literature, several methods have been proposed

for the extrapolation of magnetization curves [43]. Bézier curves could offer an additional reliable and good estimation of the extrapolated region of the magnetization curves if the saturation point is known. For that reason, we analyzed the capabilities of Bézier curves for the extrapolation of measured magnetic curve data and compared the results with the analytic functions. In this analysis, we included Bézier curves of the sixth to ninth orders, as well as the representative analytic functions, i.e., the Elliot, Langevin, and inverse hyperbolic sine functions. These were selected based on the results in Sections 4.1 and 4.2.

The analysis was performed using input subsets \mathbf{H}_{in} , and we assumed that the saturation point was known, i.e., we fixed the last point as the saturation point $J_s(H_s)$. Then, we shortened the input subset gradually. In this way, we could analyze the influence of the measured input subset's size on the extrapolated part of the curve. The methodology is presented in Section 3.5.2 in cases (d)–(f). The measured and extrapolated curves of the NO27 electrical steel, where the input data were limited to the region between $[-H_{in,max}, H_{in,max}]$, where $H_{in,max} = 15$ kA/m, are shown in Figure 13.

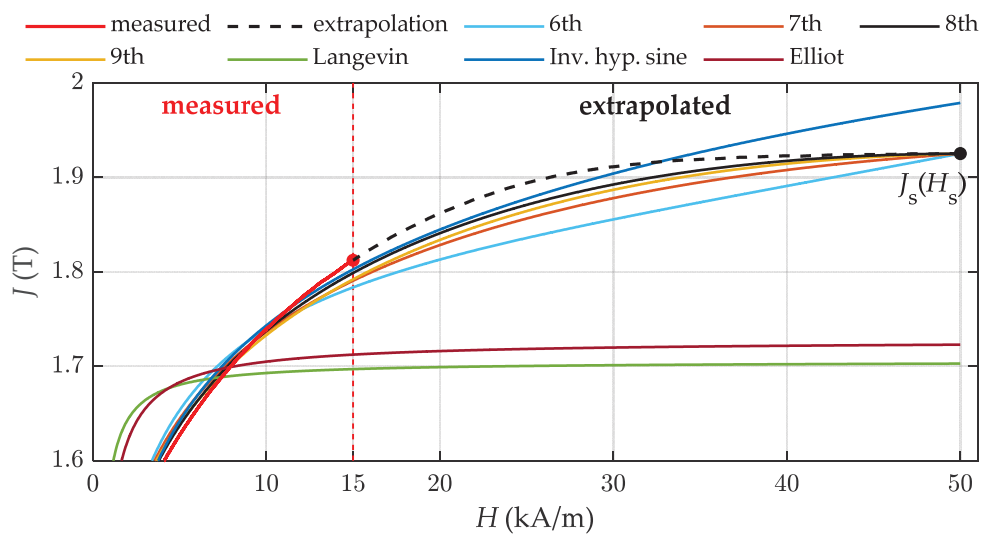


Figure 13. Extrapolation region for the anhysteretic curve with Bézier curves and analytic functions in the case where the input data were limited to the region between $[-15, 15]$ kA/m.

4.3.1. Anhysteretic Curves

First, we analyzed the goodness of fit for the full measured dataset of the anhysteretic curve, i.e., $\mathbf{H}_{eval,4} = \mathbf{H}_{meas}$ (case (d) in Section 3.5.2). The goodness of fit for these regions is presented in Figure 14a,b. The eighth- and ninth-order Bézier curves had the best goodness of fit in the whole data range, followed closely by the seventh-order and sixth-order Bézier curves. The NRMS deviation ε became constant when the input subset reached a certain range. This range was approximately $H_{in,max} = 20$ kA/m for both discussed materials. As the \mathbf{H}_{in} increased (and the extrapolation region decreased), ε decreased, which supports the conclusion from the previous analysis.

In the next step, we evaluated the deviations in two separate subregions of the approximated curves. The first was the subregion of the input data $\mathbf{H}_{eval,5} = [-H_{in,max}, H_{in,max}]$, as described in Section 3.5.2 (e). The second was the EXT subregion, as presented in Section 3.5.2 (f). The goodness of fit for $\mathbf{H}_{eval,5}$ is presented in Figure 14c,d, and for the EXT subregion $\mathbf{H}_{eval,6}$ in Figure 14e,f. For both regions, the eighth- and ninth-order Bézier curves generated the lowest NRMS error ε and offered the best estimation of the measured curve. In both subregions, the inverse hyperbolic sine function had the lowest deviation from the measured data out of the chosen analytic functions and was comparable to the results obtained with the sixth-order Bézier curve.

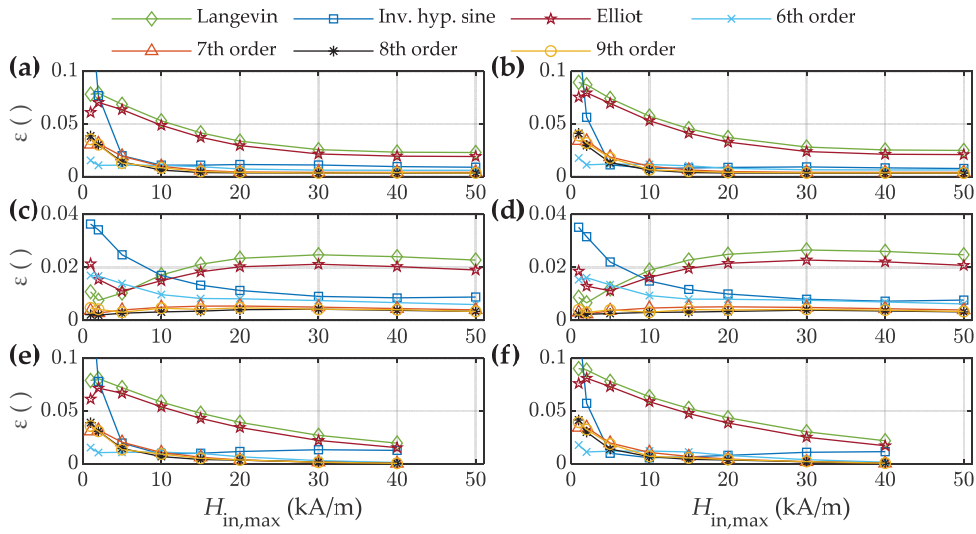


Figure 14. Calculated NRMS deviation ε within the individual input subsets $\mathbf{H}_{in} = -H_s \cup [-H_{in,max}, H_{in,max}] \cup H_s$ for the anhysteretic curve of two materials, NO35 (left column) and NO27 (right column), approximated with Bézier curves and analytic functions, including extrapolation (a,b) within the measured dataset $\mathbf{H}_{eval,4} = \mathbf{H}_{meas}$, (c,d) within the subregion $\mathbf{H}_{eval,5} = [-H_{in,max}, H_{in,max}]$ of the individual subsets, and (e,f) within the EXT subregion $\mathbf{H}_{eval,6}$ of the individual subsets.

4.3.2. Major Loop Curves

Figure 15 shows the calculated NRMS values ε obtained for the descending branch of the major loop. The conclusions are analogous to the analysis of the extrapolation of the anhysteretic curve. Overall, the eighth- and ninth-order Bézier curves offered the best goodness of fit, followed by the seventh-order Bézier curve. The sixth-order Bézier curve and the inverse hyperbolic sine function again had very similar results.

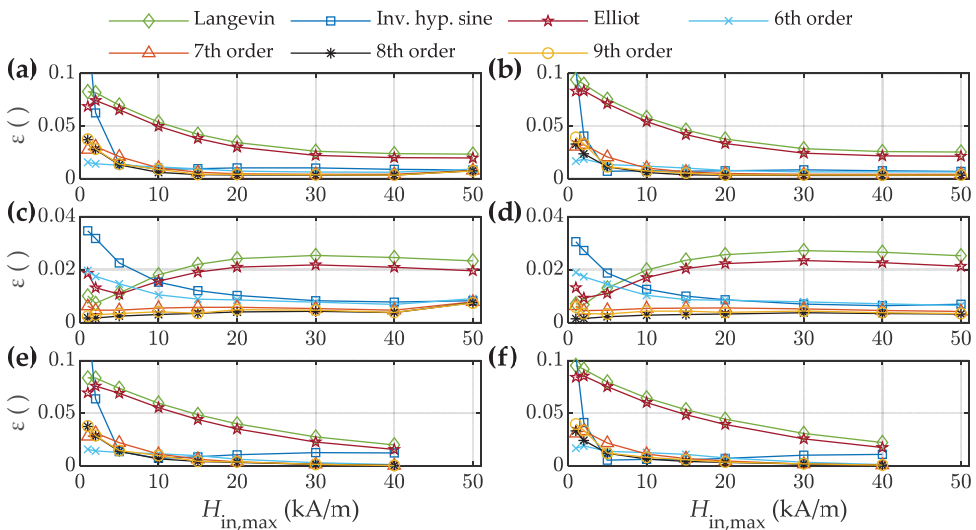


Figure 15. Calculated NRMS deviation ε within the individual input subsets $\mathbf{H}_{in} = -H_s \cup [-H_{in,max}, H_{in,max}] \cup H_s$ for the descending branch of the major loop of two materials, NO35 (left column) and NO27 (right column), approximated with Bézier curves and analytic functions, including extrapolation (a,b) within the measured dataset $\mathbf{H}_{eval,4} = \mathbf{H}_{meas}$, (c,d) within the subregion $\mathbf{H}_{eval,5} = [-H_{in,max}, H_{in,max}]$ of the individual subsets, and (e,f) within the EXT subregion $\mathbf{H}_{eval,6}$ of the individual subsets.

4.3.3. First Magnetization Curves

The results of the analysis of the first magnetization curve are presented in Figure 16. The Bézier curves again had superior results over the analytic functions in the case of the first magnetization curve. All orders from six to nine were suitable for the description of the first magnetization curve in all subsets and subregions in individual subsets. The results for the full region up to saturation are presented in Figure 16a,b, where the Bézier curves of orders seven to nine offered the best results. Slightly worse results were obtained using the sixth-order curve. In the region with the measured data (i.e., $[0, H_{in,max}]$) in Figure 16c,d, the results were in line with the full region. The extrapolation region in Figure 16e,f was the only region where one of the analytical functions, namely, the inverse hyperbolic sine function, came close to the accuracy of the Bézier curves. Among the Bézier curves, in the low-field-strength input datasets of up to $H_{in,max} = 5$ kA/m, the sixth-order Bézier curve had the lowest deviation, whereas in the more extended datasets, the seventh- to ninth-order Bézier curves again offered the best goodness of fit.

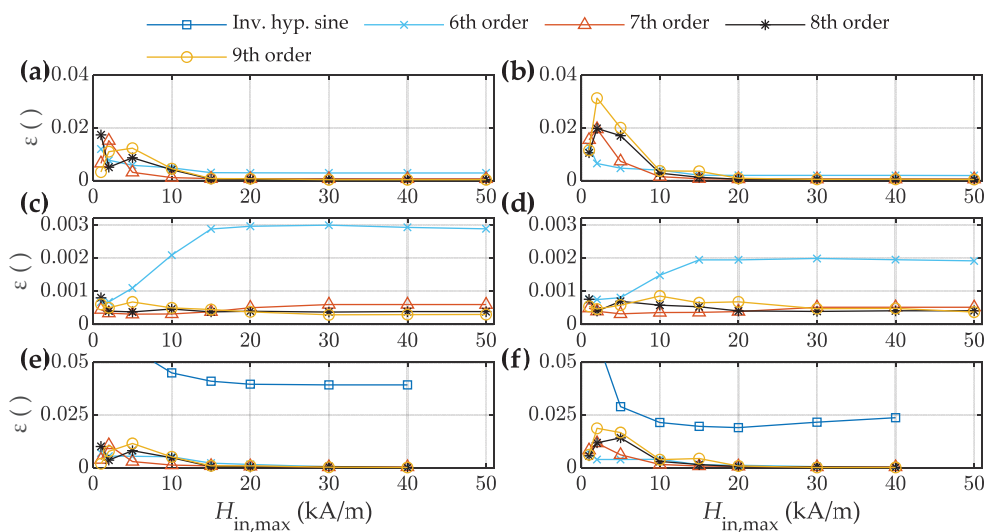


Figure 16. Calculated NRMS deviation ε within the individual input subsets $\mathbf{H}_{in} = -H_s \cup [-H_{in,max}, H_{in,max}] \cup H_s$ for the first magnetization curve of two materials, NO35 (left column) and NO27 (right column), approximated with Bézier curves and analytic functions, including extrapolation (a,b) within the measured dataset between 0 and H_s , (c,d) within the subregion between 0 and $H_{in,max}$ of the individual subsets, and (e,f) within the EXT subregion between $H_{in,max}$ and H_s of the individual subsets.

5. Discussion

Based on the results obtained within the performed analyses, the common takeaway is that both approaches, i.e., using adequate analytic functions or adequate Bézier curves, are suitable to describe or filter noisy measured data or extrapolate the nonlinear magnetic properties. Overall, Bézier curves of adequate orders (in most cases, between six and nine) offered significantly lower deviations from the measured curves compared with the analytic functions. The advantages and disadvantages of both approaches will be highlighted in this section.

Bézier curves are less sensitive to the size and range of the input dataset (limited by $H_{in,max}$) than analytic functions. This is especially highlighted in Figures 9 and 10, where it is shown that the Bézier curves had almost constant values of the NRMS deviation ε , whereas the Elliot function did not reach a constant value at different $H_{in,max}$. Further, as the order of Bézier curves increased (at a fixed maximum number of iterations of DE), starting from order nine, the goodness of fit became worse, which can be observed in Figures 9–11 (order 12 had a higher NRMS deviation ε than order 9). Therefore, not all higher orders are adequate for approximating or extrapolating the measured subsets.

A downside of analytic functions is that their final point does not reach the saturation value. This property can be observed in Figure 13. They are limited by their mathematical description. It is possible to force the functions to go through the saturation point exactly but with the tradeoff of increasing the deviations in other subregions of the curve significantly, to the extent that the description in them is useless. A special and limiting feature of Bézier curves is that their starting points and endpoints can be fixed exactly without losing the agreement with the measured data in any region (i.e., the first and last control points are interpolated, whereas the intermediate points are used to manipulate the shape and curvature of the curve). Furthermore, Bézier curves allow the slope at which the curve approaches saturation to be prescribed, as explained in Section 2.2.1. This can be both an advantage and a disadvantage. For example, a very accurate extrapolation is possible only when the saturation point of the material is known (e.g., can be calculated or estimated theoretically).

The straightforward calculation of derivatives in any point of the curve and, consequently, the curvature of the curve, allows for the precise determination of the shape of a curve under construction. Measured magnetic curves can have a lot of noise in the HP region as the maximum value of magnetic field density increases. Bézier curves have the potential to make the extraction of measured data easier. The user could set the theoretically known saturation value, the slope at which the saturation is reached, and the curvature in individual regions to obtain a symmetrical curve and, consequently, a symmetrical loop. In this way, the potential non-physical behavior of the obtained curves can be avoided (similar to the behavior of the curves in Figure 5b,d). In this work, the only prescribed limitation was not to exceed the value of magnetic polarization at saturation $J_s(H_s)$, i.e., the control points could have been placed anywhere below that point (and above the negative saturation $-J_s(-H_s)$). Additionally, pairwise symmetrical control points can be prescribed during the DE calculation to obtain symmetrical Bézier curves [40].

6. Conclusions

From the obtained results, we concluded that Bézier curves are promising candidates to adequately model the nonlinear properties of NO soft magnetic materials. Through the flexibility of curve order and adequate placement of control points, Bézier curves can approximate the shape of the magnetization curves with significantly lower deviation compared to analytic functions.

With the performed analysis, we concluded that Bézier curves from order six and higher are suitable for the approximation of the discussed magnetization curves. The approximation with those orders offers significantly improved fit based on the measured data compared with approximations with all the discussed analytic functions. In our specific case, the ninth order Bézier curve offered the best goodness of fit in all the analyzed subregions.

Bézier curves can approximate the high saturation region accurately (i.e., the extrapolation region). However, the theoretical point of saturation is required, in addition to the measurements in the HP subregion. To achieve high accuracy, it would be necessary to prescribe further boundary conditions at which the curve is generated. Examples are prescribing the slope for reaching the saturation region and adjusting the smoothness of the curvature along individual segments of the magnetization curve while calculating the control points. Our future work will focus on analyzing the conditions to generate symmetrical and accurate magnetization curves.

Author Contributions: Conceptualization, E.R. and M.P.; methodology, E.R. and M.P.; software, E.R.; validation, E.R.; formal analysis, E.R.; investigation, E.R.; resources, E.R.; data curation, E.R.; writing—original draft preparation, E.R.; writing—review and editing, E.R. and M.P.; visualization, E.R.; supervision, M.P.; project administration, M.P.; funding acquisition, M.P. All authors have read and agreed to the published version of the manuscript.

Funding: This research was funded by the Slovenian Research and Innovation Agency (ARIS) under grant numbers J7-3152 and P2-0115.

Data Availability Statement: Data available on request.

Conflicts of Interest: The authors declare no conflicts of interest.

References

1. Tellinen, J. A simple scalar model for magnetic hysteresis. *IEEE Trans. Magn.* **1998**, *34*, 2200–2206. [CrossRef]
2. Zirka, S.E.; Moroz, Y.I.; Harrison, R.G.; Chiesa, N. Inverse Hysteresis Models for Transient Simulation. *IEEE Trans. Power Deliv.* **2014**, *29*, 552–559. [CrossRef]
3. Vo, A.-T.; Fassenet, M.; Pr  ault, V.; Espanet, C.; Kedous-Lebouc, A. New formulation of Loss-Surface Model for accurate iron loss modeling at extreme flux density and flux variation: Experimental analysis and test on a high-speed PMSM. *J. Magn. Magn. Mater.* **2022**, *563*, 169935. [CrossRef]
4. Kokornaczyk, E.; Gutowski, M.W. Anhysteretic Functions for the Jiles–Atherton Model. *IEEE Trans. Magn.* **2015**, *51*, 1–5. [CrossRef]
5. Yang, J.; Shi, M.; Zhang, X.; Ma, Y.; Liu, Y.; Yuan, S.; Han, B. Demagnetization Parameters Evaluation of Magnetic Shields Based on Anhysteretic Magnetization Curve. *Materials* **2023**, *16*, 5238. [CrossRef] [PubMed]
6. M  r  e, G.; Leijon, M. Review of Hysteresis Models for Magnetic Materials. *Energies* **2023**, *16*, 3908. [CrossRef]
7. Steentjes, S.; Hameyer, K.; Dolinar, D.; Petrun, M. Iron-Loss and Magnetic Hysteresis Under Arbitrary Waveforms in NO Electrical Steel: A Comparative Study of Hysteresis Models. *IEEE Trans. Ind. Electron.* **2017**, *64*, 2511–2521. [CrossRef]
8. Bertotti, G. *Hysteresis in Magnetism: For Physicists, Materials Scientists, and Engineers*; Academic Press: Cambridge, MA, USA, 1998.
9. Tak  cs, J. A phenomenological mathematical model of hysteresis. *Compel* **2001**, *20*, 1002–1014. [CrossRef]
10. Jesenik, M.; Mernik, M.; Trlep, M. Determination of a Hysteresis Model Parameters with the Use of Different Evolutionary Methods for an Innovative Hysteresis Model. *Mathematics* **2020**, *8*, 201. [CrossRef]
11. Hofmann, M.J.; Herzog, H.-G. Modeling Magnetic Power Losses in Electrical Steel Sheets in Respect of Arbitrary Alternating Induction Waveforms: Theoretical Considerations and Model Synthesis. *IEEE Trans. Magn.* **2015**, *51*, 1–11. [CrossRef]
12. Bastos, J.P.A.; Hoffmann, K.; Leite, J.V.; Sadowski, N. A New and Robust Hysteresis Modeling Based on Simple Equations. *IEEE Trans. Magn.* **2018**, *54*, 1–4. [CrossRef]
13. Messal, O.; Vo, A.T.; Fassenet, M.; Mas, P.; Buffat, S.; Kedous-Lebouc, A. Advanced approach for static part of loss-surface iron loss model. *J. Magn. Magn. Mater.* **2020**, *502*, 166401. [CrossRef]
14. Szczyglowski, J. Use of quasi-static loops of magnetic hysteresis in loss prediction in non-oriented electrical steels. *Physica B* **2020**, *580*, 411812. [CrossRef]
15. Petrescu, L.; Cazacu, E.; Petrescu, C. Sigmoid functions used in hysteresis phenomenon modeling. In Proceedings of the 2015 9th International Symposium on Advanced Topics in Electrical Engineering (ATEE), Bucharest, Romania, 7–9 May 2015. [CrossRef]
16. Li, Q.; Li, J.-P.; Chen, L. A Bezier Curve-Based Font Generation Algorithm for Character Fonts. In Proceedings of the 2018 IEEE 20th International Conference on High Performance Computing and Communications; IEEE 16th International Conference on Smart City; IEEE 4th International Conference on Data Science and Systems (HPCC/SmartCity/DSS), Exeter, UK, 28–30 June 2018. [CrossRef]
17. Amat, N.F.I.C.; Yahya, Z.R.; Rusdi, N.A.; Helmee, N.A.; Muhamadd, W.Z.A.W. Arabic Fonts Representation in Cubic B  zier Curve using Different Soft Computing Algorithm. *IOP Conf. Ser. Mater. Sci. Eng.* **2019**, *705*, 012026. [CrossRef]
18. Vinayak, A.; Zakaria, M.A.; Baarath, K.; Majeed, A.P.P.A. A novel Bezier curve control point search algorithm for autonomous navigation using N-order polynomial search with boundary conditions. In Proceedings of the 2021 IEEE International Intelligent Transportation Systems Conference (ITSC), Indianapolis, IN, USA, 19–22 September 2021. [CrossRef]
19. Choi, J.-W.; Curry, R.; Elkaim, G. Path Planning Based on Bezier Curve for Autonomous Ground Vehicles. In Proceedings of the Advances in Electrical and Electronics Engineering—IAENG Special Edition of the World Congress on Engineering and Computer Science 2008, San Francisco, CA, USA, 22–24 October 2008. [CrossRef]
20. Han, L.; Yashiro, H.; Tehrani Nik Nejad, H.; Do, Q.H.; Mita, S. Bezier curve based path planning for autonomous vehicle in urban environment. In Proceedings of the 2010 IEEE Intelligent Vehicles Symposium, La Jolla, CA, USA, 21–24 June 2010. [CrossRef]
21. Satai, H.A.; Zahra, M.M.A.; Rasool, Z.I.; Abd-Ali, R.S.; Pruncu, C.I. B  zier Curves-Based Optimal Trajectory Design for Multirotor UAVs with Any-Angle Pathfinding Algorithms. *Sensors* **2021**, *21*, 2460. [CrossRef]
22. Coskun, O.; Turkmen, H.S. Multi-objective optimization of variable stiffness laminated plates modeled using Bezier curves. *Compos. Struct.* **2022**, *279*, 114814. [CrossRef]
23. Nuntawisuttawong, T.; Dejdumrong, N. An Approximation of B  zier Curves by a Sequence of Circular Arcs. *Inf. Technol. Control* **2021**, *50*, 213–223. [CrossRef]
24. Tiismus, H.; Kallaste, A.; Vaimann, T.; Lind, L.; Virro, I.; Rass  lkin, A.; Dedova, T. Laser Additively Manufactured Magnetic Core Design and Process for Electrical Machine Applications. *Energies* **2022**, *15*, 3665. [CrossRef]
25. Hussain, S.; Kallaste, A.; Vaimann, T. Recent Trends in Additive Manufacturing and Topology Optimization of Reluctance Machines. *Energies* **2023**, *16*, 3840. [CrossRef]
26. Matwankar, C.S.; Pramanick, S.; Singh, B. Flux-linkage Characterization and Rotor Position Estimation of Switched Reluctance Motor using B  zier Curves. In Proceedings of the 2021 IEEE 2nd International Conference on Smart Technologies for Power, Energy and Control (STPEC), Bilaspur, India, 19–22 December 2021. [CrossRef]

27. Louzazni, M.; Al-Dahidi, S. Approximation of photovoltaic characteristics curves using Bezier Curve. *Renew. Energy* **2021**, *174*, 715–732. [CrossRef]
28. Shi, N.; Lv, Y.L.; Zhang, Y.C.; Zhu, X.H. Linear fitting Rule of I-V characteristics of thin-film cells based on Bezier function. *Energy* **2023**, *278*, 127997. [CrossRef]
29. Cui, X.; Li, Y.; Xu, L. Adaptive Extension Fitting Scheme: An Effective Curve Approximation Method Using Piecewise Bézier Technology. *IEEE Access* **2023**, *11*, 58422–58435. [CrossRef]
30. Said Mad Zain, S.A.A.A.; Misro, M.Y.; Miura, K.T. Generalized Fractional Bézier Curve with Shape Parameters. *Mathematics* **2021**, *9*, 2141. [CrossRef]
31. Rahmanović, E.; Petrun, M. Approximation of nonlinear properties of soft-magnetic materials with Bézier curves. In Proceedings of the 2023 IEEE International Magnetic Conference—Short Papers (INTERMAG Short Papers), Sendai, Japan, 15–19 May 2023. [CrossRef]
32. Steentjes, S.; Petrun, M.; Glehn, G.; Dolinar, D.; Hameyer, K. Suitability of the double Langevin function for description of anhysteretic magnetization curves in NO and GO electrical steel grades. *AIP Adv.* **2017**, *7*, 056013. [CrossRef]
33. Skarlatos, A.; Theodoulidis, T. A Modal Approach for the Solution of the Non-Linear Induction Problem in Ferromagnetic Media. *IEEE Trans. Magn.* **2016**, *52*, 1–11. [CrossRef]
34. Baydas, S.; Karakas, B. Defining a curve as a Bezier curve. *J. Taibah Univ. Sci.* **2019**, *13*, 522–528. [CrossRef]
35. Ezhov, N.; Neitzel, F.; Petrovic, S. Spline Approximation, Part 2: From Polynomials in the Monomial Basis to B-splines—A Derivation. *Mathematics* **2021**, *9*, 2198. [CrossRef]
36. Kiliçoglu, Ş.; Şenyurt, S. On the matrix representation of 5th order Bézier Curve and derivatives in E^3 . *Commun. Fac. Sci. Univ. Ank. Ser. A1 Math. Stat.* **2022**, *71*, 133–152. [CrossRef]
37. Kilicoglu, S.; Yurttancikmaz, S. How to approximate cosine curve with 4th and 6th order Bezier curve in plane? *Therm. Sci.* **2022**, *26*, 559–570. [CrossRef]
38. Rovenski, V. Piecewise Curves and Surfaces. In *Modeling of Curves and Surfaces with MATLAB®*; Springer: New York, NY, USA, 2010; pp. 357–411.
39. Pijls, H.; Quan, L.P. A Computational Method with Maple for Finding the Maximum Curvature of a Bézier-Spline Curve. *Math. Comput. Appl.* **2023**, *28*, 56. [CrossRef]
40. Sanchez-Reyes, J. Detecting symmetries in polynomial Bezier curves. *J. Comput. Appl. Math.* **2015**, *288*, 274–283. [CrossRef]
41. Pandunata, P.; Shamsuddin, S.M.H. Differential Evolution Optimization for Bezier Curve Fitting. In Proceedings of the 2010 Seventh International Conference on Computer Graphics, Imaging and Visualization, Sydney, Australia, 7–10 August 2010. [CrossRef]
42. Ezhov, N.; Neitzel, F.; Petrovic, S. Spline approximation, Part 1: Basic methodology. *J. Appl. Geod.* **2018**, *12*, 139–155. [CrossRef]
43. Wang, L.; Ding, F.; Yang, D.; Wang, K.; Jiao, B.; Chen, Q. A fitting-extrapolation method of B-H curve for magnetic saturation applications. *COMPEL Int. J. Comput. Math. Electr. Electron. Eng.* **2023**, *42*, 494–505. [CrossRef]

Disclaimer/Publisher’s Note: The statements, opinions and data contained in all publications are solely those of the individual author(s) and contributor(s) and not of MDPI and/or the editor(s). MDPI and/or the editor(s) disclaim responsibility for any injury to people or property resulting from any ideas, methods, instructions or products referred to in the content.

Article

Optimization of an IPMSM for Constant-Angle Square-Wave Control of a BLDC Drive

Mitja Garmut ^{1,*}, Simon Steentjes ² and Martin Petrun ¹

¹ Institute of Electrical Power Engineering, Faculty of Electrical Engineering and Computer Science, University of Maribor, 2000 Maribor, Slovenia; martin.petrun@um.si

² Hilti Entwicklungsgesellschaft mbH, 86916 Kaufering, Germany; simon.steentjes@hilti.com

* Correspondence: mitja.garmut@um.si

Abstract: Interior permanent magnet synchronous machines (IPMSMs) driven with a square-wave control (i.e., six-step, block, or 120° control), known commonly as brushless direct current (BLDC) drives, are used widely due to their high power density and control simplicity. The advance firing (AF) angle is employed to achieve improved operation characteristics of the drive. The AF angle is, in general, applied to compensate for the commutation effects. In the case of an IPMSM, the AF angle can also be adjusted to exploit reluctance torque. In this paper, a detailed study was performed to understand its effect on the drive's performance in regard to reluctance torque. Furthermore, a multi-objective optimization of the machine's cross-section using neural network models was conducted to enhance performance at a constant AF angle. The reference and improved machine designs were evaluated in a system-level simulation, where the impact was considered of the commutation of currents. A significant improvement in the machine performance was achieved after optimizing the geometry and implementing a fixed AF angle of 10°.

Keywords: maximum torque per ampere (MTPA); interior permanent magnet synchronous machine (IPMSM); brushless direct current (BLDC) drive; rotor optimization; square-wave control; advance firing angle; neural network

MSC: 78-10

1. Introduction

One way to operate permanent magnet synchronous machines (PMSMs) is to drive them with a square-wave control (SWC) (i.e., six-step, block, or 120° control), known commonly as the brushless direct current (BLDC) drive. This drive system does not require exact continuous knowledge of the rotor position, but only six position states are determined, typically delivered by three Hall sensors. Further, only the direct current (DC) is measured, resulting in a cheap and simple implementation. Fundamental studies on the BLDC drives were provided in [1,2], where the fundamental working principles of SWC are presented. The research on this topic has been accelerated in recent years. The average-value modeling of BLDC drives for more effective machine control was introduced in [3]. A detailed analysis of different control methods for BLDC drives, where the commutation interval extends over 120°, was presented in [4]. The maximum torque per ampere (MTPA) control of BLDC drives is presented in [5]. How to reduce the torque ripple in a BLDC drive is presented in [6], and an active disturbance rejection SWC is described in [7], whereas [8] gives a state-of-the-art review of the BLDC drive technology.

As such machines are driven by the SWC, the square-wave-like currents produced in the machine's windings exhibit a commutation interval, which is a consequence of activating individual windings and a finite current rise time due to their leakage inductance. The commutation analysis of BLDC drives is presented in more detail in [9]. Reduction of

commutation torque ripple in BLDC drives through detailed analysis of the commutation interval and the implementation of an appropriate voltage vector is discussed in [10]. To compensate for the negative effects of commutation, adjusting the advance firing (AF) angle α (also called the pre-commutation angle) by a fixed value is a common strategy [11]. This adjustment aligns the back electromotive force (EMF) approximately with the commutating current in individual phases at maximum current [5,11]. However, as the relative duration of the commutation interval varies with speed and current amplitude, a single, fixed AF angle α is not the most adequate solution when operating at lower loads, i.e., in the majority of the operation range. The problem was addressed by developing a compensation method that aligns the fundamental harmonic components of the back EMF and the current precisely with an alignment AF angle α_{al} [5].

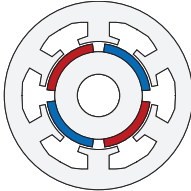
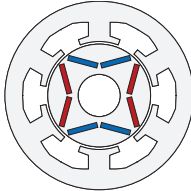
Operating machines at very high speeds is often necessary for applications that require high power densities. Due to the high speed, interior magnets are often used, resulting in interior permanent magnet synchronous machines (IPMSMs), which are characterized by their generation of magnetic and reluctance torque components. The two torque components are discussed in detail in [12]. The magnetic torque is caused by the permanent magnet, whereas the reluctance torque is caused because of the difference in the air gap along the rotor circumference. To utilize both torques fully, in general, the concept of MTPA control is applied, which is well known when the IPMSM is controlled with field-oriented control (FOC), as first shown in [13], and has been applied and researched widely. A unified theory for optimal feedforward torque control, including MTPA control, is presented in [14]. Many authors are researching this topic, the MTPA strategy for direct torque control for an IPMSM was deployed in [15], the signal injection to correct the MTPA angle in an IPMSM was deployed in [16], and the constraints for obtaining the MTPA line for PMSM control are presented in [17]. The best fit of the nonlinear MTPA line, which was then used in the control of the IPMSM, is presented in [18].

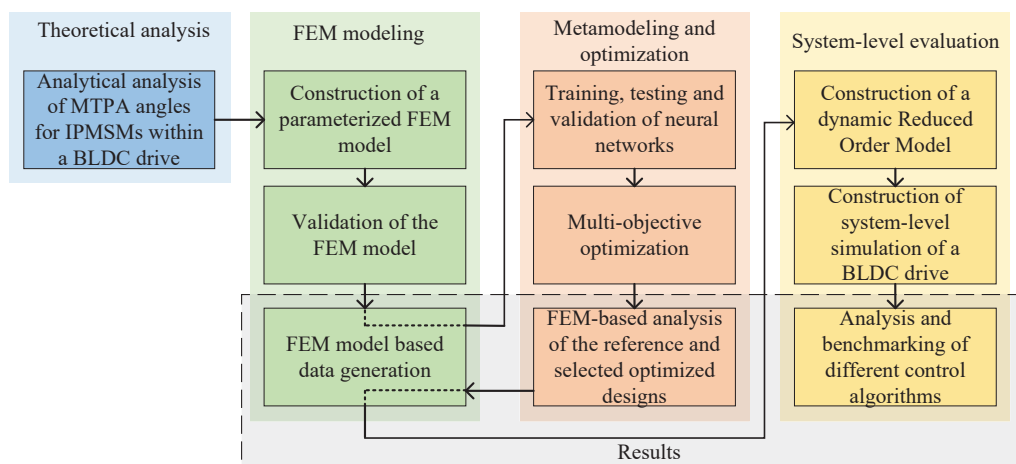
Determining the MTPA operation for IPMSMs driven with a SWC is not well-researched. In the case of IPMSMs within BLDC drives, MTPA operations can be achieved by adjusting the AF angle α , where the MTPA AF angle α_M , (hereafter referred to as the MTPA angle) is defined as the AF angle α , which results in the maximal torque at a specific current. It is comprised of the alignment AF angle α_{al} to compensate for the commutation effect and the reluctance AF angle α_r , to exploit additional reluctance torque. In [4,5], the MTPA control algorithm for SWC was firstly presented for surface permanent magnet synchronous machines (SPMSMs), where the reluctance AF angle α_r , was zero, as only the magnetic torque component was present. On the other hand, the reluctance AF angle α_r , should be adjusted according to the load current (i.e., its peak value I_p) when using IPMSMs. To highlight the distinctions between IPMSMs and SPMSMs, the key differences that influence α_M are summarized in Table 1 and presented in [12,19]. Notably, IPMSMs achieve improved performance when the reluctance AF angle α_r is considered.

The main aim of this research was to enhance the drive's performance by increasing the torque-to-current ratio for greater power efficiency, minimizing torque ripple, and maintaining the simplicity of the control system. Further information on how the drive's performance is enhanced by a greater torque-to-current ratio is presented in [1]. A systematic approach was pursued, to achieve the stated goals, as presented schematically in Figure 1.

First, the ideal square-wave currents were analyzed to show the theoretical MTPA operation. The analysis was similar to [20], where a comparative study was performed between square-wave and sinusoidal current supplies. Second, the theoretical effect was showcased on an existing experimentally validated finite element method (FEM) IPMSM model. As such machines were highly saturated due to their high power densities, and a FEM model was used to simulate the performance. Parameter identification of a saturated IPMSM was discussed in [21], where [22] used a FEM model to model the IPMSM accurately.

Table 1. Comparison between IPMSMs and SPMSMs.

	SPMSMs	IPMSMs
	mounted on the rotor surface	embedded within the rotor
magnet position		
magnetic circuit	constant reluctance, independent on the rotor position	varying reluctance, dependent on the rotor position
torque	due to permanent magnets	due to permanent magnets and varying reluctance
torque-to-current ratio	lower	higher
power density	lower	higher
flux-weakening capability	lower	higher
MTPA AF angle adjustment	none, $\alpha_r = 0$	dependent on load current, i.e., $\alpha_r(I_p)$

**Figure 1.** Schematic presentation of the applied methodology.

In the next step, a multi-objective optimization of the rotor and pole shoe geometry was performed to enhance the performance. A comprehensive tutorial of multi-objective optimization using genetic algorithms is provided in [23], where [24] provides a state-of-the-art summary of different algorithms. Machine geometry optimizations have been presented in many works. A review study is presented in [25]. An optimization to enhance the performance by employing the FEM model directly is presented in [26,27]. A multi-level multi-objective optimization, where the objectives and parameters are split into levels, is presented in [28]. The FEM analysis was also exchanged with a metamodel (i.e., the Kriging model). The presented optimization in this study was also performed based on a metamodel trained with a feedforward neural network. Exchanging a computationally expensive numerical evaluation with a neural network was presented in [29–31]. A neural network metamodel was used in a multi-objective optimization in [32]. An overview of how machine learning is used in the design optimization of electromagnetic devices is given in [33].

Third, the selected IPMSM design and the reference design were implemented in a system-level simulation, where the nonlinear IPMSM, inverter, and control were coupled, as

shown in [18,34]. How to implement the abc reference frame IPMSM model in a simulation is presented in [35], whereas [36] shows how to reduce the computation time to obtain nonlinear machine models for system-level simulation. This allowed us to analyze the effect of the communication and analyze different simple and advanced control techniques for BLDC drives.

This paper is organized as follows. Section 2 presents the theoretical background of the MTPA angle α_M , behavior in square-wave-shaped-driven IPMSMs. The experimental validation of the FEM reference IPMSM design is presented in Section 3. Furthermore, optimization is presented to achieve the set goals. The results are presented in Section 4; the results include a system-level simulation analysis, where the influence was analyzed of the non-ideal current excitations on the optimization objectives and the operation range. Section 4 highlights the conclusions.

2. Theoretical Background

2.1. Dynamic Model of an IPMSM within BLDC Drives

A typical Hall sensor-controlled BLDC drive is presented in Figure 2. The voltage–balance equation in the abc reference frame for the IPMSM is given by (1)

$$\begin{bmatrix} u_a \\ u_b \\ u_c \end{bmatrix} = \begin{bmatrix} R & 0 & 0 \\ 0 & R & 0 \\ 0 & 0 & R \end{bmatrix} \begin{bmatrix} i_a \\ i_b \\ i_c \end{bmatrix} + \begin{bmatrix} L_{aa} & L_{ab} & L_{ac} \\ L_{ba} & L_{bb} & L_{bc} \\ L_{ca} & L_{cb} & L_{cc} \end{bmatrix} \frac{d}{dt} \begin{bmatrix} i_a \\ i_b \\ i_c \end{bmatrix} + \dot{\theta} \frac{\partial}{\partial \theta} \left(\begin{bmatrix} L_{aa} & L_{ab} & L_{ac} \\ L_{ba} & L_{bb} & L_{bc} \\ L_{ca} & L_{cb} & L_{cc} \end{bmatrix} \begin{bmatrix} i_a \\ i_b \\ i_c \end{bmatrix} + \begin{bmatrix} \Psi_{am} \\ \Psi_{bm} \\ \Psi_{cm} \end{bmatrix} \right), \quad (1)$$

where $\mathbf{u}_{abc} = [u_a \ u_b \ u_c]^T$ are the phase voltages, $\mathbf{i}_{abc} = [i_a \ i_b \ i_c]^T$ are the phase currents, $\mathbf{\Psi}_m = [\Psi_{am} \ \Psi_{bm} \ \Psi_{cm}]^T$ are the flux linkages generated by the permanent magnets, θ is the rotor position (i.e., electrical angle), and the phase resistances of the stator windings are $R = \text{diag}[R \ R \ R]$ [35]. L is the inductances matrix, where L_{aa} , L_{bb} and L_{cc} are the self-inductances, $L_{ab} = L_{ba}$, $L_{ac} = L_{ca}$, and $L_{bc} = L_{cb}$ are the mutual inductances, and $\dot{\theta}$ is the electrical angular velocity of the rotor. By highlighting that $L(\theta)$ and $\mathbf{\Psi}_m(\theta)$ are dependent on the electrical rotor position θ , (1) can be expressed in matrix form by (2)

$$\mathbf{u}_{abc} = \mathbf{R}\mathbf{i}_{abc} + \frac{d}{dt}[\mathbf{L}(\theta)\mathbf{i}_{abc} + \mathbf{\Psi}_m(\theta)]. \quad (2)$$

The electromagnetic torque is defined by (3)

$$t_e = t_{em} + t_{er} = p_p \left[\mathbf{i}_{abc}^T \frac{\partial \mathbf{\Psi}_m(\theta)}{\partial \theta} + \frac{1}{2} \mathbf{i}_{abc}^T \frac{\partial \mathbf{L}(\theta)}{\partial \theta} \mathbf{i}_{abc} \right], \quad (3)$$

where t_{em} is the magnetic torque component, t_{er} is the reluctance torque component, and p_p is the number of pole pairs [35]. If $L(\theta)$ and $\mathbf{\Psi}_m(\theta)$ from (1) are combined with (3), t_e can be expressed by (4)

$$\begin{aligned} t_e = & \frac{1}{2} p_p \left[i_a^2 \frac{\partial L_{aa}}{\partial \theta} + i_b^2 \frac{\partial L_{bb}}{\partial \theta} + i_c^2 \frac{\partial L_{cc}}{\partial \theta} \right] \\ & + p_p \left[i_a i_b \frac{\partial L_{ab}}{\partial \theta} + i_b i_c \frac{\partial L_{bc}}{\partial \theta} + i_a i_c \frac{\partial L_{ac}}{\partial \theta} \right] \\ & + p_p \left[i_a \frac{\partial \Psi_{am}}{\partial \theta} + i_b \frac{\partial \Psi_{bm}}{\partial \theta} + i_c \frac{\partial \Psi_{cm}}{\partial \theta} \right]. \end{aligned} \quad (4)$$

By employing (1) and (4), one can describe the electromagnetic behavior of the IPMSM in the abc reference frame fully for any given resistances, position-dependent inductances, and position-dependent flux linkages generated by the permanent magnet. The inductances are position-dependent due to the difference in the air gap along the rotor circumference,

which is typical for all types of IPMSM. The flux linkages are fundamentally position-dependent due to the magnets rotating in the machine [1].

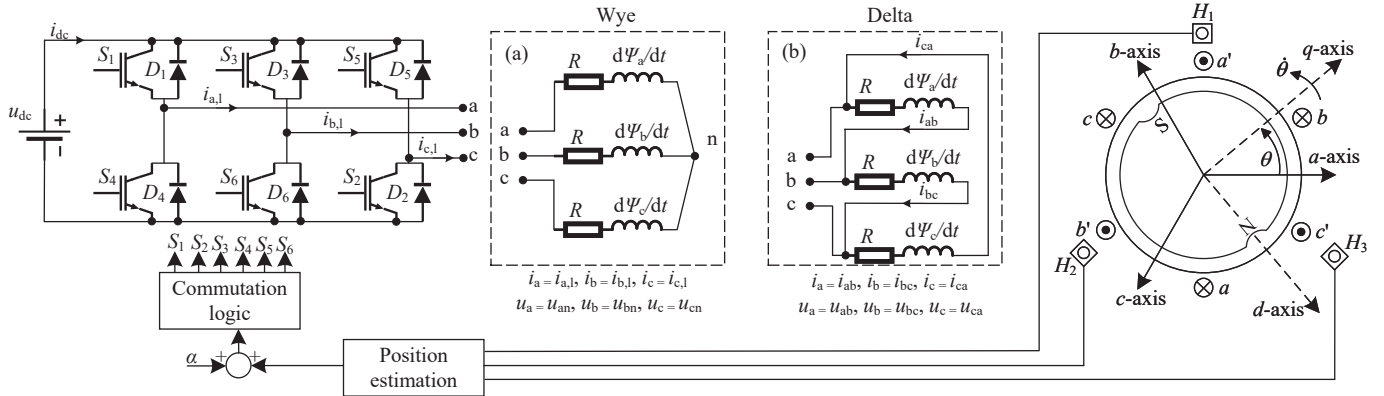


Figure 2. Schematic presentation of a typical BLDC drive, controlled by square-wave control (SWC), which is based on the Hall sensor position feedback. The windings of the machine can be connected into (a) wye and (b) delta connections. The commutation logic is presented in [3], and the position estimation is presented in [4].

2.2. MTPA Angle of an Ideal BLDC Drive

In a typical BLDC drive, an IPMSM is driven with an SWC that controls the metal oxide semiconductor field effect transistors (MOSFETs) S_1 , S_2 , S_3 , S_4 , S_5 , and S_6 , which are switched based on the signals obtained from three Hall-effect sensors, H_1 , H_2 , and H_3 , as presented in Figure 2. The delta and wye (i.e., star) winding connection types are presented in Figure 2a,b, respectively. Both are the subject of the presented analysis.

Operating the machine with SWC requires a commutation inverter that excites the machine phases with square-wave-shaped currents; which are presented in Figure 3b in their ideal form, i.e., without the commutation interval. The machine design should ideally provide a back EMF e_{abc} shape that matches the square-wave-shaped current waveform i_{abc} as closely as possible, as presented in Figure 3. If the machine was an SPMSM and the AF angle α , was zero, such a complement between the shapes of i_{abc} and e_{abc} would produce the maximal possible torque t_e . However, if the design is an IPMSM, the MTPA operation can be achieved by shifting the activation of individual phases adequately, which results in an AF angle α . The AF angle α , can be defined as the phase shift between the fundamental harmonic components of the phase currents i_{abc} and the EMF e_{abc} , as presented in Figure 3.

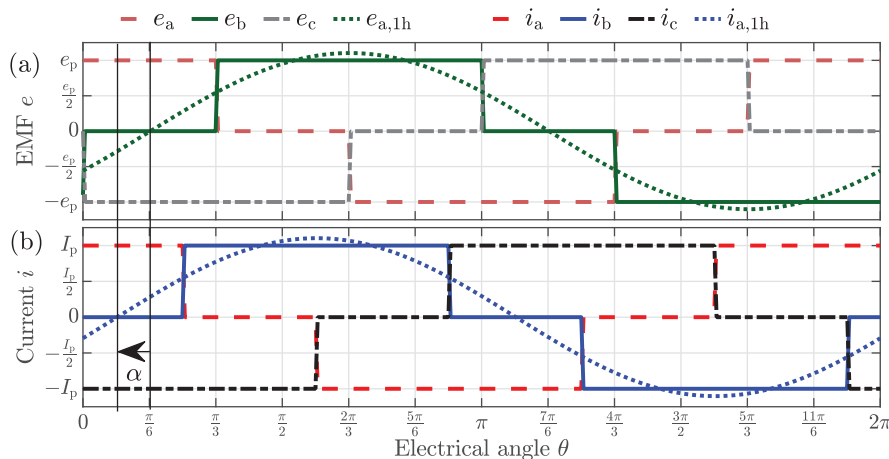


Figure 3. The shape of the variables in a theoretically ideal BLDC drive: (b) phase EMFs and (a) corresponding ideal phase currents without commutation interval. the AF angle, α , is, in general, defined as a shift between the first harmonic component of the current and the corresponding back EMF.

When operating the machine with actual currents, a commutation interval occurs, requiring a shift in the AF angle α , to align the EMFs e_{abc} adequately with the currents i_{abc} , and generate the maximal torque t_e . This angle, known as the alignment AF angle α_{al} , synchronizes the fundamental harmonic components of the back EMF e_{abc} and the current i_{abc} .

When an IPMSM is excited with ideal-shaped square-wave currents, the maximal torque t_e , is produced at a specific α , called the reluctance AF angle α_r . This shift is caused by the induced voltage due to the position-dependent inductances $L(\theta)$, presented in Figure 4b. The inductance does not impact the EMF in no load, but when the machine is operating under different loads, the shape of the EMF changes, requiring operation at an adequate α_r .

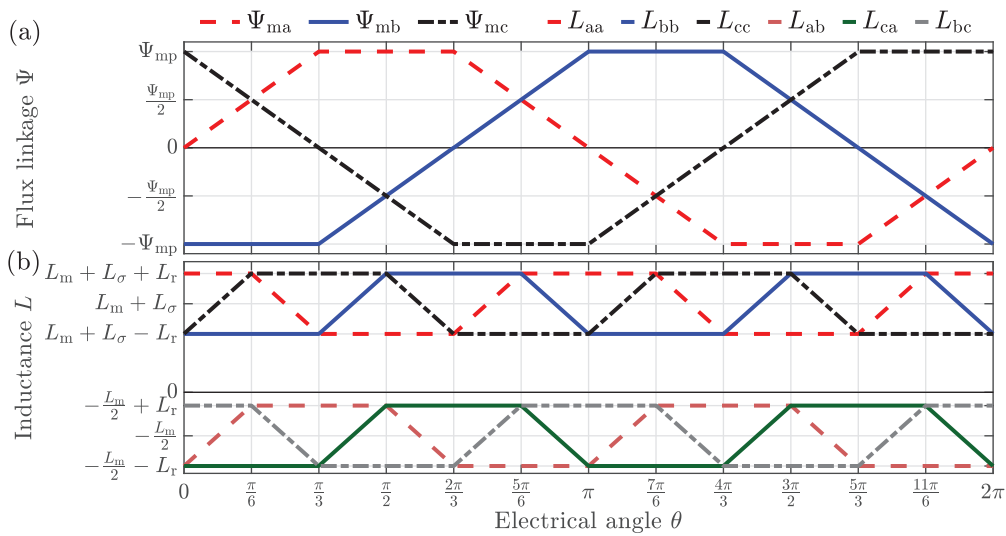


Figure 4. The shape of flux linkages and inductances in the theoretical ideal BLDC drive: (a) trapezoidal flux linkage results in square-wave EMFs, and (b) in an IPMSM, additional trapezoidal dependent inductances can be assumed, which impact the EMFs when the drive is loaded.

By considering the commutation effect and additional reluctance torque t_{er} , in an IPMSM, the total MTPA angle α_M , is defined by (5)

$$\alpha_M = \alpha_{al} + \alpha_r. \quad (5)$$

The analysis in this section treats the impact of reluctance torque t_{er} , on the α_M of an IPMSM specifically, assuming the absence of commutation effects (i.e., ideal-shaped square-wave currents are assumed). This results in the MTPA angle α_M , matching the reluctance AF angle α_r (i.e., $\alpha_M = \alpha_r$). Additionally, the following assumptions are made:

- Wye-connected windings of the IPMSM (i.e., phase currents i_{abc} , were identical to the line currents $i_{abc,l}$, as presented in Figure 2).
- The design of the IPMSM is such that $t_{em} > t_{er}$ and $L_q \geq L_d$.
- The torque t_e , exhibits periodic repetition every $\pi/3$, reflecting the symmetry in a three-phase system, as demonstrated in [36]. Consequently, the analysis can be performed for a $1/6$ electrical rotation of the rotor.
- The analysis of the AF angle α , was restricted to $\pi/3$ due to the definition of the involved variables.

The ideal square-wave currents $i_{abc}(\theta)$, presented in Figure 3b can be defined by (6)

$$\mathbf{i}_{abc}(\theta) = \begin{bmatrix} i_a \\ i_b \\ i_c \end{bmatrix} = \begin{bmatrix} \begin{cases} I_p, & 0 \leq \theta < \frac{\pi}{3} - \alpha \\ 0, & \frac{\pi}{3} - \alpha \leq \theta < \frac{\pi}{3} \end{cases} \\ \begin{cases} 0, & 0 \leq \theta < \frac{\pi}{3} - \alpha \\ I_p, & \frac{\pi}{3} - \alpha \leq \theta < \frac{\pi}{3} \end{cases} \\ \begin{cases} I_p, & 0 \leq \theta < \frac{\pi}{3} - \alpha \\ -I_p, & \frac{\pi}{3} - \alpha \leq \theta < \frac{\pi}{3} \end{cases} \end{bmatrix}, \quad (6)$$

where I_p is the peak current value. The ideal matching flux linkages $\Psi_m(\theta)$, have a trapezoidal form, resulting in a perfect square wave back EMF $e_{abc}(\theta) = \theta \frac{\partial \Psi_m(\theta)}{\partial \theta}$. Such flux linkages $\Psi_m(\theta)$, are defined by (7)

$$\Psi_m(\theta) = \begin{bmatrix} \Psi_{am} \\ \Psi_{bm} \\ \Psi_{cm} \end{bmatrix} = \begin{bmatrix} \begin{cases} \frac{3}{\pi} \Psi_{mp} \theta, & 0 \leq \theta < \frac{\pi}{3} \\ -\Psi_{mp}, & \frac{\pi}{3} \leq \theta < \frac{2\pi}{3} \end{cases} \\ \begin{cases} -\Psi_{mp}, & 0 \leq \theta < \frac{\pi}{3} \\ \frac{3}{\pi} \Psi_{mp} \theta + \Psi_{mp}, & \frac{\pi}{3} \leq \theta < \frac{2\pi}{3} \end{cases} \\ \begin{cases} \frac{3}{\pi} \Psi_{mp} \theta + \Psi_{mp}, & 0 \leq \theta < \frac{\pi}{3} \\ -\Psi_{mp}, & \frac{\pi}{3} \leq \theta < \frac{2\pi}{3} \end{cases} \end{bmatrix}, \quad (7)$$

where Ψ_{mp} is the peak flux linkage generated by the permanent magnets. The flux linkages are presented in Figure 4a.

The inductance matrix $L(\theta)$ is defined with trapezoidal self and mutual inductances by (8)

$$\begin{aligned} L_{aa} &= \begin{cases} L_m + L_\sigma + L_r, & 0 \leq \theta < \frac{\pi}{6} \\ -\frac{12L_r}{\pi} \theta + L_m + L_\sigma + 3L_r, & \frac{\pi}{6} \leq \theta < \frac{\pi}{3} \end{cases} \\ L_{bb} &= \begin{cases} L_m + L_\sigma - L_r, & 0 \leq \theta < \frac{\pi}{3} \end{cases} \\ L_{cc} &= \begin{cases} \frac{12L_r}{\pi} \theta + L_m + L_\sigma - L_r, & 0 \leq \theta < \frac{\pi}{6} \\ L_m + L_\sigma + L_r, & \frac{\pi}{6} \leq \theta < \frac{\pi}{3} \end{cases} \\ L_{ab} &= \begin{cases} \frac{12L_r}{\pi} \theta - \frac{L_m}{2} - L_r, & 0 \leq \theta < \frac{\pi}{6} \\ -\frac{L_m}{2} + L_r, & \frac{\pi}{6} \leq \theta < \frac{\pi}{3} \end{cases} \\ L_{ac} &= \begin{cases} -\frac{L_m}{2} - L_r, & 0 \leq \theta < \frac{\pi}{3} \end{cases} \\ L_{bc} &= \begin{cases} -\frac{L_m}{2} + L_r, & 0 \leq \theta < \frac{\pi}{6} \\ \frac{12L_r}{\pi} \theta - \frac{L_m}{2} + 2L_r, & \frac{\pi}{6} \leq \theta < \frac{\pi}{3} \end{cases} \end{aligned} \quad (8)$$

where L_m is the magnetizing inductance, L_σ is the leakage inductance, and L_r is the amplitude value of the fundamental harmonic of the magnetizing (reluctance) inductance. The position-dependent inductances are shown in Figure 4b.

By inserting (6) and (7) into (3) and integrating the representative interval from $\theta = 0$ to $\theta = \pi/3$ by (9)

$$t_{em,avg} = \frac{3p_p}{\pi} \int_0^{\frac{\pi}{3}} \left(i_a \frac{\partial \Psi_{am}}{\partial \theta} + i_b \frac{\partial \Psi_{bm}}{\partial \theta} + i_c \frac{\partial \Psi_{cm}}{\partial \theta} \right) d\theta, \quad (9)$$

which is valid for changes in the AF angle α from 0 to $\pi/3$, we derived (10)

$$t_{em,avg} = \left\{ \frac{3}{\pi^2} p_p I_p \Psi_{mp} (2\pi - 3\alpha), \quad 0 \leq \alpha < \frac{\pi}{3} \right\}. \quad (10)$$

The obtained average torque $t_{em,avg}$, is linearly dependent on α , and reaches maximal value at $\alpha = 0$, as presented in Figure 5a. Analogously, we derive the reluctance torque (12) by inserting (6) and (8) into (3), and integrating the representative interval from $\theta = 0$ to $\theta = \pi/3$ by (11)

$$t_{er,avg} = \frac{3p_p}{2\pi} \int_0^{\frac{\pi}{3}} \left(i_a^2 \frac{\partial L_{aa}}{\partial \theta} + i_b^2 \frac{\partial L_{bb}}{\partial \theta} + i_c^2 \frac{\partial L_{cc}}{\partial \theta} + 2i_a i_b \frac{\partial L_{ab}}{\partial \theta} + 2i_b i_c \frac{\partial L_{bc}}{\partial \theta} + 2i_a i_c \frac{\partial L_{ac}}{\partial \theta} \right) d\theta, \quad (11)$$

which is also valid for AF angle α changes from 0 to $\pi/3$. The average reluctance torque can be expressed in two sections by (12)

$$t_{er,avg} = \begin{cases} \frac{54}{\pi^2} p_p I_p^2 L_r \alpha, & 0 \leq \alpha < \frac{\pi}{6} \\ \frac{9}{\pi} p_p I_p^2 L_r, & \frac{\pi}{6} \leq \alpha < \frac{\pi}{3} \end{cases} \quad (12)$$

The obtained average torque $t_{er,avg}$, is linearly dependent on α within the interval $\alpha < \frac{\pi}{6}$, but is constant above $\frac{\pi}{6}$, as presented in Figure 5b. Overall, due to the presented assumptions $t_{er,avg}$ is smaller than $t_{em,avg}$. The total average torque $t_{e,avg}$, is defined by (13)

$$t_{e,avg} = t_{em,avg} + t_{er,avg}. \quad (13)$$

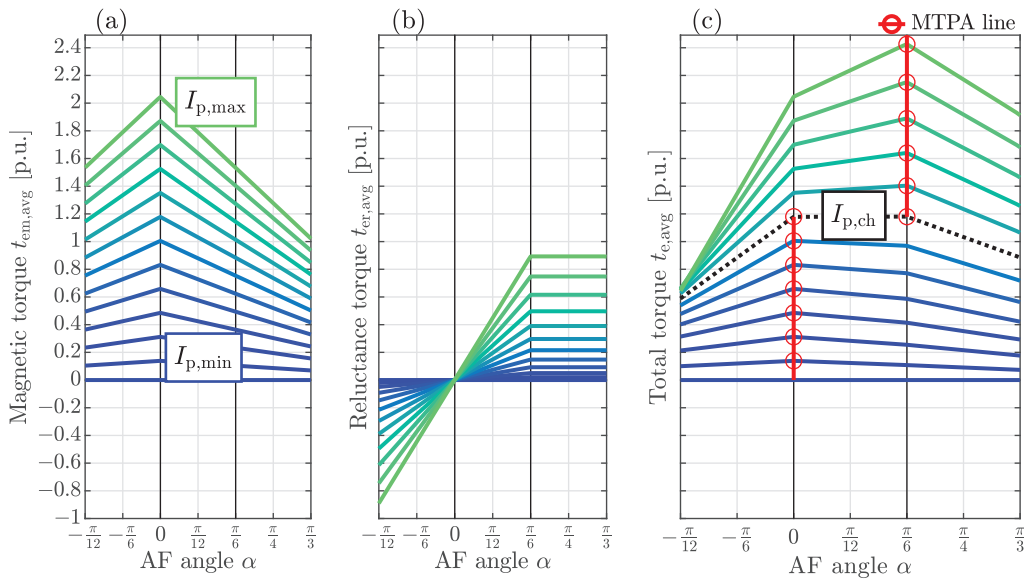


Figure 5. Torque of IPMSM with respect to the AF angle and current: (a) magnetic torque, (b) reluctance torque, and (c) total torque.

Figure 5c shows how the total electromagnetic torque $t_{e,avg}$, changes with respect to the peak current value from $I_{p,min} = 0$ p.u. to $I_{p,max} = 1.62$ p.u. and the AF angle α . The analysis of the total torque $t_{e,avg}$, was performed to determine α_M for MTPA operation. When analyzing the total torque $t_{e,avg}$, visually, the MTPA angle α_M can be determined by finding the maximal extrema of the obtained piecewise function, as presented in Figure 5c. The obtained α_M changed from 0 to $\pi/6$ discretely, where the change happened at a characteristic current $I_{p,ch}$. At $I_{p,ch}$, all AF angles α between 0 and $\pi/6$ result in the MTPA operation. The $I_{p,ch}$ can be determined mathematically by first identifying the sections of the piecewise function $t_{e,avg}$, where maximum extrema are located. Most are located on the border between two sections. $I_{p,ch}$ can be obtained by (14)

$$\frac{dt_{e,avg}}{d\alpha} = \frac{dt_{em,avg}}{d\alpha} + \frac{dt_{er,avg}}{d\alpha} = 0. \quad (14)$$

By inserting (10) and (12) into (14), we derive (15)

$$-\frac{9}{\pi^2} p_p I_p (\Psi_{mp} - 6I_p L_r) = 0. \quad (15)$$

By solving (15) for I_p , we obtain two solutions: the first is zero and the second defines the characteristic current $I_{p,ch}$, by (16)

$$I_{p,ch} = \frac{\Psi_{mp}}{6L_r}. \quad (16)$$

Only the saliency of the rotor L_r and the peak magnetic flux Ψ_{mp} influence the characteristic current $I_{p,ch}$ (i.e., $I_{p,ch}$ is dependent on the machine design).

The relationship between α , I_p and $t_{e,avg}$ from $\alpha = 0$ to $\alpha = \pi/6$ is given by (17) to further assess the relations of both the current I_p , and the AF angle α , on the total torque $t_{e,avg}$. This relation shows all possible combinations of I_p and α for a desired $t_{e,avg}$, i.e., the iso-torque lines that are presented in Figure 6.

$$\alpha(I_p, t_{e,avg}) = \left\{ \frac{\pi(\pi t_{e,avg} - 6p_p I_p \Psi_{mp})}{9p_p I_p (\Psi_{mp} - 6I_p L_r)}, \quad 0 \leq \alpha < \frac{\pi}{6} \right\} \quad (17)$$

The MTPA operation is achieved when the minimal possible I_p is used for the generation of individual $t_{e,avg}$, confirming the discrete change of α .

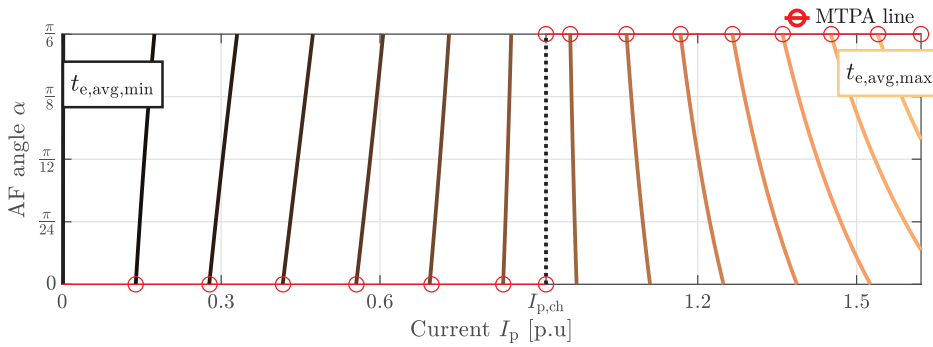


Figure 6. The effect of the current, I_p , and the AF angle, α , on the total torque, $t_{e,avg}$, from $t_{e,avg,min}$ to $t_{e,avg,max}$ is presented for a star-connected IPMSM. The MTPA line and the characteristic current are highlighted.

The relationship (17) is essential from a control perspective, as it identifies which combinations of current I_p and AF angle α provide the desired reference torque. Figure 6 presents the relationship from Figure 5c from a different viewpoint, offering an alternative perspective on the data. The MTPA points for the shown torques are at $\alpha_M = 0$ up to the $I_{p,ch}$, where the MTPA points change to $\alpha_M = \pi/6$ for all higher torque values.

2.3. Impact of the IPMSM Design on the MTPA Angle

In the next step, we analyze how different IPMSM design parameters and winding connections impact the MTPA angle α_M and the total electromagnetic torque $t_{e,avg}$. The delta connection is emphasized for the sake of generality. Five cases are analyzed, as presented in Table 2. The selected design cases highlight the effect of trapezoidal and sinusoidally shaped flux linkages, $\Psi_m(\theta)$, and inductances, $L(\theta)$, and are presented in Figure 7a,b for the variables in phase a.

Table 2. Analyzed IPMSM design cases with the corresponding equations for the flux linkage, inductances, currents, total torque, characteristic current, and AF angle.

Design Case	Winding Connection Type	Shape of $\Psi_m(\theta)$ Figure 5a	Shape of $L(\theta)$ Figure 5b	Current Figure 5c	Torque $t_{e,avg}$	Char. Current $I_{p,ch}$	AF Angle α_M
1	Wye	Trapezoidal, $\Psi_{m,Y}$ (7)	Trapezoidal, L (8)	$i_{abc,Y}$ (6)	(13)	(26)	(29)
2	Delta	Trapezoidal, $\Psi_{m,\Delta}$ (19)	Trapezoidal, L (8)	$i_{abc,\Delta}$ (18)	(22)	(26)	(29)
3	Delta	Sinusoidal, $\Psi_{m,sin}$ (20)	Trapezoidal, L (8)	$i_{abc,\Delta}$ (18)	(23)	(27)	(30)
4	Delta	Trapezoidal, $\Psi_{m,\Delta}$ (19)	Sinusoidal, L_{sin} (21)	$i_{abc,\Delta}$ (18)	(24)	(28)	(31)
5	Delta	Sinusoidal, $\Psi_{m,sin}$ (20)	Sinusoidal, L_{sin} (21)	$i_{abc,\Delta}$ (18)	(25)	/	(32)

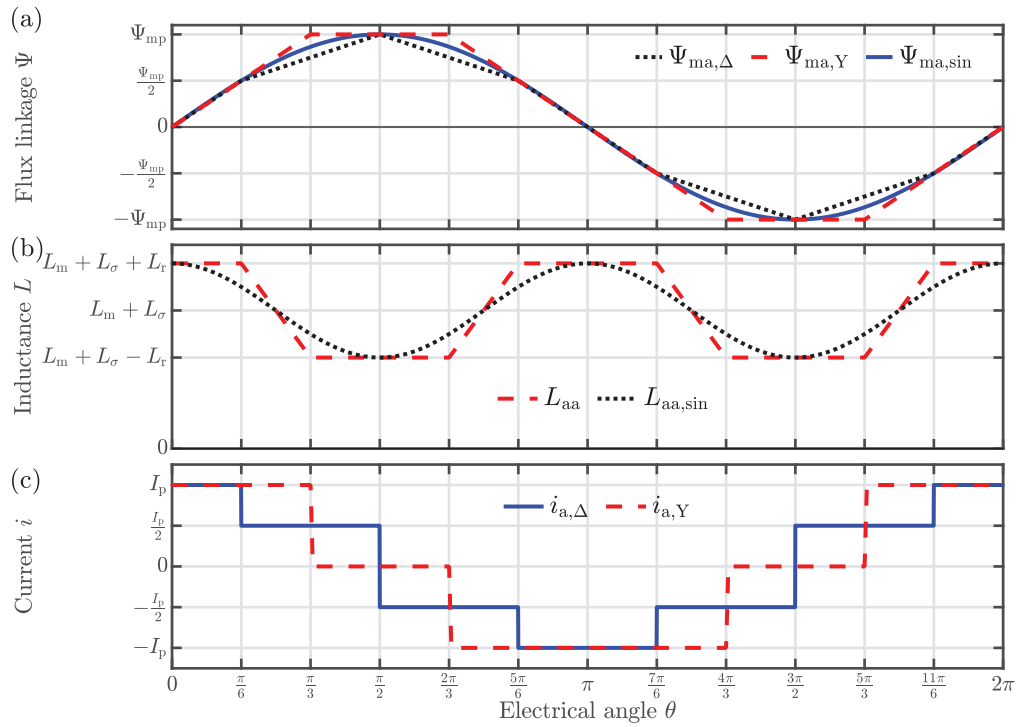


Figure 7. Theoretically ideal waveforms of the analyzed IPMSM designs: (a) permanent magnet flux linkage for a delta-connected BLDC drive, wye-connected BLDC drive, and a BLAC drive; (b) trapezoidal- and sinusoidal-dependent self-inductances of an IPMSM; and (c) corresponding currents for a delta- and wye-connected BLDC drive.

The effect of the IPMSM's winding connection is highlighted since the phase current waveforms change if the IPMSM is connected to delta or wye, as presented in Figures 2 and 7c for phase a. The delta phase current $i_{abc,\Delta}$ can be defined by (18)

$$i_{\Delta}(\theta) = \begin{bmatrix} i_{a,\Delta} \\ i_{b,\Delta} \end{bmatrix} = \begin{bmatrix} \begin{cases} I_p, & 0 \leq \theta < \frac{\pi}{6} - \alpha \\ \frac{I_p}{2}, & \frac{\pi}{6} - \alpha \leq \theta < \frac{\pi}{3} \end{cases}, & 0 \leq \alpha < \frac{\pi}{6} \\ \begin{cases} \frac{I_p}{2}, & 0 \leq \theta < \frac{\pi}{3} - \alpha \\ -\frac{I_p}{2}, & \frac{\pi}{3} - \alpha \leq \theta < \frac{\pi}{3} \end{cases}, & \frac{\pi}{6} \leq \alpha < \frac{\pi}{3} \\ \begin{cases} -\frac{I_p}{2}, & 0 \leq \theta < \frac{\pi}{6} - \alpha \\ \frac{I_p}{2}, & \frac{\pi}{6} - \alpha \leq \theta < \frac{\pi}{3} \end{cases}, & 0 \leq \alpha < \frac{\pi}{6} \\ \begin{cases} \frac{I_p}{2}, & 0 \leq \theta < \frac{\pi}{3} - \alpha \\ I_p, & \frac{\pi}{3} - \alpha \leq \theta < \frac{\pi}{3} \end{cases}, & \frac{\pi}{6} \leq \alpha < \frac{\pi}{3} \\ \begin{cases} -I_p, & 0 \leq \theta < \frac{\pi}{6} - \alpha \\ -I_p, & \frac{\pi}{6} - \alpha \leq \theta < \frac{\pi}{3} \end{cases}, & 0 \leq \alpha < \frac{\pi}{6} \\ \begin{cases} -I_p, & 0 \leq \theta < \frac{\pi}{3} - \alpha \\ -\frac{I_p}{2}, & \frac{\pi}{3} - \alpha \leq \theta < \frac{\pi}{3} \end{cases}, & \frac{\pi}{6} \leq \alpha < \frac{\pi}{3} \end{bmatrix}. \quad (18)$$

A corresponding theoretically ideal shape of $\Psi_{m,\Delta}(\theta)$ in a delta connection is presented in Figure 7a for phase a and is defined by (19)

$$\Psi_{m,\Delta}(\theta) = \begin{bmatrix} \Psi_{am,\Delta} \\ \Psi_{bm,\Delta} \\ \Psi_{cm,\Delta} \end{bmatrix} = \begin{bmatrix} \begin{cases} \frac{3}{\pi} \Psi_{mp} \theta, & 0 \leq \theta < \frac{\pi}{6} \\ \frac{3}{2\pi} \Psi_{mp} \theta + \frac{\Psi_{mp}}{4}, & \frac{\pi}{6} \leq \theta < \frac{\pi}{3} \end{cases} \\ \begin{cases} -\frac{3}{2\pi} \Psi_{mp} \theta - \frac{3\Psi_{mp}}{4}, & 0 \leq \theta < \frac{\pi}{6} \\ \frac{3}{2\pi} \Psi_{mp} \theta - \frac{5\Psi_{mp}}{4}, & \frac{\pi}{6} \leq \theta < \frac{\pi}{3} \end{cases} \\ \begin{cases} -\frac{3}{2\pi} \Psi_{mp} \theta + \frac{3\Psi_{mp}}{4}, & 0 \leq \theta < \frac{\pi}{6} \\ -\frac{3}{\pi} \Psi_{mp} \theta + \Psi_{mp}, & \frac{\pi}{6} \leq \theta < \frac{\pi}{3} \end{cases} \end{bmatrix}. \quad (19)$$

Additionally, a sinusoidally dependent $\Psi_{m,\sin}(\theta)$ was considered, which is presented in Figure 7a for phase a, and defined by (20)

$$\Psi_{m,\sin}(\theta) = \begin{bmatrix} \Psi_{am,\sin} \\ \Psi_{bm,\sin} \\ \Psi_{cm,\sin} \end{bmatrix} = \begin{bmatrix} \Psi_{mp} \sin(\theta) \\ \Psi_{mp} \sin(\theta - \frac{2\pi}{3}) \\ \Psi_{mp} \sin(\theta + \frac{2\pi}{3}) \end{bmatrix}. \quad (20)$$

The sine wave flux linkage corresponds to a brushless alternating current (BLAC) drive. Lastly, the sinusoidally dependent inductances $L_{\sin}(\theta)$ are included in the analysis, which are presented in Figure 7b for L_{aa} , and are defined by (21)

$$\begin{aligned} L_{aa} &= L_m + L_\sigma + L_r \cos(2\theta), \\ L_{bb} &= L_m + L_\sigma + L_r \cos(2(\theta - \frac{2\pi}{3})), \\ L_{cc} &= L_m + L_\sigma + L_r \cos(2(\theta + \frac{2\pi}{3})), \\ L_{ab} &= -\frac{1}{2}L_m + L_r \cos(2(\theta - \frac{\pi}{3})), \\ L_{ac} &= -\frac{1}{2}L_m + L_r \cos(2(\theta + \frac{\pi}{3})), \\ L_{bc} &= -\frac{1}{2}L_m + L_r \cos(2(\theta + \pi)). \end{aligned} \quad (21)$$

For all the presented cases, the average torque $t_{e,avg}$, characteristic currents $I_{p,ch}$, and the MTPA AF angle α_M are derived analogous to Section 2.2. The average total torque $t_{e,avg}$, for Case 1 is defined by (13). The average total torque $t_{e,avg}$, for Case 2 is defined by (22)

$$t_{e,avg,C2} = \begin{cases} \frac{9}{4\pi^2} p_p I_p \Psi_{mp} (2\pi - 3\alpha) + \frac{81}{2\pi^2} p_p I_p^2 L_r \alpha, & 0 \leq \alpha < \frac{\pi}{6} \\ \frac{9}{4\pi^2} p_p I_p \Psi_{mp} (2\pi - 3\alpha) + \frac{27}{4\pi} p_p I_p^2 L_r, & \frac{\pi}{6} \leq \alpha < \frac{\pi}{3} \end{cases}. \quad (22)$$

The average total torque $t_{e,avg}$, for Case 3 is defined by (23)

$$t_{e,avg,C3} = \begin{cases} \frac{9}{2\pi} p_p I_p \Psi_{mp} \cos(\alpha) + \frac{81}{2\pi^2} p_p I_p^2 L_r \alpha, & 0 \leq \alpha < \frac{\pi}{6} \\ \frac{9}{2\pi} p_p I_p \Psi_{mp} \cos(\alpha) + \frac{27}{4\pi} p_p I_p^2 L_r, & \frac{\pi}{6} \leq \alpha < \frac{\pi}{3} \end{cases}. \quad (23)$$

The average total torque $t_{e,avg}$, for Case 4 is defined by (24)

$$t_{e,avg,C4} = \left\{ \frac{9}{4\pi^2} p_p I_p \Psi_{mp} (2\pi - 3\alpha) + \frac{27\sqrt{3}}{8\pi} p_p I_p^2 L_r \sin(2\alpha), \quad 0 \leq \alpha < \frac{\pi}{3} \right\}. \quad (24)$$

The average total torque $t_{e,avg}$, for Case 5 is defined by (25)

$$t_{e,avg,C5} = \left\{ \frac{9}{2\pi} p_p I_p \Psi_{mp} \cos(\alpha) + \frac{27\sqrt{3}}{8\pi} p_p I_p^2 L_r \sin(2\alpha), \quad 0 \leq \alpha < \frac{\pi}{3} \right\}. \quad (25)$$

Additionally, the characteristic currents $I_{p,ch}$ for Cases 1 to 4 are evaluated by applying (14). $I_{p,ch}$ for Case 1 and Case 2 is defined by (26)

$$I_{p,ch,C1} = I_{p,ch,C2} = \frac{\Psi_{mp}}{6L_r}, \quad (26)$$

in Case 3 by (27)

$$I_{p,ch,C3} = \frac{\pi\Psi_{mp}}{9L_r} \left(\sin\left(\alpha - \frac{\pi}{3}\right) + \sin\left(\alpha + \frac{\pi}{3}\right) \right), \quad (27)$$

and in Case 4 by (28)

$$I_{p,ch,C4} = \frac{\sqrt{3}\Psi_{mp}}{3\pi L_r \cos(2\alpha)}, \quad (28)$$

where in Case 5, there is no characteristic current $I_{p,ch}$.

Further, the MTPA angles α_M for Cases 3 to 5 are evaluated by (14). The MTPA angles α_M for Cases 1 to 3 are located within the interval $\alpha_M = 0$ and $\alpha_M = \frac{\pi}{6}$. The MTPA angles α_M for Cases 1 and 2 are defined by (29)

$$\alpha_{M,C1} = \alpha_{M,C2} = \begin{cases} 0, & 0 < I_p \leq I_{p,ch} \\ \frac{\pi}{6}, & I_p \geq I_{p,ch} \end{cases}. \quad (29)$$

The MTPA angles α_M for Case 3 are defined by (30)

$$\alpha_{M,C3} = \begin{cases} \text{asin}\left(\frac{9I_p L_r}{\pi\Psi_{mp}}\right), & 0 < I_p \leq I_{p,ch,C3} \\ \frac{\pi}{6}, & I_p \geq I_{p,ch,C3} \end{cases}. \quad (30)$$

The MTPA angles α_M for Cases 4 to 5 are located within the intervals $\alpha_M = 0$ and $\alpha_M = \frac{\pi}{3}$. The MTPA angles α_M for Case 4 are defined by (31)

$$\alpha_{M,C4} = \begin{cases} 0, & 0 < I_p \leq I_{p,ch,C4} \\ \text{asin}\left(\frac{1}{2\sqrt{\pi}} \sqrt{\frac{2(3\pi I_p L_r - \sqrt{3}\Psi_{mp})}{3\pi I_p L_r}}\right), & I_p \geq I_{p,ch,C4} \end{cases}. \quad (31)$$

The MTPA angles α_M for Case 5 are defined by (32)

$$\alpha_{M,C5} = -\text{asin}\left(\frac{\sqrt{3}(\Psi_{mp} - \sqrt{54I_p^2 L_r^2 + \Psi_{mp}^2})}{18I_p L_r}\right). \quad (32)$$

Equations (13) and (22) through (32) are utilized to evaluate the dependency of the average torque $t_{e,avg}$, on the AF angle α , and the current I_p . Figure 8 illustrates these relationships, with the maximum torque per ampere (MTPA) angles α_M highlighted for all five cases. In Cases 1 and 2, where all the parameter shapes of the IPMSM are trapezoidal, a discrete change in the MTPA angle α_M from 0 to $\pi/6$ occurs. In the delta-connected IPMSM, the characteristic current $I_{p,ch}$, is identical, and the total torque $t_{e,avg}$, is lower overall compared to the wye-connected IPMSM. No discrete change in the MTPA angle α_M occurs in Cases 3 and 4. In Case 3 α_M follows an almost linear line described by (30), as it crosses $I_{p,ch}$ it settles at $\pi/6$. Case 4 shows a reverse effect of Case 3, where α_M is zero up to $I_{p,ch}$. Above this value, it follows a nonlinear line described by (31). Case 5, where all the IPMSM parameters have a sinusoidal shape, no distinct $I_{p,ch}$ is observed, and α_M follows a nonlinear line that is known from FOC and described by (32).

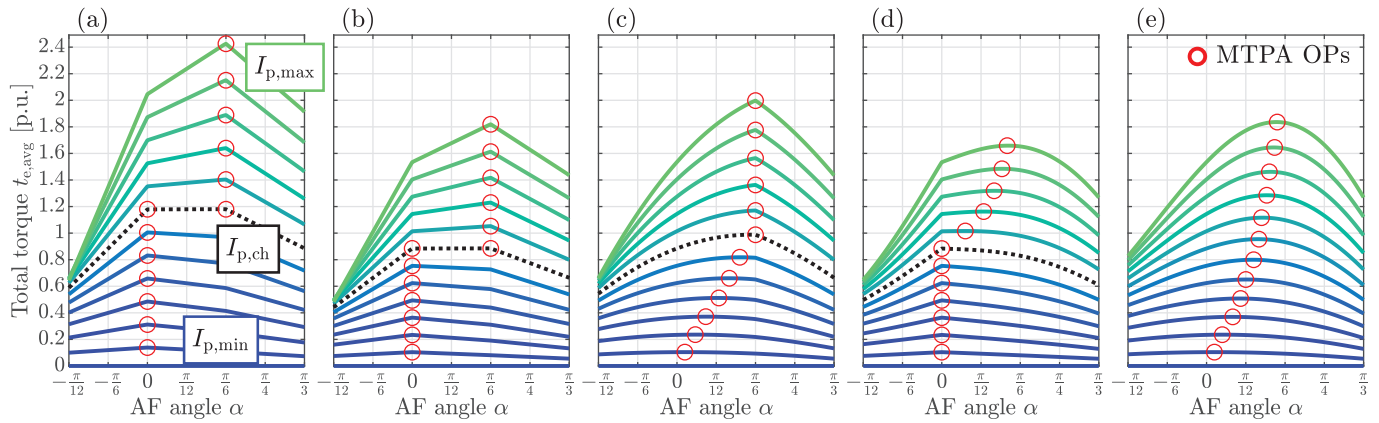


Figure 8. Comparison of the total torque $t_{e,avg}$, and MTPA angles α_M , for the analyzed IPMSM designs within a theoretically ideal BLDC drive: (a) Case 1, (b) Case 2, (c) Case 3, (d) Case 4, and (e) Case 5.

3. Optimization of an IPMSM for SWC

A parametrized FEM model of a 6-slot 4-pole IPMSM with a fractional slot non-overlapping winding and Nd-Fe-B magnets was set up in ANSYS Maxwell 2D. The FEM model was validated using measurements and a 2-step process. The validated model was optimized to obtain the specified objectives.

3.1. Experimental Validation of the Reference IPMSM Model

By performing a 2-step validation process, the FEM model was validated against a commercial IPMSM. The experimental workbench consisted of an active brake to provide load torque, a torque sensor, a rotary encoder, an SWC inverter with a single shunt current measurement, and a Hall sensor position measurement. A Dewetron measurement system was used to measure the line-to-line voltages u_{abc} , line currents $i_{abc,l}$, the load torque $t_{l,meas}$, the rotational speed ω_m , and the temperatures on the winding and the stator ϑ . The measured temperature ϑ , was used to adjust the magnet properties and the winding resistance within the FEM model.

First, the no-load condition was evaluated, where the measured back EMF e_{abc} was compared against the corresponding calculated back EMF. The comparison is presented in Figure 9a. The difference in the EMFs' root mean square (RMS) values was 4.30%. Additionally, the comparison of the calculated magnet flux linkage $\Psi_m(\theta)$ and the evaluated magnet flux linkage from the measured back EMF is presented in Figure 9b.

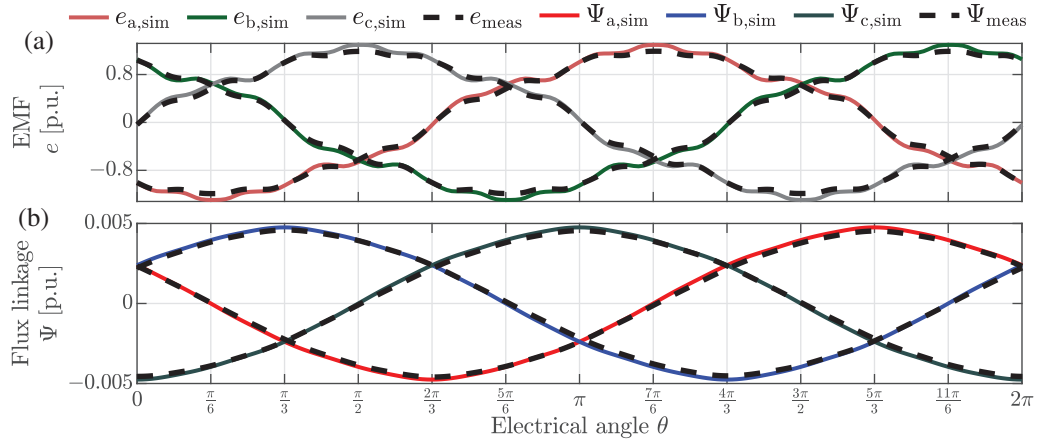


Figure 9. Comparison of measured and calculated variables in no-load: (a) back EMFs and (b) flux linkage.

Secondly, a typical operation point was measured and evaluated numerically. The measurement was performed at 60% of the thermally stable load torque $t_{l,OP}$, and the full base speed $\omega_{m,OP}$. Figure 10a shows the line currents $i_{abc,l}$ with the commutation interval angle α_C (i.e., the angle that is required for the currents to rise) highlighted and the calculated phase currents i_{abc} . The measured currents were used directly as the current excitation of the FEM model of the IPMSM. We adjusted the obtained $t_{e,sim}$, as presented in Figure 10b, to be comparable with the measured load torque $t_{l,meas}$, as the effect of iron core losses P_{Fe} , and the mechanical losses P_{mech} , were not included in the FEM simulation directly. The adjustment included the calculation of the iron core P_{Fe} , and mechanical losses P_{mech} , in the analyzed operation point. The iron core losses P_{Fe} , were calculated in post-processing with the extended iron core loss model [37,38], which considered the effect of higher harmonics. The mechanical losses P_{mech} , were calculated based on the mechanical coefficients (k_f is the viscous friction coefficient and k_C is the ventilation coefficient) determined from adequate no-load measurements (i.e., with and without magnetized magnets, with and without ventilation). The electromagnetic torque was adjusted by (33)

$$t_{e,adj} = t_{e,avg,sim} - \frac{P_{Fe}}{\omega_m} - k_f \omega_m - k_C \omega_m^2. \quad (33)$$

The obtained difference between the measured load torque $t_{l,meas}$, and the calculated adjusted electromagnetic torque $t_{e,adj}$, was 5.03%.

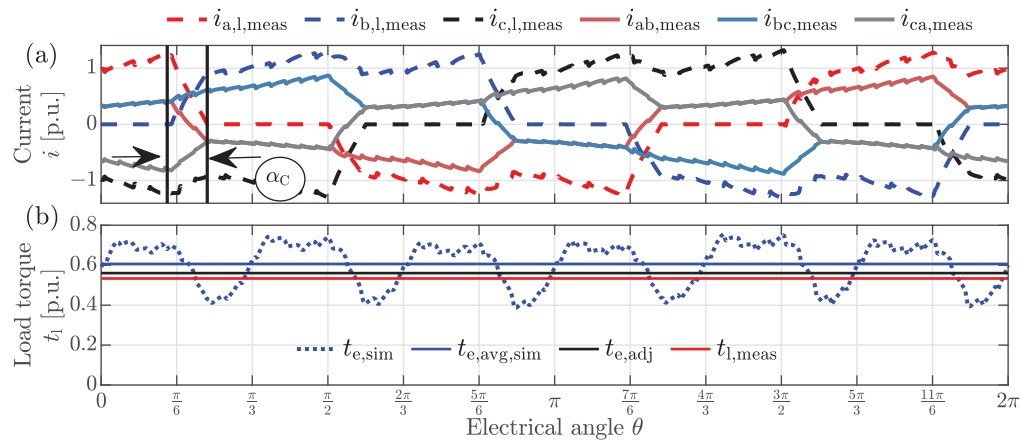


Figure 10. Comparison between (a) the measured line and, from the measurements, the calculated phase currents of a delta-connected IPMSM. (b) Simulated, adjusted, and measured torque.

3.2. IPMSM Design Optimization

The goal of the optimization was to improve the torque-to-current ratio, reduce torque ripple, and maintain the simplicity of control. The optimization was performed on a parameterized IPMSM model, as presented in Figure 11.

In this study, five parameters were optimized (four rotor parameters d_{rd} , d_{rq} , d_{ry} , θ_{rM} , and one parameter that changed the stator pole shoe θ_v). Table 3 presents the parameter values of the reference IPMSM and the upper and lower boundary conditions. Additionally, the fixed parameter values are presented in Table 3. All parameters are scaled to the inner radius of the stator $r_{s,in}$.

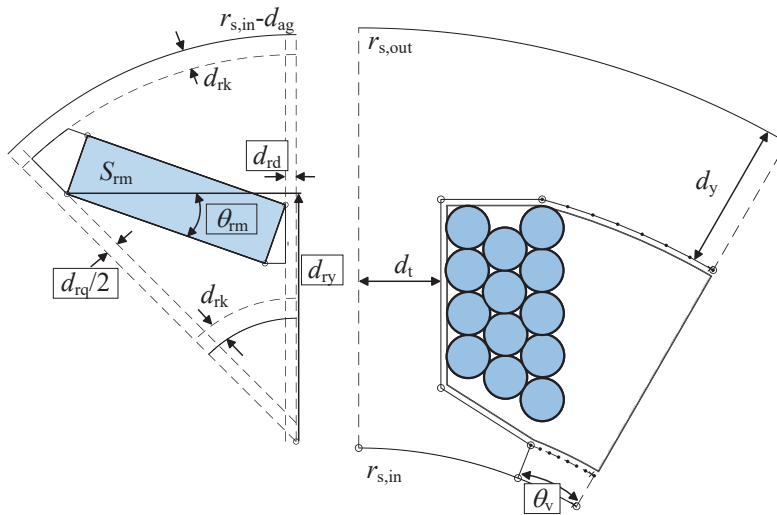


Figure 11. Parameterized geometry of the analyzed IPMSM.

Table 3. Stator and rotor parameters used for optimization of the reference design and fixed parameters.

Parameters	Description	Unit	Ref. Value	Min x_l	Max x_u
θ_v	Slot opening angle	$^\circ$	7.5	5	10
d_{rq}	q-axis bridge width	p.u.	0.074	0.026	0.184
d_{rd}	d-axis bridge width	p.u.	0	0	0.184
d_{ry}	Magnet tip height	p.u.	0.563	0.268	0.783
θ_{rm}	Magnet angle	$^\circ$	0	−25	25
$r_{r,out}$	Stator outer radius	p.u.	1.9	/	/
$r_{r,in}$	Stator inner radius	p.u.	1	/	/
d_y	Yoke width	p.u.	0.30	/	/
d_t	Tooth width	p.u.	0.23	/	/
d_{rk}	Minimal bridge width	p.u.	0.05	/	/
d_{ag}	Air gap width	p.u.	0.03	/	/
S_{rm}	Magnet area	p.u.	1	/	/

The primary aim of the optimization was to tailor a delta-connected IPMSM for the constant AF angle SWC. A two-objective optimization was performed. The FEM model of the IPMSM was excited by the phase currents of a delta-connected IPMSM, which are presented in Figure 7c, with a peak value of $I_p = 1$ p.u. The first goal was to obtain a predictable, constant MTPA angle α_M , which was addressed by choosing the first objective to achieve the maximal average electromagnetic torque $t_{e,avg}$, at $\alpha = 0^\circ$. With this, we strived to achieve that the shape of the back EMF would ensure an α_M that would be as close to zero as possible throughout the whole operation (presented in Section 2.3). The second goal and objective were to minimize the torque ripple $t_{e,ripp}$. The optimization problem was defined by (34)

$$\begin{aligned} \min : & \begin{cases} f_1(x) = -t_{e,avg}(\alpha = 0^\circ) \\ f_2(x) = t_{e,ripp}(\alpha = 0^\circ) \end{cases} \\ \text{s.t. : } & x_l \leq x \leq x_u, \end{aligned} \quad (34)$$

where $x = [d_{rd}, d_{rq}, d_{ry}, \theta_{rm}, \theta_v]$ are the optimization parameters and x_u and x_l are the upper and lower boundaries defined in Table 3. Objective 1 is defined by $f_1(x)$, where the $-t_{e,avg}$ is minimized (i.e., $t_{e,avg}$ is maximized) at $\alpha = 0^\circ$. Objective 2 is defined by $f_2(x)$, where the $t_{e,ripp}$ is minimized at $\alpha = 0^\circ$.

The optimization was performed based on the neural network-based metamodel [29], which is presented in Figure 12. Neural networks were chosen as metamodels over alterna-

tive methods following a preliminary study. The discussed neural networks were set up in the following steps.

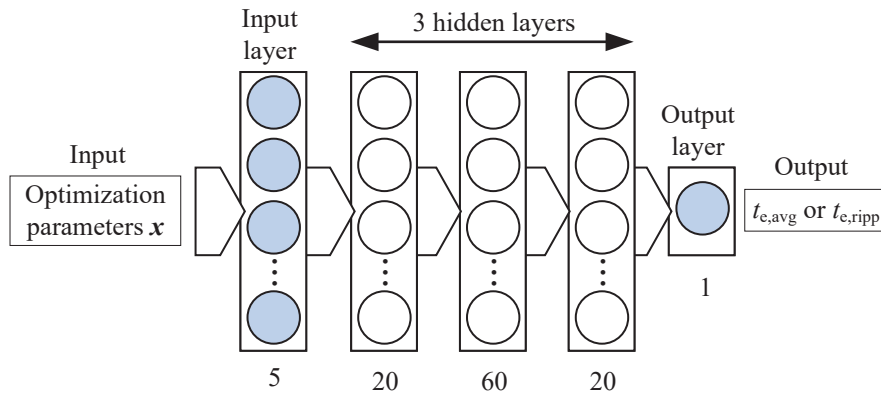


Figure 12. Neural network architecture for direct prediction of $t_{e,avg}$ and $t_{e,ripp}$.

First, a design of the experiment was performed by applying Latin hypercube sampling, where 6000 datasets, including input and output parameters $t_{e,avg}$ and $t_{e,ripp}$, were gathered from FEM models. Second, for every output, a feedforward neural network was trained with 5 inputs (i.e., optimization parameters x) and 1 output (i.e., $t_{e,avg}$ or $t_{e,ripp}$). The data were divided into training, validation, and test data in ratios of 70%, 15%, and 15%, respectively. Three hidden layers (20, 60, and 20) were used, as presented in Figure 12. The Levenberg–Marquardt training function was employed. Figure 13 shows the regression plot of the trained networks for all the data. The stability of the neural networks was ensured through input data normalization, the use of high-quality and diverse data, and the implementation of a robust neural network architecture.

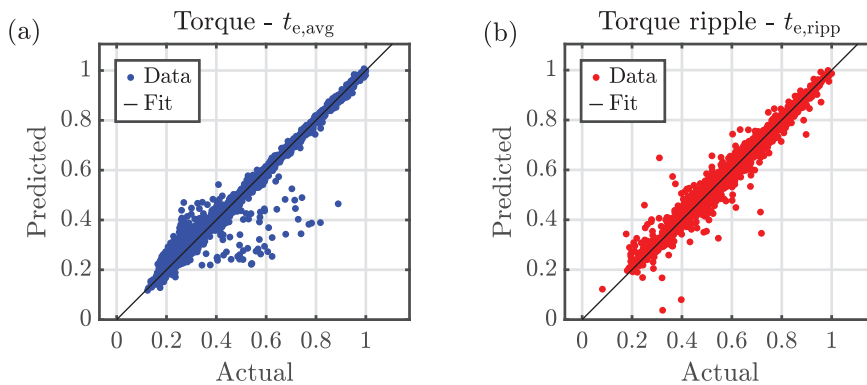


Figure 13. Regression plot of the trained neural network models for (a) torque $t_{e,avg}$, and (b) torque ripple $t_{e,ripp}$.

A two-objective optimization based on the trained neural network models was performed with Matlab’s multi-objective genetic algorithm, which is an elitist genetic algorithm, a variant of NSGA-II [39]. The maximal number of iterations was set to 100, and the population size per generation was set to 300.

4. Results

The results are presented in three parts. First, we discuss the reduction in computational time and present the selected optimized design achieved through the presented optimization process. Second, we analyze the MTPA angle α_M , for both the optimized and reference designs using the FEM evaluation. Last, we conducted a system-level simulation analysis, applying various basic and advanced control techniques for BLDC drives. This

enabled us to compare the control with a fixed AF angle in the optimized design against other established control methods used in BLDC drives.

4.1. Design Optimization and Computational Efficiency

The reduction in computation time required for the described multi-objective optimization process was the primary benefit. We replaced the FEM-based numerical evaluation with neural network metamodels. Each FEM-based numerical evaluation required 30 s, accumulating to 50 h for complete data collection. A direct optimization would require approximately 30,000 such evaluations, totaling 250 h. By adopting the metamodeling approach, the overall computation time was cut by 80%. A similar approach is presented in [32], where the total computation time was reduced by around 50%. The metamodels also facilitated the modification of optimization objectives and enabled the reuse of trained neural networks, thus further reducing the computation time significantly.

The performed optimization resulted in a Pareto front, which is presented in Figure 14. A design was selected from the Pareto front that reduced the torque ripple $t_{e,ripp}$, significantly. Further, the average electromagnetic torque $t_{e,avg}$, at $\alpha = 0^\circ$ was improved compared to the reference design, i.e., by increasing the magnetic torque $t_{em,avg}$, component of the design. The novelty of this optimization approach was to optimize the IPMSM design to increase the magnetic torque component and provide the MTPA operation at a fixed AF angle α . Other studies [4] have utilized SPMSM, which generates solely magnetic torque $t_{em,avg}$. However, SPMSMs are less effective for high-speed operations without additional reinforcement of the surface-mounted magnets, which increases the cost.

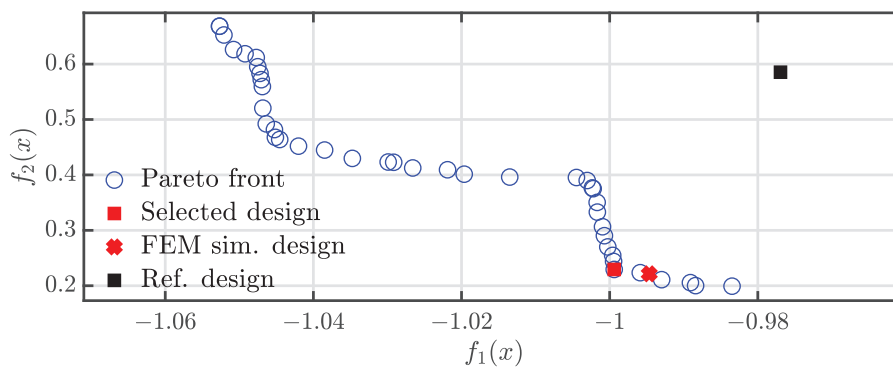
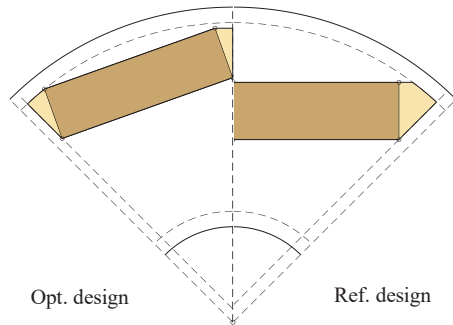


Figure 14. Pareto front of the performed optimization.

Because the neural network models inherited an error margin, the selected design re-evaluated by the FEM simulation gave a slightly different output result. The obtained FEM design is presented with the red cross and square in Figure 14. The torque ripple $t_{e,ripp}$, between the neural network and FEM models differed by 3.45%, and the average electromagnetic torque $t_{e,avg}$, differed by 0.63%. Compared to the reference design, the obtained design showed a 3% improvement of average electromagnetic torque $t_{e,avg}$, and a 164.26% improvement of torque ripple $t_{e,ripp}$. Figure 15 presents the geometry of the rotor of the reference and optimized IPMSM, and Table 4 presents the geometry parameter values of the reference and optimized IPMSM. In the optimized design, the d_{rq} became slightly narrower, and d_{rd} stayed at zero. The magnet was pushed to the outer border of the rotor, as indicated by d_{ry} and θ_{rm} .

Table 4. Comparison between the optimized geometry parameter values of the reference and optimized designs.

Par.	Unit	Ref.	Opt.
θ_v	$^\circ$	7.5	7.2
d_{rq}	p.u.	0.074	0.058
d_{rd}	p.u.	0	0
d_{ry}	p.u.	0.563	0.619
θ_{rm}	$^\circ$	0	19.7

**Figure 15.** Comparison of the geometries of rotors of the reference and optimized designs.

4.2. Analysis in the Case of an Ideally Shaped Current

The goal of the optimization was to provide a design that would allow for MTPA control of the IPMSM at a fixed angle AF angle α . To confirm this, the AF angle α analysis was performed for the reference and optimized IPMSMs, by performing a set of FEM simulations. The results are presented in Figure 16. The electromagnetic torque $t_{e,avg}$, changed with respect to the peak current value from $I_{p,min} = 0$ p.u. to $I_{p,max} = 1$ p.u., and the AF angle α , from 0° to 15° (i.e., $\pi/12$). The change in the MTPA angle α_M was observed at the characteristic current $I_{p,ch}$, which was at 0.568 p.u. for both designs. Above $I_{p,ch}$, α_M followed a nonlinear line. For the reference IPMSM α_M changed to 14° (i.e., $14\pi/180$) at the maximal $I_{p,max}$. In contrast, for the optimized IPMSM α_M only changed to 3° (i.e., $\pi/60$) at the maximal $I_{p,max}$. The behavior of α_M resembled Case 4 in Section 2.3, where the flux linkage $\Psi_m(\theta)$ had a trapezoidal shape, whereas the inductance $L(\theta)$ had a sinusoidal shape.

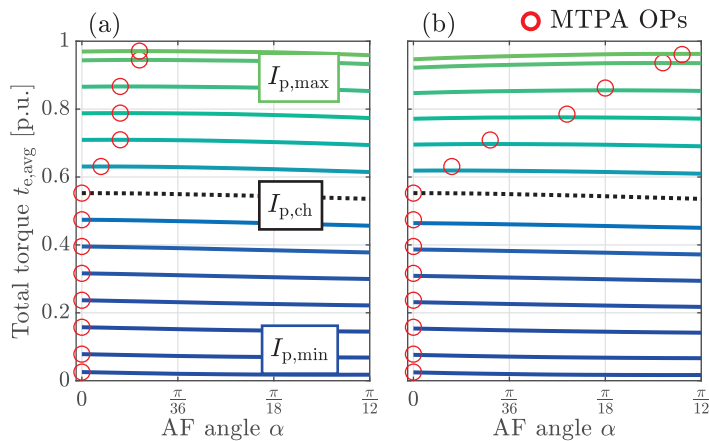
**Figure 16.** Comparison of the calculated total torque dependent on the AF angle and the current with highlighted MTPA angles for (a) the optimized design and (b) reference design.

Figure 17 presents the torque ripple $t_{e,ripp}$ analysis of the optimized and reference design generated with the FEM model. The analysis included identifying the maximum

and minimum values of $t_{e,ripp}$ and their corresponding AF angles α (the last two points have α values of the same value) in relation to $i_{a,rms}$. This approach aims to emphasize the limit values that define the reachable operation range by adjusting the AF angle α , and establishing a baseline for comparison.

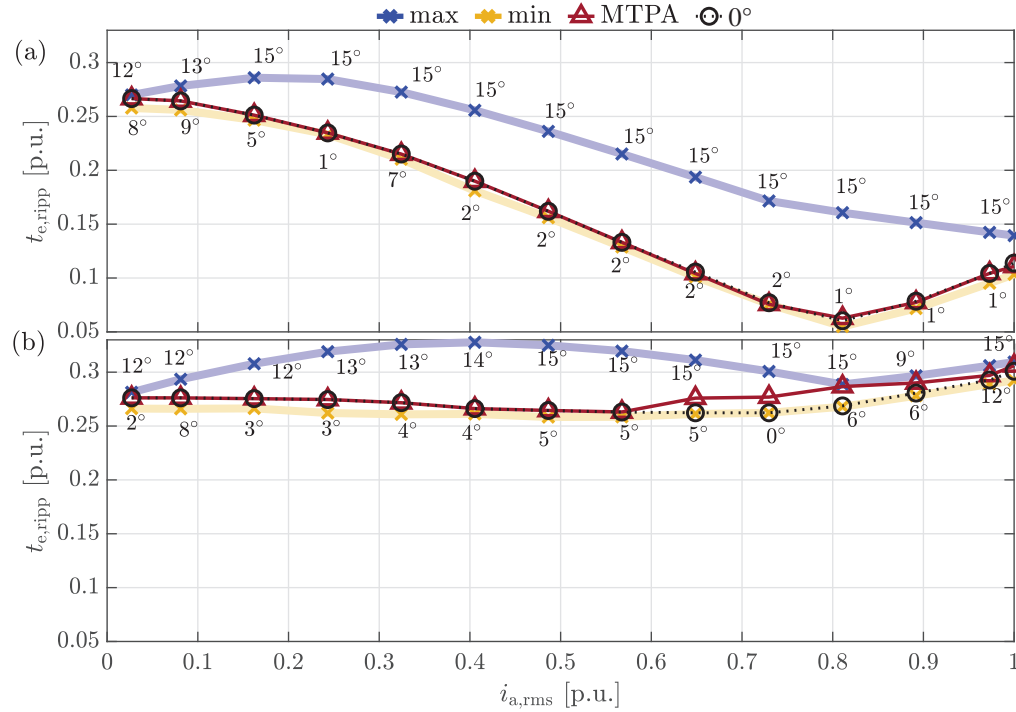


Figure 17. Comparison of minimal and maximal reachable torque ripple and actual torque ripple when adjusting the AF angle within an ideal BLDC drive with (a) the optimized design and (b) the reference design.

By comparing the minimum reachable values of both designs, it was observed that the optimized machine exhibited lower $t_{e,ripp}$, across the entire region. Therefore, the optimization achieved the second goal. For both designs, a smaller $t_{e,ripp}$ was observed at a smaller α , while higher $t_{e,ripp}$ was noted at a larger α . Additionally, two special cases were highlighted. The first was by setting α to zero, and the second was by following the MTPA line. In the optimized design, both scenarios (setting α to zero and following the MTPA path) matched the minimal achievable $t_{e,ripp}$ closely. For the reference design, the $\alpha = 0^\circ$ scenario aligned closely with the minimal $t_{e,ripp}$, while the MTPA scenario maintained close proximity to the lowest $t_{e,ripp}$ up to $I_{p,ch}$, where α_M shifted. Beyond this point, the $t_{e,ripp}$ no longer tracked the minimal value closely.

4.3. System-Level Simulation Analysis

To include the impact of the commutation interval and the corresponding effect of the alignment AF angle α_{al} in the evaluation of the BLDC drive performance with a fixed AF angle control, a system-level simulation was implemented, as presented in Figure 2. This analysis considered the impact of the real-world commutation of currents. The Simulink/Simscape environment was used to model the IPMSM, inverter, and control. First, a computationally efficient reduced order model (ROM) of the IPMSM was constructed by performing a series of FEM simulations of both analyzed IPMSM designs by varying the i_d and i_q input currents, as presented in [18,34,36]. An IPMSM model in the d-q reference frame was set up and connected to a voltage source inverter in the delta connection. The Hall sensor signals were modeled for position estimation [4]. Furthermore, different strategies for changing the AF angle α , were implemented, where the commutation logic was used to switch the transistors [3]. The DC of the BLDC drive was controlled by using

a proportional–integral controller. The adjustable input parameters were the mechanical speed ω_m and AF angle α . This setup allowed the following advantages:

- It was possible to model the nonlinear electromagnetic behavior of discussed IPMSM designs according to the respective FEM models and reproduce all the related effects in the system-level simulation.
- By varying the DC i_{dc} at a set mechanical speed $\omega_m = 0.78$ p.u., we analyzed the RMS phase currents $i_{a,rms}$, torque ripples $t_{e,ripp}$, and electromagnetic torques $t_{e,avg}$.
- The AF angle α , could be adjusted according to different strategies for benchmarking purposes.

For the purpose of this analysis, the torque-to-current coefficient k_{em} was defined by (35)

$$k_{em} = \frac{t_{e,avg}}{i_{a,rms}}. \quad (35)$$

Figure 18 presents the torque ripple $t_{e,ripp}$ and torque-to-current coefficient k_{em} of the optimized and reference design obtained through the system-level simulation. The analysis first focused on identifying the maximum and minimum achievable values of $t_{e,ripp}$ and k_{em} , and their corresponding α in relation to $i_{a,rms}$. Presenting the maximum and minimum values offered a range for evaluating various control strategies.

Three control strategies were applied and analyzed for setting the AF angle α . In the basic algorithm, α was maintained at a fixed value, thereby preserving the simplicity of the control. The reference design was controlled with a fixed $\alpha = 30^\circ$, a common value used in the industry [5]. The optimized design was controlled with two fixed α values. The first was $\alpha = 0^\circ$, according to the optimization objective, and the second was $\alpha = 10^\circ$, because at this α and the maximal allowed $i_{a,rms}$, maximal k_{em} was achieved, as presented in Figure 18a.

The second, more advanced strategy (hereafter, referred to as alignment control) was implemented to control the AF angle α , as presented in [4]. In the previous sections, the phase currents i_{abc} were assumed to be ideal-shaped, as presented in Figure 7a. In reality, the phase current i_{abc} shape is more irregular and lags behind the ideal shape due to commutation, as presented in Figure 10a. To negate the effect of real-world commutation and align the phase currents i_{abc} better with the back EMFs e_{abc} , the fundamental harmonic component of the current i_a and back EMF e_a in phase a is calculated, as presented in Figure 3. The obtained AF angle α equals the alignment AF angle α_{al} and was used to align the currents to EMFs.

The third control type upgraded the alignment control by considering the reluctance AF angle α_r , additionally (hereafter referred to as MTPA control), as presented in Figure 16. This resulted in a total MTPA angle α_M , as presented by (5).

Several key findings emerged upon assessing the performance of designs utilizing a fixed α (as indicated by the dotted lines in Figure 18). First, setting $\alpha = 30^\circ$ in the reference design did not achieve optimal performance across the entire operational range. In the whole operation range, the maximal $t_{e,ripp}$ was observed, where k_{em} was minimal at lower $i_{a,rms}$. The value of k_{em} diverged from its minimum at $i_{a,rms} = 0.4$ p.u., reaching its maximum at the highest $i_{a,rms}$. While this approach did not yield optimal results at lower currents, it maximized k_{em} at the highest $i_{a,rms}$, thereby maximizing the operational envelope in terms of the maximal torque. Second, applying a fixed $\alpha = 0^\circ$ in the optimized design also fell short of achieving optimal performance throughout the operational range, presenting an inverse effect compared to the reference design with $\alpha = 30^\circ$. In the whole operation range, minimal $t_{e,ripp}$ was achieved, where the k_{em} was maximal at lower $i_{a,rms}$. The value of k_{em} diverged from its maximal at $i_{a,rms} = 0.25$ p.u., reaching its minimum at the highest $i_{a,rms}$. While this setup offers advantages (particularly at low $i_{a,rms}$), it limits the operational envelope significantly by decreasing k_{em} at the highest allowable $i_{a,rms}$. Consequently, implementing a fixed $\alpha = 10^\circ$ in the optimized design successfully avoided narrowing the operational envelope while still leveraging the enhancements from

optimizing the IPMSM. The obtained $t_{e,ripp}$ was increased slightly, where the k_{em} was decreased slightly at a lower $i_{a,rms}$ and approached the maximal values already at low $i_{a,rms}$. The maximal k_{em} was achieved at the highest $i_{a,rms}$.

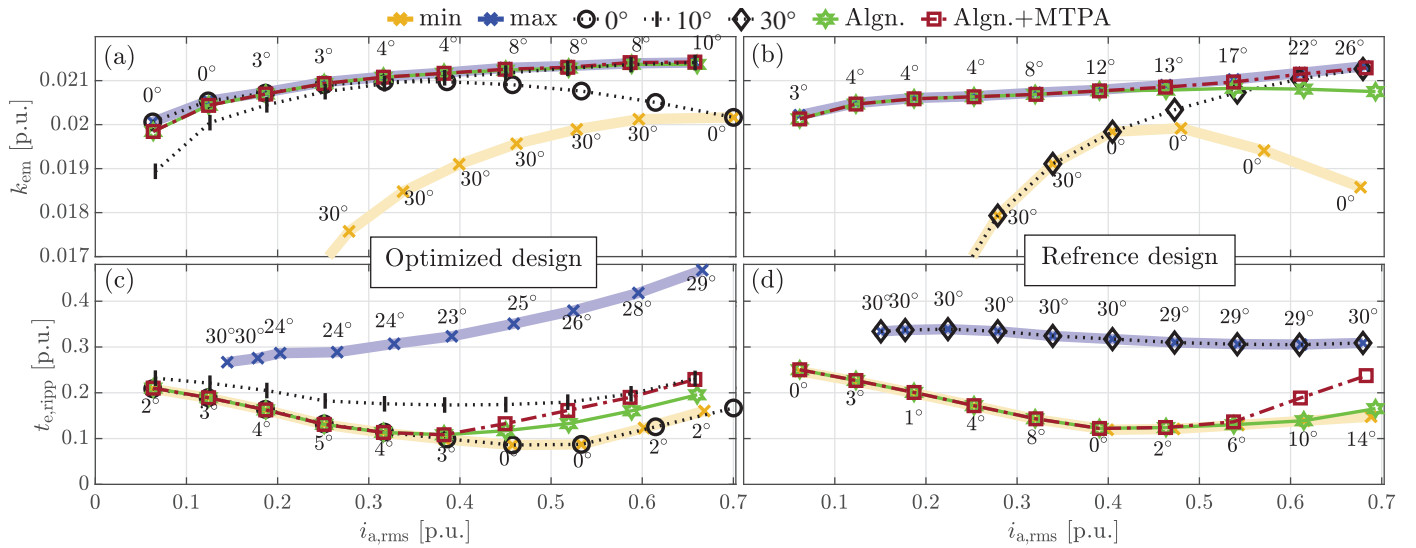


Figure 18. Comparison between reachable minimum and maximum values with the actual values obtained by applying different control strategies in the system-level simulation: (a) k_{em} for optimized design (b) k_{em} for reference design (c) $t_{e,ripp}$ for optimized design (d) $t_{e,ripp}$ for the reference design.

It can be concluded that optimizing the IPMSM using ideal-shaped currents did not translate fully to the same level of improvement in system-level simulations, particularly when controlling the drive with a fixed $\alpha = 0^\circ$. While the optimization enhanced the IPMSM to a certain degree, the impact of the commutation period affected the current shapes significantly, especially when approaching maximal currents. Further studies should incorporate the commutation effect into the optimization to capitalize fully on the motor design for SWC. However, implementing a fixed $\alpha = 0^\circ$ or $\alpha = 10^\circ$ in the optimized design resulted in k_{em} remaining relatively constant across the entire operational range. In contrast, a fixed α of 30° in the reference design led to significant variations in k_{em} throughout the operation range. This is advantageous for the control implementation in BLDC motors. Further, the relative improvement was evaluated in the performance of the optimized design with a fixed $\alpha = 10^\circ$ compared to the reference design with a fixed $\alpha = 30^\circ$. First, the relative difference ϵ_{ripp} of the torque ripple $t_{e,ripp}$ at all total torque $t_{e,avg}$ values was evaluated by (36)

$$\epsilon_{ripp} = 100 \frac{t_{e,ripp,opt} - t_{e,ripp,ref}}{t_{e,ripp,ref}}. \quad (36)$$

Second, the relative difference ϵ_{Cu} of the copper losses in the winding at all total torque $t_{e,avg}$ values was evaluated by (37)

$$\epsilon_{Cu} = 100 \frac{3Ri_{a,rms,opt}^2 - 3Ri_{a,rms,ref}^2}{3Ri_{a,rms,ref}^2}. \quad (37)$$

The copper losses were analyzed due to their direct impact on the machine's efficiency. The $t_{e,ripp,opt}$ and $i_{a,rms,opt}$ are the torque ripple and RMS currents for the optimized design with a fixed $\alpha = 10^\circ$, where $t_{e,ripp,ref}$ and $i_{a,rms,ref}$ are the torque ripple and RMS current for the reference design with a fixed $\alpha = 30^\circ$. Figure 19 presents ϵ_{ripp} and ϵ_{Cu} in dependence on the total torque $t_{e,avg}$. For the optimized design, the copper losses were reduced across the entire operational range compared to the reference design. This difference narrowed to

0% at maximum torque. At half of the maximum torque, as indicated by the blue circle in Figure 19, a 12.7% reduction was achieved in copper losses. The optimized machine exhibited reduced torque ripple across the entire operational range when compared to the reference design. The greatest reduction, observed at a torque of $t_{e,avg} = 0.43$ p.u., was a 45.5% decrease in torque ripple, as indicated by the orange square.

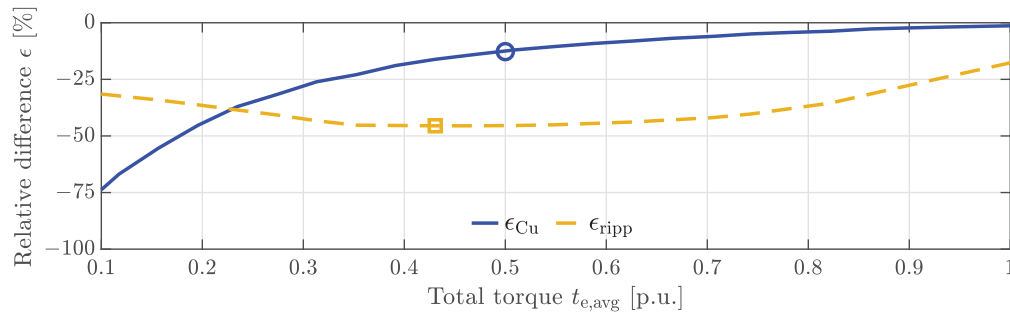


Figure 19. The relative difference between the torque ripple ϵ_{ripp} and the copper losses ϵ_{Cu} in the winding in the dependence on the total torque $t_{e,avg}$. Comparison between the optimized design with a fixed $\alpha = 10^\circ$ for control and the reference design with a fixed $\alpha = 30^\circ$ for control.

Furthermore, the performances were analyzed for two different advanced control algorithms (i.e., alignment and MTPA control). Those require additional resources along with exact knowledge of the rotor position, which can be retrieved from the Hall sensors.

Alignment control [5] was applied first. It enhanced the k_{em} of the optimized design significantly, nearly unlocking its full potential, while showing drawbacks at higher $i_{a,rms}$ for the reference design. In the optimized design, the maximum k_{em} was maintained throughout the entire operational range, whereas the $t_{e,ripp}$ remained at its lowest up to an $i_{a,rms} = 0.38$ p.u. before increasing. Conversely, in the reference design, the $t_{e,ripp}$ was nearly minimal across the entire range, but the k_{em} began to decrease from its maximum at $i_{a,rms} = 0.39$ p.u.

Second, MTPA control was applied additionally. It did not improve the performance of the optimized design while enhancing the performance of the reference design compared with the alignment control. By implementing MTPA control for the optimized design, the electromagnetic constant k_{em} remained largely unchanged compared to the alignment control. Furthermore, the $t_{e,ripp}$ increased from the minimal value after $i_{a,rms} = 0.39$ p.u. and was bigger than the $t_{e,ripp}$ generated with alignment control. No added benefit using the MTPA control for the optimized design was observed, as the k_{em} was almost maximal for MTPA and alignment control, and the MTPA control caused higher $t_{e,ripp}$. This was a direct consequence of the set optimization goals, where α_M was close to zero. In the reference design scenario, employing MTPA control increased the k_{em} across the entire region. However, it also led to an increase in $t_{e,ripp}$, starting from $i_{a,rms} = 0.57$ p.u. onward. Despite this, using MTPA control for the reference design emerged as the most effective approach.

Implementing advanced control algorithms enhanced the machine's performance significantly by compensating for commutation efficiently by adjusting the AF angles α adequately. Consequently, an almost constant k_{em} in the whole region was obtained, and the operation envelope was maximized. As the algorithms could track the optimal α , the design of the machine to change the MTPA angle α_M , did not influence their capabilities significantly. However, there was a significant difference in terms of the required control complexity to unlock the IPMSM's potential. The biggest benefit of optimizing the IPMSM to have the α_M at near zero angles was when using a fixed $\alpha = 10^\circ$, as the performance was enhanced significantly, and the simplicity of control was preserved. To achieve the desired effect of zero or near zero MTPA angles α_M , the V-shaped rotor of the IPMSM should have the magnets as close as possible to the outer radius of the rotor and no bridge between the magnet segments.

5. Conclusions

The analytical analysis of the MTPA angle α_M showed that the machine design (i.e., the shape of the IPMSMs flux linkage $\Psi_m(\theta)$ and inductances $L(\theta)$) impact the MTPA operation of a BLDC drive strongly. If $\Psi_m(\theta)$ and $L(\theta)$ have a theoretically ideal trapezoidal shape, a discrete change of the machine's MTPA angle α_M was observed from 0 to $\frac{\pi}{6}$ at $I_{p, ch}$. The connection of the IPMSM windings did not change the behavior of the MTPA angle α_M and the characteristic current $I_{p, ch}$. Also, other machine designs were assessed, featuring sinusoidal and trapezoidal shapes of flux linkages $\Psi_m(\theta)$ and inductances $L(\theta)$. In some designs, the machine's MTPA angle exhibited discrete changes, while, in others, the MTPA trajectories were nonlinear.

Similar effects were observed with the experimental validated FEM model of the IPMSM, where the behavior resembled Case 4 from the analytical analysis. By optimizing the rotor geometry and the pole shoe, the torque ripple $t_{e, ripp}$ was reduced, the torque-to-current ratio k_{em} increased, and the MTPA angle α_M was adjusted to near-zero values.

The optimization workflow was presented, which employed neural network-based metamodels, and reduced optimization time by 80%. Additionally, it allowed for various optimization setups to be performed without incurring additional time.

A system-level simulation of the reference design with fixed $\alpha = 30^\circ$ showed non-optimal performance, except for maximizing the operation envelope in terms of the maximal torque. Further, controlling the optimized design with fixed $\alpha = 10^\circ$ showed enhanced performance in all analyzed aspects, i.e., increasing k_{em} , decreasing $t_{e, ripp}$, maximizing the operation envelope, and providing an almost constant k_{em} , compared to the reference design. The optimized design with $\alpha = 10^\circ$ outperformed the reference design significantly with $\alpha = 30^\circ$, achieving a maximum reduction of 45.5% in torque ripple and a 12.7% decrease in copper losses at half of the maximum torque.

When using advanced control algorithms that required exact knowledge of the rotor angle, significant enhancement was achieved, compared with fixed α . For the reference design, the MTPA control achieved the best performance, and for the optimized design, the alignment control performed the best. In both cases, the maximal k_{em} was achieved in the whole range, along with an almost constant k_{em} and a greatly reduced $t_{e, ripp}$. The advantages required, however, a significantly increased control complexity. If a simple control is desired, optimizing the IPMSM results in significant performance enhancements.

Author Contributions: Conceptualization, M.G., S.S. and M.P.; methodology, M.G.; software, M.G.; validation, M.G. and S.S.; formal analysis, M.G.; investigation, M.G. and M.P.; resources, M.G. and M.P.; data curation, M.G.; writing—original draft preparation, M.G.; writing—review and editing, M.G., S.S. and M.P.; visualization, M.G.; supervision, S.S. and M.P.; project administration, S.S. and M.P.; funding acquisition, S.S. and M.P. All authors have read and agreed to the published version of the manuscript.

Funding: This work was supported by the Slovenian Research and Innovation Agency (ARIS) under project P2-0115 and project J7-3152.

Data Availability Statement: Third-party data: Restrictions apply to the availability of these data. Data were obtained from Hilti Entwicklungsgesellschaft mbH and are available with the permission of Hilti Entwicklungsgesellschaft mbH.

Conflicts of Interest: Author Simon Steentjes was employed by the company HILTI Entwicklungsgesellschaft mbH. The remaining authors declare that the research was conducted in the absence of any commercial or financial relationships that could be construed as a potential conflict of interest.

Abbreviations

The following abbreviations are used in this manuscript:

AF	advance firing
BLAC	brushless alternating current
BLDC	brushless direct current

DC	direct current
EMF	electromotive force
FEM	finite element method
FOC	field-oriented control
IPMSM	interior permanent magnet synchronous machine
MOSFET	metal oxide semiconductor field effect transistor
MTPA	maximum torque per ampere
PMSM	permanent magnet synchronous machine
ROM	reduced order model
RMS	root mean square
SPMSM	surface permanent magnet synchronous machine
SWC	square-wave control

References

- Hendershot, J.R.; Miller, T.J.E. *Design of Brushless Permanent-Magnet Motors*; Motor Design Books: Venice, FL, USA, 2010.
- Krause, P.C.; Wasynczuk, O.; Sudhoff, S.D.; Pekarek, S.D. *Analysis of Electric Machinery and Drive Systems*; IEEE Press and Wiley: Piscataway, NJ, USA, 2013.
- Han, Q.; Samoylenko, N.; Jatskevich, J. Average-Value Modeling of Brushless DC Motors with 120° Voltage Source Inverter. *IEEE Trans. Energy Convers.* **2008**, *23*, 423–432. [CrossRef]
- Zhou, J.; Ebrahimi, S.; Jatskevich, J. Extended Operation of Brushless DC Motors Beyond 120° Under Maximum Torque Per Ampere Control. *IEEE Trans. Energy Convers.* **2023**, *38*, 1280–1291. [CrossRef]
- Zhou, J.; Lu, J.; Ebrahimi, S.; Jatskevich, J. A Compensation of Commutation Angle in Hall-Sensor-Controlled Brushless DC Motors for Maximum Torque per Ampere Operation. In Proceedings of the 21st International Symposium INFOTEH-JAHORINA, East Sarajevo, Bosnia and Herzegovina, 16–18 March 2022.
- Baby, B.K.; George, S. Torque ripple reduction in BLDC motor with 120 degree conduction inverter. In Proceedings of the 2012 Annual IEEE India Conference (INDICON), Kochi, Kerala, India, 7–9 December 2012.
- Zhang, P.; Shi, Z.; Yu, B.; Qi, H. Research on the Control Method of a Brushless DC Motor Based on Second-Order Active Disturbance Rejection Control. *Machines* **2024**, *12*, 244. [CrossRef]
- Mohanraj, D.; Arulavid, R.; Verma, R.; Sathiyasekar, K.; Barnawi, A.B.; Chokkalingam, B.; Mihet-Popa, L. A Review of BLDC Motor: State of Art, Advanced Control Techniques, and Applications. *IEEE Access* **2022**, *10*, 54833–54869. [CrossRef]
- Jiang, W.; Huang, H.; Wang, J.; Gao, Y.; Wang, L. Commutation analysis of brushless DC motor and reducing commutation torque ripple in the two-phase stationary frame. *IEEE Trans. Power Electron.* **2017**, *32*, 4675–4682. [CrossRef]
- Heidari, R.; Ahn, J.-W. Torque ripple reduction of BLDC motor with a low-cost fast-response direct DC-link current control. *IEEE Trans. Ind. Electron.* **2024**, *71*, 150–159. [CrossRef]
- Sudhoff, S.D.; Krause, P.C. Operating modes of the brushless DC motor with a 120 degrees inverter. *IEEE Trans. Energy Convers.* **1990**, *5*, 558–564. [CrossRef]
- Dianov, A.; Tinazzi, F.; Calligaro, S.; Bolognani, S. Review and Classification of MTPA Control Algorithms for Synchronous Motors. *IEEE Trans. Power Electron.* **2022**, *37*, 3990–4007. [CrossRef]
- Morimoto, S.; Sanada, M.; Takeda, Y. Wide-speed operation of interior permanent magnet synchronous motors with high-performance current regulator. *IEEE Trans. Ind. Appl.* **1994**, *30*, 920–926. [CrossRef]
- Eldeeb, H.; Hackl, C.M.; Horlbeck, L.; Kullick, J. A Unified Theory for Optimal Feedforward Torque Control of Anisotropic Synchronous Machines. *Int. J. Control* **2018**, *91*, 2273–2302. [CrossRef]
- Khazaee, A.; Zarchi, H.A.; Markadeh, G.A.; Mosaddegh Hesar, H. MTPA Strategy for Direct Torque Control of Brushless DC Motor Drive. *IEEE Trans. Ind. Electron.* **2021**, *68*, 6692–6700. [CrossRef]
- Li, K.; Wang, Y. Maximum Torque per Ampere (MTPA) Control for IPMSM Drives Using Signal Injection and an MTPA Control Law. *IEEE Trans. Ind. Inform.* **2019**, *15*, 5588–5598. [CrossRef]
- Dianov, A.; Anuchin, A. Design of Constraints for Seeking Maximum Torque Per Ampere Techniques in an Interior Permanent Magnet Synchronous Motor. *Mathematics* **2021**, *9*, 2785. [CrossRef]
- Garmut, M.; Steentjes, S.; Petrun, M. Parameter identification for MTPA control based on a nonlinear d-q dynamic IPMSM model. *COMPEL—Int. J. Comput. Math. Electr. Electron. Eng.* **2022**, *42*, 846–860. [CrossRef]
- Jung, W.-S.; Lee, H.-K.; Lee, Y.-K.; Kim, S.-M.; Lee, J.-I.; Choi, J.-Y. Analysis and Comparison of Permanent Magnet Synchronous Motors According to Rotor Type under the Same Design Specifications. *Energies* **2023**, *16*, 1306. [CrossRef]
- Bertoluzzo, M.; Buja, G.; Keshri, R.K.; Menis, R. Sinusoidal Versus Square-Wave Current Supply of PM Brushless DC Drives: A Convenience Analysis. *IEEE Trans. Ind. Electron.* **2015**, *62*, 7339–7349. [CrossRef]
- Yan, M.; Wen, B.; Cui, Q.; Peng, X. Parameter Identification for Maximum Torque Per Ampere Control of Permanent Magnet Synchronous Machines Under Magnetic Saturation. *Electronics* **2024**, *13*, 699. [CrossRef]
- Elshebiny, H.; Szamel, L.; Ahmed, M.K.; Elwany, M.A. High Accuracy Modeling of Permanent Magnet Synchronous Motors Using Finite Element Analysis. *Mathematics* **2022**, *10*, 3880. [CrossRef]

23. Konak, A.; Coit, D.W.; Smith, A.E. Multi-objective optimization using genetic algorithms: A tutorial. *Reliab. Eng. Syst. Saf.* **2006**, *91*, 992–1007. [CrossRef]
24. Li, W.; Zhang, T.; Wang, R.; Huang, S.; Liang, J. Multimodal Multi-objective Optimization: Comparative Study of the State-of-the-art. *Swarm Evol. Comput.* **2023**, *77*, 101253. [CrossRef]
25. Bramerdorfer, G.; Zavoianu, A.-C. Surrogate-Based Multi-Objective Optimization of Electrical Machine Designs Facilitating Tolerance Analysis. *IEEE Trans. Magn.* **2017**, *53*, 1–11. [CrossRef]
26. Zheng, S.; Zhu, X.; Xu, L.; Xiang, Z.; Quan, L.; Yu, B. Multi-Objective Optimization Design of a Multi-Permanent-Magnet Motor Considering Magnet Characteristic Variation Effects. *IEEE Trans. Ind. Electron.* **2022**, *69*, 3428–3438. [CrossRef]
27. Zarko, D.; Stipetic, S.; Martinovic, M.; Kovacic, M.; Jercic, T.; Hanic, Z. Reduction of Computational Efforts in Finite Element-Based Permanent Magnet Traction Motor Optimization. *IEEE Trans. Ind. Electron.* **2018**, *65*, 1799–1807. [CrossRef]
28. Sun, X.; Shi, Z.; Lei, G.; Guo, Y.; Zhu, J. Multi-Objective Design Optimization of an IPMSM Based on Multilevel Strategy. *IEEE Trans. Ind. Electron.* **2021**, *68*, 139–148. [CrossRef]
29. Parekh, V.; Flore, D.; Schöps, S. Deep Learning-Based Prediction of Key Performance Indicators for Electrical Machines. *IEEE Access* **2021**, *9*, 21786–21797. [CrossRef]
30. Gör, H. Feasibility of Six Metaheuristic Solutions for Estimating Induction Motor Reactance. *Mathematics* **2024**, *12*, 483. [CrossRef]
31. Sasaki, H.; Hidaka, Y.; Igarashi, H. Prediction of IPM Machine Torque Characteristics Using Deep Learning Based on Magnetic Field Distribution. *IEEE Access* **2022**, *10*, 60814–60822. [CrossRef]
32. Parekh, V.; Flore, D.; Schöps, S. Deep Learning-Based Meta-Modeling for Multi-Objective Technology Optimization of Electrical Machines. *IEEE Access* **2023**, *11*, 93420–93430. [CrossRef]
33. Li, Y.; Lei, G.; Bramerdorfer, G.; Peng, S.; Sun, X.; Zhu, J. Machine Learning for Design Optimization of Electromagnetic Devices: Recent Developments and Future Directions. *Appl. Sci.* **2021**, *11*, 1627. [CrossRef]
34. Weidenholzer, G.; Silber, S.; Jungmayr, G.; Bramerdorfer, G.; Grabner, H.; Amrhein, W. A flux-based PMSM motor model using RBF interpolation for time-stepping simulations. In Proceedings of the 2013 International Electric Machines & Drives Conference, Chicago, IL, USA, 12–15 May 2013.
35. Mohammed, O.A.; Liu, S.; Liu, Z. A phase variable model of brushless dc motors based on finite element analysis and its coupling with external circuits. *IEEE Trans. Magn.* **2005**, *41*, 1576–1579. [CrossRef]
36. Sizov, G.Y.; Ionel, D.M.; Demerdash, N.A.O. Modeling and Parametric Design of Permanent-Magnet AC Machines Using Computationally Efficient Finite-Element Analysis. *IEEE Trans. Ind. Electron.* **2012**, *59*, 2403–2413. [CrossRef]
37. Steentjes, S.; Leßmann, M.; Hameyer, K. Advanced iron-loss calculation as a basis for efficiency improvement of electrical machines in automotive application. In Proceedings of the Electrical Systems for Aircraft, Railway and Ship Propulsion, Bologna, Italy, 16–18 October 2012.
38. Garmut, M.; Petrun, M. Influence of stator segmentation on iron losses in PMSMs for traction applications. *COMPEL—Int. J. Comput. Math. Electr. Electron. Eng.* **2022**, *41*, 644–658. [CrossRef]
39. gamultiobj: Find Pareto front of Multiple Fitness Functions Using Genetic Algorithm. Available online: <https://www.mathworks.com/help/gads/gamultiobj.html> (accessed on 10 April 2024).

Disclaimer/Publisher’s Note: The statements, opinions and data contained in all publications are solely those of the individual author(s) and contributor(s) and not of MDPI and/or the editor(s). MDPI and/or the editor(s) disclaim responsibility for any injury to people or property resulting from any ideas, methods, instructions or products referred to in the content.

Article

Developing and Evaluating the Operating Region of a Grid-Connected Current Source Inverter from Its Mathematical Model

Carlos R. Baier ^{1,*}, Pedro E. Melin ², Miguel A. Torres ³, Roberto O. Ramirez ¹, Carlos Muñoz ¹ and Agustín Quinteros ¹

¹ Department of Electrical Engineering, Faculty of Engineering, University of Talca, Campus Curicó, Curico 3344158, Chile; roramirez@utalca.cl (R.O.R.); carlosmunoz@utalca.cl (C.M.); aquinteros20@alumnos.utalca.cl (A.Q.)

² Department of Electrical and Electronic Engineering, Universidad del Bío-Bío, Concepción 4051381, Chile; pemelin@ubiobio.cl

³ Universidad de los Andes, Chile, Faculty of Engineering and Applied Science, Santiago 7620086, Chile; matorres@uandes.cl

* Correspondence: cbaier@utalca.cl

Abstract: Grid-connected power inverters are indispensable in modern electrical systems, playing a pivotal role in enhancing the integration of renewable energies into power grids. Their significance, primarily when functioning as grid-forming inverters, extends to maintaining the grid's inertia and strength—a distinct advancement over traditional grid-following operations. As grid-forming inverters, these devices emulate the characteristics of synchronous generators and can act as robust voltage sources, providing essential ancillary services. This behavior is particularly relevant when integrating energy storage systems on the converters' direct current side. Among the various inverter topologies, the current source inverter (CSI) has emerged as a promising yet underexplored alternative for grid-forming applications. CSIs, when paired with their AC output filters, can effectively operate as voltage sources, utilizing control strategies that facilitate the integration of renewable energies into the electrical system. Their design inherently manages output current fluctuations, reducing the need for restrictive current limitations or additional protective measures. This paper examines the operational region of CSIs, obtained through detailed modeling, to explore their advantages, challenges, and potential for enhancing grid-connected systems. Analyzing the operating region from the converter model verifies the limits of where the converter can operate in a plane of active and reactive powers. For a small prototype model operating with 7 amperes in DC and 120 V in AC, it is possible to supply or absorb active power exceeding 1000 W and manage maximum reactive power values around 500 VAR, as determined by its operating region. Simulations also confirm that small changes in the control reference, as little as 5%, towards the region's right limits cause significant oscillations in the dynamic control responses. This research aims to deepen our understanding of CSIs' operational capabilities and highlight their unique benefits in advancing grid-connected systems and promoting the integration of renewable energy using this technology.

Keywords: current source inverter (CSI); grid-forming inverters (GFM); droop control strategy; mathematical model of converters; operating region analysis; voltage and frequency support

MSC: 93-10

1. Introduction

Over the past few decades, the increasing integration of renewable energies into our power systems has posed challenges to both power quality and grid stability, while traditional grid-following inverters effectively channel power from renewable sources,

they are not inherently designed to provide essential frequency or voltage support to the power grids [1]. This absence of voltage and frequency support becomes particularly evident when grid dynamics lead to deviations from nominal frequency and voltage values. Insights gained from microgrid research have unveiled various operational modes for grid-connected inverters. These modes have introduced specific terminologies for inverter operation within microgrids, including grid-following (GFL), grid-forming (GFM), and grid-supporting (GSP) inverters. In each operational mode, grid-connected inverters display behaviors as either voltage or current sources, as illustrated in Figure 1. The key differences between these operational modes lie in their control strategies. GFL inverters traditionally use maximum power point tracking (MPPT) techniques to consistently extract maximum power from renewable generation systems. They also employ phase-locked loop (PLL) algorithms to synchronize with the grid voltage. These synchronization algorithms can generally be used in GSP inverters as well. In contrast, most GFM inverters do not require PLLs, making them more robust in maintaining stable operation under normal grid conditions.

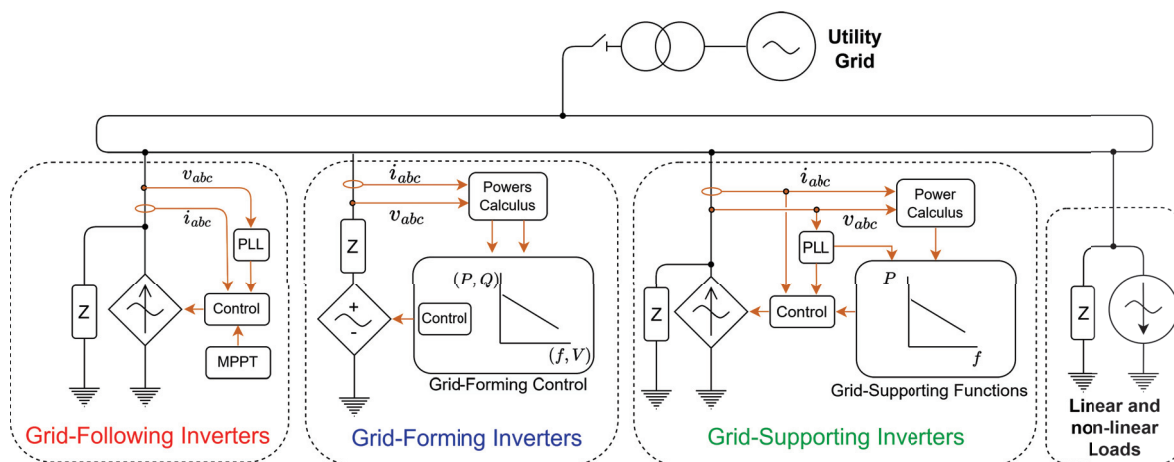


Figure 1. Configuration of inverters operating in various modes within a microgrid.

A GFL inverter maximizes power transfer from the DC side to the AC grid, consistently synchronizing with the frequency and voltage of the connected electrical grid. On the other hand, a GFM inverter demonstrates remarkable resilience by generating power even during grid disconnection or outages, supporting 'black start' scenarios [2,3]. This establishes the frequency and voltage of the microgrid if it operates in isolation from the primary grid, functioning as a reference for other connected converters. Additionally, it offers voltage and frequency support when integrated with the primary grid. Meanwhile, a GSP inverter aims to deliver power from its sources while enhancing grid stability. This can be achieved by providing targeted frequency support through its control mechanisms and converter, as depicted in Figure 1. Additionally, it can potentially offer voltage support. The GSP inverter can operate as a controlled current source, as shown in Figure 1, but it can also function as a voltage source [4]. To emphasize the different control strategies involved, Figure 1 illustrates only one option. For a more comprehensive understanding of these concepts, please refer to [5].

The predominant operation of grid-connected inverters as GFL inverters means that as the amount of renewable energy delivered through such inverters increases, the overall system inertia and the capability to handle frequency and voltage contingencies diminish [6]. However, recent studies have suggested that GFM inverters, which emulate the behavior of synchronous generators, could theoretically enable near-limitless integration of renewable energies into electric grids [7,8]. This advancement primarily leaves the challenge of renewable energy intermittency, a concern potentially mitigated by the augmented deployment of energy storage devices [9,10]. Presently, a variety of control strategies exist to achieve GFM inverters [11]. The droop control scheme stands as the most foundational

and widely recognized method [12,13]. Moreover, direct power control has seen several years of application. Yet, numerous other control schemes have emerged recently [14].

While the specific control scheme may vary to realize a GFM inverter, it is important to note that this mode can be implemented across virtually any inverter topology, as a GFM inverter is essentially an operational mode of a grid-connected inverter. Among the topologies, the VSI remains the most practical and recognized, within which most GFM strategies have been tested. However, studying the CSI for GFM is particularly attractive in this context [15]. If the perspective is expanded to grid-connected operation, it could be said that in recent years, there has been increasing interest in grid-connected CSI for enhanced grid operation [16–19]. In this regard, a comprehensive review of the state of the art is provided in Chapter 2 of this article.

This article presents a novel approach by proposing and exploring the operating regions of grid-forming inverters implemented with the CSI topology enhanced with a CLC (Capacitive-Inductive-Capacitive) filter, which is not addressed in the existing literature. Additionally, the article presents simulations to demonstrate the operation and dynamics within the working zone of the converter. The document is organized as follows: Section 1 contextualizes how power inverters can operate when connected to microgrids and electrical networks. Section 2 briefly compares the VSI and CSI topologies, delving into a detailed review of the state of the art regarding grid-connected CSIs and introducing the operation of the CSI as a grid-forming inverter. Section 3 provides a complete modeling of the grid-connected CSI, covering both dynamic performance and steady-state behavior. Section 4 explains the process of obtaining and analyzing the operating region of the current source converter. Section 5 corroborates the determination of the operating region through simulations at various operating points. Section 6 discusses and comments on the results, and Section 7 draws the document's conclusions.

2. Grid-Forming Inverters Topologies and Control Schemes

2.1. A Brief Comparison between VSI and CSI Topologies

From a topological perspective, the conventional approach to implementing a grid-forming inverter considers a voltage source inverter (VSI). Typically, the VSI incorporates an LCL filter at its AC output before serving local loads or interfacing with the primary grid, as seen in [20–22]. Alternatively, the current source inverter (CSI) has been tested as a grid-connected inverter and can be a topological option for grid-forming inverter operation [15,23,24]. Although its potential in grid-forming applications remains largely untapped, interest in CSI topology has persisted over the years for various other applications [25–27]. When functioning as a grid-forming inverter, the CSI can integrate a CLC (Capacitive-Inductive-Capacitive) filter on its AC output. This filter helps to improve the voltage and power quality provided by the inverter. Similar to its VSI counterpart, it can operate in connected and isolated modes, as depicted in Figure 2. Historically, the CSI has often been overshadowed by the VSI due to perceived technological constraints [28]. The DC-link of the CSI contains a DC current source demanding management, complemented by a series choke inductor.

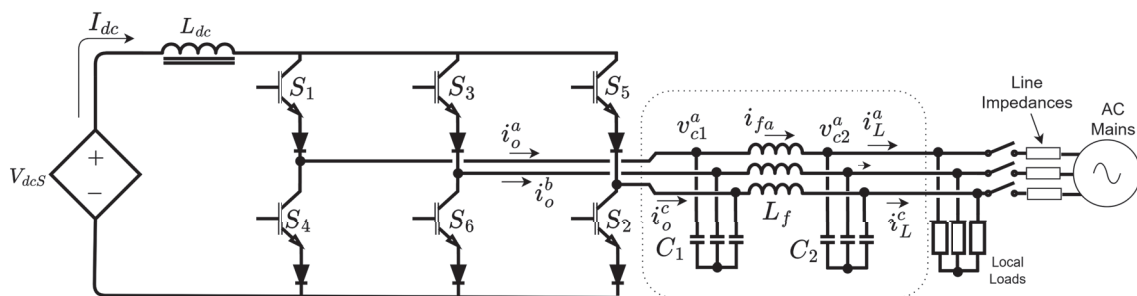


Figure 2. Current source inverter (CSI) and its possible operation as a grid-connected inverter.

The merits of the VSI in comparison to the CSI are both evident and extensively documented [28–31]. A concise comparison of the strengths and limitations of both topologies is presented in Table 1. Among the notable benefits of the VSI is the relative ease with which a converter can be implemented using this technology. The contemporary market even offers ready-to-use power modules. The efficiency of VSIs is further accentuated by incorporating DC capacitors on the DC side, which serve as filters. The maturation of capacitor technology ensures both quality and longevity for these components.

Table 1. A brief comparison of advantages and disadvantages in classic VSI and CSI topologies.

Topology	Advantages	Disadvantages
VSI	<ul style="list-style-type: none"> • Efficient dc filter with very low energy losses. • Low weight of filter (storage element). • It can be switched with frequencies (10 kHz ~ 20 kHz). • It is a more well-known technology. 	<ul style="list-style-type: none"> • Highly vulnerable to damage from short circuits. • It is necessary to regulate and/or limit the output current. • Observed reliability falls short of aspirational standards • Parallel operation is a challenge
CSI	<ul style="list-style-type: none"> • Natural short-circuit protection • It is easier to operate several in parallel on AC sides. • Very high reliability can be achieved 	<ul style="list-style-type: none"> • It is difficult to achieve high efficiency. • More complex modulation and control. • There are losses even in a zero-switching state. • The volume and weight of the DC filter are evident.

Additionally, the reduction in the equivalent series resistance of capacitors and the potential associated loss is evidence of ongoing advancements in this domain. Conversely, DC links in the CSI utilize choke inductors. Several new CSI topologies are emerging, aiming to improve or modify the design on the DC side of these converters [32–34]. Experts in power electronics opine that strides in superconductor development are imperative for choke inductors to attain a technological maturity akin to capacitors [35]. This progression is crucial to mitigating losses associated with filtering DC ripple in CSIs [36,37].

However, the CSI finds niche applications where DC-controlled current is crucial, particularly in systems that demand high reliability. As a topology, it is more reliable than the VSI [38,39]. It is anticipated that future advancements in superconductor technology will further enable the proliferation of CSIs across various applications, leveraging its inherent short-circuit protection [35,40].

2.2. Grid-Forming Control Scheme

In recent years, significant attention has been directed toward GFM inverters, as they hold the potential to facilitate the widespread integration of renewable energy into our electrical grids. These GFM inverters are attainable through advanced control strategies, while the foundational and well-established droop control strategy remains popular for achieving GFM operation, numerous alternative approaches have emerged in recent research. These alternatives empower the inverter to function as a voltage source and provide valuable grid services, including black start capability and inertia support, among other capabilities [41].

A notable control scheme that enables a CSI to function effectively as a GFM inverter is the well-known droop control strategy. Implementing this strategy in the CSI, precisely as depicted in Figure 3, eliminates the need for a traditional inner current control loop—typically used in VSI systems—thanks to the CSI’s inherent ability to regulate current both at the DC side and at the inverter’s output.

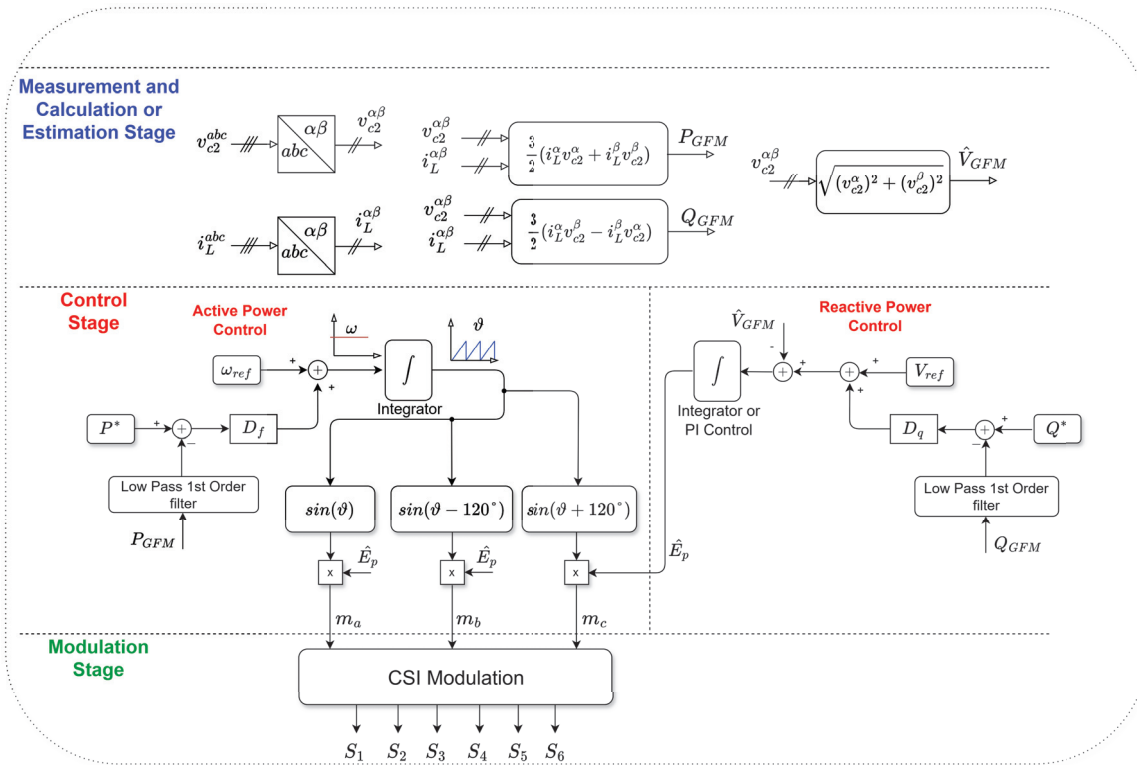


Figure 3. Droop control scheme for application in a CSI.

3. Modeling of a Grid-Connected CSI

3.1. Dynamic Behavior Modeling

A GFM inverter implemented with a CSI, through a droop control scheme as shown in Figure 3, will seek to impose its voltages v_{c2}^a , v_{c2}^b , and v_{c2}^c at the terminals at the output of its CLC filter. If this inverter operates in a microgrid connected to the main grid, then the currents i_L^a , i_L^b , and i_L^c supplied or absorbed by the CSI will be managed by the inverter's control scheme (contributing or absorbing active powers P_{GFM} and/or reactive powers Q_{GFM}). In the case that the microgrid is isolated, these same currents (and powers) will be demanded by the microgrid, altering the voltage and frequency of the inverter according to the predefined curves in the same control scheme [42]. To determine how much power (P_{GFM} and Q_{GFM}) the inverter can contribute or absorb through its operating region, it will be necessary to know its model, whether the inverter operates in a microgrid connected to the main grid or in isolation. For this purpose, a description can be made using the variables observed in Figure 4. Therefore, the three voltages in the capacitances with a value of C_1 can be expressed as follows:

$$\left. \begin{aligned} \frac{dv_{c1}^a}{dt} &= \frac{1}{C_1} (i_o^a - i_f^a) \\ \frac{dv_{c1}^b}{dt} &= \frac{1}{C_1} (i_o^b - i_f^b) \\ \frac{dv_{c1}^c}{dt} &= \frac{1}{C_1} (i_o^c - i_f^c) \end{aligned} \right\}. \quad (1)$$

If a compact notation is adopted, it is possible to present the three equations of the set expressed in (1) as a single equation as follows:

$$\frac{d\mathbf{v}_{c1}^{abc}}{dt} = \frac{1}{C_1} (\mathbf{i}_o^{abc} - \mathbf{i}_f^{abc}), \quad (2)$$

where

$$\mathbf{i}_o^{abc} = [i_o^a \quad i_o^b \quad i_o^c]^T, \quad (3)$$

corresponds to a three-phase array consisting of the output currents i_o^a , i_o^b and i_o^c , whereas

$$\mathbf{i}_f^{abc} = \begin{bmatrix} i_f^a & i_f^b & i_f^c \end{bmatrix}^T, \quad (4)$$

is an array composed of the currents passing through the filter inductances, specifically i_f^a , i_f^b , and i_f^c . Moreover, it is required that

$$\frac{d\mathbf{v}_{c1}^{abc}}{dt} = \begin{bmatrix} \frac{dv_{c1}^a}{dt} & \frac{dv_{c1}^b}{dt} & \frac{dv_{c1}^c}{dt} \end{bmatrix}^T, \quad (5)$$

which is the array of the derivatives of the voltages v_{c1}^a , v_{c1}^b and v_{c1}^c , which are the voltages across the first capacitor bank.

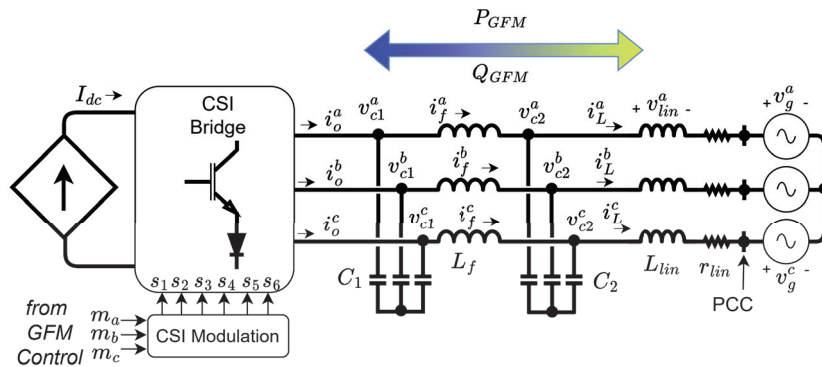


Figure 4. CSI schematic with variables needed for modeling.

Taking into account the voltages within the CLC filter, it is possible to present the state equation of the currents in the filter inductor (in a compact notation) as

$$\frac{d\mathbf{i}_f^{abc}}{dt} = \frac{1}{L_f} (\mathbf{v}_{c1}^{abc} - \mathbf{v}_{c2}^{abc}), \quad (6)$$

where \mathbf{v}_{c1}^{abc} contains the voltages v_{c1}^a , v_{c1}^b , and v_{c1}^c , while \mathbf{v}_{c2}^{abc} contains the voltages v_{c2}^a , v_{c2}^b , and v_{c2}^c . Similarly, the behavior of the voltages across the capacitor C_2 can be expressed as:

$$\frac{d\mathbf{v}_{c2}^{abc}}{dt} = \frac{1}{C_2} (\mathbf{i}_f^{abc} - \mathbf{i}_L^{abc}), \quad (7)$$

where the array of currents \mathbf{i}_L^{abc} contains the load currents of the inverter i_L^a , i_L^b , and i_L^c , contributed to or absorbed from the PCC (Point of Common Coupling).

Given the converter's connection to the Point of Common Coupling (PCC) through a line characterized by a small inductance (L_{lin}) and minimal resistance (r_{lin}), forming the line impedance and excluding the consideration of a local load for this context, as can be seen in Figure 4, the following equations are applicable within the ABC coordinate system:

$$\frac{d\mathbf{i}_L^{abc}}{dt} = \frac{1}{L_{lin}} (\mathbf{v}_{c2}^{abc} - r_{lin} \mathbf{i}_L^{abc} - \mathbf{v}_g^{abc}), \quad (8)$$

where \mathbf{v}_g^{abc} corresponds to the grid voltages to which the inverter is connected.

In the case of a perfectly balanced system, Equations (2), (6), (7), and (8) can be transformed into dq axes using compact notation. These four equations can now be expressed as:

$$\left. \begin{aligned} \frac{d\mathbf{v}_{c1}^{dq}}{dt} &= -\mathbf{W}\mathbf{v}_{c1}^{dq} + \frac{1}{C_1}(\mathbf{i}_o^{dq} - \mathbf{i}_f^{dq}) \\ \frac{d\mathbf{i}_f^{dq}}{dt} &= -\mathbf{W}\mathbf{i}_f^{dq} + \frac{1}{L_f}(\mathbf{v}_{c1}^{dq} - \mathbf{v}_{c2}^{dq}) \\ \frac{d\mathbf{v}_{c2}^{dq}}{dt} &= -\mathbf{W}\mathbf{v}_{c2}^{dq} + \frac{1}{C_2}(\mathbf{i}_f^{dq} - \mathbf{i}_L^{dq}) \\ \frac{d\mathbf{i}_L^{dq}}{dt} &= -\mathbf{W}\mathbf{i}_L^{dq} + \frac{1}{L_{lin}}(\mathbf{v}_{c2}^{dq} - r_{lin}\mathbf{i}_L^{dq} - \mathbf{v}_g^{dq}) \end{aligned} \right\}, \quad (9)$$

where \mathbf{W} is defined as a matrix with the frequency information ω , given by the following:

$$\mathbf{W} = \begin{bmatrix} 0 & -\omega \\ \omega & 0 \end{bmatrix}. \quad (10)$$

In the set of expressions provided in (9), it should be understood that the vectors \mathbf{v}_{c1}^{dq} and \mathbf{v}_{c2}^{dq} contain the voltages v_{c1}^d and v_{c1}^q in the first array, as well as v_{c2}^d and v_{c2}^q in the second array. Similarly, the current array \mathbf{i}_o^{dq} includes the currents i_o^d and i_o^q , while the term \mathbf{i}_f^{dq} encompasses i_f^d and i_f^q . Additionally, \mathbf{i}_L^{dq} accounts for the currents i_L^d and i_L^q .

Regarding the CSI, it is known that the currents \mathbf{i}_o^{abc} are imposed at the output by the inverter bridge itself, which reflects the current I_{dc} , through modulators, in each output line as follows:

$$\mathbf{i}_o^{abc} = \begin{bmatrix} i_o^a \\ i_o^b \\ i_o^c \end{bmatrix} = \begin{bmatrix} m'_a \\ m'_b \\ m'_c \end{bmatrix} I_{dc}, \quad (11)$$

where modulators m'_a , m'_b , and m'_c originate from the sinusoidal signals of the controller (the signals m_a , m_b , and m_c in Figure 3), which have an amplitude M and a possible phase shift ϕ with respect to the grid. When passing through the modulation block in the inverter, the CSI signals m'_a , m'_b , and m'_c undergo a gain G_{ac} . The effect of the inverter bridge topology on modulation, whether operating as an inverter or rectifier, introduces a 30-degree phase shift in these signals compared to the original ones from the controller [43]. Therefore, these signals can be represented as:

$$\begin{bmatrix} m'_a \\ m'_b \\ m'_c \end{bmatrix} = G_{ac}M \begin{bmatrix} \sin(\omega t + \pi/6 + \phi) \\ \sin(\omega t - \pi/2 + \phi) \\ \sin(\omega t + 5\pi/6 + \phi) \end{bmatrix}. \quad (12)$$

Taking this angle ϕ into account, these modulation signals, when transformed into dq axes, can be represented in terms of their modulation index M and the modulation type gain G_{ac} as follows:

$$\begin{bmatrix} m'_d \\ m'_q \end{bmatrix} = G_{ac}M \begin{bmatrix} \sin(\phi + \frac{\pi}{6}) \\ -\cos(\phi + \frac{\pi}{6}) \end{bmatrix}. \quad (13)$$

Then, the currents \mathbf{i}_o^{dq} can be presented as:

$$\mathbf{i}_o^{dq} = \begin{bmatrix} i_o^d \\ i_o^q \end{bmatrix} = M_G I_{dc} \begin{bmatrix} \sin(\phi_r) \\ -\cos(\phi_r) \end{bmatrix}, \quad (14)$$

where $M_G = G_{ac}M$ and $\phi_r = \phi + \frac{\pi}{6}$.

3.2. Modeling of Steady-State Behavior

In the context of steady-state analysis, it becomes feasible to formulate the system's behavior within the dq reference frame by equating the derivatives of the dynamic model

to zero. Under this condition, starting from the first expression in the group of equations in (9), the following compact expression can be derived:

$$\mathbf{i}_f^{\text{dq}} = \begin{bmatrix} i_f^d \\ i_f^q \end{bmatrix} = C_1 \omega \begin{bmatrix} v_{c1}^q \\ -v_{c1}^d \end{bmatrix} + \begin{bmatrix} i_o^d \\ i_o^q \end{bmatrix}. \quad (15)$$

Also, the output voltages $\mathbf{v}_{c2}^{\text{dq}}$ in the CLC filter, in steady state, can be expressed as follows:

$$\mathbf{v}_{c2}^{\text{dq}} = \begin{bmatrix} v_{c2}^d \\ v_{c2}^q \end{bmatrix} = L_f \omega \begin{bmatrix} i_f^q \\ -i_f^d \end{bmatrix} + \begin{bmatrix} v_{c1}^d \\ v_{c1}^q \end{bmatrix}, \quad (16)$$

whereas the output currents of the CLC filter should behave in a steady state as follows:

$$\mathbf{i}_L^{\text{dq}} = \begin{bmatrix} i_L^d \\ i_L^q \end{bmatrix} = C_2 \omega \begin{bmatrix} v_{c2}^q \\ -v_{c2}^d \end{bmatrix} + \begin{bmatrix} i_f^d \\ i_f^q \end{bmatrix}. \quad (17)$$

Finally, if the inverter is connected to a grid with \mathbf{v}_g^{dq} voltages, the steady state voltages can be expressed as follows:

$$\mathbf{v}_g^{\text{dq}} = \begin{bmatrix} v_g^d \\ v_g^q \end{bmatrix} = L_{lin} \omega \begin{bmatrix} i_L^q \\ -i_L^d \end{bmatrix} + \begin{bmatrix} v_{c2}^d - r_{lin} i_L^d \\ v_{c2}^q - r_{lin} i_L^q \end{bmatrix}. \quad (18)$$

Then, if the grid-connected CSI operates in steady state, the voltage and current values of the same inverter can be corroborated from the expressions (14) to (18).

The validity of the expressions above presupposes the presence of a modulation block within the control strategy that enables a CSI to function as a GFM converter. These expressions form the basis for delineating an operating region. Within this region, it is possible to discern the potential power outputs (P_{GFM} and Q_{GFM}) of the inverter, along with the upper limits of current magnitude contributed by both the inverter and its associated filter. Understanding this operational range is crucial during the converter's design phase and even during operation since it conveys information about its power handling capacity.

4. Operating Region of a Grid-Connected CSI

4.1. Equations to Find the Operating Region

If the filter capacitance values are chosen with a design ratio of $C_1 = 2C_2$ for the sake of analytical convenience, assuming that ω is in a steady state (remains without variation) and taking into account expressions (14) to (16), we can express the currents i_o^d and i_o^q as follows:

$$\mathbf{i}_o^{\text{dq}} = \begin{bmatrix} i_o^d \\ i_o^q \end{bmatrix} = \begin{bmatrix} v_{c2}^q \sigma_1 + i_L^d \sigma_2 \\ -v_{c2}^d \sigma_1 + i_L^q \sigma_2 \end{bmatrix}, \quad (19)$$

where

$$\left. \begin{aligned} \sigma_1 &= (2C_2 L_f \omega^2 - 3) \omega C_2 \\ \sigma_2 &= (1 - 2C_2 L_f \omega^2) \end{aligned} \right\}. \quad (20)$$

Assuming the magnitude and phase of the modulators (M and ϕ) as inputs provided by a control system, the DC current value (I_{dc}), and the grid voltages (v_g^d and v_g^q , which are the d and q voltages at the point where the converter connects to the network), are known or measurable, one can derive a system of four nonlinear equations with four unknown variables. This derivation involves considering Equations (14) and (19), and setting the

expressions outlined in (18) to zero. The resultant system can be concisely represented as follows:

$$\left. \begin{aligned} f_1(\mathbf{v}_{c2}^{dq}, \mathbf{i}_L^{dq}) &= v_{c2}^q \sigma_1 + i_L^d \sigma_2 - M_G I_{dc} \sin(\phi_r) = 0 \\ f_2(\mathbf{v}_{c2}^{dq}, \mathbf{i}_L^{dq}) &= -v_{c2}^d \sigma_1 + i_L^q \sigma_2 + M_G I_{dc} \cos(\phi_r) = 0 \\ f_3(\mathbf{v}_{c2}^{dq}, \mathbf{i}_L^{dq}) &= -v_g^d + L_{lin} \omega i_L^q + v_{c2}^d - r_{lin} i_L^d = 0 \\ f_4(\mathbf{v}_{c2}^{dq}, \mathbf{i}_L^{dq}) &= -v_g^q - L_{lin} \omega i_L^d + v_{c2}^q - r_{lin} i_L^q = 0 \end{aligned} \right\}. \quad (21)$$

Subsequently, by considering a control input where the modulator's magnitude (M) and phase (ϕ_r) are held constant in a steady state and assuming a nominal grid voltage, solving the system described above allows for the identification of an operating point.

It is important to note that, with the determined voltage and current values, one can calculate the active power (P_{GFM}) and reactive power (Q_{GFM}) that the inverter is capable of delivering or absorbing through the CLC filter as follows:

$$\begin{bmatrix} P_{GFM} \\ Q_{GFM} \end{bmatrix} = \frac{3}{2} \begin{bmatrix} v_{c2}^d i_L^d + v_{c2}^q i_L^q \\ v_{c2}^q i_L^d - v_{c2}^d i_L^q \end{bmatrix}. \quad (22)$$

The magnitude of the voltage, at the filter output itself, can also be determined as follows:

$$\hat{V}_{GFM} = \sqrt{(v_{c2}^d)^2 + (v_{c2}^q)^2} \quad (23)$$

Finally, the magnitude of the inverter output current will also be relevant from a practical point of view, as this will allow the correct selection of the semiconductors needed in the converter. This magnitude can be derived from Equation (14) and can be written as follows:

$$\hat{I}_O = M_G I_{dc}. \quad (24)$$

By evaluating all possible inputs from the system controller—varying the modulator's magnitude M from 0 to 1, varying the phase ϕ between $-\pi$ and π , and considering a nominal grid voltage—a comprehensive set of solutions can be obtained by solving the system outlined in (21) for each input configuration. These solutions collectively define what we can refer to as the full operating region, a comprehensive map of potential operating points.

Solutions can be obtained by knowing the fixed parameters and variables of a specific CSI for which the analysis is desired. For instance, in this study, an operating region can be determined for a small prototype inverter being implemented in the laboratory. The prototype has the data from Table 2.

Table 2. Parameters and fixed variables for the CSI in this document.

Parameter or Variable	Description	Values
I_{dc}	DC Source Current	7 A
C_1	Filter capacitor 1	60 μ F
C_2	Filter capacitor 2	30 μ F
L_f	Filter inductance	5 m H
G_{ac}	Modulation gain	0.866
\hat{V}_{nom}	Output magnitude voltage	120 V

4.2. Operating Region for a Specific Grid-Forming CSI

Considering the system of equations provided by the expressions in (21), and taking into account specific parameters and characteristics of the grid-connected CSI converter, including the sizes of capacitances and inductances in the CLC filter, the current I_{dc} , modulation type, gain G_{ac} , and the magnitude of the nominal operating voltage \hat{V}_{nom} , in Table 2, the system can be solved numerically. For each input involving a value M and its

phase ϕ applied to the equations in (21), the solution can be achieved by employing the Levenberg–Marquardt method in Matlab, thus determining the voltages and currents in dq axes (v_{c2}^{dq}, i_L^{dq}).

After the procedures described above are completed, it is possible to compute each solution's active and reactive powers according to Equation (22), using the obtained values for voltages and currents. By systematically evaluating all possible inputs for the modulator M and its phase ϕ and calculating the corresponding pairs of power values P_{GFM} and Q_{GFM} , these powers can be graphically represented as functions of the modulator's magnitude. The results are depicted in Figure 5.

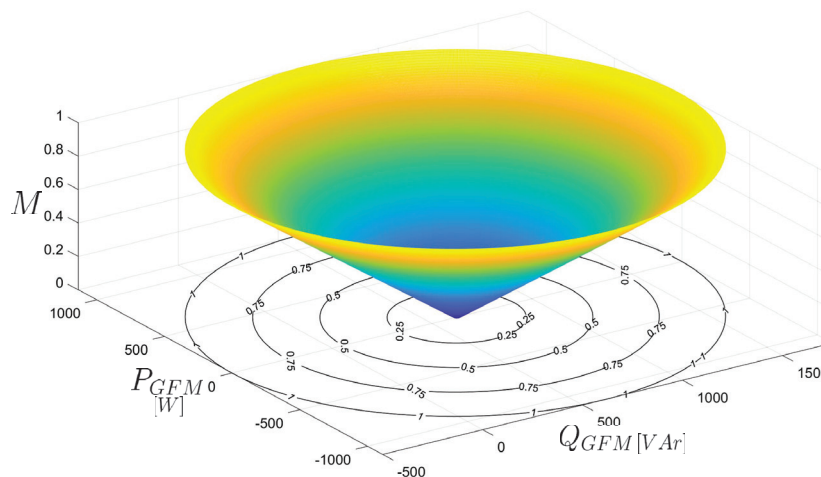


Figure 5. Modulator magnitude versus active and reactive powers.

By focusing on specific iso-value contours that represent the modulation index (M) and projecting them onto the xy -plane, where the active and reactive powers of the inverter are depicted, as demonstrated in Figure 5, well-defined limits become evident for the achievable power levels associated with the converter listed in Table 2. It is worth noting that when $M = 1$, it becomes apparent that the lowest attainable reactive power for this particular converter remains below -500 VAr. A clearer illustration related to the above is shown in Figure 6.

As observed in Figures 5 and 6, there is a substantial operating region for power, characterized by a circular shape within the reactive and active power plane. This pattern suggests a symmetric potential for power output from the converter, with consistent limits radiating in every direction from the center. However, from a practical perspective, control strategies for grid-forming converters, aimed at controlling the output voltage with reference to the active and reactive powers, typically have an operating range for modulation angles that is limited to only two quadrants. This occurs because synchronization is achieved through the active power, and with these control schemes, only one power-frequency pair is feasible for synchronization. In the region identified, there are two potential operating points with the same active power value, dependent on the ϕ_r angle of the control system. Consequently, the control can only achieve synchronism with the powers produced in the first and second quadrants of the modulators. A similar situation is observed with synchronous machines, which can operate with their load angles only in two quadrants; outside these quadrants, synchronism is lost [44,45].

Analysis of the data from the operating region reveals distinct active power values P_{GFM} as functions of the modulator angle ϕ_r across various modulation indices M , as illustrated in Figure 7. For each modulation index M , there are typically two possible active power values, except at the extremes; the maximum active power is attained when $\phi_r = 0$, and the minimum is observed at $\phi_r = \pi$.

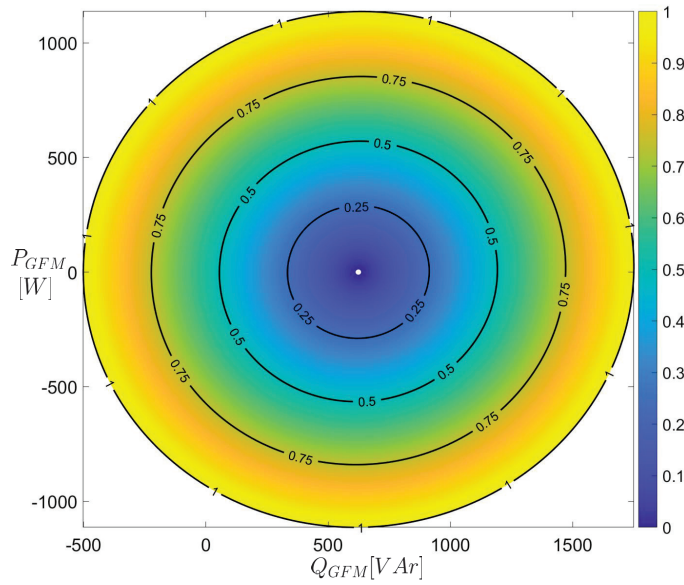


Figure 6. Full theoretical operating region for the grid-connected CSI, obtained through contours.

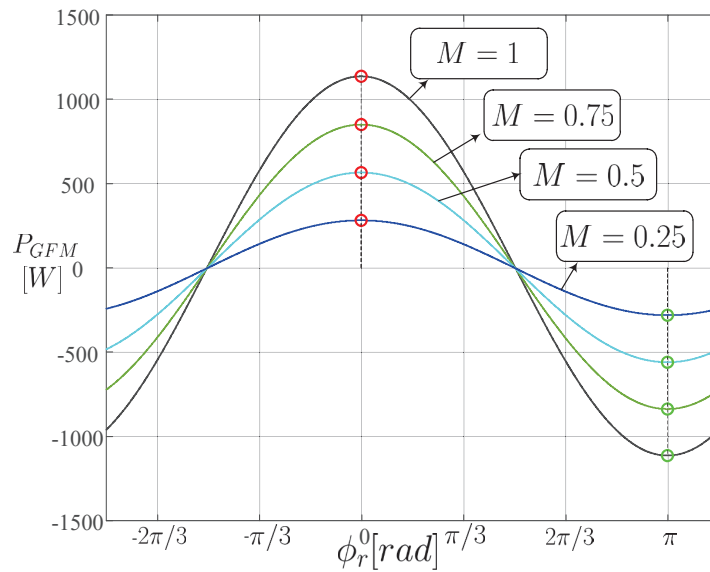


Figure 7. Output power versus modulator angle for various modulator magnitudes.

In control strategies analogous to those used in synchronous machines—such as the droop control, power synchronization control (PSC), or virtual synchronous machine control (VSM) strategies—the modulator phase angle plays a critical role similar to the power angle in synchronous machines [46]. It is understood that decreasing the modulator phase angle beyond zero radians risks losing synchrony, just as increasing it beyond π radians would. Consequently, the operational region for phase angles is inherently bounded between 0 and π radians to maintain synchronism.

Taking into account the above-described range for modulation angle, the entire region can be delineated and segmented into two zones: the sync-guaranteed region, where synchronization is assured, and the out-of-sync region, where synchronization cannot be guaranteed. The resulting graph is shown in Figure 8.

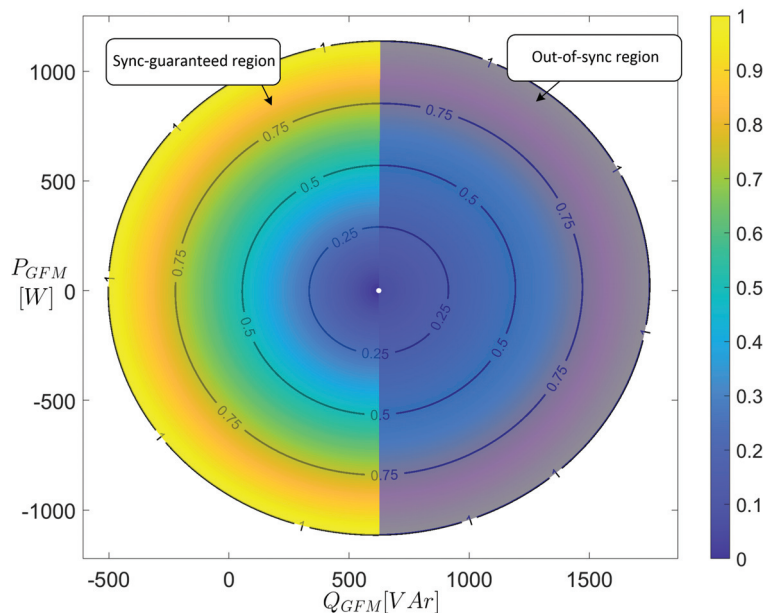


Figure 8. Operating regions with guaranteed synchronism and without synchronism for grid-forming strategies for CSI.

4.3. Effects of CLC Filter Design Variations on the Operating Region

It is important to note that the external contour and the complete operating region can shift, expand, or contract in the power plane depending on the design parameters of the CLC filter, the system's operating frequency, or the magnitude of the DC current. For example, if one compares the external contour of the operating region obtained with the CLC filter parameters from Table 2 with the contours of two regions obtained by varying the CLC filter parameters, a variation referred to in this document as 'Redu', which corresponds to a reduction in the size of the CLC filter, with filter values given as $C_1 = 40 \mu\text{F}$, $C_2 = 20 \mu\text{F}$, and $L_f = 3 \text{ mH}$, and another variation referred to in this document as 'Incr', with an increase in the size of the filter, with CLC filter values given as $C_1 = 80 \mu\text{F}$, $C_2 = 40 \mu\text{F}$, and $L_f = 7 \text{ mH}$. By obtaining the external contours of the operating regions for $M = 1$ of these two variations and superimposing them with the region obtained for Table 2, it is possible to see in Figure 9 that in the case of the 'Redu' variation (filter with reduced values), the converter's region will shift to the left, allowing it to absorb a greater magnitude of reactive power if desired but reducing the maximum and minimum possible values of active power. On the other hand, if the operating region is obtained with the filter parameters of the 'Incr' variation (filter with increased values), the external contour and the operating region will shift to the right, reducing the maximum reactive power absorption capacity but increasing the maximum and minimum active powers that the converter could supply or absorb.

In summary, obtaining the operating region for the CSI with a CLC filter allows for the evaluation of different filter designs by analyzing the external contours, as well as determining the maximum and minimum power levels, which, in part, will depend on the specific parameter designs.

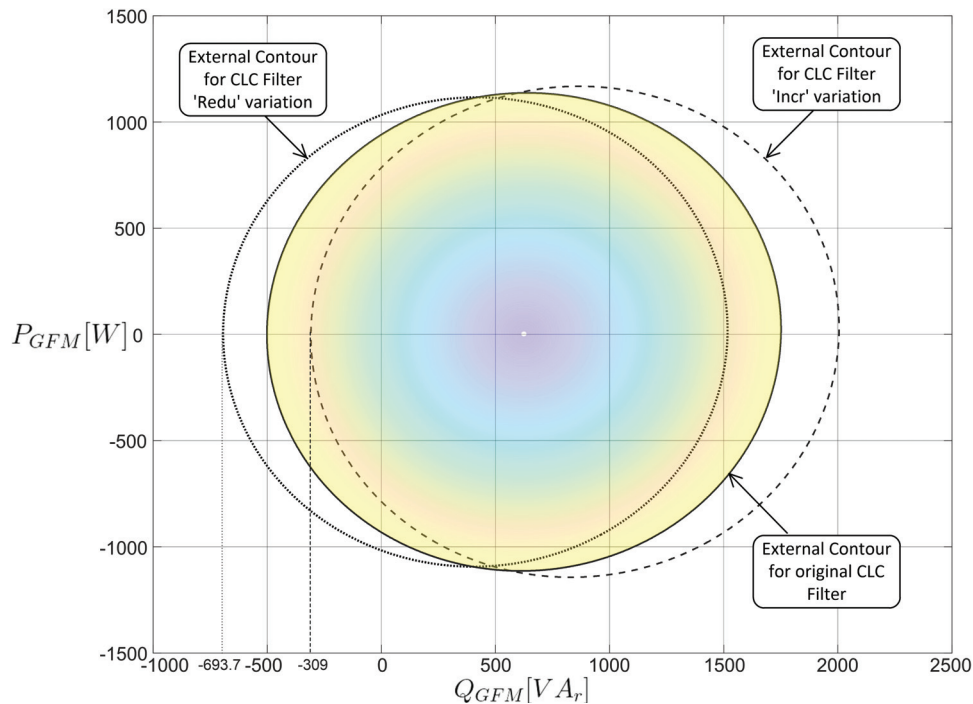


Figure 9. Shifts in the external contours of the operating region due to changes in CLC filter parameters.

5. Corroborating Results and Simulations of the Model and Operating Region

Simulation serves as an invaluable method for validating the operation of the CSI converter, utilizing the control strategy depicted in Figure 3. This validation ensures that the operating region identified aligns seamlessly with the proposed system configuration. In this study, five potential reference points have been selected for operational validation, as detailed in Table 3. In the initial section of this chapter, three distinct operating points are carefully chosen and subjected to comprehensive testing within this region. These tests include (i) test point R, located at the left boundary of the region, achieving a modulation value close to $M = 1$; (ii) test point S, exploring an operating point near the right edge, with a modulation value of $M = 0.5$; and (iii) test point T, assessing an operating point with a lower modulation value of $M = 0.25$, slightly further from the right edge than the second case. Following these steady-state tests, three dynamic response tests will be conducted, involving transitions between these points. Finally, the results will be discussed in a concise yet insightful manner.

Table 3. Power references given for the operating points to be analyzed in simulations.

Operating Point Name	Active Power (P_{GFM})	Reactive Power (Q_{GFM})
Test Point R	−300 W	−460 VAr
Test Point S	585 W	595 VAr
Test Point T	229 W	464 VAr
Test Point RE	281.9 W	626.9 VAr
Test Point OS	229 W	790.8 VAr

5.1. Steady State Tests

In the initial simulated scenario, Test 1 at test point R, the control system is configured to have the converter absorb both active and reactive power—approximately −300 W and −460 VAr, respectively. If, through the references, there were a request for slightly less active or reactive power, the control would lead to over-modulation (a value of M greater than 1). Figure 10's left panel displays waveforms that include the modulation signal m_a and its magnitude M , as well as the voltage in phase a and its magnitude (see Figure 10b), the load current in line a (Figure 10c), and the recorded values of active and reactive powers

(Figure 10d). On the right side of Figure 10, the operating region plots illustrate potential power data along the x and y axes relative to the modulation index M . The operating point where $M = 1$ is marked, aligning the active and reactive power values from the simulation in Figure 10d with the axes.

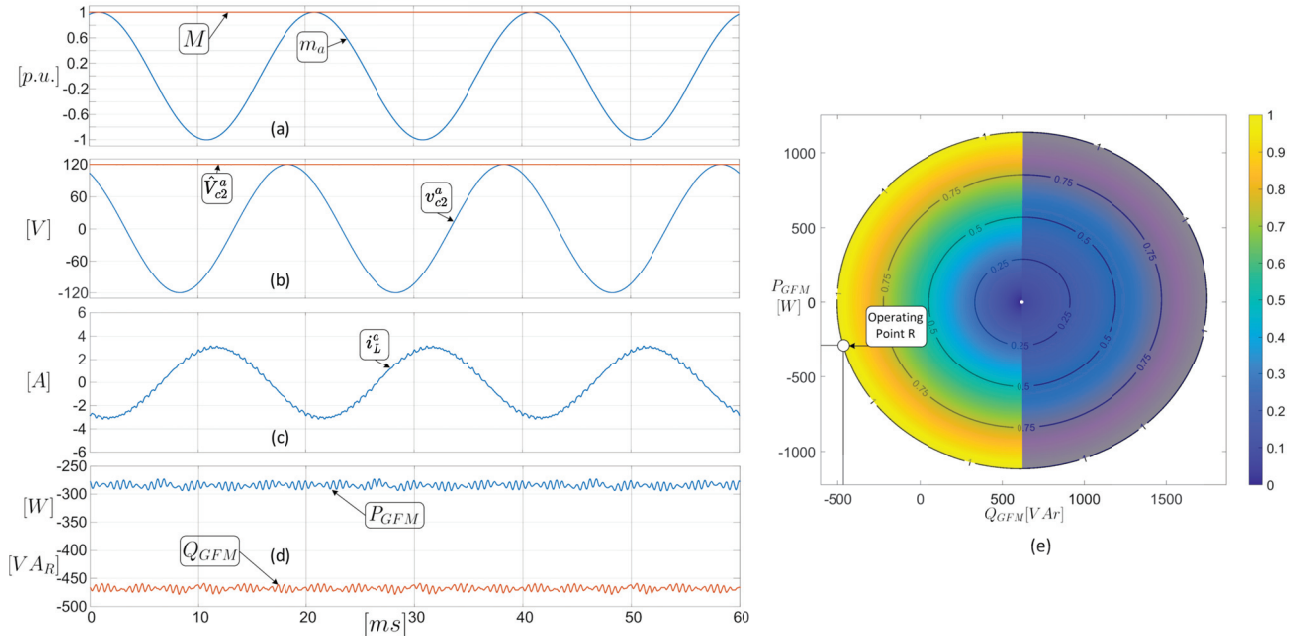


Figure 10. Test 1 waveforms and operating points. (a) Modulator and modulator magnitude; (b) output phase voltage of converter and magnitude of this voltage; (c) load current waveform in line 'a'; (d) active and reactive power of the converter; (e) operating point of the modulator magnitude as seen from its operating region.

In the second simulated scenario, Test 2 at test point S, the control scheme is adjusted to set the converter to deliver specific positive power levels: 585 W of active power and 595 VAr of reactive power. On the left side of Figure 11, fundamental waveforms are once again visible: the modulator a , its modulation index M , the voltage waveform in phase a and its magnitude, and the output current in line a . Additionally, the measured active and reactive powers are displayed in Figure 11d. Analysis of the operating region indicates that the operating point is within the synchronization-guaranteed region but quite close to the limit where the out-of-sync region begins, with the modulation index magnitude set at $M = 0.5$. This is corroborated by both Figure 11a from the simulation and Figure 11e within the operating region. The measured active and reactive power values at the converter's output precisely match the corresponding point within the system's operating area.

In the third simulated experiment, Test 3 at test point T, the control scheme adjusts the power references to achieve a modulation index (M) of 0.25, thus positioning the operating point further from the boundary where the out-of-sync region begins, compared to the previous case. The active and reactive power values are set at 229 W and 464 VAr, respectively. Figure 12 showcases the modulators, the phase 'a' voltage, the load line 'a' current, and both active and reactive power readings. An examination of Figure 12a and the power values in Figure 12d which are stably maintained by the droop control proposed in Figure 3 clearly indicates that the modulation and power values are in line with the predictions from the operating region, as illustrated in Figure 12e.

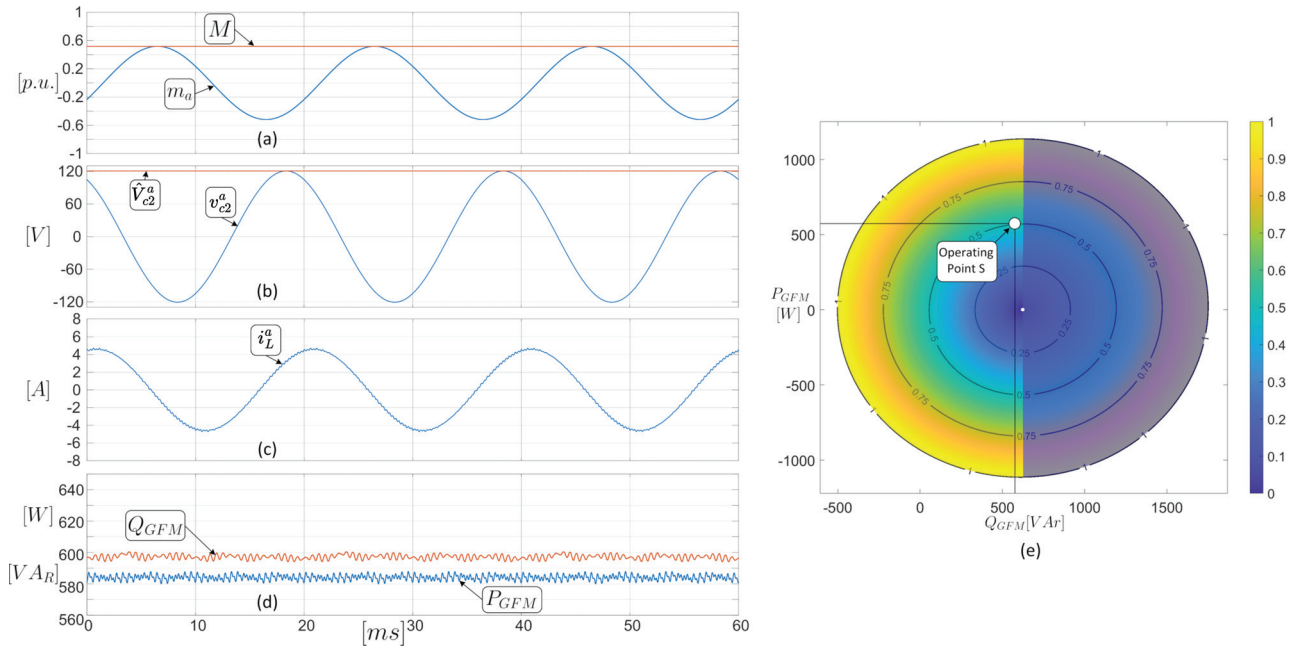


Figure 11. Test 2 waveforms and operating points. (a) Modulator and modulator magnitude; (b) output phase voltage of converter and magnitude of this voltage; (c) load current waveform in line 'a'; (d) active and reactive power of the converter; (e) operating point of the modulator magnitude as seen from its operating region.

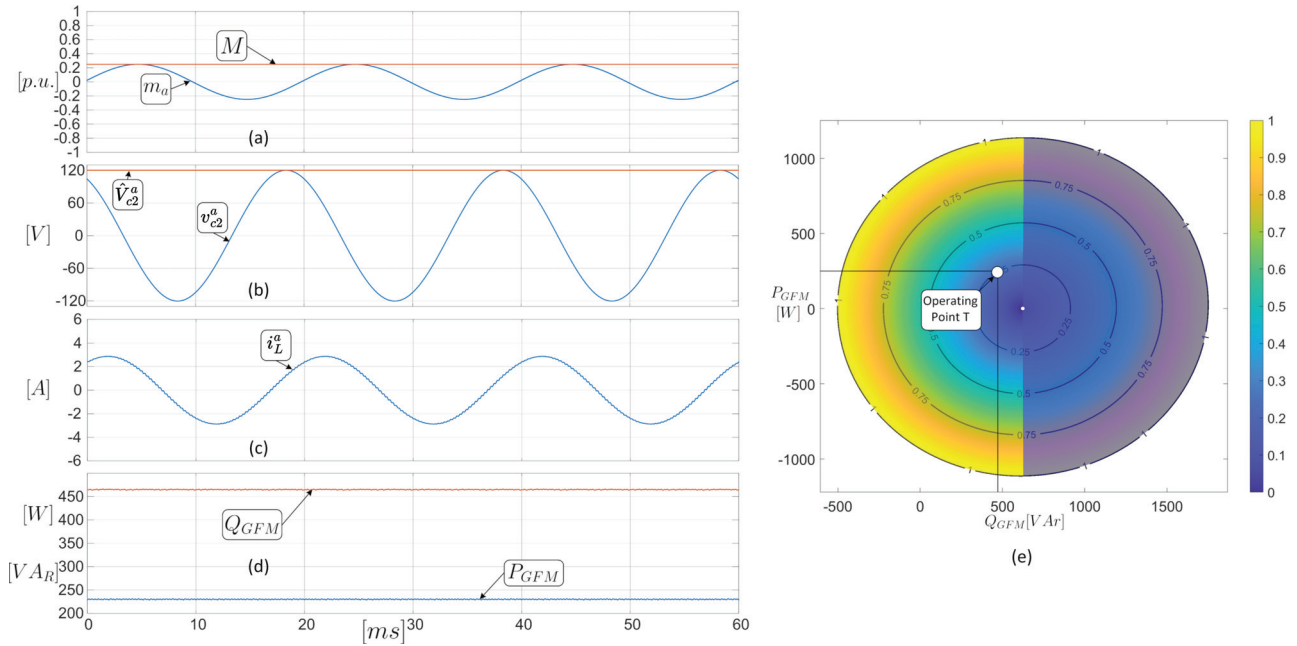


Figure 12. Test 3 waveforms and operating points. (a) Modulator and modulator magnitude; (b) output phase voltage of converter and magnitude of this voltage; (c) load current waveform in line 'a'; (d) active and reactive power of the converter; (e) operating point of the modulator magnitude as seen from its operating region.

5.2. Test in Transient State

To assess dynamic changes within and outside the operating region, four simulation tests are conducted using the control strategy depicted in Figure 3. Dynamic Test 1 evaluates the system's response to a step change from test point T to test point R. Dynamic Test 2 assesses the response to a step change from T to S. It should be noted that these three points,

R, S, and T, were previously analyzed statically in the initial tests. Dynamic Test 3 examines the response to a step change from T to an operating point at the right edge, designated as RE. Finally, Dynamic Test 4 investigates the system's response to a step change from T to an operating point OS in the out-of-sync region.

In Dynamic Test 1, as illustrated in Figure 13, the modulator M transitions from a value of 0.25 to 1 per unit (p.u.) at $t = 50$ ms, moving from test point T to test point R. The inverter output voltage remains close to the nominal value, while transients are observed in both current and power. Initially, the active and reactive powers are $P_{GFM_T} = 229$ W and $Q_{GFM_T} = 464$ VAr, respectively. These values shift to $P_{GFM_R} = -300$ W and $Q_{GFM_R} = -460$ VAr, indicating that both power outputs in the converter transition from positive to negative values.

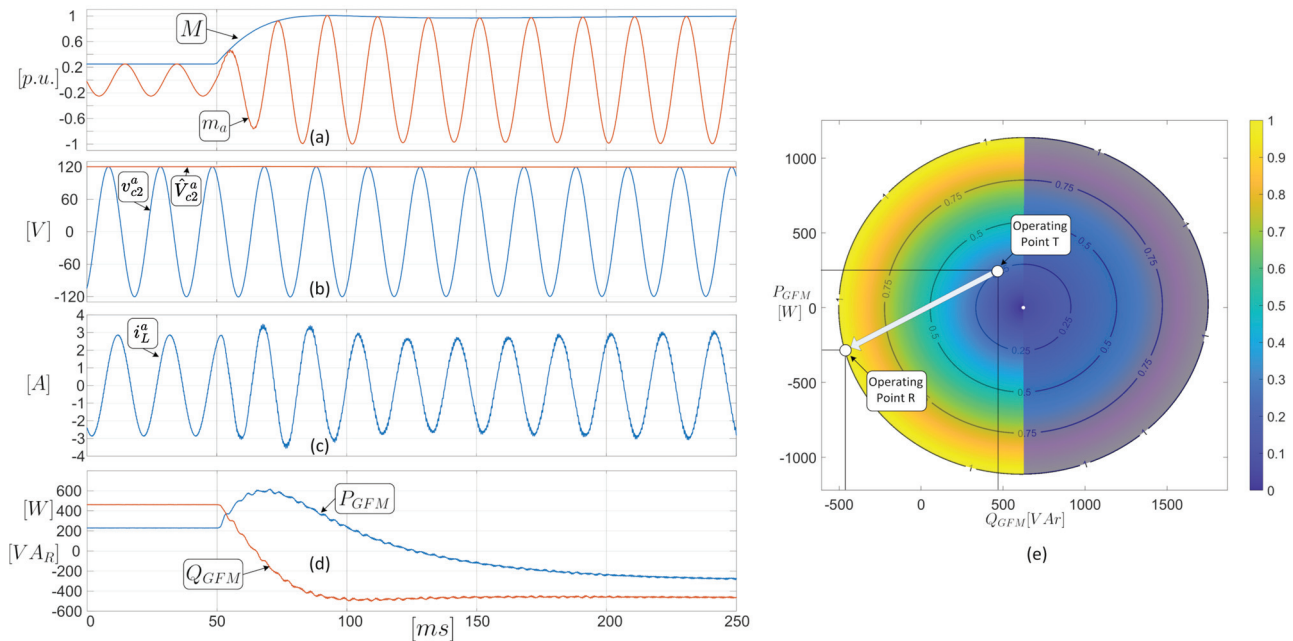


Figure 13. Dynamic Test 1 waveforms and operating points. (a) Modulator and modulator magnitude; (b) output phase voltage of converter and magnitude of this voltage; (c) load current waveform in line 'a'; (d) active and reactive power of the converter; (e) operating point of the modulator magnitude as seen from its operating region.

Dynamic Test 2 introduces a subtle shift from operating point T with $M = 0.25$ p.u. to operating point S with $M = 0.5$ p.u. This latter point is near the boundary where synchronism might be compromised. As seen in Figure 14, upon initiating the change in the control system at $t = 400$ ms, the modulator magnitude exhibits an underdamped response. Similarly, the active and reactive powers in the converter undergo an underdamped transition from point T to point S but stabilize by $t = 1900$ ms. Notably, during this transient response, the system's damping characteristics diminish as the operating point moves from a region far from the out-of-sync boundary toward it.

In Dynamic Test 3, the observations noted at the end of the previous paragraph are confirmed. This test involves transitioning from operating point T, with $M = 0.25$ p.u., to an operating point designated as RE, also at $M = 0.25$ p.u., located very close to the onset of the out-of-sync region. As illustrated in Figure 15, the waveforms of the modulator, currents, and powers display a highly underdamped response, far more pronounced than the responses observed in Figure 14.

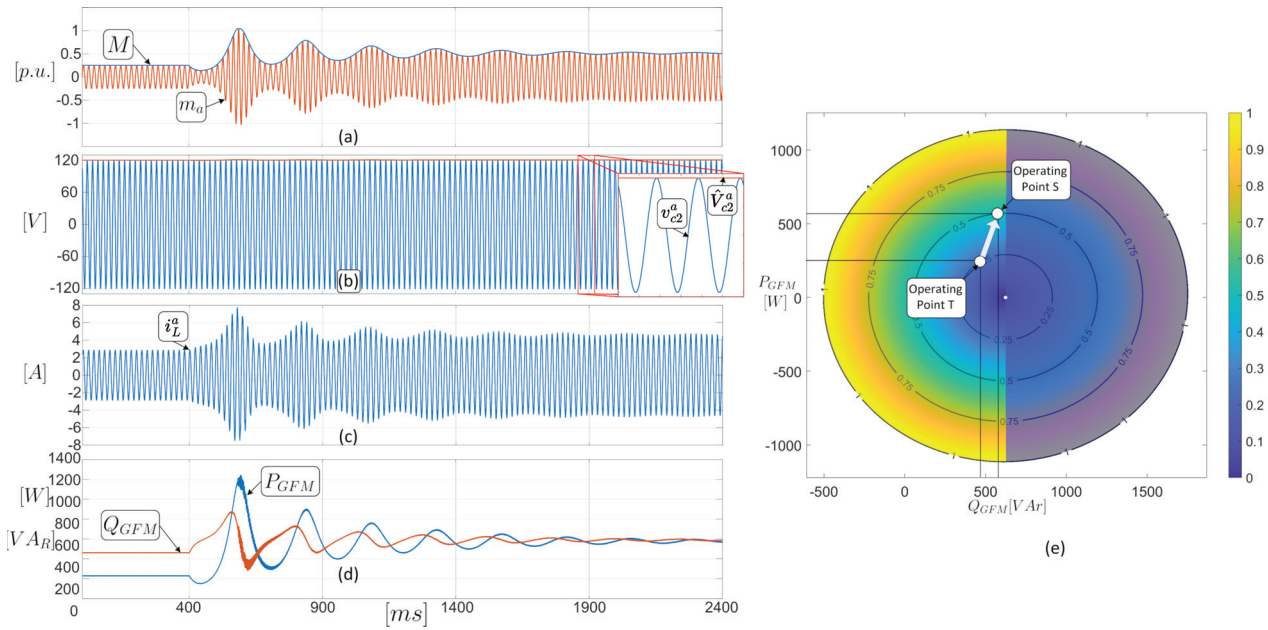


Figure 14. Dynamic Test 2 waveforms and operating points. (a) Modulator and modulator magnitude; (b) output phase voltage of converter and magnitude of this voltage; (c) load current waveform in line 'a'; (d) active and reactive power of the converter; (e) operating point of the modulator magnitude as seen from its operating region.

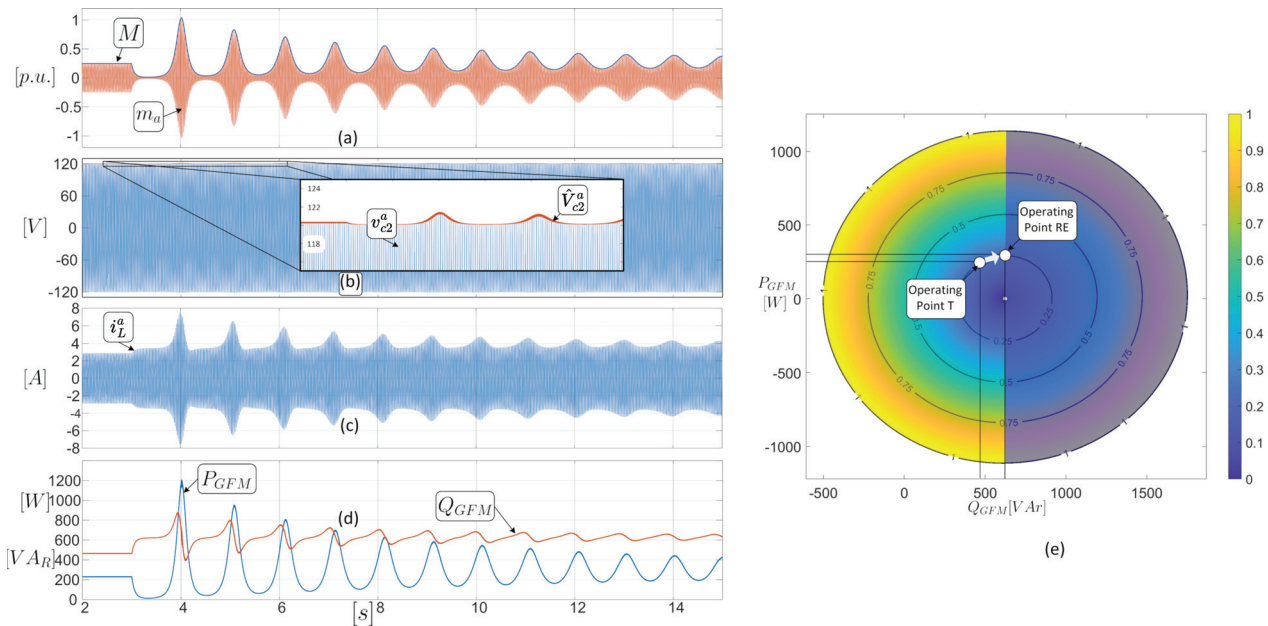


Figure 15. Dynamic Test 3 waveforms and operating points. (a) Modulator and modulator magnitude; (b) output phase voltage of converter and magnitude of this voltage; (c) load current waveform in line 'a'; (d) active and reactive power of the converter; (e) operating point of the modulator magnitude as seen from its operating region.

Observations from the last responses (from Figures 14 and 15) suggest that transitioning from an operating point within the sync-guaranteed region into the out-of-sync region may lead to control divergence. This is because proposing power references that are closer to the limit between the synchronized zones and the out-of-sync zone results in increasingly oscillatory responses or reduced damping. In Dynamic Test 4, to further demonstrate the effect of not imposing limits on the control and to illustrate the outcomes when the system operates without constraints, the upper and lower limits of the PI controller, as well as

any possible limit on the reactive power reference, have been removed. The behavior of the modulator M is clearly evident when attempting to transition from operating point T to operating point OS, as depicted in Figure 16. This transition results in indefinite divergence immediately after the change at time $t = 400$ ms. Furthermore, the responses in the currents and powers, illustrated in Figure 16, degrade, losing the expected quality following the reference change. Consequently, it is clear that operating at test point OS is unable to sustain satisfactory performance.

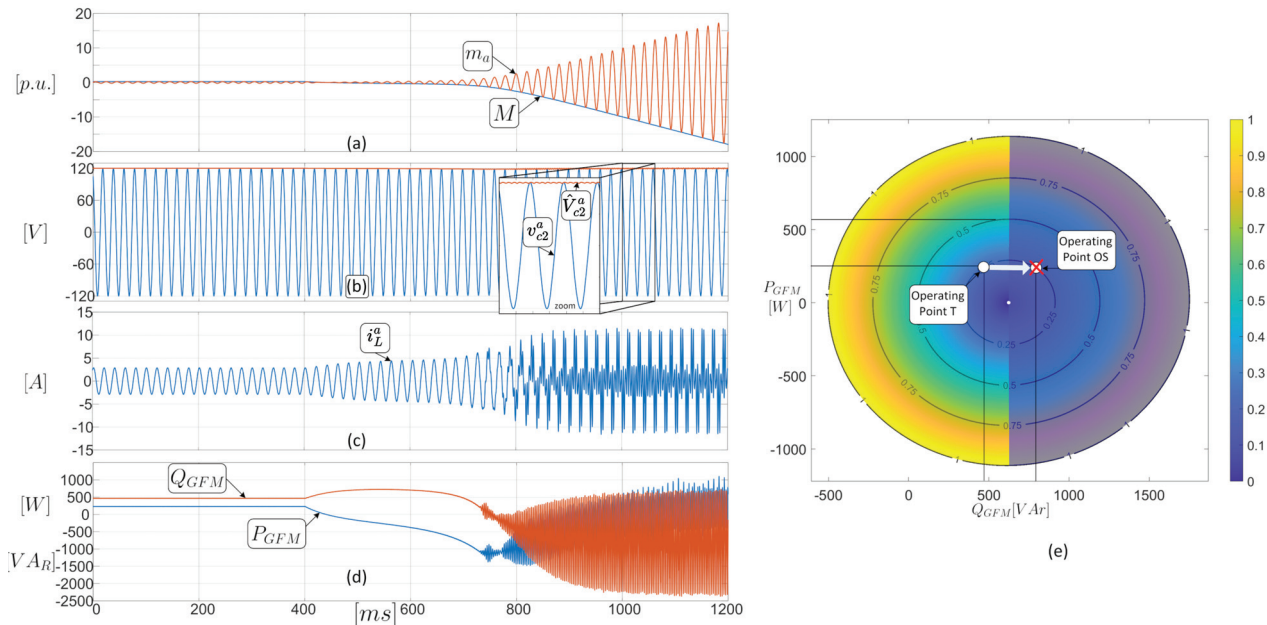


Figure 16. Dynamic Test 4 waveforms and operating points. (a) Modulator and modulator magnitude; (b) output phase voltage of converter and magnitude of this voltage; (c) load current waveform in line 'a'; (d) active and reactive power of the converter; (e) operating point of the modulator magnitude as seen from its operating region.

6. Discussion and Comments

6.1. Overview of Results

A critical observation when analyzing the operating region of a grid-connected CSI under a droop control strategy, particularly during simulations across various points within the area, is that not all sets of points deduced through mathematical modeling are feasible for inverter operation. This study has enabled the determination that by exploring possible inputs—namely, the different modulation indices and angles delivered by the system control—a specific operating point corresponding to particular active and reactive power values can be established for each input. By plotting all these operating points on a plane and projecting the modulation indices onto a third axis, a conical surface is obtained, as seen in Figure 5. Projecting the modulation index values onto the power plane reveals an operational region in a circular shape, as illustrated in Figure 6. However, given that droop control directly correlates the inverter's power with the system's frequency, synchronization is achieved through power control by only one pair of power-frequency when the inverter is synchronized with the grid. This results in the operating region being divided into two halves: one with synchronization and the other without.

The steady-state simulations confirm that the model precisely matches the tested system, achieving the active and reactive powers exactly as predicted for the given modulation indices in the operational region. Three operating points were tested: two delivering active and reactive power and one absorbing both. During transitions, or more precisely, in transient state testing, it becomes evident that moving away from the boundary dividing the guaranteed synchronism zone from the non-synchronism zone results in

more damped responses as opposed to moving towards it. Transitions from points further away to those closer to the boundary lead to completely underdamped responses. Notably, within the limit zone, where synchronization is not ensured, the operation of the converter becomes compromised.

6.2. Enhancements from Operating Region Insights

By identifying and analyzing the operating region of a CSI converter through modeling and simulation, as demonstrated in this work, there is a chance to select components more effectively. This is because the approach allows for analyzing how the region changes with different component values, enabling the determination of maximum currents through the semiconductors and the maximum and minimum power levels manageable by this inverter. In this regard, recent articles discuss the design and parameter optimization of CSIs [47,48]. This work can be considered complementary to those articles, as it proposes a method to obtain the operating region of a CSI in the active and reactive power plane, facilitating the evaluation of a particular design or the comparison with other designs. Furthermore, understanding these limitations facilitates the integration of appropriate protections directly into the control system. For example, knowing that there is an almost vertical line of reactive power, which divides the zone where synchronization is guaranteed from the zone where it is not, enables the use of the line's minimum value and, considering a safety margin, limits the reactive power in the control scheme reference. Thus, if secondary control demands a reactive power greater than what the converter can handle, a thorough analysis ensures that the reactive power is capped, preventing system desynchronization due to an incorrect reference change. Additionally, the output of the PI control in the reactive power control loop can be precisely limited to prevent modulation index M values from exceeding set maximums.

7. Conclusions

A grid-connected current source inverter (CSI) equipped with a CLC filter can function as a grid-forming inverter using a droop control strategy. This control scheme only requires voltage and frequency loops, thus eliminating the need for an inner current loop within its control architecture. This operational capability, arising from the current source converter topology's inherent current management, significantly boosts hardware protection, particularly under conditions such as short circuits or when current demands exceed the inverter's operational threshold. By employing a precise system model, an operating region is clearly defined, enabling the identification of specific maximum and minimum operational parameters crucial for the practical system design. This process involves calculating potential active and reactive power outputs or the inverter's maximum current limits based on the modulation indices issued by the system controller.

Simulation results confirm the model's accuracy and indicate that not all areas within the obtained region can maintain synchronization with the connected electrical grid. A thorough understanding of this operational area allows for setting prudent limits on control scheme references, thereby preventing operations in zones where synchronization is lost or where the modulation index (M) exceeds 1. This study presents a method for methodically acquiring and analyzing the operating region of a CSI with a CLC filter connected to a stiff grid. By analyzing the operating region with the same converter, it is observed that reducing the nominal size of the CLC filter capacitances by 33% allows the system to absorb up to 39% more reactive power. Conversely, increasing the capacitance size by 33% reduces the system's capacity to absorb reactive power to 62% of its original capacity. This approach opens the door for further detailed analyses or assessments of the impacts of various CLC filter parameters on the system's active and reactive power capabilities. Future work will involve analyzing the converter's operating region when it is fully isolated or operating in an isolated microgrid, as this aspect was not considered in the current study. This analysis will complement the results obtained and allow for a comparison of the operating regions

of the CSI and VSI converters, providing insights into the performance of both topologies in the power plane.

Author Contributions: Conceptualization, C.R.B. and P.E.M.; Methodology, C.R.B.; Software, A.Q.; Validation, P.E.M., R.O.R. and C.M.; Formal analysis, C.M.; Investigation, C.R.B.; Resources, C.R.B.; Data curation, A.Q.; Writing—original draft preparation, C.R.B.; Writing—review and editing, M.A.T., P.E.M., R.O.R., C.M. and A.Q.; Visualization, P.E.M. and R.O.R.; Supervision, C.R.B.; Project administration, C.R.B.; Funding acquisition, C.R.B., P.E.M., M.A.T. and R.O.R. All authors have read and agreed to the published version of the manuscript.

Funding: This research was partly funded by the ANID/FONDECYT Initiation project-grant number 11241077, and a grant from the Council of Andalucía-Junta de Andalucía, Consejería de Transformación Económica, Industria, Conocimiento y Universidades, Secretaría General de Universidades, Investigación y Tecnología—under Project ProyExcel_00381. Additional support was provided by the Thematic Network RIBIERSE-CYTED 723RT0150 and FONDAP SERC Chile No. 1522A0006.

Data Availability Statement: Data are contained within the article.

Acknowledgments: The support of the Energy Conversion Technology Center of the University of Talca is gratefully acknowledged.

Conflicts of Interest: The authors declare no conflicts of interest.

Abbreviations

The following abbreviations are used in this manuscript:

CSI	Current Source Inverter
GFM	Grid-Forming Inverter
GFL	Grid-Following Inverter
GSP	Grid-Supporting Inverter
VSI	Voltage Source Inverter
CLC	Capacitive Inductive Capacitive

References

1. Zhang, H.; Xiang, W.; Lin, W.; Wen, J. Grid Forming Converters in Renewable Energy Sources Dominated Power Grid: Control Strategy, Stability, Application, and Challenges. *J. Mod. Power Syst. Clean Energy* **2021**, *9*, 1239–1256. [CrossRef]
2. Peña Asensio, A.; Arnaltes Gómez, S.; Rodríguez-Amenedo, J.L. Black-start capability of PV power plants through a grid-forming control based on reactive power synchronization. *Int. J. Electr. Power Energy Syst.* **2023**, *146*, 108730. [CrossRef]
3. Sawant, J.; Seo, G.S.; Ding, F. Resilient Inverter-Driven Black Start with Collective Parallel Grid-Forming Operation. In Proceedings of the 2023 IEEE Power & Energy Society Innovative Smart Grid Technologies Conference (ISGT), Washington, DC, USA, 16–19 January 2023; pp. 1–5. [CrossRef]
4. Rocabert, J.; Luna, A.; Blaabjerg, F.; Rodríguez, P. Control of Power Converters in AC Microgrids. *IEEE Trans. Power Electron.* **2012**, *27*, 4734–4749. [CrossRef]
5. Henninger, S.; Jaeger, J. Advanced classification of converter control concepts for integration in electrical power systems. *Int. J. Electr. Power Energy Syst.* **2020**, *123*, 106210. [CrossRef]
6. Lai, N.B.; Tarrasó, A.; Baltas, G.N.; Marin Arevalo, L.V.; Rodriguez, P. External Inertia Emulation Controller for Grid-Following Power Converter. *IEEE Trans. Ind. Appl.* **2021**, *57*, 6568–6576. [CrossRef]
7. Strunz, K.; Almunem, K.; Wulkow, C.; Kuschke, M.; Valescudero, M.; Guillaud, X. Enabling 100% Renewable Power Systems Through Power Electronic Grid-Forming Converter and Control: System Integration for Security, Stability, and Application to Europe. *Proc. IEEE* **2023**, *111*, 891–915. [CrossRef]
8. Peng, F.Z.; Liu, C.C.; Li, Y.; Jain, A.K.; Vinnikov, D. Envisioning the Future Renewable and Resilient Energy Grids—A Power Grid Revolution Enabled by Renewables, Energy Storage, and Energy Electronics. *IEEE J. Emerg. Sel. Top. Ind. Electron.* **2024**, *5*, 8–26. [CrossRef]
9. Hossain, E.; Faruque, H.M.R.; Sunny, M.S.H.; Mohammad, N.; Nawar, N. A Comprehensive Review on Energy Storage Systems: Types, Comparison, Current Scenario, Applications, Barriers, and Potential Solutions, Policies, and Future Prospects. *Energies* **2020**, *13*, 3651. [CrossRef]
10. Ellis, B.E.; Pearre, N.; Swan, L. Impact of residential photovoltaic systems on net load intermittency. *Renew. Energy Focus* **2023**, *46*, 377–384. [CrossRef]
11. Unruh, P.; Nuschke, M.; Strauß, P.; Welck, F. Overview on grid-forming inverter control methods. *Energies* **2020**, *13*, 2589. [CrossRef]

12. Safamehr, H.; Izadi, I.; Ghaisari, J. Robust $V - I$ Droop Control of Grid-Forming Inverters in the Presence of Feeder Impedance Variations and Nonlinear Loads. *IEEE Trans. Ind. Electron.* **2024**, *71*, 504–512. [CrossRef]
13. Liu, T.; Wang, X. Unified Voltage Control for Grid-Forming Inverters. *IEEE Trans. Ind. Electron.* **2024**, *71*, 2578–2589. [CrossRef]
14. Rosso, R.; Wang, X.; Liserre, M.; Lu, X.; Engelken, S. Grid-Forming Converters: Control Approaches, Grid-Synchronization, and Future Trends—A Review. *IEEE Open J. Ind. Appl.* **2021**, *2*, 93–109. [CrossRef]
15. Pattabiraman, D. Current source inverter with grid forming control. *Electr. Power Syst. Res.* **2024**, *226*, 109910. [CrossRef]
16. Abdel-Moneim, M.G.; Hamad, M.S.; Abdel-Khalik, A.S.; Hamdy, R.R.; Hamdan, E.; Ahmed, S. Analysis and control of split-source current-type inverter for grid-connected applications. *Alex. Eng. J.* **2024**, *96*, 268–278. [CrossRef]
17. Xu, C.; Liu, P.; Miao, Y. Overlap Time Compensation and Characteristic Analysis for Current Source Photovoltaic Grid-Connected Inverter. *Energies* **2024**, *17*, 1768. [CrossRef]
18. Gao, H. High-frequency common-mode voltage mitigation for current-source inverter in transformerless photovoltaic system using active zero-state space vector modulation. *IET Electr. Power Appl.* **2023**, *17*, 245–255. [CrossRef]
19. Geng, Y.; Zhou, T.; Cao, F.; Xin, Y.; Wang, H. A model predictive control of three-phase grid-connected current-source inverter based on optimization theory. *IET Power Electron.* **2023**, *16*, 2650–2665. [CrossRef]
20. Ray, I. Review of Impedance-Based Analysis Methods Applied to Grid-Forming Inverters in Inverter-Dominated Grids. *Energies* **2021**, *14*, 2686. [CrossRef]
21. Lasseter, R.H.; Chen, Z.; Pattabiraman, D. Grid-Forming Inverters: A Critical Asset for the Power Grid. *IEEE J. Emerg. Sel. Top. Power Electron.* **2020**, *8*, 925–935. [CrossRef]
22. Young, H.A.; Marin, V.A.; Pesce, C.; Rodriguez, J. Simple Finite-Control-Set Model Predictive Control of Grid-Forming Inverters With LCL Filters. *IEEE Access* **2020**, *8*, 81246–81256. [CrossRef]
23. Geng, Y.; Yang, K.; Lai, Z.; Zheng, P.; Liu, H.; Deng, R. A Novel Low Voltage Ride Through Control Method for Current Source Grid-Connected Photovoltaic Inverters. *IEEE Access* **2019**, *7*, 51735–51748. [CrossRef]
24. Alemi, P.; Wang, J.; Zhang, J.; Amini, S. Performance analysis of high-power three-phase current source inverters in photovoltaic applications. *IET Circuits Devices Syst.* **2021**, *15*, 79–87. [CrossRef]
25. Fidone, G.L.; Migliazza, G.; Carfagna, E.; Benatti, D.; Immovilli, F.; Buticchi, G.; Lorenzani, E. Common Architectures and Devices for Current Source Inverter in Motor-Drive Applications: A Comprehensive Review. *Energies* **2023**, *16*, 5645. [CrossRef]
26. Killeen, P.; Ghule, A.N.; Ludois, D.C. A Medium-Voltage Current Source Inverter for Synchronous Electrostatic Drives. *IEEE J. Emerg. Sel. Top. Power Electron.* **2022**, *10*, 1597–1608. [CrossRef]
27. Migliazza, G.; Buticchi, G.; Carfagna, E.; Lorenzani, E.; Madonna, V.; Giangrande, P.; Galea, M. DC Current Control for a Single-Stage Current Source Inverter in Motor Drive Application. *IEEE Trans. Power Electron.* **2021**, *36*, 3367–3376. [CrossRef]
28. Azmi, S.A.; Ahmed, K.H.; Finney, S.J.; Williams, B.W. Comparative analysis between voltage and current source inverters in grid-connected application. In Proceedings of the IET Conference on Renewable Power Generation (RPG 2011), Edinburgh, UK, 6–8 September 2011; pp. 1–6. [CrossRef]
29. Sahan, B.; Araújo, S.V.; Nöding, C.; Zacharias, P. Comparative Evaluation of Three-Phase Current Source Inverters for Grid Interfacing of Distributed and Renewable Energy Systems. *IEEE Trans. Power Electron.* **2011**, *26*, 2304–2318. [CrossRef]
30. Tan, Q.; Mao, L.; Cai, Y.; Zhang, B.; Ruan, Z. Comparative evaluation and analysis of GaN-based VSIs and CSIs. *Energy Rep.* **2023**, *9*, 568–576. [CrossRef]
31. Dai, H.; Jahns, T.M.; Torres, R.A.; Han, D.; Sarlioglu, B. Comparative Evaluation of Conducted Common-Mode EMI in Voltage-Source and Current-Source Inverters using Wide-Bandgap Switches. In Proceedings of the 2018 IEEE Transportation Electrification Conference and Expo (ITEC), Long Beach, CA, USA, 13–15 June 2018; pp. 788–794. [CrossRef]
32. Wang, Z.; Wei, Q. X-Type Five-Level Current Source Inverter. *IEEE Trans. Power Electron.* **2023**, *38*, 6283–6292. [CrossRef]
33. Wang, Z.; Wei, Q. Γ -Type Five-Level Current Source Inverter. *IEEE Trans. Power Electron.* **2024**, *39*, 7206–7216. [CrossRef]
34. Kim, J.; Cha, H. Switching Cell Current Source Inverter With Active Power Decoupling Circuit. *IEEE Trans. Ind. Electron.* **2024**, *1*–9. [CrossRef]
35. Zheng, Z.; Xie, Q.; Huang, C.; Xiao, X.; Li, C. Superconducting Technology Based Fault Ride Through Strategy for PMSG-Based Wind Turbine Generator: A Comprehensive Review. *IEEE Trans. Appl. Supercond.* **2021**, *31*, 1–6. [CrossRef]
36. Wang, Z.; Jiang, L.; Zou, Z.; Cheng, M. Operation of SMES for the Current Source Inverter Fed Distributed Power System Under Islanding Mode. *IEEE Trans. Appl. Supercond.* **2013**, *23*, 5700404. [CrossRef]
37. Hassan, M.u.; Emon, A.I.; Luo, F.; Solovyov, V. Design and Validation of a 20-kVA, Fully Cryogenic, Two-Level GaN-Based Current Source Inverter for Full Electric Aircrafts. *IEEE Trans. Transp. Electr.* **2022**, *8*, 4743–4759. [CrossRef]
38. Potdukhe, K.C.; Munshi, A.P.; Munshi, A.A. Reliability prediction of new improved current source inverter (CSI) topology for transformer-less grid connected solar system. In Proceedings of the 2015 IEEE Power, Communication and Information Technology Conference (PCITC), Bhubaneswar, India, 15–17 October 2015; pp. 373–378. [CrossRef]
39. Marignetti, F.; Di Stefano, R.L.; Rubino, G.; Giacomobono, R. Current Source Inverter (CSI) Power Converters in Photovoltaic Systems: A Comprehensive Review of Performance, Control, and Integration. *Energies* **2023**, *16*, 7319. [CrossRef]
40. Mustafeez-UI-Hassan; Emon, A.I.; Yuan, Z.; Peng, H.; Luo, F. Performance Comparison and Modelling of Instantaneous Current Sharing Amongst GaN HEMT Switch Configurations for Current Source Inverters. In Proceedings of the 2022 IEEE Applied Power Electronics Conference and Exposition (APEC), Houston, TX, USA, 20–24 March 2022; pp. 2014–2020. [CrossRef]

41. Lin, Y.; Eto, J.H.; Johnson, B.B.; Flicker, J.D.; Lasseter, R.H.; Pico, H.N.V.; Seo, G.S.; Pierre, B.J.; Ellis, A.; Miller, J.; et al. Pathways to the Next-Generation Power System with Inverter-Based Resources: Challenges and recommendations. *IEEE Electr. Mag.* **2022**, *10*, 10–21. [CrossRef]
42. Tamrakar, U.; Shrestha, D.; Maharjan, M.; Bhattarai, B.P.; Hansen, T.M.; Tonkoski, R. Virtual Inertia: Current Trends and Future Directions. *Appl. Sci.* **2017**, *7*, 654. [CrossRef]
43. Melin, P.E.; Espinoza, J.R.; Zargari, N.R.; Sanchez, M.A.; Guzman, J.I. Modeling Issues in Three-Phase Current Source Rectifiers that use Damping Resistors. In Proceedings of the 2006 IEEE International Symposium on Industrial Electronics, Paris, France, 7–10 November 2006; Volume 2, pp. 1247–1252. [CrossRef]
44. Basler, M.J.; Schaefer, R.C. Understanding Power-System Stability. *IEEE Trans. Ind. Appl.* **2008**, *44*, 463–474. [CrossRef]
45. Shuai, Z.; Shen, C.; Liu, X.; Li, Z.; Shen, Z.J. Transient Angle Stability of Virtual Synchronous Generators Using Lyapunov's Direct Method. *IEEE Trans. Smart Grid* **2019**, *10*, 4648–4661. [CrossRef]
46. Ippolito, M.G.; Musca, R.; Zizzo, G. Generalized power-angle control for grid-forming converters: A structural analysis. *Sustain. Energy Grids Netw.* **2022**, *31*, 100696. [CrossRef]
47. Geng, Y.; Song, X.; Zhang, X.; Yang, K.; Liu, H. Stability Analysis and Key Parameters Design for Grid-Connected Current-Source Inverter with Capacitor-Voltage Feedback Active Damping. *IEEE Trans. Power Electron.* **2021**, *36*, 7097–7111. [CrossRef]
48. Riegler, B.; Muetze, A. Passive Component Optimization for Current-Source-Inverters. *IEEE Trans. Ind. Appl.* **2023**, *59*, 6113–6124. [CrossRef]

Disclaimer/Publisher's Note: The statements, opinions and data contained in all publications are solely those of the individual author(s) and contributor(s) and not of MDPI and/or the editor(s). MDPI and/or the editor(s) disclaim responsibility for any injury to people or property resulting from any ideas, methods, instructions or products referred to in the content.

Article

Derivation of Analytical Expressions for Fast Calculation of Resistance Spot Welding System Currents

Robert Brezovnik * and Jožef Ritonja

Institute of Electrical Power Engineering, Faculty of Electrical Engineering and Computer Science,
University of Maribor, Koroška Cesta 46, 2000 Maribor, Slovenia; jozef.ritonja@um.si

* Correspondence: robert.brezovnik@um.si

Abstract: The paper deals with the dynamics of a resistance spot welding system. At the core of this system is a transformer, which is powered on the primary side by a pulse-width modulated inverter and has a full-wave output rectifier on the secondary side that provides a direct welding current. The entire system is nonlinear, due to magnetic hysteresis and electronics. The electronics prevent the current from flowing in all parts of the welding transformer at separate time intervals during the voltage supply period; therefore, not all the parameters affect the dynamic of currents and voltages all the time so the system is also time-variant. To design a high-performance welding system and to predict the maximum possible welding current at a specific load, it is necessary to know the welding and primary currents. The leakage inductances of the system can reduce the maximum welding current significantly at higher frequencies and the same load. There are several methods to determine these currents, each with its drawbacks. Measurements are time-consuming, using professional software is expensive and requires time to learn and free open-source software has many limitations and does not guarantee the correctness of the results. The article presents a new, fourth option—a theoretical derivation of analytical expressions that facilitate straightforward and rapid calculation of the welding and primary currents of the resistance spot welding system with symmetrical secondary branches. The derivation of the mathematical expressions is based on the equivalent circuits that describe the system in different operating states. The results of the numerical simulations confirmed the derived expressions completely.

Keywords: DC–DC converters; pulse width modulation (PWM); welding transformers; center-tapped transformers; full-wave rectifier; resistance spot welding (RSW); leakage inductance; analytical modeling; time-variant system; equivalent circuit

MSC: 94C05

1. Introduction

Resistance spot welding (RSW) systems are essential in metal joining processes in many industries, including the automotive [1], aerospace, train industry, and manufacturing sectors. It provides a reliable and efficient method for joining sheet metals, which is crucial for product structural integrity and safety. The RSW is a vital welding technique that has been considered the dominant process for joining sheet metals in many industries, due to its high production efficiency and adequacy for automated realization. Traditional RSW also has limitations when joining different materials is needed [2,3]. Therefore, new variants of spot welding have been developed [4], such as laser spot welding, friction stir spot welding, and ultrasonic spot welding [5]. The RSW for different materials such as aluminum, titanium, steel, and various alloys requires appropriate current control, welding time [6], clamp forces, and temperature [7–9] to ensure the adequate quality of the weld nugget. Zinc-coated steels can also impact the weld quality negatively [10]. In the automotive industry, welding quality control is a critical topic. As a result, many new technologies

have been developed for real-time quality control of the welding process [11–16]. Some methods also consider welding electrode displacement [17,18]. The welding electrodes are exposed to high temperatures and forces, which causes them to degrade over time; therefore, they must be replaced at specific intervals to prevent a negative impact on welding quality [19–22].

The RSW systems can be divided into two groups [23,24]: the systems in the first group provide an alternating welding current (AC) and the systems in the second group provide a direct welding current (DC). The welding systems with an AC current can provide only low welding currents due to low frequency (50 or 60 Hz), and, therefore, large and heavy welding transformers. The large and heavy transformer is inappropriate for mounting on a moving robot's arm in the automotive industry, and, therefore, can be used only in stationary applications. Another weakness of RSW systems with AC welding current is the low power factor due to high inductance and harmonic distortion [25]. The high leakage inductances of the welding guns demand a DC welding current for high current applications, where the welding transformer with a full-wave rectifier mounted at the secondary is attached to the moving robot's arm. The welding transformer mounted on a robot's arm must be as light as possible to reduce the robot's power consumption and increase movement dynamics. The dimensions and weight of the transformer's iron core can be reduced drastically with a higher frequency of voltage supply. The standard middle-frequency RSW systems operate with a pulse width modulated (PWM) voltage supply with a switching frequency of 1 kHz. The transformer's iron core can be additionally reduced if, instead of diodes, a synchronous rectifier [26,27] is used to operate at high switching frequencies of 25 kHz. On the other hand, the high switching frequency also has a negative impact, due to high power losses on semiconductors and windings [28,29]. Additionally, the higher switching frequency of the voltage supply decreases the maximum possible welding current at the same load, due to the leakage inductances and correspondent time constants of the RSW system [30]. To design a high-performance welding system and to predict the maximum possible welding current at a specific load, it is necessary to know the welding and transformer's primary currents and their dynamics. These currents can be determined in several ways, each with its drawbacks. Measurements are time-consuming and require expensive measuring devices, which must be able to measure very high currents over 30 kA with a fast dynamic. Using professional software is also expensive and requires time to learn. The numerical calculations with software require appropriate solver settings to reduce numerical errors and achieve convergence. The free, open-source software has many limitations and does not guarantee the correctness of the results. The fourth, new option provided by this article is a theoretical derivation of analytical expressions that facilitate straightforward and rapid calculation of the welding and primary currents of the resistance spot welding system with symmetrical secondary branches. This is also the main goal and focus of this article. The derived analytical expressions for welding and primary current calculations can be implemented in any programming language. Moreover, the analytical expressions of welding and primary currents also provide a deep understanding of their dynamic behavior and the influence of the RSW system parameters on them; therefore, this article is very significant and important.

The high-power RSW systems used with a moving robot's arm consist of three main parts. The first part is the H-bridge inverter, with an integrated three-phase full-wave input rectifier that provides DC voltage to the inverter. The second part is a welding transformer, with an integrated full-wave rectifier mounted on the robot's arm. The welding transformer is separated from the inverter. Therefore, a long connecting cable is used to connect them, and its resistance and leakage inductance must be considered. The third part is the welding clamp or gun mounted on the end of the robot's arm, which delivers a high welding current from the output rectifier to the weld. All three parts of the RSW system can be represented as an equivalent circuit containing the voltage sources, ideal transformer model, equivalent resistances, and leakage inductances; the capacitances can be neglected. The diodes of the output rectifier can also be modeled as series-connected resistance and voltage sources. The

entire RSW system is nonlinear, due to magnetic hysteresis and electronics (the transistors and diodes). The electronics prevent the current from flowing in all parts of the welding transformer at separate time intervals during the voltage supply period. Therefore, all the parameters do not always affect the dynamic behavior of the currents and voltages; for that reason, the RSW system is also time-variant, and three different equivalent circuits describe the dynamic of the welding and primary current in separate intervals of the voltage supply period. These three simplified equivalent circuits can be represented as series connected resistance and inductance with a step voltage supply; therefore, their currents can be described analytically as a step voltage response of a first-order system. These three relatively simple equations define the dynamic behavior of welding and primary currents of the RSW system in each time interval of the PWM voltage supply, as well as their time series.

This article is split into 5 sections. Section 2 describes the analyzed RSW system; all three main parts of the system are presented in detail. The modeling of the RSW system is presented in Section 3, where three equivalent circuits are shown, and the values are presented of the parameters for the analyzed RSW system. The PWM voltage supply of the inverter is explained, and analytical equations for welding and primary current are derived for each time interval of the one-and-a-half voltage supply period. Section 4 contains the obtained results. The analytically calculated time series of the welding and primary currents are compared with the numerically calculated time series in Simulink, and the differences are shown. Finally, in Section 5, the concluding remarks are presented, and suggestions are provided for implementing the analytical solution.

2. Description of the Resistance Spot Welding System

This article analyzes a 130 kVA resistance spot welding transformer, which is suitable for mounting on a moving robot arm. The industrial name of the transformer is PSG6130, and it can achieve a maximum continuous DC welding current of up to 6.5 kA at a 100% duty cycle or up to 30 kA for shorter welding times. The maximum welding DC current depends on many parameters, such as welding resistance, welding time, duty cycle, and coolant temperature. The primary voltage and frequency of the transformer are 530 V and 1000 Hz. The no-load output DC voltage is 8.9 V, and the transformer's turn ratio is 55:1. The weight of the welding transformer with an integrated full-wave rectifier is 15.1 kg. The water-cooling system of the transformer requires a nominal flow of 6 L/min and causes 0.6 bar differential pressure.

The iron core of the transformer has a nonlinear core saturation function, as shown in Figure 1. To calculate the welding and transformer's primary current analytically, it is essential to prevent the transformer's iron core from saturating. A linear iron core model of the transformer is considered in the circuit model. Therefore, all leakage inductances are constant, and not dependent on the transformer's primary and secondary currents. The saturation of the iron core is also not acceptable in real RSW transformers, due to its high primary current, which can trigger over-current protection during the welding process. The iron core losses are frequency-dependent, but relatively small compared to the copper losses in the transformer's primary and secondary windings and losses in the output rectifier. The iron core losses are reduced by selecting the appropriate material and lamination. The iron core is made of grain-oriented silicon steel (EILOR) with a thickness of 0.23 mm for operation at a frequency of 1 kHz. The iron core losses can be decreased further with thinner lamination of 0.1 mm thickness, which is typically used for operation at higher frequencies than 1 kHz. The iron core losses are not considered in the modeling of the welding transformer.

The secondary winding of the welding transformer has only two turns; each is active in one-half period and is connected to a high-power diode. Both high-power diodes have the same characteristics and provide a high DC welding current at the output of the welding transformer.

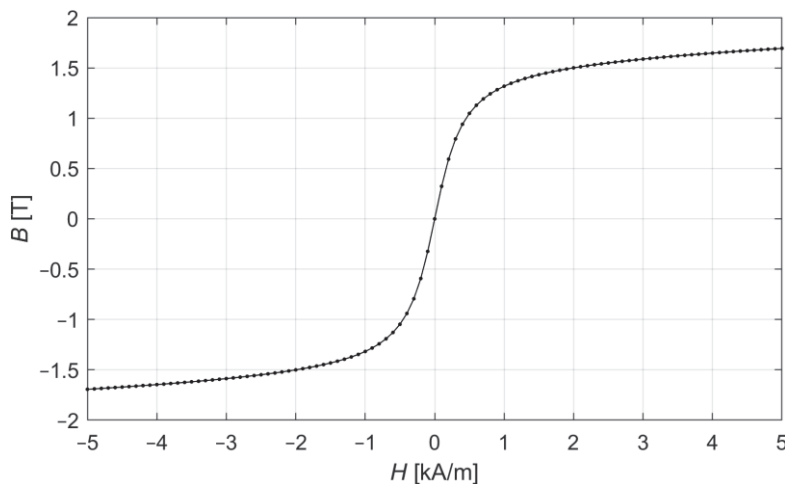


Figure 1. Nonlinear core saturation function.

A schematic presentation of the analyzed RSW system is shown in Figure 2. A three-phase input rectifier is shown on the left side of Figure with AC voltages u_{L1} , u_{L2} , and u_{L3} , which are rectified and filtered to get a DC bus voltage U_{DC} . The bus voltage U_{DC} is connected to the H-bridge inverter. The welding transformer's supply voltage u is PWM-controlled by the H-bridge inverter, composed of transistors denoted by $S_1 - S_4$. The IGBT transistors are used with antiparallel diodes $D_{H1} - D_{H4}$. The PWM supply voltage u is connected to the transformer's primary winding with a relatively long connection cable, whose resistance and leakage inductance cannot be neglected. In industry, the H-bridge inverter is located separately from the welding transformer mounted on the moving robot arm; therefore, the connection cable can be up to 30 m long. The welding transformer has a full-wave rectifier mounted on the secondary, providing high DC welding current to the welding clamps.

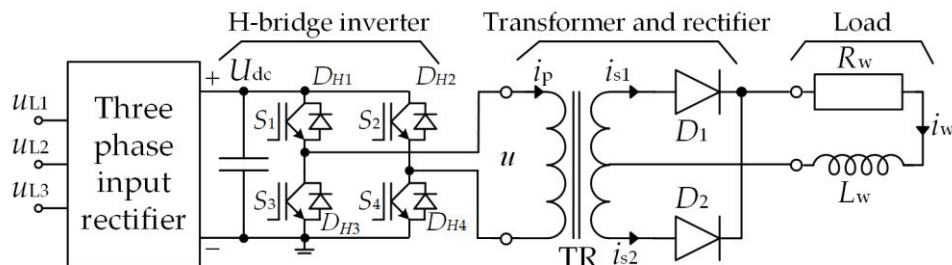


Figure 2. Schematic presentation of the analyzed RSW system.

3. Modeling of the RSW System

To calculate the welding and transformer's primary current of the RSW system analytically, the system's separate parts need to be modeled as equivalent circuits. Individual parts can be modeled as equivalent circuits with ideal resistance, inductance, and capacitance, but high-power RSW systems are physically larger and heavier. Therefore, the resistances and leakage inductances prevail over capacitances, which can be neglected. Not considering the capacitances of the RSW system is an important simplification that allows the RSW system to be described as a series of connected resistances and leakage inductances, presenting a first-order system that can be described analytically.

The circuit model of the RSW system is shown in Figure 3 and represents a series connection of the cable, transformer with rectifier, and load. The connection cable is modeled as series-connected leakage inductance L_c and resistance R_c . The transformer's primary winding is modeled as series-connected leakage inductance L_p and resistance R_p . The transformer is modeled as an ideal linear transformer with neglected iron core losses and a magnetizing current. The primary winding has $N_p = 55$ turns, and the secondary winding has two turns with a central tap; each turn is active only in one-half period;

therefore $N_{s1} = N_{s2} = 1$. Each secondary turn is modeled as a series-connected leakage inductance L_{s1} , L_{s2} and resistance R_{s1} , R_{s2} , that is connected to the rectifier diodes D_{s1} and D_{s2} . Both diodes have the same characteristics and can be modeled as series-connected resistance R_d and backward voltage source U_d . The diode's voltage source always works as a load and never as a generator. Some parts of the rectifier are common to both secondary windings and the common welding current, which causes voltage drops. Therefore, these parts of the rectifier are modeled as a series-connected leakage inductance L_{s3} and resistance R_{s3} . The load is modeled as a series-connected leakage inductance L_w and resistance R_w , considering the leakage inductance and resistance of the welding clamps (welding gun) and welding nugget.

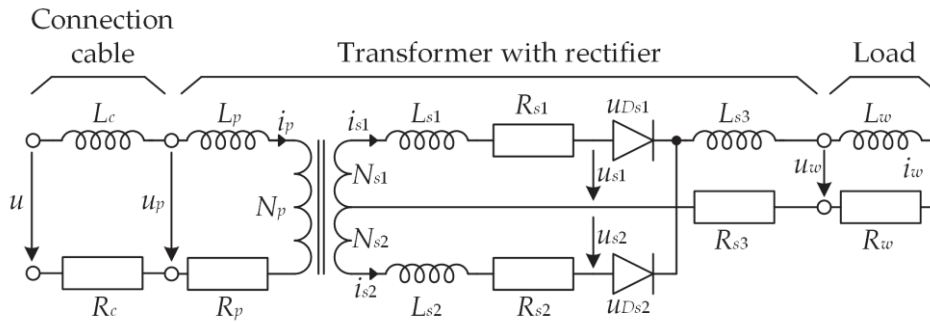


Figure 3. Extended circuit model of the RSW system.

Usually, some authors [24,31,32] combine the leakage inductance and resistance of the connection cable (L_c and R_c) with the primary winding (L_p and R_p) for simplicity or neglect them altogether. They also combine the leakage inductance and resistance of the common parts of the output rectifier (L_{s3} and R_{s3}) with the load (L_w and R_w). In this article, an extended circuit model of RSW is used, because the parameters of a specific welding transformer remain the same, although the parameter values of the connection cable or the load can change significantly if the cable or load is replaced. The separation of the parameters also allows for the analysis of the influence of each part of the RSW system on the equivalent circuit time constants and the dynamic behavior of the system.

3.1. Dynamic Model of RSW

A dynamic model of the analyzed RSW system in Figure 3 can be described in implicit form by Equations (1)–(4). Equation (1) describes the voltage balance in the primary coil of the transformer. The state variable i_p is a time-dependent primary current, S_{Fe} is the cross-section of the iron core, B is the flux density in the iron core, and u is the PWM voltage of the H-bridge; all the other parameters have been described already.

$$u = i_p R_c + L_c \frac{di_p}{dt} + i_p R_p + L_p \frac{di_p}{dt} + N_p S_{Fe} \frac{dB}{dt}. \quad (1)$$

Equations (2) and (3) describe the voltage balance in both secondary coils of the RSW transformer. The state variables i_{s1} and i_{s2} are time-dependent currents of the secondary branches, u_{Ds1} and u_{Ds2} are the voltages of both secondary diodes and are functions of the corresponding currents i_{s1} and i_{s2} . The nonlinear characteristic of the diodes is defined as serial connected diode resistance R_d and voltage source U_d , which acts as a load and never as a generator. The welding current i_w is defined as the sum of the currents in both branches $i_w = i_{s1} + i_{s2}$. All the other parameters in (2) and (3) have been described already.

$$N_{s1} S_{Fe} \frac{dB}{dt} = -L_{s1} \frac{di_{s1}}{dt} - i_{s1} R_{s1} - u_{Ds1}(i_{s1}) - i_w R_{s3} - L_{s3} \frac{di_w}{dt} - i_w R_w - L_w \frac{di_w}{dt}, \quad (2)$$

$$N_{s2} S_{Fe} \frac{dB}{dt} = L_{s2} \frac{di_{s2}}{dt} + i_{s2} R_{s2} + u_{Ds2}(i_{s2}) + i_w R_{s3} + L_{s3} \frac{di_w}{dt} + i_w R_w + L_w \frac{di_w}{dt}. \quad (3)$$

In (4), H is the magnetic field strength that is a function of the magnetic flux density B , μ_0 is the permeability of the vacuum ($\mu_0 = 4\pi 10^{-7} \frac{\text{Vs}}{\text{Am}}$), δ is an iron core air gap, and l_{av} is the average length of a magnetic flux line in the iron core.

$$N_p i_p + N_{s1} i_{s1} - N_{s2} i_{s2} = H(B) l_{av} + \frac{B}{\mu_0} 2\delta. \quad (4)$$

The welding transformer in Figure 3 is taken as ideal, with linear magnetizing characteristics without iron core losses, as described already. Some authors [24,31] model iron core losses as a parallel connected resistance R_{Fe} to the primary winding, which causes additional current flow into a transformer and voltage drops on the primary parameters. Such modeling of iron core losses comes from modeling classical transformers supplied with AC voltage, where all the transformer parameters can be referred from primary to secondary or vice versa. In the case of RSW systems, the voltage supply is not AC, but DC (PWM), and, in a certain time period, the primary current i_p is zero, but the secondary currents i_{s1} and i_{s2} are not zero. When i_p is zero, the power losses would also be zero if the R_{Fe} is connected parallel to the primary winding, but, at the same time, the secondary currents are not zero, and the main magnetic flux in the iron core is decreasing which still causes iron core losses. From that point of view, it is difficult to model iron core losses in an RSW system properly only with the parallel connected resistance R_{Fe} with a fixed value to the primary winding. That way of modeling iron core losses is possible only for one setting of voltage, frequency, and duty cycle; for different values, the resistance R_{Fe} should be changed, and that is not easy to achieve properly. For that reason, in this article, the resistance R_{Fe} is not used for modeling the iron core losses and can be neglected, as already mentioned, due to much higher copper losses in the transformer's windings and output rectifier. The measurements on the analyzed RSW system show that the iron core losses are less than 1 kW at a nominal output power of 130 kVA and a PWM frequency of 1 kHz, which is less than 0.8% of the nominal output power.

3.2. The Parameters of the Circuit Model of the RSW System

The parameter values of the extended circuit model of the RSW system in Figure 3 need to be determined according to the time series of currents and voltages measured in the real system. Determination of parameter values is a challenging task since the RSW system is a nonlinear time-variant system with relatively low resistances and leakage inductances that cannot be measured directly. The inductances that cannot be measured directly are the leakage inductance of the primary winding L_p , both secondary windings (L_{s1} , L_{s2}) and the output rectifier L_{s3} . Many papers deal with the topic of determining the parameter values of a resistance spot welding system using different optimization algorithms [31,32]. The main goal of the optimization algorithm is to find values for the model's parameters such that the difference between measured and numerically calculated time series of currents and voltages is minimal. As this paper focuses on the analytical determination of the welding current and transformer's primary current, it is, in principle, irrelevant what values are used for the model parameters. The values of the model parameters for the analyzed RSW system have already been determined [30] and are shown in Table 1. The only difference between the parameter values in the article [30] and Table 1 are the resistance and leakage inductance values of the secondary windings (R_{s1} , R_{s2} , L_{s1} , and L_{s2}), because, in Table 1, the average values are calculated and set equally for both secondary branches. In reality, the resistance and leakage inductance of secondary windings are slightly different ($R_{s1} = 27.7 \mu\Omega$, $R_{s2} = 32.76 \mu\Omega$, $L_{s1} = 12 \text{ nH}$, $L_{s2} = 14 \text{ nH}$); for analytically calculated welding and the transformer's primary current, both branches must be symmetrical with the same resistance and leakage inductance values. In Table 1, the values of all parameters are given, whereas, in the fourth column, the values are referred to the secondary side of the transformer. The per unit values are given in the fifth column; the basis for per unit calculation is the resistance and inductance of the load due to the highest value. In Table 1

are also the values of the output rectifier diode's parameters, the equivalent resistance R_d , and voltage source U_d , which is negative because it always works as a load and never as a generator.

Table 1. Circuit parameters of the RSW system.

Description	Parameter	Value	Refer to Sec.	pu
Connection cable	L_c	3.8153 μH	1.26 nH	0.00097
	R_c	9.4 m Ω	3.11 $\mu\Omega$	0.0141
Primary winding	L_p	2.5636 μH	0.85 nH	0.00065
	R_p	24.03 m Ω	7.94 $\mu\Omega$	0.036
Secondary winding 1	L_{s1}	13 nH	13 nH	0.01001
	R_{s1}	30.23 $\mu\Omega$	30.23 $\mu\Omega$	0.1371
Secondary winding 2	L_{s2}	13 nH	13 nH	0.01001
	R_{s2}	30.23 $\mu\Omega$	30.23 $\mu\Omega$	0.1371
Sec. winding common parts	L_{s3}	36.1 nH	36.1 nH	0.0278
	R_{s3}	56.2 $\mu\Omega$	56.2 $\mu\Omega$	0.2549
Load	L_w	1.2981 μH	1.2981 μH	1
	R_w	220.52 $\mu\Omega$	220.52 $\mu\Omega$	1
Diode	U_d	−0.66 V	−0.66 V	/
	R_d	37 $\mu\Omega$	37 $\mu\Omega$	0.1678

3.3. PWM Generation of Primary Voltage

It is known that the steady state of the welding current of the RSW system depends on the switching frequency f , the duty cycle D (from 0 to 1 or 0% to 100%), the H-bridge voltage U_{dc} , and all model parameters of the RSW system. The voltage supply for welding transformer u is provided by the H-bridge, where the diagonal transistors (S_1 , S_4) and (S_2 , S_3) in Figure 2 are opened and closed adequately with the PWM voltages u_{T+} and u_{T-} . The PWM has centrally positioned pulses, as is shown in Figure 4. Therefore, the start time T_{1p} and the end time T_{2p} of voltage u_{T+} (S_1 and S_4), and the start time T_{1n} and the end time T_{2n} of voltage u_{T-} (S_2 and S_3) can be calculated if the time period $T = 1/f$ and the duty cycle D are determined.

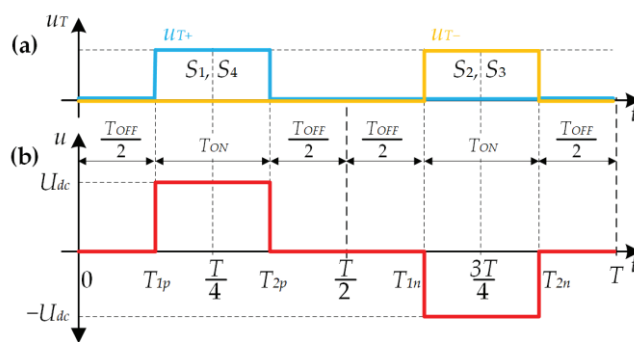


Figure 4. Time series of (a) transistor control voltage u_{T+} and u_{T-} , (b) H-bridge voltage u .

The pulse voltage u_{T+} closes the switches S_1 and S_4 between the time T_{1p} and T_{2p} that can be determined by Equations (5) and (6). Therefore, in this time interval, the voltage $u = +U_{dc}$.

$$T_{1p} = \frac{T(1-D)}{4}, \quad (5)$$

$$T_{2p} = \frac{T(1+D)}{4}. \quad (6)$$

The pulse voltage u_{T-} closes the switches S_2 and S_3 between the time T_{1n} and T_{2n} , that can be determined by Equations (7) and (8). Therefore, in this time interval, the voltage $u = -U_{dc}$, as is shown in Figure 4. From the comparison of Equations (5) and (7) and also (6) and (8), it can be seen that the difference is only $T/2$, so both half periods of the voltage u are the same, only the sign of the voltage U_{dc} is changing between $+U_{dc}$ and $-U_{dc}$.

$$T_{1n} = \frac{T(1-D)}{4} + \frac{T}{2}, \quad (7)$$

$$T_{2n} = \frac{T(1+D)}{4} + \frac{T}{2}. \quad (8)$$

In Figure 4, it can be seen that the time interval between T_{1p} and T_{2p} and also between T_{1n} and T_{2n} is denoted by T_{ON} , and represents the time interval when the voltage $+U_{dc}$ or $-U_{dc}$ is applied to the transformer. The time interval T_{ON} is defined with the time of a half period and duty cycle D , by Equation (9)

$$T_{ON} = \frac{T}{2}D. \quad (9)$$

In one one-half period outside of the time interval T_{ON} , there is a time interval T_{OFF} , when all the switches $S_1 - S_4$ are open, and the voltage $u = 0$. One-half of the time interval T_{OFF} is left of the time interval T_{ON} and one-half is right of it; it is the same in the second half of the period. Time interval T_{OFF} can be defined by Equation (10)

$$T_{OFF} = \frac{T}{2} - T_{ON} = \frac{T}{2}(1-D). \quad (10)$$

In Figure 4, the times T_{1p} , T_{2p} , T_{1n} , and T_{2n} are defined by Equations (5)–(8) only for the first period of the time series. For each subsequent time period, the times T_{1pi} , T_{2pi} , T_{1ni} , and T_{2ni} can be defined by adding $T \cdot (i-1)$ to each of them, where i is the time period of interest, as it is shown, for example, by Equation (11) for the time T_{1pi} and the same applies for T_{2pi} , T_{1ni} and T_{2ni}

$$T_{1pi} = T_{1p} + T \cdot (i-1), \quad i = 1, \dots, n. \quad (11)$$

The voltage supply for the welding transformer shown in Figure 4 has the same time interval T_{ON} in both half periods. In real applications, this is true for all time periods except the first one. The first period is usually exceptionally different, with only half of the time interval T_{ON} in the first half period, due to the nonlinear magnetic characteristics of the iron core. Assuming the remanent magnetic flux density $B_r = 0$ and the time interval T_{ON} is the same in both half periods, then, in the first half periods, the magnetic core is magnetized from the $B_r = 0$ to $B = 1$ T, for example, in the second half periods the magnetic core is demagnetized from $B = 1$ T back to $B = 0$, and so on. In this example, only the positive part of the nonlinear magnetic characteristic is used; if the T_{ON} is too long (D is too high), the magnetic core can become very saturated, and a high transformer's primary current can trigger an over current protection. To prevent the magnetic core from being magnetized only in a positive or only in a negative direction, the time interval T_{ON} in the first half period must be only half of it. In this example, if assuming the remanent magnetic flux density $B_r = 0$, half of the time interval T_{ON} causes magnetization from $B_r = 0$ to $B = 0.5$ T, for example, but, in the second half period with the full-time interval T_{ON} , the iron core is magnetized from $B = 0.5$ T to $B = -0.5$ T, and so on. In this example, the positive and negative parts of the nonlinear magnetic core are used, the iron core saturation is prevented, and the overcurrent protection is not triggered. The shorter time interval T_{ON} in the first half period can be achieved if the start of the pulse voltage u_{T+} begins at the time $\frac{T}{4}$ instead of T_{1p} in Figure 4.

3.4. Analytical Calculation of Welding and the Transformer's Primary Current of the RSW System

According to the H-bridge inverter model in Figure 2 and the welding transformer with output rectifier model in Figure 3, the Matlab/Simulink model of the RSW system can be made, as shown in Figure 5. The model of the RSW system can be made using any other appropriate software that allows time-dependent simulations of electrical circuits. On the left side of Figure 5 is the model of an H-bridge inverter with a constant DC link voltage $U_{dc} = 560$ V, the three-phase input rectifier is not modeled. The transistors or switches are modeled as voltage-controlled switches with a neglected resistance in a closed state ($1 \text{ n}\Omega$) and very high resistance in an open state ($1 \text{ G}\Omega$). Each switch has a backward diode that protects it against large, induced voltages when switching off inductive loads. The parameters of the backward diode model are set on neutral values, due to the neglected impact on the currents and voltages in the model. The forward voltage is set to 1 mV , the on-resistance is $1 \text{ n}\Omega$, and the off-resistance is $1 \text{ G}\Omega$. The welding transformer with the central tap on secondary winding is in Simulink (Figure 5), modeled as two separate ideal one-phase transformers, with primary windings connected in parallel and secondary windings connected in series. The only parameter of both transformers is the turn ratio, set to 55. All the other parameters of the RSW model in Figure 5, the resistances, leakage inductances, and diodes are set according to the values in Table 1.

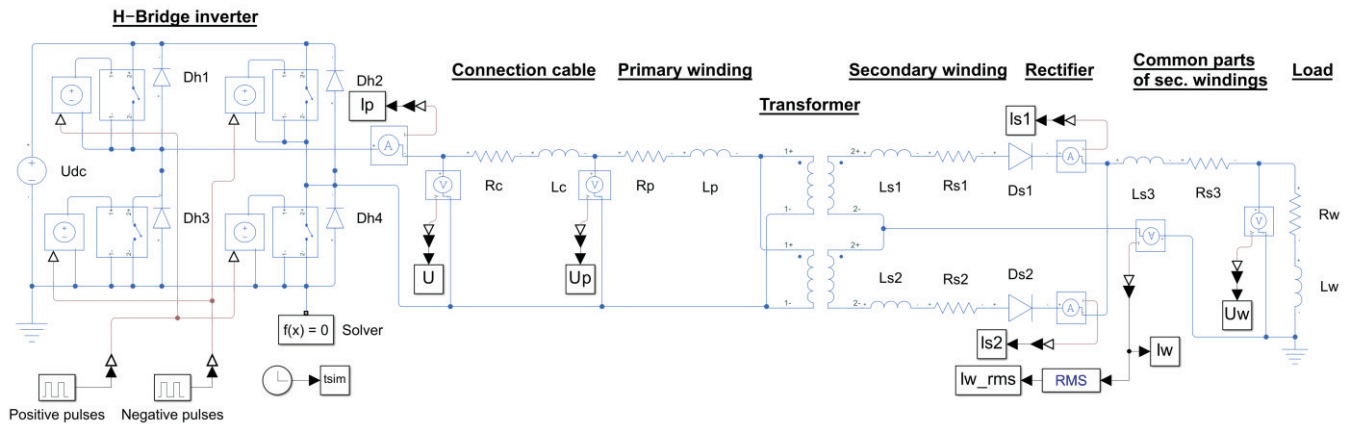


Figure 5. The Matlab/Simulink model of the RSW system.

The solver settings of the Simulink model in Figure 5 are as follows:

- Fixed-step solver: ode14x (extrapolation),
- Fixed-step size: $0.1 \mu\text{s}$, (depends on the selected PWM frequency f)
- Solver Jacobian method: auto,
- Extrapolation order: 4,
- Number of Newton's iterations: 3.

To solve the equations of the circuit model, a separate solver is used, which is connected to the circuit and can be seen as a block in the left bottom part in Figure 5, above the clock. The settings for this solver are as follows:

- Equation formulation: Time
- Index reduction method: None
- Consistency tolerance: Model AbsTol and RelTol
- Tolerance factor: 1×10^{-8}
- Use local solver: yes
- Solver type: Backward Euler
- Sample time: $0.1 \mu\text{s}$ (same as for the Simulink solver setting)
- Apply filtering: yes
- Filtering time constant 0.001

According to the Simulink model in Figure 5 and the parameters set, the numerical calculations were made at the PWM frequency $f = 1$ kHz and the duty cycle $D = 0.8$, for example. The numerically calculated time series for 20 periods are shown in Figure 6. In the first graph, the time series of the PWM voltage u is shown in the second graph, the time series of welding current i_w and both secondary windings (i_{s1} , i_{s2}) are shown, and, in the last, third graph, the time series is shown of the primary current. In Figure 6, the welding current i_w reaches the steady state value in approximately 20 time periods. Due to the relatively long time series of the transformer's voltages and currents in Figure 6, their analysis is difficult, so, in Figure 7, the same time series is shown for only one period of time for more straightforward observation.

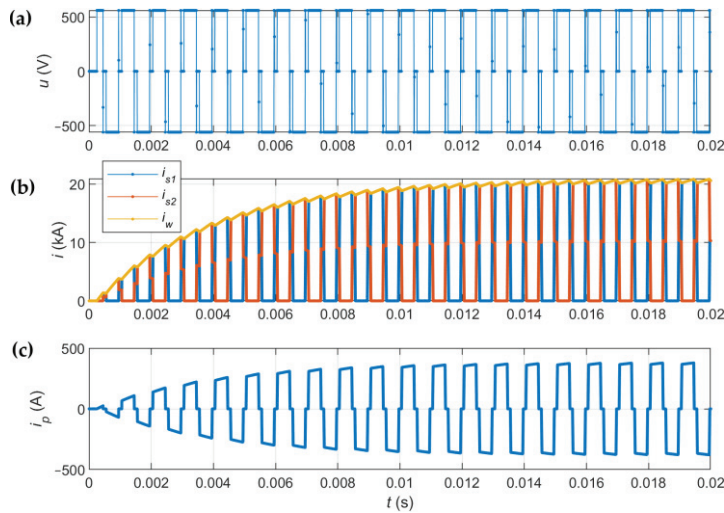


Figure 6. Time series for 20 periods of (a) H-bridge voltage u , (b) welding current i_w and both secondary currents (i_{s1} , i_{s2}), and (c) primary current i_p .

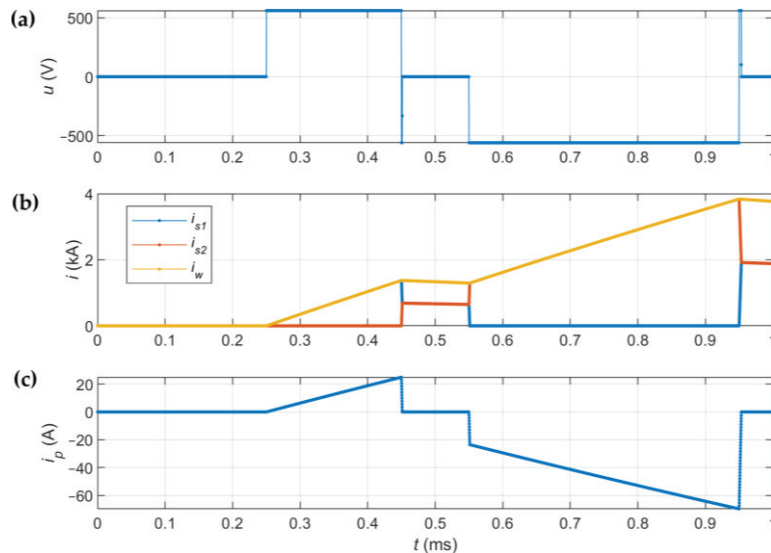


Figure 7. Time series for one period of (a) H-bridge voltage u , (b) welding current i_w and both secondary currents (i_{s1} , i_{s2}), and (c) primary current i_p .

In Figure 7, the RSW voltage and currents are shown, where it can be seen that the welding current increases relatively slowly when the positive or negative voltage u is applied and decreases relatively slowly when the voltage $u = 0$. The welding current i_w is changing according to two different time constants. The primary current i_p in the third graph in Figure 7 increases relatively slowly when the positive or negative voltage

u is applied but when the voltage u changes its value, the primary current increases or decreases relatively fast. The primary current i_p is changing according to two very different time constants. The time intervals when the primary current increases or decreases very fast are relatively short, but significantly impact the steady-state welding current. The time series of welding i_w and primary current i_p in separate time intervals look like straight lines define them and can be described analytically with linear equations; that is not true. The currents in each time interval can be described analytically as a step response of a first-order system, as explained below.

In Figure 7, some of the time intervals are very short, so it is not easy to mark the beginnings and ends of these intervals. For that reason, in Figure 8, the time series are sketched again with intentionally longer time intervals, and denotations are added at the beginning and end of each time interval for a more straightforward explanation. The time series in Figure 8 are shown for one and a half of the periods, due to the aforementioned exceptionally shorter T_{ON} time interval in the first half period to prevent iron core saturation. If the analytical solution of the welding and primary current is described for one and a half of the periods, the description for all subsequent periods is the same.

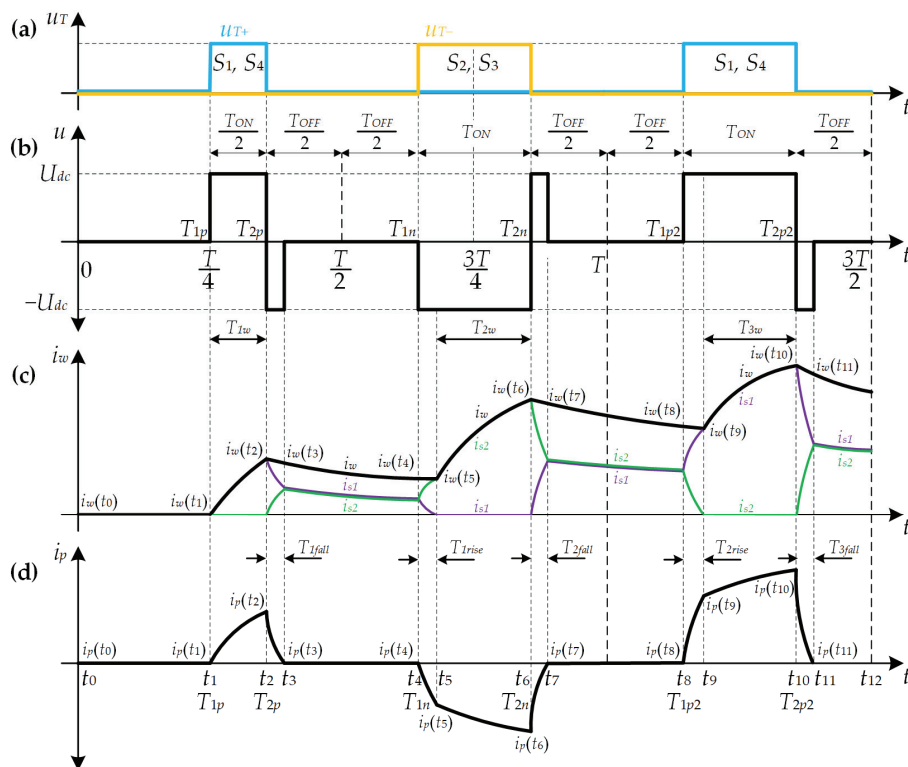


Figure 8. One and a half period of (a) transistor control voltage u_{T+} and u_{T-} , (b) H-bridge voltage u , (c) welding current i_w and both secondary currents (i_{s1} , i_{s2}), and (d) primary current i_p .

Figure 8 provides a basis for the interpretation of the individual time intervals and for the analytical determination of the dynamic behavior of the welding current and the transformer's primary winding current. The RSW system is a nonlinear time-varying system due to the diodes in the output rectifier. Therefore, not all equivalent circuit parameters influence the welding i_w and primary current i_p in each time interval. Each time interval in Figure 8 is described in the following subsections, and an analytical solution is given for the welding i_w and primary current i_p .

3.4.1. Time Interval $t_0 \leq t \leq t_1$

This time interval presents the first quarter of the period T , therefore, $t_0 = 0$ is the beginning of the time series and $t_1 = \frac{T}{4}$. All four switches ($S_1 - S_4$) are open in this time

interval, and the PWM voltage is $u = 0$. If we assume that the initial values of the welding and primary currents are zero $i_w(t_0) = i_p(t_0) = 0$, both currents remain zero at the end of the interval $i_w(t_1) = i_p(t_1) = 0$.

3.4.2. Time Interval $t_1 \leq t \leq t_2$, Increasing Welding and Primary Current

In this time interval, the switches S_1 and S_4 are closed, and the PWM voltage $u = +U_{dc}$ is applied to the welding transformer. The time $t_1 = T_{1p} = T/4$ is the beginning of the voltage pulse $u = +U_{dc}$, the time $t_2 = T_{2p}$ is the end of the voltage pulse defined by Equation (6). Due to the applied voltage, $u = +U_{dc}$, the primary i_p and welding current i_w starts to increase, and the energy from an inverter is delivered to the weld. According to the induced voltages on the transformer's secondary, the diode D_2 in Figure 3 prevents the current i_{s2} from flowing. Therefore, the equivalent circuit can be simplified, as shown in Figure 9. The diode D_1 is modeled as a serial connected resistance R_d and voltage source U_d in the simplified equivalent circuit.

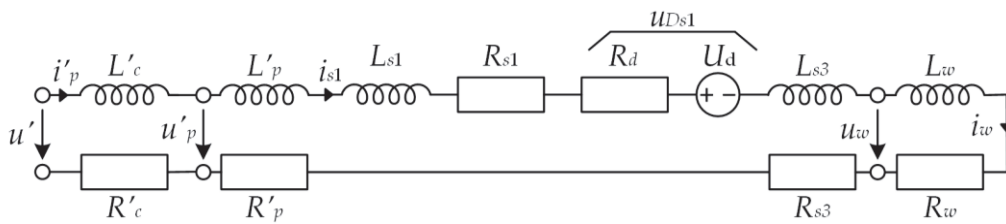


Figure 9. Simplified equivalent circuit with only one secondary branch.

In an equivalent circuit, in Figure 9, all resistances and leakage inductances are connected in series; therefore, the equivalent inductance L_1 by Equation (12) and resistance R_1 by Equation (13), can be calculated to define the time constant τ_1 , defined by Equation (14).

$$L_1 = L_c \left(\frac{N_s}{N_p} \right)^2 + L_p \left(\frac{N_s}{N_p} \right)^2 + L_{s1} + L_{s3} + L_w = 1.349 \mu\text{H}, \quad (12)$$

$$R_1 = R_c \left(\frac{N_s}{N_p} \right)^2 + R_p \left(\frac{N_s}{N_p} \right)^2 + R_{s1} + R_d + R_{s3} + R_w = 355 \mu\Omega, \quad (13)$$

$$\tau_1 = \frac{L_1}{R_1} = \frac{1.349 \mu\text{H}}{355 \mu\Omega} = 3.8 \text{ ms}. \quad (14)$$

Serial-connected equivalent resistance R_1 , inductance L_1 , and the diode's voltage source U_d define the first-order system supplied by a step voltage u' . Therefore, the time-dependent welding current i_w can be described analytically by Equation (15). In Equation (15) the voltage step is the H-bridge voltage $u = +U_{dc}$ referred as secondary u' , is reduced by the diode's voltage source $U_d = -0.66 \text{ V}$. The initial value of the welding current in Equation (15) is zero, because the welding current at the time $i_w(t_1) = 0$. The variable t in Equation (15) is general, but to calculate the welding current i_w for any time in the interval t_1 to t_2 , the variable t can be only between $t = 0$ and $t = t_2 - t_1 = T_{1w}$, where time T_{1w} is denoted in Figure 8.

$$i_w(t) = \frac{u' + U_d}{R_1} \left(1 - e^{-\frac{t}{\tau_1}} \right). \quad (15)$$

At the end of this interval, $t_1 \leq t \leq t_2$ is also the beginning of the next time interval $t_2 \leq t \leq t_3$. Therefore, it is essential to calculate the initial value of welding and primary current at the time t_2 . The initial value of welding current $i_w(t_2)$ is defined by Equation (15) if considering $t = T_{1w}$, as it is defined by Equation (16).

$$i_w(t_2) = \frac{u' + U_d}{R_1} \left(1 - e^{-\frac{T_{1w}}{\tau_1}} \right). \quad (16)$$

In Figure 9, all three currents are equal $i'_p = i_{s1} = i_w$. Therefore, Equation (15) also defines the primary current i_p , and Equation (16) also defines the initial value of the primary current $i_p(t_2)$, if they are referred to as primary ($i'_p(t_2) = i_w(t_2)$).

3.4.3. Time Interval $t_2 \leq t \leq t_3$, Fast Decreasing Primary Current

In this time interval, the inverter is in the T_{OFF} stage, so all the switches ($S_1 - S_4$) are open. The welding current i_w decreases from the initial value $i_w(t_2)$, the secondary current i_{s1} decreases fast from the initial value $i_{s1}(t_2) = i_w(t_2)$, the secondary current i_{s2} increases fast from the initial value 0. The primary current decreases fast from the initial value $i_p(t_2)$ to zero. Although all the switches ($S_1 - S_4$) are open, the primary current i_p cannot fall to zero instantly, due to the accumulated magnetic energy in the leakage inductances. The primary current now flows through the integrated antiparallel diodes of the inverter (D_{H2} and D_{H3}) in Figure 2. Therefore, the H-bridge voltage is opposite $u = -U_{dc}$. If the beginning of this time interval $t_2 = T_{2p}$ is defined by Equation (6), the end of this interval t_3 is not so trivial to determine. The end of this interval t_3 is defined by the primary current i_p , and how long it is decreasing from the initial value $i_p(t_2)$ to the zero $i_p(t_3) = 0$; this time interval is denoted by T_{1fall} in Figure 8. To derive an analytical solution for primary current i_p , the equivalent circuit must be defined, that describes the fast decreasing primary current in this time interval. The analysis shows that the equivalent circuit in Figure 10 defines the dynamic behavior of the primary current, where only specific resistances and leakage inductances have influence. The circuit parameters R_{s3} , R_w , L_{s3} , L_w , and diode's voltage source U_d do not influence the dynamic behavior of the primary current in this interval.

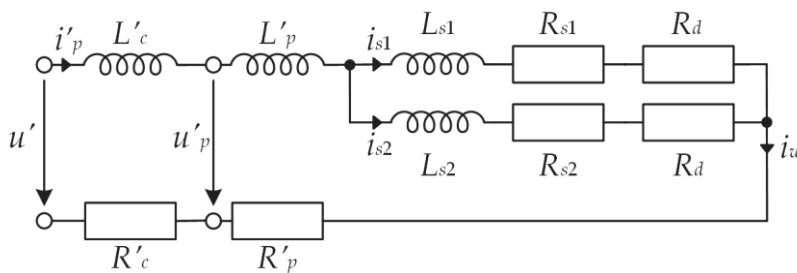


Figure 10. Equivalent circuit model defining the fast-changing primary current i_p .

In Figure 10 it can be seen that the inductances L_{s1} and L_{s2} are connected in parallel and then connected in series with L'_c and L'_p . Therefore, the equivalent inductance L_3 can be defined by Equation (17). The equivalent resistance R_3 of the circuit can also be defined by Equation (18).

$$L_3 = L_c \left(\frac{N_s}{N_p} \right)^2 + L_p \left(\frac{N_s}{N_p} \right)^2 + \frac{L_{s1}L_{s2}}{L_{s1} + L_{s2}} = 8.61 \text{ nH}, \quad (17)$$

$$R_3 = R_c \left(\frac{N_s}{N_p} \right)^2 + R_p \left(\frac{N_s}{N_p} \right)^2 + \frac{(R_{s1} + R_d)(R_{s2} + R_d)}{(R_{s1} + R_d) + (R_{s2} + R_d)} = 44.67 \text{ } \mu\Omega. \quad (18)$$

The equivalent inductance L_3 and resistance R_3 define the time constant τ_3 by Equation (19):

$$\tau_3 = \frac{L_3}{R_3} = \frac{8.61 \text{ nH}}{44.67 \text{ } \mu\Omega} = 192.73 \text{ } \mu\text{s}. \quad (19)$$

The serial-connected R_3 and L_3 present the first-order system with the step voltage supply $u = -U_{dc}$ in this time interval. Therefore, the analytical solution for primary current can be defined by Equation (20):

$$i'_p(t) = \frac{u'}{R_3} + \left(i'_p(t_2) - \frac{u'}{R_3} \right) e^{\frac{-t}{\tau_3}}. \quad (20)$$

The end of the time interval t_3 can now be derived by Equation (20). Previously, it has been mentioned that the time interval $T_{1fall} = t_3 - t_2$ is over when the primary current i_p decreases from the initial value $i_p(t_2)$ to zero. After substituting the primary current value $i'_p = i'_p(t_3) = 0$, $t = T_{1fall}$, and $u' = -U'_{dc}$ into Equation (20), we obtain a new expression from which the time interval T_{1fall} can be derived as:

$$T_{1fall} = \ln \left(\left(\frac{0 - \frac{-U'_{dc}}{R_3}}{i'_p(t_2) - \frac{-U'_{dc}}{R_3}} \right)^{-\tau_3} \right). \quad (21)$$

The end of the analyzed time interval t_3 can now be defined by Equation (22)

$$t_3 = t_2 + T_{1fall}. \quad (22)$$

Equation (20) is an analytical solution for the dynamic behavior of the primary current i_p in time interval $t_2 \leq t \leq t_3$, where the starting time $t = 0$ is at the beginning of the time interval t_2 . The initial condition $i_p(t_3)$ for the next time interval $t_3 \leq t \leq t_4$ is zero $i'_p(t_3) = 0$ but is defined by Equation (23), where considering $t = T_{1fall}$ and voltage step $u' = -U'_{dc}$:

$$i'_p(t_3) = \frac{-U'_{dc}}{R_3} + \left(i'_p(t_2) - \frac{-U'_{dc}}{R_3} \right) e^{\frac{-T_{1fall}}{\tau_3}}. \quad (23)$$

The welding current i_w is decreasing from the initial value $i_w(t_2)$ to $i_w(t_3)$ in the analyzed time interval $t_2 \leq t \leq t_3$, according to the equivalent circuit in Figure 11. From the circuit, only the parameters from the secondary define the dynamic behavior of the welding current i_w . At the same time, the primary current i_p is also flowing, and voltage is induced at the secondary, but it does not influence the welding current i_w , due to the symmetrical secondary branches. The secondary current i_{s1} is decreasing from the initial value $i_{s1}(t_2) = i_w(t_2)$ and i_{s2} is increasing from the initial value $i_{s2}(t_2) = 0$ (see Figure 8). Both currents are equal at the end of this time interval t_3 , and their values are half of the welding current $i_{s1}(t_3) = i_{s2}(t_3) = \frac{i_w(t_3)}{2}$.

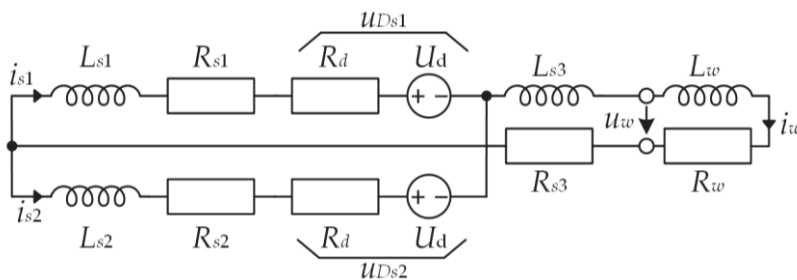


Figure 11. Equivalent circuit model defining decreasing welding current i_w .

According to the circuit in Figure 11 the equivalent inductance L_2 and resistance R_2 can be determined by Equations (24) and (25), that define the time constant τ_2 by Equation (26).

$$L_2 = \frac{L_{s1}L_{s2}}{L_{s1} + L_{s2}} + L_{s3} + L_w = 1.34 \mu\text{H}, \quad (24)$$

$$R_2 = \frac{(R_{s1} + R_d)(R_{s2} + R_d)}{(R_{s1} + R_d) + (R_{s2} + R_d)} + R_{s3} + R_w = 310.34 \mu\Omega, \quad (25)$$

$$\tau_2 = \frac{L_2}{R_2} = \frac{1.34 \mu\text{H}}{310.34 \mu\Omega} = 4.32 \text{ ms}. \quad (26)$$

Serial-connected equivalent resistance R_2 and inductance L_2 present the first-order system with the step voltage supply U_d . Therefore, an analytical solution for welding

current can be defined by Equation (27). In Equation (27) $U_d = -0.66$ V is the voltage source of the diode, which always works as a load; therefore, the welding current decreases a little faster, and the initial value of the welding current $i_w(t_2)$ is defined by Equation (16).

$$i_w(t) = \frac{U_d}{R_2} + \left(i_w(t_2) - \frac{U_d}{R_2} \right) e^{\frac{-t}{\tau_2}}. \quad (27)$$

Equation (27) is an analytical solution for the dynamic behavior of the welding current i_w in time interval $t_2 \leq t \leq t_3$, where the starting time $t = 0$ is at the beginning of the time interval t_2 . The initial condition $i_w(t_3)$ for the next time interval $t_3 \leq t \leq t_4$ is defined by Equation (28), where, considering $t = T_{1fall}$ and the voltage step is the diode's voltage source $U_d = -0.66$ V:

$$i_w(t_3) = \frac{U_d}{R_2} + \left(i_w(t_2) - \frac{U_d}{R_2} \right) e^{\frac{-T_{1fall}}{\tau_2}}. \quad (28)$$

3.4.4. Time Interval $t_3 \leq t \leq t_4$, Decreasing Welding Current

In this time interval the inverter is still in the T_{OFF} stage, so all the switches ($S_1 - S_4$) are open, and the primary current does not flow anymore $i_p = 0$. The welding current i_w still decreases according to the time constant τ_2 and Equation (27). The only difference is the initial value of the welding current $i_w(t_3)$ defined by Equation (28), and the starting time $t = 0$ is at the beginning of the time interval t_3 .

$$i_w(t) = \frac{U_d}{R_2} + \left(i_w(t_3) - \frac{U_d}{R_2} \right) e^{\frac{-t}{\tau_2}}. \quad (29)$$

The initial condition $i_w(t_4)$ for the next time interval $t_4 \leq t \leq t_5$ is defined by Equation (29), where considering $t = T_{1n} - t_3$ and voltage step is still the diode's voltage source $U_d = -0.66$ V, so we get Equation (30). The time $T_{1n} = t_4$ defines the beginning of the voltage pulse u_{T-} , when the negative $u = -U_{dc}$ is applied to the welding transformer, the time T_{1n} is defined by Equation (7) and t_3 by Equation (22).

$$i_w(t_4) = \frac{U_d}{R_2} + \left(i_w(t_3) - \frac{U_d}{R_2} \right) e^{\frac{-(T_{1n}-t_3)}{\tau_2}}. \quad (30)$$

3.4.5. Time Interval $t_4 \leq t \leq t_5$, Fast Increasing Primary Current

In this time interval, the inverter is in the T_{ON} stage, so the switches S_2 and S_3 are closed, the negative voltage $u = -U_{dc}$ is applied to the welding transformer, and the primary current increases fast from the initial value $i_p(t_4) = 0$ to the welding current $i'_p(t_5) = -i_w(t_5)$. The secondary currents are the same at the time t_4 with the value $i_{s1}(t_4) = i_{s2}(t_4) = \frac{i_w(t_4)}{2}$, the current i_{s1} decreases fast to zero $i_{s1}(t_5) = 0$, and the current i_{s2} increases fast to the value of the welding current $i_{s2}(t_5) = i_w(t_5)$. Although the voltage $u = -U_{dc}$ is applied to the transformer, the welding current still decreases, as is shown in Figure 8. The beginning $t_4 = T_{1n}$ of this time interval $t_4 \leq t \leq t_5$ is defined by Equation (7), the end time t_5 depends on the time that the primary current needs to increase from the initial value $i'_p(t_4) = 0$ to the value of the welding current $i'_p(t_5) = -i_w(t_5)$. This time interval is, in Figure 8, denoted by $T_{1rise} = t_5 - t_4 = t_5 - T_{1n}$. The welding current in this interval is defined by Equation (27) or (29). The only difference is the initial welding current $i_w(t_4)$, and the starting time $t = 0$ is at the beginning of the time interval t_4 , so we get Equation (31):

$$i_w(t) = \frac{U_d}{R_2} + \left(i_w(t_4) - \frac{U_d}{R_2} \right) e^{\frac{-t}{\tau_2}}. \quad (31)$$

The primary current increases from the initial value $i_p(t_4) = 0$ according to Equation (20), if the initial value $i'_p(t_4) = 0$ and step voltage source $u' = -U'_{dc}$ are taken into account to get Equation (32):

$$i'_p(t) = \frac{-U'_{dc}}{R_3} + \left(i'_p(t_4) - \frac{-U'_{dc}}{R_3} \right) e^{\frac{-t}{\tau_3}}. \quad (32)$$

The time interval $T_{1rise} = t_5 - T_{1n}$ is over when the primary current from the initial value $i'_p(t_4) = 0$ reaches the value of the welding current $i'_p(t_5) = -i_w(t_5)$, which is still decreasing in this time interval T_{1rise} . Therefore, Equations (31) and (32) must be equal, and $t = T_{1rise}$ must be considered to get Equation (33):

$$\frac{-U'_{dc}}{R_3} + \left(i'_p(t_4) - \frac{-U'_{dc}}{R_3} \right) e^{\frac{-T_{1rise}}{\tau_3}} = - \left(\frac{U_d}{R_2} + \left(i_w(t_4) - \frac{U_d}{R_2} \right) e^{\frac{-T_{1rise}}{\tau_2}} \right). \quad (33)$$

The time interval T_{1rise} appears on the left and right sides of Equation (33) and should be derived from it, but it is not possible, because this equation represents a transcendental equation and an analytical solution does not exist for T_{1rise} . A solution for a time interval T_{1rise} in Equation (33) can be found only numerically. When the T_{1rise} is a known value, the time t_5 can be defined by Equation (34):

$$t_5 = t_4 + T_{1rise}. \quad (34)$$

The initial value of the welding current $i_w(t_5)$ for the next time interval $t_5 \leq t \leq t_6$ is defined by Equation (31) if $t = T_{1rise}$ is considered to get Equation (35):

$$i_w(t_5) = \frac{U_d}{R_2} + \left(i_w(t_4) - \frac{U_d}{R_2} \right) e^{\frac{-T_{1rise}}{\tau_2}}. \quad (35)$$

The initial value of the primary current $i_p(t_5)$ for the next time interval is defined by Equation (32) if the $t = T_{1rise}$ is considered to get Equation (36):

$$i'_p(t_5) = \frac{-U'_{dc}}{R_3} + \left(i'_p(t_4) - \frac{-U'_{dc}}{R_3} \right) e^{\frac{-T_{1rise}}{\tau_3}}. \quad (36)$$

3.4.6. Time Interval $t_5 \leq t \leq t_6$, Increasing Welding and Primary Current

In this time interval, the inverter is still in the T_{ON} state, so the switches S_2 and S_3 are closed, the negative voltage $u = -U_{dc}$ is still applied to the welding transformer. The primary current i'_p , welding current i_w and i_{s2} are equal $-i'_p = i_w = i_{s2}$, the current of the first secondary branch is zero $i_{s1} = 0$. This time interval is like the interval $t_1 \leq t \leq t_2$. The difference is that the voltage supply is now negative $u = -U_{dc}$ and the initial condition is not zero. The analytical solution for the primary and welding currents can be defined based on the equivalent circuits in Figure 9, due to the symmetrical secondary branches $R_{s1} = R_{s2}$ and the same diode parameters R_d and U_d . Equation (15) is the analytical solution for increasing the welding current i_w in time period $t_1 \leq t \leq t_2$, where the initial current is zero.

Based on Equation (15) the analytical solution for the primary current in this time interval ($t_5 \leq t \leq t_6$) can be defined by Equation (37), if the negative voltage supply $-U'_{dc} - U_d$ and the initial current condition $i'_p(t_5)$ defined by (36) are considered:

$$i'_p = \frac{-U'_{dc} - U_d}{R_1} + \left(i'_p(t_5) - \frac{-U'_{dc} - U_d}{R_1} \right) e^{\frac{-t}{\tau_1}}. \quad (37)$$

Due to the negative voltage supply $-U'_{dc} - U_d$ in Equation (37), the initial condition $i'_p(t_5)$ and the current i'_p are negative values. The welding current is always positive, due to the output rectifier. Therefore, the analytical solution for the welding current is

$i_w = -i_p' = |i_p'|$. In Equation (37), the diode's negative voltage $U_d = -0.66$ V always works as a load, therefore, it must be subtracted from the negative voltage supply $u' = -U_{dc}'$.

Equation (37) is the analytical solution for the dynamic behavior of the welding and primary current in time interval $t_5 \leq t \leq t_6$, where the starting time $t = 0$ is at the beginning of the time interval t_5 . The initial condition $i_w(t_6) = -i_p'(t_6)$ for the next time interval $t_6 \leq t \leq t_7$ is defined by Equation (37), where, considering $t = T_{2n} - t_5$ to get Equation (38). The time T_{2n} is defined by Equation (8) and time t_5 is defined by Equation (34).

$$i_p'(t_6) = -i_w(t_6) = \frac{-U_{dc}' - U_d}{R_1} + \left(i_p'(t_5) - \frac{-U_{dc}' - U_d}{R_1} \right) e^{\frac{-(T_{2n}-t_5)}{\tau_1}}, \quad (38)$$

3.4.7. Time Interval $t_6 \leq t \leq t_7$, Fast Decreasing Primary Current

This time interval is like the interval $t_2 \leq t \leq t_3$, therefore, a detailed explanation is not necessary. The difference is that the voltage supply is positive $u' = +U_{dc}$ because, with all the switches ($S_1 - S_4$) open, the primary current flows through the integrated antiparallel diodes of the inverter (D_{H1} and D_{H4}). The primary current decreases fast from the negative initial value $i_p(t_6)$ to zero $i_p(t_7) = 0$, the welding current decreases from the initial value $i_w(t_6)$ to a new value $i_w(t_7)$, the secondary current i_{s2} decreases fast from the initial value $i_{s2}(t_6)$ to a new value $i_{s2}(t_7)$, the secondary current i_{s1} increases fast from the initial value $i_{s1}(t_6) = 0$ to a new value $i_{s1}(t_7)$. At the end of this time interval t_7 , both secondary currents are half of the welding current $i_{s1}(t_7) = i_{s2}(t_7) = \frac{i_w(t_7)}{2}$. The beginning of this time interval $t_6 = T_{2n}$ is defined by Equation (8), the end time t_7 depends on the time period $T_{2fall} = t_7 - t_6$ denoted in Figure 8. The time period T_{2fall} is, like the time period T_{1fall} , defined by the primary current, i.e., how long does it take to fall from the negative initial value $i_p(t_6)$ to zero? To define the time period T_{2fall} , the analytical solution for the falling primary current must be defined first. The primary current is falling according to the equivalent circuit in Figure 10 and Equation (20), where the voltage supply $u' = +U_{dc}$ and the initial value of the primary current $i_p'(t_6)$, defined by Equation (38), are considered to get Equation (39):

$$i_p'(t) = \frac{u'}{R_3} + \left(i_p'(t_6) - \frac{u'}{R_3} \right) e^{\frac{-t}{\tau_3}}. \quad (39)$$

The end of the time interval t_7 can now be derived by Equation (39). Previously, it has been mentioned that the time interval $T_{2fall} = t_7 - t_6$ is over when the primary current i_p decreases from the initial value $i_p'(t_6)$ to zero. If, in Equation (39), the primary current value at t_7 is zero $i_p' = i_p'(t_7) = 0$, $t = T_{2fall}$ and $u' = +U_{dc}'$, Equation (40) can be derived that defines the time interval T_{2fall}

$$T_{2fall} = \ln \left(\left(\frac{0 - \frac{+U_{dc}'}{R_3}}{i_p'(t_6) - \frac{+U_{dc}'}{R_3}} \right)^{-\tau_3} \right). \quad (40)$$

The end of the analyzed time interval t_7 can now be defined by Equation (41):

$$t_7 = t_6 + T_{2fall}. \quad (41)$$

Equation (39) is an analytical solution for the dynamic behavior of the primary current i_p in the time interval $t_6 \leq t \leq t_7$, where the starting time $t = 0$ is at the beginning of the time interval t_6 . The initial condition $i_p(t_7)$ for the next time interval $t_7 \leq t \leq t_8$ is zero $i_p'(t_7) = 0$, but is defined by Equation (42), where, considering $t = T_{2fall}$ and voltage step $u' = +U_{dc}$:

$$i_p'(t_7) = \frac{u'}{R_3} + \left(i_p'(t_6) - \frac{u'}{R_3} \right) e^{\frac{-T_{2fall}}{\tau_3}}. \quad (42)$$

The welding current i_w is decreasing in this time interval, although $u' = +U_{dc}$ and the primary current i_p is also flowing, and voltage is induced at the secondary, but it does not influence the welding current due to the symmetrical secondary branches. The welding current is decreasing according to the same Equation (43) as in all previous time intervals between the time t_2 and t_5 , only the initial welding current is different $i_w(t_6)$, defined by Equation (38).

$$i_w(t) = \frac{U_d}{R_2} + \left(i_w(t_6) - \frac{U_d}{R_2} \right) e^{\frac{-t}{\tau_2}}. \quad (43)$$

Equation (43) is an analytical solution for the dynamic behavior of the primary current i_w in the time interval $t_6 \leq t \leq t_7$, where the starting time $t = 0$ is at the beginning of the time interval t_6 . The initial condition $i_w(t_7)$ for the next time interval $t_7 \leq t \leq t_8$ is defined by Equation (43) if $t = T_{2fall}$ is considered to get Equation (44)

$$i_w(t_7) = \frac{U_d}{R_2} + \left(i_w(t_6) - \frac{U_d}{R_2} \right) e^{\frac{-T_{2fall}}{\tau_2}}. \quad (44)$$

3.4.8. Time Interval $t_7 \leq t \leq t_8$, Decreasing Welding Current

This time interval is like the interval $t_3 \leq t \leq t_4$, therefore, a detailed explanation is not necessary. The primary current is not flowing $i_p = 0$. The welding current is still decreasing according to the time-constant τ_2 and Equation (45), where the initial welding current $i_w(t_7)$ defined by Equation (44) is considered. The starting time $t = 0$ is at the beginning of the time interval t_7 .

$$i_w(t) = \frac{U_d}{R_2} + \left(i_w(t_7) - \frac{U_d}{R_2} \right) e^{\frac{-t}{\tau_2}}. \quad (45)$$

The initial condition $i_w(t_8)$ for the next time interval $t_8 \leq t \leq t_9$ is defined by Equation (45), where considering $t = t_8 - t_7$ to get Equation (46). The time $t_8 = T_{1p2}$ is defined by Equation (11), where $T_{1p2} = T_{1p} + T$, and time t_7 is defined by Equation (41).

$$i_w(t_8) = \frac{U_d}{R_2} + \left(i_w(t_7) - \frac{U_d}{R_2} \right) e^{\frac{-(t_8-t_7)}{\tau_2}}. \quad (46)$$

3.4.9. Time Interval $t_8 \leq t \leq t_9$, Fast Increasing Primary Current

This time interval starts at time $t_8 = T_{1p2}$ when the positive voltage supply $u = +U_{dc}$ is applied to the transformer in the second period due to the closed switches S_1 and S_4 , like in the first half of the first period. The difference between the start of the positive voltage supply $u = +U_{dc}$ in the first and second periods is the initial condition of welding current at $t_1 = T_{1p}$ and $t_8 = T_{1p2}$. In the first period, the initial value of the welding current at time t_1 is zero $i_w(t_1) = 0$. Therefore, there is no time interval for the fast-increasing primary current i_p . In the second period at the time t_8 , the welding current i_w is not zero $i_w(t_8) > 0$; therefore, the primary current i_p increases fast from zero $i'_p(t_8) = 0$ to the value of the welding current $i'_p(t_9) = i_w(t_9)$. The fast increase of the primary current i_p is the difference between the first and second periods at the beginning of the positive voltage supply $u = +U_{dc}$. Therefore, the explanation and analytical solutions for the welding i_w and primary current i_p are given for one and a half periods instead of only one period.

The time interval $t_8 \leq t \leq t_9$ is like $t_4 \leq t \leq t_5$. The only difference is the positive voltage supply $u = +U_{dc}$ and the initial value of the welding current at the time t_8 ; therefore, a detailed explanation is unnecessary. This analyzed time interval $t_8 \leq t \leq t_9$ ends when the primary current from the initial value zero $i'_p(t_8) = 0$ reaches the value of the welding current $i'_p(t_9) = i_w(t_9)$ in time $T_{2rise} = t_9 - t_8$, denoted in Figure 8. To define the T_{2rise} the analytical solution for the decreasing welding current i_w and fast increasing primary

current i_p must be defined first. The welding current decreases according to Equation (31) if the initial value of the welding current $i_w(t_8)$ is considered to get Equation (47)

$$i_w(t) = \frac{U_d}{R_2} + \left(i_w(t_8) - \frac{U_d}{R_2} \right) e^{\frac{-t}{\tau_2}}. \quad (47)$$

The primary current i_p increases fast from the initial value $i_p(t_8) = 0$ according to Equation (32), if the initial value $i'_p(t_8) = 0$ and positive step voltage source $u' = +U'_{dc}$ are considered to get Equation (48)

$$i'_p(t) = \frac{+U'_{dc}}{R_3} + \left(i'_p(t_8) - \frac{+U'_{dc}}{R_3} \right) e^{\frac{-t}{\tau_3}}. \quad (48)$$

The time interval $T_{2rise} = t_9 - t_8$ is over when the primary current from the initial value $i'_p(t_8) = 0$ reaches the value of the welding current $i'_p(t_9) = i_w(t_9)$, which is still decreasing in this time interval T_{2rise} . Therefore, Equations (47) and (48) must be equal, and $t = T_{2rise}$ must be considered to get Equation (49)

$$\frac{+U'_{dc}}{R_3} + \left(i'_p(t_8) - \frac{+U'_{dc}}{R_3} \right) e^{\frac{-T_{2rise}}{\tau_3}} = \frac{U_d}{R_2} + \left(i_w(t_8) - \frac{U_d}{R_2} \right) e^{\frac{-T_{2rise}}{\tau_2}}. \quad (49)$$

The time interval T_{2rise} appears on the left and right sides of Equation (49) and should be derived from it, but it is not possible because this equation represents a transcendental equation and an analytical solution for T_{2rise} does not exist. A solution for T_{2rise} can only be found numerically. When the T_{2rise} is a known value, the time t_9 can be defined by Equation (50), where $t_8 = T_{1p2}$ and $T_{1p2} = \frac{T(1-D)}{4} + T$ is defined by Equations (5) and (11)

$$t_9 = t_8 + T_{2rise} = T_{1p2} + T_{2rise}. \quad (50)$$

The initial value of the welding current $i_w(t_9)$ for the next time interval $t_9 \leq t \leq t_{10}$ is defined by Equation (47) if $t = T_{2rise}$ is considered to get Equation (51)

$$i_w(t_9) = \frac{U_d}{R_2} + \left(i_w(t_8) - \frac{U_d}{R_2} \right) e^{\frac{-T_{2rise}}{\tau_2}}. \quad (51)$$

The initial value of the primary current $i'_p(t_9)$ for the next time interval is defined by Equation (48) if the $t = T_{2rise}$ is considered to get Equation (52)

$$i'_p(t_9) = \frac{+U'_{dc}}{R_3} + \left(i'_p(t_8) - \frac{+U'_{dc}}{R_3} \right) e^{\frac{-T_{2rise}}{\tau_3}}. \quad (52)$$

3.4.10. Time Interval $t_9 \leq t \leq t_{10}$, Increasing Welding and Primary Current

This time interval is like the interval $t_1 \leq t \leq t_2$ in the first half of the first period, only the initial primary current $i'_p(t_9)$ is not zero. Equation (53) is an analytical solution for the primary and welding current $i'_p = i_w$ in this analyzed interval, and the starting time $t = 0$ is at the time t_9

$$i'_p = \frac{+U'_{dc} + U_d}{R_1} + \left(i'_p(t_9) - \frac{+U'_{dc} + U_d}{R_1} \right) e^{\frac{-t}{\tau_1}}. \quad (53)$$

The initial value of the welding $i_w(t_{10})$ and primary current $i'_p(t_{10})$ for the next time interval $t_{10} \leq t \leq t_{11}$ are defined by Equation (53) if $t = T_{2p2} - t_9 = T_{3w}$ is considered to get Equation (54). The time $T_{2p2} = T_{2p} + T$ is defined by Equation (11), and the time t_9 is defined by Equation (50)

$$i'_p = \frac{+U'_{dc} + U_d}{R_1} + \left(i'_p(t_9) - \frac{+U'_{dc} + U_d}{R_1} \right) e^{\frac{-(T_{2p2}-t_9)}{\tau_1}}. \quad (54)$$

4. Results

The analytical solution for welding and the transformer's primary current of the RSW system is given in previous subsections. The analytical solution is provided as equations that describe the time response of the welding and primary current in separate time intervals of the voltage-supplied period. In these time intervals, the RSW system is linear and the currents change according to the step voltage response of the first-order system. If the time series of the currents in the individual intervals are connected, the time series of the welding i_w and primary currents i_p are obtained, which should be the same as the numerically calculated time series using the Simulink model in Figure 5. The comparison of analytically and numerically (Simulink) calculated time series of the welding i_w and the primary currents i_p are shown in Figure 12, for the same example and parameter settings as in Figure 6.

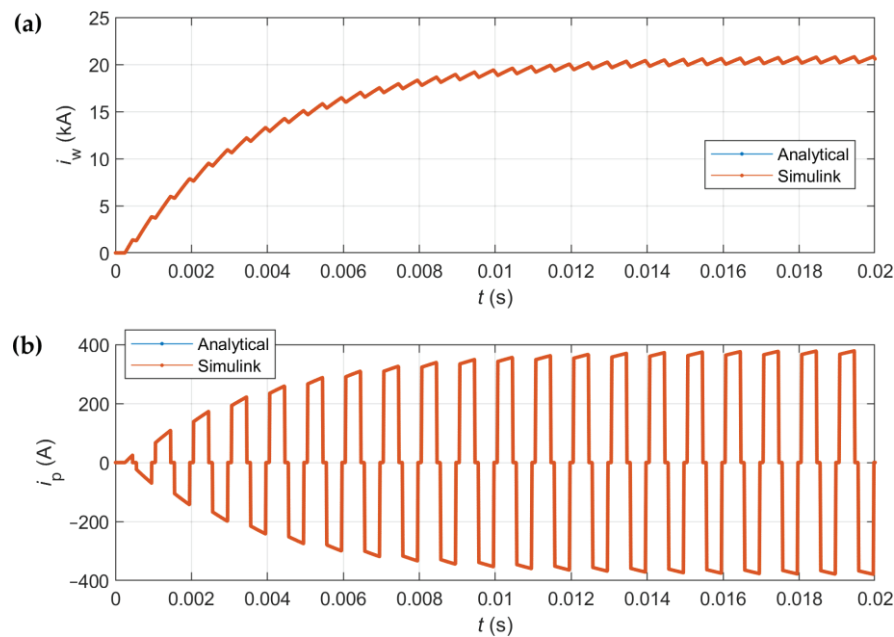


Figure 12. The comparison of analytically and numerically (Simulink) calculated (a) welding i_w and (b) primary currents i_p .

The comparison of time series in Figure 12 shows that the analytically calculated welding and primary currents are practically the same; it is not possible to see any difference between them. The time series in the red color overlaps the blue time series, so it cannot be seen. For a more precise comparison of the analytically and numerically calculated time series of currents, the differences are calculated and shown in Figure 13. From the calculated differences in welding current Δi_w it can be seen that the maximum difference does not exceed 1 A. The maximum welding current in the steady state in Figure 12a is more than 20 kA, so, the maximum difference 1 A presents less than 0.005% of the maximum welding current. From the calculated difference of the primary current Δi_p in Figure 13b, it can be seen that the maximum difference is around 2 A in only six-time intervals that step out; in all other cases, the difference is less than 0.1 A. The maximum primary current in a steady state in Figure 12b is around 378 A, so, the maximum difference 2 A presents around 0.53%, and 0.1 A presents less than 0.03% of the maximum primary current.

The reason for the differences between the analytically and numerically calculated welding and primary currents is the numerical errors of the solvers in Simulink. In Simulink settings, the fixed time step of both solvers is used ($0.1 \mu\text{s}$) to calculate the time series of the currents and voltages. If the times, T_{1p} , T_{2p} , T_{1n} , T_{2n} in the first and all subsequent periods in Figure 4 are not precisely a multiple of the fixed time step, the numerical error can cause the differences in time intervals T_{ON} in Figure 4, when the voltage $u = U_{dc}$ or $u = -U_{dc}$

is applied to the welding transformer. The different time intervals T_{ON} in each period of PWM voltage supply causes different time intervals (T_{1w} , T_{2w} , T_{3w} in Figure 8). When the welding current increases, it influences the time series of the welding and primary currents. To minimize the numerical errors in Simulink, the fixed time step must be short enough; if not, the numerical errors increase, and so do the differences between the analytical and numerically calculated time series of the welding and primary currents. The analytical approach to calculate the time series of the welding and secondary currents does not have such numerical problems depending on the fixed time step size. The times, T_{1p} , T_{2p} , T_{1n} , T_{2n} , in the first and all subsequent periods are determined precisely independent of the fixed step size, so the start and end times of each time interval in Figure 8 are not affected by the fixed step size as they are in Simulink.

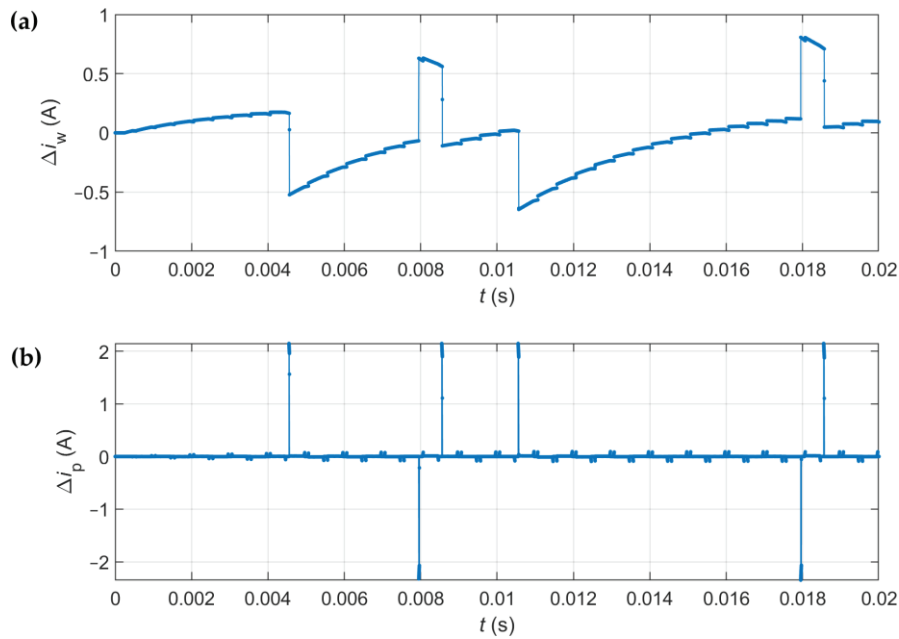


Figure 13. The difference between the analytically and numerically (Simulink) calculated (a) welding, and (b) primary currents.

The time intervals in Figure 8 are not always present in the same sequence; for example, the welding current in Figure 8 is, from the time t_1 forward, always greater than zero. That is true if the duty cycle D is greater than the minimal duty cycle D_{min} , which assures a continuous steady state welding current without time interval with $i_w = 0$ in the period of the PWM voltage supply. At the duty cycle D_{min} , the welding current decreases in the T_{OFF} time interval, and only touches the value $i_w = 0$ and immediately starts to increase in the next half period, as is shown in Figure 14. If the duty cycle D is less than D_{min} , the welding current in a steady state is not continuous anymore, and there are time intervals with the $i_w = 0$. Such discontinuous conduction mode of welding current i_w is not usable in practice but can also be calculated analytically. If the duty cycle $D < D_{min}$, the time intervals with fast-increasing primary current (T_{1rise} , T_{2rise} in Figure 8) do not exist, as is shown in Figure 14.

Like the minimal duty cycle D_{min} , there is also the maximal duty cycle D_{max} . The increase of the duty cycle D from 0 to D_{max} causes an increase in the steady state welding current's root mean square (RMS) I_w . If the duty cycle increases further from D_{max} to $D = 1$, the steady state welding current I_w does not increase anymore but stays the same. At the maximal duty cycle D_{max} , the steady state primary current decreases fast in the time intervals T_{1fall} , T_{2fall} , and T_{3fall} in Figure 8, but crosses the value $i_w = 0$, and starts to increase fast immediately in the opposite direction in time intervals T_{1rise} and T_{2rise} in Figure 8, without the time intervals when $i_p = 0$. The comparison of analytically and

numerically (Simulink) calculated time series of the welding i_w and primary currents i_p is shown in Figure 15, where the duty cycle is $D = D_{max} = 0.9619$, and there is no time interval with $i_p = 0$ in the steady-state welding current I_w .

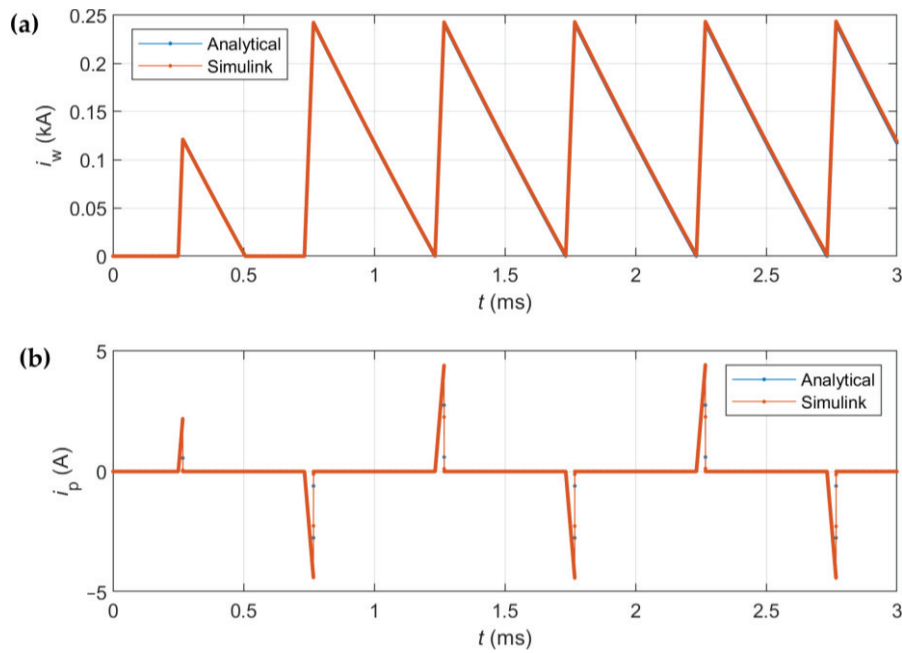


Figure 14. The comparison of analytically and numerically (Simulink) calculated (a) welding i_w and (b) primary currents i_p at the minimal duty cycle $D_{min} = 0.06889$.

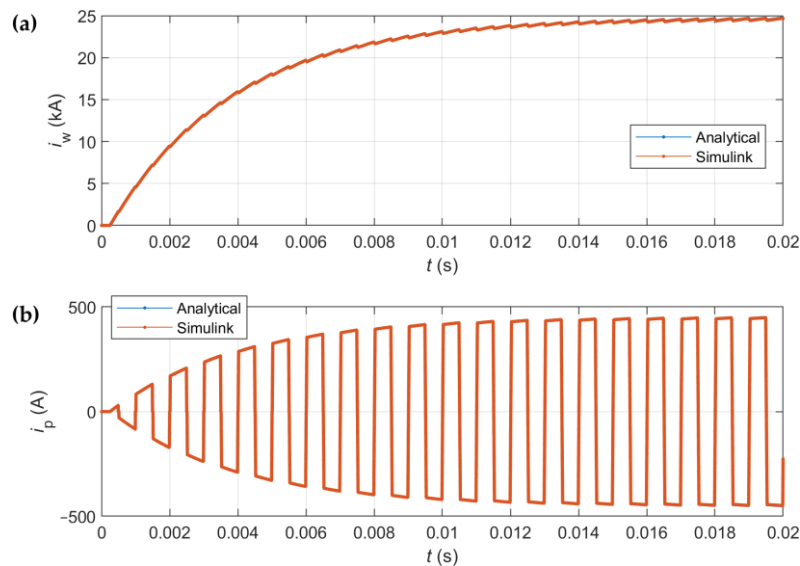


Figure 15. The comparison of analytically and numerically (Simulink) calculated (a) welding i_w and (b) primary currents i_p at the maximal duty cycle $D_{max} = 0.9619$. Due to minimal differences, the red time series (Simulink) overlaps the blue time series (Analytical).

According to Figures 14 and 15, the analytical approach can be used to calculate the time series of the welding i_w and primary currents i_p , even when the duty cycle D is smaller than D_{min} or greater than D_{max} , and some time intervals are not present in each voltage supply period.

5. Conclusions

In this paper, a 130 kVA resistance spot welding system is analyzed in terms of the possibility of describing the time series of the welding and the primary current of the transformer analytically. The resistance spot welding systems are used mainly in the automotive industry for welding car bodies, where the welding transformer is attached to a moving robotic arm. The RSW system consists of an inverter, a welding transformer, an output diode rectifier, and welding clamps with electrodes. The PWM controls the welding current with centrally positioned pulses. The weight of the iron core of the welding transformer mounted on the robotic arm can be reduced with a higher frequency of voltage supply, but leakage inductances of the welding transformer reduce the maximum welding current that can be achieved at the same load. To predict the maximum possible welding current at a specific load and to design a high-performance welding system, it is necessary to know the dynamics of the welding and the primary currents of the RSW system. The design of the welding transformer with the output rectifier defines the equivalent resistances and leakage inductances of the RSW system that determine the dynamics of the currents and the maximum welding current at a specific load.

The current and voltage dynamics of the RSW system can be analyzed by expensive and time-consuming measurements or by expensive and complex software tools that are not easy to use. Free software tools usually have several limitations, and do not guarantee the correctness of the results; therefore, they are not used in commercial projects. This paper presents a fourth, new possibility to determine the dynamic responses of the welding and primary current of a welding transformer analytically. In high-power resistance spot welding systems, resistances and leakage inductances are dominant, while capacitances can be neglected. For this reason, an RSW can be modeled with an equivalent circuit, with equivalent resistances and leakage inductances, and the diodes of a diode rectifier can be modeled as serially connected resistances and a voltage source. Due to the output diode rectifier, RSW systems are nonlinear and time-varying systems, so all equivalent circuit parameters do not affect the dynamics of the currents and voltages in all the time intervals of the voltage supply period. In the one-half period of the voltage supply, only one secondary branch is active, and, in the second-half period, only the second secondary branch of the transformer is active. Due to the time-varying system, three different equivalent circuits can be determined at individual intervals of the voltage supply period, which determine the dynamics of the welding and primary currents of the transformer. These three equivalent circuits can be determined as serially connected equivalent resistance and inductance, that present a first-order system supplied by a step voltage; therefore, the analytical solution can be determined for the current response. These three relatively simple analytical solutions for step responses of the first-order system allow analytical determination of the time series of welding and the transformer's primary current. The presented analytical solution is limited to symmetrical secondary branches of the welding transformer. Therefore, the resistance and leakage inductance of both secondary branches must be the same, and the DC voltage supply of the inverter must be constant in each separate time interval of the voltage supply period. The values of the RSW system equivalent circuit parameters can change with time but must stay constant in separate time intervals. Therefore, the temperature-dependent resistance of the weld nugget or the voltage drop of the H-bridge DC link can be considered.

The analytical solution has many advantages compared to numerical calculations with Simulink, where the solver selection and fixed time step size cause numerical errors in the time series of welding and primary currents, or even cause the numerical calculation not to converge to a solution. The derived analytical equations allow calculations of welding and primary currents of the RSW system but also give a thorough understanding of how its parameters influence the current dynamic. The analytical solution can be implemented in any programming language and benefits from multi-core processors. When the initial conditions and the equations for currents in each time interval of the time series of welding

and primary currents are determined, the values of the currents inside each time interval can be calculated simultaneously on different cores of processors for fast computation.

In future work, the derived analytical solutions can be extended to include phenomena not considered in this manuscript. The voltage drops on the switching transistors of the H-bridge can be easily considered with an additional equivalent resistance of the transistors in conduction mode. The same is true for the antiparallel diodes of the inverter; the equivalent resistance and the backward voltage source of the diodes can be considered with their actual values. In this example, the time constant is not the same anymore if the primary current is flowing from the inverter to the transformer or from the transformer to the inverter due to the different resistances of the transistors and antiparallel diodes. The iron core losses could be considered in the analytical solutions as additional equivalent resistance or with the more sophisticated method. The non-linear magnetic curve of the iron core could also be considered in the calculations if the time intervals are divided into smaller intervals and some values of the parameters are changed according to the iron core saturation in each interval.

Author Contributions: Conceptualization, R.B. and J.R.; Data curation, R.B.; Formal analysis, R.B.; Funding acquisition, J.R.; Investigation, R.B.; Methodology, R.B. and J.R.; Project administration, J.R.; Resources, R.B.; Software, R.B.; Supervision, J.R.; Validation, R.B.; Visualization, R.B.; Writing—original draft, R.B.; Writing—review and editing, R.B. and J.R. All authors have read and agreed to the published version of the manuscript.

Funding: This research was funded in part by the Slovenian Research and Innovation Agency (ARIS) under Grants numbers P2-0115 and L2-7556 and in part by BOSCH Rexroth.

Data Availability Statement: Data available on request.

Conflicts of Interest: The authors declare no conflicts of interest.

References

1. Soomro, I.A.; Pedapati, S.R.; Awang, M. A review of advances in resistance spot welding of automotive sheet steels: Emerging methods to improve joint mechanical performance. *Int. J. Adv. Manuf. Technol.* **2022**, *118*, 1335–1366. [CrossRef]
2. Sakurai, S.; Ike, Y.; Yoshida, K.; Iyota, M. Weldability and Mechanical Properties of Fe/Al Dissimilar Joints by Resistance Spot Weld Bonding. *Eng. Proc.* **2023**, *43*, 47. [CrossRef]
3. Lambiase, F.; Scipioni, S.I.; Lee, C.-J.; Ko, D.-C.; Liu, F. A State-of-the-Art Review on Advanced Joining Processes for Metal-Composite and Metal-Polymer Hybrid Structures. *Materials* **2021**, *14*, 1890. [CrossRef]
4. Arumugam, A.; Pramanik, A. A Review on the Recent Trends in Forming Composite Joints Using Spot Welding Variants. *J. Compos. Sci.* **2024**, *8*, 155. [CrossRef]
5. Kwon, H.; Shah, U.; Liu, X.; Malpica, J.; Lester, P.; Bonam, H. Experimental Analysis on Ultrasonic Resistance Spot Welding of Aluminum Alloys. *Weld. J.* **2023**, *102*, 217–233. [CrossRef]
6. Mezher, M.T.; Pereira, A.; Trzepieciński, T.; Acevedo, J. Artificial Neural Networks and Experimental Analysis of the Resistance Spot Welding Parameters Effect on the Welded Joint Quality of AISI 304. *Materials* **2024**, *17*, 2167. [CrossRef] [PubMed]
7. Mezher, M.T.; Carou, D.; Pereira, A. Exploring Resistance Spot Welding for Grade 2 Titanium Alloy: Experimental Investigation and Artificial Neural Network Modeling. *Metals* **2024**, *14*, 308. [CrossRef]
8. Matsukage, T.; Sakurai, S.; Traui, T.; Iyota, M. Mechanical Properties of Resistance-Spot-Welded Joints of Aluminum Castings and Wrought Alloys. *Eng. Proc.* **2023**, *43*, 52. [CrossRef]
9. Prabhakaran, M.; Jeyasimman, D.; Varatharajulu, M. Insights and Implications: Unraveling Critical Factors in Resistance Spot Welding of Dissimilar Metals through SS 347 and DSS 2205 Welds. *Eng. Proc.* **2023**, *59*, 27. [CrossRef]
10. Kucera, V.; Zofkova, Z.; Digiovanni, C.; He, L.; Vojtěch, D. Investigation of Liquid Metal Embrittlement during Resistance Spot Welding of Martensitic Steel with Zn Jet Vapor-Deposited Coating. *Metals* **2021**, *11*, 1813. [CrossRef]
11. Chang, F.; Zhou, G.; Ding, K.; Li, J.; Jing, Y.; Hui, J.; Zhang, C. A CNN-LSTM and Attention-Mechanism-Based Resistance Spot Welding Quality Online Detection Method for Automotive Bodies. *Mathematics* **2023**, *11*, 4570. [CrossRef]
12. Dong, J.; Hu, J.; Luo, Z. Quality Monitoring of Resistance Spot Welding Based on a Digital Twin. *Metals* **2023**, *13*, 697. [CrossRef]
13. Martín, Ó.; De Tiedra, P. Advances in the Control and Improvement of Quality in the Resistance Spot Welding Process. *Metals* **2022**, *12*, 1810. [CrossRef]
14. Stavropoulos, P.; Sabatakakis, K. Quality Assurance in Resistance Spot Welding: State of Practice, State of the Art, and Prospects. *Metals* **2024**, *14*, 185. [CrossRef]
15. Teren, T.; Penter, L.; Peukert, C.; Ihlenfeldt, S. A Finite-Difference Based Parallel Solver Algorithm for Online-Monitoring of Resistance Spot Welding. *Materials* **2022**, *15*, 6348. [CrossRef] [PubMed]

16. Wen, J.; Jia, H. Real-time monitoring system for resistance spot welding quality. *Eng. Res. Express* **2023**, *5*, 015006. [CrossRef]
17. Ibáñez, D.; García, E.; Soret, J.; Martos, J. Real-Time Condition Monitoring System for Electrode Alignment in Resistance Welding Electrodes. *Sensors* **2022**, *22*, 8412. [CrossRef] [PubMed]
18. Kim, S.; Hwang, I.; Kim, D.-Y.; Kim, Y.-M.; Kang, M.; Yu, J. Weld-Quality Prediction Algorithm Based on Multiple Models Using Process Signals in Resistance Spot Welding. *Metals* **2021**, *11*, 1459. [CrossRef]
19. Zhao, D.; Vdonin, N.; Bezgans, Y.; Radionova, L.; Glebov, L. Correlating Electrode Degradation with Weldability of Galvanized BH 220 Steel during the Electrode Failure Process of Resistance Spot Welding. *Crystals* **2022**, *13*, 39. [CrossRef]
20. Zhao, D.; Vdonin, N.; Slobodyan, M.; Butsykin, S.; Kiselev, A.; Gordynets, A. Assessing Electrode Characteristics in Continuous Resistance Spot Welding of BH 340 Steel Based on Dynamic Resistance. *J. Manuf. Mater. Process.* **2023**, *7*, 218. [CrossRef]
21. Zhao, D.; Vdonin, N.; Slobodyan, M.; Butsykin, S.; Kiselev, A.; Gordynets, A.; Wang, Y. Dynamic resistance signal-based wear monitoring of resistance spot welding electrodes. *Int. J. Adv. Manuf. Technol.* **2024**, *133*, 3267–3281. [CrossRef]
22. Bachchhav, B.D.; Chaitanya, S.V.; Salunkhe, S.; Chandrakumar, P.; Pagáč, M.; Nasr, E.A. Wear Performance of Cu–Cd, Cu–Be and Cu–Cr–Zr Spot Welding Electrode Materials. *Lubricants* **2023**, *11*, 291. [CrossRef]
23. Zhou, K.; Li, H. A Comparative Study of Single-Phase AC and Medium Frequency DC Resistance Spot Welding Using Finite Element Modeling. *IEEE Access* **2020**, *8*, 107260–107271. [CrossRef]
24. Zhou, K.; Yao, P. Review of Application of the Electrical Structure in Resistance Spot Welding. *IEEE Access* **2017**, *5*, 25741–25749. [CrossRef]
25. Ko, W.-H.; Gu, J.-C.; Lee, W.-J. Energy efficiency improvement of a single-phase ac spot welding machine by using an advanced thyristor switched detuning capacitor bank. *IEEE Trans. Ind. Appl.* **2018**, *54*, 1958–1965. [CrossRef]
26. Wagner, M.; Bernet, S.; Kolb, S. High frequency transformer with synchronous rectifier for resistance spot welding. In Proceedings of the 2013 Africon, Pointe-Aux-Piments, Mauritius, 9–12 September 2013. Available online: <https://ieeexplore.ieee.org/stampPDF/getPDF.jsp?tp=&arnumber=6757716&ref=> (accessed on 10 July 2024). [CrossRef]
27. Wagner, M.; Kolb, S. Efficiency improvements for high frequency resistance spot welding. In Proceedings of the 2013 15th European Conference on Power Electronics and Applications (EPE), Lille, France, 2–6 September 2013. [CrossRef]
28. Stepien, M.; Grzesik, B.; Mikno, Z. A Numerical Determination of Power Distribution in the Resistance Welding Machine Output Circuit. In Proceedings of the 2018 IEEE 18th International Power Electronics and Motion Control Conference (PEMC), Budapest, Hungary, 26–30 August 2018. [CrossRef]
29. Stepien, M.; Mikno, Z.; Grzesik, B. Experimental Determination of Efficiency and Power Losses in Resistance Welding Machines. In Proceedings of the 2019 Electric Power Quality and Supply Reliability Conference (PQ) & 2019 Symposium on Electrical Engineering and Mechatronics (SEEM), Kardla, Estonia, 12–15 June 2019. [CrossRef]
30. Brezovnik, R.; Cernelic, J.; Petrun, M.; Dolinar, D.; Ritonja, J. Impact of the Switching Frequency on the Welding Current of a Spot-Welding System. *IEEE Trans. Ind. Electron.* **2017**, *64*, 9291–9301. [CrossRef]
31. Wang, X.; Zhou, K. Electrical Parameter Identification of Medium-Frequency DC Resistance Spot Welding System Using Intelligent Algorithm. *IEEE/ASME Trans. Mechatron.* **2021**, *26*, 1791–1802. [CrossRef]
32. Petrun, M.; Dezelak, K.; Dolinar, D.; Stumberger, G. Determining the Parameters of a Resistance Spot Welding Transformer Using Differential Evolution. *IEEE Trans. Magn.* **2014**, *50*, 1–4. [CrossRef]

Disclaimer/Publisher’s Note: The statements, opinions and data contained in all publications are solely those of the individual author(s) and contributor(s) and not of MDPI and/or the editor(s). MDPI and/or the editor(s) disclaim responsibility for any injury to people or property resulting from any ideas, methods, instructions or products referred to in the content.

Article

Fast Analysis and Optimization of a Magnetic Gear Based on Subdomain Modeling

Manh-Dung Nguyen ¹, Woo-Sung Jung ¹, Duy-Tinh Hoang ¹, Yong-Joo Kim ², Kyung-Hun Shin ^{3,*} and Jang-Young Choi ^{1,*}

¹ Department of Electrical Engineering, Chungnam National University, Daejeon 34134, Republic of Korea; nguyendung@o.cnu.ac.kr (M.-D.N.); woosung0712@o.cnu.ac.kr (W.-S.J.); hoangduytinh@o.cnu.ac.kr (D.-T.H.)

² Department of Biosystem Machinery Engineering, Chungnam National University, Daejeon 34134, Republic of Korea; babina@cnu.ac.kr

³ Department of Electrical Engineering, Changwon National University, Changwon 51140, Republic of Korea

* Correspondence: kshin@changwon.ac.kr (K.-H.S.); choi_jy@cnu.ac.kr (J.-Y.C.)

Abstract: This study presents a two-dimensional analytical method for fast optimization, taking into consideration the influence of the eddy current in a magnet and iron loss within a coaxial magnetic gear. Subdomain modeling was utilized to obtain vector potentials in the air-gap, magnet, and modulation regions by solving Maxwell's equations. After that, the magnet, rotor, and modulation losses were predicted and then compared using a finite element method simulation within three topologies with gear ratios ranging from five to six. The authors improved the machine performance, specifically the torque density, by employing a multi-objective function with particle swarm optimization. The flux density obtained using subdomain modeling in just 0.5 s benefits the optimization process, resulting in a torque-density optimal model after around 3 h. A 3/19/16 prototype targeting a low-speed, high-torque, permanent generator application was fabricated to verify the analytical and simulation results.

Keywords: analytical modeling; design optimization; electromagnetic fields; finite element analysis; iron loss; magnet loss; magnetic gear; mathematical modeling; subdomain modeling

MSC: 35-04

1. Introduction

In contrast to traditional mechanical gears, magnetic gears (MGs) transmit power between high-torque, low-speed rotations and low-torque, high-speed rotations through the interaction of magnetic fields rather than physical contact between interlocking teeth. The potential benefits of magnetic gears include inherent overload protection, decreased maintenance requirements, enhanced reliability, and physical isolation between shafts. Consequently, magnetic gears can be promising candidates for use in gearless or direct-drive magnetically geared machines (MGMs) due to their advantageous power density. The concept of the coaxial magnetic gear was initially introduced in 1968 [1], with its operational principles and potential further explained in previous work [2,3].

Over the last twenty years, many studies have been conducted to investigate various power, topology, and application ranges. A comprehensive overview of the evolution and numerous approaches to MGs has also been published [4–6]. Prototypes of magnetic gears have been investigated for many other potential uses, such as aircraft propulsion (NASA) [7,8], wind [9–12], wave [13–15], marine [16], traction [17–21], and space [22–24] applications. The torque density of MGs was reviewed and compared in a previous study [25]. Three typical examples published in [10,26] and [27] achieved torque densities of 110 kNm/m³, 141 kNm/m³, and 239 kNm/m³, respectively. In addition to coaxial radial flux MGs, some

papers have also paid attention to other structures: the work in [28–31] investigated axial flux counterparts; however, the performance of the axial analog was much lower than the conventionally radial counterparts [31]. Consequently, linear topologies, which are the best candidates for wave generators, were introduced [15,32–35]. Prior work has presented [36,37] and minimized [2,38,39] cogging torque by strategically selecting the number of pole pairs, unequal-space-type pole pieces, and skewing.

When analyzing electrical machines in general or MGs in particular, the air-gap flux density is always the first and most essential quantity that designers concern themselves with. The aforementioned studies mainly employed FEM simulation, resulting in significant computational time or magnetic equivalent circuits, which do not predict accurately. The analytical method, on the other hand, offers faster running times and results that agree well with FEM simulations, making it a promising solution for MG pre-design and optimization. Two analytical methods are mainly studied. The first method (subdomain modeling) is based on directly solving Maxwell's equations and the boundary and interface conditions by using the Fourier series expansion method. Researchers have applied the subdomain method to various cases, such as radial and axial magnetic gears, eccentricity effects in magnetic gears, and magnetically geared machines, as demonstrated in [40–43]. The second method (harmonic modeling), which solves permeability modeling using the complex Fourier series and Cauchy product, allows the consideration of nonlinear characteristics in the core [44,45]. Based on the analytical results, the authors of [43,46] optimized the output power using particle swarm optimization (PSO) and genetic algorithms (GAs). Dealing with mechanical analyses, the authors of [47] utilized 3D FEM, which required several hours to obtain results; the authors of [48] employed the subdomain method to predict stress and deformation in the modulation in seconds; and the authors of [49] experimentally verified a laminated structure in modulation after simulating a relevantly simplified model.

This paper extensively examines a coaxial MG, employing both subdomain and harmonic reduction methods to predict the air-gap flux density and enhance the computational efficiency. Following this approach, the core-loss and eddy-current effects were analyzed across different configurations, and the machine underwent optimization to boost torque density. Ultimately, a 3/16/19 prototype was manufactured, and the torque capacity results obtained from the FEM simulation and the proposed method were verified via the test bench.

2. Principle of Magnetic Gear

The magnetic gear shown in Figure 1a is composed of three parts: an inner rotor with Z_{pi} pole pairs of the permanent magnet; an outer rotor with Z_{po} pole pairs of the permanent magnet; and modulation with P_m poles. The transmission of flux between the inner rotor and the outer rotor and vice versa requires a minimum of three pole numbers as follows [2]:

$$Z_{pi} + Z_{po} = P_m \quad (1)$$

If the modulation is fixed and machine losses are ignored, the gear ratio of the inner and outer rotors is given by [3]

$$G = \frac{\omega_i}{\omega_o} = \frac{T_o}{T_i} = \frac{Z_{po}}{Z_{pi}} \quad (2)$$

where T_o and T_i are the electromagnetic torque of the external and internal rotors, respectively.

To reduce the cogging torque, selecting a magnet pole number that does not result in an integer gear ratio has been recommended [2], which is helpful when selecting a pole-pair combination. For instance, for a gear ratio requirement of six, three pole-pair combinations ($(Z_{pi}/Z_{po}/P_m) = \{(2/11/13); (3/16/19); (3/17/20)\}$) should be selected. In the current study, the authors also verified these combinations related to loss calculations, as discussed in Section 4.

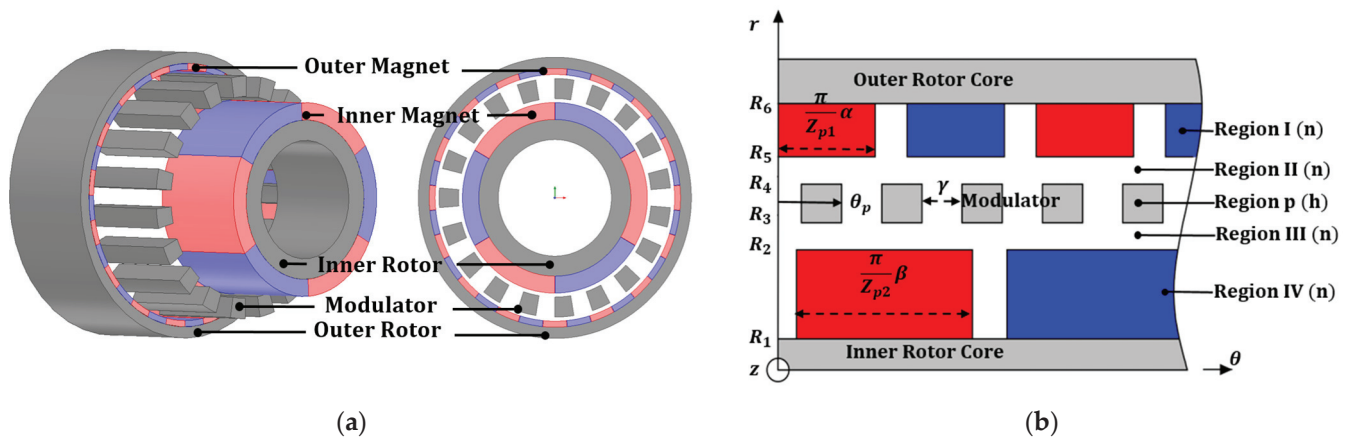


Figure 1. (a) Magnetic gear configuration and (b) a simplified model.

3. Subdomain Modeling

Figure 1b shows the MG and simplified analytical models employed in the subdomain method. Before obtaining the solutions, the following assumptions were made:

- The end effects are neglected;
- The problem is 2D in cylindrical coordinates;
- The magnetic vector potential A , current density J , magnetization vector M , and magnetic flux density vector B have the following non-zero components:

$$A = [0, 0, A_z]; J = [0, 0, J_z]; M = [M_r, M_t, 0]; B = [B_r, B_t, 0];$$

- The core materials have infinite permeability;
- The shaft is a non-magnetic material.

3.1. Governing Partial Differential Equations (PDEs)

By conducting a 2D analysis in cylindrical coordinates, the partial differential equations (PDEs) for the five regions are expressed as follows:

$$\frac{\partial^2 A_z^{I,IV}}{\partial r^2} + \frac{\partial A_z^{I,IV}}{r \partial r} + \frac{\partial^2 A_z^{I,IV}}{r^2 \partial \theta^2} = \frac{\mu_0}{r} \left(M_t^I + \frac{\partial M_r^{I,IV}}{\partial \theta} \right) \quad (3)$$

$$\frac{\partial^2 A_z^{II,III}}{\partial r^2} + \frac{\partial A_z^{II,III}}{r \partial r} + \frac{\partial^2 A_z^{II,III}}{r^2 \partial \theta^2} = 0 \quad (4)$$

$$\frac{\partial^2 A_z^p}{\partial r^2} + \frac{\partial A_z^p}{r \partial r} + \frac{\partial^2 A_z^p}{r^2 \partial \theta^2} = 0 \quad (5)$$

where M_r and M_t are the radial and tangential magnetizations of the parallel magnet, respectively, whose description can be found in [43,48]. The general PDE solution is the sum of the homogeneous and particular solutions. Owing to the magnetic excitation in the magnet regions, the solutions contain both homogeneous and particular solutions, whereas in the air-gap regions, homogeneous solutions alone are sufficient. The assumption of infinite permeability in the core leads to tangential-direction boundary conditions in the modulation region, $\frac{\partial A_z^p}{\partial \theta} \Big|_{\theta=\theta_p} = \frac{\partial A_z^p}{\partial \theta} \Big|_{\theta=\theta_p+\alpha}$. Therefore, the vector potential of each region can be expressed as

$$A_z^{I,IV} = \sum_{n=1,2}^{\infty} \left(r^n A_n^{I,IV} + r^{-n} B_n^{I,IV} + P_n^s \right) \sin(n\theta) + \left(r^n C_n^{I,IV} + r^{-n} D_n^{I,IV} + P_n^c \right) \cos(n\theta) \quad (6)$$

$$A_z^{II,III} = \sum_{n=1,2}^{\infty} \left(r^n A_n^{II,III} + r^{-n} B_n^{II,III} \right) \sin(n\theta) + \left(r^n C_n^{II,III} + r^{-n} D_n^{II,III} \right) \cos(n\theta) \quad (7)$$

$$A_z^p = A_0^p + \ln(r) B_0^p + \sum_{h=1,2}^{\infty} \left(r^{h\frac{\pi}{\alpha}} C_h^p + r^{-h\frac{\pi}{\alpha}} D_h^p \right) \cos\left(h\frac{\pi}{\alpha}(\theta - \theta_p)\right) \quad (8)$$

where P_n^s and P_n^c were presented in [48].

The continuity of the vector potential radial components leads to the following boundary conditions:

$$r = R_6 \rightarrow \frac{\partial A_z^I}{\mu_r \partial r} + \mu_0 M_t^I = 0 \quad (9)$$

$$r = R_5 \rightarrow \begin{cases} \frac{\partial A_z^I}{\mu_r \partial r} + \mu_0 M_t^I = \frac{\partial A_z^{II}}{\partial r} \\ A_z^{II} = A_z^I \end{cases} \quad (10)$$

$$r = R_4 \rightarrow \begin{cases} \frac{\partial A_z^{II}}{\partial r} = \sum_{p=1,2}^{P_m} \frac{\partial A_z^p}{\partial r} \\ A_z^p = A_z^{II} \end{cases} \quad (11)$$

$$r = R_3 \rightarrow \begin{cases} A_z^p = A_z^{III} \\ \frac{\partial A_z^{III}}{\partial r} = \sum_{p=1,2}^{P_m} \frac{\partial A_z^p}{\partial r} \end{cases} \quad (12)$$

$$r = R_2 \rightarrow \begin{cases} A_z^{III} = A_z^{IV} \\ \frac{\partial A_z^{IV}}{\mu_r \partial r} + \mu_0 M_t^{IV} = \frac{\partial A_z^{III}}{\partial r} \end{cases} \quad (13)$$

$$r = R_1 \rightarrow \frac{\partial A_z^{IV}}{\mu_r \partial r} + \mu_0 M_t^{IV} = 0 \quad (14)$$

3.2. Flux Density and Improving Computational Time

The flux density at the air gap and magnet are deduced from

$$B_r^{I,IV} = \frac{\partial A_z^{I,IV}}{r \partial \theta}; B_t^{I,IV} = -\frac{\partial A_z^{I,IV}}{\partial r} \quad (15)$$

In total, there are 20 coefficients in (6)–(8). If the harmonic number is $N = 150$ and $K = 3$, the matrix size is $16N + 4P_m K \times 16N + 4P_m K$ (2628×2628). Conversely, a small matrix size results in an inaccurate solution. However, the larger the size, the greater the computational time. In this study, the harmonic number N was first reduced; then, the proposed approach was employed, as discussed in the following sections.

In [50,51], the harmonic content of the machine was categorized into two groups: the source term, including the magnets, and the spatial aspects, which encompass the machine's geometry and winding distribution. Understanding the machine structure can help to predict the harmonics that contribute to the output parameters. Therefore, non-useful harmonics can be detected.

Subsequently, a 3/16/19 specification, whose parameters are listed in Table 1, is computed. As shown in Figure 2, there is good agreement between the subdomain method and FEM simulation results in terms of flux density. Additionally, the radial and tangential flux densities were analyzed via the fast Fourier transform (FFT) to evaluate the contribution of the harmonic order. Notably, the FFT analysis results for the flux densities at the air gap and magnet show that not all harmonics contribute to the total flux density; however, they consume more computational time. For the flux density derivation, if only dominant harmonics having an amplitude of over 2% of the maximum amplitude remain, the computational time is reduced from 1.6 to 0.5 s without effecting the accuracy. This time reduction benefits the optimization thereafter.

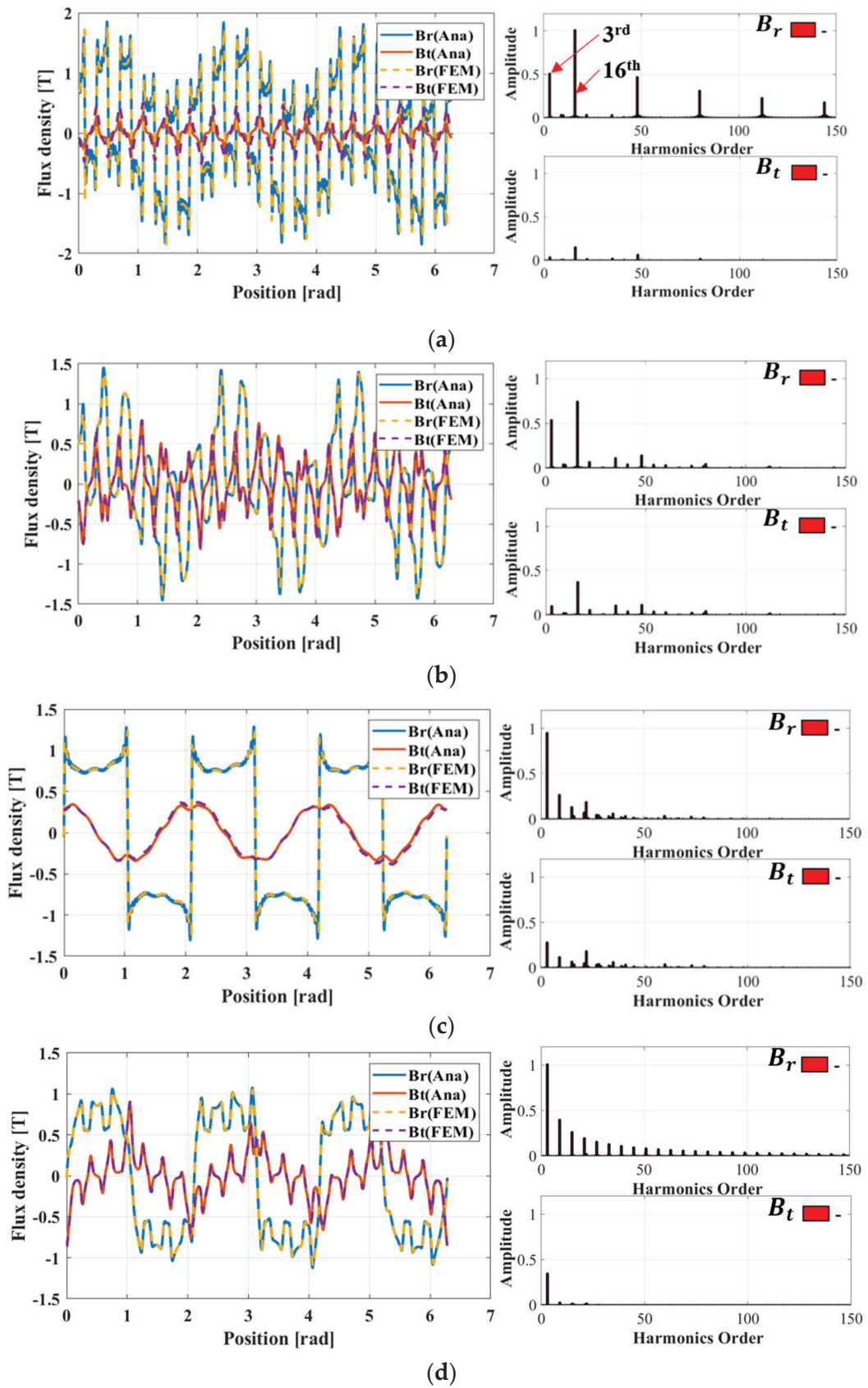


Figure 2. Radial, tangential flux density, and FFT analysis at (a) the external magnet, (b) the outer air gap, (c) the inner air gap, and (d) the internal magnet.

Table 1. Specification parameters.

Quantity	Symbol	Unit	Value
Outer rotor radius	R_7	mm	39.0
Outer external magnet radius	R_6	mm	32.2
Inner external magnet radius	R_5	mm	30.7
Outer modulation radius	R_4	mm	29.7
Inner modulation radius	R_3	mm	24.7
Outer internal magnet radius	R_2	mm	23.7
Inner internal magnet radius	R_1	mm	19.5
Inner rotor radius	R_0	mm	10.0
Stack length	L_{stk}	mm	77.0
Remanent of magnets	B_0	T	1.25
Magnet relative permeability	μ_r	-	1.03
Vacuum permeability	μ_0	$\text{kg}\cdot\text{m}\cdot\text{s}^{-2}\cdot\text{A}^{-2}$	4×10^{-7}
Outer magnet pole pair	Z_{po}	-	11/16/17
Inner magnet pole pair	Z_{pi}	-	2/3/3
Modulation pole	P_m	-	13/19/20
Outer magnet pitch ratio	α	-	1.0
Inner magnet pitch ratio	β	-	1.0
Modulation pitch	γ	$2\pi/P_m$ rad	0.5

4. Loss Definition

The loss in MGs is mainly composed of three components: modulation loss, rotor yoke loss, and eddy-current loss in the magnet. During operation, the modulation is stationary; therefore, its flux flow behavior is identical to that of the stator teeth of synchronous machines. The rotor yoke loss in conventional machines is often neglected owing to non-frequency-generating synchronous rotation. Conversely, the fluxes flowing through the rotors in the MG are coupled to each other. This interconnection causes more than one frequency in each rotor yoke, thereby generating a significant loss. This can be seen clearly in the rotor yoke flux density shown in Figure 3, in which the flux of the three-pole-pair inner magnet flows through the modulation, and then interacts with the outer magnet and results in third-order harmonic occurrence. The magnets exhibited a similar phenomenon, which significantly influenced the eddy-current effect. The detailed implementation is discussed in the following sections.

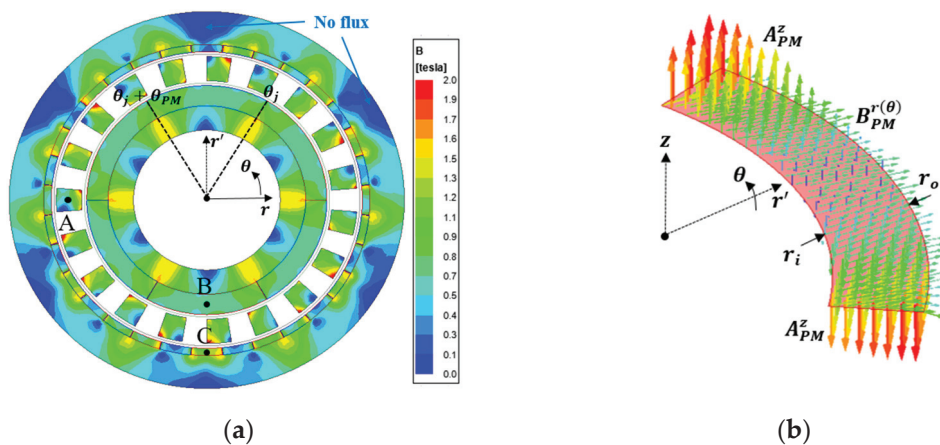


Figure 3. (a) Flux density distribution of an MG and (b) an illustration of one magnet segment in the magnet loss calculation.

4.1. Modulation Loss

The core loss can generally be estimated as the sum of the hysteresis, eddy-current, and excess losses [52]. Notably, the flux density variation in the machine is not purely

sinusoidal. Therefore, the harmonic effects should be reflected to predict the eddy-current and excess losses, as follows:

$$P_{core} = P_h + P_c + P_e = V_{core} \left(C_{dc} k_h f B_m^2 + \sum_{v=1}^{odd} k_c (fv)^2 B_{mv}^2 + k_e (fv)^{\frac{3}{2}} B_{mv}^{\frac{3}{2}} \right) \quad (16)$$

where V_{core} is the volume. The coefficients k_h , k_c , and k_e are the hysteresis, eddy current, and excess factors, respectively, which can be derived using the curve-fitting technique and loss data provided by the manufacturer [53,54]. In this study, the coefficients employed in the FEM and calculations were defined as $k_h = 386$, $k_c = 0.061$, and $k_e = 15.8$. f is the electrical frequency of modulation flux, which is calculated the same way as that of a synchronous machine. B_m is the peak flux density. v and B_{mv} are the harmonic order and the corresponding flux density, respectively, obtained via FFT analysis with respect to time. Finally, C_{dc} represents the bias effect of the DC-component flux density and is defined as $C_{dc} = 1 + 0.65 B_{dc}^2$. In this study, the modulation characterized the AC magnetic field; therefore, $B_{dc} = 0$. Additionally, alternating and rotating fields based on the time harmonic loci were introduced [45,46,53–56]. However, this effect was not considered in this study.

Because of the infinite permeability assumption at the start, the subdomain method does not allow direct flux density prediction at modulation. A secondary approach using the flux linkage results for two adjacent slots was employed to compute the maximum value. The flux linkage and density at point A in Figure 3a can be expressed as follows:

$$\Phi_p = \frac{L_{stk}}{\frac{R_4^2 - R_3^2}{2} \gamma} \iint_{R_3; \theta_p}^{R_4; \theta_p + \gamma} A_r^p(\theta, z) r dr d\theta \quad (17)$$

$$B_p^m = \frac{\Phi_p + \Phi_{p+1}}{2} \frac{1}{L_{stk} \frac{R_4 + R_3}{2} \gamma} \quad (18)$$

A new value is obtained for each new rotor position. After one electrical period, an array containing the flux density values is achieved. In (16), the maximum value in the array can be used as B_m , whereas all array elements are analyzed by FFT to deduce the harmonics and their amplitudes, which are denoted as v and B_{mv} , respectively.

4.2. Rotor Yoke Loss

The rotor yoke parts are assumed to have infinite permeability. Therefore, flux density, in particular core loss, is predicted through an equivalent transformation. First, the flux densities at radii R_1 and R_6 are defined by the vector potentials of regions I and IV, as shown in Figure 1b.

$$B_r^{I(IV)} = \frac{\partial A_z^{I(IV)}}{r \partial \theta} \bigg|_{r=R_6}^{r=R_1} ; B_t^{I(IV)} = -\frac{\partial A_z^{I(IV)}}{\partial r} \bigg|_{r=R_6}^{r=R_1} \quad (19)$$

Similar to the flux densities of the external and internal magnets in Figure 2a,d, the flux densities are composed of many harmonics. These flux densities, which are considered to be the two largest components, can be estimated as the sum of the Z_{po}^{th} - and Z_{pi}^{th} -order harmonics, as shown in Figure 3. Owing to the synchronous speed of each rotor, one harmonic does not generate a frequency; consequently, the corresponding order harmonic is eliminated. For example, in an external rotor with pole-pair number Z_{po} , the Z_{po}^{th} -order harmonic is neglected in the loss calculation. In an internal rotor with pole-pair number Z_{pi} , the Z_{pi}^{th} -order harmonic is removed. The frequencies of both rotors match the frequencies of the magnets, which are expressed as

$$f_{I(IV)} = f \frac{P_m}{Z_{po(i)}} \quad (20)$$

The maximum rotor yoke flux density can be obtained by

$$B_{r(t)_{-ry}}^I = B_{r(t)}^{I(Z_{pi}^{th})} \frac{\pi R_7}{Z_{pi}} \frac{2}{\pi} \frac{1}{2} \frac{1}{R_7 - R_0}; B_{r(t)_{-ry}}^{IV} = B_{r(t)}^{IV(Z_{po}^{th})} \frac{\pi R_1}{Z_{po}} \frac{2}{\pi} \frac{1}{2} \frac{1}{R_1 - R_0} \quad (21)$$

The first equation in (21) can be explained in more detail as follows: $B_{r(t)}^{I(Z_{pi}^{th})}$ is the radial (or tangential) flux density in the external rotor yoke, which remains in the Z_{pi}^{th} order after the FFT analysis. Supposing that all fluxes traverse through the rotor yoke, $\frac{\pi R_7}{Z_{po}} \frac{2}{\pi}$ is the average flux linkage calculation. This flux flows equally to the two sides of the yoke and is represented by $\frac{1}{2} \frac{1}{R_8 - R_7}$.

The flux densities in (16) are replaced by the radial and tangential flux densities in (21), and the core loss is expressed as

$$P_{core} = V_{core} \left(C_{dc} k_h f_{I(IV)} \left(\left(B_{r_{ry}}^{I(IV)} \right)^2 + \left(B_{t_{ry}}^{I(IV)} \right)^2 \right) + k_c f_{I(IV)}^2 \left(\left(B_{r_{ry}}^{I(IV)} \right)^2 + \left(B_{t_{ry}}^{I(IV)} \right)^2 \right) + k_e f_{I(IV)}^{\frac{3}{2}} \left(\left(B_{r_{ry}}^{I(IV)} \right)^{\frac{3}{2}} + \left(B_{t_{ry}}^{I(IV)} \right)^{\frac{3}{2}} \right) \right) \quad (22)$$

The coefficient C_{dc} is defined in a manner similar to the modulation loss calculation. However, in the rotor yoke, the flux density consists of both AC and DC terms; therefore, B_{dc} should be defined.

4.3. Magnet Loss

As mentioned previously, the coupling effect between the magnet numbers of the two rotors generates a frequency in the magnet. In this machine, the magnet layers are modeled in regions I and IV; therefore, the flux density and frequency can be calculated directly. First, the frequencies of the inner and outer magnets are given by

$$f_{mi(o)} = f \frac{P_m}{Z_{pi(o)}} \quad (23)$$

When the rotors rotate, the flux density at the middle points of the magnet (points B and C in Figure 3a) is also analyzed using FFT to deduce the harmonic order and their amplitudes, which were expressed as v and B_{mv}^{PM} , respectively. Notably, the components related to the magnetization in (6) do not contribute to the eddy-current loss; therefore, they can be removed from the flux density calculation in the magnet loss section.

$$A_{PM}^{I,IV} = \sum_{n=1,2}^{\infty} \left(r^n A_n^{I,IV} + r^{-n} B_n^{I,IV} \right) \sin(n\theta) + \left(r^n C_n^{I,IV} + r^{-n} D_n^{I,IV} \right) \cos(n\theta) \quad (24)$$

Then, calculation of the eddy current in the magnets can be approached as shown in Figure 3.

$$J_{PM} = -\sigma_{PM} \frac{\partial A_{PM}}{\partial t} + C(t) \quad (25)$$

where σ_{PM} is the conductivity of the magnet and $C(t)$ is a term ensuring the total current zero within every single magnet. In the coordinate $Or\theta$, $C(t)$ can be expressed by

$$C(t) = \frac{2}{\theta_{PM}} \frac{1}{r_o^2 - r_i^2} \int_{r_i}^{r_o} \int_{\theta_j}^{\theta_j + \theta_{PM}} \sigma_{PM} \frac{\partial A_{PM}}{\partial t} r dr d\theta \quad (26)$$

Figure 3b shows the flux density vector and vector potential in a magnet piece. It can be seen that the vector potential is symmetrical along the z -axis, which describes the zero-current characteristic in the magnet piece. By re-choosing a new coordinate $Or'\theta$, the integral equation of $C(t)$ can be rewritten as follows:

$$C(t) = \frac{2}{\theta_{PM}} \frac{1}{r_o^2 - r_i^2} \int_{r_i}^{r_o} \int_{-\frac{\theta_{PM}}{2}}^{\frac{\theta_{PM}}{2}} \sigma_{PM} \frac{\partial A_{PM}}{\partial t} r dr d\theta \quad (27)$$

In this new coordinate, $A_{PM}(\theta) = -A_{PM}(-\theta)$; $C(t)$, therefore, equals zero. Consequently, the eddy-current loss in the magnet segment is expressed simply as

$$P_{eddy} = \frac{L_{stk}}{\sigma_{PM}} \int_{r_i}^{r_o} \int_{-\frac{\theta_{PM}}{2}}^{\frac{\theta_{PM}}{2}} \left(\sigma_{PM} \frac{\partial A_{PM}}{\partial t} \right)^2 r dr d\theta \quad (28)$$

Assuming that the tangential flux density does not contribute to the eddy-current effect, the vector potential in (28) can be approximated as $\partial A_{PM} = r\theta \partial \sum v B_{mv}^{PM}$. Finally, the eddy-current loss is given by

$$P_{eddy} = L_{stk} \sigma_{PM} \int_{r_i}^{r_o} \int_{-\frac{\theta_{PM}}{2}}^{\frac{\theta_{PM}}{2}} \left(\frac{\partial}{\partial t} \sum v B_{mv}^{PM} \right)^2 r^3 dr d\theta = L_{stk} \sigma_{PM} \frac{r_o^4 - r_i^4}{4} \frac{\theta_{PM}^3}{12} \sum \frac{\left(2\pi f_{mo(i)} v B_{mv}^{PM} \right)^2}{2} \quad (29)$$

4.4. Loss Verification via FEM

Simulations were performed to validate the MG core loss. Three topologies characterizing the low cogging torque [2], whose parameters are listed in Table 1, were verified for various cases, as shown in Figure 4. The losses as a function of the rotor speed are shown in Figure 5. In general, the analytical results show good agreement with the FEM results, even though in high-speed operation resulting in a high electrical frequency the loss calculation error is slightly larger. The possible reasons are that (i) the estimated coefficients in the curve fitting step at high frequencies have a larger error than the low-frequency ones, and (ii) the loss depends exponentially on the frequency; thus, higher frequencies lead to a higher error possibility. Consequently, the influence of machine parameters on the loss can be summarized as follows:

- Compared to the full-pitch magnet in Figure 5a,c,e, decreasing the magnet pitch in the rotors in Figure 5b,d,f reduces the losses. This can be attributed to the fact that a smaller magnet pitch results in a smaller flux density.
- The loss of the small pole-pair combination $[Z_{po}; Z_{pi}] = [11; 2]$ is significantly larger than that of groups $[16; 3]$ and $[17; 3]$ along all modulation frequency ranges. This is due to the contribution of the rotor yoke and magnet losses to the total loss. In (22) and (29), the losses depend on the rotor frequency, which is governed by the electrical frequency and pole-pair numbers in (20) and (23), respectively. Accordingly, as the number of pole pairs in the rotor decreases, the rotor frequency increases. This difference does not arise from modulation loss, as it can be attributed to the similarity of the electrical and modulation frequencies in (16).

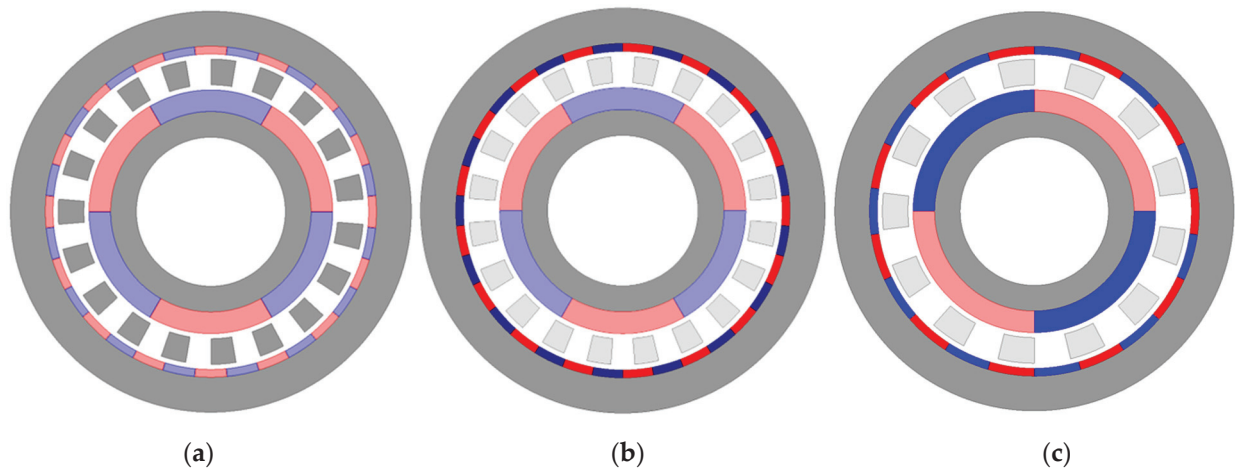


Figure 4. Topologies using in loss verification: (a) 3/19/16, (b) 3/20/17, and (c) 2/13/11.

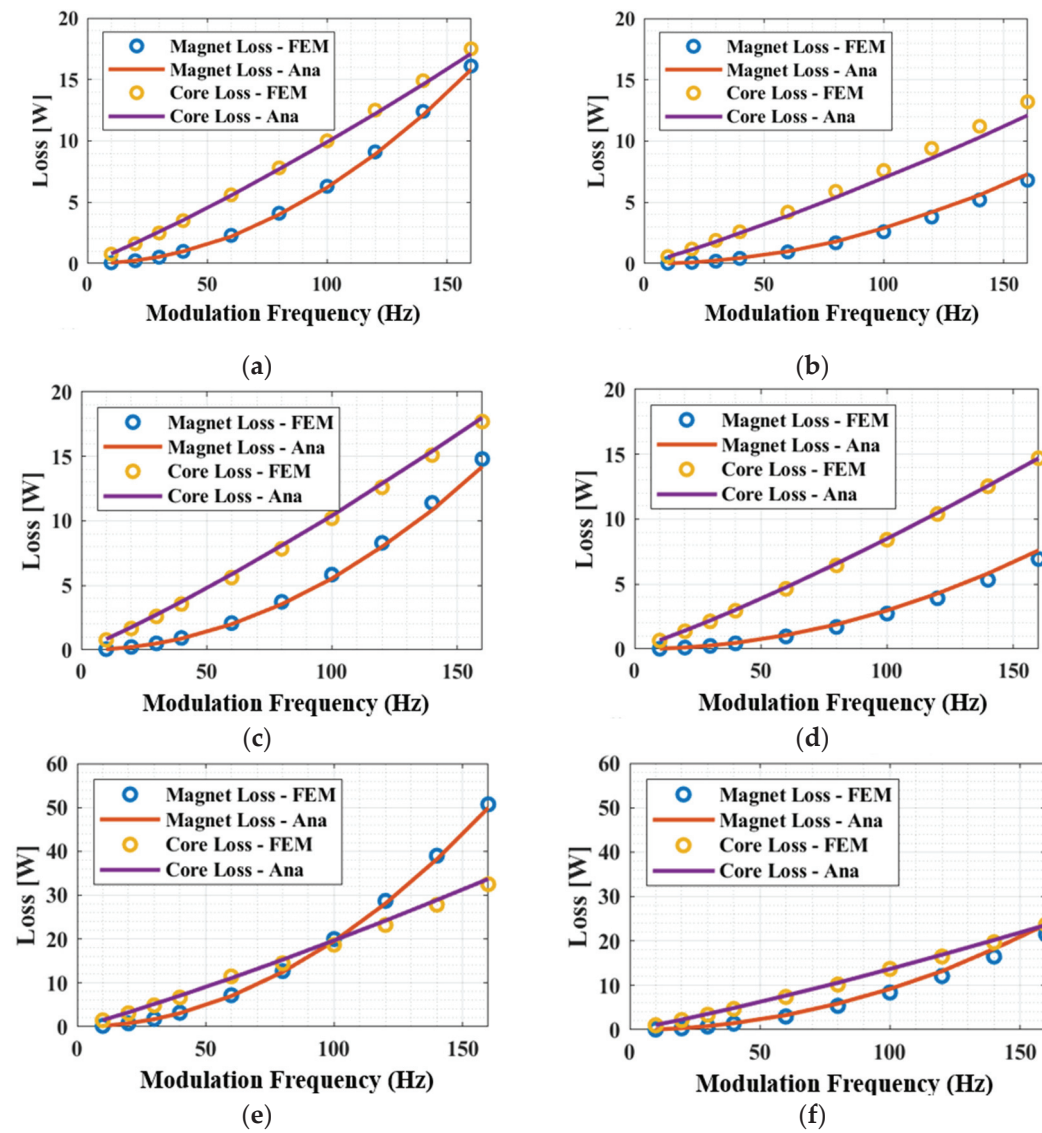


Figure 5. Loss comparison of the proposed method and FEM in the topologies having parameters $[Z_{po}; Z_{pi}; P_m; \alpha; \beta]$ as follows: (a) [16; 3; 19; 1.0; 1.0], (b) [16; 3; 19; 0.8; 0.7], (c) [17; 3; 20; 1.0; 1.0], (d) [17; 3; 20; 0.8; 0.8], (e) [11; 2; 13; 1.0; 1.0], and (f) [11; 2; 13; 0.8; 0.67].

It is worth noting that at the same primary speed, the modulation frequency of the [11; 2] pair is much lower than that of the other pairs. Consequently, a significant loss reduction can be achieved in this scenario. Therefore, the results shown in Figure 5 should not be used as a reference when selecting a particular specification. Determining the optimal choice requires a more comprehensive understanding of machine features such as cogging torque, power density, and efficiency.

5. Optimization Process

5.1. Variables, Objective Functions, and Constraints

After ensuring that the proposed mathematical model was accurate, an optimal solution of the 3/16/19 specification, whose parameters and optimal variables are listed in Tables 1 and 2, respectively, was investigated in terms of efficiency and torque density. The objective function, equality function, and inequality constraints are expressed as

$$\begin{aligned} \max_{X=[x_1, \dots, x_7]} f(X) &= \left[\frac{P_e}{\pi R_8^2 l_{stk}}; \frac{P_e}{P_e + Loss} \right] \\ \text{subject to} & \\ 55 < \text{Magnet volume} \left[\text{dm}^3 \right] &< 65 \\ R_7 - R_6 &= \frac{\pi \alpha}{Z_{po}}; R_1 - R_0 = \frac{\pi \beta}{Z_{pi}} \end{aligned} \quad (30)$$

Table 2. Value range of optimization.

Quantity	Symbol	Unit	Value
Outer magnet pitch ratio	$x_1 = \alpha$	-	0.7–1.0
Inner magnet pitch ratio	$x_2 = \beta$	-	0.7–1.0
Modulation pitch	$x_3 = \gamma$	$2\pi/P_m$ rad	0.4–0.6
Outer diameter	$x_4 = R_7$	mm	23–100
Outer magnet width	$x_5 = R_6 - R_5$	mm	0.75–3
Modulation width	$x_6 = R_4 - R_3$	mm	2.5–10.0
Inner magnet width	$x_7 = R_2 - R_1$	mm	2.0–8.0

To prevent saturation, the rotor yoke thickness is set to the corresponding magnet pitch width. In PSO, a collection of particles representing potential solutions iteratively adjust their positions based on local and global information. Each particle moves toward its own best-known position and the overall best-known position within the swarm. Through iterations, the swarm gradually converges toward an optimal solution.

5.2. Optimization Results

The optimal flowchart employed in this study is illustrated in [43]. The swarm population size in one iteration and the maximum number of iterations were set to 15 and 20, respectively. Consequently, it took approximately 3 h to obtain an optimal specification, the dimensions of which are listed in Table 3, and a Pareto curve is shown in Figure 6. The two Pareto fronts in Figure 6a are observed on the yz and xz planes in Figure 6b and 6c, respectively. The dots represent all particles generated in the program. The red dots denote the points of maximum torque density when the magnetic field volume was varied. The efficiency was calculated as shown in Figure 6d. In general, multi-objective optimization is a compromise between two quantities. As can be seen, the maximum torque density and efficiency points do not occur synchronously. An increasing efficiency can result in a reduction in torque density and vice versa. Based on these requirements, the most suitable point was selected. For instance, in Figure 6, we chose and verified a green-dot point, whose structure is compared in Figure 7. The optimal solution has a larger diameter and shorter length than the initial solution. Table 4 presents the optimization performance at an outer rotor speed of 300 rpm in terms of the torque, torque density, magnet volume, total loss, and efficiency obtained using the subdomain method and FEM. The optimal machine

generated a higher output torque of approximately 5%, whereas it saved more magnetic resources by approximately 10%. Furthermore, the efficiency remained almost constant with a difference of <1%. Notably, these results show that the analytical and simulation results are in excellent agreement.

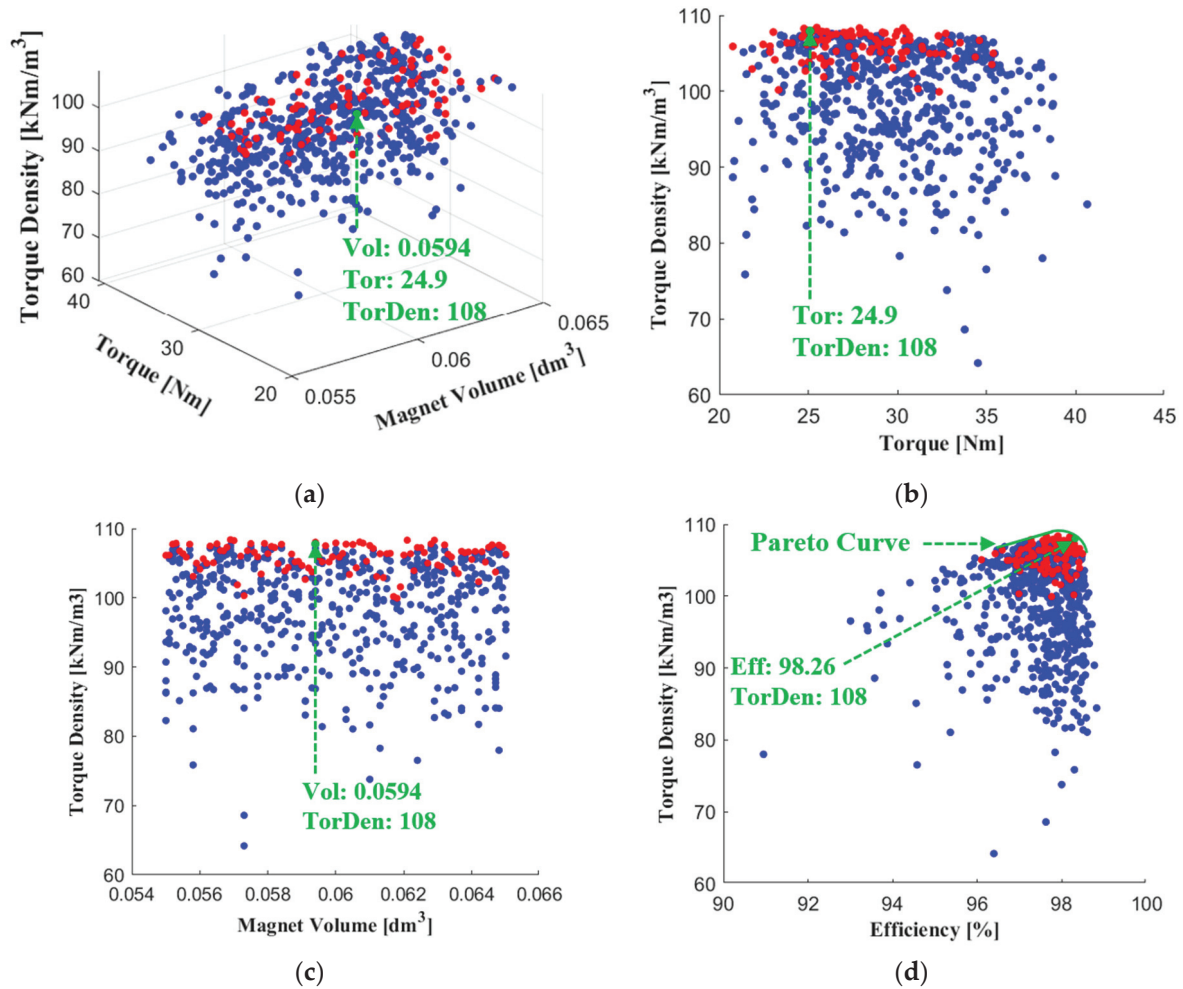


Figure 6. Optimization results of the PSO algorithm. (a) Torque density with respect to torque and magnet volume; (b,c) corresponding yz and xz planes; and (d) Pareto curve of torque density and efficiency.

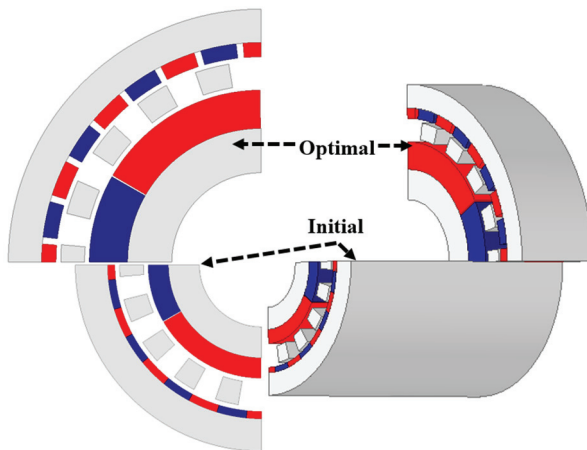


Figure 7. Structural comparison of initial and optimal machines.

Table 3. Dimension comparison between the initial and optimal models.

Quantity	Symbol	Unit	Initial	Optimal
Outer rotor radius	R_7	mm	39.0	53.0
Outer external magnet radius	R_6	mm	32.2	46.0
Inner external magnet radius	R_5	mm	30.7	43.0
Outer modulation radius	R_4	mm	29.7	42.0
Inner modulation radius	R_3	mm	24.7	37.0
Outer internal magnet radius	R_2	mm	23.7	36.0
Inner internal magnet radius	R_1	mm	19.5	28.0
Inner rotor radius	R_0	mm	10.0	18.7
Stack length	L_{stk}	mm	77.0	25.6
Outer magnet pitch ratio	α	-	1.00	0.84
Inner magnet pitch ratio	β	-	1.00	1.00
Modulation pitch	γ	$2\pi/P_m$ rad	0.50	0.53

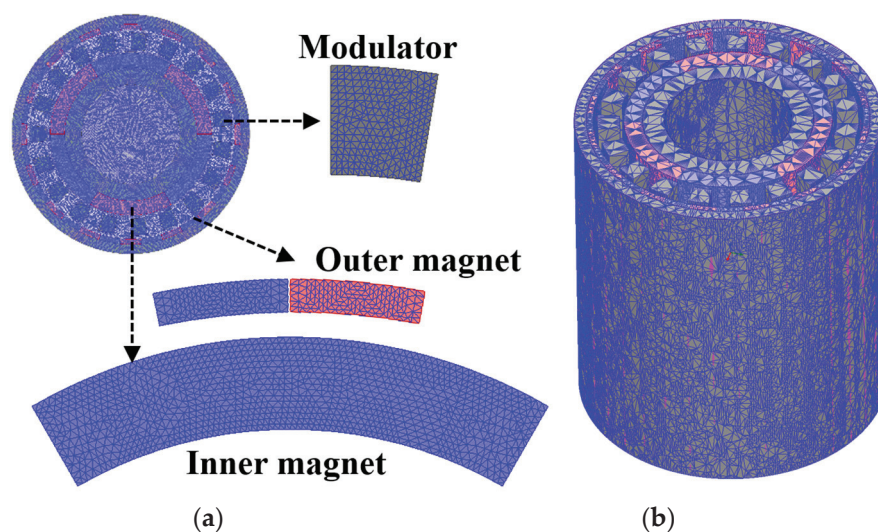
Table 4. Optimization performance.

Characteristic	Initial Design		Optimal Design	
	Subdomain	FEM	Subdomain	FEM
Torque—Nm	23.7	23.4	24.9	24.3
Torque density—kNm/m ³	64	64	108	108
Magnet volume—dm ³	66.1	66.1	54.9	59.4
Total loss—W	10.04	10.39	13.66	13.65
Efficiency—%	98.67	98.61	98.26	98.26

6. Experimental Validation

6.1. Three-Dimensional Simulation

The 3/16/19 specification is given in Table 1; however, the adjusted $R_7 = 35$ (mm) was simulated in 2D and 3D FEM, whose mesh settings are shown in Figure 8a and b, respectively. Meanwhile, the torque characteristics were calculated via subdomain modeling combined with the harmonic reduction method and then compared with the FEM results. As shown in Figure 9, there is a good agreement between the computation and simulation results. The 3D analysis gave an output torque that was approximately 7% lower than that of the subdomain method. Based on these results, the following conclusions can be drawn.

**Figure 8.** Mesh operation of the 3/16/19 specification in (a) 2D (119,068 elements) and (b) 3D (1,029,637 elements).

- The harmonic reduction approach result matches that of the original analytical approach while decreasing the running time.
- Saturation occurred because of the small rotor yoke thickness, which weakened the flux linkage. Therefore, in general, the FEM produced a slightly smaller torque.
- Three-dimensional FEM was taken into account by the endcap effect. Its torque was also reduced compared with the 2D results.
- The computational times of the 2D FEM, 3D FEM, and analytical method were 4 min, more than 60 min, and 25 s, respectively. This further highlights the subdomain modeling priority.

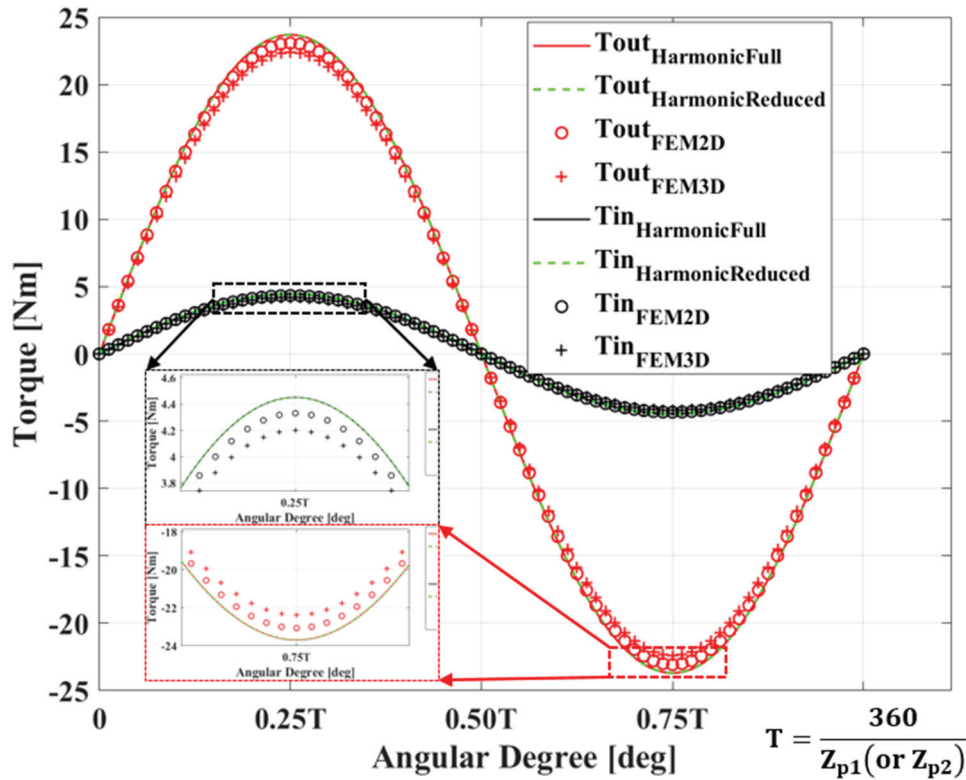


Figure 9. Torque characteristic comparison.

6.2. Comparison of Analysis and Experimental Results

In this study, a prototype was fabricated, as shown in Figure 10. The experimental process was as follows. The driving motor is the primary source of input torque in the outer rotor. Then, the MG transferred power from the outer side to the inner side. The MG output was used as the input power for the generator, which was connected to an adjustable load. Consequently, the generator and load system can be considered as the MG load. When the resistance value (generator load) or rotational speed (generator BEMF) fluctuates, the MG load also fluctuates. Owing to mechanical limitations, the outer-rotor speed range was restricted to 1000 rpm.

Figure 11a shows the outer rotor response when the inner rotor speed is varied. These results confirm the working principle of the MG. The rotor pole-pair combination was designed as 3/16 with an expected transformation ratio of $16/3 \approx 5.33$. All four points at 200, 400, 600, and 800 rpm show excellent agreement with the designed ratio.

To verify the maximum torque capacity of the MG, the load resistance was decreased, and the rotor speed was simultaneously increased to approximately 1000 rpm. This increase in speed was implemented slowly to ensure safety. The maximum torque was captured immediately as the rotor was synchronously lost. In Figure 11b, the captured maximum torque is 4.15 Nm at the 2- Ω resistance and 891-rpm speed point, which is close to the calculation (4.45 Nm). Notably, in the no-load results, the MG torque appeared to be

relatively large, indicating an unpredictable impact of mechanical factors on the system. Therefore, experiments on loss and efficiency were not considered in this study.

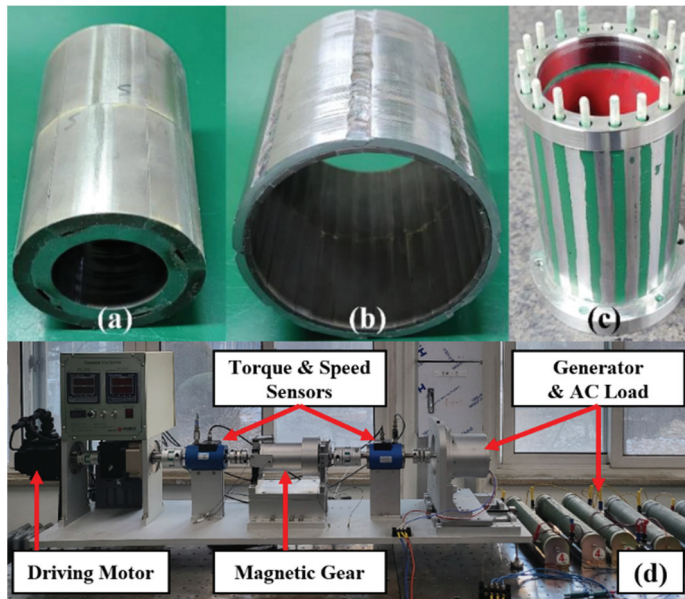


Figure 10. Test bench: (a) inner rotor, (b) outer rotor, (c) modulation, and (d) experimental system.

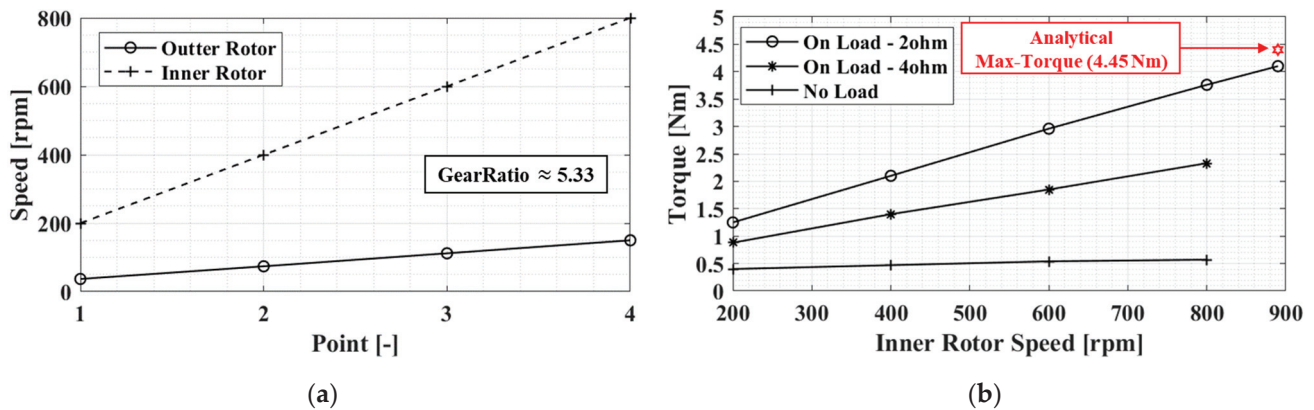


Figure 11. (a) Corresponding speed of inner and outer rotors in various load conditions and (b) evolution of inner rotor torque various speeds.

7. Conclusions

The proposed subdomain approach combined with the harmonic reduction method was efficient in obtaining the magnetic gear characteristics. Loss calculations for the magnets, modulation, and rotor yokes were introduced based on the flux density in every region. Furthermore, compared with the 2D and 3D FEM simulations, the torque and loss computational time was reduced from dozens of minutes to roughly seven seconds, while maintaining excellent accuracy. This allows for the application of PSO techniques, which saves time exponentially. Consequently, the optimal model reached between 66 and 108 kNm/m³ of the torque density and used fewer magnets than the initial model. Based on the methodology and findings of this study, the following future research avenues are suggested:

- Consider the non-linear characteristics of magnetic materials;
- Consider the endcap effects for flux leakage prediction;
- Consider the mechanical loss in the optimization and then verify this quantity experimentally;

- Consider the demagnetization risk in the magnets.

Author Contributions: Conceptualization, M.-D.N.; methodology, M.-D.N.; validation, M.-D.N., W.-S.J., and D.-T.H.; formal analysis, M.-D.N.; investigation, M.-D.N.; writing—original draft preparation, M.-D.N.; writing—review and editing, K.-H.S. and J.-Y.C.; visualization, M.-D.N.; supervision, Y.-J.K., K.-H.S., and J.-Y.C. All authors have read and agreed to the published version of the manuscript.

Funding: This work was supported by the BK21 FOUR Program by Chungnam National University Research Grant, 2022.

Data Availability Statement: Data are contained within the article.

Conflicts of Interest: The authors declare no conflicts of interest.

References

- Martin, T. Magnetic Transmission. U.S. Patent 3 378 710, 16 April 1968.
- Atallah, K.; Howe, D. A novel high-performance magnetic gear. *IEEE Trans. Magn.* **2001**, *37*, 2844–2846. [CrossRef]
- Rasmussen, P.O.; Andersen, T.O.; Jorgensen, F.T.; Nielsen, O. Development of a high-performance magnetic gear. *IEEE Trans. Ind. Appl.* **2005**, *41*, 764–770.
- Praslicka, B.; Gardner, M.C.; Johnson, M.; Toliyat, H.A. Review and Analysis of Coaxial Magnetic Gear Pole Pair Count Selection Effects. *IEEE J. Emerg. Sel. Top. Power Electron.* **2022**, *10*, 1813–1822.
- Wang, Y.; Filippini, M.; Bianchi, N.; Alotto, P. A Review on Magnetic Gears: Topologies, Computational Models, and Design Aspects. *IEEE Trans. Ind. Appl.* **2019**, *55*, 4557–4566.
- Tlali, P.M.; Wang, R.-J.; Gerber, S. Magnetic gear technologies: A review. In Proceedings of the 2014 International Conference on Electrical Machines (ICEM), Berlin, Germany, 2–5 September 2014; pp. 544–550.
- Scheidler, J.; Asnani, V.; Tallerico, T. NASA’s magnetic gearing research for electrified aircraft propulsion. In Proceedings of the 2018 AIAA/IEEE Electric Aircraft Technologies Symposium (EATS), Cincinnati, OH, USA, 12–14 July 2018; pp. 1–12.
- Scheidler, J.; Cameron, Z.; Tallerico, T. Dynamic testing of a high-specific-torque concentric magnetic gear. In Proceedings of the Annual Forum & Technology Display—The Future of Vertical Flight, Philadelphia, PA, USA, 13–16 May 2019; pp. 1–8. [CrossRef]
- Kjaer, A.B.; Korsgaard, S.; Nielsen, S.S.; Demsa, L.; Rasmussen, P.O. Design fabrication test and benchmark of a magnetically geared permanent magnet generator for wind power generation. *IEEE Trans. Energy Convers.* **2020**, *35*, 24–32.
- Li, K.; Modaresahmadi, S.; Williams, W.B.; Wright, J.D.; Som, D.; Bird, J.Z. Designing and experimentally testing a magnetic gearbox for a wind turbine demonstrator. *IEEE Trans. Ind. Appl.* **2019**, *55*, 3522–3533.
- Li, K.; Modaresahmadi, S.; Williams, W.B.; Bird, J.Z.; Wright, J.D.; Barnett, D. Electromagnetic analysis and experimental testing of a flux focusing wind turbine magnetic gearbox. *IEEE Trans. Energy Convers.* **2019**, *34*, 1512–1521. [CrossRef]
- Wang, R.-J.; Gerber, S. Magnetically geared wind generator technologies: Opportunities and challenges. *Appl. Energy* **2014**, *136*, 817–826. [CrossRef]
- Johnson, M.; Gardner, M.C.; Toliyat, H.A.; Englebreton, S.; Ouyang, W.; Tschida, C. Design construction and analysis of a large-scale inner stator radial flux magnetically geared generator for wave energy conversion. *IEEE Trans. Ind. Appl.* **2018**, *54*, 3305–3314. [CrossRef]
- Uppalapati, K.K.; Bird, J.Z.; Jia, D.; Garner, J.; Zhou, A. Performance of a magnetic gear using ferrite magnets for low speed ocean power generation. In Proceedings of the 2012 IEEE Energy Conversion Congress and Exposition (ECCE), Raleigh, NC, USA, 15–20 September 2012; pp. 3348–3355.
- Li, W.; Chau, K.T.; Jiang, J.Z. Application of Linear Magnetic Gears for Pseudo-Direct-Drive Oceanic Wave Energy Harvesting. *IEEE Trans. Magn.* **2011**, *47*, 2624–2627. [CrossRef]
- McGilton, B.; Crozier, R.; McDonald, A.; Mueller, M. Review of magnetic gear technologies and their applications in marine energy. *IET Renew. Power Gener.* **2018**, *12*, 174–181.
- Rasmussen, P.O.; Mortensen, H.H.; Matzen, T.N.; Jahns, T.M.; Toliyat, H.A. Motor integrated permanent magnet gear with a wide torque-speed range. *Proc. IEEE Energy Convers. Congr. Expo.* **2009**, 1510–1518.
- Rasmussen, P.O.; Frandsen, T.V.; Jensen, K.K.; Jessen, K. Experimental evaluation of a motor-integrated permanent-magnet gear. *IEEE Trans. Ind. Appl.* **2013**, *49*, 850–859.
- Frandsen, T.V.; Rasmussen, P.O.; Jensen, K.K. Improved motor integrated permanent magnet gear for traction applications. In Proceedings of the 2012 IEEE Energy Conversion Congress and Exposition (ECCE), Raleigh, NC, USA, 15–20 September 2012; pp. 3332–3339.
- Frandsen, T.V.; Mathe, L.; Berg, N.I.; Holm, R.K.; Matzen, T.N.; Rasmussen, P.O.; Jensen, K.K. Motor integrated permanent magnet gear in a battery electrical vehicle. *IEEE Trans. Ind. Appl.* **2015**, *51*, 1516–1525. [CrossRef]
- Chmelicek, P.; Calverley, S.D.; Dragan, R.S.; Atallah, K. Dual rotor magnetically geared power split device for hybrid electric vehicles. *IEEE Trans. Ind. Appl.* **2019**, *55*, 1484–1494. [CrossRef]

22. Esnoz-Larraya, J.; Valiente-Blanco, I.; Cristache, C.; Sanchez-Garcia-Casarrubios, J.; Rodriguez-Celis, F.; Diez-Jimenez, E.; Perez-Diaz, J.L. Optimagdrive: High-performance magnetic gears development for space applications. In Proceedings of the ESMATS, Hatfield, UK, 20–22 September 2017; pp. 1–5.
23. Dragan, R.S.; Clark, R.E.; Hussain, E.K.; Atallah, K.; Odavic, M. Magnetically geared pseudo direct drive for safety critical applications. *IEEE Trans. Ind. Appl.* **2019**, *55*, 1239–1249. [CrossRef]
24. Puchhammer, G. Magnetic gearing versus conventional gearing in actuators for aerospace applications. In Proceedings of the 42nd Aerospace Mechanism Symposium, Baltimore, MD, USA, 14–16 May 2014.
25. Painter, D.S. A Comparative Study of the Performance Capabilities of Magnetic Gears. Bachelor’s Thesis, Portland State University, Portland, OR, USA, 2016.
26. Jian, L.; Chau, K.T.; Li, W.; Li, J. A Novel Coaxial Magnetic Gear Using Bulk HTS for Industrial Applications. *IEEE Trans. Appl. Supercond.* **2010**, *20*, 981–984.
27. Uppalapati, K.K.; Bird, J.Z.; Wright, J.; Pitchard, J.; Calvin, M.; Williams, W. A magnetic gearbox with an active region torque density of 239 Nm/L. In Proceedings of the 2014 IEEE Energy Conversion Congress and Exposition (ECCE), Pittsburgh, PA, USA, 14–18 September 2014; pp. 1422–1428.
28. Kouhshahi, M.B.; Bird, J.Z.; Acharya, V.M.; Li, K.; Calvin, M.; Williams, W.; Modaresahmadi, S. An axial flux focusing magnetically geared generator for low input speed applications. *IEEE Trans. Ind. Appl.* **2020**, *56*, 138–147.
29. Johnson, M.; Gardner, M.C.; Toliyat, H.A. Design and analysis of an axial flux magnetically geared generator. *IEEE Trans. Ind. Appl.* **2017**, *53*, 97–105.
30. Zhu, D.; Yang, F.; Du, Y.; Xiao, F.; Ling, Z. An axial-field flux-modulated magnetic gear. *IEEE Trans. Appl. Supercond.* **2016**, *26*, 0604405. [CrossRef]
31. Bomela, W.; Bird, J.Z.; Acharya, V.M. The performance of a transverse flux magnetic gear. *IEEE Trans. Magn.* **2014**, *50*, 4000104.
32. RHolehouse, C.; Atallah, K.; Wang, J. A linear magnetic gear. In Proceedings of the 2012 XXth International Conference on Electrical Machines, Marseille, France, 2–5 September 2012; pp. 563–569.
33. Holehouse, R.C.; Atallah, K.; Wang, J. Design and Realization of a Linear Magnetic Gear. *IEEE Trans. Magn.* **2011**, *47*, 4171–4174.
34. Niu, S.; Ho, S.L.; Fu, W.N. Performance Analysis of a Novel Magnetic-Geared Tubular Linear Permanent Magnet Machine. *IEEE Trans. Magn.* **2011**, *47*, 3598–3601.
35. Li, W.; Chau, K.T.; Li, J. Simulation of a Tubular Linear Magnetic Gear Using HTS Bulks for Field Modulation. *IEEE Trans. Appl. Supercond.* **2011**, *21*, 1167–1170.
36. Gerber, S.; Wang, R.-J. Cogging Torque Definitions for Magnetic Gears and Magnetically Geared Electrical Machines. *IEEE Trans. Magn.* **2018**, *54*, 8103209.
37. Niguchi, N.; Hirata, K. Cogging Torque Analysis of Magnetic Gear. *IEEE Trans. Ind. Electron.* **2012**, *59*, 2189–2197.
38. Dai, B.; Nakamura, K.; Suzuki, Y.; Tachiya, Y.; Kuritani, K. Cogging Torque Reduction of Integer Gear Ratio Axial-Flux Magnetic Gear for Wind-Power Generation Application by Using Two New Types of Pole Pieces. *IEEE Trans. Magn.* **2022**, *58*, 8002205.
39. Jungmayr, G.; Loeffler, J.; Winter, B.; Jeske, F.; Amrhein, W. Magnetic Gear: Radial Force, Cogging Torque, Skewing, and Optimization. *IEEE Trans. Ind. Appl.* **2016**, *52*, 3822–3830.
40. Lubin, T.; Mezani, S.; Rezzoug, A. Analytical Computation of the Magnetic Field Distribution in a Magnetic Gear. *IEEE Trans. Magn.* **2010**, *46*, 2611–2621.
41. Lubin, T.; Mezani, S.; Rezzoug, A. Development of a 2-D Analytical Model for the Electromagnetic Computation of Axial-Field Magnetic Gears. *IEEE Trans. Magn.* **2013**, *49*, 5507–5521.
42. Jing, L.; Gong, J.; Ben, T. Analytical Method for Magnetic Field of Eccentric Magnetic Harmonic Gear. *IEEE Access.* **2020**, *8*, 34236–34245.
43. Nguyen, M.D.; Kim, S.M.; Shin, H.S.; Shin, K.H.; Phung, A.T.; Choi, J.Y. Maximizing the output power of magnetically geared generator in low-speed applications using subdomain modeling and particle swarm optimization. *AIP Adv.* **2024**, *14*, 025117.
44. Zhao, H.; Liu, C.; Song, Z.; Yu, J. A Fast Optimization Scheme of Coaxial Magnetic Gears Based on Exact Analytical Model Considering Magnetic Saturation. *IEEE Trans. Ind. Appl.* **2021**, *57*, 437–447.
45. Djelloul-Khedda, Z.; Boughrara, K.; Dubas, F.; Kechroud, A.; Tikellaline, A. Analytical Prediction of Iron-Core Losses in Flux-Modulated Permanent-Magnet Synchronous Machines. *IEEE Trans. Mag.* **2019**, *55*, 6300112.
46. Desvaux, M.; Sire, S.; Hlioui, S.; Ahmed, H.B.; Multon, B. Development of a Hybrid Analytical Model for a Fast Computation of Magnetic Losses and Optimization of Coaxial Magnetic Gears. *IEEE Trans. Energy. Convers.* **2019**, *34*, 25–35.
47. Lee, J.I.; Shin, K.H.; Bang, T.K.; Ryu, D.W.; Kim, K.H.; Hong, K.; Choi, J.Y. Design and Analysis of the Coaxial Magnetic Gear Considering the Electromagnetic Performance and Mechanical Stress. *IEEE Trans. Appl. Supercond.* **2020**, *30*, 3700105.
48. Nguyen, M.-D.; Kim, S.-M.; Lee, J.-I.; Shin, H.-S.; Lee, Y.-K.; Lee, H.-K.; Shin, K.-H.; Kim, Y.-J.; Phung, A.-T.; Choi, J.-Y. Prediction of Stress and Deformation Caused by Magnetic Attraction Force in Modulation Elements in a Magnetically Geared Machine Using Subdomain Modeling. *Machines* **2023**, *11*, 887. [CrossRef]
49. Modaresahmadi, S.; Barnett, D.; Baninajar, H.; Bird, J.Z.; Williams, W.B. Structural modeling and validation of laminated stacks in magnetic gearing applications. *Int. J. Mech. Sci.* **2021**, *192*, 106133.
50. Hannon, B.; Sergeant, P.; Dupré, L. Time- and Spatial-Harmonic Content in Synchronous Electrical Machines. *IEEE Trans. Magn.* **2017**, *53*, 8101011.

51. Hannon, B.; Sergeant, P.; Dupré, L. Computational-Time Reduction of Fourier-Based Analytical Models. *IEEE Trans. Energy Convers.* **2018**, *33*, 281–289.
52. Shin, K.-H.; Hong, K.; Cho, H.-W.; Choi, J.-Y. Core Loss Calculation of Permanent Magnet Machines Using Analytical Method. *IEEE Trans. Appl. Supercond.* **2018**, *28*, 5205005.
53. Maxwell Help. Core Loss Coefficients for Electrical Steel. 2024. Available online: <https://ansyshelp.ansys.com/account/secured?returnurl=/Views/Secured/Electronics/v212/en/home.htm#./Subsystems/Maxwell/Content/CoreLossCoefficientsforElectricalSteel.htm> (accessed on 1 September 2024).
54. Guo, Y.G.; Zhu, J.G. Core losses in claw pole permanent magnet machines with soft magnetic composite stators. *IEEE Trans. Magn.* **2003**, *39*, 3199–3201.
55. Chen, Y.; Pillay, P. An improved formula for lamination core loss calculations in machines operating with high frequency and high flux density excitation. In Proceedings of the IEEE IAS 37th Annual Meeting 2002, Pittsburgh, PA, USA, 13–18 October 2002; Volume 2, pp. 759–766.
56. Cho, H.W. Characteristic Analysis of High-Speed PM Synchronous Motor Considering Power Losses and SVPWM Inverter. Ph.D. Dissertation, Chungnam National University, Daejeon, Republic of Korea, 2007.

Disclaimer/Publisher’s Note: The statements, opinions and data contained in all publications are solely those of the individual author(s) and contributor(s) and not of MDPI and/or the editor(s). MDPI and/or the editor(s) disclaim responsibility for any injury to people or property resulting from any ideas, methods, instructions or products referred to in the content.

Article

Fast Prediction of Characteristics in Wound Rotor Synchronous Condenser Using Subdomain Modeling

Manh-Dung Nguyen ¹, Tae-Seong Kim ¹, Kyung-Hun Shin ^{2,*}, Gang-Hyeon Jang ³ and Jang-Young Choi ^{1,*}

¹ Department of Electrical Engineering, Chungnam National University, Daejeon 34134, Republic of Korea; nguyendungmanh@o.cnu.ac.kr (M.-D.N.); myxotjd@o.cnu.ac.kr (T.-S.K.)

² Department of Electrical Engineering, Changwon National University, Changwon 51140, Republic of Korea

³ Convergence Technology Laboratory, Korea Electric Power Research Institute, Daejeon 34056, Republic of Korea; gh.jang@kepeco.co.kr

* Correspondence: kshin@changwon.ac.kr (K.-H.S.); choi_jy@cnu.ac.kr (J.-Y.C.)

Abstract: Wound rotor synchronous condensers (WRSCs) are DC-excited rotor machines that utilize rotor winding instead of permanent magnets. Their voltage regulator controls the rotor field to generate or absorb reactive power, thereby regulating grid voltage or improving power factor. A key characteristic of a WRSC is the compounding curve, which shows the required rotor current under specific stator current and voltage conditions. This paper presents an approach for quickly calculating the electromagnetic parameters of a WRSC using a mathematical method. After determining magnetic flux density, induced voltage, and inductance through analytical methods, the Park and Clarke transformations are applied to derive the dq -frame quantities, enabling prediction of active and reactive powers and compounding curve characteristics. The 60 Hz model was evaluated through comparison with finite element method (FEM) simulations. Results of flux density, induced voltage, and the compounding curve under varying rotor and stator current conditions showed that the proposed method achieved comparable performance to FEM simulation while reducing computational time by half.

Keywords: compounding curve; finite element method; subdomain modeling; wound rotor synchronous condenser

MSC: 35-04

1. Introduction

Growing environmental concerns and the impacts of climate change are driving the shift from fossil-fuel-based power generation to renewable energy sources. Integrating renewable energy into power systems worldwide helps reduce greenhouse gas emissions and addresses the significant CO₂ emissions of the energy sector, offering sustainable and eco-friendly electricity to power electronic systems. Achieving net-zero emissions by 2050 is essential to limiting global temperature rise, prompting significant changes in the global energy landscape. By 2050, variable renewable energy sources like wind and solar power are expected to dominate the energy mix, with global electricity production projected to increase by 70%. However, the intermittency of renewable energy requires innovative solutions to maintain grid stability, including advanced energy storage and flexible demand management. Consequently, increasing the installed capacity of renewable energy sources in power systems has become a global priority [1–4].

Most renewable energy resources (RERs) connect to power systems through power electronic converters, which lack the inertia provided by traditional fossil fuel generators. The high penetration of RERs, coupled with the retirement of aging fossil-fuel-based generators, has reduced power system inertia. Moreover, most RERs are located in rural areas and connect to power systems via long transmission lines. These long lines have high

impedance, which lowers the power system's short circuit ratio [5]. As a result, transmitting active power through the system consumes significant reactive power, reducing the AC grid's dynamic reactive power reserve and making voltage stability a critical issue [6].

A synchronous condenser is a machine used as a reactive power compensation device to enhance AC power system performance. It provides two primary functions: load compensation and voltage support. Load compensation improves power factor, balances loads, and eliminates current harmonics in nonlinear industrial loads. Voltage support aims to reduce voltage fluctuations at transmission line terminals [7,8], increase the maximum transmittable active power, and enhance AC system stability [9].

Studies in [10,11] discuss converting existing or retired synchronous generators into synchronous condensers. This conversion involves evaluating and modifying auxiliary equipment, accelerating the generator slightly above synchronous speed, powering the excitation system, and synchronizing the condenser with the transmission system. The system maintains the desired terminal voltage of the condenser using automatic voltage regulation controls.

In analyzing electrical machines, particularly synchronous condensers, air-gap flux density is crucial for designers, as it enables determination of parameters such as voltage, torque, and power. Previous studies have mainly relied on finite element method (FEM) simulations, which can be time-consuming, or on magnetic equivalent circuit approaches [12], which often lack precision. Analytical methods offer faster computation with results that align closely with FEM simulations, making them an attractive option for pre-design, analysis, and optimization of wound rotor synchronous condensers (WRSCs). Two main analytical approaches have been explored: subdomain modeling and harmonic modeling.

Subdomain modeling involves solving Maxwell's equations and boundary/interface conditions using Fourier series expansion. This approach has been applied to surface permanent magnet (SPM) motors [13]. The second approach, harmonic modeling, addresses permeability issues using a complex Fourier series and a Cauchy product, allowing consideration of nonlinear core characteristics. It was initially introduced in analyzing switched reluctance motors (SRMs) [14]. Based on these analytical approaches, ref. [15] optimized cogging torque by investigating the slot opening and magnet pitch ratio, while [16–18] optimized output power in magnetically geared machines (MG) and SPMs. For multi-physics analysis, ref. [19] applied the subdomain method to predict stress and deformation in MGMs, and [20] solved for thermal distribution in the stator slot of SPMs.

To the best of our knowledge, analytical methods have not been applied to WRSCs. Thus, this study extensively analyzes a WRSC using a subdomain approach to predict air-gap flux density, voltage, and power-factor-related characteristics. Section 2 presents the main content in four subsections. The Section 2.1 introduces the application of partial differential equations (PDEs) to WRSCs. The Section 2.2 establishes an equation system to solve for unknown coefficients based on boundary conditions. The Section 2.3 defines WRSC parameters, and the fourth presents the compounding curve calculation. Finally, Section 3 presents FEM simulation results validating the proposed method.

2. Subdomain Modeling

2.1. Governing Partial Differential Equations (PDEs)

Figure 1 describes the WRSC and its simplified models employed in the subdomain modeling. Initially, the following assumptions were made:

- The end effects are ignored;
- The problem is two-dimensional (2-D) in polar coordinates;
- Magnetic vector potential A , current density J , and magnetic flux density vector B have the following non-zero components: $A = [0, 0, A_z]$; $J = [0, 0, J_z]$; $B = [B_r, B_\theta, 0]$;
- The core materials have infinite permeability.

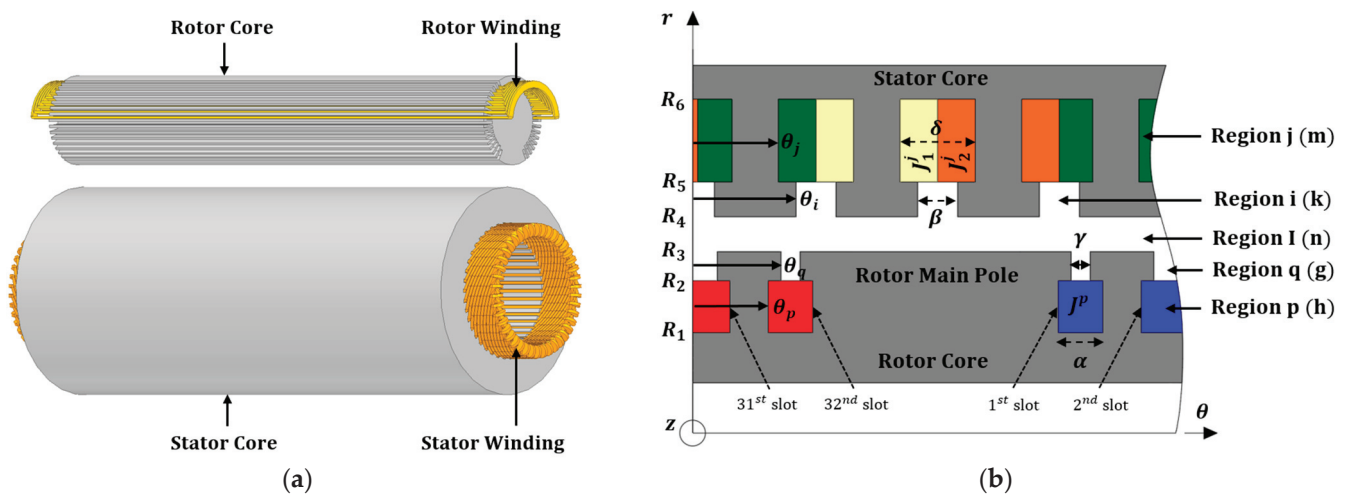


Figure 1. (a) Wound rotor synchronous condenser and (b) a simplified model.

The WRSC model, as illustrated in Figure 1b, is divided into five subdomains: rotor, rotor opening, air gap, stator opening, and stator slots. Each subdomain is represented by a vector potential of the form $A_z^p, A_z^q, A_z^I, A_z^i, A_z^j$, with respective harmonic components h, g, n, k, m . The model includes N_r rotor and N_s stator slots, where indices p, q, i , and j denote specific rotor and stator slots with initial positions $\theta_p, \theta_q, \theta_i$, and θ_j . A 2-D analysis in polar coordinates is used to derive partial differential equations (PDEs) for each region:

$$\frac{\partial^2 A_z^p}{\partial r^2} + \frac{\partial A_z^p}{r \partial r} + \frac{\partial^2 A_z^p}{r^2 \partial \theta^2} = -\mu_0 J_z^p \quad (1)$$

$$\frac{\partial^2 A_z^q}{\partial r^2} + \frac{\partial A_z^q}{r \partial r} + \frac{\partial^2 A_z^q}{r^2 \partial \theta^2} = 0 \quad (2)$$

$$\frac{\partial^2 A_z^I}{\partial r^2} + \frac{\partial A_z^I}{r \partial r} + \frac{\partial^2 A_z^I}{r^2 \partial \theta^2} = 0 \quad (3)$$

$$\frac{\partial^2 A_z^i}{\partial r^2} + \frac{\partial A_z^i}{r \partial r} + \frac{\partial^2 A_z^i}{r^2 \partial \theta^2} = 0 \quad (4)$$

$$\frac{\partial^2 A_z^j}{\partial r^2} + \frac{\partial A_z^j}{r \partial r} + \frac{\partial^2 A_z^j}{r^2 \partial \theta^2} = -\mu_0 J_z^j \quad (5)$$

The air gap and slot-opening regions can be modeled using Laplace's equation, while the rotor-stator slot subdomains can be represented by Poisson's equation. To facilitate the Fourier series expansion of the vector potential, the right-hand side of Poisson's equation must be reformulated in Fourier form.

In the double-layer stator winding, the current density in the j -th slot is expressed as

$$J_z^j = \left(J_0^j + \sum_{m=1,2}^{\infty} J_m^j \cos\left(\frac{m\pi}{\delta}(\theta - \theta_j)\right) \right) i_z$$

where

$$J_0^j = \frac{J_0^{j-layer1} + J_0^{j-layer2}}{2} \quad (6)$$

$$J_m^j = \begin{cases} \frac{2}{m\pi} \left(J_0^{j-layer1} - J_0^{j-layer2} \right) \sin\left(\frac{m\pi}{2}\right) & \leftrightarrow \text{non overlapping} \\ 0 & \leftrightarrow \text{overlapping} \end{cases}$$

In the single-layer rotor winding, the current sheet is simply described as $J_z^p = J_0^p i_z$.

2.2. General Solutions

The infinite permeability assumption in the core leads to tangential-direction boundary conditions.

$$\left. \frac{\partial A_z^p}{\partial \theta} \right|_{\theta=\theta_p} = \left. \frac{\partial A_z^p}{\partial \theta} \right|_{\theta=\theta_p+\alpha} \quad (7)$$

$$\left. \frac{\partial A_z^q}{\partial \theta} \right|_{\theta=\theta_q} = \left. \frac{\partial A_z^q}{\partial \theta} \right|_{\theta=\theta_q+\gamma} \quad (8)$$

$$\left. \frac{\partial A_z^i}{\partial \theta} \right|_{\theta=\theta_i} = \left. \frac{\partial A_z^i}{\partial \theta} \right|_{\theta=\theta_i+\beta} \quad (9)$$

$$\left. \frac{\partial A_z^j}{\partial \theta} \right|_{\theta=\theta_j} = \left. \frac{\partial A_z^j}{\partial \theta} \right|_{\theta=\theta_j+\delta} \quad (10)$$

Applying these four boundary conditions to Equations (1)–(5), general solutions of PDEs are expressed as a sum of homogeneous and particular solutions.

$$A_z^p = A_0^p + \ln(r) B_0^p - \frac{\mu_0}{4} r^2 J_0^p + \sum_{h=1,2}^{\infty} \left(r^{h\frac{\pi}{\alpha}} C_h^p + r^{-h\frac{\pi}{\alpha}} D_h^p \right) \cos\left(h\frac{\pi}{\alpha}(\theta - \theta_p)\right) \quad (11)$$

$$A_z^q = A_0^q + \ln(r) B_0^q + \sum_{g=1,2}^{\infty} \left(r^{g\frac{\pi}{\gamma}} C_g^q + r^{-g\frac{\pi}{\gamma}} D_g^q \right) \cos\left(g\frac{\pi}{\gamma}(\theta - \theta_q)\right) \quad (12)$$

$$A_z^I = \sum_{n=1,2}^{\infty} \left(r^n A_n^I + r^{-n} B_n^I \right) \sin(n\theta) + \left(r^n C_n^I + r^{-n} D_n^I \right) \cos(n\theta) \quad (13)$$

$$A_z^i = A_0^i + \ln(r) B_0^i + \sum_{k=1,2}^{\infty} \left(r^{k\frac{\pi}{\beta}} C_k^i + r^{-k\frac{\pi}{\beta}} D_k^i \right) \cos\left(k\frac{\pi}{\beta}(\theta - \theta_i)\right) \quad (14)$$

$$A_z^j = A_0^j + \ln(r) B_0^j - \frac{\mu_0}{4} r^2 J_0^j + \sum_{m=1,2}^{\infty} \left(r^{m\frac{\pi}{\delta}} C_m^j + r^{-m\frac{\pi}{\delta}} D_m^j + \frac{\mu_0 r^2 J_m^j}{(m\frac{\pi}{\delta})^2 - 4} \right) \cos\left(m\frac{\pi}{\delta}(\theta - \theta_j)\right) \quad (15)$$

In total, there are 20 coefficients in (11)–(15). Thus, to determine a unique solution requires us to derive 20 corresponding equations. The continuity of the vector potential radial components results in the following boundary conditions:

$$r = R_1 \rightarrow \frac{\partial A_z^p}{\partial r} = 0 \quad (16)$$

$$r = R_2 \rightarrow \begin{cases} \frac{\partial A_z^p}{\partial r} = \frac{\partial A_z^q}{\partial r} \\ A_z^q = A_z^p \end{cases} \quad (17)$$

$$r = R_3 \rightarrow \begin{cases} A_z^q = A_z^I \\ \frac{\partial A_z^I}{\partial r} = \sum_{p=1,2}^{N_r} \frac{\partial A_z^p}{\partial r} \end{cases} \quad (18)$$

$$r = R_4 \rightarrow \begin{cases} \frac{\partial A_z^I}{\partial r} = \sum_{i=1,2}^{N_s} \frac{\partial A_z^i}{\partial r} \\ A_z^i = A_z^I \end{cases} \quad (19)$$

$$r = R_5 \rightarrow \begin{cases} A_z^i = A_z^j \\ \frac{\partial A_z^j}{\partial r} = \frac{\partial A_z^i}{\partial r} \end{cases} \quad (20)$$

$$r = R_6 \rightarrow \frac{\partial A_z^j}{\partial r} = 0 \quad (21)$$

By employing integrals $sni(n, \theta_i, \beta)$, $rni(n, \theta_i, \beta)$, $gkni(k, n, \theta_i, \beta)$, $fkni(k, n, \theta_i, \beta)$, and $Fmk(m, k, \beta, \delta)$ in [19] to shorten equations, 20 equations are given in Appendices A and B.

2.3. Matrix Representation and Solving Electromagnetic Quantities

Reformulating the above equations into matrix and vector forms makes it possible to obtain analytical solutions using MATLAB R2022b. For instance, in a WRSM model with $N_r = 32$ rotor and $N_s = 42$ stator slots and harmonic order numbers $G = H = K = M = 5$ and $N = 100$, the result is a column matrix \mathbf{X} with $4(N + N_r G + N_r H + N_s K + N_s M) = 3360$ elements.

$$\mathbf{X} = \left[A_n^I B_n^I C_n^I D_n^I A_0^p B_0^p C_0^p D_0^p A_0^q B_0^q C_0^q D_0^q A_0^i B_0^i C_0^i D_0^i A_0^j B_0^j C_0^j D_0^j \right]^T \quad (22)$$

After solving the coefficients, flux density at the air gap (radius is R_e) is derived as:

$$B_\theta = -\frac{\partial A^I}{\partial r} = -\frac{1}{R_e} \sum_{n=1,2}^{\infty} \left(R_e^n A_n^I - R_e^{-n} B_n^I \right) \sin(n\theta)n + \left(R_e^n C_n^I - R_e^{-n} D_n^I \right) \cos(n\theta)n \quad (23)$$

$$B_r = \frac{1}{R_e} \frac{\partial A^I}{\partial \theta} = \frac{1}{R_e} \sum_{n=1,2}^{\infty} \left(R_e^n A_n^I + R_e^{-n} B_n^I \right) \cos(n\theta)n - \left(R_e^n C_n^I + R_e^{-n} D_n^I \right) \sin(n\theta)n \quad (24)$$

To compute the induced voltage in a three-phase motor with stack length L_{stk} , the flux through each slot cross-section at a given rotor position θ_0 was calculated. Uniform current density across the slot area was assumed, allowing for the flux in the j -th slot to be determined by integrating the vector potential across the slot area, as given in Equation (15).

$$\begin{aligned} \Phi_j &= T_{pole} \frac{I_{stk}}{A_{slot}} \iint A_r^j(\theta, z) r dr d\theta \\ &= \frac{L_{stk}}{\frac{R_6^2 - R_5^2}{2}} \left(A_0^j \frac{R_6^2 - R_5^2}{2} + B_0^j \left(\ln(R_6) \frac{R_6^2}{2} - \ln(R_5) \frac{R_5^2}{2} + \frac{R_6^2 - R_5^2}{4} \right) - J_0^j \frac{\mu_0 (R_6^4 - R_5^4)}{16} \right) \end{aligned} \quad (25)$$

The phase flux is calculated as the sum of fluxes in slots associated with each phase. A connecting matrix $[C]$ with the dimensions $3 \times N_s$ was used to present the stator winding distribution in the slots, as shown in [13], where indices 1 and -1 denote positive and negative, and 0 denotes a phase absence in the slot. T_{slot} represents the phase-winding turns per slot, and the phase fluxes are expressed as:

$$\begin{bmatrix} \Phi_A \\ \Phi_B \\ \Phi_C \end{bmatrix}_{3 \times 1} = T_{slot} [C]_{3 \times N_s} [\Phi_j]_{N_s \times 1} \quad (26)$$

The induced voltage can be defined at a given rotor speed ω_m as follows:

$$\begin{bmatrix} U_A \\ U_B \\ U_C \end{bmatrix}_{3 \times 1} = \frac{N_r}{2} \omega_m \frac{d}{d\theta_0} \begin{bmatrix} \Phi_A \\ \Phi_B \\ \Phi_C \end{bmatrix}_{3 \times 1} \quad (27)$$

Notably, without stator current contribution in the no-load condition, the induced voltage becomes BEMF.

2.4. Compounding Curve

Figure 2 illustrates three compounding curves, where the red, blue, and orange lines represent power factors of 1 and 0.95 leading (WRSC generates reactive power), and 0.95 lagging (WRSC absorbs reactive power), respectively. For instance, at a stator load of 105 A, the rotor generates 86 A to achieve a power factor of 1. If the rotor current

exceeds 86 A, the machine becomes overexcited, and excess reactive power flows to the grid. Conversely, if the rotor current is below 86 A, the machine becomes under-excited, lowering its operating voltage below the grid voltage, prompting the grid to supply reactive power to compensate for the power deficit in the machine.

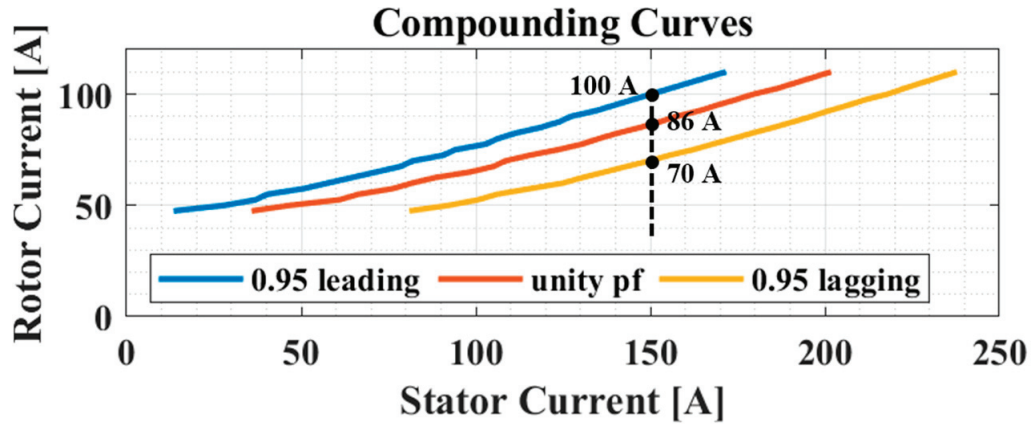


Figure 2. Illustration of compounding curves.

The compounding curve is essential for assessing WRSC performance, allowing designers to estimate the field current necessary for a given stator load to achieve a desired electrical system power factor. This section presents the procedure for deriving the unity power factor line and applies it to salient and non-salient rotors. The procedure involves:

- Transforming phase quantities (flux, voltage, and current) obtained from subdomain modeling into the dq -frame under current excitation.
- Deriving and transforming self- and mutual inductances into the dq -frame.
- Building and solving a d-axis current function with a reactive power of zero from the voltage and power equations in the dq -frame.

By aligning the rotor pole with phase A in the initial position, the quantities of voltage, current, flux, and inductance can be transferred to the dq -frame using Park and Clarke transformations [21]. By assuming that machine saturation is neglected, Park and Clarke transformations are given as follows:

$$UI\lambda_{dqz} = \frac{2}{3} \begin{bmatrix} \cos(\theta_0) & \cos(\theta_0 - \frac{2\pi}{3}) & \cos(\theta_0 + \frac{2\pi}{3}) \\ -\sin(\theta_0) & -\sin(\theta_0 - \frac{2\pi}{3}) & -\sin(\theta_0 + \frac{2\pi}{3}) \\ 1/2 & 1/2 & 1/2 \end{bmatrix} \begin{bmatrix} UI\lambda_a \\ UI\lambda_b \\ UI\lambda_c \end{bmatrix} \quad (28)$$

$$\begin{bmatrix} L_d & M_{dq} & M_{dz} \\ M_{qd} & L_q & M_{qz} \\ M_{zd} & M_{zq} & L_z \end{bmatrix} = \sqrt{\frac{2}{3}} \begin{bmatrix} 1 & \cos(\frac{2\pi}{3}) & \cos(\frac{4\pi}{3}) \\ 0 & \sin(\frac{2\pi}{3}) & \sin(\frac{4\pi}{3}) \\ 1/\sqrt{2} & 1/\sqrt{2} & 1/\sqrt{2} \end{bmatrix} \begin{bmatrix} L_{aa} & M_{ab} & M_{ac} \\ M_{ba} & L_{bb} & M_{bc} \\ M_{ca} & M_{cb} & L_{cc} \end{bmatrix} \sqrt{\frac{2}{3}} \quad (29)$$

To calculate the winding self-inductance and mutual inductances in (29), the authors apply an excitation current of 1 A to the first winding, while setting the currents in all other windings to zero, excluding rotor current effects from the analysis. For example, phase A is set to 1 A, while phases B and C and the rotor current are set to zero. The obtained flux linkages of phases A, B, and C (ψ_a, ψ_b, ψ_c) are then used to calculate the inductance as follows:

$$\begin{bmatrix} L_{aa} & L_{ab} & L_{ac} \end{bmatrix} = \frac{\begin{bmatrix} \psi_a & \psi_b & \psi_c \end{bmatrix}}{1A} \quad (30)$$

Additionally, rotor flux linkage (ψ_f), used to derive rotor inductance, $M_{df} = \psi_f / I_f$, is calculated by setting all stator winding currents to zero and applying only a 1 A current to the rotor. The flux linkage of phase A is considered the rotor flux linkage.

In high-power machines, reactance is dominant, and stator resistance can be neglected; therefore, the voltage equation is given by:

$$\begin{bmatrix} U_d \\ U_q \end{bmatrix} \approx \omega_e \begin{bmatrix} -L_q i_q \\ L_d i_d + M_{df} i_f \end{bmatrix} \quad (31)$$

Consequently, the active and reactive powers are defined as:

$$\begin{aligned} P &= 1.5(U_d i_d + U_q i_q) \\ Q &= 1.5(U_q i_d - U_d i_q) \end{aligned} \quad (32)$$

Table 1 shows the operating modes of the machine's power. To operate as a capacitor bank, the machine generates reactive power (negative Q). This is achieved by applying a sufficiently large negative d -axis current along with a specific rotor current. For a constant stator current, this capacitor-like operation can also be achieved by applying a sufficient rotor current.

Table 1. Machine mode definition.

Mode	Power Factor	P	Q
Motor	Lagging	>0	>0
Motor	Leading	>0	<0
Generator	Lagging	<0	>0
Generator	Leading	<0	<0

To achieve a unity power factor ($PF = 1$), commutation in WRSC is defined by a zero reactive power, $Q = 0$. This condition, combined with the voltage constraint $v_d^2 + v_q^2 = V_{smax}^2$, allows the d -axis stator current to be modeled as a function of rotor current.

$$\left(L_d^2 - L_d L_q \right) i_d^2 + M_{df} i_f (2L_d - L_q) i_d + M_{df} i_f^2 - \frac{V_{smax}^2}{\omega_e^2} = 0 \quad (33)$$

By adjusting the rotor current i_f , the d -axis current can be solved using Equation (33), and the q -axis current can be obtained from Equation (32). These computations form a compounding curve that maps the current relationship between the rotor and stator. In salient-pole rotor machines, where dq -frame inductances are nearly identical, Equation (33) reduces to a first-order equation, simplifying analysis.

3. FEM Simulation Comparison

To validate these principles, specifications for a one-pole-pair WRSC, as listed in Table 2, were simulated using a 2-D finite element method (FEM) model with the mesh setting depicted in Figure 3a. Due to mechanical constraints in MW-class WRSC, the air gap was intentionally designed to be large (up to 100 mm). The FEM simulation took 66 s to compute flux density, flux at the air gap, and induced voltage (see Figures 3b and 4). By contrast, the subdomain modeling approach achieved these calculations in 33 s, showcasing the computational efficiency of the proposed method in WRSC pre-design.

Figure 3b illustrates the flux density distribution at current conditions $i_f = 1$ kA; $i_d = i_q = -0.5$ kA. The salient-pole rotor caused flux linkage to concentrate in the rotor pole and teeth near the pole, inducing mild saturation in the teeth. Under typical conditions, machines avoid saturation, making the assumption of infinite permeability in subdomain modeling suitable. However, when the field current or stator current is increased, saturation intensifies, resulting in accuracy discrepancies in the subdomain method (see Figure 4e,f).

The compounding curves derived from the subdomain method were closely aligned with the FEM results, as seen in Figure 5. To maintain a unity power factor while increasing stator current, the field current must also rise. Additionally, rotor current must increase at higher stator voltages. Calculations for these curves, derived from Equation (33), involve

computing the dq -axis currents for each rotor current, then determining the stator current. The analysis covered phase peak voltages of 10, 15, 18, and 22 kV, revealing that the machine can support stator currents up to 5 kA with a maximum field current of 1.3 kA. The mathematical method obtained these results in under 1 s, which represents a significant time advantage in deriving compounding curves.

Table 2. WRSC parameters.

Quantity	Symbol	Unit	Value
Inner rotor slot radius	R_1	mm	269.50
Outer rotor radius	R_2	mm	425.25
Inner stator slot radius	R_3	mm	525.25
Outer stator slot radius	R_4	mm	700.50
Outer stator radius	R_5	mm	1119.50
Stack length	L_{stk}	mm	6402.40
Vacuum permeability	μ_0	$\text{kg}\cdot\text{m}\cdot\text{s}^{-2}\cdot\text{A}^{-2}$	$4\pi \times 10^{-7}$
Rotor slot number	N_r	-	32
Stator slot number	N_s	-	42
Rotor slot pitch ratio	α	$\pi/180$ rad	4.64
Rotor opening slot pitch ratio	γ	$\pi/180$ rad	4.64
Stator opening slot pitch ratio	β	$2\pi/N_s$ rad	0.46
Stator slot pitch ratio	δ	$2\pi/N_s$ rad	0.46
Rotor slot winding turn	T_{slot}^r	-	5/7 *
Stator slot winding turn	T_{slot}^s	-	2

* The 1st, 16th, 17th, and 32nd slots each contain five turns. The remaining slots accommodate seven turns.

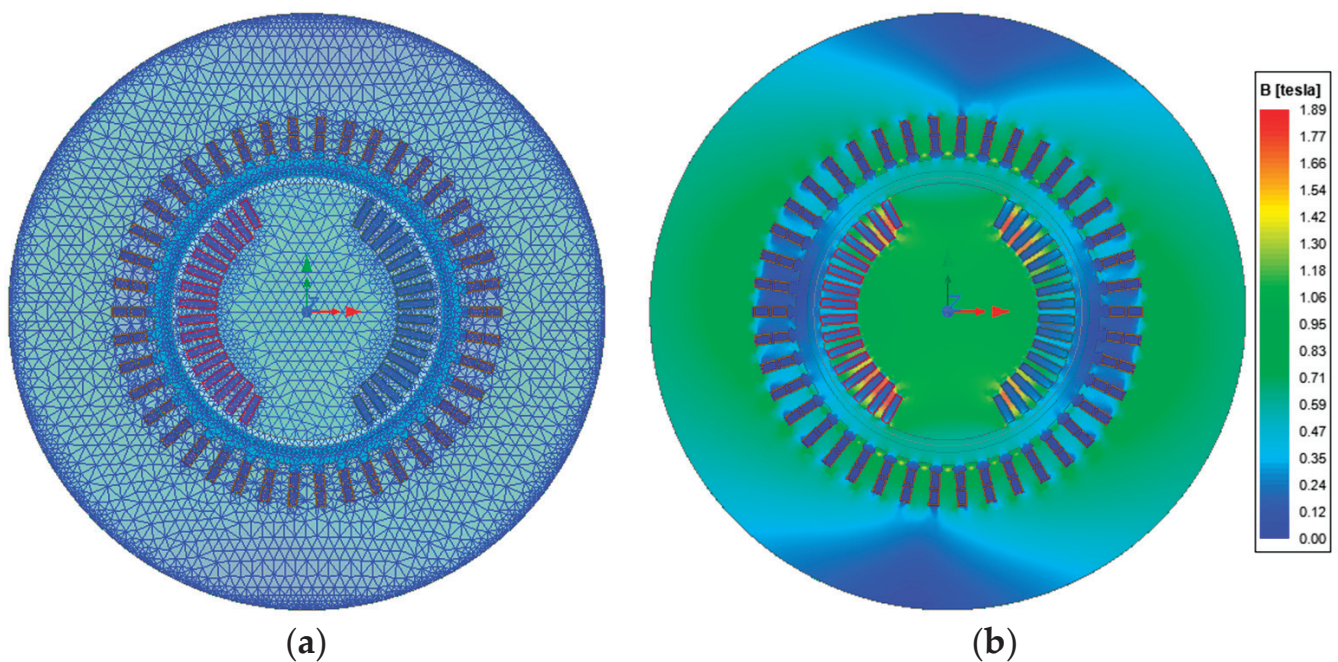


Figure 3. (a) Mesh operation (29,242 elements) and (b) flux density distribution at $i_f = 1$ kA; $i_d = i_q = -0.5$ kA.

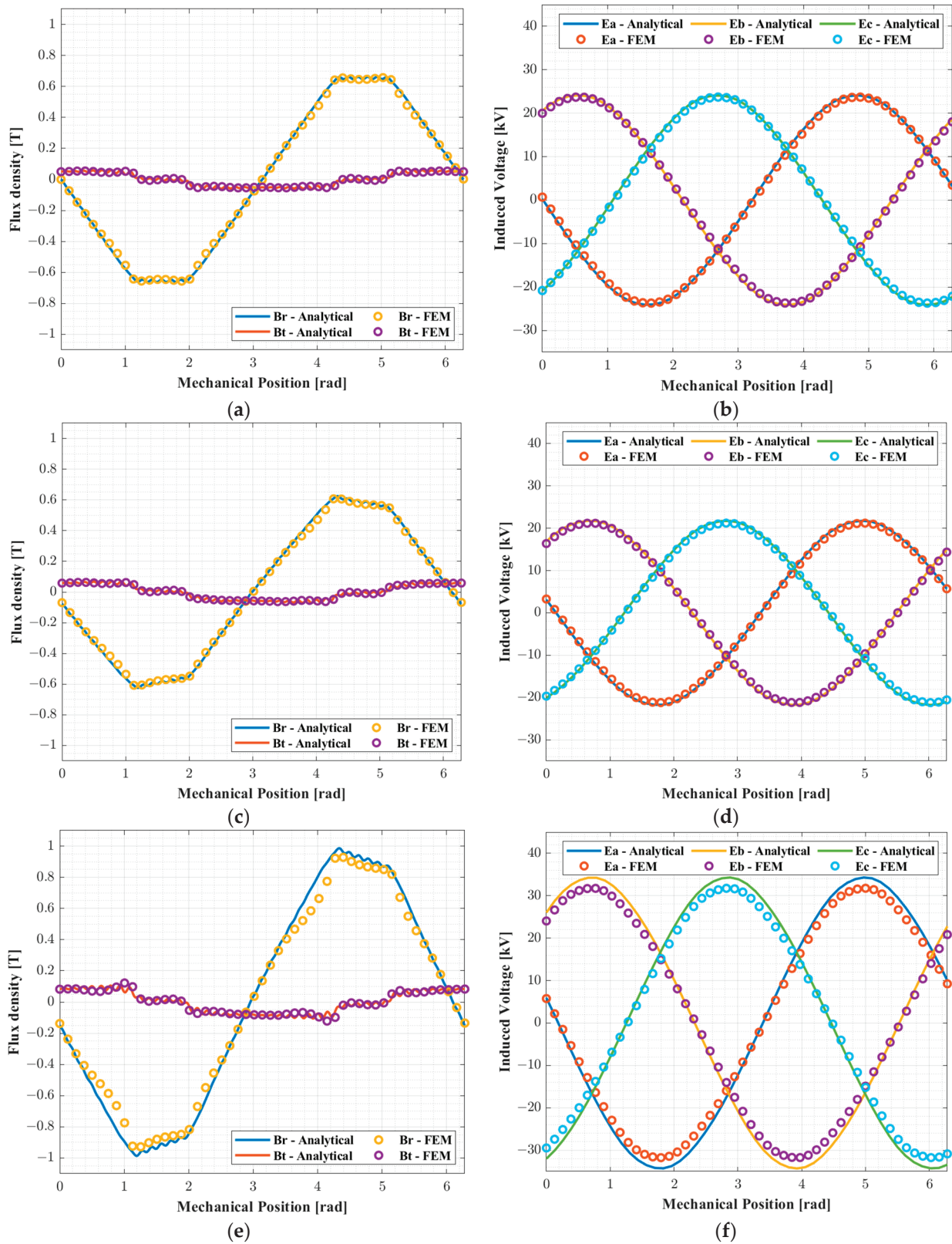


Figure 4. Flux density at the air gap and induced voltage in case of (a,b) $i_f = 1 \text{ kA}; i_d = i_q = 0 \text{ kA}$, (c,d) $i_f = 1 \text{ kA}; i_d = i_q = -0.5 \text{ kA}$, and (e,f) $i_f = 1.5 \text{ kA}; i_d = -0.5; i_q = -1 \text{ kA}$, respectively.

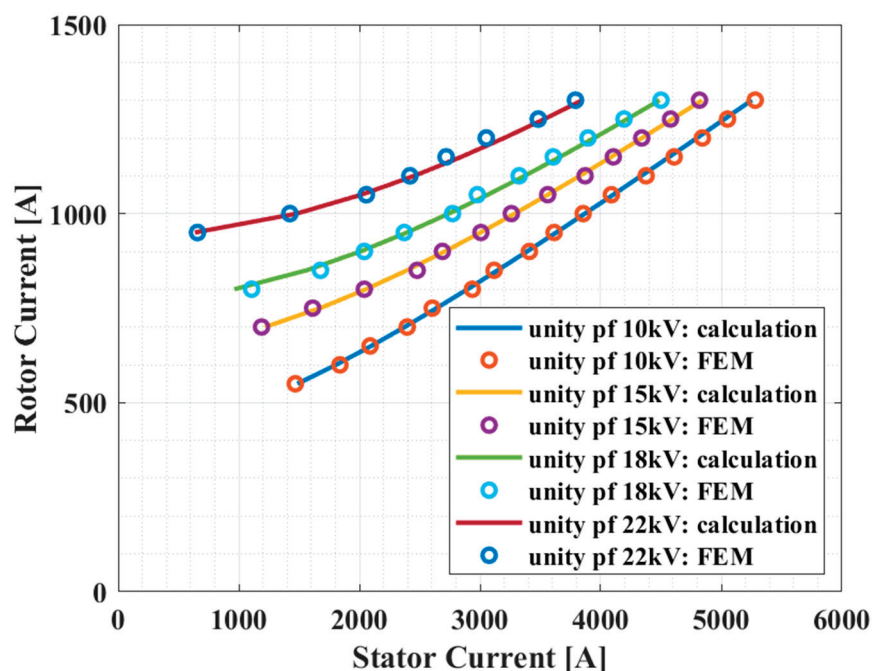


Figure 5. Compounding curves of the calculation and the FEM under different conditions of maximum stator voltage.

4. Conclusions

Overall, the proposed mathematical method offers a fast and effective approach for characterizing WRSC properties, including flux density, induced voltage, inductance, and compounding curves. Under low rotor and stator current conditions, the subdomain method aligns well with 2-D FEM results. However, as rotor and stator currents increase, saturation can induce errors of up to 10% in the flux density and induced voltage results. The unity-power-factor compounding curves were accurate across varying conditions. These results were obtained because of the unity power factor and suppression of demagnetization by the d-axis stator current, which weakens flux linkage and limits saturation.

Compared to 2-D FEM simulations, the mathematical method cut computation time from 66 to 33 s, facilitating faster optimizations in the WRSC design process. The reduced time can lead to exponential efficiency gains, enabling designers to employ optimization techniques more effectively.

Future research based on these findings could explore:

- Nonlinear magnetic material characteristics;
- Deriving leading and lagging compounding curves for power factor;
- Optimization techniques for a more efficient WRSC design;
- Experimental verification of the subdomain method on a test bench.

Author Contributions: Conceptualization, M.-D.N., T.-S.K., K.-H.S., G.-H.J. and J.-Y.C.; methodology, M.-D.N.; validation, M.-D.N.; writing—original draft preparation, M.-D.N. and T.-S.K.; writing—review and editing, K.-H.S., G.-H.J. and J.-Y.C.; supervision, K.-H.S. and J.-Y.C. All authors have read and agreed to the published version of the manuscript.

Funding: This work was supported by Korea Institute of Energy Technology Evaluation and Planning (KETEP) grant funded by the Korean government (MOTIE) (20223A10100040, Development of design technology for converting retired thermal plant into synchronous condenser plant).

Data Availability Statement: Data are contained within the article.

Conflicts of Interest: The authors declare no conflicts of interest.

Appendix A

The following integrals are presented to shorten equations in Appendix B:

$$sni(n, \theta_i, \beta) = \int_{\theta_i}^{\theta_i+\beta} \sin(n\theta) d\theta = \frac{1}{n} (\cos(n\theta_i) - \cos(n(\theta_i + \beta))) \quad (A1)$$

$$rni(n, \theta_i, \beta) = \int_{\theta_i}^{\theta_i+\beta} \cos(n\theta) d\theta = \frac{1}{n} (\sin(n(\theta_i + \beta)) - \sin(n\theta_i)) \quad (A2)$$

$$gkni(k, n, \theta_i, \beta) = \int_{\theta_i}^{\theta_i+\beta} \sin(n\theta) \cos\left(k\frac{\pi}{\beta}(\theta - \theta_i)\right) d\theta$$

$$= \begin{cases} \frac{\beta}{2} \left(\sin(n\theta_i) - \frac{1}{2k\pi} (\cos(n(\theta_i + 2\beta)) - \cos(n\theta_i)) \right) \leftrightarrow k\pi = n\beta \\ \frac{n\beta^2}{(k\pi)^2 - (n\beta)^2} \left((-1)^k (n(\theta_i + 2\beta)) - \cos(n\theta_i) \right) \leftrightarrow k\pi \neq n\beta \end{cases} \quad (A3)$$

$$fkni(k, n, \theta_i, \beta) = \int_{\theta_i}^{\theta_i+\beta} \cos(n\theta) \cos\left(k\frac{\pi}{\beta}(\theta - \theta_i)\right) d\theta$$

$$= \begin{cases} \frac{\beta}{2} \left(\cos(n\theta_i) + \frac{1}{2k\pi} (\sin(n(\theta_i + 2\beta)) - \sin(n\theta_i)) \right) \leftrightarrow k\pi = n\beta \\ \frac{-n\beta^2}{(k\pi)^2 - (n\beta)^2} \left((-1)^k \sin(n(\theta_i + 2\beta)) - \sin(n\theta_i) \right) \leftrightarrow k\pi \neq n\beta \end{cases} \quad (A4)$$

$$Fmk(m, k, \beta, \delta) = \int_{\theta_i}^{\theta_i+\beta} \cos\left(k\frac{\pi}{\beta}(\theta - \theta_i)\right) \cos\left(m\frac{\pi}{\delta}(\theta - \theta_j)\right) d\theta$$

$$= \begin{cases} \frac{\beta}{2} \cos\left(\frac{k\pi}{2\beta}(\beta - \delta)\right) \leftrightarrow \frac{m}{\delta} = \frac{k}{\beta} \\ \frac{m\frac{\pi}{\delta}}{(m\frac{\pi}{\delta})^2 - (k\frac{\pi}{\beta})^2} \left((-1)^k \sin\left(\frac{m\pi}{2\delta}(\beta + \delta)\right) + \sin\left(\frac{m\pi}{2\delta}(\beta - \delta)\right) \right) \leftrightarrow \frac{m}{\delta} \neq \frac{k}{\beta} \end{cases} \quad (A5)$$

Appendix B

Twenty respective equations to determine a unique solution are rewritten as:

$$\frac{1}{R_1} B_0^p - \frac{\mu_0}{2} R_1 J_0^p = 0 \quad (A6)$$

$$R_1^{h\frac{\pi}{\alpha}-1} h \frac{\pi}{\alpha} C_h^p + R_1^{-h\frac{\pi}{\alpha}-1} \left(-h\frac{\pi}{\alpha}\right) D_h^p = 0 \quad (A7)$$

$$\frac{1}{R_2} B_0^p - \frac{\mu_0}{2} R_2 J_0^p = \frac{\gamma}{\alpha} \frac{1}{R_2} B_0^q \quad (A8)$$

$$R_2^{h\frac{\pi}{\alpha}-1} h \frac{\pi}{\alpha} C_h^p + R_2^{-h\frac{\pi}{\alpha}-1} \left(-h\frac{\pi}{\alpha}\right) D_h^p = \frac{2}{\alpha} \frac{1}{R_2} B_0^q \frac{\alpha}{h\pi} 2\cos\left(\frac{h\pi}{2}\right) \sin\left(\frac{h\pi}{2} \frac{\gamma}{\alpha}\right)$$

$$+ \sum_{g=1,2}^{\infty} \left(R_2^{g\frac{\pi}{\gamma}-1} g \frac{\pi}{\gamma} C_g^q + R_2^{-g\frac{\pi}{\gamma}-1} \left(-g\frac{\pi}{\gamma}\right) D_g^q \right) \frac{2}{\alpha} Fmk(h, g, \gamma, \alpha) \quad (A9)$$

$$A_0^q + \ln(R_2) B_0^q = A_0^p + \ln(R_2) B_0^p - \frac{\mu_0}{4} R_2^2 J_0^p$$

$$+ \sum_{h=1,2}^{\infty} \left(R_2^{h\frac{\pi}{\alpha}} C_h^p + R_2^{-h\frac{\pi}{\alpha}} D_h^p \right) \frac{1}{\gamma} \frac{\alpha}{h\pi} 2\cos\left(\frac{h\pi}{2}\right) \sin\left(\frac{h\pi}{2} \frac{\gamma}{\alpha}\right) \quad (A10)$$

$$R_2^{g\frac{\pi}{\gamma}} C_g^q + R_2^{-g\frac{\pi}{\gamma}} D_g^q = \sum_{h=1,2}^{\infty} \left(R_2^{h\frac{\pi}{\alpha}} C_h^p + R_2^{-h\frac{\pi}{\alpha}} D_h^p \right) \frac{2}{\gamma} Fmk(h, g, \gamma, \alpha) \quad (A11)$$

$$R_3^{n-1} n A_n^I + R_3^{-n-1} (-n) B_n^I = \sum_{p=1,2}^{N_r} \frac{1}{R_3} B_0^q \frac{2}{2\pi} sni(n, \theta_q, \gamma)$$

$$+ \sum_{q=1,2}^{N_r} \sum_{g=1,2}^{\infty} \left(R_3^{g\frac{\pi}{\gamma}-1} g \frac{\pi}{\gamma} C_g^q + R_3^{-g\frac{\pi}{\gamma}-1} \left(-g\frac{\pi}{\gamma}\right) D_g^q \right) \frac{2}{2\pi} gkni(g, n, \theta_q, \gamma) \quad (A12)$$

$$R_3^{n-1}n\mathbf{C}_n^I + R_3^{-n-1}(-n)\mathbf{D}_n^I = \sum_{q=1,2}^{N_r} \frac{1}{R_3} \mathbf{B}_0^q \frac{2}{2\pi} rni(n, \theta_q, \gamma) + \sum_{q=1,2}^{N_r} \sum_{g=1,2}^{\infty} \left(R_3^{g\frac{\pi}{\gamma}-1} g \frac{\pi}{\gamma} \mathbf{C}_g^q + R_3^{-g\frac{\pi}{\gamma}-1} \left(-g \frac{\pi}{\gamma} \right) \mathbf{D}_g^q \right) \frac{2}{2\pi} fgni(g, n, \theta_q, \gamma) \quad (\text{A13})$$

$$\mathbf{A}_0^q + \ln(R_3) \mathbf{B}_0^q = \left(R_3^n \mathbf{A}_n^I + R_3^{-n} \mathbf{B}_n^I \right) \frac{1}{\gamma} sni(n, \theta_q, \gamma) + \left(R_3^n \mathbf{C}_n^I + R_3^{-n} \mathbf{D}_n^I \right) \frac{1}{\gamma} rni(n, \theta_q, \gamma) \quad (\text{A14})$$

$$R_3^{g\frac{\pi}{\gamma}} \mathbf{C}_g^q + R_3^{-g\frac{\pi}{\gamma}} \mathbf{D}_g^q = \left(R_3^n \mathbf{A}_n^I + R_3^{-n} \mathbf{B}_n^I \right) \frac{2}{\gamma} gkni(g, n, \theta_q, \gamma) + \left(R_3^n \mathbf{C}_n^I + R_3^{-n} \mathbf{D}_n^I \right) \frac{2}{\gamma} fgni(g, n, \theta_q, \gamma) \quad (\text{A15})$$

$$R_4^{n-1}n\mathbf{A}_n^I + R_4^{-n-1}(-n)\mathbf{B}_n^I = \sum_{i=1,2}^{N_s} \frac{1}{R_4} \mathbf{B}_0^i \frac{2}{2\pi} sni(n, \theta_i, \beta) + \sum_{i=1,2}^{N_s} \sum_{k=1,2}^{\infty} \left(R_4^{k\frac{\pi}{\beta}-1} k \frac{\pi}{\beta} \mathbf{C}_k^i + R_4^{-k\frac{\pi}{\beta}-1} \left(-k \frac{\pi}{\beta} \right) \mathbf{D}_k^i \right) \frac{2}{2\pi} gkni(k, n, \theta_i, \beta) \quad (\text{A16})$$

$$R_4^{n-1}n\mathbf{C}_n^I + R_4^{-n-1}(-n)\mathbf{D}_n^I = \sum_{i=1,2}^{N_s} \frac{1}{R_4} \mathbf{B}_0^i \frac{2}{2\pi} rni(n, \theta_i, \beta) + \sum_{i=1,2}^{N_s} \sum_{k=1,2}^{\infty} \left(R_4^{k\frac{\pi}{\beta}-1} k \frac{\pi}{\beta} \mathbf{C}_k^i + R_4^{-k\frac{\pi}{\beta}-1} \left(-k \frac{\pi}{\beta} \right) \mathbf{D}_k^i \right) \frac{2}{2\pi} fgni(k, n, \theta_i, \beta) \quad (\text{A17})$$

$$\mathbf{A}_0^i + \ln(R_4) \mathbf{B}_0^i = \sum_{n=1,2}^{\infty} \left(R_4^n \mathbf{A}_n^I + R_4^{-n} \mathbf{B}_n^I \right) \frac{1}{\beta} sni(n, \theta_i, \beta) + \left(R_4^n \mathbf{C}_n^I + R_4^{-n} \mathbf{D}_n^I \right) \frac{1}{\beta} rni(n, \theta_i, \beta) \quad (\text{A18})$$

$$R_4^{k\frac{\pi}{\beta}} \mathbf{C}_k^i + R_4^{-k\frac{\pi}{\beta}} \mathbf{D}_k^i = \sum_{n=1,2}^{\infty} \left(R_4^n \mathbf{A}_n^I + R_4^{-n} \mathbf{B}_n^I \right) \frac{2}{\beta} gkni(k, n, \theta_i, \beta) + \left(R_4^n \mathbf{C}_n^I + R_4^{-n} \mathbf{D}_n^I \right) \frac{2}{\beta} fgni(k, n, \theta_i, \beta) \quad (\text{A19})$$

$$\mathbf{A}_0^j + \ln(R_5) \mathbf{B}_0^j = \mathbf{A}_0^j + \ln(R_5) \mathbf{B}_0^j - \frac{\mu_0}{4} R_5^2 J_0^j + \sum_{m=1,2}^{\infty} \left(R_5^{m\frac{\pi}{\delta}} \mathbf{C}_m^j + R_5^{-m\frac{\pi}{\delta}} \mathbf{D}_m^j + \frac{\mu_0}{(m\frac{\pi}{\delta})^2 - 4} R_5^2 J_m^j \right) \frac{2}{m\pi} \frac{\delta}{\beta} \cos\left(\frac{m\pi}{2}\right) \sin\left(\frac{m\pi}{2} \frac{\beta}{\delta}\right) \quad (\text{A20})$$

$$R_5^{k\frac{\pi}{\delta}} \mathbf{C}_k^j + R_5^{-k\frac{\pi}{\delta}} \mathbf{D}_k^j = \frac{2}{\beta} \sum_{m=1,2}^{\infty} \left(R_5^{m\frac{\pi}{\delta}} \mathbf{C}_m^j + R_5^{-m\frac{\pi}{\delta}} \mathbf{D}_m^j + \frac{\mu_0}{(m\frac{\pi}{\delta})^2 - 4} R_5^2 J_m^j \right) Fmk(m, k, \beta, \delta) \quad (\text{A21})$$

$$\frac{1}{R_5} \mathbf{B}_0^j - \frac{\mu_0}{2} R_5 J_0^j = \frac{\beta}{\delta} \frac{1}{R_5} \mathbf{B}_0^j \quad (\text{A22})$$

$$R_5^{m\frac{\pi}{\delta}} m \frac{\pi}{\delta} \mathbf{C}_m^j + R_5^{-m\frac{\pi}{\delta}} \left(-m \frac{\pi}{\delta} \right) \mathbf{D}_m^j + \frac{\mu_0 2 R_5 J_m^j}{(m\frac{\pi}{\delta})^2 - 4} = \frac{1}{R_5} \mathbf{B}_0^j \frac{4}{m\pi} \cos\left(\frac{m\pi}{2}\right) \sin\left(\frac{m\pi}{2} \frac{\beta}{\delta}\right) + \sum_{k=1,2}^{\infty} \left(R_5^{k\frac{\pi}{\delta}-1} k \frac{\pi}{\delta} \mathbf{C}_k^j + R_5^{-k\frac{\pi}{\delta}-1} \left(-k \frac{\pi}{\delta} \right) \mathbf{D}_k^j \right) \frac{2}{\delta} Fmk(m, k, \beta, \delta) \quad (\text{A23})$$

$$\frac{1}{R_6} \mathbf{B}_0^j - \frac{\mu_0}{2} R_6 J_0^j = 0 \quad (\text{A24})$$

$$R_6^{m\frac{\pi}{\delta}} m \frac{\pi}{\delta} \mathbf{C}_m^j + R_6^{-m\frac{\pi}{\delta}} \left(-m \frac{\pi}{\delta} \right) \mathbf{D}_m^j + \frac{\mu_0 2 R_6 J_m^j}{(m\frac{\pi}{\delta})^2 - 4} = 0 \quad (\text{A25})$$

References

1. Sajjad, H.; Si, M.; Majid, F.; Aaron, Z.; Behrooz, B. Virtual Synchronous Generator Versus Synchronous Condensers: An Electromagnetic Transient Simulation based Comparison. *CIGRE Sci. Eng.* **2022**, *24*, 2022.
2. Cho, H.W.; Bang, T.K.; Lee, J.I.; Shin, K.H.; Lee, H.S.; Hur, J.S.; Haran, K.S. Design and Preliminary Experiments of a Rotating Armature Partial Superconducting Air-Core Generator. *IEEE Trans. Appl. Supercond.* **2022**, *32*, 5202505. [CrossRef]
3. Soleimani, H.; Habibi, D.; Ghahramani, M.; Strengthening, A.A. Power Systems for Net Zero: A Review of the Role of Synchronous Condensers and Emerging Challenges. *Energies* **2024**, *17*, 3291. [CrossRef]

4. Nedd, M.; Booth, C.; Bell, K. Potential Solutions to the Challenges of Low Inertia Power Systems with a Case Study Concerning Synchronous Condensers. In Proceedings of the 2017 52nd International Universities Power Engineering Conference (UPEC), Heraklion, Greece, 28–31 August 2017.
5. Hadavi, S.; Saunderson, J.; Sani, A.M.; Bahrani, B. A Planning Method for Synchronous Condensers in Weak Grids Using Semi-Definite Optimization. *IEEE Trans. Power Syst.* **2023**, *38*, 1632–1641. [CrossRef]
6. Nguyen, H.T.; Yang, G.; Nielsen, A.H.; Jensen, P.H. Combination of Synchronous Condenser and Synthetic Inertia for Frequency Stability Enhancement in Low-Inertia Systems. *IEEE Trans. Sustain. Energy* **2019**, *10*, 997–1005. [CrossRef]
7. Xu, G.; Yuan, Z.; Zhu, X.; Hu, P.; Liu, W.; Li, W.; Zhan, Y.; Zhao, H. Influence of Rotor Damping Bars on Rotor Temperature Rise of Synchronous Condenser After Single-Phase Short-Circuit Fault. *IEEE Trans. Ind. Appl.* **2023**, *59*, 5832–5841. [CrossRef]
8. Tao, Z.; Wang, T.; Cai, D.; Chen, R. Research on Reactive Power Optimization of Synchronous Condensers in HVDC Transmission Based on Reactive Power Conversion Factor. *Energies* **2024**, *17*, 4294. [CrossRef]
9. Teleke, S.; Abdulahovic, T.; Thiringer, T.; Svensson, J. Dynamic Performance Comparison of Synchronous Condenser and SVC. *IEEE Trans. Power Deliv.* **2008**, *23*, 1606–1612. [CrossRef]
10. Stein, J. *Turbine-Generator Topics for Power Plant Engineers*; EPRI: Palo Alto, CA, USA, 2014.
11. Marken, P.E.; Depoian, A.C.; Skliutas, J.; Verrier, M. Modern Synchronous Condenser Performance Considerations. In Proceedings of the 2011 IEEE Power and Energy Society General Meeting, Detroit, MI, USA, 24–28 July 2011.
12. Kim, S.-M.; Kim, T.-S.; Jung, W.-S.; Nguyen, M.-D.; Kim, Y.-J.; Shin, K.-H.; Choi, J.-Y. Electromagnetic analysis of permanent magnet-assisted synchronous reluctance motor based on magnetic equivalent circuit. *AIP Adv.* **2024**, *14*, 025229. [CrossRef]
13. Lubin, T.; Mezani, S.; Rezzoug, A. 2-D Exact Analytical Model for Surface-Mounted Permanent-Magnet Motors with Semi-Closed Slots. *Magnetics. IEEE Trans. Magn.* **2011**, *47*, 479–492. [CrossRef]
14. Sprangers, R.L.J.; Paulides, J.J.H.; Gysen, B.L.J.; Lomonova, E.A. Magnetic Saturation in Semi-Analytical Harmonic Modeling for Electric Machine Analysis. *IEEE Trans. Magn.* **2016**, *52*, 1–10. [CrossRef]
15. Shin, K.-H.; Park, H.-I.; Cho, H.-W.; Choi, J.-Y. Analytical Calculation and Experimental Verification of Cogging Torque and Optimal Point in Permanent Magnet Synchronous Motors. *IEEE Trans. Magn.* **2017**, *53*, 1–4. [CrossRef]
16. Nguyen, M.-D.; Kim, S.-M.; Shin, H.-S.; Shin, K.-H.; Phung, A.-T.; Choi, J.-Y. Maximizing the output power of magnetically geared generator in low-speed applications using subdomain modeling and particle swarm optimization. *AIP Adv.* **2024**, *14*, 025117. [CrossRef]
17. Nguyen, M.-D.; Jung, W.-S.; Hoang, D.-T.; Kim, Y.-J.; Shin, K.-H.; Choi, J.-Y. Fast Analysis and Optimization of a Magnetic Gear Based on Subdomain Modeling. *Mathematics* **2024**, *12*, 2922. [CrossRef]
18. Hoang, D.-T.; Nguyen, M.-D.; Woo, J.-H.; Shin, H.-S.; Shin, K.-H.; Phung, A.-T.; Choi, J.-Y. Volume optimization of high-speed surface-mounted permanent magnet synchronous motor based on sequential quadratic programming technique and analytical solution. *AIP Adv.* **2024**, *14*, 025319. [CrossRef]
19. Nguyen, M.-D.; Kim, S.-M.; Lee, J.-I.; Shin, H.-S.; Lee, Y.-K.; Lee, H.-K.; Shin, K.-H.; Kim, Y.-J.; Phung, A.-T.; Choi, J.-Y. Prediction of Stress and Deformation Caused by Magnetic Attraction Force in Modulation Elements in a Magnetically Geared Machine Using Subdomain Modeling. *Machines* **2023**, *11*, 887. [CrossRef]
20. Nguyen, M.-D.; Woo, J.-H.; Shin, H.-S.; Lee, Y.-K.; Lee, H.-K.; Shin, K.-H.; Phung, A.-T.; Choi, J.-Y. Thermal analysis and experimental verification of permanent magnet synchronous motor by combining lumped-parameter thermal networks with analytical method. *AIP Adv.* **2023**, *13*, 025140. [CrossRef]
21. Nguyen, M.-D.; Hoang, D.-T.; Kim, S.-M.; Jung, W.-S.; Shin, K.-H.; Kim, Y.-J.; Choi, J.-Y. Nonlinear Modeling and Analysis Considering Coupling Stator Flux of Wound-Rotor Synchronous Motors. In Proceedings of the 2024 International Conference on Electrical Machines (ICEM), Torino, Italy, 1–4 September 2024; pp. 1–7. [CrossRef]

Disclaimer/Publisher’s Note: The statements, opinions and data contained in all publications are solely those of the individual author(s) and contributor(s) and not of MDPI and/or the editor(s). MDPI and/or the editor(s) disclaim responsibility for any injury to people or property resulting from any ideas, methods, instructions or products referred to in the content.

Article

Mathematical Modelling and Optimisation of Operating Parameters for Enhanced Energy Generation in Gas Turbine Power Plant with Intercooler

Anthony O. Onokwai ^{1,2,3,*}, Udochukwu B. Akuru ^{1,*} and Dawood A. Desai ²

¹ Department of Electrical Engineering, Tshwane University of Technology, Pretoria 0183, South Africa

² Department of Mechanical and Mechatronics Engineering, Tshwane University of Technology, Pretoria 0183, South Africa; desaida@tut.ac.za

³ Department of Mechanical Engineering, Pan Atlantic University, Lekki 105101, Nigeria

* Correspondence: onokwaiao@tut.ac.za (A.O.O.); akuruub@tut.ac.za (U.B.A.)

Abstract: This study developed an optimal model for gas turbine power plants (GTPPs) with intercoolers, focusing on the challenges related to power output, thermal efficiency and specific fuel consumption. The study combined response surface methodology (RSM) and central composite design (CCD) with advanced metaheuristic algorithms, including ANFIS, ANFIS PSO and ANFIS GA, to model nonlinear interactions of key parameters, including the pressure ratio, ambient temperature, turbine inlet temperature and the effectiveness of the intercooler. Optimal values of thermal efficiency (47.8%), power output (165 MW) and specific fuel consumption (0.16 kg/kWh) were attained under conditions of a pressure ratio of 25, an ambient temperature 293 K, a turbine inlet temperature of 1550 K and 95% intercooler effectiveness. The RSM, being the initial model, was able to predict but lacked precision when compared with the nonlinear influences that were modelled by ANFIS PSO and ANFIS GA, with power output, thermal efficiency and specific fuel consumption (sfc) having corresponding R^2 values of 0.979, 0.987 and 0.972. The study demonstrated the potential of extending metaheuristic algorithms to provide sustainable solutions to energy system problems and reduced emissions through gas turbine power plant (GTPP) optimisation.

Keywords: central composite design (CCD); gas turbine power plant (GTPP); intercooler; modelling; optimisation; power output; response surface methodology (RSM); specific fuel consumption; thermal efficiency

MSC: 37A60; 70-08; 70-10; 76-10; 74P10

1. Introduction

The ever-increasing electricity consumption in the world makes it imperative to push for more efficient power generation technologies [1–3]. The International Energy Agency (IEA) also highlighted that global electricity demand is predicted to increase more than 50% over the subsequent quarter-century, mainly from developing countries. This has placed huge pressure on energy systems to improve efficiency, minimise fuel use and reduce emissions [4–6]. Gas turbines, because of their flexibility, high ratio of power per output and lower pollution, continue to attract interest in power generation. However, conversion and operational losses due to inherent thermodynamic inefficiencies of heat-to-electricity conversion and other factors continue to pose major challenges [7,8]. These inefficiencies

are most felt in areas such as Africa, where energy demand is increasing. Yet, proper solutions that will have minimal impact on the environment are desired [9,10].

Gas turbines (GT) work on the Brayton cycle, a thermodynamic cycle in which air is compressed, and then, fuel is added and ignited to produce energy [11]. In gas-turbine performance, relevant aspects include pressure ratio, which compares intake pressure to exhaust pressure; ambient temperature, affecting combustion and efficiency; turbine inlet temperature, associated with a high-pressure turbine or HP turbine; and the intercooler, employed to cool the compressed air in an intercooler recuperative system for less work on the compressor. While there is rigorous research dedicated to improving individual components of gas turbine systems, a vast majority of suggested approaches do not account for the fact that these components are dependent upon the interrelation of multiple variables. A holistic approach is necessary to fully exploit the potential efficiency gains of gas turbine systems, especially in light of increasing global energy demands.

Empirical research has explored various aspects of gas turbine optimisation, with mixed successes. Ref. [12] investigated combined cycles for improving gas turbine thermal efficiency, concluding that integrating steam cycles significantly enhances overall system performance. Ref. [13] researched the impact of cooling technologies on the operation of gas turbines in hot climatic regions, like the Middle Eastern regions, finding that evaporative cooling systems enhance power output by reducing the intake air temperature. Ref. [14] conducted a comprehensive review of GT power plants, focusing on modelling and simulating GT performance. The review examined both simple and complex cycle GT power plants, including two-shaft, regenerative, reheat and intercooler configurations. Particular attention was given to how operating conditions affect GT performance, with an emphasis on both simple and complex cycles. The study highlighted performance improvements for GT power plants, particularly in varying ambient conditions and more advanced configurations.

Ref. [15] explored the impact of environmental conditions on gas turbine performance in hot, arid climates, focusing on Karbala. Using Aspen HYSYS, they simulated a fogging air intake cooling system. The results showed that cooling the intake air increased the net power and thermal efficiency and reduced fuel consumption and the heat rate by 7%, especially when temperatures exceeded 30 °C and humidity was below 40%.

In the work of [16], a theoretical analysis of the effect of pressure ratio and the ambient temperature on the efficiency of the gas turbine was presented. It was deduced that higher pressure ratios yield better results, although how ambient temperature affects the efficiency of the turbine is still unclear. Ref. [17] analysed how turbine inlet temperature and the effectiveness of the intercooler affected the energy efficiency. The results showed that, with higher values of turbine inlet temperatures, the overall thermal efficiency of the cycles increases, but the above study was constrained by being a limited parameter study that only incorporated two variables at a time.

Current research in micro gas turbines includes hydrogen-enriched gaseous fuel injection and the use of machine learning for the optimisation of compatibility, while the efficiency of combustion processes signals increased thrust at lower emissions. Hydrogen is a high-energy-density fuel that has a high flame speed, to the extent that flame stability is enhanced, blow out is reduced and the problems associated with partial combustion under lean burn conditions are appropriately addressed [18]. CFD simulations have been used to enhance the fuel injector's hydrogen distribution, though challenges like backfiring risks still remain [19]. The performance prediction of micro gas turbines (MGTs) has been enhanced by the use of machine-learning (ML) techniques, especially long short-term memory (LSTM) networks, for various parameters like turbine inlet temperature and the fuel flow rates. These models effectively accommodate dynamic parameter conditions

and enhance thermal performance while decreasing specific fuel consumption rates. Also, microalgae-based fuels have emerged as a renewable source of energy, which reduces the emission of CO₂ and ensures optimum performance. LSTM networks address the variability of fuel properties, such as viscosity and calorific value, for improved operation and fuel blend [20].

Furthermore, gradient descent algorithms enhance optimisation for the MGT systems. Variant techniques like stochastic gradient descent and adaptive methods (Adagrad, Adam, RMSprop, etc.) enhance the convergence. The integration of gradient descent with metaheuristic optimisation such as PSO further handles both non-convex and multi-modal cost surfaces, optimising vital turbine parameters for cleaner and greater efficiency in energy generation [21].

The response surface methodology (RSM) is a strong technique that is intended for the investigation of systems characterised by more than one operating parameter, conveys the relationship of the influencing factors with the performance characteristics and establishes equations that quantify the correlation between the input variables and output responses. RSM is an optimisation model through which empirical models and numerical optimisation are employed to predict the effect of certain conditions on particular responses [18].

Ref. [19] investigated the interaction effect of pressure ratio and turbine inlet temperature on the performance of a gas turbine using RSM. While the study validated the inputs suggesting that it was possible to achieve as much as a 30% improvement in the thermal efficiency when both parameters were optimised, the work did not address other factors, such as ambient temperature and intercooler efficiency for practical applications.

Ref. [20] extended the study by applying RSM for the improvement of thermal and exergy efficiency of gas turbines but is limited in terms of the number of operational parameters. The research only considered pressure ratio and turbine inlet temperature, factors that, although crucial, do not capture the synergy between the multi-number operation parameters that form the basis of the efficiency of the gas turbine.

The research carried out in [21] established a survey concerning the effect of different operating parameters on gas turbine efficiency. Ref. [21] stated that, while the pressure ratio, ambient temperature and turbine inlet temperature can be analysed individually, optimising them using RSM is an area that has not extensively been explored.

Notwithstanding, RSM still has a limitation in handling complex relationships between responses and control factors. For instance, although RSM has capabilities in establishing polynomial regression equations and optimisation within a specific domain of the variables, it is not efficient in capturing the high nonlinearity and multimodality of the gas turbines. These are interactions between variables such as turbine inlet temperature and pressure ratio, where high levels of these interactions may be synergistic or antagonistic in nature. Thus, they cannot solely be modelled using the standard RSM. Further, the RSM is less effective when the independent variables are discrete or when the variables interact in such a way as to produce noncontinuous responses. For such cases, meta-heuristic or optimisation techniques like genetic algorithm (GA), particle swarm optimisation (PSO), ant colony optimisation (ACO) and others promise more effective and efficient solutions than the standard methods in the multi-dimensional and non-linear optimisation problems. When working with gas turbine systems, which are characterised by complex thermal and mechanical interactions, these algorithms are able to locate global optima better than the RSM [22].

Studied works have demonstrated metaheuristic algorithms solve combinatorial optimisation problems in an efficient manner, if the decision variables are discrete instead of continuous, by converting the continuous values into binary ones and taking candidate solution vectors [23,24]. Moreso, metaheuristic optimisation algorithms are applied to solv-

ing numerous difficulties, with an established impact in engineering, finance, healthcare, telecommunications and computing [25]. These techniques do not specifically address the main problems but use iterative search methods to adjust to desired solutions where necessary, especially for solving (nondeterministic polynomial time) NP-hard issues in energy generation, production management and bioinformatics [26]. In the past decades, metaheuristic algorithms have been regarded as relevant solution providers for NP problems that need the high power of exponential steps for achieving versatile and beneficial optimisation approaches for complex issues. Furthermore, metaheuristic optimisation algorithms have indicated the potential to solve most problems found in gas turbine power plants and hydropower generation, defined as nonlinear and multi-modal optimisation problems [27].

Ref. [28] developed an algorithm to compute greenhouse control with model predictive control (MPC) embedded with PSO. The aim was to achieve the highest possible crop output with the lowest possible expenditure on energy. The results showed that the proposed PSO-MPC algorithm has outperformed the rule-based and GA. This was supported by the results of experiments indicating the feasibility of using the proposed methods for the further enhancement of energy and yield efficiency in agriculture.

Ref. [29] analysed the exergy, exergoeconomic and exergoenvironmental multiobjective optimisation of a gas turbine cycle using multiobjective PSO. The results showed that raising the compressor's pressure ratio and the turbine's inlet temperature decreases CO₂ emissions and enhances energy efficiency. However, the gains level off as the levels increase. The analysis considers cost, time and environmental considerations but is carried out under certain assumptions, has a limited range, uses static economic variables and does not consider lifecycle costing. It was concluded that exit strategies for affordable, sustainable energy design have potential and that these results warrant future study under practical conditions.

In ref. [30], PSO and GA were employed for the optimisation of the economic and environmental performance of power generation. The results established that PSO had a faster convergence to the best solution and lower costs and emission levels compared with GA. The study utilised real-world data and validation using IEEE test systems. Limitations include the exclusion of some real constraints, such as line losses and areas that cannot be supplied. However, the opportunity for metaheuristics to effectively dispatch is outlined in the study, as well as recommendations for greater reality and enhanced algorithms.

The current study combines RSM with metaheuristic optimisation algorithms such as the adaptive neuro-fuzzy inference system (ANFIS), ANFIS with GA and ANFIS with PSO (ANFIS-PSO) to investigate the non-linear correlation of operating conditions and responses in the gas turbine power plant, including power output, thermal efficiency and specific fuel consumption. This work establishes RSM and metaheuristic algorithms as methods for developing suitable mathematical models for improving gas turbine performance and offering practical implications for the industry. There is promise for concurrent optimisation approaches and techniques to optimise performance and design, as well as create new processes. This work not only contributes in response to energy problems and encourages sustainable development of the world's energy systems but also offers clear modelling that can be implemented by stakeholders, especially in the developing world, where the generation of energy is a core determinant of economic growth.

2. Materials and Methods

2.1. Overview of the Power Gas Plant

A cycle model of a gas turbine power plant with an effect intercooler, along with a detailed parametric study, is presented in this paper. The effects of parameter (design and operation conditions) on the power output, compression work, specific fuel consumption

and thermal efficiency are evaluated. In this study, the implementation of intercooling increases the power-generating efficiency of the suggested gas turbine power plant when compared to the non-intercooled gas turbine power plant configurations. The intercooler gas turbine cycle is analysed, and a new approach for improvement of their thermodynamic performances based on the first law of thermodynamics is presented. Different affected parameters are simulated, including different compressor pressure ratios, ambient temperatures, air–fuel ratios, turbine inlet temperature, and cycle peak temperature ratios were analysed. The obtained results are presented and analysed. Further increasing the cycle peak temperature ratio and total pressure ratio can still improve the performance of the intercooled gas turbine cycle.

Intercoolers are an integral part of the gas turbine power plant. This facility is situated in a region with rich natural gas and river resources so the turbines will be highly operational. The operational data used in this study were collected from the GT section operator's manual logbook containing daily reading. All of these recorded data were put for analysis and the principles of boundaries, and the second law of thermodynamics was applied. The gas turbine power plant utilises the Brayton cycle, and its constituent parts are the compressor, combustion chamber, gas turbine and generator (load), as shown in Figure 1. The interconnections of these components guarantee a fine and optimal operation of the components, which ensures a sophisticated and efficient operation of the gas turbine power plant [31], the optimisation of the resources and compliance with the gas turbine power station on the fundamentals of thermodynamics for garnering the highest effective utilisation of the available resources [32].

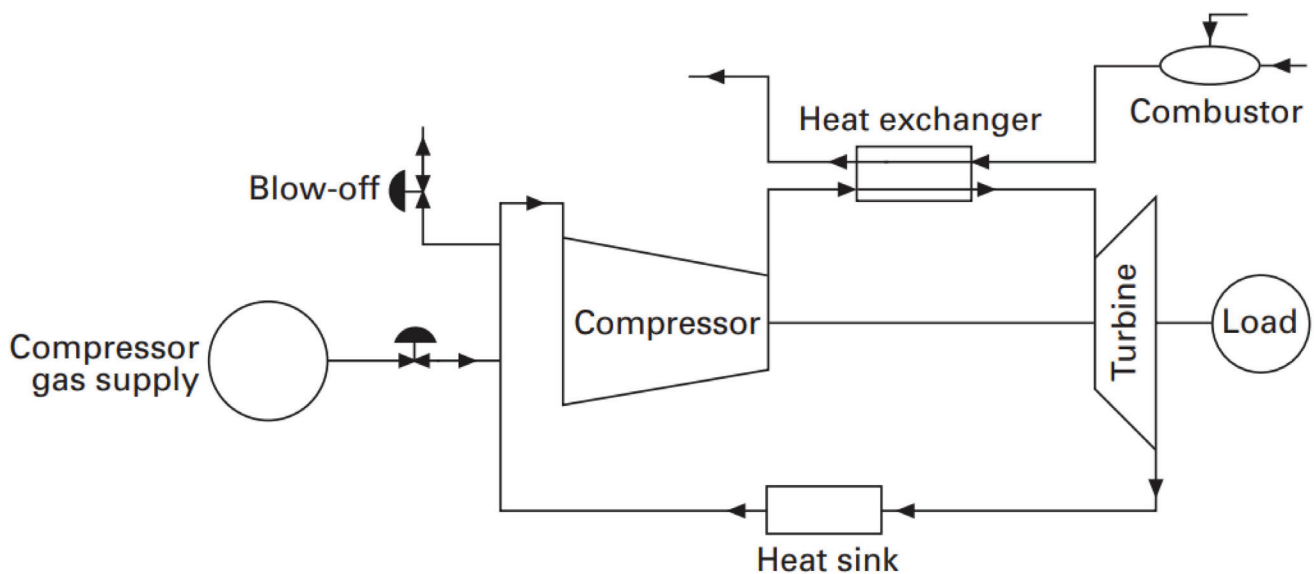


Figure 1. The schematic illustration of the gas turbine plant.

2.2. Modelling and Optimisation Process

The experimental design was developed using the design of experiment (DOE) and the central composite design (CCD) for both single and multiple combinations of the operating parameters. This was followed by the use of the RSM to estimate the responses such as power output (P), specific fuel consumption (sfc) and thermal efficiency (η). Under these experimental conditions, four independent parameters of the gas power plant were identified and optimised, namely the pressure ratio (r_p), ambient temperature (T_1), turbine inlet temperature (T_3) and intercooler effectiveness (ϵ). The rationale for CCD stemmed from its multiple strengths, namely time and cost perspectives, as well as the sensitivity and accuracy of the calculated results to various operating conditions. Also, one of the

advantages of using CCD is that the method ensures a minimum number of test runs [33]. Before applying the RSM, the experimental work, which was used in the present investigation, was selected from the database of the Design Expert software version 7.0.3 (Stat-Ease). after thoughtful consideration.

The study involved three responses in CCD (P , sfc and η) and four operating parameters (r_p , T_1 , T_3 and ϵ). Each varied at three levels, namely high, moderate and low, and were denoted as +1, 0 and −1. The modelling and optimisation of operational factors occurred in two stages. The initial step involved establishing a mathematical relationship between the responses and independent factors using Equation (1) [34]

$$y = f(x_1, x_2, x_3, \dots \dots \dots x_n) \quad (1)$$

where y is the response, and f is the unknown function of response.

$x_1, x_2, x_3, \dots \dots \dots x_n$ are known as independent factors, and n is the number of independent factors.

The independent factors were considered to be continuous and subject to control within the experiments with minimal errors, aligning with the insights presented by [35]. In the subsequent phase, the estimation of coefficients in a mathematical model took place, employing a second-order model or quadratic equation. This mathematical model serves the purpose of predicting, optimising, and discerning the primary interaction factors, namely the independent factors, and elucidating their impact on gas power plant efficiency, as depicted in Equation (2) and as stated by [36]

$$y = \beta_0 + \sum_{i=1}^k \beta_i x_i + \sum_{i=1}^k \beta_{ii} x_i^2 + \sum_{i=1}^k \sum_{j>1}^k \beta_{ij} x_i x_j + \epsilon_i \quad (2)$$

where x_i and x_j are coded independent factors, and y denotes thermal efficiency, power output and specific fuel consumption, recognised as the dependent variable or response. The coefficients include β_0 as the constant term, β_i and β_{jj} for the linear and quadratic effects, respectively, and β_{ij} for interaction effects. k signifies the number of independent factors, while ϵ_i accounts for the random error inherent in the experiment.

The coefficient of determination, R^2 , serves as an indicator of the polynomial's fit quality. The model's performance was assessed through a thorough analysis of the results using an ANOVA. The selection of predetermined independent factors for the experiments was grounded in their reported impact on gas power plant efficiency.

The data derived from the RSM are underpinned by 30 experimental runs, as outlined in Equation (3) [37].

$$\begin{aligned} N &= 2^k + 2k + n_c \\ &= 2^4 + 2(4) + 6 = 30 \end{aligned} \quad (3)$$

n_c signifies the repeated number of experiments at the centre points. The total comprises the conventional $2k$ factorial, centred around the origin. This design allows for the generation of a quadratic number of independent factors, as elucidated.

2.3. Thermodynamic Modelling of the Gas Power Plant

The enhancement of the network output in a gas turbine cycle can be achieved by mitigating the negative work, specifically the compressor work. One approach for minimising compression work, as outlined by [38], involves employing a multistage compression process with intercooling. The gas power plant encompasses components such as a low-pressure compressor (LPC), an intercooler, a high-pressure compressor (HPC), a combustion chamber and a turbine [39]. Intercooling is an important feature of gas turbine power plants in which compressed air is cooled between compression stages before entering the next

stage of compression. Intercooling lowers the temperature and specific volume of the air, causing less work to be required for further compression. This leads to a substantially greater plant net-power output. Since compression is generally the most energy-demanding process in a gas turbine, the reduction in heat buildup through intercooling reduces the overall workload, hence enhancing the efficiency of the entire system. Specifically, the intercooler, which is a heat exchanger, transfers heat to a cooling medium, which reduces the work of compression. This reduction is shown in the form of a smaller area under the pressure–volume (p–V) curve and, hence, leads to the enhancement of the overall net power output. Intercooling also cools the high-pressure compressor inlet temperature and helps to preserve the efficiency and lifespan of important components of the gas turbine, which is crucial for uninterrupted long-term operation. Implementing intercooling can significantly boost the power output of a gas turbine, cost of operation and overall plant performance, which are vital to modern energy systems [40].

For a constant compression ratio, an elevated inlet temperature corresponds to an augmented demand for compression work, and conversely, a lower inlet temperature reduces this requirement. The thermodynamic processes integral to multistage intercooled compression are delineated in Figure 2.

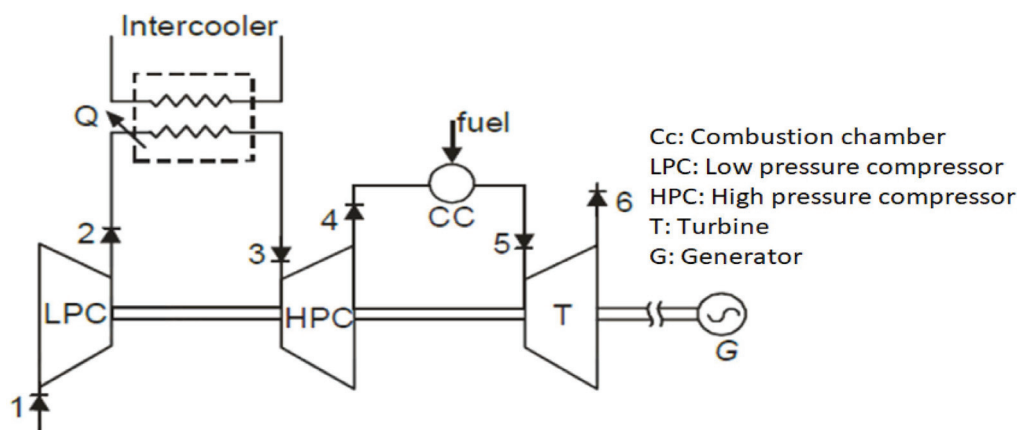


Figure 2. Schematic diagram of a gas turbine cycle featuring intercooling [28].

In the initial stage, air compression transpires in the LPC. The compressed air, exiting the LPC at state '2', proceeds to the HPC and undergoes cooling in the intercooler. Here, the compressed air temperature diminishes to state '3' at a constant pressure. In the case of perfect intercooling, states '3' and '1' share identical temperatures, an indication of compression in two stages. As a result of this two-stage compression, the compressed and cooled air exhibits a reduced volume. This enables the compression to be conducted in a more compact compressor, thereby necessitating less energy. Consequently, the introduction of an intercooler leads to a decrease in the work required for compression. While intercooling amplifies the net output, it is essential to acknowledge that the heat supplied, when intercooling is present, surpasses that in a single-stage compression scenario. Therefore, although the net output experiences an upswing, thermal efficiency tends to decline due to the added heat supply.

The tangible impact of intercooling on compression work is visually evident in the p–V diagram, exemplified by area 2342 in Figure 3a. Area 2343' represents the work saved due to intercooling between the compression stages, as seen in Figure 3a [38].

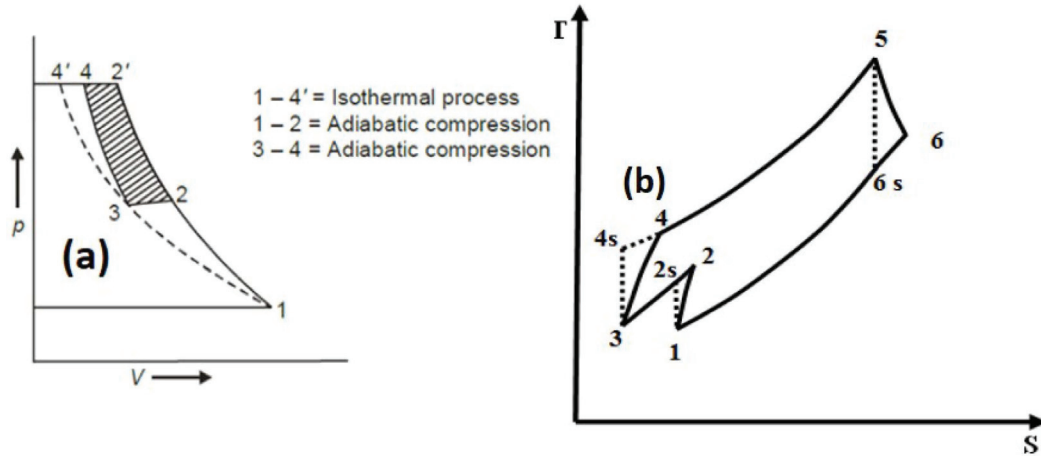


Figure 3. (a) p-V diagram. (b) T-S diagram.

2.4. Analysis of Gas Turbines Power Plant with Intercooler

This study focuses on a regenerative gas plant that incorporates both reheating during the expansion cycle and intercooling during the compression cycle. The synergy of these processes results in a noteworthy enhancement of both network output and thermal efficiency.

The intercooler effectiveness is denoted as ε , the compressor efficiency as η_c and the turbine efficiency as η_t . Both the ideal and actual processes are illustrated with dashed and full lines, respectively, in the T-S diagram in Figure 3b. These parameters, expressed in terms of temperature (Equations (4) and (5)), are defined according to [41]

$$\eta_c = \frac{T_{2s} - T_1}{T_2 - T_1} = \eta_{clp}; \quad \eta_{chp} = \frac{T_{4s} - T_3}{T_4 - T_3} \quad (4)$$

$$\eta_t = \frac{T_5 - T_6}{T_5 - T_{6s}}; \quad x = \frac{T_2 - T_3}{T_2 - T_1} \quad (5)$$

Here, η_{clp} and η_{chp} denote the efficiency of the low- and high-pressure compressors, respectively.

The work necessary to operate the compressor is expressed in Equation (6):

$$W_c = c_{pa} T_1 \left(\frac{r_p^{\frac{\gamma_a - 1}{\gamma_a}}}{\eta_c} - 1 \right) \left[2 + (1 - x) \left(\frac{r_p^{\frac{\gamma_a - 1}{\gamma_a}}}{\eta_c} - 1 \right) \right] \quad (6)$$

Ref. [42]'s method was used to calculate the specific heat of the air, as shown in Equation (7).

$$c_{pa} = 1.019 \times 10^3 - 0.138 T_a + 1.984 \times 10^{-4} T_a^2 + 4.240 \times 10^{-7} T_a^3 - 3.7631984 \times 10^{-10} T_a^4 \quad (7)$$

The turbine's output was determined using Equations (8) and (9), as suggested by [43].

$$W_t = c_{pg} T_5 \left[\eta_t \left(1 - \frac{1}{\left(r_p^2 \right)^{\frac{\gamma_g - 1}{\gamma_g}}} \right) \right] \quad (8)$$

$$W_t = c_{pg} T_{TIT} \left[\eta_t \left(1 - \frac{1}{\left(r_p^2 \right)^{\frac{\gamma_g - 1}{\gamma_g}}} \right) \right] \quad (9)$$

where $T_{TIT} = T_5$ is referred to as the turbine inlet temperature.

The network was determined using Equation (10). The network compares the generated energy with compression and other losses, and the net output depends on the pressure ratio, ambient temperature and effectiveness of the intercooler. Decreasing the level of compression work, through intercooling or optimal pressure ratios, increases the energy that is available for power generation.

$$W_n = c_{pg} T_{TIT} \left[\eta_t \left(1 - \frac{1}{\left(r_p^2 \right)^{\frac{\gamma_g - 1}{\gamma_g}}} \right) \right] - c_{pa} T_1 \left(\frac{r_p^{\frac{\gamma_a - 1}{\gamma_a}} - 1}{\eta_c} \right) \left[2 + (1 - x) \left(\frac{r_p^{\frac{\gamma_a - 1}{\gamma_a}} - 1}{\eta_c} \right) \right] \quad (10)$$

Since the combustion chamber functions on the principle of heat transfer from fuel to air, Equation (11) can be simplified to reflect this specific scenario. In essence, all the heat energy provided by the burning fuel is absorbed by the incoming air.

$$Q_{add} = c_{pgm} \left[T_{IT} - T_1 + T_2 \left(\frac{r_p^{\frac{\gamma_a - 1}{\gamma_a}} - 1}{\eta_c} \right) \left[(2 - x) + (1 - x) \left(\frac{r_p^{\frac{\gamma_a - 1}{\gamma_a}} - 1}{\eta_c} \right) \right] \right] \quad (11)$$

where c_{pgm} is the mean specific heat capacity at constant pressure for the gas mixture (kJ/kg·K).

Equation (10) was used to determine the power output, as stated by [44].

$$Power = m_a \cdot W_{net} \quad (12)$$

The air-to-fuel ratio (AFR) was calculated based on Equation (13) [14].

$$AFR = \frac{LHV}{Q_{add}} \quad (13)$$

Additionally, *sfc* was determined through:

$$sfc = \frac{3600}{(AFR \cdot W_{net})} \quad (14)$$

where m_a is denoted as the air mass flow rate, LHV represents the higher heating value and AFR signifies the air–fuel ratio.

The thermal efficiency of the cycle was obtained using Equation (15) and was stated by [14].

$$\eta_{th} = \frac{c_{pg} T_{TIT} \left[\eta_t \left(1 - \frac{1}{\left(r_p^2 \right)^{\frac{\gamma_g - 1}{\gamma_g}}} \right) \right] - c_{pa} T_1 \left(\frac{r_p^{\frac{\gamma_a - 1}{\gamma_a}} - 1}{\eta_c} \right) \left[2 + (1 - x) \left(\frac{r_p^{\frac{\gamma_a - 1}{\gamma_a}} - 1}{\eta_c} \right) \right]}{c_{pgm} \left[T_{IT} - T_1 + T_2 \left(\frac{r_p^{\frac{\gamma_a - 1}{\gamma_a}} - 1}{\eta_c} \right) (2 - x) + (1 - x) \left(\frac{r_p^{\frac{\gamma_a - 1}{\gamma_a}} - 1}{\eta_c} \right) \right]} \quad (15)$$

The specific heat of the gas is 1.148, and its specific heat ratio is 1.326. As for air, its specific heat is 1.005 kJ/kg·K, with a specific heat ratio of 1.38.

This investigation looks at refining the operational variables in a gas turbine power plant utilising an intercooler while employing the RSM in conjunction with the CCD. The purpose is to optimise energy creation and raise the thermal and exergy efficiencies while lowering the specific fuel demands. Here, we present important procedures carried out during the study, including establishing a model and determining the experimental factors.

2.5. Design of ANFIS Models for Analysis of Gas Turbines Power Plant with Intercooler

2.5.1. ANFIS

The core of the methodology begins with ANFIS, a model that integrates neural network learning with fuzzy logic. ANFIS can effectively model the complex, nonlinear relationships between the gas turbine's operating parameters such as pressure ratio, intercooler effectiveness and ambient and turbine temperatures and responses such as power output, thermal efficiency and specific fuel consumption by adapting its structure based on data patterns. This adaptability is essential in gas turbine power plant settings, where environmental and operational conditions vary widely [45]. Using historical data, ANFIS learns to associate different combinations of operating parameters, such as pressure ratio, ambient and turbine temperatures with specific power output, thermal efficiency and specific fuel consumption levels. The model does this by generating fuzzy if-then rules that map input variables to output predictions.

The input/output membership functions describe how inputs (e.g., pressure ratio, ambient temperature, turbine inlet temperature and intercooler effectiveness) are related to the outputs, such as power output, thermal efficiency and sfc. The inputs are assigned degrees of truth by membership functions building up fuzzy rules such as "If pressure ratio is high then thermal efficiency is high". Rule generation combines input combinations to find out the probable outputs; the model adjusts the parameters while using the training data to reduce the error margin. Through incorporating these operational parameters, ANFIS helps to model interactions that result in improvements in the prediction accuracy of key performance aspects, such as output power, thermal efficiency and sfc of gas turbine power plants under diverse conditions. These rules are underpinned by membership functions that assign degrees of truth to each condition, making ANFIS particularly adept at capturing the nuanced dynamics within a gas turbine power plant. During training, ANFIS uses optimisation algorithms to iteratively refine these rules and membership functions to minimise prediction error. ANFIS applies both fuzzy logic and artificial neural networks to model non-linear relationships in data sets of gas turbine power plants.

However, while ANFIS is powerful in adapting to data, its reliance on initial parameters can limit accuracy. The criterion influencing ANFIS's accuracy is that the initial membership functions and the rule parameters serve as model parameters. Such parameters are generally predefined based on heuristic or domain-specific knowledge. If the initial parameters are not well chosen or do not contain an adequate level of variance for the equations in the data set, the model may converge to a suboptimal solution. This sensitivity to initial conditions also results in a lower ability to predict in systems with high complexity or noise where the relationships between inputs and outputs are less well-defined or highly non-linear [46].

To address this, the methodology incorporates optimisation techniques, namely PSO and GA, to further refine ANFIS's structure and boost its performance [18]. Gas turbines exhibit relations between different parameters, which are rather non-linear, and the interaction between different parameters may not be easily separable. That is why the inclusion of PSO and GA are beneficial in ANFIS framework.

2.5.2. ANFIS-PSO: Improved Tuning Using PSO

The ANFIS limitation was addressed by setting up the initial parameters. PSO is then integrated, hence, reducing the parameter optimisation problem. PSO is a global optimisation technique that is based on the social model, particularly bird flocking. It can manage optimisation problems featuring large numbers of search variables with non-linear qualities. Therefore, using it within the ANFIS framework makes sense to fine-tune the best set of parameters for the present work.

In the ANFIS-PSO model, the PSO algorithm was used to identify the optimal membership function and rule parameters that act as a base for ANFIS. The process began by creating a swarm of particles, where a particle represented a possible solution. These particles search and move through the solution space according to their own best solutions stored within them (local best) and the best solutions found by all the particles in the search space (global best) in order to minimise a fitness function, i.e., the mean squared error between the predicted and actual power output [47].

As the cost function of the PSO, the mean absolute error decreases in each iteration, as the system adapts to new particle positions. This fine-tuning enabled the ANFIS-PSO model to predict higher accuracy compared to the classical ANFIS model because of the PSO-enabled adjustment of the network parameters to optimise the model during the dynamic conditions of gas turbine power plants in the real-time operational space. Optimisation of the PSO results leads to a more effective adaptation of ANFIS to alterations in parameters like pressure ratio or turbine inlet temperature settings with regard to the prediction of power output, thermal efficiency and sfc.

2.5.3. ANFIS-GA: Optimisation with GA

Here, GA is embedded to develop the ANFIS-GA model to improve the model. GA is an evolutionary optimisation technique that is based on the natural selection that can be used to optimise the solution space and for finding the best solution in an oversised structure, such as gas turbine power plants.

In ANFIS-GA, only GA is used to optimise the same membership functions and rule parameters as in ANFIS-PSO, but the best situation will be generated and evolved from a population. Each of these individuals will be associated with a specific set of parameters of ANFIS, and the population is optimised through selection, crossover and mutation operations [48]. The best solutions are selected based on fitness (prediction accuracy) for replicating all population sizes, while crossover recombines the attributes of two parent solutions into offspring that potentially excel the parents, and mutation enforces random changes to prevent the drifting of the population. GA evolves over numerous generations to get the closest-possible parameters to an optimal solution, in terms of the accurate tuning of ANFIS-GA, for enhanced predictive capability [49]. The ANFIS-GA model stands out as the most useful in circumstances where the conditions are ever-changing. It can model potential dependencies between them, where trends much more sophisticated than simple direct correlations may apply to the power output, thermal efficiency and sfc of gas turbine power plants.

2.5.4. Evaluation and Comparison of Actual and Predicted Models

After developing the ANFIS, ANFIS-PSO and ANFIS-GA models, their results are compared in terms of predictive accuracy and reliability. As for the evaluation criteria to estimate each model's performance, root mean square error (RMSE) and mean absolute error (MAE), which reflect how close the predicted curves are to the actual power output, thermal efficiency and sfc data are applied. Normally, the two hybrid models that have been proposed here, namely ANFIS-PSO and ANFIS-GA, should outperform the ANFIS model,

since optimum values of some of the parameters are incorporated in the model. To examine the generality of the models, a k-fold cross-validation technique is also used, whereby the data set is divided into K subsets and the model is trained and tested k times on the subsets. This approach makes it possible to establish whether the models are overtrained on one part of a given dataset, hence guaranteeing their real-world application [24].

3. Results

3.1. Experimental Design Matrix and Corresponding Responses

The experimental design presented in Table 1 examines the relationship between four key operational parameters: r_p , T_1 , T_3 and ε . These parameters were then manipulated in sequence to study their effects on the power output and thermal efficiency of the gas power plant. The maximum power output (165 MW) of the gas turbine was obtained at a pressure ratio of 25 and an ambient temperature of 293 K, with the turbine inlet temperature at 1550 K and an intercooler effectiveness of 55%. This combination equally relates to how a high-pressure ratio and low ambient temperature increase the rating of the power plant. Additionally, thermal efficiency peaked at 47.8% under slightly different conditions: different at a pressure ratio of 25 with an ambient temperature of 293 K, a turbine inlet temperature of 1550 K and an intercooler effectiveness of 95%. Likewise, a maximum sfc of 0.35 kg/kWh was observed at a r_p of 5, a T_1 of 313 K, a T_3 of 1150 K, and an ε of 95%. This indicates that, although enhancements of the intercooler improve thermal efficiency, it slightly lowers the power rating because of compressor deterioration. The results showed that elevating the pressure ratio enhances the power output, with values obtained between 121 MW and 165 MW. It also became evident that the overall temperature or low ambient conditions have a further advantage in both power output and thermal efficiency due to the low intake air temperature compressor workload. Hence, optimum energy conversion occurs. Moreover, these temperatures constantly result in higher power generation and more thermal energy is available for expansion in turbines. When coupled with high levels of pressure ratio, operational thrust and thermal efficiency are enhanced.

Table 1. Experimental design matrix and the corresponding responses.

Std	Run	Factor 1	Factor 2	Factor 3	Factor 4	Response 1	Response 2	Response 3
		A: Pressure Ratio (r_p)	B: Ambient Temp (T_1)	C: Turbine Temperature (T_3)	D: Intercooler Effectiveness (ε)	Thermal Efficiency (η)	sfc	Power Output
			K	K	%	%	kg/kW·h	MW
2	1	25	293	1150	55	47.1	0.23	156
16	2	25	313	1550	95	43.8	0.28	153
22	3	15	303	1550	75	37.9	0.17	145
6	4	25	293	1550	55	45.3	0.22	165
7	5	5	313	1550	55	31.7	0.29	150
19	6	15	293	1350	75	36.2	0.18	147
27	7	15	303	1350	75	26.8	0.29	138
20	8	15	313	1350	75	22.9	0.26	129
24	9	15	303	1350	95	35.3	0.25	126
12	10	25	313	1150	95	41.3	0.32	144
17	11	5	303	1350	75	21.6	0.26	125
30	12	15	303	1350	75	26.4	0.19	135
5	13	5	293	1550	55	44.2	0.22	155

Table 1. Cont.

Std	Run	Factor 1	Factor 2	Factor 3	Factor 4	Response 1	Response 2	Response 3
		A: Pressure Ratio (rp)	B: Ambient Temp (T ₁)	C: Turbine Temperature (T ₃)	D: Intercooler Effectiveness (ε)	Thermal Efficiency (η)	sfc	Power Output
			K	K	%	%	kg/kW·h	MW
3	14	5	313	1150	55	20.9	0.31	142
10	15	25	293	1150	95	46.4	0.29	154
28	16	15	303	1350	75	26.3	0.19	136
15	17	5	313	1550	95	35.1	0.32	140
26	18	15	303	1350	75	26.5	0.2	136
8	19	25	313	1550	55	40.6	0.23	158
11	20	5	313	1150	95	33.1	0.35	121
29	21	15	303	1350	75	26.7	0.21	135
14	22	25	293	1550	95	47.8	0.24	157
25	23	15	303	1350	75	26.6	0.2	135
4	24	25	313	1150	55	34.6	0.28	155
23	25	15	303	1350	55	22.1	0.17	146
18	26	25	303	1350	75	39.5	0.16	149
9	27	5	293	1150	95	40.7	0.33	141
1	28	5	293	1150	55	30.8	0.3	153
21	29	15	303	1150	75	23.4	0.27	128
13	30	5	293	1550	95	45.3	0.28	151

3.2. Statistical Model Development for Power Output and Thermal Efficiency

Equations (16)–(18) delineate the mathematical model employed for predicting responses, while Tables 2–4 provide a summary of the outcomes derived using an analysis of variance (ANOVA). This comprehensive analysis assesses the influence of individual and interactive factors on the responses. In this study, the choice of employing the quadratic model to the CCD technique is justified by its recognised suitability for optimisation [47].

Table 2. ANOVA for reduced quadratic model for power output (P).

Source	Sum of Squares	df	Mean Square	F-Value	p-Value	Remark
Model	3901.69	8	391.96	14.55	<0.0001	significant
A-Pressure ratio	709.39	1	709.39	26.33	<0.0001	significant
B-Ambient temperature	420.50	1	420.50	15.61	0.0007	significant
C-Turbine temperatures	355.56	1	355.56	13.20	0.0016	significant
D-Intercooler effectiveness	480.50	1	480.50	17.83	0.0004	significant
AB	351.06	1	351.06	12.95	0.0020	significant
AD	27.56	1	27.56	1.10	0.3433	not significant
BD	481.50	1	481.50	24.33	0.0002	significant
B ²	1075.56	1	1075.56	39.92	<0.0001	significant
Residual	39.05	21	26.94			
Lack of Fit	32.22	16	3.02	2.69	0.1157	not significant
Pure Error	6.83	5	1.37			
Cor Total	3940	74				

$R^2 = 97.9\%$; adjusted $R^2 = 90.98\%$; predicted $R^2 = 79.98\%$; CV% = 4.41; adeq precision = 10.03.

In Table 2, the ANOVA results for power output show a significant model, with an F-value of 14.55 and a p-value of less than 0.0001, indicating a reliable model. Key

contributors to power output include the pressure ratio (A), ambient temperature (B), turbine inlet temperature (C) and intercooler effectiveness (D). The interaction effects between ambient temperature and pressure ratio (AB), as well as the interaction between ambient temperature and intercooler effectiveness (BD), were also significant. The model demonstrates a high R^2 value of 0.979, meaning that 97.9% of the variability in power output is explained by the model. The adequate precision score of 10.03 further reinforces the strong signal-to-noise ratio, indicating a robust model.

Table 3. ANOVA for reduced quadratic model for thermal efficiency (η).

Source	Sum of Squares	df	Mean Square	F-Value	p-Value	Remarks
Model	1537.06	7	245.73	20.54	<0.0001	significant
A-Pressure ratio	382.72	1	382.72	32.00	<0.0001	significant
B-Ambient temperature	353.78	1	353.78	29.58	<0.0001	significant
C-Turbine temp.	158.42	1	158.42	13.24	0.0015	significant
D-Intercooler effectiveness	147.35	1	147.35	12.32	0.0021	significant
AC	119.84	1	119.84	10.02	0.0047	significant
AD	251.02	16	251.02	15.69	<0.0001	significant
C ²	123.93	1	123.93	10.36	0.0041	significant
Residual	29.72	22	11.96			
Lack of Fit	29.54	17	1.16	1.02	0.3233	not significant
Pure Error	0.1750	5	0.0350			
Cor Total	1566.78	29				

$R^2 = 98.7\%$; adjusted $R^2 = 93.47\%$; predicted $R^2 = 80.47\%$; CV% = 2.53; adeq precision = 14.5774.

Similarly, Table 3 shows the ANOVA results for thermal efficiency, where the model is also highly significant, with an F-value of 20.54 and a p -value of less than 0.0001. The pressure ratio, ambient temperature, turbine inlet temperature and intercooler effectiveness all significantly influence thermal efficiency. Additionally, interactions between pressure ratio and turbine inlet temperature (AC) and pressure ratio and intercooler effectiveness (AD) were found to be significant. The R^2 value of 0.987 indicates that the model accounts for 98.7% of the variation in thermal efficiency, while the adequate precision of 14.57 supports the model's reliability.

Table 4. ANOVA for reduced quadratic model for specific fuel consumption (sfc).

Source	Sum of Squares	df	Mean Square	F-Value	p-Value	Remarks
Model	0.0666	7	0.0095	12.98	<0.0001	significant
A-Pressure ratio	0.0093	1	0.0093	12.74	0.0017	significant
B-Ambient temperature	0.0068	1	0.0068	9.29	0.0059	significant
C-Turbine temperatures	0.0103	1	0.0103	14.02	0.0011	significant
D-Intercoolereffectiveness	0.0093	1	0.0093	12.74	0.0017	significant
AB	0.0043	1	0.0043	5.81	0.0247	significant
BC	0.0090	1	0.0090	12.72	0.0018	significant
BD	0.0045	1	0.0045	5.83	0.0244	significant
Residual	0.0161	22	0.0007			
Lack of Fit	0.0088	17	0.0005	0.3526	0.9515	not significant
Pure Error	0.0073	5	0.0015			
Cor Total	0.0827	29				

$R^2 = 97.2\%$; adjusted $R^2 = 89.95\%$; predicted $R^2 = 74.95\%$; CV% = 4.86; adeq precision = 9.734.

Table 4 also gives the ANOVA results of the reduced quadratic model for sfc . The results show that the model fits the data: $F = 12.98$ and $p < 0.0001$, which means that, overall, the included factors play an important role in determining sfc . Based on the results of the analysis shown in Table 4, several variables and the interrelationships between them are considered noteworthy. The pressure ratio (A) and turbine temperatures (C) show

particularly high impact, with p -values of 0.0017 and 0.0011, respectively. Temperature (B) and intercooler effectiveness (D) further influence sfc , with p -values of 0.0017 and 0.0059, respectively. Moreover, the effects of pressure ratio on AB and BC on turbine temperature and BD on intercooler effectiveness were also significant, indicating that these variables depend on one another in some manner. The model shows a good fit based on the performance criteria, such as MAE = 0.945, RMSE = 1.191 and $R^2 = 0.972$, signifying that a 97.2% variance of sfc is accounted for by the model.

It is established that all the models are very consistent compared to the mean given by the low coefficients of variation (CV%), with 4.41% for power output, 2.53% for thermal efficiency and 4.86% for specific fuel consumption, confirming the models' precision and reliability in predicting the outcomes. Furthermore, the lack of fit values for both models was not significant, supporting the models' accuracy in representing the experimental data. The p -values are lower than 0.05, which indicates a good signal-to-noise ratio of adequate precision values of 10.03 and 14.57, respectively. Also, the R^2 values of 0.979 for power output and 0.987 for thermal efficiency indicate a very good model fit and its capacity to replicate the experiment data. The lack-of-fit test yields a p -value of 0.9515 (Table 4), suggesting no significant systematic errors, which supports the model's validity for the data.

Overall, the results highlight the model's accuracy in analysing sfc while emphasising the importance of individual factors and their interactions. The adjusted R^2 shows the degree of variance of the independent factors and the predicted R^2 degree to which a model accurately predicts new observations. The fluctuations between these two results have about a difference of 0.20, which signifies good model conformity. Regarding power output, there is a good agreement, with a 0.12 difference between the adjusted R^2 (0.9098) and the predicted R^2 (0.7898). Also, in the case of thermal efficiency (Table 3), the predicted R^2 (0.9347) is closely matching with the adjusted R^2 (0.8047), with a difference of 0.13. The model has been found to be non-arbitrary, consistent and capable of reproducing the data of the experiment. Likewise, for sfc (Table 4), the adjusted R^2 of 0.8995, which is fairly high for the model, considered the number of predictors in the data. In addition, the high value of the adjusted R^2 of 74.95% proves that the model is also highly predictive. Moreover, an adequate precision value of 9.734 means that it has a good signal-to-noise ratio.

$$P = 136.17 + 6.28A - 4.83B + 4.44C - 5.17D + 12.22B^2 + 1.56AB + 1.31BD \quad (16)$$

$$\eta = 28.08 + 4.618A - 4.43B + 2.96C + 2.86D + 10.26C^2 - 1.42AC - 0.93AD \quad (17)$$

$$sfc = 0.207 - 0.023A + 0.021B - 0.024C + 0.023D + 0.035AB + 0.003BC - 0.04BD \quad (18)$$

where the variables P , η and sfc denote power output (in MW), thermal efficiency (as a percentage) and specific fuel consumption (in kg/kWh), respectively. Additionally, A, B, C and D represent the coded factors associated with pressure ratio (r_p), ambient temperature (in Kelvin), turbine inlet temperature (in Kelvin) and intercooler effectiveness (ϵ), respectively. It is important to note that a positive (+) sign in the mathematical model signifies a synergistic effect, while a negative (−) sign indicates antagonistic effects. For example, higher pressure ratios (A) in the compressors cause air temperatures to rise so that the energy needed for compression may be high, and hence, this decreases the efficiency that comes with higher turbine inlet temperatures (C). While turbine inlet temperatures enhance thermal efficiency, there is some loss due to compressor work, owing to pressures at higher levels. This negative interaction shows that the pressure ratio and the turbine inlet temperature have to be optimised, such that further increases will not reduce efficiency drastically. This modelling reflects their influencing interactions to enhance the functionality and efficiency of the gas turbine within these systems.

3.3. Influence of Individual Parameters on the Performance of the Gas Power Plant with Intercooler

The impact of different operational parameters for the gas power plant with an intercooler is illustrated in Figures 4–7. The values are useful in order to enhance the effects of these parameters on the performance of the gas power plant. The effect of pressure ratio on power output and thermal efficiency is depicted in Figure 4. With an increase in pressure ratio from 5 to 30, the power output rises. This rise is due to the improvement of the energy, which is utilised to expand with the increased pressure ratio, thus making the expansion process of the gas in the turbine more efficient. Likewise, the thermal efficiency of the cycle varies from 25% at the lower pressure ratio of 15 to over 45% at the pressure ratio of 30. This illustrates how it is possible to raise both the power and the efficiency of a gas turbine by the rising pressure ratio.

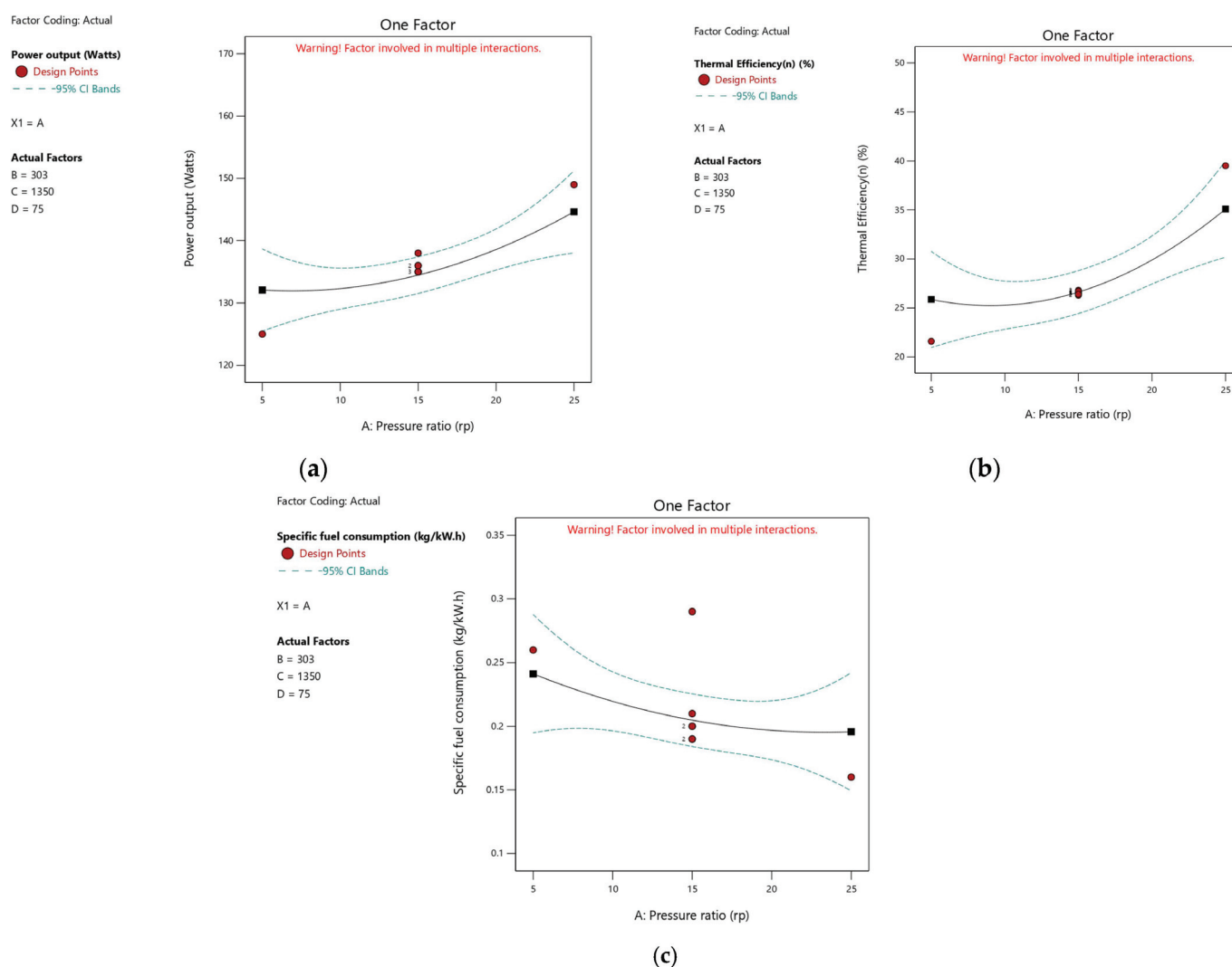


Figure 4. Influence of pressure ratio on the (a) power output, (b) thermal efficiency and (c) specific fuel consumption.

Figure 5 shows the effect of ambient temperature on power output and thermal efficiency. The power output reduces with the increase in ambient temperature, ranging from 15 °C up to 45 °C. The power output from the temperature range of 15 °C is equivalent to 240 MW, while that from a 45 °C temperature is around 160 MW. This inverse correlation between the ambient temperature and power output is due to the fact that, as the temperature increases, the work needed to compress the air decreases the energy available for power generation. With the increase in ambient temperature, the thermal efficiency of

the gas turbine follows the decline manner and is below 40% at 15 °C and below 30% at 45 °C. It was observed that lower ambient temperatures increase both power and thermal efficiency, underlining the desirability of operating the gas turbine in cooler surroundings.

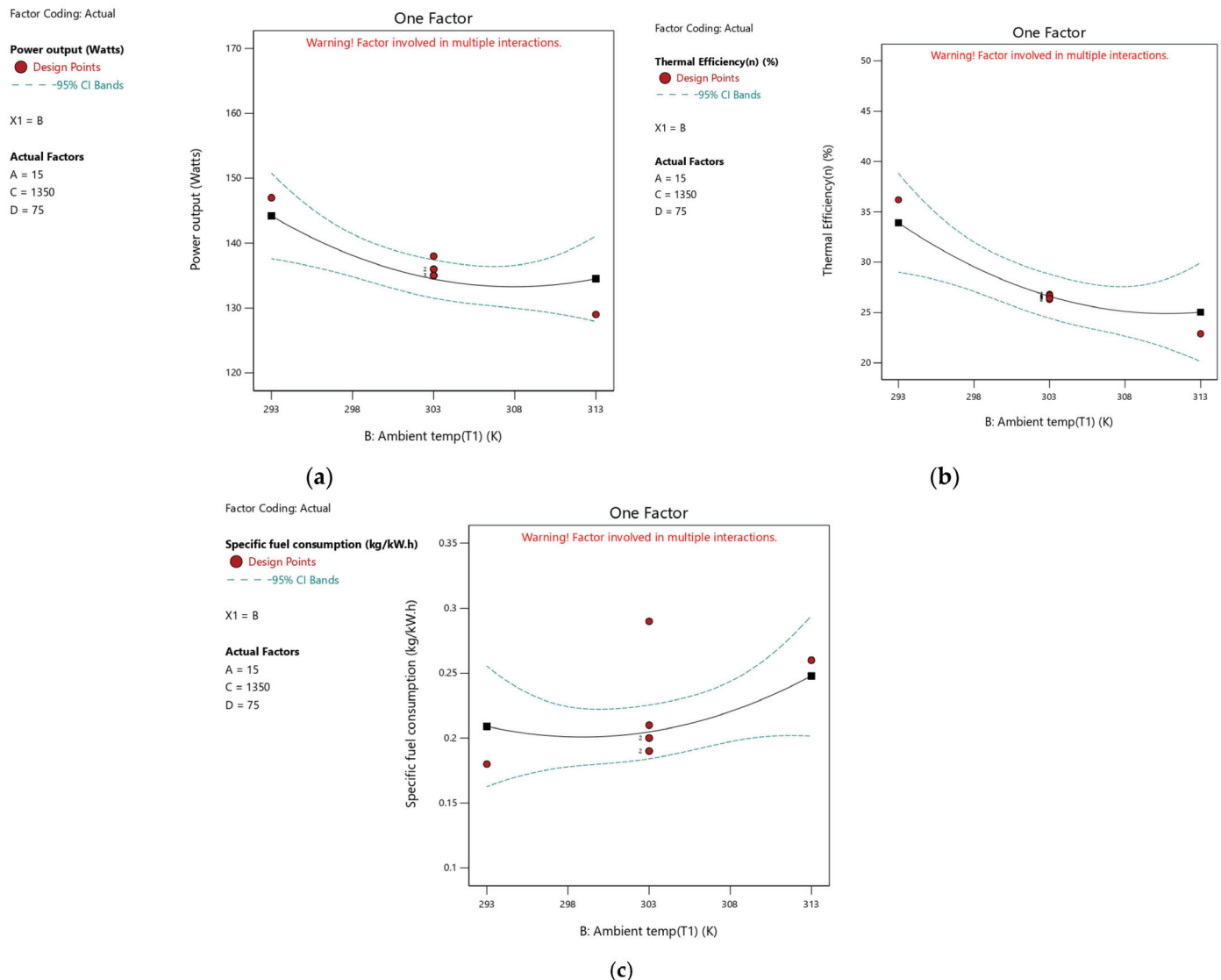


Figure 5. Influence of ambient temperature on the (a) power output, (b) thermal efficiency and (c) specific fuel consumption.

The effect of turbine inlet temperature on power output and thermal efficiency is shown in Figure 6. The power of the gas turbine increases significantly from 150 to 300 MW as the turbine inlet temperature rises from 1100 to 1600 K. This increase results from the higher thermal energy available for expansion at higher turbine inlet temperatures, a factor that greatly enhances the power produced. The thermal efficiency also rises and goes from about 30% with 1100 K to over 50% with 1600 K. This indicates that substantial improvements in both the power produced and thermal efficiency can be realised just by improving the turbine inlet temperatures.

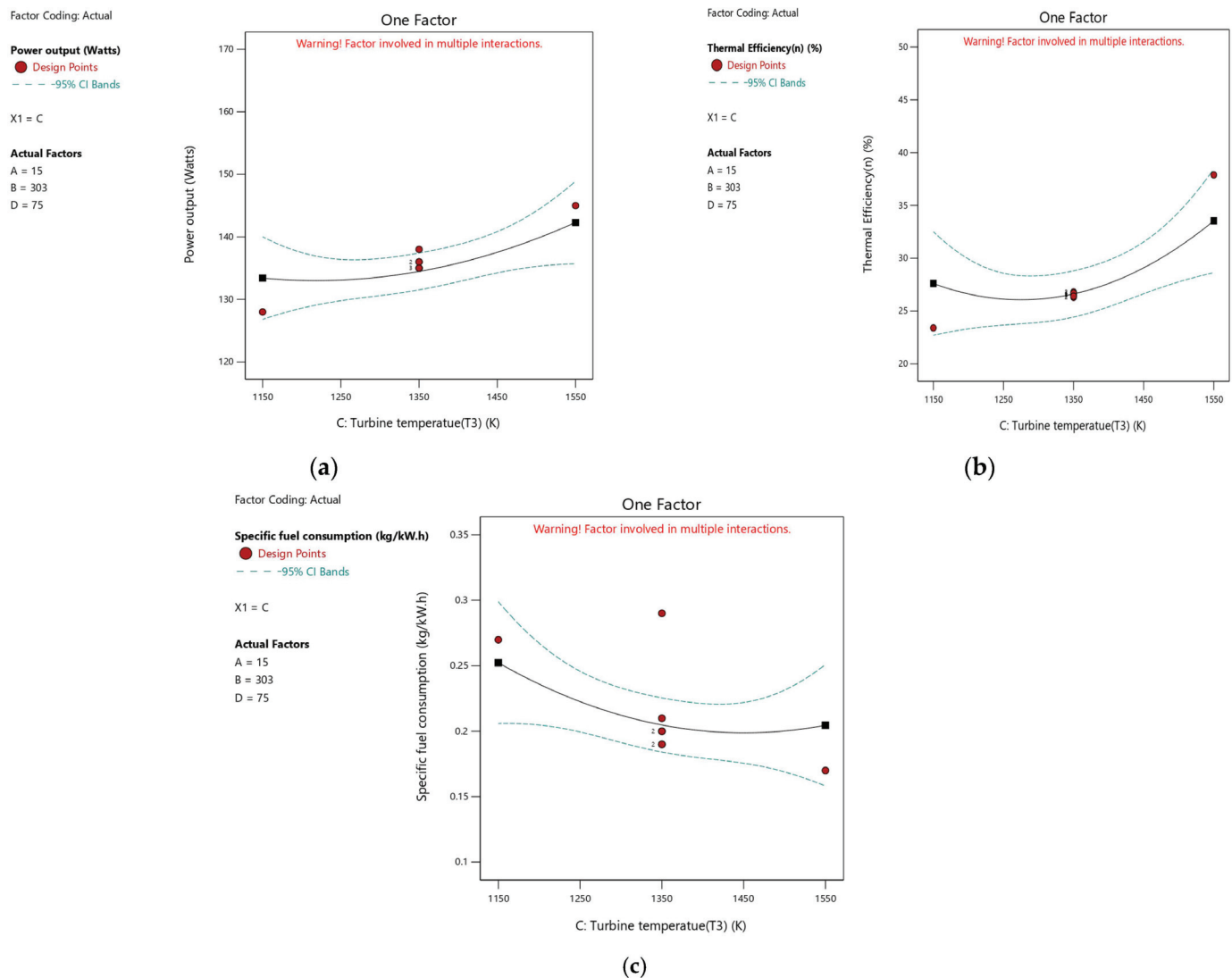


Figure 6. Influence of turbine inlet temperature on the (a) power output, (b) thermal efficiency and (c) specific fuel consumption.

The effect of intercooler effectiveness on power output and thermal efficiency is also depicted in Figure 7. An increase in the intercooler effectiveness from 0.5 to 1.0 and slightly reduced the power output from 200 to 180 MW. It was due to the production of less-energetic compressed air due to more heat extracted from the compressed air, leaving it with less energy to work in the turbine. But with the increase of intercooler effectiveness, the thermal efficiency increased from 35 to 45%. Thus, even though the intercooler's effectiveness enhances the efficiency of the system, it must be balanced to prevent excessive minimisation of the power output. Conversely, a gradual increase in ambient temperature and intercooler effectiveness (ranging from 293 to 313 K and 55% to 95%, respectively) correlated with a rise in specific fuel consumption, ranging from 22.1 to 47.8 kg/kW·h, as the total pressure ratio decreased from 25 to 5 [41].

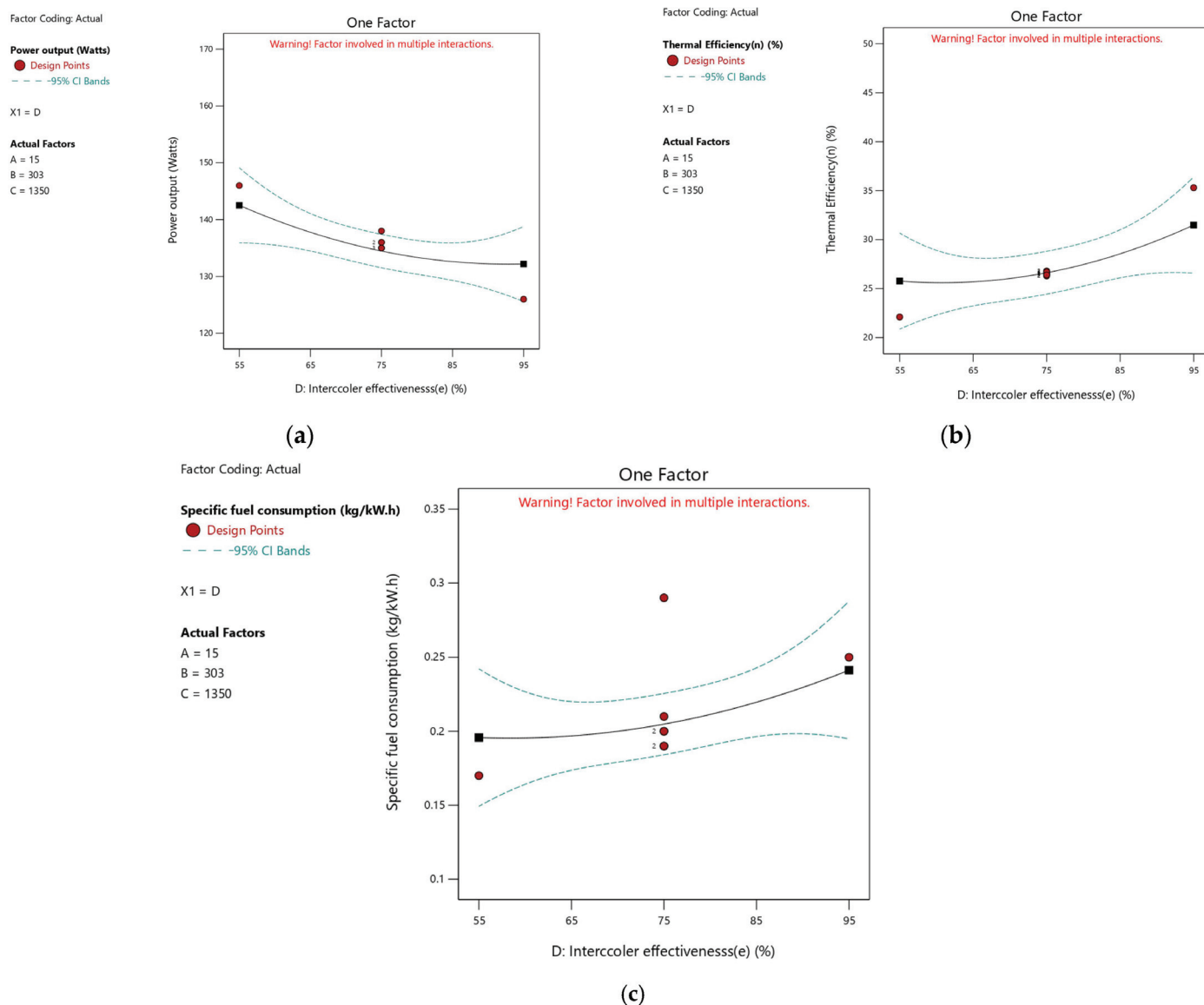


Figure 7. Influence of intercooler effectiveness on the (a) power output, (b) thermal efficiency and (c) specific fuel consumption.

3.4. Influence of Two Most Significant Factors on the Performance of the Gas Turbine Power Plant with Intercooler

Figures 8–14 present 3D response surface plots and 2D contour plots of the interdependence of the crucial parameters that influence the gas turbine power plant's performance. This inverse relationship between the pressure ratio and the effectiveness of the intercooler shows that, while the intercooler cools the air by lowering the compressor's work, the intercooler is also capable of increasing the power output whenever the pressure ratio is raised.

The interactive effect of the pressure ratio and the ambient temperature on the power output of a gas turbine power plant is depicted in Figure 8a,b. The figure shows that power output is highly responsive to higher pressure ratios and lower ambient temperatures. When the pressure ratio is 25 and the ambient temperature of 293 K, the power output rises from 130 MW to 147 MW. The maximum output power is found to be 147 MW at constant intercooler effectiveness, and the power output was maximum (147 MW), when the pressure ratio and the ambient temperature were 25 and 1350 K, respectively. On the other hand, lower pressure ratios integrated with higher ambient temperatures translate to

a significant loss of power production capability. This inverse-like condition is observed since lower ambient temperatures mean lesser compression load, which improves the energy for expansion in the turbine. The results obtained reflect the need to keep the pressure ratios and ambient conditions at their optimal levels to get the best results from the driving gas turbines. In particular, an increase in pressure ratio enhances the energy conversion efficiency during expansion, while low ambient temperatures decrease the compressor's energy requirements. This synergy also confirms that power generation is optimised under certain operating conditions.

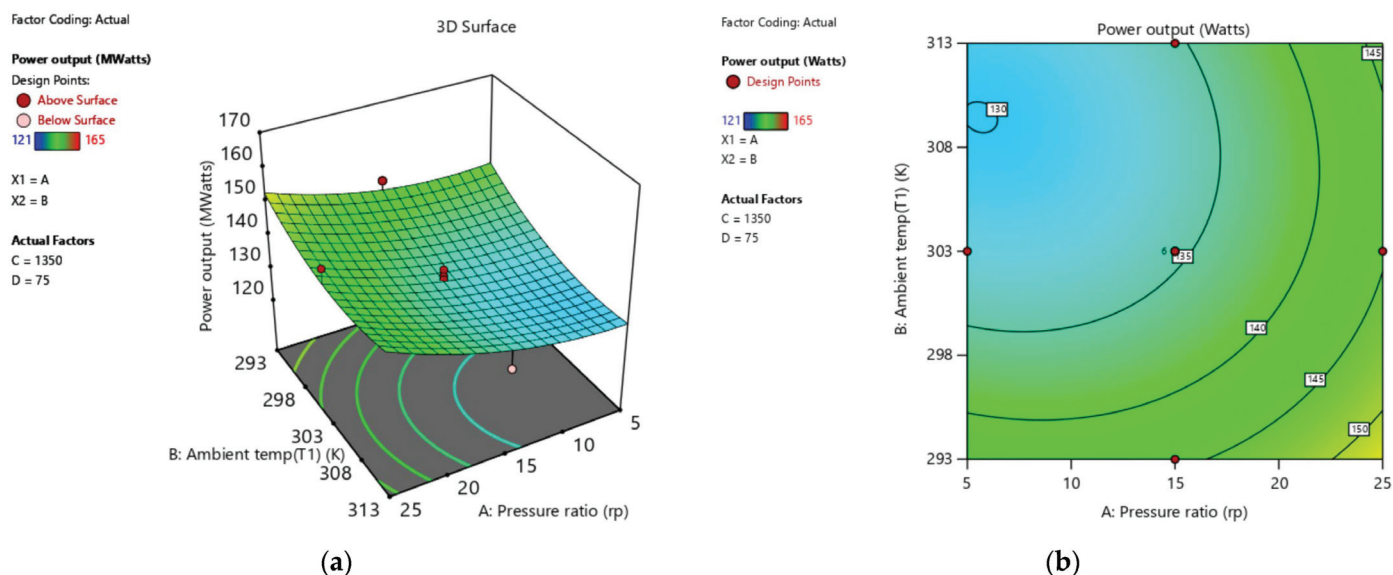


Figure 8. (a) 3D surface plot of power output (MW) against pressure ratio and ambient temperature (K); (b) 2D contour plot of power output (MW) against pressure ratio and ambient temperature (K).

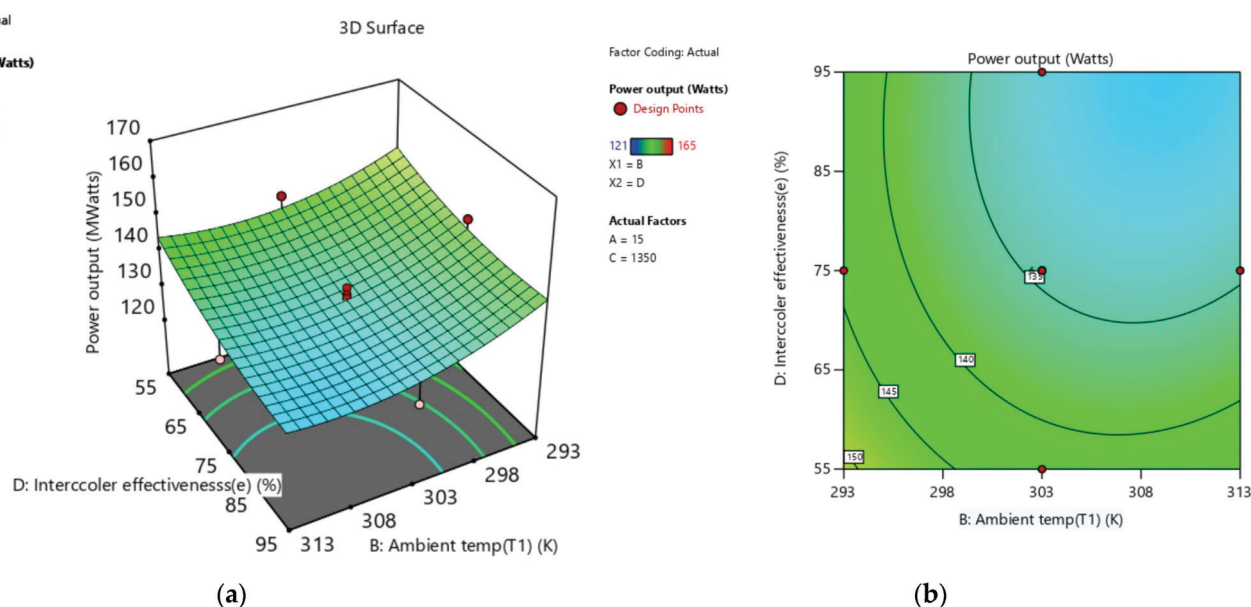


Figure 9. (a) 3D surface plot of power output (MW) against ambient temperature and intercooler effectiveness (%); (b) 2D contour plot of power output (MW) against ambient temperature and intercooler effectiveness (%).

The interactions of pressure ratio and intercooler effectiveness in determining power output are depicted in Figure 9a,b. The results depict that the power output is optimum when the pressure ratio rises from 5 to 25, and the effectiveness of an intercooler decreases

from 95% to as low as 55%. The results obtained for the present power plant indicate that the maximum power output of 145 MW was obtained at a turbine inlet temperature (TIT) of 1350 K and ambient temperature of 303 K. These results indicate that, even though the intercooling minimises the compressor work, there is no significant effect of increased intercooler efficiency (e.g., 95%), due to the reduced thermal energy available for turbine expansion. When the intercooler effectiveness decreases to around 55% and power output rises, more thermal energy is conserved for turbine work. This clearly shows problems with air-cooled intercooler efficiency, which depends on gas turbine operating parameters such as pressure ratio and ambient temperature. The main function of an intercooler is to cool the compressed air between the stages of compressing so that its temperature and specific volume are decreased, thus lowering the compressor work and improving the thermodynamic efficiency. However, very efficient intercooling certainly reduces the temperature of the air entering the combustion chamber and, hence, reduces the thermal energy needed to expand the turbine. Since the turbine produces power by expanding hot gases, a low inlet temperature results in low amounts of energy being required for conversion into mechanical work, thereby decreasing power output. Consequently, high effectiveness in the intercooler leads to a higher efficiency in the compressor and thermal efficiency, but it has negative impacts on the efficiency of a turbine. The range of optimal intercooler effectiveness (55–95%) balances the trade-off between these two effects and provides increased efficiency and sufficient power output. These findings show the necessity for tactful optimisation of the intercooler's characteristics and the stability of the required operating parameters to provide the maximum power in gas turbine combined cycles [50].

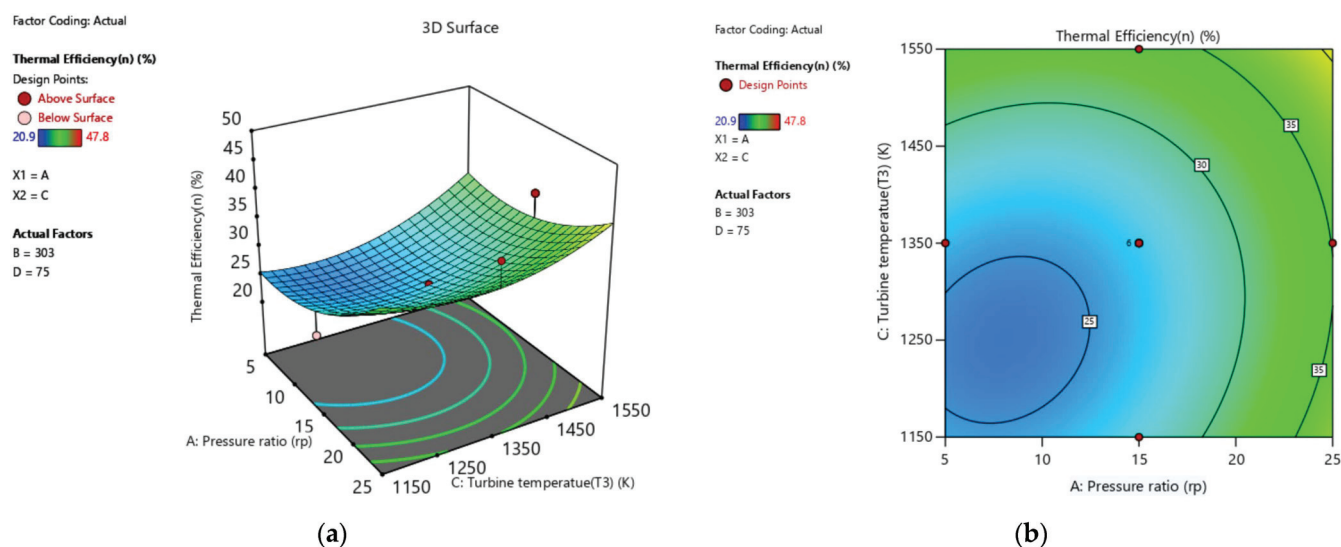


Figure 10. (a) 3D surface plot of thermal efficiency (%) against pressure ratio (r_p) and turbine inlet temperature, and (b) 2D contour plot of thermal efficiency (%) against pressure ratio (r_p) and turbine inlet temperature.

Figure 10a,b shows the interactive influences of turbine inlet temperature and pressure ratio on the thermal efficiency of the power plant gas turbine. It was observed that thermal efficiency rises with higher turbine inlet temperatures and pressure ratios. The optimum value of thermal efficiency of 47% was observed for a TIT with a 1550 K pressure ratio of 25 and a constant ambient temperature of 293 K but with an intercooler effectiveness level of 95%. The results demonstrate that, at lower pressure ratios, the efficiency of the power plant is moderate. However, above a pressure ratio of 15, the plant efficiency becomes steeper. This is attributed to the fact that a greater TIT offers more thermal energy for the expansion stage in the turbine and, hence, better energy conversion. The finding emphasises that

high values of TIT and pressure ratios ensure that the gas turbine operates at the highest level of thermal efficiency. However, much care has to be taken to avoid reducing material strength or undergoing stresses due to heat while operating at such high values of the said quantities. Thus, optimisation offers a route for enhancing energy efficiency and sector performance in gas turbine power plants.

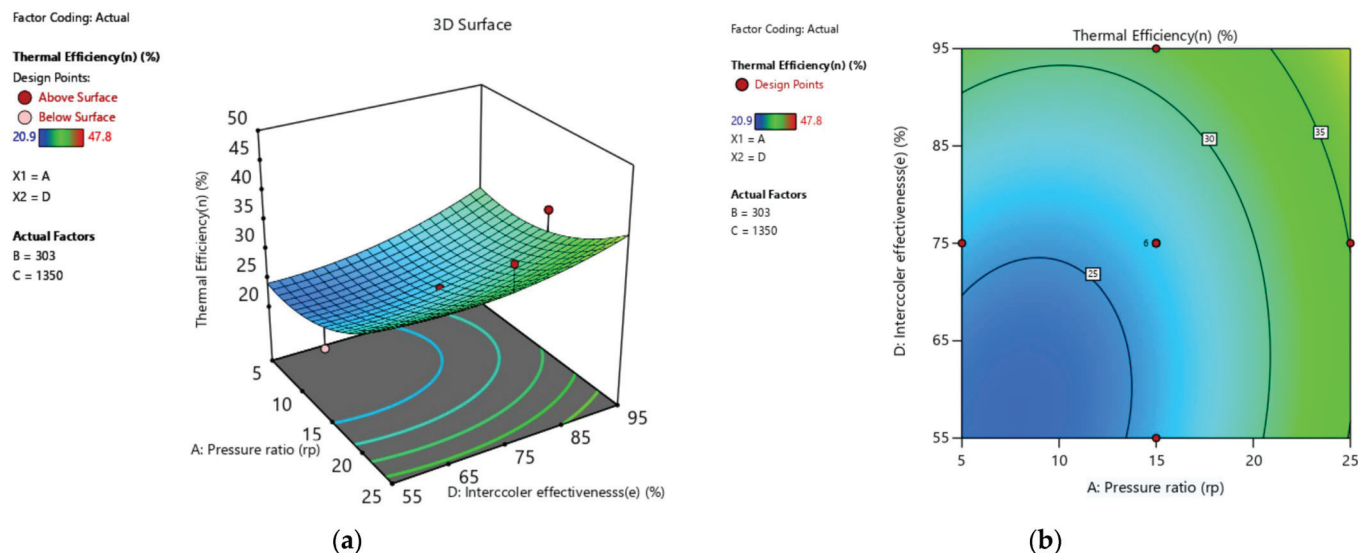


Figure 11. (a) 3D surface plot of thermal efficiency (%) against pressure ratio and intercooler effectiveness (ϵ), and (b) 2D contour plot of thermal efficiency (%) against pressure ratio and intercooler effectiveness (ϵ).

The influence of the combination of pressure ratio and intercooler effectiveness on the thermal efficiency is shown in Figure 11a,b. It is realised that the thermal efficiency increases as the pressure ratio is high and, at the same time, isolates the effectiveness of the intercooler. The maximum thermal efficiency of 47.8% was obtained when the pressure ratio was at the maximum of 25, intercooler effectiveness at 55% and with a constant ambient temperature and turbine inlet temperature of 293 K and 1550 K, respectively. The result shows that, although intercooling reduces the work that the compressor performs, extreme cooling reduces the amount of heat that is available for expansion by the turbine, thereby reducing the thermal efficiency. At lower intercooler effectiveness, less heat is removed, and therefore, more work is performed at higher pressure ratios. This finding shows that there is always a trade-off between intercooler effectiveness and thermal efficiency, an indication that there must be a careful balancing of intercooler effectiveness to arrive at an optimum system. Additionally, it reveals that higher pressure ratios are necessary for increased thermal efficiency when the effectiveness of the intercooler is well managed.

The interaction between pressure ratio and ambient temperature on the sfc of a gas turbine power plant is depicted in Figure 12a,b. The study shows that, at a pressure of 15 and ambient temperature of 303 K, sfc is lowest at 0.28 kg/kWh, with a steady TIT of 1350 K and an intercooler efficiency of 75%. Specific fuel consumption increases as the ambient temperature increases and the pressure ratio decreases. This is because an enhanced ambient temperature raises the pressure ratio in compression work, hence, lowering the energy for turbine expansion. Reduced pressure ratios compound the energy losses that are inevitable with the generation of power. Thus, more fuel is consumed per unit of power generated. Hence, the pressure ratios must be kept moderate and ambient conditions stable to maximise fuel economy. Operating at a pressure ratio of 15 balances fuel consumption while maintaining system efficiency, especially for a moderate ambient temperature. Furthermore, maintaining the TIT at 1350 K keeps energy losses negligible,

provided the working fluid undergoes expansion, and intercooler effectiveness is set at 75% to give sufficient cooling without massive thermal energy loss. This demonstrates that, under stable turbine inlet conditions, increasing the pressure ratio positively influences fuel efficiency at moderate ambient temperatures.

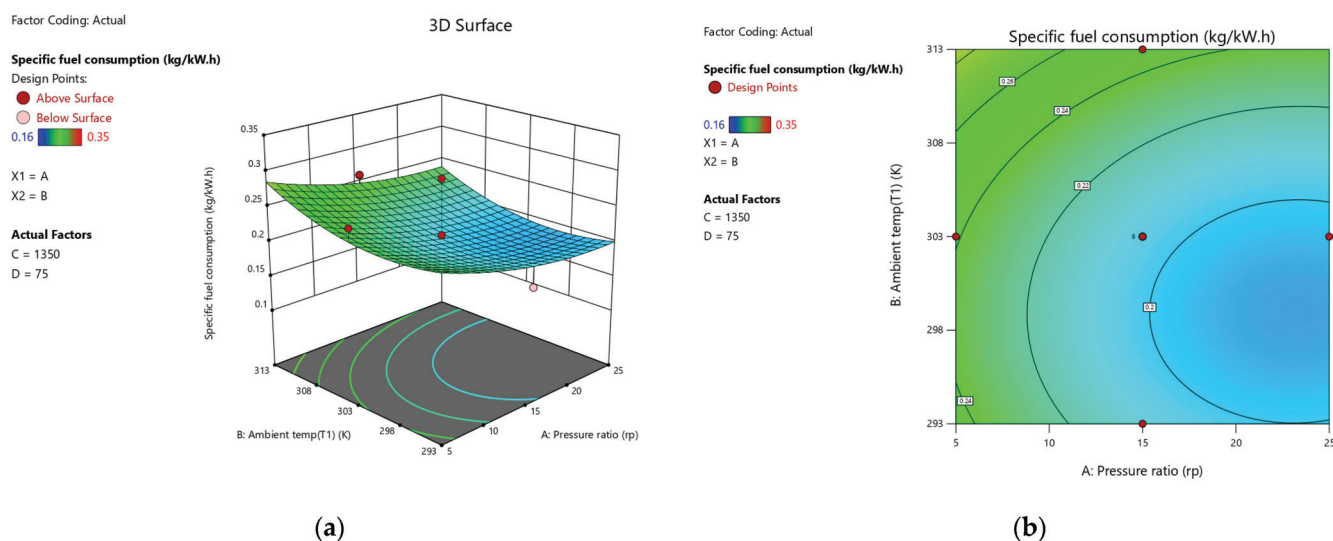


Figure 12. (a) 3D surface plot of specific fuel consumption (kg/kW·h) against pressure ratio and ambient temperature (K), and (b) 2D contour plot of specific fuel consumption (kg/kW·h) against pressure ratio and ambient temperature (K).

The effect of ambient temperature and TIT on the sfc of gas turbine systems is depicted in Figure 13a,b. The results demonstrate that, with an ambient temperature increase, the sfc improves, primarily at a lower TIT. A minimum sfc of 0.25 kg/kW·h was obtained with a pressure ratio of 15, a TIT of 1350 K, and an ambient temperature of 293 K. Higher ambient temperatures put a higher load on the compressor stage. Therefore, the energy available for the turbine expansion is lowered, and hence, more fuel is used. This is compounded by a lower TIT, meaning that there is the least thermal energy for conversion into useful work. However, at a TIT of 1350 K, moderate conditions of sfc are achieved while burning fuel efficiently and maintaining maximum energy output. These results underline the need for a high TIT and a moderate pressure ratio to maximise the fuel consumption as ambient conditions change.

Figure 14a,b examines the effect of both ambient temperature and intercooler effectiveness on sfc. The findings show that the sfc rises with an increasing ambient and TIT, especially when both conditions are at a high level. An optimum sfc of 0.25 kg/kW·h was obtained at a pressure ratio of 15, a TIT of 1350 K, and an ambient temperature of about 293 K. More energy is used in relation to air compression at higher ambient temperatures, resulting in less energy being available for turbine expansion and leading to more fuel consumption. Similarly, with a higher TIT, more thermal energy is available for expansion, but the cost, in terms of fuel, required to sustain operations at those conditions is also increased. These results show the relationship between these operating parameters, in which increased temperature offers greater turbine efficiency at the expense of increased specific fuel consumption. The result also shows that, for a low sfc while generating high power, the TIT, ambient temperature and pressure ratio must be set at their optimum level. It became clear that, for best performance, these parameters must be optimised to achieve the best fuel consumption and turbine efficiency.

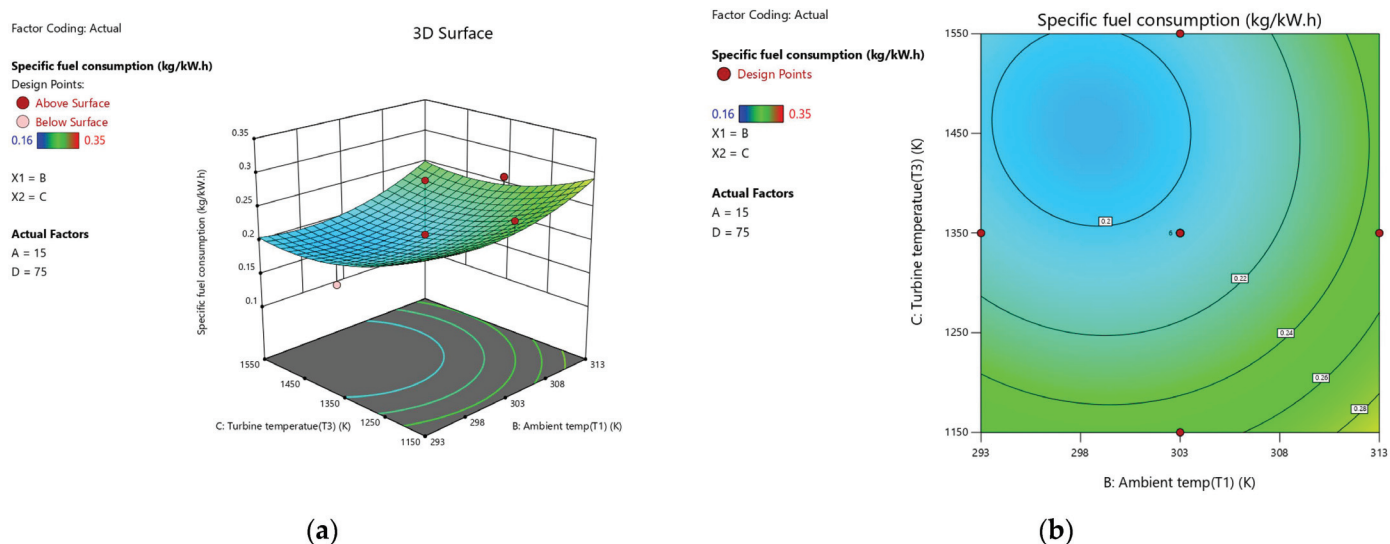


Figure 13. (a) 3D surface plot of specific fuel consumption (kg/kW·h) against ambient temperature (K) and turbine temperature (K), and (b) 2D contour plot of specific fuel consumption (kg/kW·h) against ambient temperature (K) and turbine temperature (K).

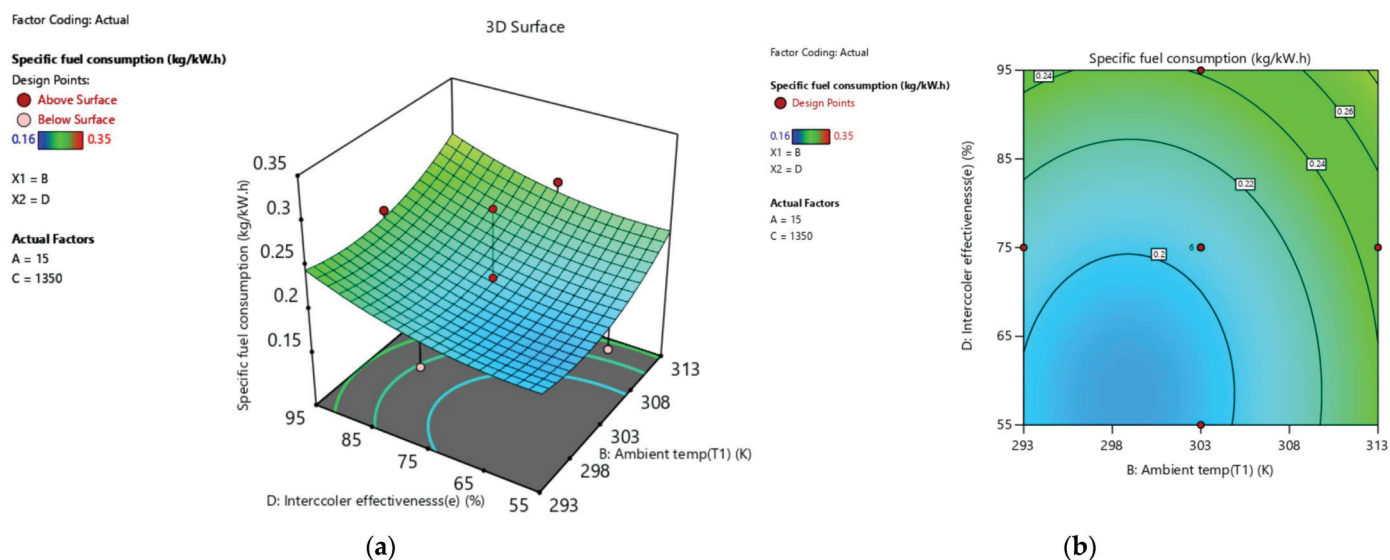


Figure 14. (a) 3D surface plot of specific fuel consumption (kg/kW·h) against ambient temperature (K) and turbine temperature (K), and (b) 2D contour plot of specific fuel consumption (kg/kW·h) against ambient temperature (K) and turbine temperature (K).

3.5. Comparison Analysis Between Experimental and RSM Predicted Performance

The RSM was used to analyse the actual and the predicted power output, thermal efficiency and sfc. Tables 5–7 provide multiple experimental runs, where each entry was the actual and predicted values with the residual value (actual value minus predicted value). The basic statistical values, such as leverage, Cook's distance and Studentised residuals, indicate how accurate the model is and how much impact every data unit has. The residuals show to what extent the predicted data are in tandem with the actual data. Small residuals indicate that, overall, the RSM model satisfactorily estimates power output, thermal efficiency and sfc, whereas the point values identified as outliers based on larger Studentised residuals and Cook's distance values are minor. The power in brackets (Tables 5–7) appears when the value of DFFITS exceeds the critical threshold (values) and this means that the observation significantly influences the fitted values of the regression model.

Table 5. Comparison between actual and RSM predicted values for power output.

Run Order	Actual Value for Power Output	Predicted Value for Power Output	Residual	Leverage	Internally Studentised Residuals	Externally Studentised Residuals	Cook's Distance	Influence on Fitted Value DFFITS	Standard Order
1	156.00	160.23	−4.23	0.659	−1.627	−1.733	0.341	−2.407 ⁽¹⁾	2
2	153.00	152.99	0.0102	0.659	0.004	0.004	0.000	0.005	16
3	145.00	142.30	2.70	0.485	0.846	0.837	0.045	0.813	22
4	165.00	162.99	2.01	0.659	0.774	0.763	0.077	1.060	6
5	150.00	149.77	0.2325	0.659	0.090	0.087	0.001	0.120	7
6	147.00	144.19	2.81	0.485	0.880	0.873	0.049	0.848	19
7	138.00	134.47	3.53	0.096	0.835	0.826	0.005	0.270	27
8	129.00	134.53	−5.53	0.485	−1.733	−1.873	0.189	−1.819	20
9	126.00	132.19	−6.19	0.485	−1.942	−2.169	0.237	−2.107	24
10	144.00	141.73	2.27	0.659	0.876	0.869	0.099	1.206	12
11	125.00	132.08	−7.08	0.485	−2.221	−2.620	0.310	−2.544 ⁽¹⁾	17
12	135.00	134.47	0.5263	0.096	0.125	0.120	0.000	0.039	30
13	155.00	158.06	−3.06	0.659	−1.178	−1.195	0.179	−1.660	5
14	142.00	139.50	2.50	0.659	0.961	0.959	0.119	1.332	3
15	154.00	152.77	1.23	0.659	0.475	0.462	0.029	0.642	10
16	136.00	134.47	1.53	0.096	0.361	0.351	0.001	0.115	28
17	140.00	136.56	3.44	0.659	1.325	1.362	0.226	1.892	15
18	136.00	134.47	1.53	0.096	0.361	0.351	0.001	0.115	26
19	158.00	160.95	−2.95	0.659	−1.135	−1.147	0.166	−1.593	8
20	121.00	121.55	−0.5453	0.659	−0.210	−0.203	0.006	−0.282	11
21	135.00	134.47	0.5263	0.096	0.125	0.120	0.000	0.039	29
22	157.00	160.28	−3.28	0.659	−1.264	−1.291	0.205	−1.794	14
23	135.00	134.47	0.5263	0.096	0.125	0.120	0.000	0.039	25
24	155.00	154.43	0.5658	0.659	0.218	0.211	0.006	0.293	4
25	146.00	142.53	3.47	0.485	1.090	1.097	0.075	1.065	23
26	149.00	144.64	4.36	0.485	1.368	1.413	0.118	1.372	18
27	141.00	138.84	2.16	0.659	0.833	0.824	0.089	1.145	9
28	153.00	151.55	1.45	0.659	0.560	0.547	0.040	0.760	1
29	128.00	133.42	−5.42	0.485	−1.698	−1.826	0.181	−1.773	21
30	151.00	150.10	0.8991	0.659	0.346	0.336	0.015	0.467	13

ANOVA: single factor
SUMMARY

Groups	Count	Sum	Average	Variance
Column 1	30	4305	143.5	127.6379
Column 2	30	4305	143.5	117.4334

ANOVA

Source of Variation	SS	df	MS	F	p-value	F crit
Between Groups	2.73×10^{-12}	1	2.73×10^{-12}	2.23×10^{-14}	1	4.006873
Within Groups	7107.067	58	122.5356			
Total	7107.067	59				

The power values are presented in Table 5, where the actual values of power output vary from 121 to 165, and the predicted power output values are close to the actual values, indicating the effectiveness and accuracy of the models. The residuals, which are the differences between the observation and fitted values, are relatively small, and with the exception of a few cases, are less than one. For instance, Run 1, with the residual −4.23, and Run 9 has a greater discrepancy, equal to −6.19. Also, Run 1 and Run 11 have symbols ⁽¹⁾ because their DFFITS values are −2.407 and −2.544, respectively, which indicates that these two Runs have significant effect on model prediction. Nevertheless, as has been depicted by the ANOVA analysis (Table 5), there is no statistically significant difference between the actual and the predicted values. The F-value is as low as 2.23×10^{-14} , and the p-value

equals 1, which means that any variation that was identified does not stem from systematic errors produced by the faulty model (Table 5).

Table 6. Comparison between actual and RSM predicted values for thermal efficiency.

Run Order	Actual Value for Thermal Efficiency	Predicted Value for Thermal Efficiency	Residual	Leverage	Internally Studentised Residuals	Externally Studentised Residuals	Cook's Distance	Influence on Fitted Value DFFITS	Standard Order
1	47.10	43.91	3.19	0.659	1.653	1.766	0.352	2.453 ⁽¹⁾	2
2	43.80	43.73	0.0668	0.659	0.035	0.033	0.000	0.046	16
3	37.90	33.55	4.35	0.485	1.836	2.015	0.212	1.957	22
4	45.30	48.78	−3.48	0.659	−1.801	−1.965	0.417	−2.729 ⁽¹⁾	6
5	31.70	30.54	1.16	0.659	0.601	0.588	0.046	0.817	7
6	36.20	33.91	2.29	0.485	0.965	0.962	0.059	0.935	19
7	26.80	26.62	0.1789	0.096	0.057	0.055	0.000	0.018	27
8	22.90	25.05	−2.15	0.485	−0.905	−0.899	0.051	−0.873	20
9	35.30	31.49	3.81	0.485	1.607	1.706	0.162	1.657	24
10	41.30	42.41	−1.11	0.659	−0.576	−0.563	0.043	−0.782	12
11	21.60	25.87	−4.27	0.485	−1.800	−1.964	0.204	−1.907	17
12	26.40	26.62	−0.2211	0.096	−0.070	−0.068	0.000	−0.022	30
13	44.20	42.27	1.93	0.659	1.000	1.000	0.129	1.390	5
14	20.90	19.07	1.83	0.659	0.949	0.945	0.116	1.313	3
15	46.40	48.42	−2.02	0.659	−1.044	−1.047	0.140	−1.455	10
16	26.30	26.62	−0.3211	0.096	−0.102	−0.099	0.000	−0.032	28
17	35.10	37.47	−2.37	0.659	−1.229	−1.252	0.194	−1.739	15
18	26.50	26.62	−0.1211	0.096	−0.039	−0.037	0.000	−0.012	26
19	40.60	40.52	0.0765	0.659	0.040	0.038	0.000	0.053	8
20	33.10	30.48	2.62	0.659	1.358	1.401	0.237	1.945	11
21	26.70	26.62	0.0789	0.096	0.025	0.024	0.000	0.008	29
22	47.80	48.81	−1.01	0.659	−0.524	−0.511	0.035	−0.710	14
23	26.60	26.62	−0.0211	0.096	−0.007	−0.006	0.000	−0.002	25
24	34.60	34.73	−0.1276	0.659	−0.066	−0.064	0.001	−0.089	4
25	22.10	25.77	−3.67	0.485	−1.547	−1.630	0.150	−1.583	23
26	39.50	35.09	4.41	0.485	1.860	2.048	0.217	1.989	18
27	40.70	39.96	0.7432	0.659	0.385	0.374	0.019	0.519	9
28	30.80	31.72	−0.9221	0.659	−0.477	−0.465	0.029	−0.646	1
29	23.40	27.61	−4.21	0.485	−1.776	−1.931	0.198	−1.876	21
30	45.30	46.03	−0.7276	0.659	−0.377	−0.366	0.018	−0.508	13
ANOVA: single factor SUMMARY									
Groups		Count	Sum	Average	Variance				
Column 1		30	1026.9	34.23	76.45045				
Column 2		30	1026.91	34.23033	70.79907				
ANOVA									
Source of Variation		SS	df	MS	F	p-value	F crit		
Between Groups		1.67 × 10 ^{−6}	1	1.67 × 10 ^{−6}	2.26 × 10 ^{−8}	0.99988	4.006873		
Within Groups		4270.236	58	73.62476					
Total		4270.236	59						

The ANOVA analysis for thermal efficiency is displayed in Table 6, where the actual values of thermal efficiency range between 20.90 and 47.80 and the predicted thermal efficiencies follow the same trend. The results showed that most of the residuals are relatively small, although some runs depict higher deviations. For instance, Run 26 has a residual of 4.41, which means there is a rather high deviation between the actual and estimated values. However, the analysis of variance shows no significant difference between the actual and predicted values for thermal efficiency. The F-value (2.26×10^{-8}), as *p*-value well as the (0.999 88), shows that the probabilities of the model are statistically relevant to the actual

values (Table 6). Therefore, comparing the result of incorporated power output with the actual test data and thermal efficiency estimations, it could be obviously concluded that the RSM model has enough accuracy, since there is not a large gap between the actual and predicted values. The observed variations in a few residuals, hence, do not affect the predictability and reproducibility of the model and can be widely used to predict gas power plant performance.

Table 7. Comparison between actual and RSM predicted values for specific fuel consumption.

Run Order	Actual Value	Predicted Value	Residual	Leverage	Internally Studentised Residuals	Externally Studentised Residuals	Cook's Distance	Influence on Fitted Value DFFITS	Standard Order
1	0.2300	0.2385	−0.0085	0.659	−0.463	−0.450	0.028	−0.625	2
2	0.2800	0.2789	0.0011	0.659	0.062	0.060	0.000	0.083	16
3	0.1700	0.2046	−0.0346	0.485	−1.543	−1.626	0.150	−1.579	22
4	0.2200	0.1894	0.0306	0.659	1.674	1.793	0.360	2.491 ⁽¹⁾	6
5	0.2900	0.2789	0.0111	0.659	0.609	0.596	0.048	0.828	7
6	0.1800	0.2091	−0.0291	0.485	−1.296	−1.328	0.106	−1.290	19
7	0.2900	0.2048	0.0852	0.096	2.866	4.116 ⁽²⁾	0.058	1.345	27
8	0.2600	0.2480	0.0120	0.485	0.537	0.524	0.018	0.509	20
9	0.2500	0.2413	0.0087	0.485	0.388	0.377	0.009	0.366	24
10	0.3200	0.3179	0.0021	0.659	0.115	0.111	0.002	0.155	12
11	0.2600	0.2413	0.0187	0.485	0.834	0.825	0.044	0.802	17
12	0.1900	0.2048	−0.0148	0.096	−0.499	−0.486	0.002	−0.159	30
13	0.2200	0.2312	−0.0112	0.659	−0.615	−0.601	0.049	−0.835	5
14	0.3100	0.3229	−0.0129	0.659	−0.706	−0.693	0.064	−0.963	3
15	0.2900	0.2878	0.0022	0.659	0.123	0.119	0.002	0.165	10
16	0.1900	0.2048	−0.0148	0.096	−0.499	−0.486	0.002	−0.159	28
17	0.3200	0.3207	−0.0007	0.659	−0.037	−0.036	0.000	−0.049	15
18	0.2000	0.2048	−0.0048	0.096	−0.162	−0.157	0.000	−0.051	26
19	0.2300	0.2346	−0.0046	0.659	−0.250	−0.242	0.008	−0.336	8
20	0.3500	0.3672	−0.0172	0.659	−0.941	−0.938	0.114	−1.302	11
21	0.2100	0.2048	0.0052	0.096	0.174	0.168	0.000	0.055	29
22	0.2400	0.2362	0.0038	0.659	0.206	0.200	0.005	0.277	14
23	0.2000	0.2048	−0.0048	0.096	−0.162	−0.157	0.000	−0.051	25
24	0.2800	0.2711	0.0089	0.659	0.488	0.475	0.031	0.660	4
25	0.1700	0.1957	−0.0257	0.485	−1.147	−1.160	0.083	−1.127	23
26	0.1600	0.1957	−0.0357	0.485	−1.593	−1.688	0.160	−1.640	18
27	0.3300	0.3346	−0.0046	0.659	−0.250	−0.242	0.008	−0.336	9
28	0.3000	0.2878	0.0122	0.659	0.670	0.657	0.058	0.913	1
29	0.2700	0.2524	0.0176	0.485	0.785	0.774	0.039	0.752	21
30	0.2800	0.2755	0.0045	0.659	0.244	0.237	0.008	0.329	13

ANOVA: single factor
SUMMARY

Groups	Count	Sum	Average	Variance
0.23	29	7.26	0.250345	0.002939
0.2385	29	7.2516	0.250055	0.002427

ANOVA

Source of Variation	SS	df	MS	F	p-value	F crit
Between Groups	1.22×10^{-6}	1	1.22×10^{-6}	0.000453	0.983086	4.012973
Within Groups	0.15024	56	0.002683			
Total	0.150241	57				

Comparing the variance (Table 7) between groups (actual and predicted means and variances) and within groups (variances of the two data sets) shows a very low F-value (almost equal to zero) and a *p*-value of 0.983, suggesting that there is no significant difference between the actual and the predicted values. Such a high value of *P* implies that the model

prediction is highly accurate, and the result of the model matches with the actual data. Also, Run 7 is indicated by ⁽²⁾ due to the very high DFFITS of 4.116, which means that this run has significantly impacted the fitted models.

Figure 15a–c shows the comparison between the predicted and experimental values for power output, sfc and thermal efficiency of the gas turbine via RSM. The existence of this strong correlation confirms the effectiveness of the RSM in modelling the intricate thermodynamic and operating interactions in a gas turbine system. Therefore, the model's ability and reliability to predict gas turbine power plant performance affirm its usefulness for optimising the operational conditions.

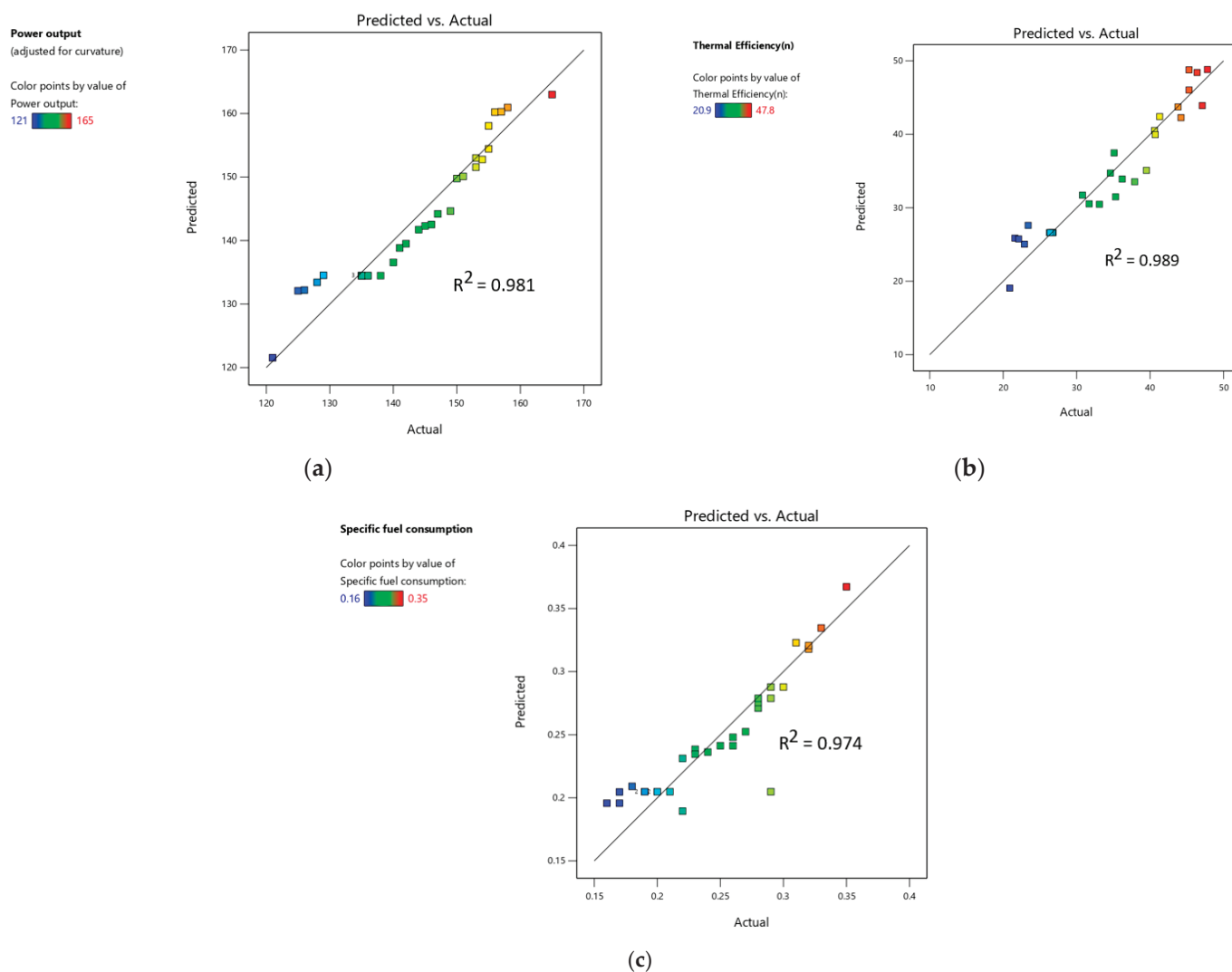


Figure 15. Actual vs. predicted (a) power output, (b) thermal efficiency and (c) sfc.

The normal probability plots of residuals for power output, thermal efficiency and sfc are presented in Figure 16a–c. the residuals closely fit along the straight line on the plots and represent the random, normally distributed errors. This confirms the appropriateness of employing the model for future prediction, with no indication of a consistent pattern of bias. The plots of even residual distribution also ensure homoscedasticity, as there is evidence of similarity in the variance of error across the values on the y -axis that are being predicted. These findings validate the applicability of the quadratic RSM in identifying the performance efficiency of gas turbine power plants and enabling the optimisation of operational conditions. The accurate prediction helps operators to make precise estimations of performance indicators, as well as to correct such essential parameters as turbine inlet

temperature, pressure ratio and intercooler effectiveness. The optimisation process can drive improvements in the efficiency of the plant, accompanied by a decrease in sfc and an increase in power. Furthermore, the model's precise predictive capability makes it feasible for practical use in monitoring and evaluating real-time performance and for making timely adjustments to mitigate operational wastes and greenhouse gas emissions. This is vital to achieving the economic and environmental efficiency of gas turbine power plants in present-day power systems.

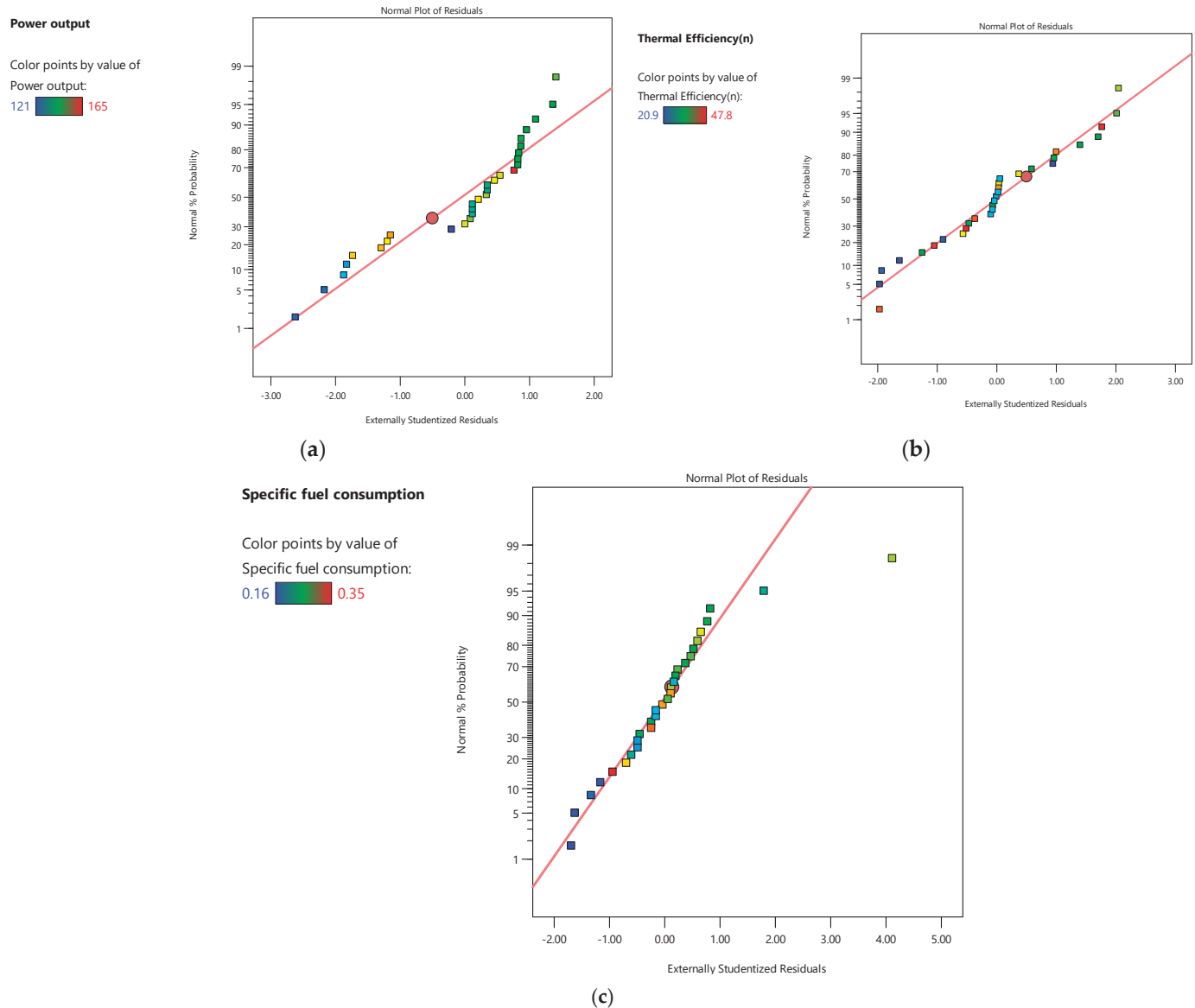


Figure 16. Normal probability plot of residuals (a) power output, (b) thermal efficiency and (c) sfc.

3.6. Comparison Analysis Between Experimental, RSM and ANFIS Models Predicted Performance

The comparative performance of gas power plants via the RSM, ANFIS, ANFIS-PSO and ANFIS-GA models, based on the results presented in Tables 8–10, revealed significant improvement in the state-of-the-art in predictive modelling, as influenced by this study. The enhancement of the traditional methodology comprised the integration of metaheuristic optimisation techniques, such as PSO and GA, with ANFIS for the improvement of the prediction accuracy across diverse gas power plant operating parameters.

Table 8. Comparison between actual, RSM, ANFIS, ANFIS-PSO and ANFIS-GA for power output.

Std	Run	Actual Values for Power Output (MW)	RSM Values for Power Output (MW)	ANFIS Values for Power Output (MW)	ANFIS-PSO Values for Power Output (MW)	ANFIS-GA Values for Power Output (MW)
2	1	156	160.23	155.7	156.3	156.4
16	2	153	152.99	152.4	152.8	152.7
22	3	145	142.30	145.3	145.2	144.8
6	4	165	162.99	164.6	165.3	165.3
7	5	150	149.77	149.7	150.2	150.4
19	6	147	144.19	146.3	147.2	146.7
27	7	138	134.47	137.8	137.8	137.5
20	8	129	134.53	128.5	129.2	128.6
24	9	126	132.19	126.1	126.3	126.2
12	10	144	141.73	143.4	143.6	143.8
17	11	125	132.08	124.6	125.2	124.5
30	12	135	134.47	134.8	135.1	134.6
5	13	155	158.06	154.5	154.7	154.8
3	14	142	139.50	141.4	141.6	141.7
10	15	154	152.77	153.2	154.2	153.6
28	16	136	134.47	135.7	136.1	135.4
15	17	140	136.56	139.8	140.1	139.5
26	18	136	134.47	135.5	135.8	135.8
8	19	158	160.95	157.2	157.7	157.4
11	20	121	121.55	120.4	121.1	120.7
29	21	135	134.47	134.6	135.2	134.6
14	22	157	160.28	156.7	157.3	157.3
25	23	135	134.47	134.8	135.2	134.7
4	24	155	154.43	154.1	154.8	154.6
23	25	146	142.53	145.8	146.2	146.3
18	26	149	144.64	148.3	148.6	149.2
9	27	141	138.84	140.6	141.3	140.9
1	28	153	151.55	152.3	153.2	152.8
21	29	128	133.42	127.6	128.3	128.4
13	30	151	150.10	150.2	150.8	150.6

ANOVA: single factor for Table 8
SUMMARY

Groups	Count	Sum	Average	Variance		
156	29	4149	143.069	126.4236		
160.23	29	4144.77	142.9231	111.2865		
155.7	29	4136.2	142.6276	124.2049		
156.3	29	4150.1	143.1069	125.0721		
156.4	29	4143.4	142.8759	127.6755		
ANOVA						
Source of Variation	SS	df	MS	F	p-value	F crit
Between Groups	4.192921	4	1.04823	0.008527	0.999854	2.436317
Within Groups	17,210.55	140	122.9325			
Total	17,214.75	144				

The comparative analysis of the presented models' accuracy in terms of power output prediction with minimal deviations from the actual values is summarised in Table 8. The results show that ANFIS-PSO and ANFIS-GA outperform the RSM and ANFIS models. For instance, for actual power output, which is 156 W in Run 1, both ANFIS-PSO 156.3 MW and ANFIS-GA 156.4 MW achieve better results than RSM, whose deviation is 160.23 W. Also, for Run 4, both ANFIS-PSO and ANFIS-GA accurately matched the actual value of 165 W in the data set, making them highly reliable and accurate in predicting the power output of the gas turbine. The ANOVA result also supports the analysis of these models, and there is no significant difference between the various groups (p -value = 0.999854). The strengths

indicated by the superior performance of these models, in terms of their accuracy, flexibility of the metaheuristic algorithms and consistency of the ANFIS in terms of the capability of modelling nonlinear relationships and providing consistent predictions, are noteworthy in this study for integrating metaheuristic algorithms with ANFIS. By maintaining plant performance levels at optimal ranges, energy losses and resource wastage are limited. This advancement can enable operators to optimise the input variables, for instance the fuel flow and the load conditions.

Table 9. Comparison between actual, RSM, ANFIS, ANFIS-PSO and ANFIS-GA for thermal efficiency.

Std	Run	Actual Values for Thermal Efficiency (%)	RSM Values for Thermal Efficiency (%)	ANFIS Values for Thermal Efficiency (%)	ANFIS-PSO Values for Thermal Efficiency (%)	ANFIS-GA Values for Thermal Efficiency (%)
2	1	47.10	43.91	47.1	47.3	47.1
16	2	43.80	43.73	43.5	43.8	43.6
22	3	37.90	33.55	37.6	38.1	37.7
6	4	45.30	48.78	45.3	45.4	45.3
7	5	31.70	30.54	31.5	31.7	31.8
19	6	36.20	33.91	36.4	36.4	36.2
27	7	26.80	26.62	26.8	26.8	26.6
20	8	22.90	25.05	23.1	23.1	23.1
24	9	35.30	31.49	35.2	35.4	35.5
12	10	41.30	42.41	41.3	41.5	41.3
17	11	21.60	25.87	21.7	21.8	21.4
30	12	26.40	26.62	26.5	26.4	26.4
5	13	44.20	42.27	44.2	44.4	44.3
3	14	20.90	19.07	21.1	21.1	21.1
10	15	46.40	48.42	46.4	46.4	46.4
28	16	26.30	26.62	26.3	26.3	26.3
15	17	35.10	37.47	35.3	35.2	35.1
26	18	26.50	26.62	26.5	26.5	26.5
8	19	40.60	40.52	40.7	40.6	40.6
11	20	33.10	30.48	33.2	33.3	33.3
29	21	26.70	26.62	26.5	26.7	26.5
14	22	47.80	48.81	47.5	47.6	47.8
25	23	26.60	26.62	26.4	26.5	26.4
4	24	34.60	34.73	34.7	34.6	34.6
23	25	22.10	25.77	22.4	22.3	22.3
18	26	39.50	35.09	39.5	39.5	39.5
9	27	40.70	39.96	40.8	40.7	40.5
1	28	30.80	31.72	30.6	30.8	30.8
21	29	23.40	27.61	23.6	23.4	23.4
13	30	45.30	46.03	45.5	45.3	45.3

ANOVA: single factor for Table 9
SUMMARY

Groups	Count	Sum	Average	Variance			
47.1	29	979.8	33.78621	73.06123			
43.91	29	983	33.89655	69.86593			
47.1	29	980.1	33.79655	72.19177			
47.3	29	981.6	33.84828	72.68544			
47.1	29	979.6	33.77931	72.82099			
ANOVA							
Source of Variation	SS	df	MS	F	p-value	F crit	
Between Groups	0.289931	4	0.072483	0.001005	0.999998	2.436317	
Within Groups	10,097.51	140	72.12507				
Total	10,097.8	144					

Table 10. Comparison between actual, RSM, ANFIS, ANFIS-PSO and ANFIS-GA for specific fuel consumption.

Std	Run	Actual Values for Specific Fuel Consumption (kg/kW·h)	RSM Values for Specific Fuel Consumption (kg/kW·h)	ANFIS Values for Specific Fuel Consumption (kg/kW·h)	ANFIS-PSO Values for Specific Fuel Consumption (kg/kW·h)	ANFIS-GA Values for Specific Fuel Consumption (kg/kW·h)
2	1	0.2300	0.2385	0.235	0.231	0.230
16	2	0.2800	0.2789	0.285	0.282	0.281
22	3	0.1700	0.2046	0.185	0.179	0.169
6	4	0.2200	0.1894	0.222	0.23	0.229
7	5	0.2900	0.2789	0.305	0.296	0.291
19	6	0.1800	0.2091	0.192	0.186	0.178
27	7	0.2900	0.2048	0.286	0.286	0.291
20	8	0.2600	0.2480	0.276	0.271	0.262
24	9	0.2500	0.2413	0.244	0.242	0.249
12	10	0.3200	0.3179	0.317	0.324	0.321
17	11	0.2600	0.2413	0.272	0.268	0.261
30	12	0.1900	0.2048	0.209	0.200	0.191
5	13	0.2200	0.2312	0.224	0.222	0.221
3	14	0.3100	0.3229	0.303	0.312	0.311
10	15	0.2900	0.2878	0.282	0.293	0.289
28	16	0.1900	0.2048	0.185	0.192	0.191
15	17	0.3200	0.3207	0.336	0.319	0.321
26	18	0.2000	0.2048	0.194	0.213	0.210
8	19	0.2300	0.2346	0.223	0.233	0.231
11	20	0.3500	0.3672	0.346	0.351	0.350
29	21	0.2100	0.2048	0.220	0.212	0.211
14	22	0.2400	0.2362	0.237	0.242	0.241
25	23	0.2000	0.2048	0.204	0.202	0.199
4	24	0.2800	0.2711	0.296	0.284	0.278
23	25	0.1700	0.1957	0.184	0.175	0.171
18	26	0.1600	0.1957	0.157	0.154	0.161
9	27	0.3300	0.3346	0.323	0.326	0.331
1	28	0.3000	0.2878	0.318	0.298	0.310
21	29	0.2700	0.2524	0.284	0.276	0.272
13	30	0.2800	0.2755	0.273	0.278	0.281

ANOVA: single factor for Table 10
SUMMARY

Groups	Count	Sum	Average	Variance		
0.23	29	7.26	0.250345	0.002939		
0.2385	29	7.2516	0.250055	0.002427		
0.235	29	7.382	0.254552	0.002851		
0.231	29	7.346	0.25331	0.002795		
0.23	29	7.302	0.251793	0.002947		
ANOVA						
Source of Variation	SS	df	MS	F	p-value	F crit
Between Groups	0.000429	4	0.000107	0.038412	0.99716	2.436317
Within Groups	0.390874	140	0.002792			
Total	0.391303	144				

Another of the most important operating parameters defined for gas turbines includes thermal efficiency, which is described in Table 9 and which influences directly the fuel consumption and emissions. The novelty of this study is further evident in the precise predictions of thermal efficiency, as shown. The results of ANFIS-GA and ANFIS-PSO are more accurate and reliable than other models and present values closest to the actual values. For example, in Run 14, the actual efficiency value was 47.80%, correlating very

well with the value from ANFIS-GA (47.8%), whereas RSM achieved 48.81%. Likewise, in Run 1, ANFIS and ANFIS-GA accurately predicted the actual value (47.10%), showing more reliability and reproducibility than RSM's lower actual value prediction of 43.91%. For the ANOVA results, a p -value of 0.999998 also indicates that all of the models are statistically equivalent, but the values obtained via hybridisation are more accurate in comparison with the RSM. The use of GA and PSO optimisation techniques in this study helps to enhance decision making regarding thermal efficiency by raising the predictive rates impressively. This precision enables the power plants to control the combustion processes, minimise unnecessary fuel consumption and meet the requirements envisaged by emission standards.

The specific fuel consumption outlined in Table 10 can be used when analysing the economic and environmental performance of the gas turbines. Table 10 also demonstrates the further advancement of the study of predictive modelling. As shown in Run 3, the ANFIS-GA model predicted a value of 0.169 kg/kWh, which is close to the actual value of 0.170 kg/kWh. The ANFIS-GA model performed better for this problem compared to the RSM. Likewise, in Run 26, the ANFIS-GA well-predicted 0.161 kg/kWh, while the actual value is 0.1600 kg/kWh. All other models showed a higher error. The obtained p -value from the ANOVA is 0.99716, proving the reliability of the models under growing conditions. The result from the error analysis displays the ANFIS-GA model as being more accurate because it has smaller errors of prediction. This accuracy helps to maximise fuel efficiency, minimise operation expenses, and lower the overall emissions of power plants.

The novelty of this research is that PSO and GA are combined with ANFIS, which enhance the learning capability and, consequently, the predictive accuracy of this system. To perform this, these hybrid models are shown to perform an innovative modelling ability compared to the traditional RSM and the standalone ANFIS model, which effectively captures complex, nonlinear relationships. The results (Tables 8–10) demonstrate the high accuracy in estimating and determining the power output, thermal efficiency and sfc. The improvements achieved in this work provided a framework for model predictive control in gas turbine power plants. The good agreement of the observed values with ANFIS-PSO and ANFIS-GA prediction further indicate the ability of these models to overcome various gas turbine operating parameters. Moreover, the findings of the ANOVA indicate that these models are significant and reliable for real-world applications.

This research makes a positive contribution to the predictive tools and methodologies that are available to gas turbine power plants to minimise prediction errors to meet the demand for maximised efficiency. More so, the p -values of the ANOVA output imply the statistical significance and confirm the reliability of the hybrid models developed for application on real-life data sets. Such development helps to enable an optimal time earlier for timely maintenance schedule decisions and improving the fuel efficiency and load management, leading to decrease in the operational cost and, hence, improving sustainability. The study presents innovation through its hybridisation approach, which enhances model predictability, in addition to maintaining flexibility at different operating conditions in gas turbines. These models also give improved reliability and accuracy for variations such as pressure ratio, intercooler effectiveness, turbine and ambient temperature which are important in running efficient power plants.

4. Optimum Conditions of Operating Parameters

The optimal operating conditions for maximising the power output and thermal efficiency are shown in Figure 17. Based on the findings, the optimal conditions were identified at the specific levels of pressure ratio, ambient temperature, turbine temperature and regenerator effectiveness. These factors were precisely determined as follows: 25, 293 K,

1550 K and 55, respectively. Incorporating these parameters in the gas power plant would optimise the quality of the power output and thermal efficiency to 162.9 MW and 48.8%, respectively. Additionally, it is imperative to monitor how these optimised parameters interact within the gas power plant operational framework, as any factors below or above these range would reduce the thermal efficiency of the power plant.

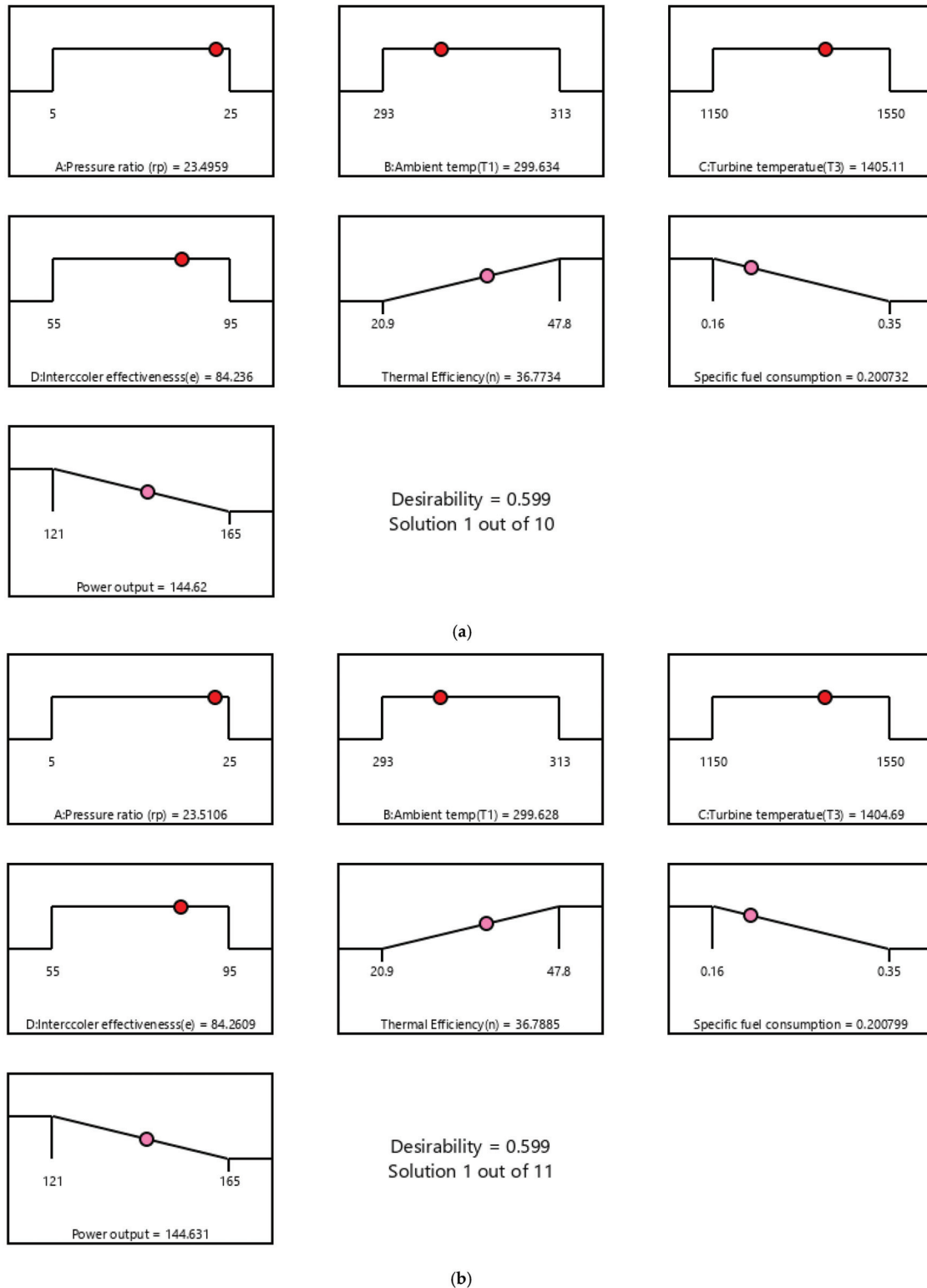


Figure 17. Cont.

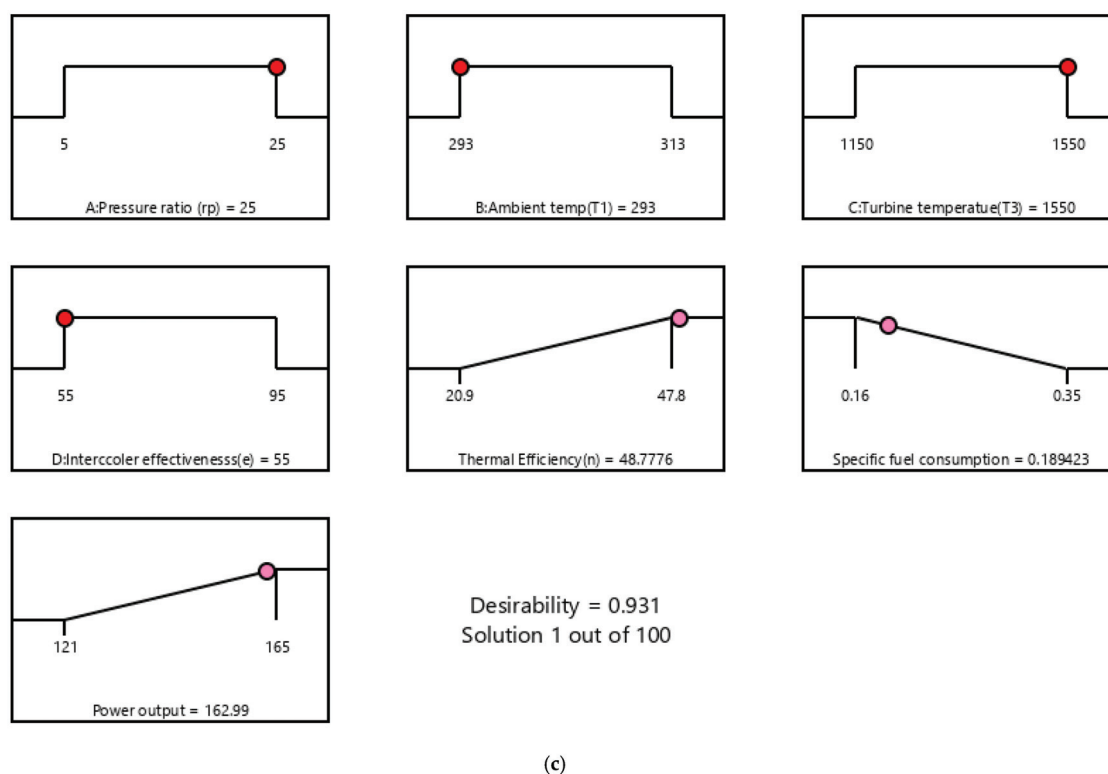


Figure 17. (a) Thermal Efficiency (b) Specific fuel consumption (c) Power output.

5. Conclusions

In this study, a novel optimisation approach to tackle identified inefficiencies in GTPPs with intercoolers, including power output, thermal efficiency and sfc, was developed. The work built upon previous methodologies by applying RSM and metaheuristic algorithms, such as ANFIS, ANFIS PSO and ANFIS GA. These advanced models proved to be adequate for the identification of non-linear relationships of pertinent gas turbine power plant operating parameters, such as pressure ratio, ambient temperature, turbine inlet temperature and the intercooler effectiveness. At the optimal parameters of pressure ratio 25, ambient temperature 293 K, turbine inlet temperature 1550 K and intercooler effectiveness of 95%, the thermal efficiency of the combined cycle is 47.8%, with a power output of 165 MW and a specific fuel consumption of 0.16 kg/kWh. Thus, both ANFIS PSO and ANFIS GA produced higher R^2 values compared to RSM, with R^2 values of 0.979, 0.987 and 0.972 for power output, thermal efficiency and sfc, respectively. These combined mathematical models performed particularly well in fine-tuning of the solutions for highly complex and interdependent integrated operational environments. This approach enables the design of flexible and adaptable solutions for optimising GTPPs with tremendous potentials for power generation for industries and utilities. It defines a roadmap for sustainable energy system designs, thereby providing a connection between the emergent innovations and the energy problems in regions with growing energy demands. This study helps improve the generation of energy, minimise emissions, and contribute to the global sustainable development goals, in terms of SDG Goal 7 (affordable and clean energy), as well as Africa's Agenda 2063 on energy security and economic development.

Future studies will focus on transient performance analysis using dynamic simulations under various ambient conditions. Also, energy and exergy analyses can be used to improve the performance and efficiency of the gas turbine. These approaches will advance the usable nature of the mathematical models and strengthen the understanding regarding performance and viability in power systems.

Author Contributions: Conceptualisation, A.O.O.; formal analysis, A.O.O.; funding acquisition, U.B.A. and D.A.D.; investigation, A.O.O., U.B.A. and D.A.D.; methodology, A.O.O. and U.B.A.; project administration, A.O.O.; resources, A.O.O., U.B.A. and D.A.D.; software, A.O.O. and D.A.D.; supervision, U.B.A. and D.A.D.; validation, U.B.A. and D.A.D.; visualisation, A.O.O. and U.B.A.; writing—original draft, A.O.O.; writing—review and editing, A.O.O., U.B.A. and D.A.D. All authors have read and agreed to the published version of the manuscript.

Funding: This research received no external funding.

Data Availability Statement: The original contributions presented in the study are included in the article; further inquiries can be directed to the corresponding author.

Acknowledgments: The authors appreciate Tshwane University of Technology, South Africa, for the support provided for this study.

Conflicts of Interest: The authors declare that the research was conducted in the absence of any commercial or financial relationships that could be construed as a potential conflict of interest.

References

1. Baakeem, S.; Orfi, J.; Alaqel, S.; Al-Ansary, H. Impact of Ambient Conditions of Arab Gulf Countries on the Performance of Gas Turbines Using Energy and Exergy Analysis. *Entropy* **2017**, *19*, 32. [CrossRef]
2. Olusanya, O.O.; Onokwai, A.O.; Anyaegbuna, B.E.; Iweriolor, S.; Omoniyi, E.B. Modelling and optimization of operating parameters for improved steam energy production in the food and beverage industry in a developing country. *Front. Energy Res.* **2024**, *12*, 1417031.
3. Onokwai, A.O.; Okonkwo, U.C.; Osueke, C.O.; Olayanju, T.M.A.; Ezugwu, C.A.; Diarah, R.S.; Banjo, S.O.; Onokpate, E.; Olabamiji, T.S.; Ibiwoye, M.; et al. Thermal analysis of solar box cooker in Omu-Aran Metropolis. *J. Phys. Conf. Ser.* **2019**, *1378*, 032065. [CrossRef]
4. Dirisu, J.O.; Oyedepo, S.O.; Olawole, O.C.; Somefun, T.E.; Peter, N.J.; Babatunde, D.; Nwaokocha, C.N.; Onokwai, A.O.; Obanor, E.; Alam, M.; et al. A comprehensive review of biofuel utilization for household cooking in developing countries: Economic and environmental impacts. *Process Saf. Environ. Prot.* **2024**, *191*, 585–604. [CrossRef]
5. Elwardany, M.; Nassib, A.M.; Mohamed, H.A. Exergy analysis of a gas turbine cycle power plant: A case study of power plant in Egypt. *J. Therm. Anal. Calorim.* **2024**, *149*, 7433–7447. [CrossRef]
6. Ndwandwe, B.; Akuru, U.B.; Ramphele, L.; Thango, B.A.; Memane, N.P.; Okoro, O.I. Power Transformer Design Implementation for Large-Scale Solar Power Plant Grid Integration. In Proceedings of the 2021 International Conference on Electrical, Computer and Energy Technologies (ICECET), Cape Town, South Africa, 9–10 December 2021; IEEE: New York, NY, USA; 2021; pp. 1–5. [CrossRef]
7. Omar, H.; Kamel, A.; Alsanousi, M. Performance of Regenerative Gas Turbine Power Plant. *Energy Power Eng.* **2017**, *9*, 136–146. [CrossRef]
8. Oosthuizen, C.; Van Wyk, B.; Hamam, Y.; Desai, D.; Alayli, Y. The Use of Gridded Model Output Statistics (GMOS) in Energy Forecasting of a Solar Car. *Energies* **2020**, *13*, 1984. [CrossRef]
9. Mashiachidi, M.; Desai, D. Fatigue life prediction of mistuned steam turbine blades subjected to deviations in blade geometry. *Sci. Eng. Technol.* **2023**, *3*, 24–35. [CrossRef]
10. Oyedepo, S.O.; Fagbenle, R.O.; Adefila, S.S.; Alam, M.M.d.; Dunmade, I.S. Thermo-economic and environmental assessment of selected gas turbine power plants in Nigeria. *Prog. Ind. Ecol. Int. J.* **2018**, *12*, 361. [CrossRef]
11. Kosowski, K.; Piwowarski, M. Design Analysis of Micro Gas Turbines in Closed Cycles. *Energies* **2020**, *13*, 5790. [CrossRef]
12. Al-attab, K.A.; Zainal, Z.A. Externally fired gas turbine technology: A review. *Appl. Energy* **2015**, *138*, 474–487. [CrossRef]
13. Alaabidy, W.; Antipov, Y.A.; Al-Rubaiawi, M.; Frolov, M. Gas turbine suitable for the ambient conditions prevailing in Arab Gulf countries: A prognostic analysis. *J. Appl. Eng. Sci.* **2023**, *21*, 982–998. [CrossRef]
14. Ibrahim, T.K.; Rahman, M.M.; Mohammed, M.K.; Basrawi, F. Statistical analysis and optimum performance of the gas turbine power plant. *Int. J. Automot. Mech. Eng.* **2022**, *13*, 3215–3225. [CrossRef]
15. Kadhim, H.J.; Abbas, A.K.; Kadhim, T.J.; Rashid, F.L. Evaluation of Gas Turbine Performance in Power Plant with High-Pressure Fogging System. *Math. Model. Eng. Probl.* **2023**, *10*, 605–612. [CrossRef]
16. Goucem, M. Influence of the Ambient Temperature on the Efficiency of Gas Turbines. *Fluid. Dyn. Mater. Process* **2024**, *20*, 2265–2279. [CrossRef]
17. Ibrahim, T.K.; Basrawi, F.; Awad, O.I.; Abdullah, A.N.; Najafi, G.; Mamat, R.; Hagos, F. Thermal performance of gas turbine power plant based on exergy analysis. *Appl. Therm. Eng.* **2017**, *115*, 977–985. [CrossRef]

18. Hu, L.; Chen, F.; Meng, Y.; Sang, Z. Expansion of stable operational range in MILD hydrogen combustion based on catalytic techniques. *Int. J. Hydrogen Energy* **2024**, *84*, 334–343. [CrossRef]
19. Hagani, B.N.; Bousbaa, H.; Bencherif, M. Numerical Study of Hydrogen enrichment and injector nozzle number impacts on non-premixed turbulent combustion characteristics in a Gas Turbine cannular Combustion Chamber. *EARTH Sci. Hum. Constr.* **2024**, *4*, 78–87. [CrossRef]
20. Venkatesan, E.P.; Murugesan, P.; Pichika, S.V.V.S.N.; Janaki, D.V.; Javed, Y.; Mahmoud, Z.; Saleel, C.A. Effects of Injection Timing and Antioxidant on NOx Reduction of CI Engine Fueled with Algae Biodiesel Blend Using Machine Learning Techniques. *Sustainability* **2022**, *15*, 603. [CrossRef]
21. Syed, T.; Krujatz, F.; Ihadjadene, Y.; Mühlstädt, G.; Hamed, H.; Mädler, J.; Urbas, L. A review on machine learning approaches for microalgae cultivation systems. *Comput. Biol. Med.* **2024**, *172*, 108248. [CrossRef] [PubMed]
22. Onokwai, A.O.; Olusanya, O.O.; Onifade, M.K.; Anyaegbuna, B.E.; Onoriode, A.; Agholor, D. Comparative analysis of response surface methodology and adaptive neuro-fuzzy inference system for predictive fault detection and optimization in beverage industry. *Front. Mech. Eng.* **2024**, *10*, 1428717. [CrossRef]
23. Alsaghir, A.; Bahk, J.H. Performance Optimization and Exergy Analysis of Thermoelectric Heat Recovery System for Gas Turbine Power Plants. *Entropy* **2023**, *25*, 1583. [CrossRef]
24. Mishra, S.; Sharma, A.; Kumari, A.; Sanjay. Response surface methodology based optimization of air-film blade cooled gas turbine cycle for thermal performance prediction. *Appl. Therm. Eng.* **2020**, *164*, 114425. [CrossRef]
25. Boyce, M.P. *Gas Turbine Engineering Handbook*, 2nd ed.; Gulf Professional Publishing: Boston, MA, USA, 2002; 799p.
26. Cuevas, E.; Ascencio-Piña, C.R.; Pérez, M.; Morales-Castañeda, B. Considering radial basis function neural network for effective solution generation in metaheuristic algorithms. *Sci. Rep.* **2024**, *14*, 16806. [CrossRef]
27. Rahman, M.A.; Sokkalingam, R.; Othman, M.; Biswas, K.; Abdullah, L.; Abdul Kadir, E. Nature-Inspired Metaheuristic Techniques for Combinatorial Optimization Problems: Overview and Recent Advances. *Mathematics* **2021**, *9*, 2633. [CrossRef]
28. Tomar, V.; Bansal, M.; Singh, P. Metaheuristic Algorithms for Optimization: A Brief Review. In Proceedings of the RAISE-2023, Dubai, United Arab Emirates, 4–5 October 2023; MDPI: Basel, Switzerland, 2024; p. 238. [CrossRef]
29. Hadroug, N.; Hafaifa, A.; Guemana, M.; Kouzou, A.; Salam, A.; Chaibet, A. Heavy duty gas turbine monitoring based on adaptive neuro-fuzzy inference system: Speed and exhaust temperature control. *Math—Ind. Case Stud.* **2017**, *8*, 8. [CrossRef]
30. Peres, F.; Castelli, M. Combinatorial Optimization Problems and Metaheuristics: Review, Challenges, Design, and Development. *Appl. Sci.* **2021**, *11*, 6449. [CrossRef]
31. Al-Aqeeli, Y.H.; Mahmood Agha, O.M.A. Optimal Operation of Multi-reservoir System for Hydropower Production Using Particle Swarm Optimization Algorithm. *Water Resour. Manag.* **2020**, *34*, 3099–3112. [CrossRef]
32. Gong, L.; Yu, M.; Kollias, S. Optimizing Crop Yield and Reducing Energy Consumption in Greenhouse Control Using PSO-MPC Algorithm. *Algorithms* **2023**, *16*, 243. [CrossRef]
33. Shamoushaki, M.; Ehyaei, M. Exergy, economic and environmental (3E) analysis of a gas turbine power plant and optimization by MOPSO algorithm. *Therm. Sci.* **2018**, *22 Pt A*, 2641–2651. [CrossRef]
34. Hussain, S.; Al-Hitmi, M.; Khaliq, S.; Hussain, A.; Asghar Saqib, M. Implementation and Comparison of Particle Swarm Optimization and Genetic Algorithm Techniques in Combined Economic Emission Dispatch of an Independent Power Plant. *Energies* **2019**, *12*, 2037. [CrossRef]
35. Al-Doori, W.H.A.R. Parametric Performance of Gas Turbine Power Plant with Effect Intercooler. *Mod. Appl. Sci.* **2011**, *5*, 173. [CrossRef]
36. Mikielewicz, D.; Kosowski, K.; Tucki, K.; Piwowarski, M.; Stępień, R.; Orynycz, O.; Włodarski, W. Gas Turbine Cycle with External Combustion Chamber for Prosumer and Distributed Energy Systems. *Energies* **2019**, *12*, 3501. [CrossRef]
37. Azizi, M.W.; Bensouici, M.; Bensouici, F.Z. Thermoexergetic analysis and multi-objective optimization of steam power plant performances. *AIUB J. Sci. Eng.* **2024**, *23*, 124–134. [CrossRef]
38. Boubacar Laougé, Z.; Çiğgin, A.S.; Merdun, H. Optimization and characterization of bio-oil from fast pyrolysis of Pearl Millet and *Sida cordifolia* L. by using response surface methodology. *Fuel* **2020**, *274*, 117842. [CrossRef]
39. Bensouici, M.; Azizi, M.W.; Bensouici, F.Z. Performance Analysis and Optimization of Regenerative Gas Turbine Power Plant using RSM: Optimization of regenerative gas turbine power plant. *Int. J. Automot. Mech. Eng.* **2023**, *20*, 10671–10683. [CrossRef]
40. Lee, X.J.; Lee, L.Y.; Hiew, B.Y.Z.; Gan, S.; Thangalazhy-Gopakumar, S.; Kiat Ng, H. Multistage optimizations of slow pyrolysis synthesis of biochar from palm oil sludge for adsorption of lead. *Bioresour. Technol.* **2017**, *245*, 944–953. [CrossRef]
41. Okokpuije, I.P.; Onokwai, A.O.; Onokpiti, E.; Babaremu, K.; Ajisegiri, E.S.; Osueke, C.O.; Akinlabi, S.A.; Akinlabi, E.T. Modelling and optimisation of intermediate pyrolysis synthesis of bio-oil production from palm kernel shell. *Clean. Eng. Technol.* **2023**, *16*, 100672. [CrossRef]
42. Singh, D.K.; Tirkey, J.V. Performance optimization through response surface methodology of an integrated coal gasification and CI engine fuelled with diesel and low-grade coal-based producer gas. *Energy* **2022**, *238*, 121982. [CrossRef]

43. Wang, W.; Chen, L.; Sun, F.; Wu, C. Power optimization of an irreversible closed intercooled regenerated brayton cycle coupled to variable-temperature heat reservoirs. *Appl. Therm. Eng.* **2005**, *25*, 1097–1113. [CrossRef]
44. Dabwan, Y.N.; Zhang, L.; Pei, G. A novel inlet air cooling system to improve the performance of intercooled gas turbine combined cycle power plants in hot regions. *Energy* **2023**, *283*, 129075. [CrossRef]
45. Kotowicz, J.; Job, M.; Brzęczek, M.; Nawrat, K.; Mędrych, J. The methodology of the gas turbine efficiency calculation. *Arch. Thermodyn.* **2016**, *37*, 19–35. [CrossRef]
46. Adefarati, T.; Bansal, R.C. Energizing Renewable Energy Systems and Distribution Generation. In *Pathways to a Smarter Power System*; University of Pretoria: Pretoria, South Africa, 2019; pp. 29–62. [CrossRef]
47. Velásquez, L.; Rubio-Clemente, A.; Tobón, D.; Botero, F.; Arrieta, C.; Chica, E. Experimental Optimization of the Propeller Turbine Performance Using the Response Surface Methodology. *Sustainability* **2024**, *16*, 8476. [CrossRef]
48. Kumar, M.; Mishra, P.K.; Upadhyay, S.N. Pyrolysis of *Saccharum munja*: Optimization of process parameters using response surface methodology (RSM) and evaluation of kinetic parameters. *Bioresour. Technol. Rep.* **2019**, *8*, 100332. [CrossRef]
49. Samitha Weerakoon, A.H.; Assadi, M. Trends and advances in micro gas turbine technology for sustainable energy solutions: A detailed review. *Energy Convers. Manag. X* **2023**, *20*, 100483. [CrossRef]
50. Owoseni, A.T.; Olabode, O.; Akintola, K.G.; Enikanselu, P.A. An improved adaptive neuro-fuzzy inference system using probability trajectory-based clustering ensemble. *Sci. Afr.* **2020**, *9*, e00520. [CrossRef]

Disclaimer/Publisher’s Note: The statements, opinions and data contained in all publications are solely those of the individual author(s) and contributor(s) and not of MDPI and/or the editor(s). MDPI and/or the editor(s) disclaim responsibility for any injury to people or property resulting from any ideas, methods, instructions or products referred to in the content.

Article

Improved Design of an Eddy-Current Speed Sensor Based on Harmonic Modeling Technique

Duy-Tinh Hoang ¹, Manh-Dung Nguyen ¹, Yong-Joo Kim ², Anh-Tuan Phung ^{3,*}, Kyung-Hun Shin ^{4,*} and Jang-Young Choi ^{1,*}

¹ Department of Electrical Engineering, Chungnam National University, Daejeon 34134, Republic of Korea; hoangduytinh@o.cnu.ac.kr (D.-T.H.); nguyenmanhdung@o.cnu.ac.kr (M.-D.N.)

² Department of Biosystem Machinery Engineering, Chungnam National University, Daejeon 34134, Republic of Korea; babina@cnu.ac.kr

³ Department of Electrical Engineering, Hanoi University of Science and Technology, Hanoi 11657, Vietnam

⁴ Department of Electrical Engineering, Changwon National University, Changwon 51140, Republic of Korea

* Correspondence: tuan.phunganh1@hust.edu.vn (A.-T.P.); kshin@changwon.ac.kr (K.-H.S.); choi_jy@cnu.ac.kr (J.-Y.C.)

Abstract: This study proposes an improved design of an eddy-current speed sensor (ECSS) by adding a ferromagnetic core to the stator, resulting in a sensitivity enhancement ranging from three to sixty times compared to a reference model according to shaft materials. An improved analytical model (AM) based on harmonic modeling (HM) is developed to account for the effects of core permeability, validated through finite element analysis (FEA), demonstrating excellent agreement between the two methods. Based on this model, the optimal dimensions of the proposed design are obtained, and comprehensive analyses of shaft materials and excitation source parameters are performed. The results show that the magnetic shaft offers the highest sensitivity, while a nonmagnetic shaft with low conductivity ensures optimal linearity. Meanwhile, a nonmagnetic shaft with high conductivity leads to low sensitivity and higher linearity errors. Furthermore, a high-frequency excitation source enhances output linearity but necessitates careful selection based on the shaft materials. The dynamic characteristics of the proposed design under different operating conditions are analyzed using a coupled Ansys Twin Builder and Maxwell 2D model. The proposed design and AM significantly improve ECSS performance and the analyzing tool, providing a robust and practical solution for precise speed measurement in various applications.

Keywords: analytical model; conductive shaft; eddy current; ferromagnetic core; finite element method; harmonic modeling; harmonic modeling; speed sensor

MSC: 35J05

1. Introduction

Over the past few decades, permanent magnet synchronous machines (PMSMs) have been extensively developed and are now the backbone of various applications due to their high efficiency, power density, and precise control capabilities [1,2]. However, induction machines (IMs) remain widely used in industry, accounting for approximately 80% of industrial applications [3]. This preference is largely due to their low production costs, simple structure and control, and high durability under extreme temperatures and harsh environments. To ensure the optimal performance of IMs under varying load conditions, accurate and reliable speed measurement is crucial.

Sensorless estimation techniques have been widely studied because of their non-intrusive and contactless structure. Nevertheless, these methods face significant challenges, such as complex hardware requirements for signal processing, susceptibility to electrical faults in stator windings, and slow response times under dynamic conditions [4]. Conventional measurements rely on devices such as DC tachometers [5,6], optical encoders, variable reluctance sensors [7–10], and resolvers [11–14] that need a connection to the shaft. DC tachometers, although widely used, incur high maintenance costs due to their brush structure, while optical encoders are particularly sensitive to environmental factors such as dust and dirt. Variable reluctance sensors and resolvers are cost effective, reliable, and robust but require complicated signal processing [15].

Recently, eddy-current speed sensors (ECSSs) have emerged as a novel solution with contactless and non-intrusive approaches. Overall, there are two types, categorized based on the excitation source. The first type [4,15–20] is excited by a high-frequency source (HFS), and the other [21–24] operates using a permanent magnet (PM) source. Evidently, the latter is simpler and more compact, but it also has drawbacks. Low-frequency or static excitation fields can introduce interference errors in the Hall effect [15], resulting in a limited linear range, while the PM is further susceptible to temperature changes. Although the first type requires a wave generator for excitation, it mitigates temperature effects due to the stable magnetic field maintained by a constant excitation current. Furthermore, with HFS, the first offers higher accuracy, with a maximum linearity deviation of only 0.15% compared to 1.89% of the PM type in the same 3000 rpm testing range, as shown in [17,24], respectively. Hence, the operating range can be extended beyond that of the PM type. These types of ECSSs feature several topologies applied to various objects, such as conductive surfaces [16,18], solid conductive shafts [17,19,20], and hollow conductive shafts [15]. These sensors can achieve excellent linearity, with errors smaller than 0.15% [15], a wide detection range, and minimal impact from shaft eccentricity [17]. However, these sensors generally have low sensitivity, often producing signals in the range of several $\mu\text{V}/\text{rpm}$. As a result, signal amplification is necessary, which not only increases the cost of signal processing but also makes the system more vulnerable to interference from external magnetic fields.

Additionally, the design, optimization, and analysis of ECSS require computational tools such as finite element analysis (FEA) or analytical models (AMs). FEA, whether in 2D or 3D, offers significant advantages in terms of high accuracy and the ability to model complex geometries. Nevertheless, its primary limitation lies in the long computation time, especially when addressing dominant eddy-current effects, which involve intricate interactions between magnetic fields and conductive materials. In contrast, AMs are often preferred for simpler problems due to their computational efficiency. Many AMs have been developed based on the subdomain method (SDM) for ECSS [17,19,20] and electrical machines, considering both magnetostatic [25–27] and time-dependent problems [28,29]. Despite the maturity, the limitations of SDM in accounting for core permeability restrict its applications. Fortunately, the harmonic modeling (HM) technique has recently been proposed as a novel approach to consider permeability. Since the first research [30] was introduced in 2016, many extended studies have been conducted to consider permeability, saturation effects [31–34], and irreversible demagnetization [35]. However, most of these studies are performed under magnetostatic assumptions, neglecting the time dependency of the problem, which prevents them from being applied to the ECSS analysis.

This paper proposes an improved design based on the ECSS introduced in [17] by integrating a low-reluctance core into the stator, resulting in a sensitivity increase of three to sixty times compared to a reference model [17]. Furthermore, an improved analytical model based on HM that considers core permeability is presented to account for the effects of the low-reluctance core accurately. Validation through FEA demonstrates the

exceptional accuracy of the proposed AM. Steady-state analyses performed by the AM are used to evaluate the effects of shaft material and excitation-source parameters on the design performance and determine the optimal dimensions of the proposed design.

Furthermore, dynamic characteristics of the improved ECSS, which were not extensively addressed in previous studies [15,17,19,20], are captured using a coupled Ansys Twinbuilder and Maxwell 2D model. This coupled approach allows for a comprehensive evaluation of sensor performance under varying operating conditions, highlighting the advantages of the proposed design in both steady-state and dynamic scenarios.

2. Proposed Design and Operation Principle

This study is based on an ECSS described in [17], with the excitation and pick-up coils positioned perpendicularly, as shown in Figure 1a. The induced eddy currents in conductive objects consist of two components: the transformer component resulting from the time variation in the source field and the motional component arising from the relative movement between the conductive object and the excitation field [36]. The transformer component produces a symmetric flux distribution in the conductive object, whereas the motional component introduces asymmetry [37,38], which leads to a net flux through the pick-up coil that is greater than zero, thereby inducing a voltage. Obviously, there are two ways to increase this voltage: increasing the motional speed of the object or strengthening the excitation field. Since the speed cannot be controlled in ECSS, the proposed design enhances the excitation field strength by incorporating low-reluctance paths, such as teeth and yoke, effectively guiding the magnetic flux, as depicted in Figure 1b. A detailed 3D representation of the new structure is shown in Figure 1c. This improved structure improves the sensor's sensitivity and provides a robust frame to support the windings.

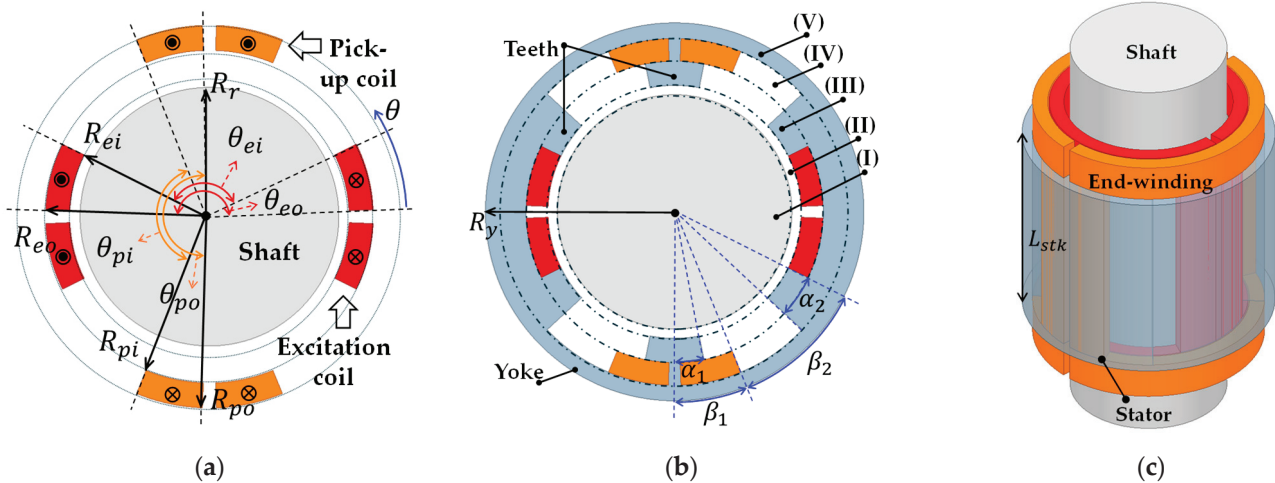


Figure 1. (a) Reference design [17]; (b) proposed design; and (c) 3D model of the proposed design.

The operational principle of the proposed design is depicted in Figure 2. A high-frequency current is injected into the excitation coils to generate a stable magnetic field. At zero speed, Figure 2a illustrates the symmetric magnetic flux distribution generated solely by the transformer component, resulting in zero flux linkage in the pick-up coil. Meanwhile, when the shaft rotates, the motional component creates an asymmetric flux distribution, as shown in Figure 2b, which induces a voltage in the pick-up coils. This induced voltage is proportional to the shaft speed, making the sensor highly suitable for accurate speed measurement.

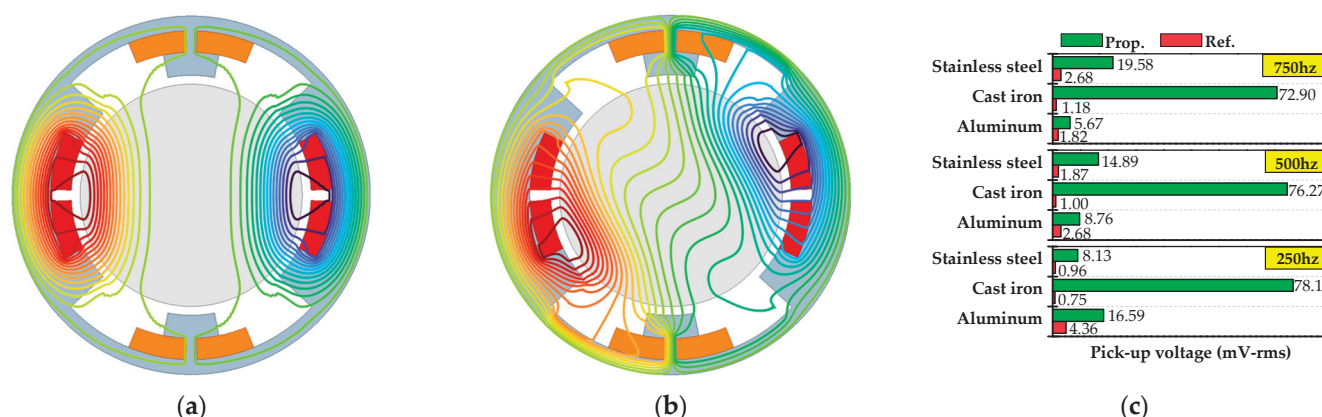


Figure 2. Analytical results under a 750 Hz, 150 mA excitation source: flux distribution of the proposed design with the aluminum shaft at (a) zero speed, (b) 20,000 rpm, and (c) pick-up voltage comparison between the reference [17] and proposed design with different shafts at 3000 rpm.

Figure 2c compares the output voltage waveforms of the proposed and reference designs [17] for different shaft materials: nonmagnetic shafts (aluminum and stainless steel) and a magnetic shaft (cast iron). The excitation source is set to an amplitude of 150 mA, with the shaft speed at 3000 rpm. Across all tested frequencies, the proposed design consistently produces a significantly higher output voltage than the reference design. Specifically, the minimum and maximum increases are 3.1 and 61.8 times at 750 Hz, 3.3 and 76.3 times at 500 Hz, and 3.8 and 104.2 times at 250 Hz. Therefore, these results demonstrate that the proposed design substantially improves ECSS performance while maintaining the same power consumption.

3. 2D Analytical Model Using Harmonic Modeling

The analytical model is performed in the 2D cylindrical coordinate system, and the symbols utilized in this section are shown in Table 1. As depicted in Figure 1b, the sensor is divided into five regions: (I) shaft, (II) air gap, (III) excitation coil region, (IV) pick-up coil region, and (V) yoke. Due to the small excitation source used in the sensor, saturation effects in the ferromagnetic parts can be neglected. Therefore, permeability in the ferromagnetic parts is considered uniform, denoted as μ_{st} , and to simplify the problem further, the following assumptions are made:

- In each region, permeability is variant in tangential and invariant in radial directions.
- The end effects are neglected.

Table 1. Nomenclature.

Symbol	Explanation	Symbol	Explanation
$r/\theta/z$	Radius/tangential and axial directions	σ	Conductivity
j	Imaginary unit	ω_r	Electric angular velocity of moving object
\vec{A}	Magnetic vector potential	A	Matrix form of magnetic vector potential
\vec{B}	Magnetic flux density	B	Matrix form of magnetic flux density
\vec{H}	Magnetic field strength	H	Matrix form of magnetic field strength
\vec{J}_z	Current density vector	J	Matrix form of current density
μ	Permeability	J_{ext}	Matrix form of external current density
$\hat{\mu}_n$	CFS coefficient of n th harmonic	A^T	Transpose matrix of matrix A
$\hat{\mu}_n^{rec}$	Inverse coefficient of n th harmonic	$\mu_{c,r}$	Permeability convolution matrix in radial direction
μ_0	Vacuum permeability	$\mu_{c,\theta}$	Permeability convolution matrix in tangential direction
μ_{sh}	Shaft permeability	K_θ	Diagonal matrix of N

Table 1. Cont.

Symbol	Explanation	Symbol	Explanation
μ_{st}	Stator permeability	I_T	First kind of Bessel function
$\hat{J}_{z,n}$	CFS coefficient of n th harmonic	K_T	Second kind of Bessel function
J_{ext}	External excitation source	N_t^p	Number of turns in the pick-up coil
k, n	Time and spatial harmonic orders	N_t^e	Number of turns in the excitation coil
ω_s, f_s	Time-based velocity and frequency	L_{stk}	Stack length of the sensor
\Re	Real part	ϕ_i^p	Flux passing through a conductor i of the pick-up coil
ψ^p	Flux linkage through the pick-up coil	ψ^e	Flux linkage through the excitation coil
N	Highest harmonic order	I	Excitation current

3.1. Complex Fourier Series Representation

The magnetic vector potential, magnetic flux density, magnetic field strength, and current density distribution can be expressed in terms of the complex Fourier series (CFS), which considers time dependency t as follows.

$$\vec{A} = A_z(r, \theta, t) \vec{u}_z \quad (1)$$

$$\vec{B} = B_r(r, \theta, t) \vec{u}_r + B_\theta(r, \theta, t) \vec{u}_\theta \quad (2)$$

$$\vec{H} = H_r(r, \theta, t) \vec{u}_r + H_\theta(r, \theta, t) \vec{u}_\theta \quad (3)$$

where $\vec{u}_z, \vec{u}_r, \vec{u}_\theta$ are unit vectors, and expressions $X(r, \theta, t)$ in Equations (1)–(3) are given by.

$$X(r, \theta, t) = \sum_{k=-\infty}^{\infty} \sum_{n=-\infty}^{\infty} \hat{X}_{k,n}(r) e^{j(k\omega_s t - n\theta)} \quad (4)$$

where k is the time-harmonic order, n is the spatial-harmonic order, and $\omega_s = 2\pi f_s$ is the time-based rotational speed of the excitation field.

Assuming that the sensor is excited by a single harmonic, Equation (4) is simplified as.

$$X(r, \theta, t) = \sum_{n=-\infty}^{\infty} \hat{X}_n(r) e^{j(\omega_s t - n\theta)} \quad (5)$$

For practical calculations, the finite Fourier series are utilized.

$$X(r, \theta, t) = \Re \left\{ \sum_{n=-N}^N \hat{X}_n(r) e^{j(\omega_s t - n\theta)} \right\} \quad (6)$$

where N is the highest harmonic order considered.

Equation (6) is rewritten in the matrix form as follows.

$$X(r, \theta, t) = \Re \left\{ e^{j\omega_s t} \mathbf{X}^T \cdot \mathbf{E} \right\} \quad (7)$$

$$\mathbf{X} = [\hat{X}_{-N} \dots \hat{X}_N]^T; \mathbf{E} = [e^{jN\theta} \dots 1 \dots e^{-jN\theta}]^T \quad (8)$$

Therefore, the CFS coefficient vectors of electromagnetic quantities can be written as $A_z, B_r, B_\theta, H_r, H_\theta$, and J_z , respectively. Additionally, permeability distribution in each region only varies in the tangential direction and is given by $\mu(\theta) = \mu$.

Cauchy's product theorem and Fourier factorization method are used to express the relationship between the field strength \mathbf{H} and flux density \mathbf{B} as follows [31].

$$\mathbf{B}_r = \mu_{c,r} \mathbf{H}_r; \mathbf{B}_\theta = \mu_{c,\theta} \mathbf{H}_\theta \quad (9)$$

where $\mu_{c,r}$, $\mu_{c,\theta}$ are the convolution matrices of permeability Fourier series coefficients on the radial and tangential directions, respectively, expressed as

$$\mu_{c,r} = \begin{bmatrix} \hat{\mu}_0 & \cdots & \hat{\mu}_{-2N} \\ \vdots & \ddots & \vdots \\ \hat{\mu}_{2N} & \cdots & \hat{\mu}_0 \end{bmatrix} \quad (10)$$

$$\mu_{c,\theta} = \begin{bmatrix} \hat{\mu}_0^{rec} & \cdots & \hat{\mu}_{-2N}^{rec} \\ \vdots & \ddots & \vdots \\ \hat{\mu}_{2N}^{rec} & \cdots & \hat{\mu}_0^{rec} \end{bmatrix} \quad (11)$$

3.2. Excitation Source and Permeability Convolution Matrix

Figure 3a shows the current density distribution in Region (III), and CFS coefficients $\hat{J}_{z,n}$ are given by.

$$\hat{J}_{z,n} = \begin{cases} 0 & ; n = 0 \\ \frac{J_0}{\pi n} \left[\sin\left(\frac{n(\pi-\theta_{ei})}{2}\right) + \sin\left(\frac{n(\pi+\theta_{ei})}{2}\right) - \sin\left(\frac{n(\pi-\theta_{eo})}{2}\right) - \sin\left(\frac{n(\pi+\theta_{eo})}{2}\right) \right] & ; n \neq 0 \end{cases} \quad (12)$$

where $J_0 = \frac{N_t^e I(t)}{(\theta_{eo} - \theta_{ei})(R_{eo}^2 - R_{ei}^2)/4}$; N_t^e is the number of turns of the excitation coils.

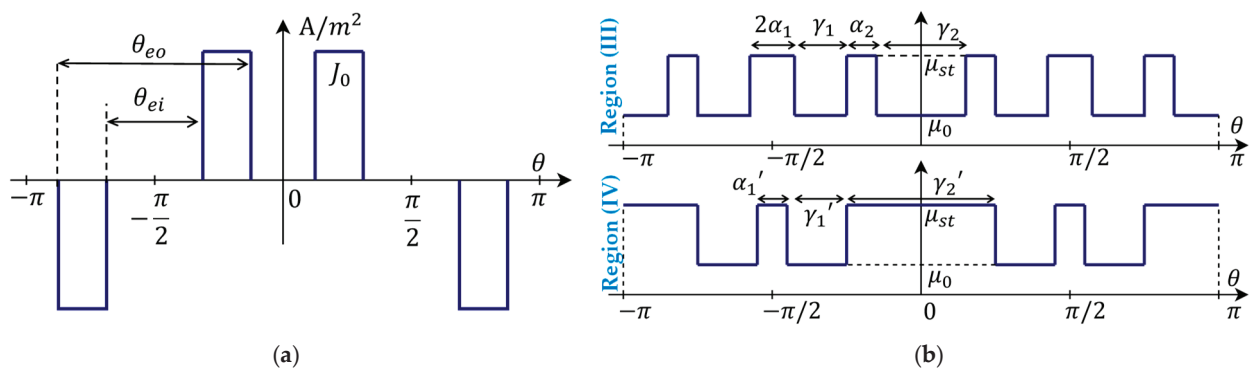


Figure 3. (a) Current density distribution in Region (III). (b) Permeability distribution in Region (III) and Region (IV).

From the permeability distribution in Regions (III) and (IV) described in Figure 3b, the CFS coefficients of permeability in Region (III) are written as

$$\hat{\mu}_0^{III} = \frac{2\mu_{st}(\alpha_1 + \alpha_2) + \mu_0(\gamma_2 + 2\gamma_1)}{\pi}; n = 0 \quad (13)$$

$$\begin{aligned} \hat{\mu}_n^{III} = & \frac{1}{n\pi} \sum_{i=1}^2 e^{jn\theta_{i1}} [\mu_0 \sin n(\alpha_1 + \gamma_1) + (\mu_{st} - \mu_0) \sin(n\alpha_1)] \\ & + e^{jn\theta_{i2}} [\mu_{st} \sin n\left(\frac{\gamma_2}{2} + \alpha_2\right) + (\mu_0 - \mu_{st}) \sin\left(\frac{n\gamma_2}{2}\right)]; n \neq 0 \end{aligned} \quad (14)$$

For Region (IV):

$$\hat{\mu}_0^{IV} = \frac{\mu_{st}(\alpha_1' + \gamma_2') + 2\mu_0\gamma_1'}{\pi}; n = 0 \quad (15)$$

$$\hat{\mu}_n^{IV} = \frac{1}{n\pi} \sum_{i=1}^2 e^{jn\theta_{i1}} \left[\mu_0 \sin n\left(\gamma_1' + \frac{\gamma_2'}{2}\right) + (\mu_{st} - \mu_0) \sin\left(n\frac{\gamma_2'}{2}\right) \right] + e^{jn\theta_{i2}} \mu_{st} \sin n\frac{\alpha_1'}{2}; n \neq 0 \quad (16)$$

where $\theta_{i1}^i = (i-1)\pi$ and $\theta_{i2}^i = (2i-1)\pi/2$.

The inverse coefficient μ_n^{rec} in Equation (11) is obtained by replacing μ_0 and μ_{st} with their inverse value $1/\mu_0$, $1/\mu_{st}$ in Equations (13)–(16).

3.3. Solution Derivation of Partial Differential Equations (PDE)

The magnetic field is derived from Ampere's law as follows:

$$\nabla \times \vec{H} = \vec{J} \quad (17)$$

$$\frac{\partial H_\theta}{\partial r} + \frac{H_\theta}{r} - \frac{1}{r} \frac{\partial H_r}{\partial \theta} = J_{ext} - \sigma \left(\frac{\partial A}{\partial t} + \omega_r \frac{\partial A}{\partial \theta} \right) \quad (18)$$

where J_{ext} is the external excitation source, such as current density, and the second component on the right-hand side represents the induced eddy current in the conductive object resulting from both temporal and spatial variation. σ , ω_r are the conductivity and the electric angular speed of the moving object.

From Equations (6) and (7), the components of Equation (18) are developed as follows:

$$\frac{\partial H_\theta}{\partial r} = e^{j\omega_s t} \frac{\partial \mathbf{H}_\theta^T}{\partial r} \mathbf{E}; \quad \frac{\partial H_r}{\partial \theta} = -j e^{j\omega_s t} \mathbf{H}_r^T \mathbf{K}_\theta \mathbf{E} \quad (19)$$

$$J_{ext} = e^{j\omega_s t} \mathbf{J}_{ext}^T \mathbf{E} \quad (20)$$

$$\frac{\partial A}{\partial t} = j\omega_s e^{j\omega_s t} \mathbf{A}_z^T \mathbf{E}; \quad \frac{\partial A}{\partial \theta} = -j e^{j\omega_s t} \mathbf{A}_z^T \mathbf{K}_\theta \mathbf{E} \quad (21)$$

where \mathbf{K}_θ is the diagonal matrix of N , $\mathbf{K}_\theta = \text{diag}(-N \dots N)$.

Using Equations (19)–(21), Equation (18) can be expressed without the time and spatial dependency as follows.

$$\frac{\partial H_\theta}{\partial r} + \frac{H_\theta}{r} + j \frac{1}{r} \mathbf{K}_\theta \mathbf{H}_r = J_{ext} - j\sigma(\omega_s - \omega_r \mathbf{K}_\theta) \mathbf{A}_z \quad (22)$$

The relationship between flux density and magnetic vector potential is written as.

$$\vec{B} = \nabla \times \vec{A} \quad (23)$$

$$B_r = \frac{1}{r} \frac{\partial A_z}{\partial \theta}; \quad B_\theta = -\frac{\partial A_z}{\partial r} \quad (24)$$

In matrix form, Equation (24) is given by

$$\mathbf{B}_r = -j \frac{1}{r} e^{j\omega_s t} \mathbf{K}_\theta \mathbf{A}_z; \quad \mathbf{B}_\theta = -\frac{\partial \mathbf{A}_z}{\partial r} \quad (25)$$

Replace Equation (24) into Equation (9), \mathbf{H}_r and \mathbf{H}_θ are obtained as

$$\mathbf{H}_r = -j \frac{1}{r} \mu_{c,r}^{-1} \mathbf{K}_\theta \mathbf{A}_z; \quad \mathbf{H}_\theta = -\mu_{c,\theta}^{-1} \frac{\partial \mathbf{A}_z}{\partial r} \quad (26)$$

Substituting Equation (26) into Equation (22), the final partial differential equation is derived.

$$\frac{\partial^2 \mathbf{A}_z}{\partial r^2} + \frac{1}{r} \frac{\partial \mathbf{A}_z}{\partial r} - \frac{1}{r^2} \mathbf{V} \mathbf{A}_z = -\mu_{c,\theta} [\mathbf{J}_{ext} - j\sigma(\omega_s - \omega_r \mathbf{K}_\theta) \mathbf{A}_z] \quad (27)$$

where $\mathbf{V} = \mu_{c,\theta} \mathbf{K}_\theta \mu_{c,r}^{-1} \mathbf{K}_\theta$.

From Equation (27), the PDEs for each Region (I)–(V) are listed in Equations (28)–(30), respectively.

$$\frac{\partial^2 A_z}{\partial r^2} + \frac{1}{r} \frac{\partial A_z}{\partial r} - \frac{1}{r^2} V A_z = j \sigma_{sh} \mu_{sh} (\omega_s - \omega_r K_\theta) A_z \quad ; \text{for (I)} \quad (28)$$

$$\frac{\partial^2 A_z}{\partial r^2} + \frac{1}{r} \frac{\partial A_z}{\partial r} - \frac{1}{r^2} V A_z = 0 \quad ; \text{for (II), (IV), (V)} \quad (29)$$

$$\frac{\partial^2 A_z}{\partial r^2} + \frac{1}{r} \frac{\partial A_z}{\partial r} - \frac{1}{r^2} V A_z = \mu_{c,\theta} J_{ext} \quad ; \text{for (III)} \quad (30)$$

where σ_{sh} and μ_{sh} are the conductivity and permeability of the shaft material.

Using the method of separation of variables to solve Equations (28)–(30), the corresponding solutions are given by

$$A_z^k = I_T(\alpha r) a^k + K_T(\alpha r) b^k \quad ; k = (\text{I}) \quad (31)$$

$$A_z^k = \left(\frac{r}{R_{outer}} \right)^{\lambda^k} a^k + \left(\frac{r}{R_{inner}} \right)^{-\lambda^k} b^k \quad ; k = (\text{II}), (\text{IV}), (\text{V}) \quad (32)$$

$$A_z^k = W^k \left(\frac{r}{R_{eo}} \right)^{\lambda^k} a^k + W^k \left(\frac{r}{R_{ei}} \right)^{-\lambda^k} b^k + r^2 F^k \quad ; k = (\text{III}) \quad (33)$$

where I_T and K_T are the first and second kinds of Bessel function with orders of $T = |K_\theta|$, $\alpha = (j \sigma_{sh} \mu_{sh} (\omega_s - \omega_r K_\theta))^{0.5}$. R_{outer} and R_{inner} are the outer and inner radii of the k -th regions. W^k, λ^k are the eigenvector matrix and diagonal eigenvalue of $(V^k)^{0.5}$. F^k is the particular solution of Equation (30), given by

$$F^k = (V^k - 4I)^{-1} J_{ext} \quad (34)$$

3.4. Boundary Conditions (BCs)

To obtain the electromagnetic field in the sensor, boundary conditions (BCs) on the continuity of the radial flux density component B_r and tangential field strength H_r are applied to four interfaces at R_r, R_{ei}, R_{eo} , and R_{po} . Moreover, Dirichlet BCs are used for both the outer boundary of the Region (V) and the infinitesimal radius of the Region (I). The solution is derived by solving the following ten conditions.

$$A_z^I|_{r \rightarrow 0} = 0; A_z^V|_{r=R_y} = 0 \quad (35)$$

$$A_z^I|_{r=R_r} - A_z^{II}|_{r=R_r} = 0; H_z^I|_{r=R_r} - H_z^{II}|_{r=R_r} = 0 \quad (36)$$

$$A_z^{II}|_{r=R_{ei}} - A_z^{III}|_{r=R_{ei}} = 0; H_z^{II}|_{r=R_{ei}} - H_z^{III}|_{r=R_{ei}} = 0 \quad (37)$$

$$A_z^{III}|_{r=R_{eo}} - A_z^{IV}|_{r=R_{eo}} = 0; H_z^{III}|_{r=R_{eo}} - H_z^{IV}|_{r=R_{eo}} = 0 \quad (38)$$

$$A_z^{IV}|_{r=R_{po}} - A_z^V|_{r=R_{po}} = 0; H_z^{IV}|_{r=R_{po}} - H_z^V|_{r=R_{po}} = 0 \quad (39)$$

These ten BCs are used to obtain a linear system $AX = B$ to determine all unknown coefficients X of magnetic vector potential in all regions. This system is implemented in MATLAB R2023b, in which A is the square matrix of the coefficient factor, and B is a column vector of the constant values with the size of $10(2N + 1)$ and $(2N + 1)$, respectively. Increasing the harmonic order N enhances the solution's accuracy but also increases computation time. To address the zero-harmonic issue in the truncated CFS, a small value, such as 10^{-10} , is assigned to the zero harmonic instead of setting it to zero [32].

3.5. Derivation of Pick-Up Voltage and Excitation Coil Inductance

The pick-up voltage is a crucial parameter of the sensor. The flux passing through one solid conductor i of the pick-up coil is expressed by

$$\varphi_i^p = \frac{L_{stk}}{S_p^{con}} \int_{\theta_{pi}^i}^{\theta_{pi}^i + \frac{\theta_{po} - \theta_{pi}}{2}} \int_{R_{pi}}^{R_{po}} A_z^{IV}(r, \theta) r dr d\theta \quad (40)$$

where $S_p^{con} = (\theta_{po} - \theta_{pi}) (R_{po}^2 - R_{pi}^2) / 4$ is the area of a solid conductor.

From the winding connection of the pick-up coil, the total flux linkage is given by

$$\psi^p = N_t^p (\varphi_1^p + \varphi_2^p - \varphi_3^p - \varphi_4^p) \quad (41)$$

where N_t^p is the number of turns in the pick-up coil.

Finally, the induced voltage in the pick-up coil is derived.

$$E_p = - \frac{d\psi^{IV}}{dt} \quad (42)$$

To find the inductance of the excitation coil L_e , similar steps are used to obtain total flux linkage ψ^e first, and then the excitation coil inductance is derived by.

$$L_e = \frac{\psi^e}{I} \quad (43)$$

where I is the exciting current.

4. Analytical Model Verification by FEA

To verify the accuracy of the analytical model, the results obtained from AM and 2D time-transient FEA are compared. The current supplied to the excitation coils is set to 750 Hz and 150 mA. The main parameters of the proposed design and the shaft material properties are listed in Tables 2 and 3, respectively.

Table 2. Proposed design parameters.

Parameter	Symbol	Unit	Value
Shaft radius	R_r	mm	15.0
Inner and outer radius of the excitation coil region	R_{ei} / R_{eo}	mm	16.2/19.0
Inner and outer radius of the pick-up coil region	R_{pi} / R_{po}	mm	19.3/22.2
Stator yoke radius	R_y	mm	24.2
Inner and outer span angle of the excitation coil	$\theta_{ei} / \theta_{eo}$	deg.	127.5/175.1
Inner and outer span angle of the pick-up coil	$\theta_{pi} / \theta_{po}$	deg.	135.2/175.8
Stack length	L_{stk}	mm	39.0
Number of turns of the excitation coil	N_t^e	-	90
Number of turns of the pick-up coil	N_t^p	-	105

Table 3. Shaft material parameters.

Parameter	Symbol	Unit	Value
Cast-aluminum conductivity	σ	S/m	22×10^6
Cast-iron conductivity	σ	S/m	15×10^5
Stainless-steel conductivity	σ	S/m	15×10^5
Relative cast-aluminum permeability	μ_r	-	1.0
Relative cast-iron permeability	μ_r	-	60.0
Relative stainless-steel permeability	μ_r	-	1.0

At 3000 rpm, the flux density distributions in the air gap are shown in Figure 4a,b for two shaft materials: aluminum and cast iron. The flux density produced with the cast-iron

shaft is significantly higher than that with the aluminum shaft. This is caused by the higher permeability of the cast iron ($\mu_r = 60$), resulting in low reluctance paths for the flux flow. In contrast, with the aluminum shaft, the permeabilities of aluminum and air are equal ($\mu = 1$), leading to a very high reluctance in the rotor and minor flux density.

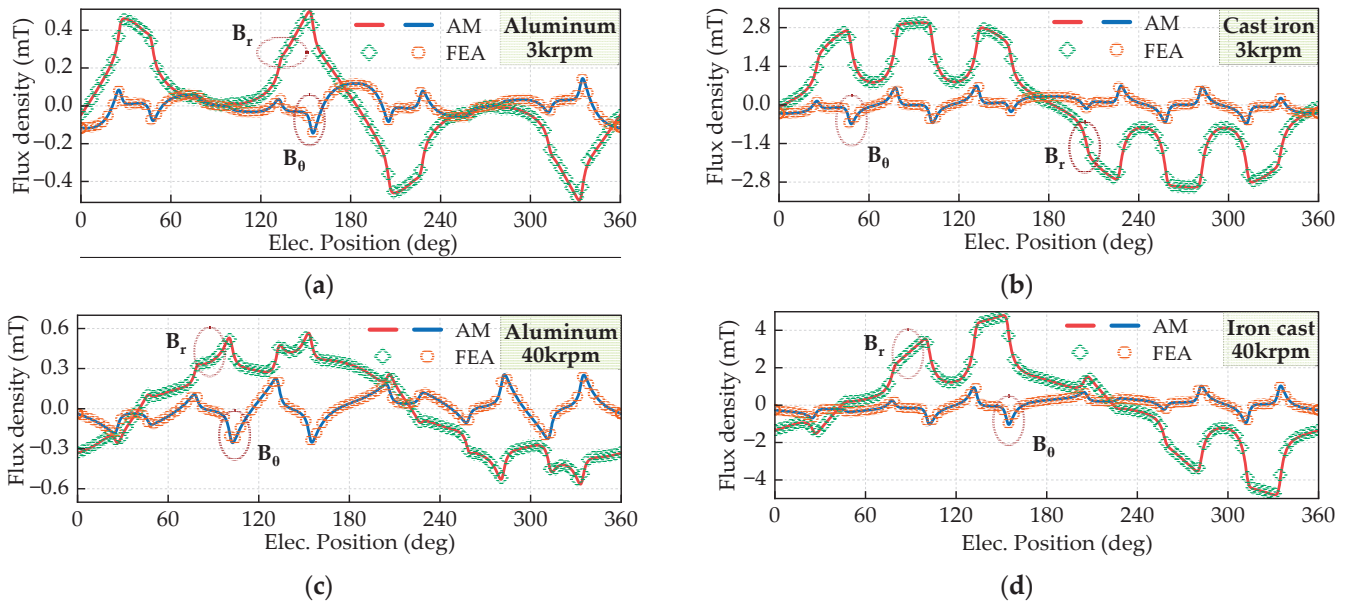


Figure 4. Flux density distribution in the air gap with different shaft materials at (a,b) 3000 rpm and (c,d) 40,000 rpm under the excitation current of 750 Hz, 150 mA.

When the shaft speed is set at 40,000 rpm, the rotation frequency approaches the stator frequency, and eddy effects are diminished. As a result, the flux density in the air gap increases for both shaft materials, as shown in Figure 4c,d. Additionally, at the higher speed, a more significant tail effect [23] is generated in the aluminum shaft, leading to substantial growth of the tangential component. Notably, the AM results show excellent agreement with the FEA results, confirming the model's validity.

For a clearer perspective, the relationship between pick-up voltage (root-mean-square value) and speed is illustrated in Figure 5. A linear relationship between pick-up voltage and speed is observed for both materials, with cast iron producing a much greater output due to its high permeability, as shown in Figure 5a. Moreover, as shown in Figure 5b, the AM predictions agree well with FEA, and the highest differences are around 0.8%.

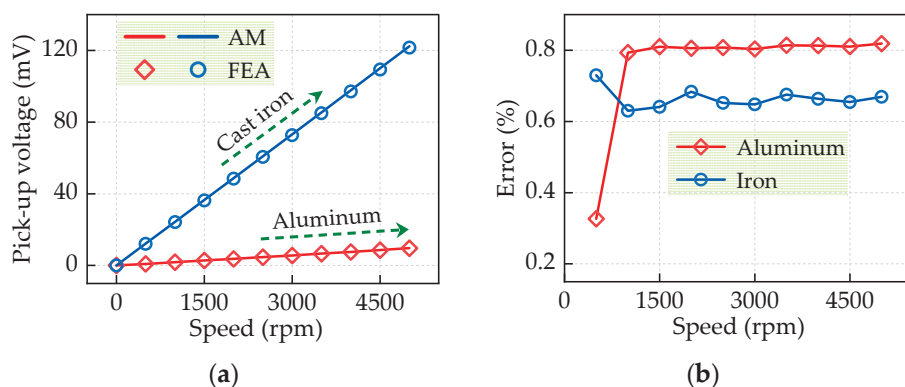


Figure 5. (a) Pick-up coil voltage and (b) difference between FEA and AM results according to speed with different shaft materials under the excitation current of 750 Hz, 150 mA.

While 2D models are less accurate than 3D calculations, 3D transient FEA is computationally intensive and time consuming [17]. Consequently, the AM is used to analyze the steady-state characteristics of the sensor in the following section.

5. Steady-State Analysis

5.1. Effects of Stator Dimensions on Sensitivity Coefficient and Excitation Coil Inductance

The sensitivity coefficient (SC: the ratio between pick-up voltage and rotation speed) and the excitation coil inductance (ECI) are two critical parameters of the ECSS. Higher sensitivity enhances the signal-to-noise ratio and increases resistance to electromagnetic interference, while lower ECI enables quicker response times by reducing the required stabilization time for the excitation current. To study the variations in SC and ECI with respect to stator dimensions, the width of the teeth in front of the pick-up coil is defined as $K_{sp1} = \alpha_1 / \beta_1$, and for the teeth in front of the excitation coil, the ratio is $K_{sp2} = \alpha_2 / \beta_2$, as shown in Figure 1b. At 3000 rpm and with an excitation current of 750 Hz and 150 mA, SC and ECI are shown in Figure 6 for varying K_{sp1} and K_{sp2} .

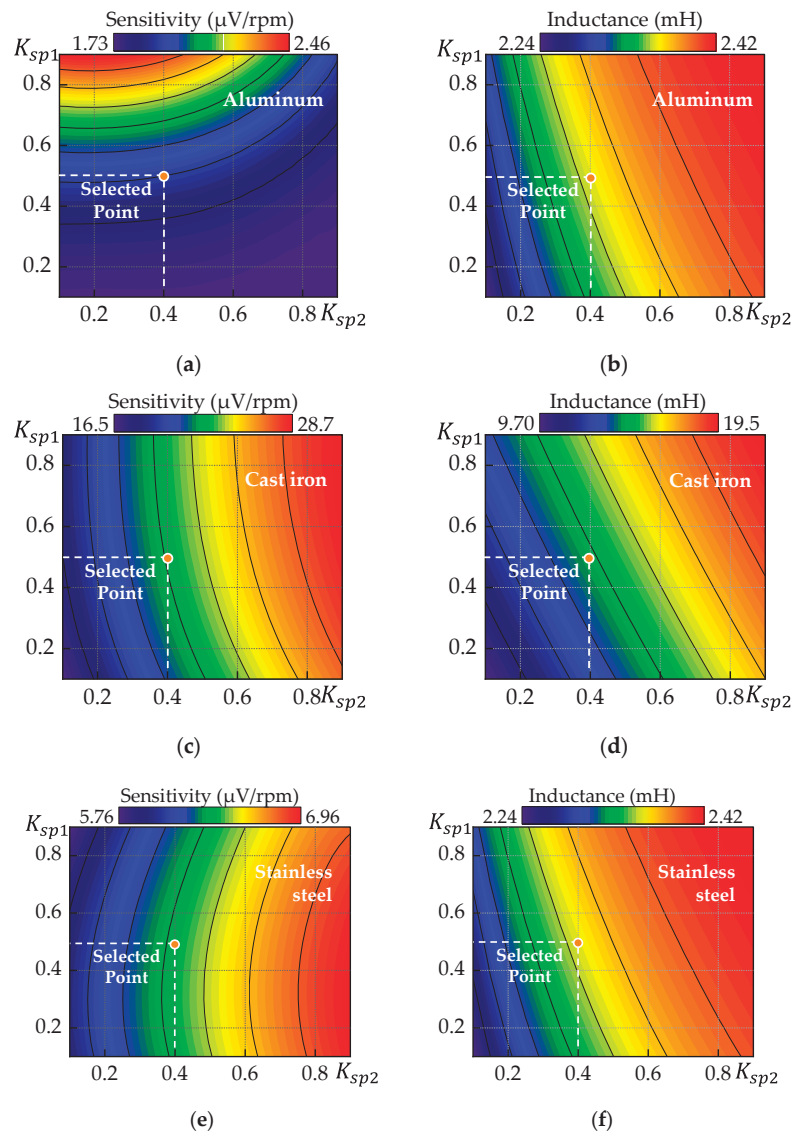


Figure 6. Sensitivity coefficient (V_{rms}/rpm) and excitation coil inductance (ECI) according to the teeth width ratios at 3000 rpm and an excitation of 750 Hz, 150 mA with shaft material of (a,b) aluminum, (c,d) cast iron, and (e,f) stainless steel.

In Figure 6c,e, SC is proportional to K_{sp2} for cast-iron and stainless-steel shafts, whereas SC shows a dependency on K_{sp1} for the aluminum shaft, as depicted in Figure 6a. The reasons are explained as follows.

- At 750 Hz current source, the penetration depths $\delta = 1/\sqrt{\pi f \sigma \mu_0 \mu_r}$ for aluminum, cast iron, and stainless steel are 3.92 mm, 1.94 mm, and 15.0 mm, respectively. This value represents the depth where the magnetic field strength decreases significantly.
- For the aluminum shaft, the small penetration depth leads to pronounced skin effects, concentrating the magnetic field near the surface of the shaft and significantly weakening the field in the air gap despite the larger excitation pole, as shown in Figure 7a. However, SC increases with the width of the pickup pole due to the greater flux linkage obtained.

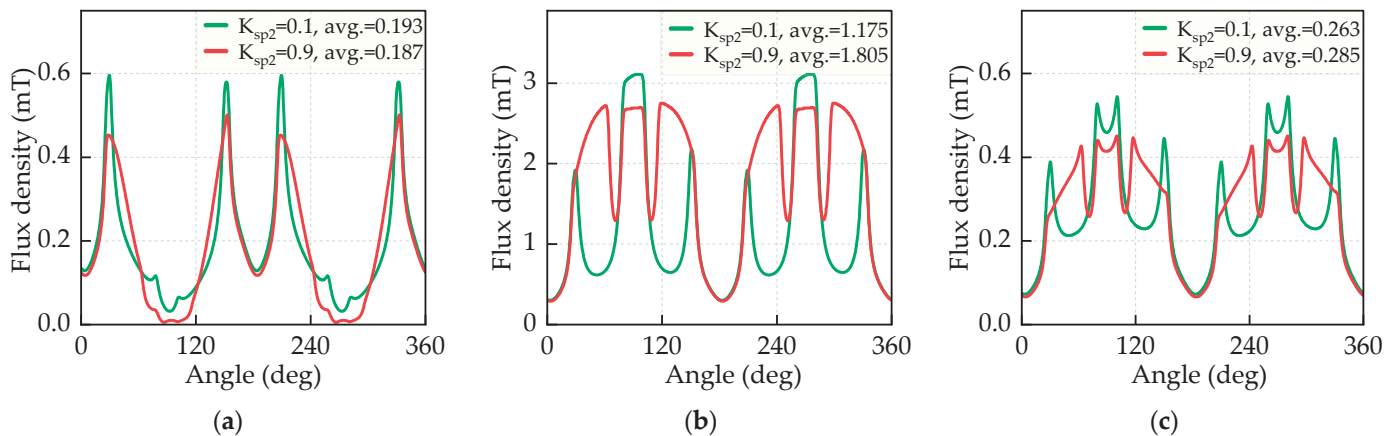


Figure 7. Magnetic flux density distribution (absolute value) at the air gap with two K_{sp2} values, (a) aluminum shaft, (b) cast iron shaft, and (c) stainless steel shaft.

- For the cast-iron shaft, SC increases notably with the excitation pole, primarily due to the low reluctance in the rotor and stator, which facilitates higher magnetic flux density (MFD). Although cast iron has the smallest penetration depth, the larger excitation pole induces a higher MFD in the air gap (see Figure 7b), thereby enhancing sensitivity.
- For the stainless-steel shaft, the considerable penetration depth minimizes skin effects, flux penetration is deep, and flux attenuation is negligible. Consequently, the extent of the excitation pole is directly proportional to SC, which increases due to the higher MFD in the air gap (see Figure 7c).

Regarding ECI, because the permeabilities of aluminum and stainless steel are similar to that of air, their ECI variations are identical and significantly smaller than those observed with the cast-iron shaft, which has much greater permeability (Figure 6b,d,f). Generally, the ECI increases with K_{sp1} and K_{sp2} due to the low reluctance along the magnetic path.

Despite the increased SC achieved by enlarging the teeth widths, the ECI also rises because wider teeth increase the magnetic path length and inductance. Consequently, a trade-off between SC and ECI is made by selecting the optimal values of $K_{sp1} = 0.5$ and $K_{sp2} = 0.4$. These dimensions are adopted for the analyses in the subsequent sections.

5.2. Effects of Shaft Material and Excitation Frequency on Sensitivity Coefficient and Linearity

The effects of shaft material and excitation frequency on the SC of the sensor are shown in Figure 8. First, in all cases, SC is inversely proportional to the conductivity of the shaft because higher conductivity intensifies eddy effects. This trend is similarly observed with increasing frequency from 250 Hz to 750 Hz, further exacerbating eddy effects.

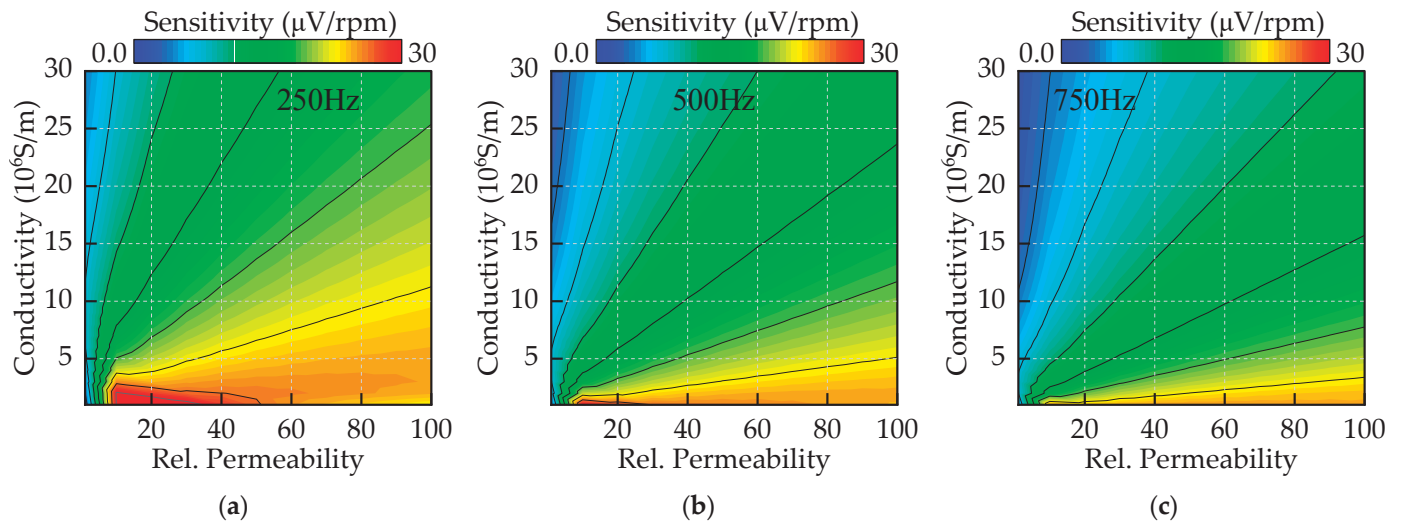


Figure 8. Sensitivity coefficient (V_{rms}/rpm) variations according to the relative permeability and conductivity of the shaft with an excitation frequency of (a) 250 Hz, (b) 500 Hz, and (c) 750 Hz.

Shaft permeability generally enhances SC by lowering magnetic reluctance, facilitating greater flux linkage. However, SC is not strictly proportional to permeability. As shown in Figure 8a,b, excessively high permeability can lead to magnetic saturation or serious skin effects, with the highest output occurring at a permeability of roughly $20\mu_0$. Therefore, the optimal SC can be achieved without relying on excessively high-permeability materials, which would increase the inductance of the excitation coil.

In [17], the pick-up coils are connected to a lock-in amplifier to extract the DC components of the induced voltage, as depicted in Figure 9. Furthermore, [17] indicates that the real component of the induced voltage, U_r , exhibits higher sensitivity and lower linearity errors than the imaginary counterpart, U_i . Consequently, this study focuses on extracting U_r to evaluate the sensitivity and linearity of the proposed design.

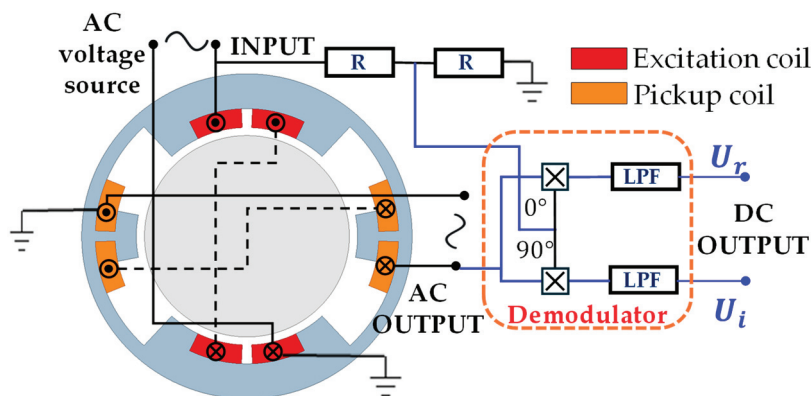


Figure 9. Schematic circuit model to extract DC components: pick up coils connected to the lock-in amplifier [17].

Figure 10 shows the real components U_r and linearity errors as speed functions under the same excitation-current amplitude of 150 mA. The cast-iron shaft induces the highest outputs U_r because of the high permeability. Additionally, for aluminum and cast-iron shafts in Figure 10a,b, U_r increases as the excitation frequency decreases, attributed to the reduction in eddy effects. Meanwhile, with the stainless-steel shaft in Figure 10c, where eddy-current effects are negligible, the output U_r grows with increasing excitation frequency.

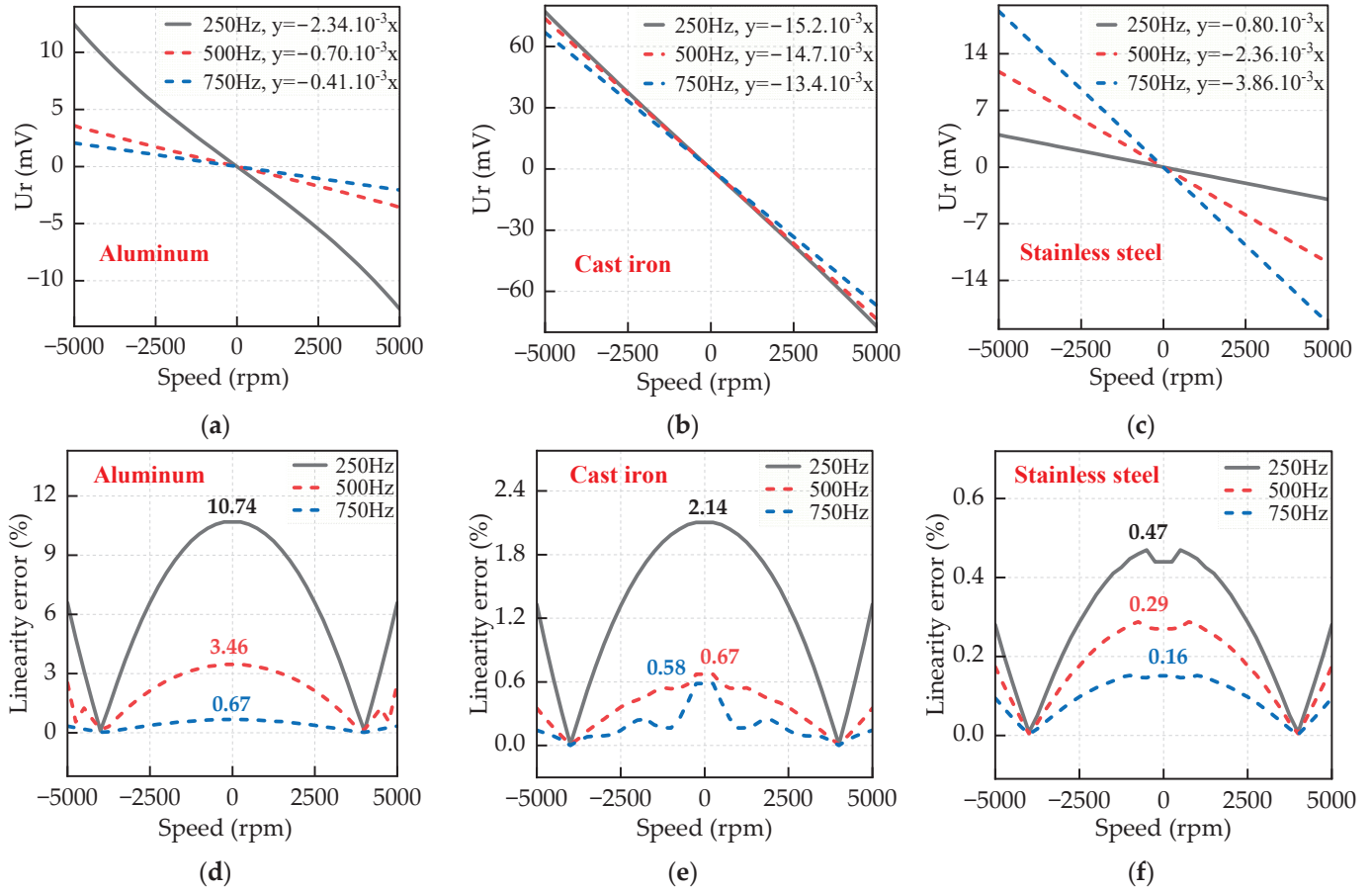


Figure 10. (a–c) Real components of output voltage and (d–f) linearity error according to speed with different shaft materials.

Regarding linearity error, this value is calculated based on the best-fitted linear line, $f_t(n)$, of the output U_r according to speed, as defined by the following equation.

$$\varepsilon = \left| \frac{f_t(n) - U_r(n)}{f_t(n)} \right| \cdot 100\% \quad (44)$$

As shown in Figure 10d–f, the aluminum shaft exhibits the highest nonlinearity across all frequencies, with a maximum error of 10.7% at 250 Hz. Conversely, the stainless-steel shaft demonstrates excellent linearity characteristics, with a maximum error of 0.47%, the lowest among all materials, at 250 Hz. For the cast-iron shaft, the nonlinearity is relatively low, with a maximum error of 2.14%. It is noteworthy that increasing the excitation frequency improves the linearity of the sensor. Compared to [17], using the same 750 Hz excitation frequency and an aluminum shaft, the sensitivity increases by a factor of 3.1, despite the linearity error rising from 0.2% to 0.67%. However, this linearity is still relatively low compared to a commercial magnetic speed sensor with a 1% linearity error [17] and another ECSS configuration [19] with 0.5%.

6. Dynamic-State Analysis

To investigate the dynamic characteristics of the eddy-current speed sensor, the circuit in Figure 9 is implemented in Ansys Twinbuilder, coupled with Maxwell 2D. A reference speed is applied to the shaft, and the estimated speed is calculated as the ratio of the real component U_r to the sensitivity coefficient (V/rpm). To mitigate the delay effects of the

low-pass filter (LPF), it is replaced by an averaging block, which computes the average value of U_r over each cycle, $1/f$.

The performance of the speed sensor is shown in Figure 11. First, as depicted in Figure 11d–f, the estimation error is significantly higher at low speeds due to reduced signal strength and increased noise interference. Since the induced voltage frequency is twice the excitation frequency, the response time is directly influenced by the excitation frequency. Consequently, increasing the excitation frequency from 250 Hz to 750 Hz significantly improves the sensor's accuracy across all tested shaft materials, with estimation errors during the $T = 0.1$ – 0.8 s period reduced to less than 0.8%.

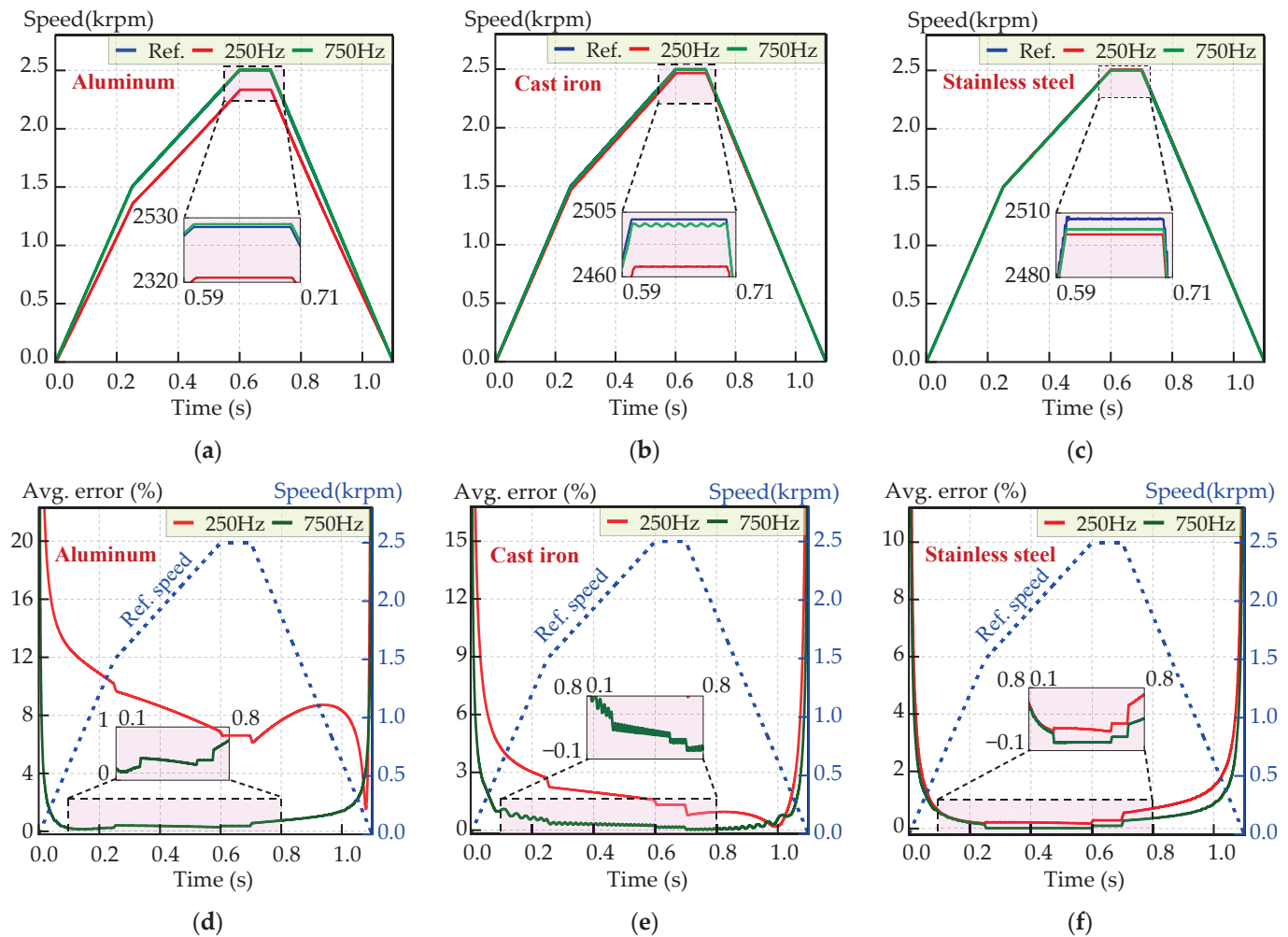


Figure 11. (a–c) Reference speed and the estimated speeds, and (d–f) estimation errors.

Second, comparing performance across shaft materials, the aluminum shaft paired with a 250 Hz excitation frequency shows the highest estimation errors, primarily due to the material's high conductivity and low permeability, with errors exceeding 6% during T period, as shown in Figure 11d. In contrast, the stainless-steel shaft demonstrates the best dynamic performance, with estimation errors remaining below 0.8% during the T period, regardless of the excitation frequency (250 Hz or 750 Hz; see Figure 11f). The performance of the cast-iron shaft lies between that of the aluminum and stainless-steel shafts.

In conclusion, using a shaft material with low conductivity and permeability, such as stainless steel, provides the best estimation performance, as its low conductivity and permeability minimize eddy-current effects and improve flux linkage stability.

7. Conclusions

This study developed an improved design of an eddy-current speed sensor (ECSS) to overcome the low sensitivity problem. The sensitivity of the proposed design is up to 104 times greater than that of the reference model without increasing power consumption. This is achieved by adding a ferromagnetic core to the stator, strengthening the signal while keeping the system efficient.

An improved analytical model based on harmonic modeling was introduced to better account for the effects of core permeability. Using this model, the effects of shaft materials and excitation frequency on the sensor's performance were analyzed in addition to obtaining the optimal sensor dimensions. The results indicate that cast iron exhibits the highest sensitivity due to its high permeability. In contrast, stainless steel provides the best linearity because of its low conductivity and reduced eddy effects.

Furthermore, this study also investigates the dynamic behavior of the sensor using coupled simulations in Ansys, which has been largely ignored in most studies. Analyzing the excitation frequency shows that higher frequencies improve dynamic precision but may reduce output strength due to stronger eddy currents.

These findings offer valuable insights into ECSS behaviors under different conditions. Future research should focus on experimental validation of the model.

8. Discussion

Although many studies have been conducted on eddy-current speed sensors (ECSSs), several critical research areas still require further investigation. While 3D FEA models provide the most accurate results, they are very time consuming. To address this, semi-analytical 3D models are needed to reduce computation time while maintaining accuracy. The authors of [15] proposed an analytical model that includes end effects for ECSSs using the subdomain method. However, as mentioned earlier, this model does not account for core permeability.

Low excitation frequencies can raise linearity errors, but connecting the sensor directly to the electrical grid to eliminate external waveform generators presents a promising solution to simplify ECSS systems. This configuration could reduce system complexity and cost and improve reliability. Future studies could explore combining different materials in a shaft for this purpose. As shown in [19], a rotating iron shaft with a copper coating can enhance both sensitivity and linearity.

Finally, thanks to the simple design of ECSS, particularly without permanent magnet excitation, it is well suited for high-temperature environments. However, the effects of temperature changes on ECSS performance still need to be explored. Temperature fluctuations can affect the permeability and conductivity of materials, leading to potential drift in sensor measurements.

Author Contributions: Conceptualization, D.-T.H.; methodology, D.-T.H.; validation, D.-T.H. and M.-D.N.; formal analysis, D.-T.H.; investigation, D.-T.H.; writing—original draft, D.-T.H.; writing—review and editing, Y.-J.K., A.-T.P., K.-H.S. and J.-Y.C.; visualization, D.-T.H.; supervision, Y.-J.K., A.-T.P., K.-H.S. and J.-Y.C. All authors have read and agreed to the published version of the manuscript.

Funding: This study was conducted with the support of the National Research Foundation of Korea and funding from the government (Ministry of Science and ICT) under Grant No. RS-2023-00258052.

Data Availability Statement: Data are contained within the article.

Conflicts of Interest: The authors declare no conflicts of interest.

References

- Villani, M.; Tursini, M.; Fabri, G.; Castellini, L. High reliability permanent magnet brushless motor drive for aircraft application. *IEEE Trans. Ind. Electron.* **2012**, *59*, 2073–2081. [CrossRef]
- Chau, K.T.; Member, S.; Chan, C.C.; Liu, C.; Member, S. Overview of Permanent-Magnet Brushless Drives for Electric and Hybrid Electric Vehicles. *IEEE Trans. Ind. Electron.* **2008**, *55*, 2246–2257. [CrossRef]
- Zhao, N.; Schofield, N. An Induction Machine Design with Parameter Optimization for a 120-kW Electric Vehicle. *IEEE Trans. Transp. Electr.* **2020**, *6*, 592–601. [CrossRef]
- Mirzaei, M.; Ripka, P. A Comparative Study of Eddy Current Speed Sensors for Rotating Speed Measurement of Iron Shafts. In Proceedings of the ITEC Asia-Pacific, Chiang Mai, Thailand, 28 November–1 December 2023.
- Lord, W.; Robert Chatto, N.B. Alternatives to Analog DC Tachogenerators. *IEEE Trans. Ind. Appl.* **1975**, *IA-11*, 470–478. [CrossRef]
- Robinson, C.E. Analog Tachometers. *IEEE Trans. Ind. Gen. Appl.* **1966**, *IGA-2*, 144–146. [CrossRef]
- Addabbo, T.; Di Marco, M.; Fort, A.; Landi, E.; Mugnaini, M.; Vignoli, V.; Ferretti, G. Instantaneous Rotation Speed Measurement System Based on Variable Reluctance Sensors for Torsional Vibration Monitoring. *IEEE Trans. Instrum. Meas.* **2019**, *68*, 2363–2373. [CrossRef]
- Ni, Z.; Wang, X.; Wu, R.; Du, L. Modeling and Characteristic Analysis of Variable Reluctance Signal Variation of Rolling Bearing Outer Ring Fault. *IEEE Access.* **2022**, *10*, 49542–49550. [CrossRef]
- Costello, J.J.; Pickard, A.C. A Novel Speed Measurement System for Turbomachinery. *IEEE Sens. Lett.* **2018**, *2*, 1–4. [CrossRef]
- Bucak, I.Ö. Position error compensation via a variable reluctance sensor applied to a hybrid vehicle electric machine. *Sensors* **2010**, *10*, 1918–1934. [CrossRef] [PubMed]
- Tootoonchian, F. Proposal of a new affordable 2-pole resolver and comparing its performance with conventional wound-rotor and VR resolvers. *IEEE Sens. J.* **2018**, *18*, 5284–5290. [CrossRef]
- Bahari, M.; Tootoonchian, F. Performance Analysis of an Outer Rotor Variable Reluctance Resolver. *IEEE Sens. J.* **2022**, *22*, 17761–17768. [CrossRef]
- Farhadi-Beiranvand, A.; Alipour-Sarabi, R.; Nasiri-Gheidari, Z.; Tootoonchian, F. Selection of Excitation Signal Waveform for Improved Performance of Wound-Rotor Resolver. In Proceedings of the PEDSTC, Shiraz, Iran, 12–14 February 2019.
- Ge, X.; Zhu, Z.Q.; Ren, R.; Chen, J.T. Analysis of windings in variable reluctance resolver. *IEEE Trans. Magn.* **2015**, *51*, 1–10. [CrossRef]
- Mirzaei, M.; Ripka, P. Three-Dimensional Analytical Modeling of Rotational Eddy Current Speed Sensor. *IEEE Sens. J.* **2024**, *24*, 10277–10286. [CrossRef]
- Mirzaei, M.; Ripka, P.; Grim, V. A novel eddy current speed sensor with a ferrite E-core. *IEEE Magn. Lett.* **2020**, *11*, 1–5. [CrossRef]
- Mirzaei, M.; Ripka, P.; Grim, V. A Novel Structure of an Eddy Current Sensor for Speed Measurement of Rotating Shafts. *IEEE Trans. Energy Convers.* **2023**, *38*, 170–179. [CrossRef]
- Tuysuz, A.; Flankl, M.; Kolar, J.W.; Mutze, A. Eddy-current-based contactless speed sensing of conductive surfaces. In Proceedings of the SPEC, Auckland, New Zealand, 5–8 December 2016.
- Mirzaei, M.; Ripka, P.; Grim, V.; Chirtsov, A. Design and Optimization of an Eddy Current Speed Sensor for Rotating Rods. *IEEE Sens. J.* **2020**, *20*, 12241–12251. [CrossRef]
- Mirzaei, M.; Grim, V. Speed Measurement of Rotating Hollow Shafts Using an Eddy Current Sensor. *IEEE/ASME Trans. Mechatron.* **2023**, *28*, 568–578. [CrossRef]
- Rocha, T.J.; Ramos, H.G.; Ribeiro, A.L.; Pasadas, D.J. Evaluation of Subsurface Defects Using Diffusion of Motion-Induced Eddy Currents. *IEEE Trans. Instrum. Meas.* **2016**, *65*, 1182–1187. [CrossRef]
- Gong, C.; Tüysüz, A.; Flankl, M.; Stolz, T.; Kolar, J.W.; Habetler, T. Experimental Analysis and Optimization of a Contactless Eddy-Current-Based Speed Sensor for Smooth Conductive Surfaces. *IEEE Trans. Ind. Electron.* **2020**, *67*, 8817–8828. [CrossRef]
- Feng, B.; Deng, K.; Wang, S.; Chen, S.; Kang, Y. Theoretical Analysis on the Distribution of Eddy Current in Motion-Induced Eddy Current Testing and High-Speed MFL Testing. *J. Nondestruct. Eval.* **2022**, *41*, 59. [CrossRef]
- Feng, B.; Deng, K.; Xie, L.; Xie, S.; Kang, Y. Speed Measurement Method for Moving Conductors Based on Motion-Induced Eddy Current. *IEEE Trans. Instrum. Meas.* **2023**, *72*, 1–8. [CrossRef]
- Hoang, D.T.; Nguyen, M.D.; Woo, J.H.; Shin, H.S.; Shin, K.H.; Phung, A.T.; Choi, J.Y. Volume optimization of high-speed surface-mounted permanent magnet synchronous motor based on sequential quadratic programming technique and analytical solution. *AIP Adv.* **2024**, *14*, 025319. [CrossRef]
- Lubin, T.; Mezani, S.; Rezzoug, A. Exact analytical method for magnetic field computation in the air gap of cylindrical electrical machines considering slotting effects. *IEEE Trans. Magn.* **2010**, *46*, 1092–1099. [CrossRef]
- Lubin, T.; Mezani, S.; Rezzoug, A. 2-D exact analytical model for surface-mounted permanent-magnet motors with semi-closed slots. *IEEE Trans. Magn.* **2011**, *47*, 479–492. [CrossRef]
- Lubin, T.; Mezani, S.; Rezzoug, A. Analytic calculation of eddy currents in the slots of electrical machines: Application to cage rotor induction motors. *IEEE Trans. Magn.* **2011**, *47*, 4650–4659. [CrossRef]

29. Roshandel, E.; Mahmoudi, A.; Kahourzade, S.; Soong, W.L. Saturation Consideration in Modeling of the Induction Machine Using Subdomain Technique to Predict Performance. *IEEE Trans. Ind. Appl.* **2022**, *58*, 261–272. [CrossRef]
30. Sprangers, R.L.J.; Paulides, J.J.H.; Gysen, B.L.J.; Lomonova, E.A. Magnetic Saturation in Semi-Analytical Harmonic Modeling for Electric Machine Analysis. *IEEE Trans. Magn.* **2016**, *52*, 1–10. [CrossRef]
31. Hoang, D.T.; Nguyen, M.D.; Kim, S.M.; Jung, W.S.; Shin, K.H.; Kim, Y.J.; Choi, J.Y. Nonlinear Analytical Solution for Permanent Magnet Synchronous Machines Using Harmonic Modeling. In Proceedings of the ICEM, Torino, Italy, 1–4 September 2024.
32. Zhao, H.; Liu, C.; Song, Z.; Yu, J. A Fast Optimization Scheme of Coaxial Magnetic Gears Based on Exact Analytical Model Considering Magnetic Saturation. *IEEE Trans. Ind. Appl.* **2021**, *57*, 437–447. [CrossRef]
33. Guo, B.; Du, Y.; Djelloul-Khedda, Z.; Peng, F.; Dong, J.; Huang, Y.; Dubas, F.; Boughrara, K. Nonlinear Semianalytical Model for Axial Flux Permanent-Magnet Machine. *IEEE Trans. Ind. Electron.* **2022**, *69*, 9804–9816. [CrossRef]
34. Wang, W.; Cheng, M.; Li, X.; Tong, M.; Qi, J. Nonlinear Analytical Solution of Magnetic Field and Performances of a Spoke Array Vernier Permanent Magnet Machine. *IEEE Trans. Energy Convers.* **2021**, *36*, 173–185. [CrossRef]
35. Hoang, D.-T.; Nguyen, M.-D.; Kim, S.-M.; Bang, T.-K.; Kim, Y.-J.; Shin, K.-H.; Choi, J.-Y. Irreversible Demagnetization Prediction Due to Overload and High-Temperature Conditions in PMSM Based on Nonlinear Analytical Model. *IEEE Trans. Energy Convers.* **2024**, *in press*. [CrossRef]
36. Davey, K.R. Analytic Analysis of Single and Three Phase Induction Motors. *IEEE Trans. Magn.* **1998**, *34*, 3721–3727. [CrossRef]
37. Marcsa, D.; Kuczmann, M. Formulations for the 2-D Analysis of Solid-Rotor Induction Machines. *IEEE Trans. Magn.* **2009**, *45*, 3329–3333. [CrossRef]
38. Raisanen, V.; Suuriniemi, S.; Kurz, S.; Kettunen, L. Rapid Computation of Harmonic Eddy-Current Losses in High-Speed Solid-Rotor Induction Machines. *IEEE Trans. Energy Convers.* **2013**, *28*, 782–790. [CrossRef]

Disclaimer/Publisher’s Note: The statements, opinions and data contained in all publications are solely those of the individual author(s) and contributor(s) and not of MDPI and/or the editor(s). MDPI and/or the editor(s) disclaim responsibility for any injury to people or property resulting from any ideas, methods, instructions or products referred to in the content.

Article

A Rotational Speed Sensor Based on Flux-Switching Principle

Duy-Tinh Hoang ¹, Joon-Ku Lee ^{2,*}, Kwang-Il Jeong ², Kyung-Hun Shin ^{3,*} and Jang-Young Choi ^{1,*}

¹ Department of Electrical Engineering, Chungnam National University, Daejeon 34134, Republic of Korea; hoangduytinh@o.cnu.ac.kr

² Korea Atomic Energy Research Institute, Daejeon 34057, Republic of Korea; hisunny@kaeri.re.kr

³ Department of Electrical Engineering, Changwon National University, Changwon 51140, Republic of Korea

* Correspondence: jklee@kaeri.re.kr (J.-K.L.); kshin@changwon.ac.kr (K.-H.S.); choi_jy@cnu.ac.kr (J.-Y.C.)

Abstract: This study proposes a rotational speed measurement machine based on the flux-switching principle with a 6-stator-slot/19-rotor-pole (6s/19p) topology. With a rotor shape similar to a variable reluctance sensor (VRS), the proposed machine features a simple and robust structure while ensuring the same output frequency as VRS. Additionally, compared to the conventional 12s/10p topology, the 6s/19p configuration reduces permanent magnet (PM) consumption by half while maintaining high induced voltage characteristics. A non-linear analytical model (NAM), which incorporates the harmonic modeling (HM) technique and an iterative process, is presented. This model more accurately captures the rectangular shape of the PM and stator teeth while accounting for core saturation effects. Based on this model, the optimal dimensions of the proposed machine are investigated to achieve the best performance for speed measurement applications. A coupling FEA simulation between Ansys Maxwell and Twin Builder further analyzes the machine's performance. Compared to a commercial product of the same size, the proposed machine achieves 31.5% higher output voltage while ensuring lower linearity errors. Moreover, superior load characteristics are observed, with a voltage drop of only 1.58% at 1500 rpm and 30 mA. The proposed machine and NAM provide an improved solution and analytical tool for speed measurement applications.

Keywords: analytical model; finite element analysis; flux switching; harmonics modeling; magnetic sensor

MSC: 35-04

1. Introduction

Accurate rotational speed measurement plays a vital role in various industrial, automotive, and aerospace applications, ensuring efficient control, monitoring, and fault detection of rotating machinery [1,2]. Speed sensors are essential for field-oriented control (FOC) and direct torque control (DTC) strategies, where real-time rotational speed data are used to regulate torque and flux linkage [3]. Any deviation or error in speed measurement can lead to performance degradation, increased energy consumption, and potential system instability, making robust and accurate speed-sensing technologies critical.

Over the years, various speed-sensing technologies have been developed, each offering distinct advantages and limitations. Optical encoders, which use light-based detection to determine rotational speed, provide high accuracy and resolution. However, their performance is significantly affected by environmental conditions such as dust, dirt, oil, and vibrations, making them less reliable in harsh industrial environments [4]. Another

common approach is sensorless speed estimation [5], where the rotational speed is inferred from machine parameters such as back electromotive force (EMF) or motor current signals. While sensorless techniques reduce hardware complexity, their drawbacks include low fault tolerance and low dynamic response due to complex signal processing. Additionally, Hall-effect sensors are widely used and provide contactless operation. However, they typically generate low output voltages and can be affected by electromagnetic interference.

Recently, speed sensors based on the eddy current effect have been extensively studied. These sensors operate on the principle of eddy current induction in a moving conductive object, which causes an asymmetric magnetic flux density distribution and then induces a voltage in the pick-up winding [6–8]. However, the output voltage is very low, and some configurations require external excitation, leading to higher power consumption and increased system complexity. Moreover, eddy current effects are influenced by multiple factors, making it challenging to predict sensor behavior, thereby reducing overall effectiveness accurately.

In parallel, variable reluctance sensors (VRS) have emerged as reliably magnetic sensors [9]. With permanent magnet (PM) excitation, they offer self-excitation and low linearity errors. However, they generate non-sinusoidal signals and relatively low output voltages, necessitating advanced signal processing techniques. Some VRS designs feature solid rotors, which intensify eddy current effects and degrade measurement accuracy [2,10]. Moreover, Magneto-resistive (MR) sensors, including Giant MR, Anisotropic MR, and Tunnel MR [11,12] offer excellent resolution, compact form factors, and stable operation under mechanical stress and vibration. MR sensors employ a PM to create the predefined magnetic field pattern, and a semiconductor detector tracks the variation in the field as a function of the rotor angle. Most MR-based angle sensors require the magnet to be mounted on the rotating part, making them less suitable for through-shaft sensing. In addition, the usage constraints of these sensors emerge from different reasons such as sensitivity to external interference, the influence of parasitics that arise due to IC layouts, and large power requirements in electro-magnet-based design [13].

To address these challenges, this paper proposes a novel speed sensor based on the flux-switching principle [14]. The proposed sensor features a 6-stator-slot/19-rotor-pole (6s/19p) topology, as illustrated in Figure 1. Its rotor structure is identical to a VRS but is laminated to minimize eddy current effects, ensuring a robust design. The multi-pole configuration and the presence of a stator yoke contribute to sinusoidal waveforms and high output voltage, overcoming the limitations of conventional VRS. Moreover, like VRS, the output frequency is also proportional to the number of rotor teeth. Additionally, compared to the conventional 12s/10p topology [15,16], the proposed 6s/19p structure reduces PM consumption by half, making it a more cost-effective solution [17,18].

In addition, conventional subdomain methods (SDMs) with infinite permeability consumptions [19] have commonly been used for analytical models (AM). Recently, the harmonic modeling (HM) technique [20,21], which accounts for the nonlinear behavior of magnetic materials, has been considered an alternative tool for SDMs and finite element analysis (FEA). Consequently, this study proposes an improved nonlinear analytical model (NAM) employing HM to predict machine performance accurately. This model considers core saturation effects and precisely represents the rectangular PM and stator tooth geometry, enhancing analytical accuracy. The validity of this model is confirmed by comparing it with FEA. Using this model, the optimal design parameters of the machine are identified to achieve the best speed measurement performance.

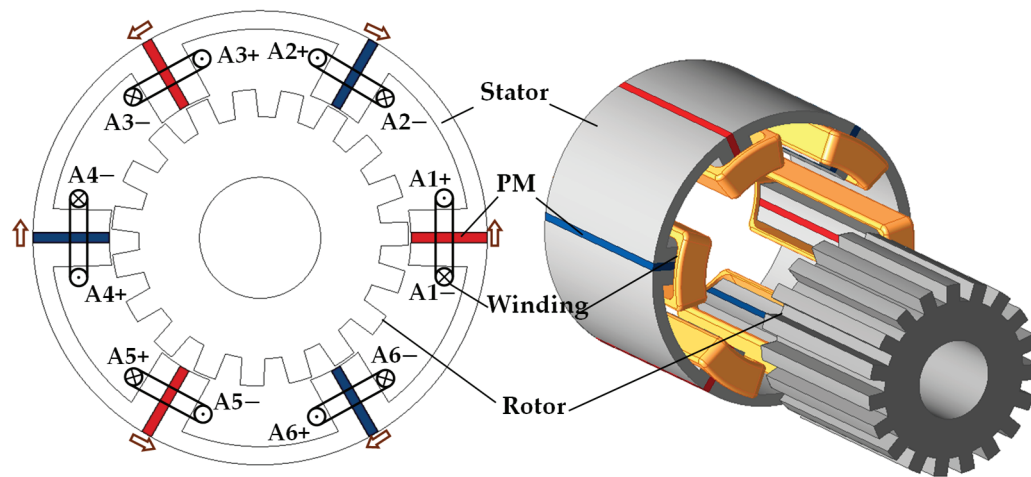


Figure 1. Proposed machine for speed measurement.

To validate the performance of the optimized design, test scenarios are implemented under fixed and varying load conditions using Ansys Maxwell and Twin Builder. In the ideal constant load, the results demonstrate that the proposed sensor achieves 31.5% higher output voltage than a commercial product and a low linearity error of 0.63%, ensuring improved signal clarity and sensitivity. Moreover, it exhibits superior load characteristics, with only a 1.58% voltage drop at 1500 rpm and 30 mA load current, ensuring reliable operation under various conditions.

The proposed speed sensor presents a promising solution for high-precision rotational speed measurement, offering superior robustness, accuracy, and efficiency compared to conventional sensors. The developed nonlinear analytical model is also a powerful tool for future optimization and designing next-generation speed sensors.

2. Machine Topology and Working Principle

2.1. Machine Topology

The structure utilized in this study is based on a 6s/19p C-core flux-switching permanent magnet machine (FSPMM), as shown in Figure 1. Herein, six poles are sandwiched between six segments of the C-shape magnetic cores. Compared to the E-core structure [22], the C core eliminates fault-tolerant teeth, resulting in a larger slot area, improved cooling capability, and material savings. Meanwhile, a double-layer concentrated winding is employed to achieve a short end-winding configuration, reducing both winding resistance and end-winding inductance. The permanent magnets (PMs) are magnetized in alternating directions, as indicated by the arrows in Figure 1. Unlike the conventional 12s/10p combination, the number of rotor poles N_r for the C-core design is not strictly constrained to be close to the number of stator slots N_s as typically different by ± 2 . As demonstrated in [23], the 6s/13p C-core type has been shown to deliver significantly better performance than the conventional 12s/10p machine. The selection of N_s and N_r follows the criteria outlined in [24].

$$N_s = 2mK; N_r = (nN_s \pm 1)K \quad (1)$$

$$1.6N_s < N_r < 4N_s; \text{mod}(N_r, m) \neq 0 \quad (2)$$

where m is the number of phases, n , K are integer values. Therefore, a machine with six stator slots has several stator/rotor pole combinations including, 6/11, 6/13, 6/17, and 6/19 for balance electromotive force. Since more rotor poles generally result in better performance [24], the 6/19 combination is chosen for the speed sensor.

2.2. Working Principle

Figure 2 illustrates the operating principle of the proposed machine through the flux line distribution at four rotor positions, denoted as P1–P4: (P1) $\theta_e = 0^\circ$, (P2) $\theta_e = 90^\circ$, (P3) $\theta_e = 180^\circ$, and (P4) $\theta_e = 270^\circ$. At positions P1 and P3, the flux passing through coils A1 and A4 is short-circuited, resulting in zero effective flux. In contrast, at positions P2 and P4, the effective flux splits into two symmetric paths, represented by the red and yellow lines, flowing through two adjacent poles. This behavior differs from that of the E-core structure [24], where the flux primarily links only one side of the coil axis and flows dominantly through a fault-tolerant tooth. As the rotor rotates, the linkage flux alternates between maximum and minimum values, known as “flux-switching”.

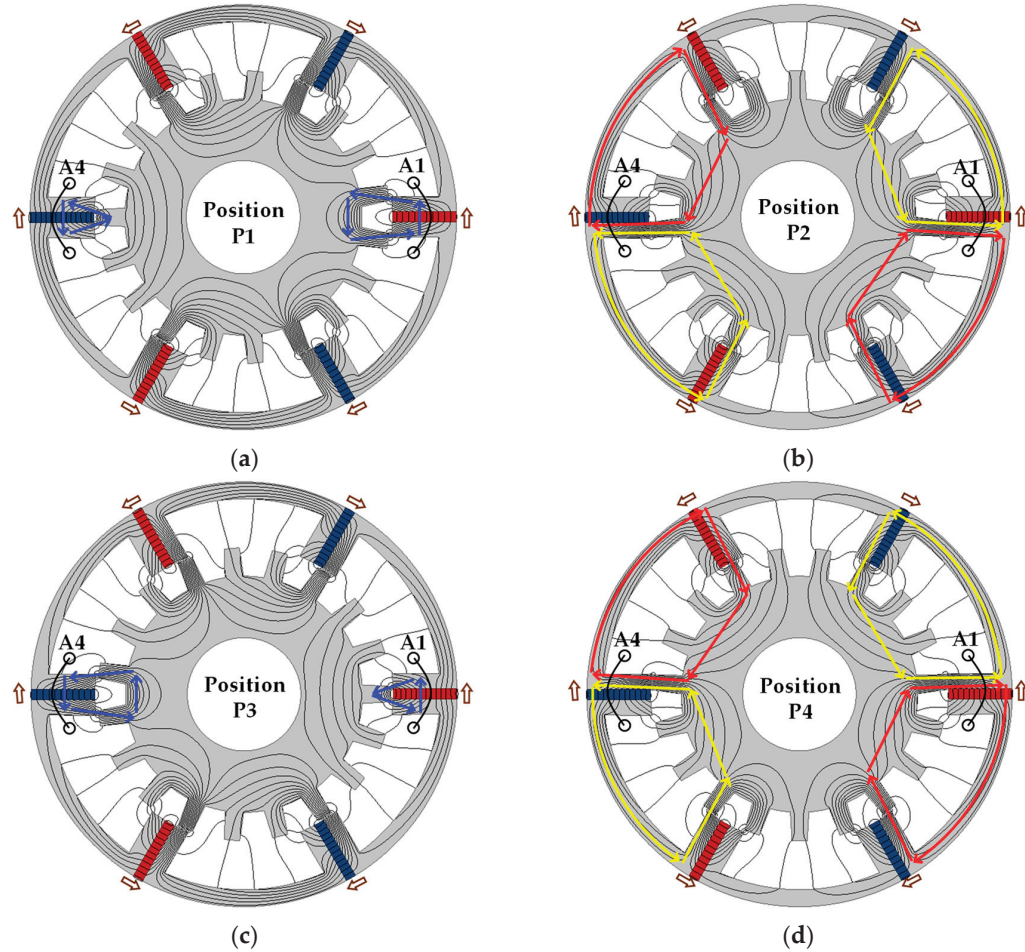


Figure 2. No-load flux distributions at four rotor positions of the proposed machine: (a) $\theta_e = 0^\circ$; (b) $\theta_e = 90^\circ$; (c) $\theta_e = 180^\circ$; and (d) $\theta_e = 270^\circ$.

Figure 3 illustrates the flux waveform of coils A1, A4, and their series-connection A1 + A4. As shown in Figure 3b, although the linkage flux in an individual coil contains significant even harmonics (second, fourth, and sixth harmonics), the flux waveform of the series-connected coils consists exclusively of odd harmonics, resulting in a highly pure sinusoidal flux waveform. This occurs because the even-order harmonics in individual coils have a phase shift of 180° , causing them to cancel each other out when connected in series [25], as confirmed by the Fourier analysis in Figure 3b.

Similarly, the fluxes induced in coil pairs A2 + A5 and A3 + A6 exhibit the same characteristics. Compared to pair A1 + A4, the flux generated by pair A2 + A5 leads by 120° due to its spatial position. Meanwhile, despite the leading spatial position, the flux of pair A3 + A6 lags behind that of A2 + A5 by 60° due to its inverted wound direction. When

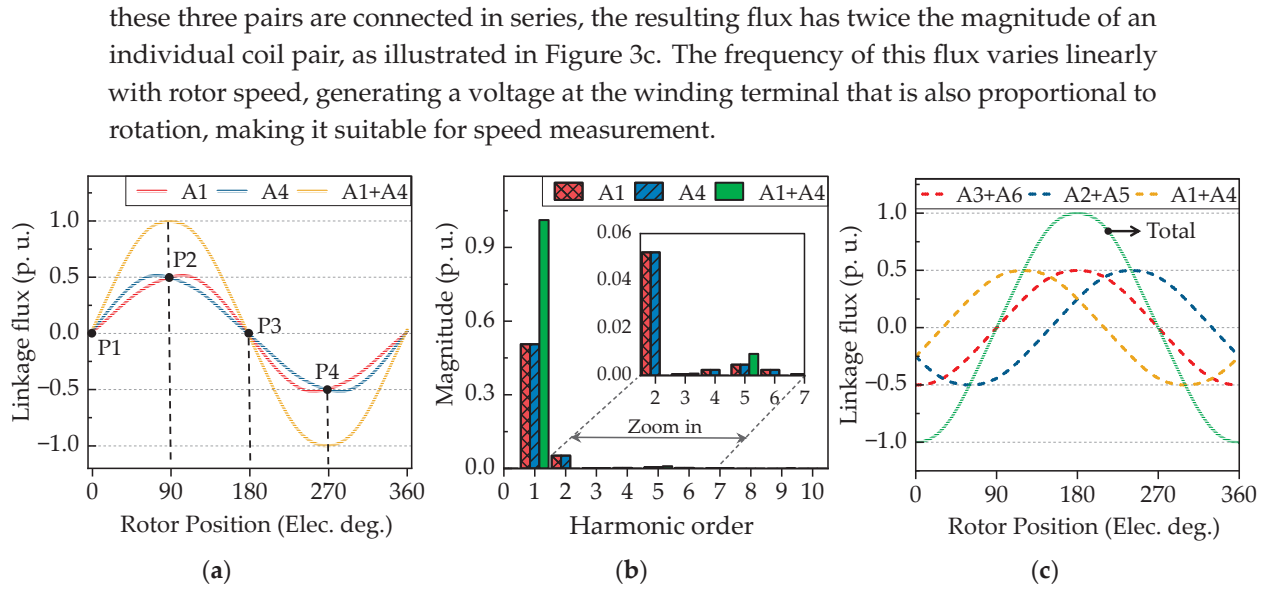


Figure 3. No-load flux analysis of the proposed machine. (a,b) Flux waveforms and its Fourier analysis of the two opposite coils and their series connection, respectively. (c) Flux waveforms of three coil pairs and their series connection denoted by the green line.

3. Analytical Modeling of Proposed Machine

3.1. Linear Analytical Model

3.1.1. Simplification and Layer Division

To construct a mathematical model for the proposed machine, several assumptions and simplifications are made to ease the analysis [20,21,26].

Since the rotor yoke size is typically designed to avoid saturation, its permeability is assumed to be infinite.

The stator yoke is considered isotropic, with constant magnetic permeability corresponding to the linear region of the $B(H)$ curve.

In each region, permeability is variable in the tangential direction but constant in the radial direction.

End effects and eddy effects are neglected.

The PMs have uniform magnetization, and their relative permeability is constant.

Mathematically, the machine is divided into five regions in the 2D cylindrical coordinate system illustrated in Figure 4, and the symbols utilized in this section are shown in Table 1. To account for the rectangular shape of the stator teeth and PMs, the stator slot region (III) is divided into multiple subregions. For rotor teeth, discretization of this region is not required because of the short radial length and the absence of PMs. The equivalent dimensions in the simplified geometry are derived from the practical model as follows.

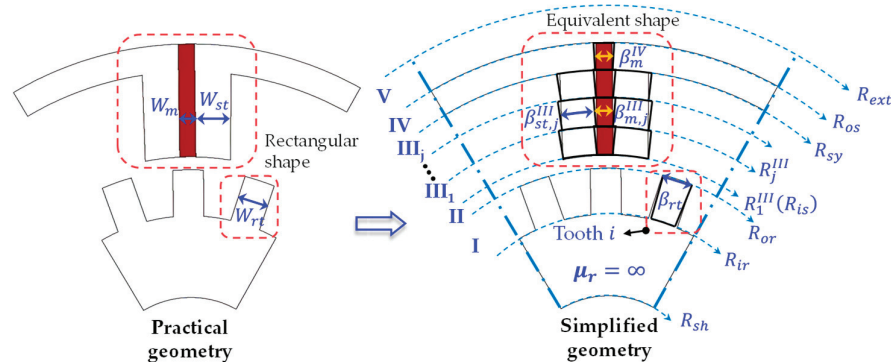


Figure 4. Geometry simplification and layer division.

Table 1. Nomenclature.

Symbol	Explanation	Symbol	Explanation
$r/\theta/z$	Radius/tangential and axial directions	μ_i^{rt}	Permeability of the i th rotor tooth
j	Imaginary unit	θ_r^{ini}	Initial rotor position
\vec{A}	Magnetic vector potential	A	Matrix form of magnetic vector potential
\vec{B}	Magnetic flux density	B	Matrix form of magnetic flux density
\vec{H}	Magnetic field strength	H	Matrix form of magnetic field strength
\vec{J}_z	Current density vector	M_r	Matrix form of radial component of magnetization
μ	Permeability	M_θ	Matrix form of tangential component of magnetization
$\hat{\mu}_n$	CFS coefficient of n th harmonic	A^T	Transpose matrix of matrix A
$\hat{\mu}_n^{rec}$	Inverse coefficient of n th harmonic	$\mu_{c,r}$	Permeability convolution matrix in radial direction
μ_0	Vacuum permeability	$\mu_{c,\theta}$	Permeability convolution matrix in tangential direction
β_{st}	Span angle of stator teeth	K_θ	Diagonal matrix of N
β_{rt}	Span angle rotor teeth	G	Particular solution of Poisson's equation
β_m	Span angle of PM	W^k	Eigenvector matrix of matrix $(V^k)^{0.5}$
K	Number of subregions	λ^k	Diagonal eigenvalue of matrix $(V^k)^{0.5}$
N	Highest harmonic order	k	Region index
R_g	Radius at the middle of airgap	L_{stk}	Stack length of the sensor
T_{cog}	Cogging torque	$\varphi_{i,j}$	Flux passing through one coil side in the i th slot, j th layer
ψ, E	Flux linkage and EMF of the winding	ψ_j	Total flux passing through j th layer
L	Winding inductance	C_i	Winding connecting matrix of j th layer

The radius of each subregion is

$$R_j^{III} = R_{is} + (j - 1)(R_{sy} - R_{is})/K \quad (3)$$

where K is the number of subregions.

The arc pole angle corresponding to each subregion can be computed by

$$\beta_{st,j}^{III} = 2\arcsin(W_{st}/2/R_j^{III}); \beta_{m,j}^{III} = 2\arcsin(W_m/2/R_j^{III}) \quad (4)$$

The other dimensions are given by

$$\beta_{rt} = 2\arcsin(W_{rt}/2/R_{or}) \quad (5)$$

$$\beta_m^{IV} = 2\arcsin(W_m/2/R_{sy}) \quad (6)$$

3.1.2. Rotor Slot (I), Airgap (II) and External Regions (VI)

The vector potential under matrix form A_z satisfies the following Poisson's equation.

$$\frac{\partial^2 A_z^k}{\partial r^2} + \frac{1}{r} \frac{\partial A_z^k}{\partial r} - \frac{1}{r^2} V^k A_z^k = 0; k = (I), (II), (V) \quad (7)$$

where $V^k = \mu_{c,\theta} K_\theta \mu_{c,r}^{-1} K_\theta$, K_θ is the diagonal matrix of the greatest harmonic number N . $\mu_{c,\theta}$, $\mu_{c,r}$ are permeability convolution matrices of Fourier series coefficients (FSCs) in the considered region k , given by.

$$\mu_{c,r} = \begin{bmatrix} \hat{\mu}_0 & \cdots & \hat{\mu}_{-2N} \\ \vdots & \ddots & \vdots \\ \hat{\mu}_{2N} & \cdots & \hat{\mu}_0 \end{bmatrix}; \mu_{c,\theta} = \begin{bmatrix} \hat{\mu}_0^{rec} & \cdots & \hat{\mu}_{-2N}^{rec} \\ \vdots & \ddots & \vdots \\ \hat{\mu}_{2N}^{rec} & \cdots & \hat{\mu}_0^{rec} \end{bmatrix} \quad (8)$$

where $\hat{\mu}_n^{rec}$ is the inverse coefficient of the n th harmonic.

Using the method of separation of variables to solve Equation (7), the general solution is expressed as

$$A_z^k = W^k \left(\frac{r}{R_{outer}^k} \right)^{\lambda^k} a^k + W^k \left(\frac{r}{R_{inner}^k} \right)^{-\lambda^k} b^k; k = (I), (II), (V) \quad (9)$$

where a, b are unknown coefficients, R_{outer}^k, R_{inner}^k are outer and inner radii of region k , W^k, λ^k are eigenvector matrix and diagonal eigenvalue of $(V^k)^{0.5}$.

The convolution matrices for regions (II) and (V) are given by

$$\mu_{c,\theta}; \mu_{c,r} = \mu_0 I; \quad (10)$$

where I is the unit matrix.

From the permeability distribution in Figure 5, FSCs for region (I) are computed by.

$$\hat{\mu}_0^I = \frac{1}{2\pi} \sum_{i=1}^{N_r} \mu_0 \beta_{rl} + \mu_i^{rt} \beta_{rt} \quad (11)$$

$$\hat{\mu}_n^I = \frac{1}{2\pi j n} \sum_{i=1}^{N_r} \mu_0 \left(e^{jn\gamma_i^r} - e^{jn(\theta_i^r - \frac{\beta_{rl}}{2})} \right) + \mu_i^{rt} \left(e^{jn(\gamma_i^r + \beta_{rt})} - e^{jn\gamma_i^r} \right) \quad (12)$$

where $\beta_{rl} = 2\pi/N_r - \beta_{rt}$, $\gamma_i^r = \theta_i^r + \beta_{rl}/2$, $\theta_i^r = (i-1)2\pi/N_r + \theta_r^{ini}$, μ_i^{rt} is the permeability of the i th rotor tooth, and θ_r^{ini} is the initial rotor position.

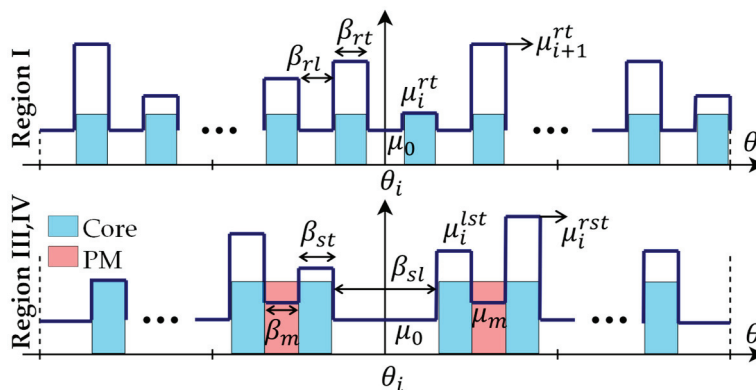


Figure 5. Permeability distribution in Region (I), Region (III), and Region (IV).

3.1.3. Stator Slot and Stator Yoke Regions (III), (IV)

The magnetic vector potential A_z satisfies the following Poisson's equation.

$$\frac{\partial^2 A_z^k}{\partial r^2} + \frac{1}{r} \frac{\partial A_z^k}{\partial r} - \frac{1}{r^2} V^k A_z^k = -\frac{\mu_0}{r} (jU^k M_r^k + M_\theta^k); k = (III), (IV) \quad (13)$$

where $U^k = \mu_{c,\theta} K_\theta \mu_{c,r}^{-1}$. The general solution of (13) is given by

$$A_z^k = W^k \left(\frac{r}{R_{outer}^k} \right)^{\lambda^k} a^k + W^k \left(\frac{r}{R_{inner}^k} \right)^{-\lambda^k} b^k + rG^k; k = (III), (IV) \quad (14)$$

where G^k is the particular solution of (13), defined by

$$G^k = j\mu_0 [V^k - I]^{-1} U^k M_r^k + \mu_0 [V^k - I]^{-1} M_\theta^k \quad (15)$$

where M_r^k and M_θ^k are the magnetization matrices of radial and tangential components of the magnetization vector M .

$$M_r^k = [\hat{M}_{r,-N}^k \dots \hat{M}_{r,N}^k]; M_\theta^k = [\hat{M}_{\theta,-N}^k \dots \hat{M}_{\theta,N}^k]; k = (\text{III}), (\text{IV}) \quad (16)$$

$$\hat{M}_{\theta,n}^k = \frac{1}{2\pi j n} \sum_{i=1}^{N_s} \frac{B_r(-1)^{i+1}}{\mu_0} e^{jn(\theta_i^k + \frac{\beta_{sl}^k}{2} + \beta_{st}^k)} (e^{jn\beta_m^k} - 1); \hat{M}_{r,n}^k = 0 \quad (17)$$

From the permeability distribution shown in Figure 5, FSCs for subregion j in Region (III) are derived from

$$\hat{\mu}_0^j = \frac{1}{2\pi} \sum_{i=1}^{N_s} \mu_0 \beta_{sl,j}^{III} + \mu_m \beta_{m,j}^{III} + (\mu_{i,j}^{lst} + \mu_{i,j}^{rst}) \beta_{st,j}^{III}; \quad \hat{\mu}_n^{III,j} = \frac{1}{2\pi j n} \sum_{i=1}^{N_s} P_i^j + Q_i^j \quad (18)$$

$$P_i^j = \mu_0 \left(e^{jn\gamma_i^j} - e^{jn(\theta_i^j - \frac{\beta_{sl}^j}{2})} \right) + \mu_m \left(e^{jn(\tau_i^j + \beta_m^j)} - e^{jn\tau_i^j} \right) \quad (19)$$

$$Q_i^j = \mu_{i,j}^{lst} \left(e^{jn\tau_i^j} - e^{jn\gamma_i^j} \right) + \mu_{i,j}^{rst} \left(e^{jn(\tau_i^j + \beta_{m,j}^{III} + \beta_{st,j}^{III})} - e^{jn(\tau_i^j + \beta_{m,j}^{III})} \right) \quad (20)$$

where $\gamma_i^j = \theta_i^s + \beta_{sl,j}^{III}/2$, $\tau_i^j = \theta_i^s + \beta_{sl,j}^{III}/2 + \beta_{st,j}^{III}$, and $\theta_i^s = (i-1)2\pi/N_s$. $\mu_{i,j}^{lst}$ and $\mu_{i,j}^{rst}$ are the permeability values of the iron parts at the left- and right-hand side of a magnet.

For Region IV, because the saturation is focused on the parts closing to the airgap, such as teeth [27,28], the stator yoke is usually in the linear range of $B(H)$ curve. A finite permeability value, such as $\mu_{sy} = 3000$, can be set for all iron parts in this region. The FSCs for the convolution matrices in this region are derived by

$$\hat{\mu}_0^{IV} = \frac{1}{2\pi N_s} \left(\mu_m \beta_m^{IV} + \mu_{sy} \left(\frac{2\pi}{N_s} - \beta_m^{IV} \right) \right) \quad (21)$$

$$\hat{\mu}_n^{IV} = \frac{1}{2\pi j n} \sum_{i=1}^{N_r} \mu_m \left(e^{jn(\gamma_i^{IV} + \beta_m^{IV})} - e^{jn\gamma_i^{IV}} \right) + \mu_{sy} \left(e^{jn\gamma_i^{IV}} - e^{jn(\tau_i^{IV} + \frac{\beta_m^{IV}}{2})} \right) \quad (22)$$

where $\gamma_i^{IV} = \theta_i^s + \pi/N_s - \beta_m^{IV}/2$, $\tau_i^{IV} = \theta_i^s - \pi/N_s$.

3.1.4. Boundary Conditions (BCs)

The BCs of the continuity of magnetic vector potential and magnetic field strength are applied to interfaces at R_{or} , R_j^{III} , R_{sy} , and R_{os} . Additionally, at R_{ir} , the Neumann condition is employed due to the assumption of infinite permeability, and at R_{ext} the Dirichlet condition is used. R_{ext} is assumed to be a considerable distance where the magnetic field is negligible compared to the machine field. The resulting boundary conditions are expressed as follows.

$$H_\theta^I|_{r=R_{ir}} = 0; A_z^V|_{r=R_{ext}} = 0 \quad (23)$$

$$A_z^I|_{r=R_{or}} - A_z^{II}|_{r=R_{or}} = 0; H_z^I|_{r=R_{or}} - H_z^{II}|_{r=R_{or}} = 0 \quad (24)$$

$$A_z^{II}|_{r=R_{is}} - A_z^{III,1}|_{r=R_{is}} = 0; H_z^{II}|_{r=R_{is}} - H_z^{III,1}|_{r=R_{is}} = 0 \quad (25)$$

$$A_z^{III,j}|_{r=R_{j+1}^{III}} - A_z^{III,j+1}|_{r=R_{j+1}^{III}} = 0; H_z^{III,j}|_{r=R_{j+1}^{III}} - H_z^{III,j+1}|_{r=R_{j+1}^{III}} = 0 \quad (26)$$

$$A_z^{III,j}|_{r=R_{sy}} - A_z^{IV}|_{r=R_{sy}} = 0; H_z^{III,j}|_{r=R_{sy}} - H_z^{IV}|_{r=R_{sy}} = 0 \quad (27)$$

$$A_z^{IV}|_{r=R_{os}} - A_z^V|_{r=R_{os}} = 0; H_z^{IV}|_{r=R_{os}} - H_z^V|_{r=R_{os}} = 0 \quad (28)$$

Finally, the unknown coefficients in (9) and (14) are determined by solving the system of (23)–(28).

3.1.5. Nonlinear Solution Derivation

After constructing a linear model with permeability as an input, the flux density obtained in the stator and rotor teeth is used to update the permeability of these iron parts based on the $B(H)$ curve of the material. This iterative process is applied using the relaxation method to find the converged solution of the magnetic field. The detailed iterative process has been thoroughly presented in [20,21] and therefore is not repeated in this paper. The magnetic material used for the core is 35PN440 steel, with the characteristic curves illustrated in Figure 6.

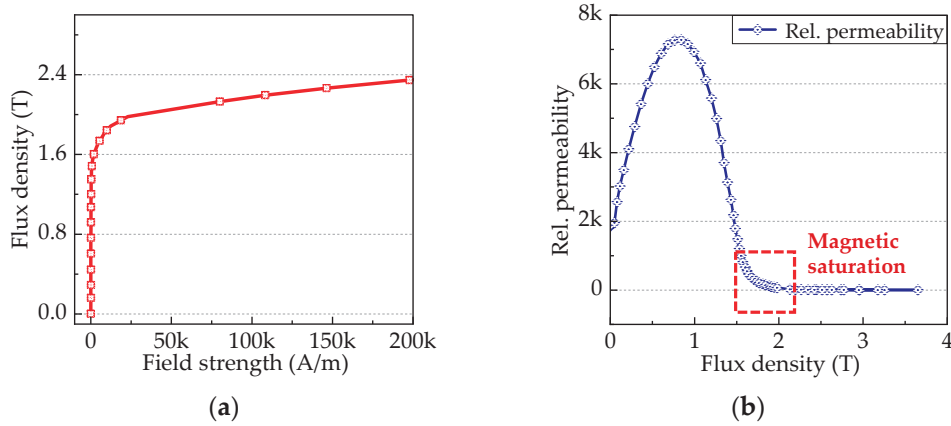


Figure 6. Magnetic properties of 35PN440. (a) $B(H)$ curve; and (b) $\mu(B)$ curve.

3.2. Performance Derivation

The proposed analytical model calculates several performance criteria, including cogging torque, output voltage, and winding inductance, which are calculated using Equations (29)–(35). For clarity, the overall computation process is illustrated in the flowchart shown in Figure 7.

The cogging torque is computed by

$$T_{cog} = \frac{l_{stk} R_g^2}{\mu_0} \int_0^{2\pi} B_{\theta}^{II}(R_g, \theta) B_r^{II}(R_g, \theta) d\theta \quad (29)$$

The output voltage can be deducted as follows.

First, the flux passing through one coil side in the i th slot is expressed as

$$\varphi_{i,1}^{III,j} = \frac{L_{stk}}{A_{slot}^{III,j}} \int_{\theta_i^s - \frac{\beta_{sl}^k}{2}}^{\theta_i^s} \int_{R_{inner}}^{R_{outer}} A_z^{III,j}(\theta, r) r dr d\theta \quad (30)$$

$$\varphi_{i,2}^{III,j} = \frac{L_{stk}}{A_{slot}^{III,j}} \int_{\theta_i^s}^{\theta_i^s + \frac{\beta_{sl}^k}{2}} \int_{R_{inner}}^{R_{outer}} A_z^{III,j}(\theta, r) r dr d\theta \quad (31)$$

where $A_{slot}^{III,j}$ is the slot area in the j th subregion and L_{stk} is the stack length.

The total flux passing through the winding is written as

$$\psi = \sum_{k=1 \rightarrow j} N_t (\varphi_1^{III,j} + \varphi_2^{III,j}) \quad (32)$$

where N_t is the number of turns per coil.

$$\varphi_1^{III,j} = C_1 [\varphi_{i,1}^{III,j}, \dots, \varphi_{N_s,1}^{III,j}]^T; \varphi_2^{III,j} = C_2 [\varphi_{i,2}^{III,j}, \dots, \varphi_{N_s,2}^{III,j}]^T \quad (33)$$

$$C_1 = \begin{bmatrix} -1 & 1 & -1 & -1 & 1 & -1 \end{bmatrix}; C_2 = \begin{bmatrix} 1 & 1 & -1 & 1 & 1 & -1 \end{bmatrix}$$

Then the output voltage of the winding is derived as

$$E = -d\psi/dt \quad (34)$$

After nonlinear solutions are found, the PM excitation is extruded and replaced by a small current I , the obtained linkage flux is used to calculate the winding inductance as

$$L = \psi_I / I \quad (35)$$

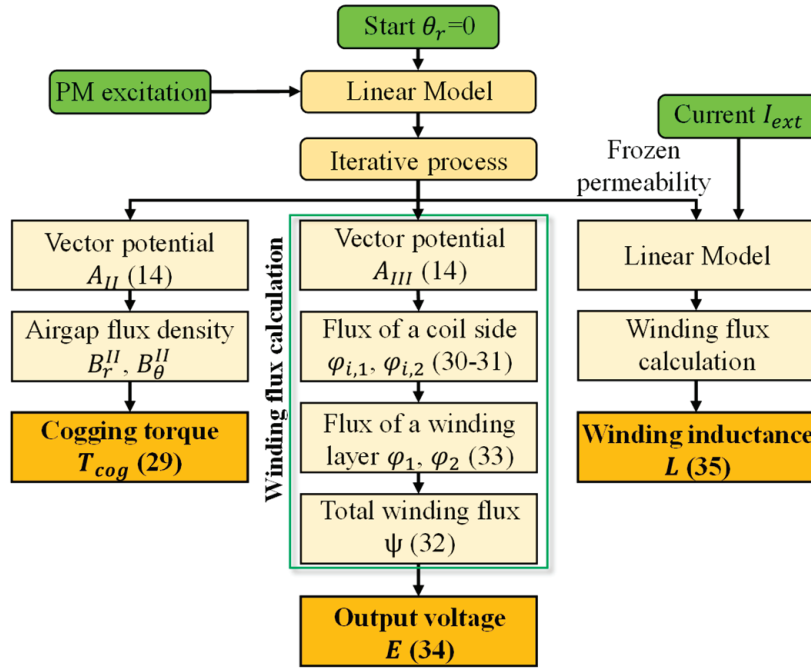


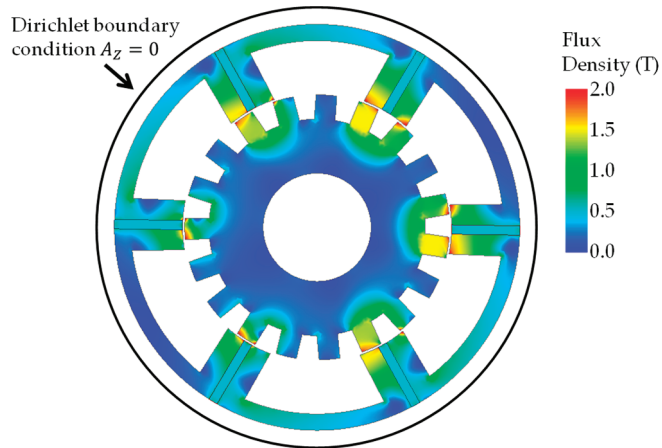
Figure 7. Flowchart for performance derivation.

4. FEA Verification

To demonstrate the accuracy of the proposed model and investigate the effects of the stator teeth layer number, three cases corresponding to one, two, and three layers are analyzed in this section. In each case, the results from analytical models are compared with those from a 2D finite element (FE) model in Ansys Maxwell. Since the proposed sensor operates under permanent magnet excitation, no external current source is applied to the windings. The simulation domain includes the stator, rotor, air gap, and external space with the Dirichlet boundary condition ($A_z = 0$) applied to the outer boundary of the problem space. The rotor is assigned a mechanical rotational speed, and transient simulation is used to observe the induced voltage waveform, flux density distribution, and other field quantities over time. The main parameters of the benchmark model are detailed in Table 2, where the outer stator diameter and stack length are selected based on a commercial AC tachogenerator [29]. Figure 8 illustrates the flux density distribution of the FE model under PM excitation. The results show that mild saturation occurs at the stator and rotor teeth, reaching approximately 1.6 T. In contrast, the highest flux density in the yoke is around 1.0 T, significantly lower than that in the teeth and well below the saturation threshold. This supports the assumption of infinite permeability made in Section 3.1.1.

Table 2. Initial design parameters.

Parameter	Symbol	Value
Stack length (mm)	L_{stk}	43.0
Outer/inner stator radius (mm)	R_{os}	37.5/24.9
Outer/inner rotor radius (mm)	R_{or}	24.4/20.0
Stator/Rotor teeth width (mm)	W_{rt}	3.70/3.85
PM width (mm)	W_{PM}	1.75
Stator yoke thickness (mm)	H_{ys}	3.0
PM remanence (T)	B_r	1.28
Number of turns per coil	N_t	63

**Figure 8.** Flux density distribution of the FE model.

4.1. Magnetic Field Analysis

Figure 9 shows the magnetic field distributions (MFD) at the airgap, obtained from analytical and FE models, in radial and tangential directions, respectively. Overall, all three cases agree acceptably with the FE model. However, the accuracy of the analytical results improves as the number of stator teeth layers increases. Specifically, the largest deviations occur when only one stator teeth layer is used, as this configuration introduces the most significant differences in the PM area. Whereas, with three layers, the analytical model more accurately approximates the geometry of the stator teeth and the PMs, resulting in excellent consistency between the analytical and FE models.

Furthermore, the Fast Fourier Transform (FFT) analysis of the MFD is illustrated in Figure 10. Unlike conventional machine types such as surface-mounted permanent magnet (SPM) or interior permanent magnet (IPM) machines, the air-gap flux of FSPMM contains various harmonics due to the flux modulation effect [30,31]. First, the dominant harmonics are the odd multiples of the stator pole pair number (PPN), or PPN of PMs, P_s , which is determined by

$$P_s = N_s / 2 \quad (36)$$

The PPN of armature winding is defined by.

$$P_w = |P_r - P_s| \quad (37)$$

Meanwhile, multiple working harmonics exist in the air gap flux. These harmonics contribute to EMF generation by ensuring that the PPN of the magnetic field excited by the PMs under rotor modulation, denoted as $P_{i,j}^s$, matches that of the magnetic field excited by the armature winding, denoted as $P_{m,k}^w$, and that both fields rotate at the same speed [32].

$$P_{i,j}^s = |iP_s \pm jP_r|; P_{m,k}^w = |mP_w \pm kP_r| \quad (38)$$

where $P_r = N_r$, $i, m = 1, 3, 5, \dots, \infty$, and $j, k = 0, 1, 2, \dots, \infty$;

FFT analysis reveals the same trend: as the number of layers increases, the AM results become closer to those obtained from the FE model. Notably, while the single-layer case exhibits the largest deviation from the FE results, the two-layer model significantly improves accuracy and shows only a minor difference compared to the three-layer case.

To further evaluate the effects of the layer number on the AM, the computation time and normalized root mean square of error (NRMSE) [33] of the MFD for each case are recorded as a function of the number of harmonics, as illustrated in Figure 11. The accuracy of the proposed model is estimated by

$$\text{NRMSE} = \sqrt{\frac{\sum [B_{ana}(i) - B_{FE}(i)]^2}{\sum B_{FE}(i)^2}} \quad (39)$$

where $B_{ana}(i)$ and $B_{FE}(i)$ are values of the i th estimation of magnetic flux density obtained by analytical and FE models, respectively.

The results indicate that the NRMSE of all cases begins to converge around $N = 250$, with the deviation between the two-layer and three-layer cases being smaller than that between the one-layer and two-layer cases. Regarding computation time, it exhibits a direct proportionality to the number of harmonics, as an increase in harmonics leads to a larger matrix size in the Equation system (23)–(28). Moreover, in terms of computational efficiency, the two-layer case offers a significant reduction in computation time compared to the three-layer counterpart while maintaining high accuracy. Although the one-layer case has the shortest computation time, its NRMSE converges at a much higher value than the other cases, resulting in a notable loss of accuracy.

As a result, the two-layer solution presents the best trade-off between accuracy and computational efficiency. Therefore, this configuration is adopted for the subsequent analyses in this paper.

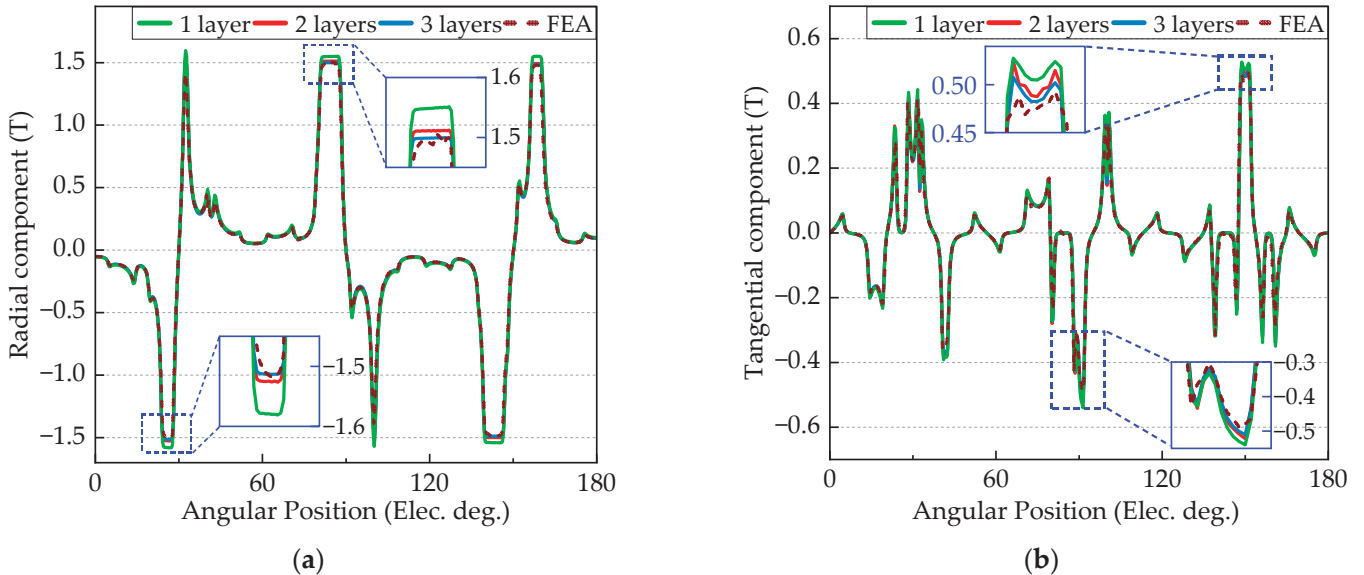


Figure 9. Airgap flux density waveform. (a) Radial component. (b) Tangential component.

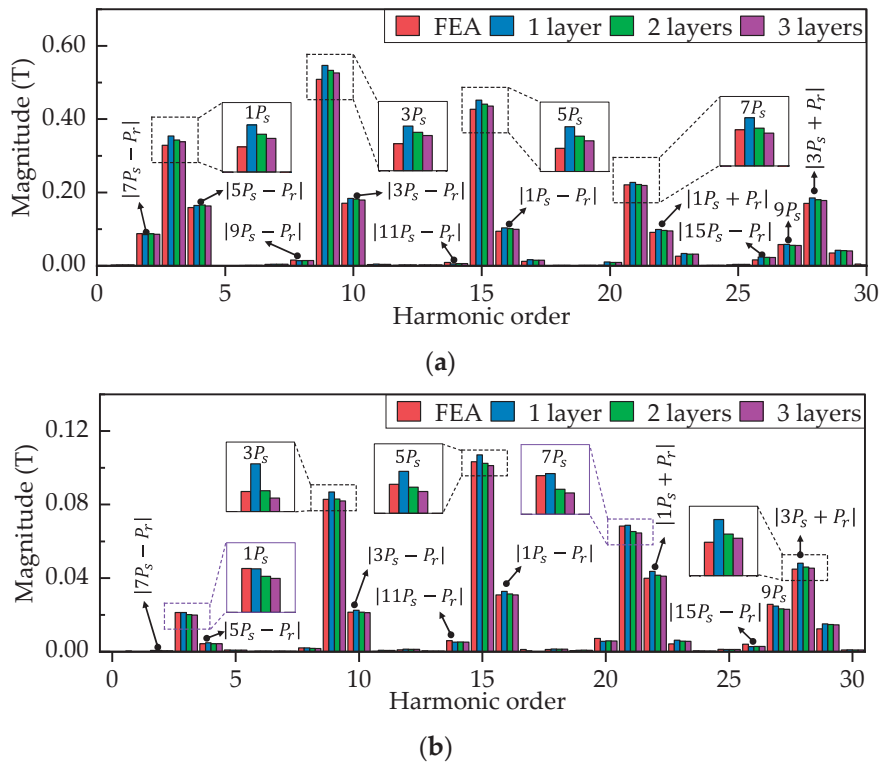


Figure 10. Airgap FFT analysis. (a) Radial component. (b) Tangential component.

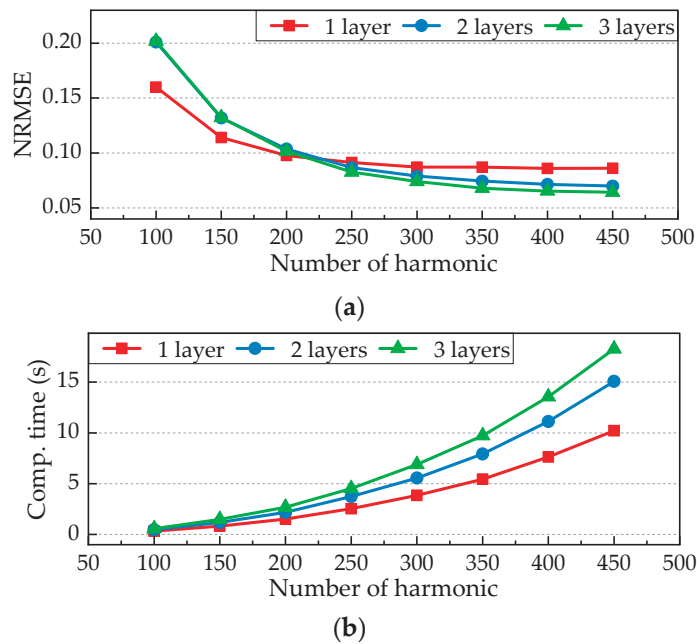


Figure 11. Effects of the number of harmonics on (a) RMSE of radial MFD and (b) computation time.

4.2. Performance Comparison

At a rotational speed of 1500 rpm, the EMF in the stator winding is illustrated in Figure 12a. Meanwhile, the stator winding inductance and cogging torque waveforms are shown in Figure 12b,c, respectively. It is observed that the EMF waveforms derived from both the AM and FEA show excellent agreement. A slight discrepancy is noted in the stator winding inductance, where the FEA result (17.32 mH) is lower than the AM prediction (17.49 mH), yielding a deviation of 0.81%.

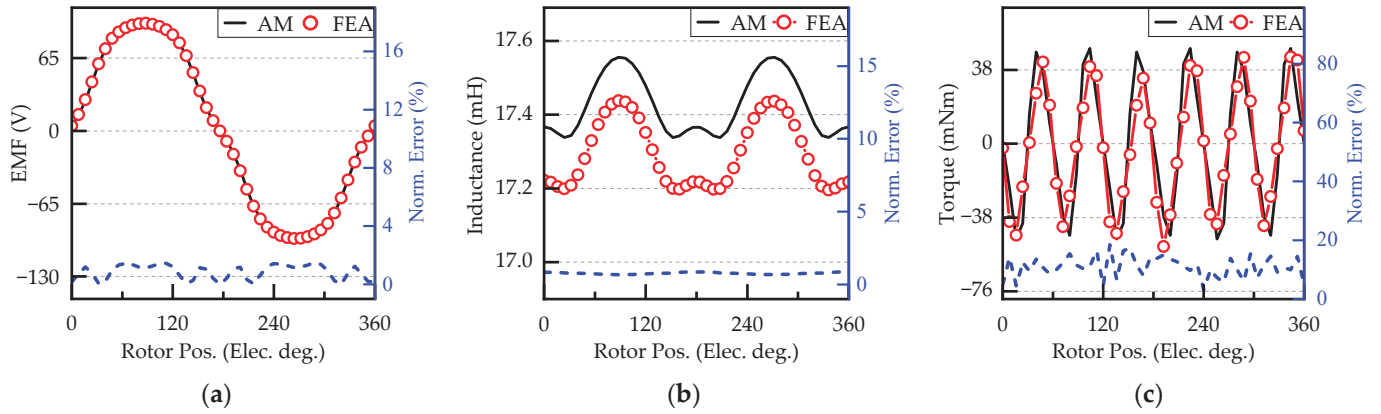


Figure 12. Comparison between analytical and FE models. (a) EMF waveform; (b) winding inductance; and (c) cogging torque.

Regarding cogging torque, a slight difference between the two models is observed. This deviation is primarily attributed to higher-order harmonics in the airgap flux, in which the AM is inherently limited due to its finite harmonic order N . Nevertheless, the AM still provides accurate and reliable predictions, making it suitable for further evaluations and design optimizations.

5. Parametric Optimization

In this section, the proposed AM is used to conduct parametric analyses and optimize the shape of the machine. Generally, the output voltage should be maximized while minimizing the cogging torque and winding inductance. A small cogging torque reduces machine vibration, while lower winding inductance leads to a smaller voltage drop in the winding when the output is connected to a load. Furthermore, the output voltage waveform is optimized to be as sinusoidal as possible, reducing noise by decreasing the total harmonic distortion (THD).

The initial machine parameters are listed in Table 2, where the split ratio R_{is}/R_{os} , the rotor teeth width W_{rt} , stator teeth width W_{st} , and PM width W_{PM} are considered as the optimal variables. The optimal objectives include cogging torque, the magnitude of the first-order EMF, THD, and winding inductance. Refs. [16,27,34] show that the combinations of stator teeth, rotor teeth, and PM widths are more sensitive to the performance of FSPM machines. Therefore, the optimization of the proposed machine follows this procedure: first, the ratio $k_{rm} = W_{rt}/W_{PM}$ and split ratio are selected according to the four optimal objectives at a specific ratio of $k_{rs} = W_{rt}/W_{st}$. This process is repeated at different k_{rs} ratios to determine the optimized machine geometry.

5.1. Split Ratio and Rotor Teeth Ratio

In this part, the two coefficients of split ratio and k_{rm} ratio are considered as variables. Herein, the split ratio is changed by fixing the outer stator radius while the k_{rm} is adjusted by changing the rotor teeth width W_{rt} . The k_{rs} is set to 1.

First, the maximum teeth flux density limitation is chosen under saturation point 1.6 T of the materials. This value should be limited to minimize core losses and ensure computation efficiency. When the machine is more saturated, additional harmonics at the airgap are produced, which the analytical model cannot capture, causing a greater error in cogging torque prediction.

The maximum flux density on stator/rotor teeth is depicted in Figure 13, where the saturated range occurs mainly for small k_{rm} and split ratios. When the split ratio gets

smaller, the radial length of PM increases, producing more flux. As a result, a small tooth is insufficient for flux flow.

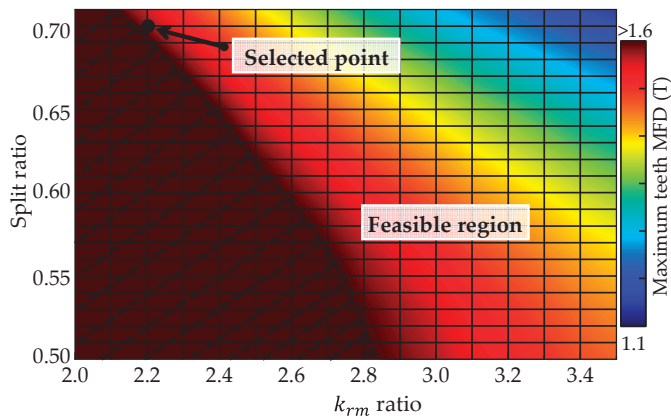


Figure 13. Variation of maximum teeth flux density according to split ratio and k_{rm} ratio.

Figure 14 shows the variations of the 1st-order EMF, THD, cogging torque, and winding inductance, where the EMF and inductance improve with a greater split ratio and smaller k_{rm} . Cogging torque and THD are inversely proportional to the split ratio. Based on the feasible region, an optimal point is chosen at $k_{rm} = 2.2$ and split ratio = 0.7, with 1st EMF = 98.3 V, THD = 8.14%, cogging torque = 32.4 mNm and inductance = 15.3 mH.

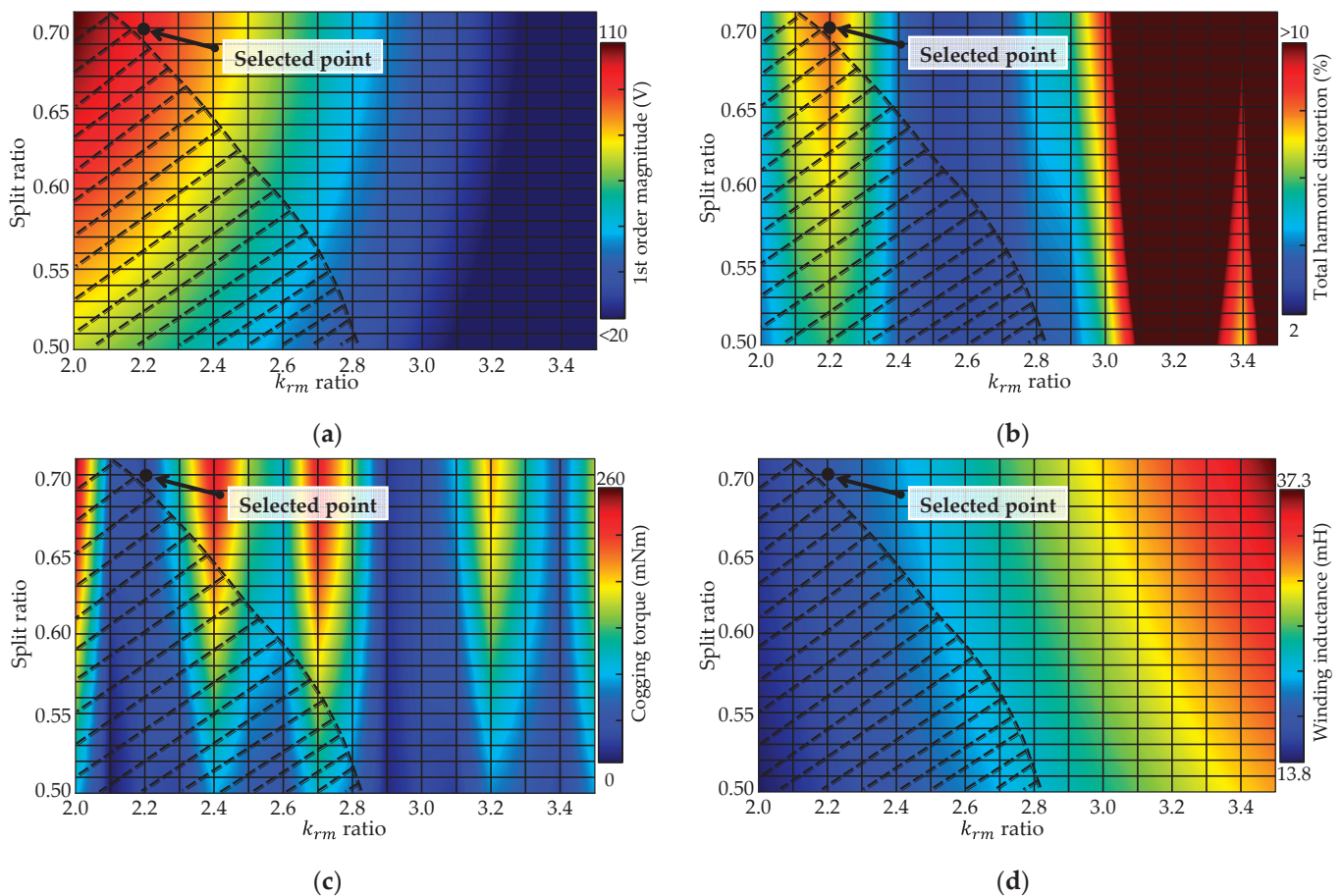


Figure 14. Variations of (a) 1st EMF, (b) THD of EMF, (c) cogging torque, and (d) winding inductance according to split ratio and k_{rm} ratio.

5.2. Stator and Rotor Teeth Width

The process in Section 4.1 is repeated in this part but with a different stator and rotor teeth ratio $k_{rs} = \beta_{rt} / \beta_{st}$. Specifically, with a rotor teeth width $\beta_{rt} = k_{rm} \beta_m$, the stator teeth width is determined by $\beta_{st} = k_{rs} \beta_{rt}$. For each k_{rs} value, an optimal solution is selected based on the optimal objectives, as illustrated in Figure 14. With the range of $k_{rs} = 0.9$ to 1.4, the obtained solutions are shown in Figure 15. From the results, a final solution is chosen with $k_{rs} = 1.2$, $k_{rt} = 2.1$, and split ratio = 0.7 with the characteristics: 1st EMF = 111.6 V, THD = 3.3%, cogging torque = 61.4 mNm, and winding inductance = 12.95 mH. Although the cogging torque is higher than the case $k_{rs} = 1$, the three remaining aspects have improved much. Using FEA to validate the final design, the obtained results are 1st EMF = 110.5 V, THD = 1.53%, cogging torque = 78.4 mNm, and winding inductance = 12.78 mH, demonstrating the effectiveness of the optimization.

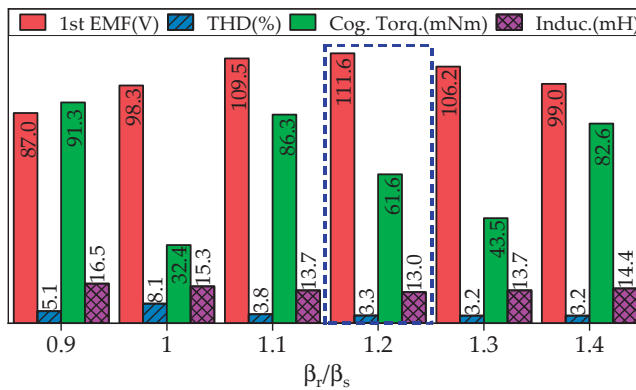


Figure 15. Best solutions at different k_{rs} ratios.

6. Performance of Optimal Design

Because the analytical model cannot capture the eddy current effects of the PM on the stator, a FE coupling model between Ansys Maxwell 2D and Twinbuilder is built to extract the performance of the proposed speed sensor. Additionally, considering the low power of the speed sensor, the AWG (American wire gauge) 34 conductor with a 0.16 mm diameter is selected for the stator winding. Due to the small size of the conductor, the additional length of one turn caused by the end-winding height can be neglected. The stator resistance is determined by

$$R_{wind} = \rho_{co} L_{wind} / S_{cond} \quad (40)$$

$$L_{wind} = N_s N_t [2(L_{stk} + 2W_{st} + W_{PM})] \quad (41)$$

where ρ_{co} is the copper resistivity, and L_{wind} is the total length of the winding. With the chosen conductor size and the design dimensions, the stator winding resistance is 40.25 Ω .

6.1. Voltage Characteristics (Constant Load Characteristics)

Figure 16 shows the output voltage characteristics against the speed from 100 rpm to 3000 rpm under a constant load of 1 mA. It is evident that the proposed design exhibits brilliant linearity and output voltage, with the output ranging from 5.16 to 156.0 Vrms. The maximum error recorded is 0.63% at 100 rpm. Compared to the product [29], the output voltage is 31.5% higher, while the maximum linearity error is smaller than that of the commercial product by 1%. It is noted that a higher voltage drop at stator resistance causes a higher deviation at low speeds. Compared to the design in [8], although the sensor volume is approximately three times larger, the proposed design achieves over 3000 times higher output sensitivity without requiring any external excitation source. Additionally,

the linearity performance is comparable, with a maximum linearity error of 0.63% in the proposed model versus 0.67% in [8].

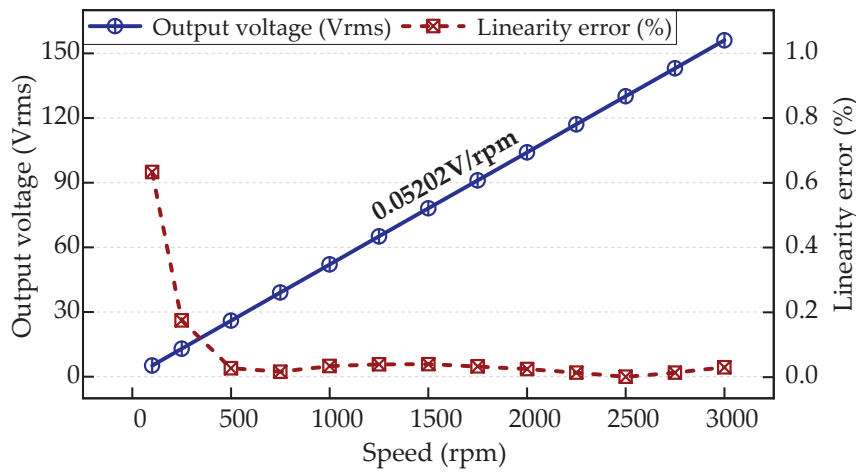


Figure 16. Output voltage and linearity error according to speed.

6.2. Varying Load Characteristics

Figure 17 shows the voltage drop of the proposed design according to the speed and load under two cases of load resistance: 2500 Ω and 5000 Ω . At the heavier load, the load current increases from 5 mA to 60 mA, and the voltage drop changes from 1.28% to 1.68%. Specifically, at 1500 rpm and 30 mA, the voltage drop is 1.58%, compared to 2.5% for the product [29], and this ratio changes negligibly despite the higher load current. At the lighter load, the voltage drop is much lower than at the first load across the speed range, with a maximum of 0.83%. These characteristics of the proposed design are comparable to commercial products.

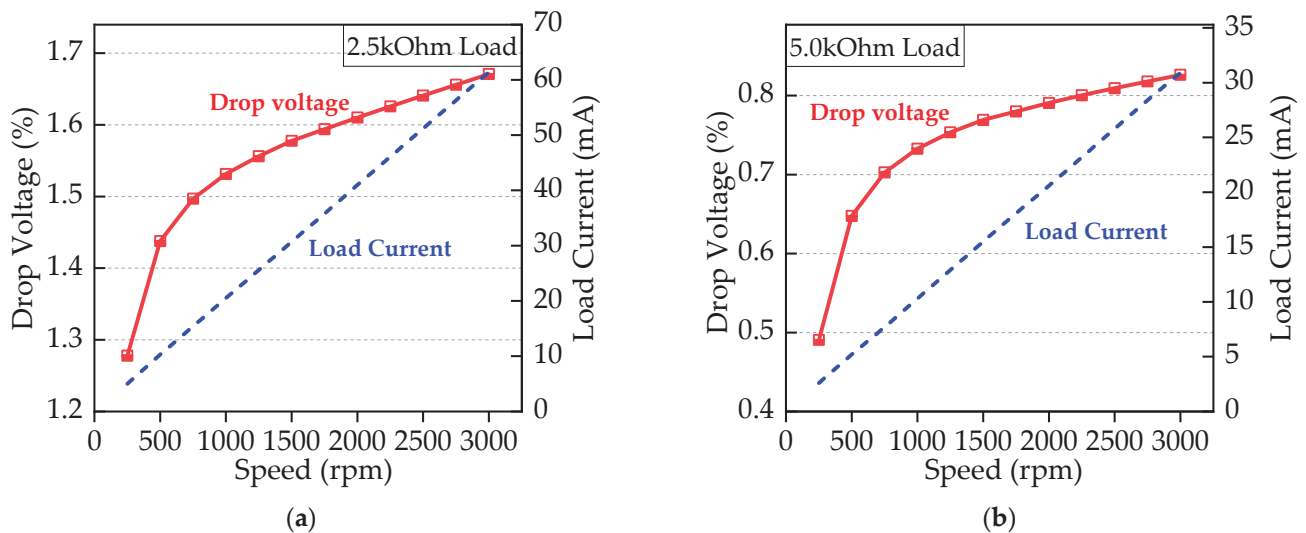


Figure 17. Drop voltage and load current according to speed at (a) 2500 Ohm and (b) 5000 Ohm load resistance.

7. Conclusions

This paper introduced a flux-switching-based speed sensor with a 6-stator-slot/19-rotor-pole (6s/19p) topology to provide a high-performance, cost-effective alternative to conventional speed measurement technologies. By leveraging the flux-switching principle, the proposed design achieves higher output voltage, improved linearity, and reduced permanent magnet (PM) consumption. To accurately model the sensor's electromagnetic

behavior, a nonlinear analytical model (NAM) based on harmonic modeling (HM) was developed. This model effectively accounts for core saturation effects and the rectangular geometry of PMs and stator teeth, ensuring better agreement with finite element analysis (FEA) results. Among the analytical models tested, the two-layer model was identified as the best trade-off between computational efficiency and accuracy, demonstrating high fidelity to FEA simulations. Performance evaluations confirmed that the optimal design achieves a 31.5% higher output voltage than a commercial product while maintaining a low linearity error (0.63%) and minimal voltage drop (1.58% at 1500 rpm, 30 mA). The sensor also demonstrated excellent sinusoidal output waveforms, reducing signal processing complexity and making it highly suitable for industrial, automotive, and aerospace applications requiring precise speed feedback. Future work will focus on experimental validation, investigating the effects of temperature variations, mechanical tolerances, and manufacturing constraints on the proposed design.

8. Discussion

While this study primarily focuses on electromagnetic design and simulation-based validation, several aspects have been considered to support its feasibility for practical applications. From a manufacturing perspective, the design incorporates a 0.5 mm air gap, with dimensional tolerances maintained within ± 0.05 mm—values well within standard CNC machining and common fixture-based assembly capabilities. This demonstrates the feasibility of constructing the sensor using standard mechanical fabrication techniques. With a low current constraint of less than 50 mA, AWG-34 copper wire was chosen for the coil design. The resulting current density remains below 2.5 A/mm^2 , which ensures thermal safety and supports long-term operation. Although fine-gauge wire is more mechanically sensitive, encapsulating the winding with epoxy or potting compound effectively mitigates vibration and strain, improving durability. For applications demanding greater robustness, slightly thicker wire (e.g., AWG-32) may be used with minimal effect on electromagnetic performance or power efficiency.

The proposed design also offers several advantages that make it appealing for industrial applications. Its contactless and self-excited operation makes it particularly suitable for harsh environments, where contamination, vibration, and limited power availability may render optical or Hall-effect sensors impractical. In particular, the sensor shows strong potential for use in induction motor (IM) control systems, such as V/f control, where reliable and cost-effective speed feedback is required without requiring high-resolution encoders.

However, several areas require further investigation. First, no prototype has yet been fabricated, and future work is needed to evaluate the sensor's mechanical, thermal, and long-term stability under real-world operating conditions. Second, the current electromagnetic model assumes temperature-invariant material properties. In practical scenarios, temperature variations can affect magnet remanence and coil resistance, leading to output voltage drift and sensitivity degradation. Third, although the design performs well at moderate speeds, it is not optimized for high-speed applications. As speed increases, the corresponding rise in signal frequency leads to a greater voltage drop across the coil inductance, which attenuates the usable output signal and may affect linearity. Addressing this issue may require winding optimization or geometric redesign to mitigate frequency-dependent losses.

Author Contributions: Conceptualization, D.-T.H.; methodology, D.-T.H.; validation, D.-T.H.; formal analysis, D.-T.H.; investigation, D.-T.H.; writing—original draft, D.-T.H.; writing—review and editing, J.-K.L., K.-I.J., K.-H.S. and J.-Y.C.; visualization, D.-T.H.; supervision, J.-K.L., K.-H.S. and J.-Y.C. All authors have read and agreed to the published version of the manuscript.

Funding: This study was conducted with the support of the National Research Foundation of Korea and funding from the government (Ministry of Science and ICT) under Grant No. RS-2023-00258052.

Data Availability Statement: The original contributions presented in this study are included in the article. Further inquiries can be directed to the corresponding authors.

Conflicts of Interest: The authors declare no conflicts of interest.

References

1. Feng, B.; Deng, K.; Xie, L.; Xie, S.; Kang, Y. Speed Measurement Method for Moving Conductors Based on Motion-Induced Eddy Current. *IEEE Trans. Instrum. Meas.* **2023**, *72*, 6005608. [CrossRef]
2. Addabbo, T.; Di Marco, M.; Fort, A.; Landi, E.; Mugnaini, M.; Vignoli, V.; Ferretti, G. Instantaneous Rotation Speed Measurement System Based on Variable Reluctance Sensors for Torsional Vibration Monitoring. *IEEE Trans. Instrum. Meas.* **2019**, *68*, 2363–2373. [CrossRef]
3. Nam, K.H. *AC Motor Control and Electrical Vehicle Applications*, 1st ed.; CRC Press: Boca Raton, FL, USA, 2010; pp. 109–126.
4. Sun, L. Analysis and improvement on the structure of variable reluctance resolvers. *IEEE Trans. Magn.* **2008**, *44*, 2002–2008.
5. Wang, H.; Zuo, Y.; Zheng, Y.; Lin, C.; Ge, X.; Feng, X.; Yang, Y.; Woldegiorgis, A.; Chen, D.; Li, S. A Delay-Based Frequency Estimation Scheme for Speed-Sensorless Control of Induction Motors. *IEEE Trans. Ind. Appl.* **2022**, *58*, 2107–2121. [CrossRef]
6. Mirzaei, M.; Ripka, P.; Grim, V. A Novel Structure of an Eddy Current Sensor for Speed Measurement of Rotating Shafts. *IEEE Trans. Energy Convers.* **2023**, *38*, 170–179. [CrossRef]
7. Tüysüz, A.; Flankl, M.; Kolar, J.W.; Mütze, A. Eddy-current-based contactless speed sensing of conductive surfaces. In Proceedings of the SPEC, Auckland, New Zealand, 5–8 December 2016.
8. Hoang, D.-T.; Nguyen, M.-D.; Kim, Y.-J.; Phung, A.-T.; Shin, K.-H.; Choi, J.-Y. Improved Design of an Eddy-Current Speed Sensor Based on Harmonic Modeling Technique. *Mathematics* **2025**, *13*, 844. [CrossRef]
9. Costello, J.J.; Pickard, A.C. A Novel Speed Measurement System for Turbomachinery. *IEEE Sens. Lett.* **2018**, *2*, 2501204. [CrossRef]
10. Ni, Z.; Wang, X.; Wu, R.; Du, L. Modeling and Characteristic Analysis of Variable Reluctance Signal Variation of Rolling Bearing Outer Ring Fault. *IEEE Access.* **2022**, *10*, 49542–49550. [CrossRef]
11. Djamal, M. Ramli Development of sensors based on giant magnetoresistance material. *Procedia Eng.* **2012**, *32*, 60–68. [CrossRef]
12. Kapsalis, V.C. Advances in Magnetic Field Sensors. *J. Phys. Conf. Ser.* **2017**, *939*, 1108–1116. [CrossRef]
13. Kumar, A.S.A.; George, B.; Mukhopadhyay, S.C. Technologies and Applications of Angle Sensors: A Review. *IEEE Sens. J.* **2021**, *21*, 7195–7206. [CrossRef]
14. Amara, Y.; Hoang, E.; Gabsi, M.; Lécrivain, M.; Allano, S. Design and comparison of different flux-switch synchronous machines for an aircraft oil breather application. *Eur. Trans. Electr. Power* **2005**, *15*, 497–511. [CrossRef]
15. Chen, J.T.; Zhu, Z.Q. Winding configurations and optimal stator and rotor pole combination of flux-switching PM brushless AC machines. *IEEE Trans. Energy Convers.* **2010**, *25*, 293–302. [CrossRef]
16. Hua, W.; Cheng, M.; Zhu, Z.Q.; Howe, D. Design of flux-switching permanent magnet machine considering the limitation of inverter and flux-weakening capability. In Proceedings of the 2006 IEEE IAS, Tampa, FL, USA, 8–12 October 2006.
17. Taras, P.; Li, G.J.; Zhu, Z.Q. Comparative Study of Fault-Tolerant Switched-Flux Permanent-Magnet Machines. *IEEE Trans. Ind. Electron.* **2017**, *64*, 1939–1948. [CrossRef]
18. Chen, J.T.; Zhu, Z.Q.; Iwasaki, S.; Deodhar, R.P. Influence of slot opening on optimal stator and rotor pole combination and electromagnetic performance of switched-flux PM brushless AC machines. *IEEE Trans. Ind. Appl.* **2011**, *47*, 1681–1691. [CrossRef]
19. Hoang, D.T.; Nguyen, M.D.; Woo, J.H.; Shin, H.S.; Shin, K.H.; Phung, A.T.; Choi, J.Y. Volume optimization of high-speed surface-mounted permanent magnet synchronous motor based on sequential quadratic programming technique and analytical solution. *AIP Adv.* **2024**, *14*, 025319. [CrossRef]
20. Hoang, D.T.; Nguyen, M.D.; Kim, S.M.; Jung, W.S.; Shin, K.H.; Kim, Y.J.; Choi, J.Y. Nonlinear Analytical Solution for Permanent Magnet Synchronous Machines Using Harmonic Modeling. In Proceedings of the ICEM, Torino, Italy, 1–4 September 2024.
21. Hoang, D.-T.; Nguyen, M.-D.; Kim, S.-M.; Bang, T.-K.; Kim, Y.-J.; Shin, K.-H.; Choi, J.-Y. Irreversible Demagnetization Prediction Due to Overload and High-Temperature Conditions in PMSM Based on Nonlinear Analytical Model. *IEEE Trans. Energy Convers.* **2024**, *in press*.
22. Chen, J.T.; Zhu, Z.Q.; Iwasaki, S.; Deodhar, R.P. A novel E-core switched-flux PM brushless AC machine. *IEEE Trans. Ind. Appl.* **2011**, *47*, 1273–1282. [CrossRef]
23. Chen, J.T.; Zhu, Z.Q. Comparison of all and alternate poles wound flux-switching PM machines having different stator and rotor pole numbers. In Proceedings of the ECCE 2009, San Jose, CA, USA, 20–24 September 2009.
24. Xu, Z.; Cheng, M.; Tong, M. Design Consideration for E-Core Outer-Rotor Flux-Switching Permanent Magnet Machines From the Perspective of the Stator-Poles and Rotor-Teeth Combinations. *IEEE Trans. Ind. Appl.* **2025**, *61*, 161–171. [CrossRef]

25. Chen, J.T.; Zhu, Z.Q.; Howe, D. Stator and rotor pole combinations for multi-tooth flux-switching permanent-magnet brushless AC machines. *IEEE Trans. Magn.* **2008**, *44*, 4659–4667. [CrossRef]
26. Djelloul-Khedda, Z.; Boughrara, K.; Dubas, F.; Kechroud, A.; Souleyman, B. Semi-Analytical Magnetic Field Predicting in Many Structures of Permanent-Magnet Synchronous Machines Considering the Iron Permeability. *IEEE Trans. Magn.* **2018**, *54*, 1–21. [CrossRef]
27. Fei, W.; Luk, P.C.K.; Shen, J.X.; Wang, Y.; Jin, M. A novel permanent-magnet flux switching machine with an outer-rotor configuration for in-wheel light traction applications. *IEEE Trans. Ind. Appl.* **2012**, *48*, 1496–1506. [CrossRef]
28. Hua, W. An Outer-Rotor Flux-Switching Permanent-Magnet-Machine With Light Traction. *IEEE Trans. Ind. Electron.* **2017**, *64*, 69–80. [CrossRef]
29. GE1214–Mechanically Connected Tachogenerator with Alternating Voltage Output Signal. Available online: <https://www.noris-group.com/products-and-systems/sensors/encoders-and-tachogenerators/ge1214> (accessed on 10 March 2025).
30. Li, D.; Qu, R.; Li, J. Topologies and analysis of flux-modulation machines. In Proceeding of the ECCE 2015, Montreal, QC, Canada, 20–24 September 2015.
31. Cheng, M.; Han, P.; Hua, W. General Airgap Field Modulation Theory for Electrical Machines. *IEEE Trans. Ind. Electron.* **2017**, *64*, 6063–6074. [CrossRef]
32. Shi, Y.; Jian, L.; Wei, J.; Shao, Z.; Li, W.; Chan, C.C. A New Perspective on the Operating Principle of Flux-Switching Permanent-Magnet Machines. *IEEE Trans. Ind. Electron.* **2016**, *63*, 1425–1437. [CrossRef]
33. Du, Y.; Huang, Y.; Guo, B.; Djelloul-Khedda, Z.; Peng, F.; Yao, Y.; Dong, J. Magnetic Field Prediction in Cubic Spoke-Type Permanent-Magnet Machine Considering Magnetic Saturation. *IEEE Trans. Ind. Electron.* **2024**, *71*, 2208–2219. [CrossRef]
34. Hua, W.; Cheng, M.; Zhu, Z.Q.; Howe, D. Analysis and optimization of back EMF waveform of a flux-switching permanent magnet motor. *IEEE Trans. Energy Convers.* **2008**, *23*, 727–733. [CrossRef]

Disclaimer/Publisher’s Note: The statements, opinions and data contained in all publications are solely those of the individual author(s) and contributor(s) and not of MDPI and/or the editor(s). MDPI and/or the editor(s) disclaim responsibility for any injury to people or property resulting from any ideas, methods, instructions or products referred to in the content.

Article

Design of a High-Efficiency External Rotor Interior Permanent Magnet Synchronous Motor Without Magnetic Leakage Flux Path

Kyoung-Soo Cha ^{1,†}, Jae-Hyun Kim ^{2,†}, Soo-Gyung Lee ³ and Min-Ro Park ^{4,*}

¹ Advanced Mobility System Group, Korea Institute of Industrial Technology, Daegu 42994, Republic of Korea; kscha@kitech.re.kr

² School of Mechanical Engineering, Yeungnam University, Gyeongsan 38541, Republic of Korea; jaehyun@yu.ac.kr

³ Global R&D Center, POSCO, Incheon 21985, Republic of Korea; soogyunglee@posco.com

⁴ Department of Electrical Engineering, Soonchunhyang University, Asan 31538, Republic of Korea

* Correspondence: minro@sch.ac.kr

† These authors contributed equally to this work.

Abstract: This paper proposes a high-efficiency design for an external rotor interior permanent magnet synchronous motor (IPMSM) that eliminates the magnetic leakage flux path. The conventional model based on an external rotor surface-mounted permanent magnet synchronous motor (SPMSM) is analyzed using a statistical method. Design directions are derived by comparing efficiencies at two major operating points with different motor characteristics. A V-shaped IPMSM is then proposed to increase the permanent magnet volume and reduce magnetic leakage. Design optimization is conducted using Gaussian process models (GPMs) constructed with a Latin hypercube design (LHD), and the optimal design is determined using a gradient descent algorithm. A prototype is fabricated to confirm manufacturability, and the improved efficiency of the proposed design is experimentally verified. The results demonstrate that the proposed IPMSM significantly outperforms the conventional SPMSM in terms of efficiency across both operating points.

Keywords: design optimization; efficiency; external rotor permanent magnet synchronous motor; gaussian process model; V-shaped rotor type

MSC: 49S05

1. Introduction

As the industrial requirement for high-performance electric motors has been growing in recent years, various types of electric motors, such as the permanent magnet synchronous motor (PMSM), have been widely investigated. Electric motors are classified according to their rotating part as being either external rotor or internal rotor types. Compared with internal rotor motors, external rotor motors have a larger stator slot area, which is responsible for increasing the torque-producing capability [1–4].

Numerous researchers have studied the applications of external rotor machines, which require high torque and high efficiency. The most common application of these types of motors is the in-wheel motor of electrical vehicles [5–10]. Similarly, external rotor machines are used in the propulsion systems of electrical bicycles [11]. According to refs. [12,13], wind turbine generators and air conditioner motor fans also constitute external rotating machines. In addition, external rotor machines are used in washing machines with direct

drive characteristics [14,15]. Because wet grinding requires both high and constant torque at low speeds without a belt or gear mechanism, external rotor configurations are suitable [16].

For those aforementioned applications, previous researchers have studied various types of external rotor machines. The design of an external rotor switched reluctance motor was proposed in [13]. Considering the design requirements related to electromagnetic and mechanical issues, a synchronous reluctance motor design was established in [4]. Permanent magnet (PM)-assisted synchronous reluctance motors were compared according to the PM material in [6]; the authors concluded that high torque density can be achieved even with ferrite magnet-based external rotor machines. The external rotor Vernier PM machine was studied to reduce end winding in [17].

In terms of PM machines, most of the related research has focused on surface-mounted permanent magnet synchronous motors (SPMSMs) [18–29]. Here, the main points for investigation included predicting the electromagnetic characteristics and conducting noise analysis. Considering the structural differences between internal and external rotor PM machines, the analytical calculation of the magnetic field of an external rotor PM machine was examined in [19–21]. Moreover, noise analysis of an external rotor PM machine was conducted in [22,23]. Concerning motor design, little research has been conducted [24–26]. According to ref. [24], the maximum achievable air gap magnetic flux density of an external rotor SPMSM is limited by the split ratio.

Interior permanent magnet synchronous motors (IPMSMs) are well known to be alternatives to SPMSMs to overcome the limited air gap magnetic flux density. These studies present the rotor structure to enhance the advantages of IPMSMs. In [30], two-layered PMs were used to increase the volume of PMs. Moreover, two-layered and hybrid PMs were used in [31]. The V-shaped topology is also favorable in that the volume of PMs can be increased [32,33]. However, the magnetic leakage flux may be large in external rotor IPMSMs owing to the small magnetic reluctance of the magnetic leakage flux path. This is due to the large cross-sectional area of the magnetic leakage flux path in the external rotor.

In [34], the external rotor structure without the magnetic leakage flux path was proposed. However, some of the aspects were insufficient and required improvement. First, the effects of each circuit parameter on efficiency were examined by changing only one circuit parameter, while the other remaining parameters were constant. However, the variation in the other parameters has to be considered, because the effect of one parameter can vary depending on the values of the other parameters. Further, detailed explanations of the sensitivity analysis and design optimization process were absent. Moreover, the improved efficiency of the proposed IPMSM was verified only through finite element analysis (FEA).

This study presents a high-efficiency design for an external rotor V-shaped IPMSM without the magnetic leakage flux path. The targeted system is a home appliance having two main operating points: these are the high-torque-and-low-speed point and the low-torque-and-high-speed point. One of the most important requirements for a home appliance is high efficiency [35]. As the motor characteristics such as current and loss vary depending on the operating points, these characteristics must be considered in the motor design process.

In conventional external rotor machines, surface-mounted PMSMs (SPMSMs) are widely used due to their mechanical simplicity and ease of manufacturing. However, they suffer from limited magnetic flux density because of the constrained permanent magnet (PM) volume, which restricts further efficiency improvement. To address this limitation, interior PMSMs (IPMSMs) with V-shaped PM arrangements have been proposed, as they allow higher PM volume and stronger flux density. Nonetheless, when applied to external rotor configurations, these V-shaped IPMSMs introduce magnetic leakage flux paths due

to structural connections between rotor cores. This leakage significantly degrades the magnetic performance and system efficiency.

To overcome this issue, this study proposes a novel external rotor V-shaped IPMSM design that eliminates the magnetic leakage flux path while maintaining mechanical robustness. The proposed rotor structure separates the core into upper and lower parts, where the lower core—adhered only to the PMs—is structurally stabilized by centrifugal force during rotation, as shown in Figure 1. The manufacturability of the design is confirmed through prototype fabrication.

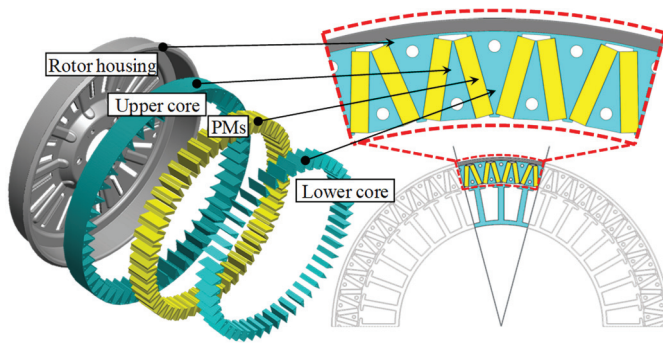


Figure 1. Proposed V-shaped IPMSM without the magnetic leakage flux path.

The conventional model currently used for the target system is analyzed based on statistical methods. From this analysis, design directions to simultaneously improve the efficiency at the two main operating points are derived. As the efficiency at the high-torque-and-low-speed point is lower than that at the high-speed-and-low-torque point, priority is given to improving the low-speed efficiency.

Design variables are selected based on sensitivity analysis, and Gaussian process models (GPMs) are constructed using a Latin hypercube design (LHD). These models provide more accurate prediction performance than conventional response surface models (RSMs) [36,37]. A gradient-based optimization algorithm is applied to obtain the optimal design solution. Experimental validation is conducted to confirm both the structural feasibility and efficiency improvement of the proposed machine compared to the conventional SPMSM.

In this study, the primary design objectives are as follows: (1) to eliminate the magnetic leakage flux path in an external rotor IPMSM through a novel V-shaped rotor topology, (2) to improve the efficiency at two representative operating points: low-speed/high-torque and high-speed/low-torque points, (3) to enhance torque density without sacrificing structural robustness, and (4) to ensure manufacturability for home appliance applications. These objectives are addressed by combining statistical analysis, GPM-based optimization, and experimental validation.

2. Analysis of Conventional External SPMSM

Figure 2a shows the conventional SPMSM that is currently being used for the targeted home appliance. As the targeted system mainly operates at two points, the efficiency of the conventional model had to be improved at the two main operating points, high-torque-and-low-speed point A and low-torque-and-high-speed point B, as shown in Figure 2b. In this section, the conventional model is analyzed based on a statistical method. The motor characteristics such as the current and the loss are calculated using the d- and q-axis equivalent circuit method combined with FEA [38]. Contrary to the stator using laminated cores, the rotor housing of the conventional model consists of carbon steel, which is an unlaminated core. As the unlaminated carbon steel has a magnetic property, the PMs were

directly attached to the rotor housing. Considering the costs, it was decided to use ferrite magnets and aluminum coils. Because the residual induction of ferrite PMs is low and the resistivity of aluminum coils is high, the efficiency of the conventional SPMSM is low at both points. Especially, the efficiency at point A is lower than that at point B. Accordingly, priority consideration is given to point A efficiency when deciding design directions for efficiency improvement.

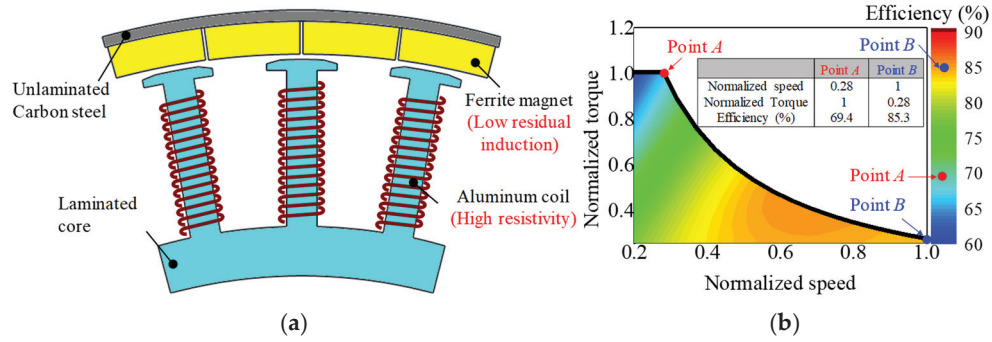


Figure 2. Conventional SPMSM: (a) Configuration; (b) Efficiency map and characteristics curve.

2.1. Characteristics

The characteristics of the conventional SPMSM are analyzed according to the d - and q -axis equivalent circuit method using Equations (1)–(6):

$$T = P_n [\Psi_a I_{oq} + (L_d - L_q) I_{od} I_{oq}] \quad (1)$$

$$V_o = \omega_e \sqrt{(L_d I_{od} + \Psi_a)^2 + (L_q I_{oq})^2} \quad (2)$$

$$I_{od} = -I_o \sin \beta, I_{oq} = I_o \cos \beta \quad (3)$$

$$I_{cd} = -\frac{\omega_e L_q I_{oq}}{\left(\frac{V_o^2}{W_{iron}}\right)}, I_{cq} = \frac{\omega_e (L_d I_{od} + \Psi_a)}{\left(\frac{V_o^2}{W_{iron}}\right)} \quad (4)$$

$$I_d = I_{od} + I_{cd}, I_q = I_{oq} + I_{cq} \quad (5)$$

$$W_{ohmic} = R_a (I_d^2 + I_q^2), R_a = \rho_{al} \frac{l_{coil}}{A_{coil}} \quad (6)$$

where T is torque, P_n is the number of pole pairs, and V_o is induced voltage. Ψ_a is the linkage flux at no load. The d - and q -axis inductances L_d and L_q , respectively, and the iron loss W_{iron} were calculated using FEA. I_o denotes the magnitude of the magnetizing current, and β denotes the current phase angle. I_{od} and I_{oq} are the d - and q -axis magnetizing currents, respectively, and I_{cd} and I_{cq} denote the d - and q -axis equivalent iron loss currents, respectively. By summing the magnetizing current and equivalent iron loss current, I_d and I_q denote the d - and q -axis input currents, respectively. ω_e and ω_m denote the electrical and mechanical angular frequencies, respectively. W_{ohmic} denotes the ohmic loss, R_a denotes the phase resistance, ρ_{al} is the resistivity of aluminum, l_{coil} is the length of the coil, and A_{coil} is the cross-sectional area of the coil.

The current at each operating point is determined by the circuit parameters. The d -axis current was maintained at zero for low-speed point A in accordance with the maximum-torque-per-ampere control method. For high-speed point B, the negative d -axis current was used to suppress the induced voltage according to the flux-weakening control method.

In this paper, two losses of the PMSM that much affected motor efficiency were considered: ohmic loss and iron loss. The ohmic and iron losses of the conventional SPMSM are shown in Figure 3. The ohmic loss of the PMSM is generated in the stator

winding coils and determined by the resistance and input current. The resistance is related to the length and the cross-sectional area of the coils, as well as the resistivity of the coil material. The magnitude of the current is determined by the circuit parameters and operating point. As shown in Figure 3a, it is evident that the ohmic loss increases as the torque increases, since the output torque is proportional to the current. As a result, the ohmic loss is the largest at point A, and has a greater effect on point A efficiency than the iron loss. The other loss is the iron loss generated in the stator and rotor core. The magnitude and frequency of the magnetic flux density on the cores affect the amount of iron loss, which means that the iron loss is determined by the material properties and the rotating speed. As the rotating speed increases, the fundamental frequency of the SPMSM also increases, which leads to a significant rise in iron loss, as shown in Figure 3b.

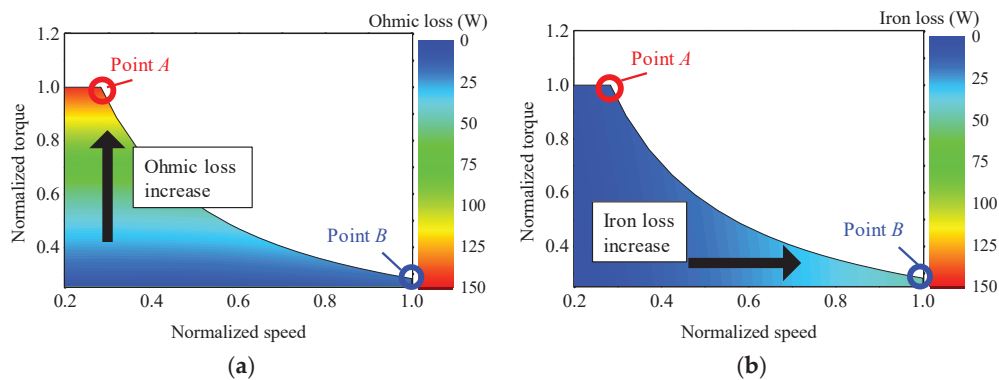


Figure 3. Loss of conventional SPMSM: (a) Ohmic loss; (b) Iron loss.

In summary, the ohmic loss refers to the resistive power loss generated in the stator winding conductors due to the current flow, while the iron loss originates from hysteresis and eddy current phenomena occurring in the magnetic cores of the stator and rotor under alternating flux conditions. These definitions are consistently applied throughout the paper. As shown in Figure 3b, the iron loss is the largest at point B and has a greater effect on point B efficiency.

2.2. Main Effects and Design Directions for Parameters

To determine the design directions for improving the efficiency at both points A and B, the effects of the circuit parameters on each efficiency are statistically investigated [39]. The circuit parameters are selected from Equations (1)–(6): these are the linkage flux at no load, the resistance, the d -axis inductance, the q -axis inductance, and the iron loss. The three-level design is written based on the orthogonal array method, and the 18 design of experiments (DOE) samples are presented in Figure 4a.

Following the DOE table constructed using the orthogonal array method, the circuit parameters are varied across 18 samples, and the efficiencies at point A and B are calculated using the equivalent circuit combined with FEA. To analyze the influence of each parameter independently, main effects analysis is conducted. Each parameter has three levels (levels 0, 1, and 2), and the samples are grouped accordingly. Within each level group, the average efficiency is calculated. The difference in these averages across levels represents the “main effect” of that parameter on efficiency. Figure 4b shows this procedure using the no-load linkage flux (P1) as an example. The plot shows how the average efficiency changes with increasing parameter level, indicating the degree and direction of its influence. Through this process, the main effects of each parameter are analyzed considering variation in the other parameters [40].

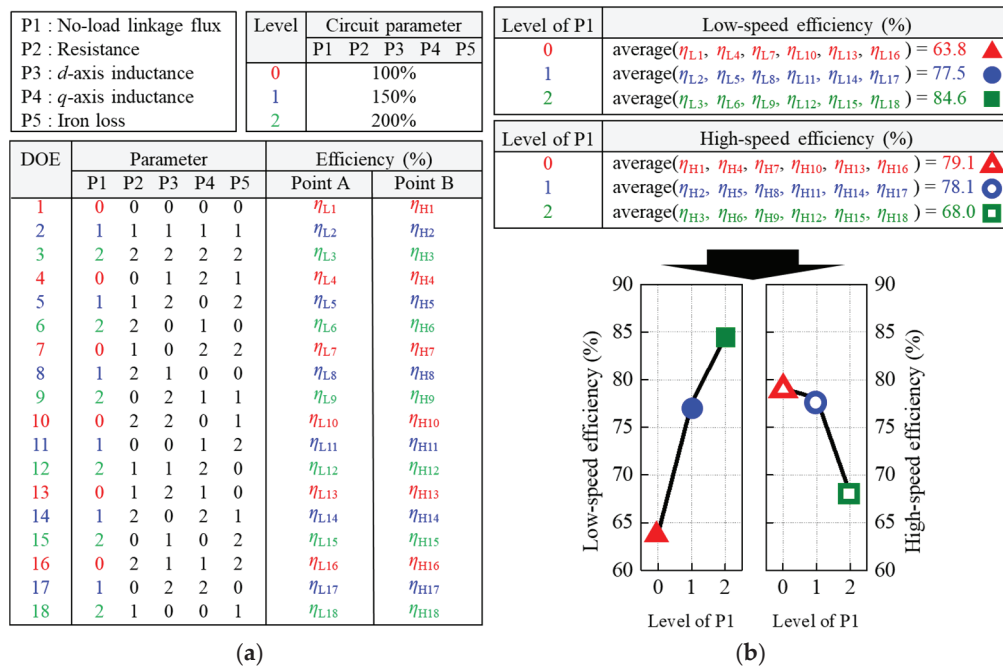


Figure 4. Procedure of main effects analysis: (a) Design of experiment table for the circuit parameters; (b) Main effects plot.

In Figure 5, the main effects of all five parameters are summarized. Parameters that increase efficiency are shown in red, while those that decrease efficiency are shown in blue. This analysis forms the basis for determining the design directions in the next step. Accordingly, a large no-load linkage flux and a small resistance are required for the improvement of the efficiency at point A. The remaining parameters are shown to have a small effect on point A efficiency. On the other hand, point B efficiency is significantly affected by most of the parameters.

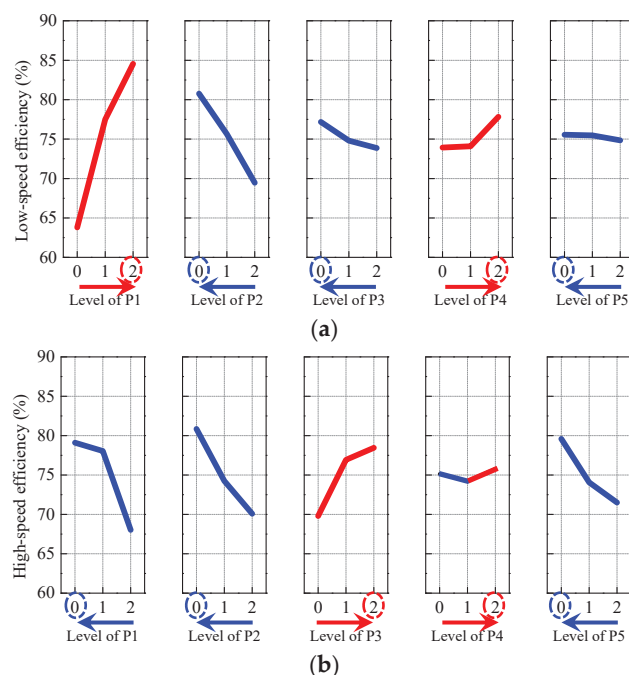


Figure 5. Main effects plot of parameters: (a) Efficiency at point A; (b) Efficiency at point B.

As the point *A* efficiency is lower than the point *B* efficiency, point *A* efficiency improvement is considered a priority in this study. In the target application—a washing machine—point *A* corresponds to the washing mode, which operates under low-speed and high-torque conditions. Point *B*, on the other hand, corresponds to the spinning mode, which operates at high speed and low torque. Although the output power at both points is similar, the washing mode is used more frequently and for a longer duration. Consequently, the efficiency at point *A* has a greater impact on the total energy consumption, making it the primary target for improvement. Thus, the no-load linkage flux has to be increased to enhance the torque production at point *A*, where the motor operates under low-speed, high-torque conditions. However, increasing the no-load flux also raises the back electromotive force (BEMF), especially at high-speed operation (point *B*). To suppress this elevated BEMF and maintain proper control, a higher negative *d*-axis current is required through flux-weakening control. This additional current can lead to increased core saturation and iron loss, which degrade the efficiency at point *B*. Therefore, to minimize total loss at high speed, other parameters such as phase resistance and inductance must be reduced. By reducing the resistance and inductance, the induced voltage can be effectively limited. This trade-off ensures improved efficiency at both operating points.

To determine the design directions, the material cost is considered in addition to efficiency. This is because low cost is as important a requirement for a home appliance as motor efficiency. Table 1 presents the unit cost of the materials for PM machines [41]. For the conventional model, the ferrite magnets, aluminum coils, and S60 core were used. Considering the material costs, it is hard to change the PM and coil materials. Instead, changing the core material within similar grades is reasonable because the unit cost of the core is the lowest. Accordingly, the following design directions are determined in this section:

1. Increasing the air gap magnetic flux produced by PMs.
2. Decreasing coil turns.
3. Changing the core material from S60 to S18.

Table 1. Unit cost of materials.

Part	Material	Cost Rate
Permanent magnets	Ferrite	\$10/kg
	Rare earth	\$50/kg
Coil	Aluminum	\$3/kg
	Copper	\$7/kg
Core	S60	\$0.7/kg
	S18	\$0.8/kg

By increasing the air gap magnetic flux produced by the PMs, the no-load linkage flux can be enhanced even though the number of coil turns are reduced. The reduced number of coil turns results in an increase in coil diameter and a decrease in coil length, thereby reducing resistance overall. The reduced number of coil turns decreases not only the resistance but also the inductance. In addition to the large no-load linkage flux, the reduced inductance causes the high-speed efficiency to decrease. This is because the induced voltage of the PMSM has to be suppressed to operate at high-speed point *B*. Considering (2), the induced voltage can be suppressed using the negative *d*-axis current. When the no-load linkage flux is large and the inductance is small, the required magnitude of the *d*-axis current has to be large at high speeds. This causes the magnetic flux density in the cores to increase. However, the iron loss is unlikely to increase by changing the core material,

although the magnetic flux density increases. As a result, it is possible to improve the efficiency at both points *A* and *B*.

3. Proposed V-Shaped IPMSM Without Magnetic Leakage Flux Path

In accordance with the design directions determined in the previous Section 2, a rotor structure for a large air gap magnetic flux produced by the PMs is introduced in this section. Among the many types of IPMSMs in existence, the spoke type is well known for its flux-concentrating effect. Therefore, many researchers have adopted the spoke type for internal rotor machines [42]. However, the spoke type is inappropriate to use for external rotors owing to the large magnetic leakage flux generation, as illustrated in Figure 6a. This is because the magnetic reluctance of the leakage flux path is small. Figure 6b shows that the air gap magnetic flux is limited no matter the length of the path in a restricted space for the rotor. To avoid a large amount of magnetic leakage flux, the existing V-shaped rotor topology is favorable for external rotating machines [32,33]. By arranging the PMs into a V-shape, the cross-sectional area of the magnetic leakage flux path is reduced compared to the spoke type. But still, the magnetic leakage flux in the existing V-shaped rotor is caused by the connection structure that exists for the structural stability of the rotor.

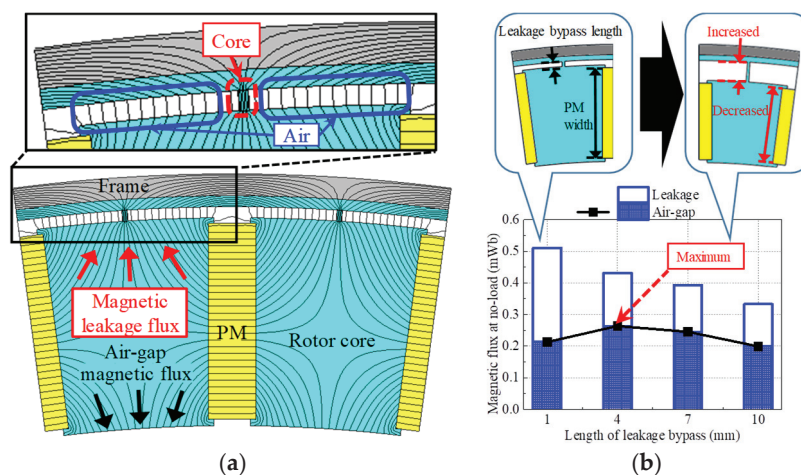


Figure 6. Magnetic characteristics of external rotor spoke-type PMSM at no load: (a) Magnetic flux lines; (b) Magnetic flux according to leakage bypass length.

In this study, a V-shaped rotor without the magnetic leakage flux path is proposed, as shown in Figure 7a. By eliminating the connection structure, the rotor core is separated into the two parts: the upper core and the lower core. Even though the lower core is only adhesive to the PMs, its structural stability is sufficient. Eliminating the connection structure is feasible only in the external rotor because the centrifugal force of the lower core is applied outward. This means that the lower core is forced toward the PMs that support the lower core. Thus, scattering of the lower core scarcely occurs.

The magnetic reluctance of the path between the upper and lower cores is large enough to reduce the magnetic leakage flux. Accordingly, the air gap magnetic flux produced by the PMs is increased, as shown in Figure 7b. In this comparison, the PM and core material, rotor size, and pole arc were the same. The stator core is assumed to be flat and has an infinite relative permeability property. In the existing V-shaped rotor that includes the connection structure in the rotor core, 17% of the magnetic leakage flux is generated. Whereas only 4% of the magnetic leakage flux is generated in the proposed V-shaped rotor without the magnetic leakage flux. A leakage flux of 39% occurs in the spoke type with the magnetic leakage flux path, and a leakage flux of 17% occurs in the V-shaped type with the magnetic

leakage flux path. Therefore, the air gap magnetic flux produced by the PMs is the largest when applying the proposed V-shaped rotor.

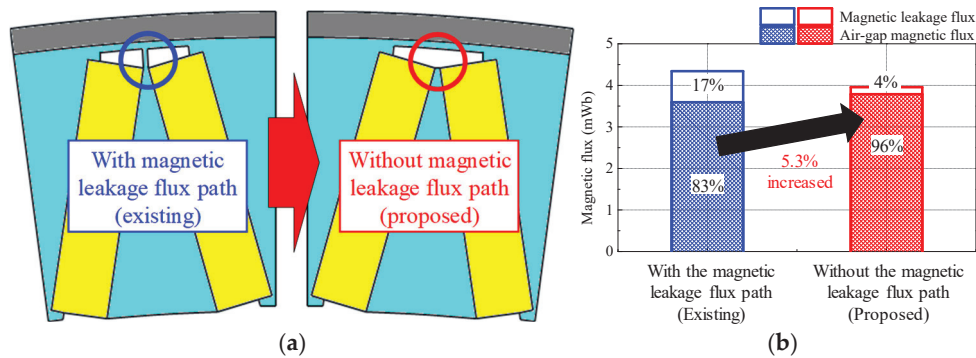


Figure 7. Comparison of magnetic flux characteristics according to rotor type: (a) Configuration; (b) Magnetic flux by PMs.

4. Design Optimization Using Gaussian Process Model

In this section, a surrogate model-based design optimization is conducted to improve the efficiency at the two main operating points: high-torque-and-low-speed point *A* and low-torque-and-high-speed point *B*. As the surrogate model of efficiency, GPMs are employed. The LHD is adopted as the sampling method for constructing the GPMs. During the LHD-based sampling process, the current density is fixed to the same value used in the conventional model. The *d*- and *q*-axis equivalent circuit method combined with FEA is used for calculating the efficiency at each of the LHD sampling points. Figure 8 presents the design optimization process. First, sensitivity analysis of the efficiency at points *A* and *B* is conducted considering the different motor characteristics according to the operating points. From the sensitivity analysis results, the significant design variables are selected. Using the selected significant design variables, the GPMs of each efficiency are built. As the sampling technique for GPM construction, the LHD method is adopted. Then, a gradient-based optimization is conducted. As a result, the optimum design model of the proposed V-shaped IPMSM without the magnetic leakage flux path is determined in this section.

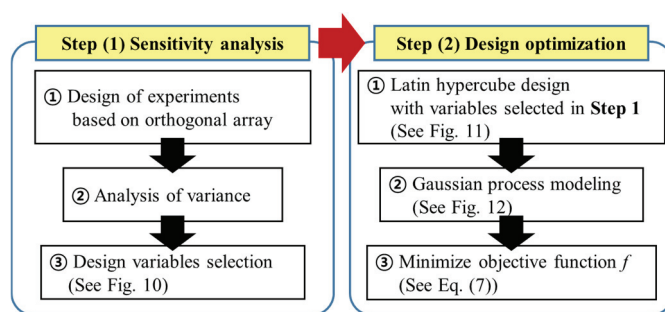


Figure 8. Optimal design process.

4.1. Sensitivity Analysis

The computational costs required for design optimization are related to the number of design variables. To reduce the computational cost, the design variables that have statistically significant effects on point *A* and *B* efficiencies are selected in this section. The constant geometry dimensions and candidates for design variables are presented in Figure 9. Based on analysis on variance (ANOVA), the sensitivity of each efficiency is investigated considering the seven candidates. Based on the orthogonal array method, 36 DOE points were constructed. After calculating the probability value (*p*-value) of the seven

candidate variables using ANOVA, those with p -values less than the significance level of 0.05 were considered to have statistically significant effects on efficiency [39,40]. For point A (low-speed operation), five variables were selected: pole angle, yoke thickness, slot opening, stator eccentricity, and rotor chamfer b . For point B (high-speed operation), six variables were significant: pole angle, yoke thickness, slot opening, stator eccentricity, and both rotor chamfers a and b . These parameters were chosen for the optimization process because they directly impact the magnetic circuit geometry and flux distribution. Their variation leads to notable changes in iron loss, flux-weakening performance, and output torque, which are key to achieving optimal efficiency across both operating conditions.

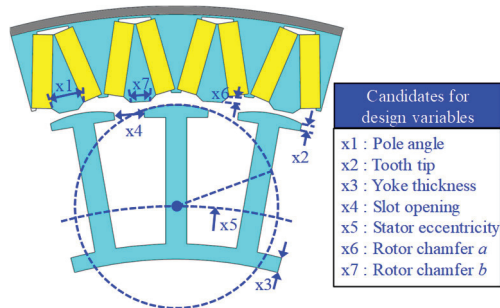


Figure 9. Geometry dimension for proposed V-shaped IPMSM without leakage bypass.

Figure 10 presents the ANOVA results for each efficiency, showing the design variables that are significant for low- and high-speed efficiency. It is evident that pole angle, yoke thickness, slot opening, stator eccentricity, and rotor chamfer b are significant for low-speed efficiency. Similarly, six design variables are significant for high-speed efficiency: pole angle, yoke thickness, slot opening, stator eccentricity, and rotor chamfers a and b . The tooth tip has a negligible effect on the efficiency at both speeds; therefore, its initial value is used in the design optimization.

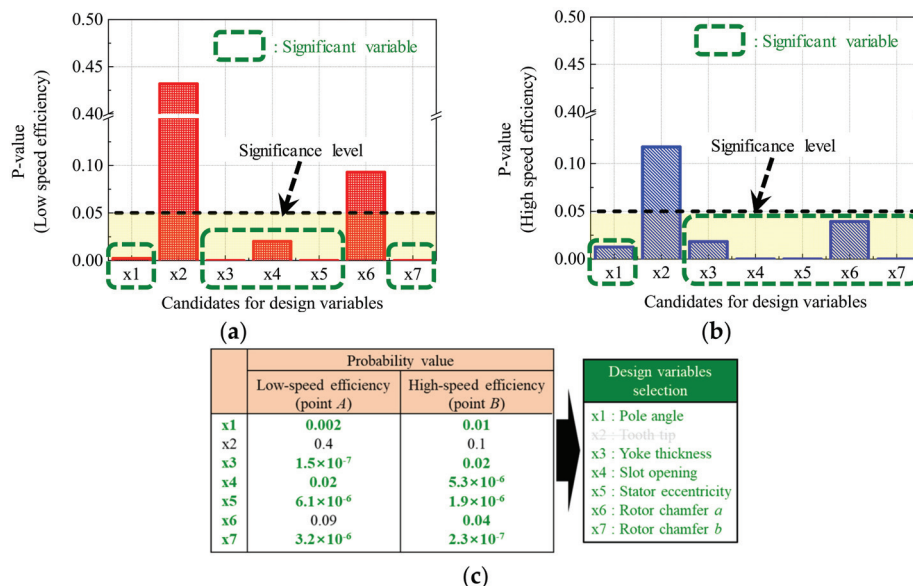


Figure 10. Sensitivity analysis results: (a) Low-speed efficiency (point A); (b) High-speed efficiency (point B); (c) Selection of design variables.

4.2. Gaussian Process Model

Using the selected design variables, the GPMs for each efficiency are constructed in this section. A GPM is a proper model to replace an FEA simulation in which the random

error is nonexistent and repeated experimentation is unnecessary [40]. The LHD is adopted as the sampling technique, which is well known as being suitable for GPMs [35]. As shown in Figure 11, the design points are well spread out across the entire design region. The respective efficiencies at the sampling points are calculated with FEA, and Figure 12 shows the constructed GPMs.

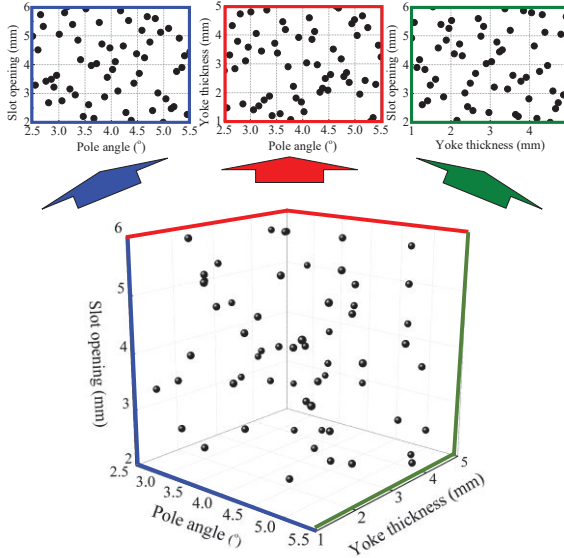


Figure 11. Latin hypercube design points according to pole angle, yoke thickness, and slot opening.

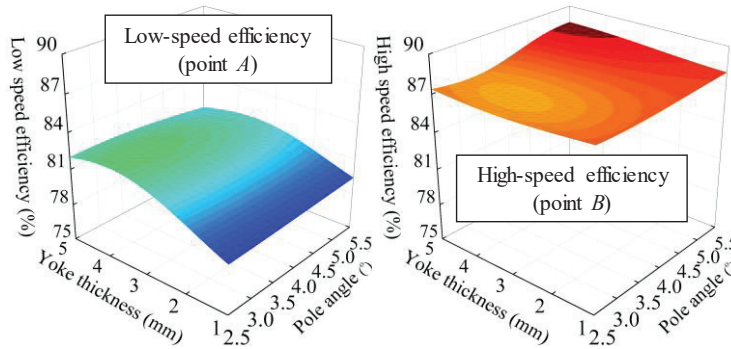


Figure 12. Gaussian process models according to pole angle and yoke thickness.

Then, the accuracies of the constructed GPMs are evaluated based on the leave-one-out cross-validation method [43]. The normalized root mean square error (NRMSE) of the GPM is defined in Equation (7):

$$\text{NRMSE} = \sqrt{\frac{1}{n_s} \cdot \sum_{i=1}^{n_s} \left(\frac{Y(x_i) - \hat{Y}^{(-i)}(x_i)}{\text{mean}\{Y(x)\}} \right)^2} \cdot 100\% \quad (7)$$

where \mathbf{x} denotes the vector of design variables. $\mathbf{Y}(\mathbf{x})$ denotes the vector of the efficiency at points A and B . n_s denotes the number of sampling points. x_i denotes the input value at the i th sample point, and $Y(x_i)$ is the response at the i th sample point calculated in FEA. $\hat{Y}^{(-i)}(x_i)$ is the predicted response at the i th sample point from the GPM constructed using the sampling points without $(x_i, Y(x_i))$. The NRMSEs of the GPM for the point A and B efficiencies are calculated as 5.2%, and 0.8%, respectively. Thus, the GPMs are verified to be adequately accurate.

4.3. Design Optimization

Considering the efficiency at the two main operating points, the objective function is defined by Equation (8):

$$\text{minimize } F(b) = -w_1 \cdot \frac{f_1(b)}{\max(f_1)} - w_2 \cdot \frac{f_2(b)}{\max(f_2)} \quad (8)$$

where F is the objective function, and \mathbf{b} is the vector of the design variables. f_1 and f_2 denote the functions of the point A and point B efficiencies, respectively. w_1 and w_2 are the weighting factors of f_1 and f_2 , respectively.

A flow chart of the optimization is shown in Figure 13. First, the design variables are initialized. With the constructed GPMs, the values of the efficiency at points A and B are predicted. Thus, the defined objective function is calculated. Then, a gradient of the objective function is calculated. Until the gradient value of the objective function is less than epsilon, the computation of the search direction, determination of the step size, and updating of the design variables are continued. If the gradient value converges, the optimization ends. As a result, the objective function is minimized and the optimum point is found, as shown in Figure 14. The optimized design variables are presented in Table 2.

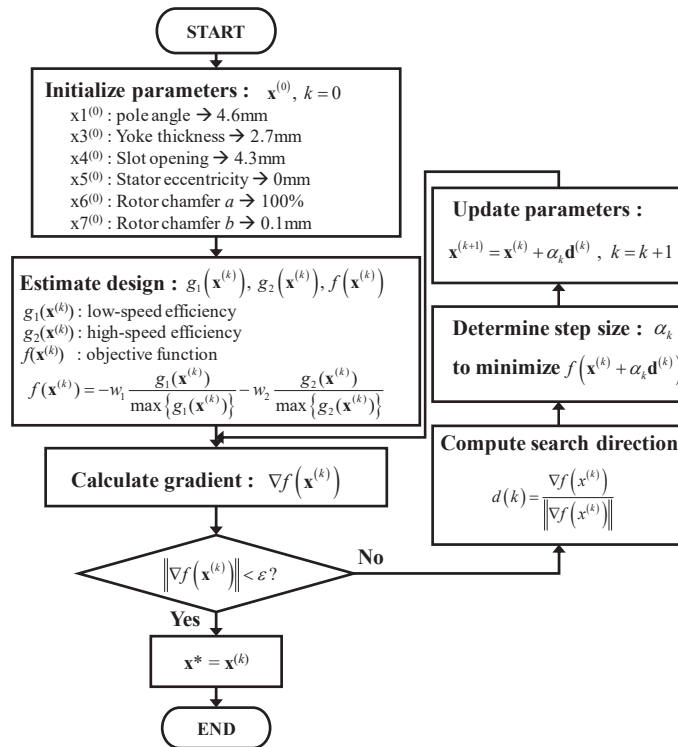


Figure 13. Optimization process.

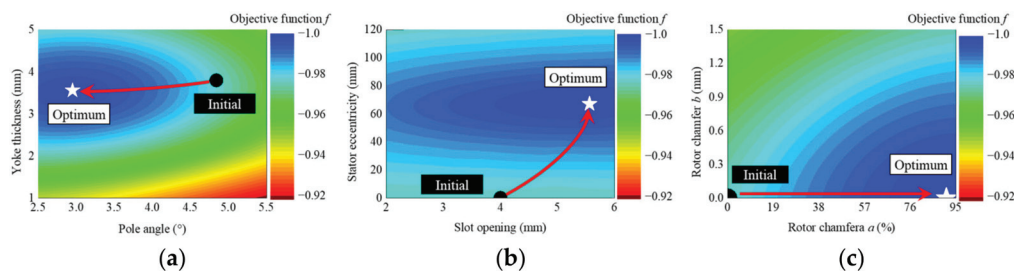


Figure 14. Design optimization: (a) Pole angle and Yoke thickness; (b) slot opening and stator eccentricity; (c) Rotor chamfers a and b .

Table 2. Design optimization results.

Design Variable	Initial Design	Optimum Design
x1 Pole angle ($^{\circ}$)	4.8	3.0
x3 Yoke thickness (mm)	3.8	3.6
x4 Slot opening (mm)	4	5.6
x5 Stator eccentricity (mm)	0	67.2
x6 Rotor chamfer a (%)	0	91
x7 Rotor chamfer b (mm)	0	0

4.4. Simulation Results

Using FEA, the optimized V-shaped IPMSM without the magnetic leakage flux path is analyzed and compared with the experimental results. A prototype of the improved model was fabricated, as shown in Figure 15a. As proposed, the magnetic leakage flux path is nonexistent in the rotor. In Figure 15b, it is evident that the no-load BEMF predicted using FEA has an error of 0.5% with the experimental result, whereas the resistance has an error of 2.1%. These errors were calculated based on the test results as reference. As shown in Figure 15c, the efficiency at each operating point can be predicted through the simulation: 84.5% at low-speed point *A* and 86.5% at low-speed point *B*. Each predicted efficiency has an error less than 1%p compared with the test results. Therefore, the simulation results of the improved model are validated.

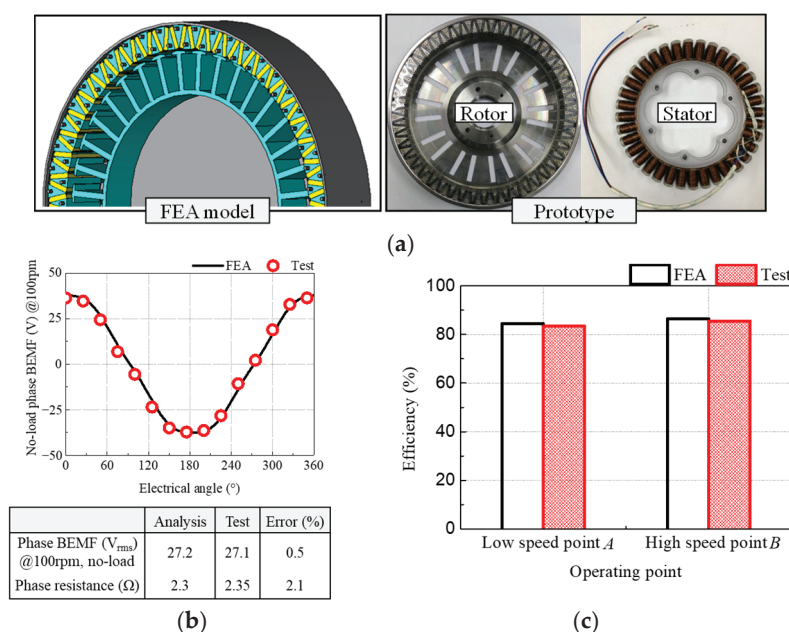


Figure 15. Improved model: (a) FEA model and prototype; (b) No-load back-electromotive force and resistance; (c) Efficiency.

5. Experimental Verification

In this section, the optimized V-shaped IPMSM without the magnetic leakage flux path is termed the improved model. Then, the efficiencies of the improved model and the conventional model are experimentally tested and compared. Both models are optimized, respectively. The prototypes of both models are presented in Figure 16a. The set-ups for the no load and load tests are presented in Figure 16b. For the no load test, a DC motor is used to rotate the test motor. The test motor is connected to a Y-connected resistor, which has a very large resistance. While the test motor is rotated, the voltage of the Y-connected resistor is measured using an oscilloscope. The measured voltage represents the BEMF. For

the load test, both the conventional and proposed models are evaluated under the same inverter-fed conditions to ensure a fair comparison. The torque, speed, and input power are measured, and the efficiency at each operating point are calculated according to the following equation:

$$\eta = \frac{T \cdot \omega}{P_{in}} \cdot 100\% \quad (9)$$

where η is the efficiency, T is the torque, ω is the rotating speed, and P_{in} is the input power. As shown in Figure 17a, the increased flux and reduced resistance of the improved model, compared with the conventional model, are validated by measuring the BEMF and phase resistance. The BEMF of the proposed model is enhanced by 27%, and the resistance is reduced by 47%. Figure 17b illustrates the degree of improvement in the efficiency of the proposed model. By conducting the design optimization for the efficiency at low- and high-speed operating points where the motor characteristics are different, the overall efficiency of the proposed model is increased throughout the torque and speed. Compared with the conventional model, the efficiency of the proposed model is improved by 14%p at low-speed point A, 1.4%p at high-speed point B, and 10.2%p on average.

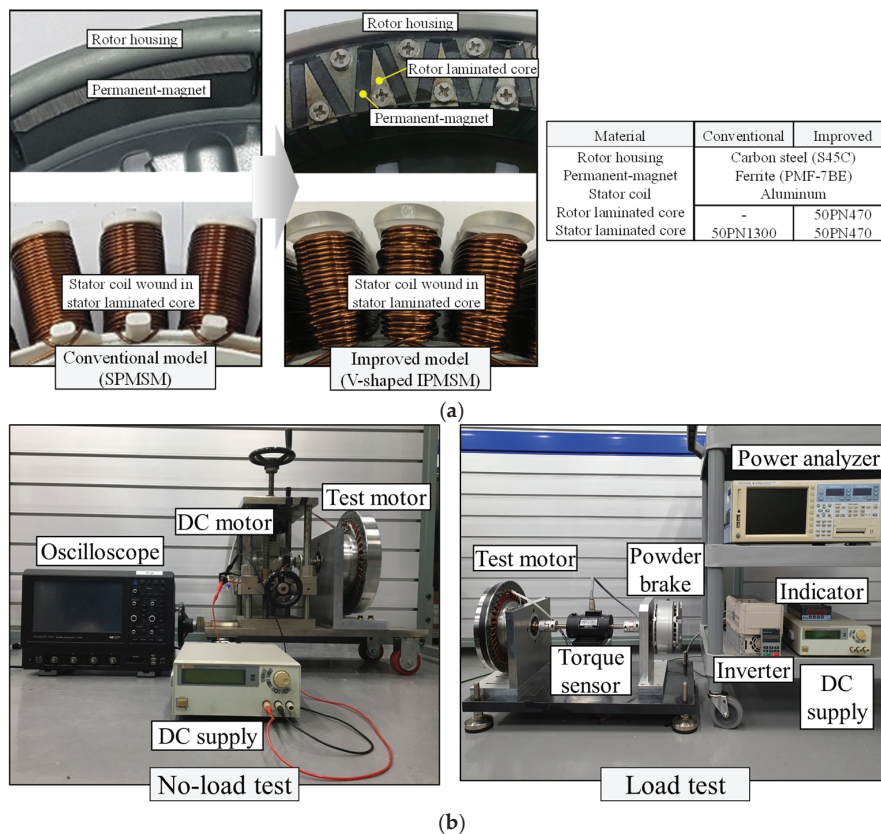


Figure 16. Prototype and test set-up: (a) Prototypes of conventional and improved models; (b) No load and load test set-ups.

The efficiency improvement mechanisms differ across the two operating points. At low speed, the increased back-EMF allows the motor to deliver the required torque with lower current. Combined with the reduced phase resistance, this leads to significantly lower ohmic loss and higher efficiency. At high speed, although the increased no-load flux raises the risk of higher iron loss and d-axis current, these effects are mitigated by using a low-loss core material and reducing the resistance. As a result, both iron and ohmic losses decrease, resulting in improved efficiency at high speed as well.

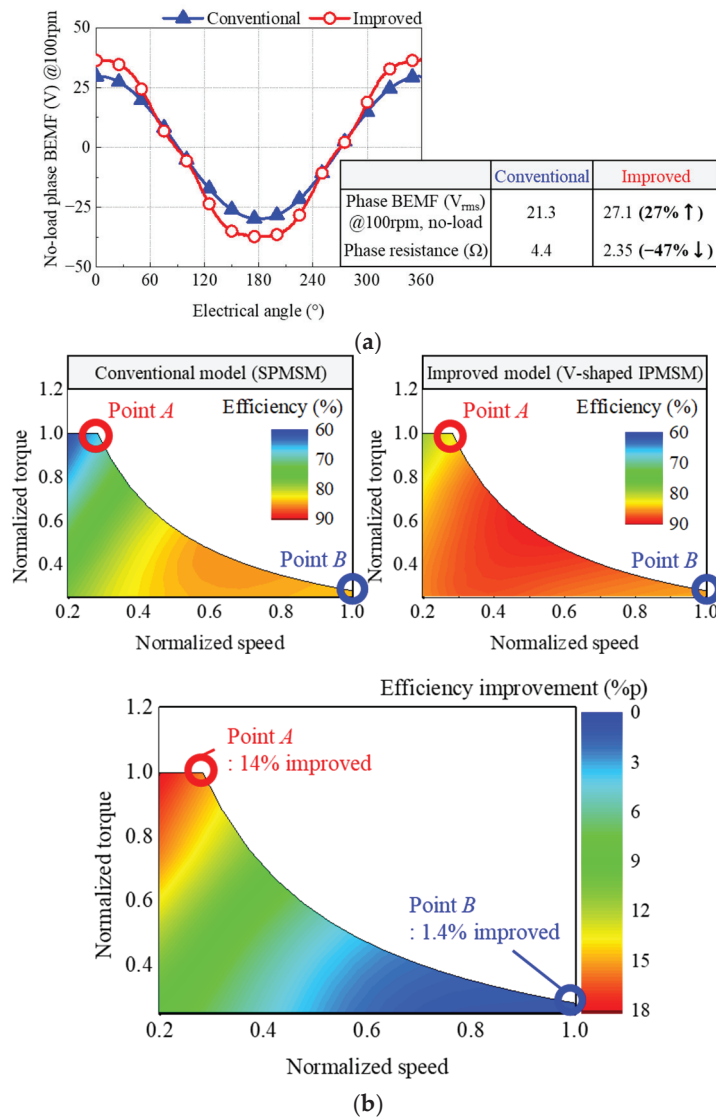


Figure 17. Experimental results of conventional and improved models. (a) No-load back-electromotive force and resistance; (b) Efficiency.

6. Conclusions

This paper presents a high-efficiency design for an external rotor machine for a home appliance having two main operating points. By analyzing the conventional model using the statistical method, the design directions were determined. According to the design directions, a V-shaped IPMSM without the magnetic leakage flux path was proposed. Then, design optimization was conducted to decide the optimum design model of the proposed V-shaped IPMSM without the magnetic leakage flux path. By fabricating and testing prototypes of both the conventional and the improved models, the validity of the improved model was confirmed. Compared with the conventional model, the average efficiency of the improved model was improved by 10.2%p. At high-torque-and-the-low-speed point A, the efficiency improved by 14%p, and at low-torque-and-the-high-speed point B, the efficiency improved by 1.4%p. Moreover, the torque density of the proposed V-shaped PMSM without leakage bypass was increased compared with the conventional PMSM by 26.6%, from 12.4 kNm/m^3 to 15.7 kNm/m^3 . As the other important requirement is low cost, a high-efficiency design that considers the cost is required in future work.

Author Contributions: Conceptualization, S.-G.L. and M.-R.P.; methodology, S.-G.L.; software, K.-S.C.; validation, J.-H.K.; resources, K.-S.C.; data curation, J.-H.K.; writing—original draft preparation, K.-S.C. and J.-H.K.; writing—review and editing, M.-R.P.; visualization, S.-G.L.; supervision, M.-R.P.; project administration, M.-R.P.; funding acquisition M.-R.P. All authors have read and agreed to the published version of the manuscript.

Funding: This work was supported by the Soonchunhyang University Research Fund.

Data Availability Statement: Data are contained within the article.

Conflicts of Interest: Author Soo-Gyung Lee was employed by the company Global R&D Center. The remaining authors declare that the research was conducted in the absence of any commercial or financial relationships that could be construed as a potential conflict of interest. The Global R&D Center had no role in the design of the study; in the collection, analyses, or interpretation of data; in the writing of the manuscript, or in the decision to publish the results.

References

- Shen, Y.; Zhu, Z.Q. Analytical prediction of optimal split ratio for fractional-slot external rotor PM brushless machines. *IEEE Trans. Magn.* **2011**, *47*, 4187–4190. [CrossRef]
- Kong, Y.; Lin, M.; Guo, R.; Li, N.; Xu, D. Design and optimization of an outer-rotor permanent magnet synchronous machine with an amorphous stator core. *IEEE Trans. Appl. Supercond.* **2018**, *28*, 1–5. [CrossRef]
- Lee, T.Y.; Ki, M.; Seo, M.; Kim, Y.J.; Jung, S.Y. Motor design and characteristics comparison of outer-rotor-type BLDC motor and BLAC motor based on numerical analysis. *IEEE Trans. Appl. Supercond.* **2016**, *26*, 1–6. [CrossRef]
- Aghazadeh, H.; Afjei, E.; Siadatan, A. Sizing and detailed design procedure of external rotor synchronous reluctance machine. *IET Electr. Power Appl.* **2019**, *13*, 1105–1113. [CrossRef]
- Sone, K.; Takemoto, M.; Ogasawara, S.; Takezaki, K.; Akiyama, H. A ferrite PM in-wheel motor without rare earth materials for electric city commuters. *IEEE Trans. Magn.* **2012**, *48*, 2961–2964. [CrossRef]
- Bonthu, S.S.R.; Arafat, A.; Choi, S. Comparisons of rare-earth and rare-earth-free external rotor permanent magnet assisted synchronous reluctance motors. *IEEE Trans. Ind. Electron.* **2017**, *64*, 9729–9738. [CrossRef]
- Xue, X.D.; Cheng, K.W.E.; Ng, T.W.; Cheung, N.C. Multi-objective optimization design of in-wheel switched reluctance motors in electric vehicles. *IEEE Trans. Ind. Electron.* **2010**, *57*, 2980–2987. [CrossRef]
- Beniakar, M.E.; Kakosimos, P.E.; Kladas, A.G. Strength pareto evolutionary optimization of an in-wheel PM motor with unequal teeth for electric traction. *IEEE Trans. Magn.* **2015**, *51*, 1–4. [CrossRef]
- Chung, S.U.; Moon, S.H.; Kim, D.J.; Kim, J.M. Development of a 20-pole–24-slot SPMSM with consequent pole rotor for in-wheel direct drive. *IEEE Trans. Ind. Electron.* **2016**, *63*, 302–309. [CrossRef]
- Öksüztepe, E. In-wheel switched reluctance motor design for electric vehicles by using a Pareto-based multiobjective differential evolution algorithm. *IEEE Trans. Veh. Technol.* **2017**, *66*, 4706–4715. [CrossRef]
- Wrobel, R.; Mellor, P.H. Design considerations of a direct drive brushless machine with concentrated windings. *IEEE Trans. Energy Convers.* **2008**, *23*, 1–8. [CrossRef]
- Chen, J.; Nayar, C.V.; Xu, L. Design and finite-element analysis of an outer-rotor permanent-magnet generator for directly coupled wind turbines. *IEEE Trans. Magn.* **2000**, *36*, 3802–3809. [CrossRef]
- Chen, H.; Gu, J.J. Switched reluctance motor drive with external rotor for fan in air conditioner. *IEEE/ASME Trans. Mechatron.* **2012**, *18*, 1448–1458. [CrossRef]
- Lim, M.S.; Kim, J.H.; Hong, J.P. Experimental characterization of the slinky-laminated core and iron loss analysis of electrical machine. *IEEE Trans. Magn.* **2015**, *51*, 1–4. [CrossRef]
- Ahn, H.J.; Lee, D.M. A new bumpless rotor-flux position estimation scheme for vector-controlled washing machine. *IEEE Trans. Ind. Electron.* **2016**, *12*, 466–473. [CrossRef]
- Raj, M.A.; Kavitha, A. Effect of rotor geometry on peak and average torque of external-rotor synchronous reluctance motor in comparison with switched reluctance motor for low-speed direct-drive domestic application. *IEEE Trans. Magn.* **2017**, *53*, 1–8. [CrossRef]
- Li, D.; Qu, R.; Li, J.; Xu, W. Consequent-pole toroidal-winding outer-rotor Vernier permanent-magnet machines. *IEEE Trans. Ind. Appl.* **2015**, *51*, 4470–4481. [CrossRef]
- Li, L.; Zhang, J.; Zhang, C.; Yu, J. Research on electromagnetic and thermal issue of high-efficiency and high-power-density outer-rotor motor. *IEEE Trans. Appl. Supercond.* **2016**, *26*, 1–5. [CrossRef]
- Ma, C.; Chen, C.; Li, Q.; Gao, H.; Kang, Q.; Fang, J.; Cui, H.; Teng, K.; Lv, X. Analytical calculation of no-load magnetic field of external rotor permanent magnet brushless direct current motor used as in-wheel motor of electric vehicle. *IEEE Trans. Magn.* **2018**, *54*, 1–6. [CrossRef]

20. Moayed-Jahromi, H.; Rahideh, A.; Mardaneh, M. 2-D analytical model for external rotor brushless PM machines. *IEEE Trans. Energy Convers.* **2016**, *31*, 1100–1109. [CrossRef]
21. Boughrara, K.; Ibtouen, R.; Zarko, D.; Touhami, O.; Rezzoug, A. Magnetic field analysis of external rotor permanent-magnet synchronous motors using conformal mapping. *IEEE Trans. Magn.* **2010**, *46*, 3684–3693. [CrossRef]
22. Zuo, S.; Lin, F.; Wu, X. Noise analysis, calculation, and reduction of external rotor permanent-magnet synchronous motor. *IEEE Trans. Ind. Electron.* **2015**, *62*, 6204–6212. [CrossRef]
23. Lin, F.; Zuo, S.; Deng, W.; Wu, S. Modeling and analysis of acoustic noise in external rotor in-wheel motor considering Doppler effect. *IEEE Trans. Ind. Electron.* **2018**, *65*, 4524–4533. [CrossRef]
24. Chu, W.; Zhu, Z.; Shen, Y. Analytical optimisation of external rotor permanent magnet machines. *IET Electr. Syst. Transp.* **2013**, *3*, 41–49. [CrossRef]
25. Kim, K.C.; Lim, S.B.; Koo, D.H.; Lee, J. The shape design of permanent magnet for permanent magnet synchronous motor considering partial demagnetization. *IEEE Trans. Magn.* **2006**, *42*, 3485–3487. [CrossRef]
26. Yoo, J.H.; Park, C.S.; Jung, T.U. Permanent magnet structure optimization for cogging torque reduction of outer rotor type radial flux permanent magnet generator. In Proceedings of the 2017 IEEE International Electric Machines and Drives Conference, Miami, FL, USA, 21–24 May 2017.
27. Wu, S.; Song, L.; Cui, S. Study on improving the performance of permanent magnet wheel motor for the electric vehicle application. *IEEE Trans. Magn.* **2007**, *43*, 438–442. [CrossRef]
28. Ma, C.; Cui, H.; Zheng, P.; Zhang, Y.; Gao, H. Influence of static eccentricity on unbalanced magnetic force of external rotor permanent magnet brushless direct current motor used as in-wheel motor. *IET Electr. Power Syst.* **2019**, *13*, 538–550. [CrossRef]
29. Ifedi, C.J.; Mecrow, B.C.; Brockway, S.T.M.; Boast, G.S.; Atkinson, G.J.; Kostic-Perovic, D. Fault-tolerant in-wheel motor topologies for high-performance electric vehicles. *IEEE Trans. Ind. Appl.* **2013**, *49*, 1249–1257. [CrossRef]
30. Ishii, S.; Hasegawa, Y.; Nakamura, K.; Ichinokura, O. Characteristics of novel flux barrier type outer rotor IPM motor with rare-earth and ferrite magnets. In Proceedings of the 2012 International Conference on Renewable Energy Research and Applications, Nagasaki, Japan, 11–14 November 2012.
31. Yu, D.; Huang, X.; Zhang, X.; Zhang, J.; Lu, Q.; Fang, Y. Optimal design of outer rotor interior permanent magnet synchronous machine with hybrid permanent magnet. *IEEE Trans. Appl. Supercond.* **2019**, *29*, 1–5. [CrossRef]
32. Yang, Y.; Rahman, M.M.; Lambert, T.; Bilgin, B.; Emadi, A. Development of an external rotor V-shape permanent magnet machine for E-bike application. *IEEE Trans. Energy Convers.* **2018**, *33*, 1650–1658. [CrossRef]
33. Chen, Q.; Liu, G.; Zhao, W.; Sun, L.; Shao, M.; Liu, Z. Design and comparison of two fault-tolerant interior-permanent-magnet motors. *IEEE Trans. Ind. Electron.* **2014**, *61*, 6615–6623. [CrossRef]
34. Lee, S.G.; Park, M.R.; Cha, K.S.; Kim, J.H.; Hong, J.P. Design of the high efficiency IPMSM considering the operating point with different characteristic. In Proceedings of the 2019 IEEE International Electric Machines and Drives Conference, San Diego, CA, USA, 12–15 May 2019.
35. Bangura, J.F. Design of high-power density and relatively high-efficiency flux-switching motor. *IEEE Trans. Energy Convers.* **2006**, *21*, 416–425. [CrossRef]
36. Jones, B.; Johnson, R.T. Design and analysis for the Gaussian process model. *Qual. Reliab. Eng. Int.* **2009**, *25*, 515–524. [CrossRef]
37. Zhang, X. Comparison of response surface method and Kriging method for approximation modeling. In Proceedings of the 2017 IEEE 2nd International Conference on Power and Renewable Energy, Chengdu, China, 20–23 September 2017.
38. Park, M.R.; Kim, H.J.; Choi, Y.Y.; Hong, J.P.; Lee, J.J. Characteristics of IPMSM according to rotor design considering nonlinearity of permanent magnet. *IEEE Trans. Magn.* **2016**, *52*, 1–4. [CrossRef]
39. Roy, R.K. *Design of Experiments Using the Taguchi Approach: 16 Steps to Product and Process Improvement*; John Wiley & Sons: New York, NY, USA, 2001.
40. Montgomery, D.C. *Design and Analysis of Experiments*, 9th ed.; John Wiley & Sons: New York, NY, USA, 2017.
41. Johnson, M.; Gardner, M.C.; Toliyat, H.A. Design comparison of NdFeB and ferrite radial flux surface permanent magnet coaxial magnetic gears. *IEEE Trans. Ind. Appl.* **2018**, *54*, 1254–1263. [CrossRef]
42. Kim, H.J.; Kim, D.Y.; Hong, J.P. Structure of concentrated-flux-type interior permanent-magnet synchronous motors using ferrite permanent magnets. *IEEE Trans. Magn.* **2014**, *50*, 1–4. [CrossRef]
43. Queipo, N.V.; Haftka, R.T.; Shyy, W.; Goel, T.; Vaidyanathan, R.; Tucker, P.K. Surrogate-based analysis and optimization. *Prog. Aerosp. Sci.* **2005**, *41*, 1–43. [CrossRef]

Disclaimer/Publisher’s Note: The statements, opinions and data contained in all publications are solely those of the individual author(s) and contributor(s) and not of MDPI and/or the editor(s). MDPI and/or the editor(s) disclaim responsibility for any injury to people or property resulting from any ideas, methods, instructions or products referred to in the content.

MDPI AG
Grosspeteranlage 5
4052 Basel
Switzerland
Tel.: +41 61 683 77 34

Mathematics Editorial Office
E-mail: mathematics@mdpi.com
www.mdpi.com/journal/mathematics



Disclaimer/Publisher's Note: The title and front matter of this reprint are at the discretion of the Guest Editors. The publisher is not responsible for their content or any associated concerns. The statements, opinions and data contained in all individual articles are solely those of the individual Editors and contributors and not of MDPI. MDPI disclaims responsibility for any injury to people or property resulting from any ideas, methods, instructions or products referred to in the content.



Academic Open
Access Publishing

mdpi.com

ISBN 978-3-7258-4684-9